1975ApJ...196..351C

THE ASTROPHYSICAL JOURNAL, **196**:351–361, 1975 March 1

A CROSS-DISPERSED ECHELETTE SPECTROGRAPH AND A STUDY OF THE SPECTRUM OF THE QSO 1331+170

R. F. CARSWELL,* R. L. HILLIARD, P. A. STRITTMATTER,† D. J. TAYLOR, AND R. J. WEYMANN
Steward Observatory, University of Arizona

Received 1974 July 30; revised 1974 September 5

ABSTRACT

A simple modification of the Cassegrain spectrograph of the Steward Observatory 90-inch (2.3 m) telescope is described. The system utilizes a grating operating in the 5–13th orders and a quartz prism to cross-disperse these orders in an echelle format. Complete spectral coverage from 3100 Å to about 9000 Å on a 40-mm image tube is possible with a dispersion of 44 Å mm^{-1} at 4200 Å.

With this equipment, an image-tube spectrogram of the absorption-rich quasi-stellar object 1331+170 has been obtained. A large number of previously undetected absorption lines are shown to be present in this object. The two absorption systems, noted by Strittmatter *et al.*, at $z_A = 1.7754$ and $z_B = 1.7851$ are confirmed; but despite the improved coverage only one further probable system, with $z_C = 1.3273$, could be found. Evidence for line locking between the absorption lines of the two well-established redshift systems, and between the absorption and emission line systems, is discussed. The strong Lα absorption feature common to systems A and B is similar to that of Lα in system A ($z = 2.309$) in PHL 957. System B seems to arise in a pure H I cloud and in this respect is also similar to system A in PHL 957.

Subject headings: instruments — quasi-stellar sources or objects — redshifts

I. INTRODUCTION

The ~16.6-mag quasar 1331+170 was first observed spectroscopically as part of a study of quasar candidates by Baldwin *et al.* (1973), who determined an emission-line redshift of 2.081 for this object. The absorption-line spectrum was the subject of a more detailed study by Strittmatter *et al.* (1973), who identified two very probable absorption line systems with redshifts of 1.7755 and 1.7851, and one possible system at 1.9653 based on three lines. It appeared from the data available that an extremely broad Lα absorption might be common to both of the definite absorption systems, though this is in a region of the spectrum not well covered by their observations. It also appeared that the two redshift systems constituted an example of line locking, in this case probably on the Mg II λ2798 doublet.

We present here the results of further study of 1331+170 using spectroscopic material obtained with a cross-dispersed echelette spectrograph at the Cassegrain focus of the Steward Observatory 90-inch (2.3 m) telescope. The resolution and spectral coverage are considerably greater than was formerly possible at Steward Observatory, and a large number of previously undetected absorption lines are shown to be present.

II. THE CROSS-DISPERSED ECHELETTE SPECTROGRAPH

The utility of echelle spectrographs for high-dispersion spectroscopy has recently received increasing recognition. They have the following advantages: First, the very high dispersive power of the echelle grating allows high dispersion with only moderate focal length cameras so that high throughput can be achieved. Second, the echelle format allows relatively large regions of the spectrum to be imaged on photocathodes. Third, the compact size of echelle spectrographs allows them to be used at the Cassegrain focus; and fourth, problems with overlapping orders are eliminated, at least when prismatic cross-dispersing elements are employed. The last three of these advantages apply equally to applications in moderate-dispersion spectroscopy where broad spectral coverage is required. A typical such application, as described below, is the search for, or analysis of, QSO absorption spectra. In the present configuration, full spectral coverage from the atmospheric limit to about 9000 Å is possible. At comparable dispersion in the blue with the unmodified spectrograph only about 1000 Å can be covered in a single exposure. Of course, the value of such spectral coverage can only be fully realized with a linear detector which has a good red response. The spectral coverage of the system as described here is restricted by the limited dynamic range of the photographic plate. If, for example, a good signal-to-noise ratio is required where the spectrum is fairly weak, then information is lost in regions where the system response is higher due to overexposure of the photographic plate. In the application described below, coverage of the red region of the spectrum was sacrificed in order to retain information in the blue and ultraviolet.

To enable such a system to be put into operation as quickly and economically as possible, it was decided to adopt a modular design which required minimum modification of the existing image-tube spectrograph, and which allowed switches between the conventional

---

* Visiting Astronomer, Kitt Peak National Observatory which is operated by the Association of Universities for Research in Astronomy, Inc., under contract to the National Science Foundation

† Alfred P. Sloan Research Fellow.

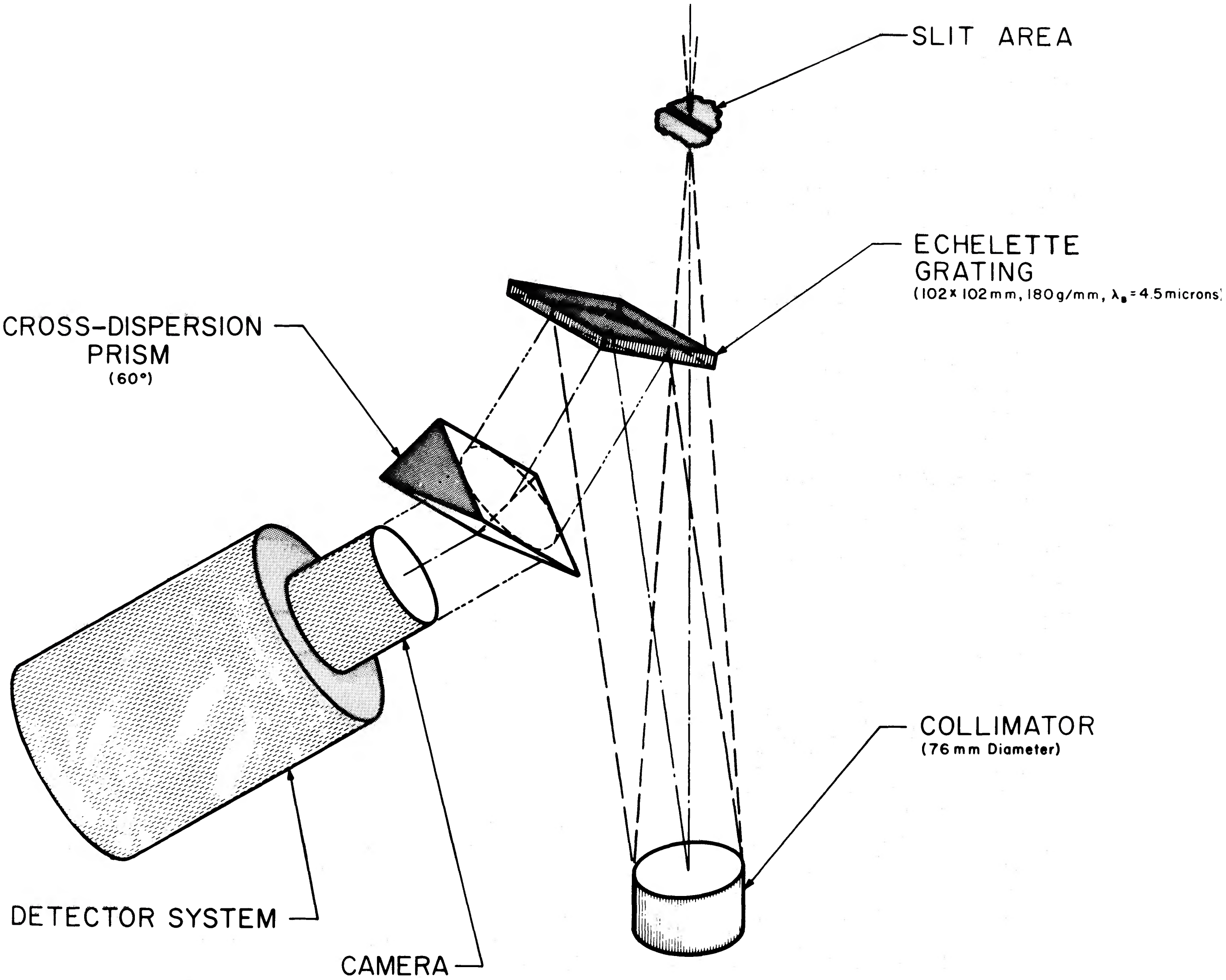

FIG. 1.—Schematic diagram for the cross-dispersed echelette

mode and cross-dispersed mode to be made simply. The design goal was to achieve full spectral coverage from 3100 Å to about 9000 Å with sufficient cross-dispersive power to allow order separation of about 0.4 mm between the last two usable orders in the red and the largest possible linear dispersion consistent with the photocathode size. A 60° quartz prism and a 180 grooves mm^{-1} Bausch and Lomb grating blazed at 4.5 μ (Littrow) in the first order satisfy these criteria reasonably well.

These considerations led to the design shown schematically in figure 1. A separate module holding the 60° quartz prism can be bolted onto the normal camera port and the image-tube camera then mounted to this module.

The properties of the cross-dispersed format are listed in table 1. The present image tube (an RCA 33063) has poor response longward of $\sim$7000 Å so that the fifth and sixth orders are not utilized. The introduction of the prism between the camera and grating increases somewhat the off-axis vignetting in the system. Despite this, the speed is still only slightly less than the spectrograph used with a conventional grating giving the same dispersion. The light losses due to the prism are offset by the fact that no filter is needed for order separation. There is no detectable degradation of the image quality, nor, as far as we can tell, has there been any change in the mechanical stability of the system. (The limiting factor on stability in normal operation is in fact the image tube; but judging from the nightsky lines, even this does not seriously affect the results on 2–3 hour exposures.)

TABLE 1

PROPERTIES OF THE CROSS-DISPERSED SPECTROGRAPH

Order	Order Separation (mm)	Dispersion (Å mm⁻¹)	Central Wavelength (Å)	Range Observed (Å)
13		33.7	3230	3100–3350
	0.91			
12		36.5	3525	3350–3700
	0.82			
11		40.0	3875	3700–4050
	0.74			
10		43.7	4250	4050–4450
	0.66			
9		48.8	4700	4450–4950
	0.59			
8		54.9	5275	4950–5600
	0.53			
7		62.7	6000	5600–6400
	0.48			
6		73.2	7050	...
	0.43			
5		87.4	8450	...

III. OBSERVATIONS

A spectrogram of 1331+170 (SI 868) widened 0.35 mm was obtained with this system during a 75-minute exposure in 1973 March and is reproduced in figure 2 (plate 5). Good quality coverage extends from the atmospheric cutoff at 3100 Å to about 5200 Å, with a plate resolution of about 45 μ; the continuum shows weakly to about 7000 Å. An iron-argon comparison source was used to give the comparison "dots" on either side of the object spectrum, and these may be seen even in the fifth order at about 8000 Å. The O I λ5577 nightsky line appears strongly in both the seventh and eighth orders, and the Na D nightsky lines are clearly resolved in the seventh order.

Comparison of this spectrum with that previously published by Strittmatter *et al.* (1973) shows the necessity for higher resolution (dispersion) studies of absorption line spectra in objects such as 1331+170. The broad emission lines show up less clearly, as might be expected at higher dispersion. The strong Lα emission line at 3750 Å is, however, clearly visible in both the 11th and 12th orders; the N V λ1240 emission line is also evident in the former. The Si VI λ1397 emission line at 4300 Å is rather weak but still discernible on either side of the strong C IV $\lambda\lambda$1548, 1550 absorption doublet in the 10th order spectrum. The ninth order contains the C IV λ1549 emission line although this is rather weaker than Lα. The wide Lα absorption mentioned by Strittmatter *et al.* shows in both 12th and 13th orders, and a large number of ultraviolet absorption lines that were not seen on earlier spectra are also evident here. The measured wavelengths of all absorption features are listed in table 2 along with the wavelengths published previously. Where wavelengths have been measured in more than one order, the value measured for the higher order is listed first, followed by that for the lower. Possible weaker lines are listed in parentheses. The quoted wavelengths for lines in the 13th order spectrum are likely to be less accurate, since these were determined using the 12th order comparison spectrum and a scaling factor of 12/13. This was necessary because of the absence of strong lines in the far-ultraviolet in the comparison spectrum. An estimate of accuracy was obtained by applying the same method to the 12th order spectrum using the 11th order comparison, measured at the same time, and comparing this with the direct measurement. The error that arises from this procedure should in all cases be less than 0.5 Å in any wavelength. No attempt was made to measure any absorption lines in the seventh order, since the spectrum is too underexposed there to be certain of their presence; only fairly prominent lines in the eighth order were measured for this same reason. Three of the absorption lines that were listed by Strittmatter *et al.* are not clearly present on well exposed parts of this spectrogram, and so they have been omitted from the table. We should emphasize, however, that because we have only one spectrogram at this dispersion we have included only very obvious absorption features in table 2. Many weaker features may in fact be real but have not been noted in the table.

The echelette spectrum was traced using the PDS microdensitometer at Kitt Peak National Observatory. An 8 μ × 8 μ entrance aperture was used, and the region of interest was scanned in a rectangular raster each line of which was approximately perpendicular to the grating dispersion. The results were recorded on magnetic tape. Selection of spectral order, elimination of ion events, wavelength calibration, and conversion to relative intensity using a standard step-wedge calibration was then carried out on the University of Arizona CDC 6400 computer. An attempt was made to remove the instrumental response by correcting the continuum level to the same value everywhere. Figure 3 shows the relative intensity tracing that resulted from this procedure. From this it was possible to determine approximate equivalent widths for the stronger narrow absorption lines, and the results are also listed in table 2. Many of the absorption lines are blended, however, and in these cases only a rough measure of the equivalent width is possible. The calibration was inevitably unreliable at high densities on the photographic plate, so the intensities, for example, in strong emission lines, particularly Lα, are very uncertain. This accounts for the discrepancy between the profile of the Lα emission line as it appears in the 12th order, where it is on the end of the spectral range, and in the 11th, where it is near the middle. A combination of the uncertainties of the instrumental response at the end of one order, and the calibration at high densities, produces a difference of about a factor of 2 in the equivalent width of this one line. The equivalent widths of absorption lines which appear in the Lα emission feature should also be treated with some caution, since they too depend strongly on the calibration curve. In regions of good exposure, however, our absorption-line equivalent widths are in excellent agreement with those given by Strittmatter *et al.* (1973) on the basis of the Lick image dissector

1975ApJ...196..351C

TABLE 2

ABSORPTION LINES IN 1331+170

					Strittmatter *et al.*				
Orders	Wavelength	W_λ(Å)	Wavelength	W_λ(Å)	Wavelength	W_λ(Å)	Adopted Wavelength	Adopted W_λ(Å)	Comments
13	3152.2	. . .					3152.2	. . .	Near atmospheric cutoff
	3172.5	1.7					3172.5	1.7	
	(3179.4)	. . .					(3179.4)	. . .	
	3189.3	0.7					3189.3	0.7	
	3195.9	1.6:					3195.9	1.6:	
	3199.5	0.5:					3199.5	0.5:	
	3202.9	0.8:					3202.9	0.8:	
	(3206.5)	. . .					(3206.5)	. . .	
	3221.8	1.2:					3221.8	1.2:	
	3227.7	0.8					3227.7	0.8	
	3244.1	1.5					3244.1	1.5	
	3263.2	0.7:					3263.2	0.7:	
	3266.2	. . .					3266.2	. . .	
	3274.6	0.4:					3274.6	0.4:	May be affected by ion events
	3286.1	1.2					3286.1	1.2	
	3294.7	0.3					3294.7	0.3	
	3303.5	1.2:					3303.5	1.2:	Possible structure in blue wing
	3307.7	1.0:					3307.7	1.0:	
	3311.4	0.9:					3311.4	0.9:	
	3315.1	0.7:					3315.1	0.7:	
	3322.5	1.7:					3322.5	1.7:	
	3328.4	2.4:					3328.4	2.4:	
	3331.6						3331.6		
	3337.4	1.0					3337.4	1.0	
	(3340.1)	. . .					(3340.1)	. . .	
	3347.7	. . .					3347.7	. . .	On wing of strong Lα absorption
13/12	3366:	~50	3373:	~50	3370:	. . .	3370:	~50	
12	3422.7	0.5:					3422.7	0.5:	
	3432.7	0.6					3432.7	0.6	
	3461.0	0.7					3461.0	0.7	
	3478.9	1.6					3478.9	1.6	
12	3490.9	0.9					3490.9	0.9	
	3494.6	0.2:					3494.6	0.2:	Wing of 3497
	3497.2	1.8:			3496.6	. . .	3497.2	1.8:	
	3510.2	0.7					3510.2	0.7	
	(3524.3)	. . .					(3524.3)	. . .	
	(3535.9)	. . .					(3535.9)	. . .	
	(3545.0)	. . .					(3545.0)	. . .	
	3548.9	0.8					3548.9	0.8	
	3562.1	0.7					3562.1	0.7	
12/11	3603.1	5.5:	3602.6	5.3:	3602.2	. . .	3602.9	5.4:	
	3610.8	2.9:	3610.6	2.7:			3610.7	2.8:	
	3614.7	1.3:	3614.6	1.2:			3614.7	1.2:	
	3620.8	1.2	3620.5	1.0			3620.7	1.1	
	3627.3	1.3	3627.2	1.0			3627.3	1.1	
	3633.3	0.4:	3633.5	0.4			3633.4	0.4:	
	(3638.5)	0.3:	3638.9	0.4:			3638.9	0.3:	
	3675.3	1.6:	3675.6	1.4	3673.3	. . .	3675.5	1.4	
	3680.9	0.6:	(3680.7)	0.5:	3682.7	. . .	3680.9	0.5:	
	3695.8	1.3:	3686.1	0.7			3686.0	0.9:	
	3704.1	2.5	3704.1	2.4	3703.7	. . .	3704.1	2.4	
	3717.2	1.4	3717.3	1.4	3717.6	. . .	3717.3	1.4	
	3729.5	0.9	3729.5	0.7	3730.1	. . .	3729.5	0.8	
	3736.9	0.3	3736.9	0.4			3736.9	0.3	
	3764.7	1.5	3765.4	1.1	3765.2	. . .	3765.1	1.3	
11	3784.5	0.2			3784.8		3784.5	0.2	
	3792.6	0.2:			3790.9		3792.6	0.2:	
	3868.1	1.6			3868.5	. . .	3868.1	1.6	
	(3883.0)	. . .					(3883.0)	. . .	
	3888.9	0.4:					3888.9	0.4:	
	3893.2	0.8:			3892.0		3893.2	0.8:	
10	(4141.3)	. . .					(4141.3)	. . .	
	(4155.9)	. . .					(4155.9)	. . .	
	(4161.7)	. . .					(4161.7)	. . .	
	4237.5	1.5			4238.0	1.5	4237.5	1.5	

TABLE 2—*Continued*

Orders	Wavelength	W_λ(Å)	Wavelength	W_λ(Å)	Strittmatter *et al.* Wavelength	Strittmatter *et al.* W_λ(Å)	Adopted Wavelength	Adopted W_λ(Å)	Comments
10.........	4252.4	0.5			4251.0	...	4252.4	0.5	
10/9.......	4296.4	3.6:	4296.4	3.3:	4297.1	7.7	4296.4	3.5:	
	4303.5	2.9:	4303.5	2.8:	4303.7		4303.5	2.9:	
	(4349.1)	...	(4347.2)	...			(4348.2)	...	
	4464.5	0.5:	4464.4	0.8	4464.5	...	4464.5	0.8	
9..........	4536.6	1.0:			4537.1	1.3	4536.6	1.3	
	4637.6	1.5			4637.6	1.8	4637.6	1.6	
	4653.6	1.2			4654.1	1.6	4653.6	1.3	
9/8........	4877.3	3.3	4876.9	3.6:	4877.9	3.0	4877.1	3.3	
	4889.7	2.5	4889.1	2.8:	4891.8	1.9	4889.4	2.5	
					5339	0.6	5339	0.6	
					5353	1.5	5353	1.5	
					5545	1.5	5545	1.5	
					6507.6	5.1	6507.6	5.1	
					6526.4	2.4	6526.4	2.4	
					(6575.5)	...	(6575.5)	...	
					6591.7	1.7	6591.7	1.7	
					6614.1	2.4	6614.1	2.4	
					6637.3	1.8	6637.3	1.8	
					(6867.6)	...	(6867.6)	...	
					7179.6	1.8	7179.6	1.8	
					7217.3	1.5	7217.3	1.5	
					7245.5	1.3	7245.5	1.3	
					7761.7	3.6	7761.7	3.6	
					7795.0	6.0	7785.0	6.0	
					7805.8	2.9	7805.8	2.9	

scanner data. The photometric accuracy of the image tube data thus appears satisfactory except in regions of very high plate density.

IV. ABSORPTION-LINE REDSHIFTS

From an analysis of the line list in table 2 we have been able to establish three absorption redshift systems that are probably present in 1331+170; these are listed in table 3. The *f*-values for the lines identified have been taken from Wiese, Smith, and Glennon (1966), Wiese, Smith, and Miles (1969), and for Fe II lines, De Boer *et al.* (1974) and Morton and Smith (1974). Some differences exist between the first two and last references, especially in the *f*-values quoted for the Si II lines. However, the values given by Wiese *et al.* (1969) for this ion were chosen since they are more consistent with the ultraviolet observations of ζ Oph (Smith 1972) than the *f*-values given by Morton and Smith.

Two absorption systems have already been described by Strittmatter *et al.* (1973). Their system A, with mean redshift $\langle z_A \rangle = 1.7754$ and system B, with $\langle z_B \rangle = 1.7851$, are confirmed here. Features listed by them as being possibly present show clearly on this newer spectrogram, and the additional coverage in the ultraviolet has enabled us to identify absorption lines of Si II λλ1190.4, 1193.3 in both systems, and Si III λ1206.4 in system A. The very broad absorption feature centered at about 3370 Å appears to be about 50 Å wide and includes contributions from Lα in both systems A and B. Some possible structure may be present within the feature, but this is probably due to the presence of nightsky features in this region of the spectrum.

The fact that the line at 3303.5 Å has a greater equivalent width than 3311.4 Å causes some difficulty in attempting to identify these with Si II λλ1190.4, 1193.3 in system A. It is, however, possible that the 3303.5 Å line is blended with one from some other system. In system B there is no such inconsistency in the ratio of line strengths, but the Si II λλ1190.4, 1193.3 lines are perhaps rather stronger than expected when compared with the Si II λ1260.4 line. There is, however, considerable structure in the spectrum of 1331+170 near the region of interest, and this may cause inaccuracies in both the strengths and wavelengths of lines.

Also noteworthy is the lack of Fe II line identifications in the ultraviolet despite the large number of candidate lines in the 1050–1150 Å region of the spectrum (Morton and Smith 1974; Grewing and Strittmatter 1973) and the many Fe II identifications at longer wavelengths. Since the *f*-values for most of these lines are believed to be less than 0.1 (De Boer *et al.* 1974), our failure to detect them is not too surprising. The strongest Fe II line in this region, with rest wavelength 1144.9 Å, is present in both systems A and B, though in the case of system A the wavelength agreement is not very good.

A search was made for fine-structure lines of O I, Si II, and C II in both redshift systems, but no clear evidence for any such lines was found. In both systems the O I λ1304.9 line would be blended with Si II λ1304.4 at our resolution, though if it were present in any strength it would affect the measurement of the

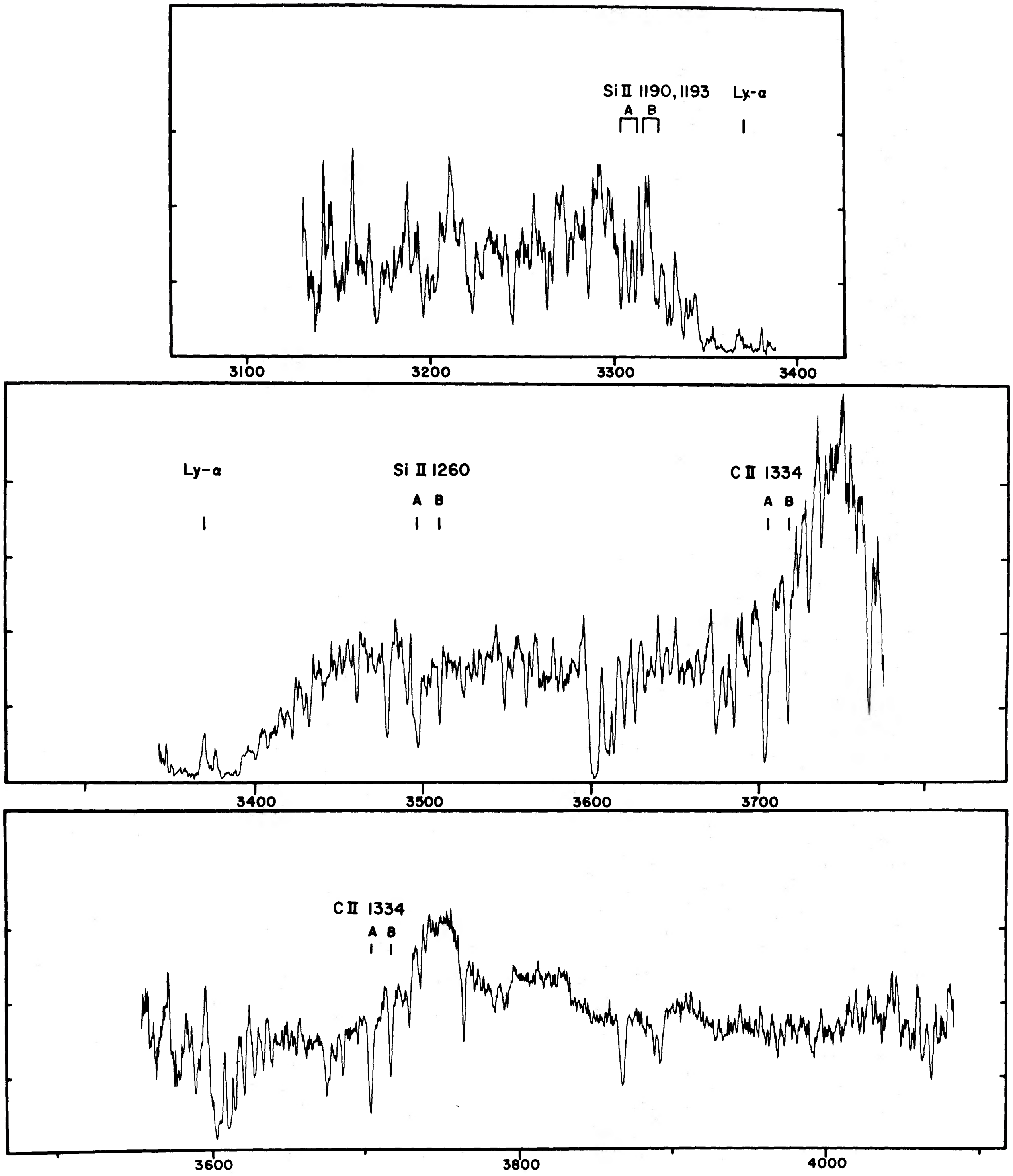

FIG. 3*a*.—PDS microdensitometer tracings of the 13th to 11th orders on a corrected relative intensity scale as described in the text.

1975ApJ...196..351C

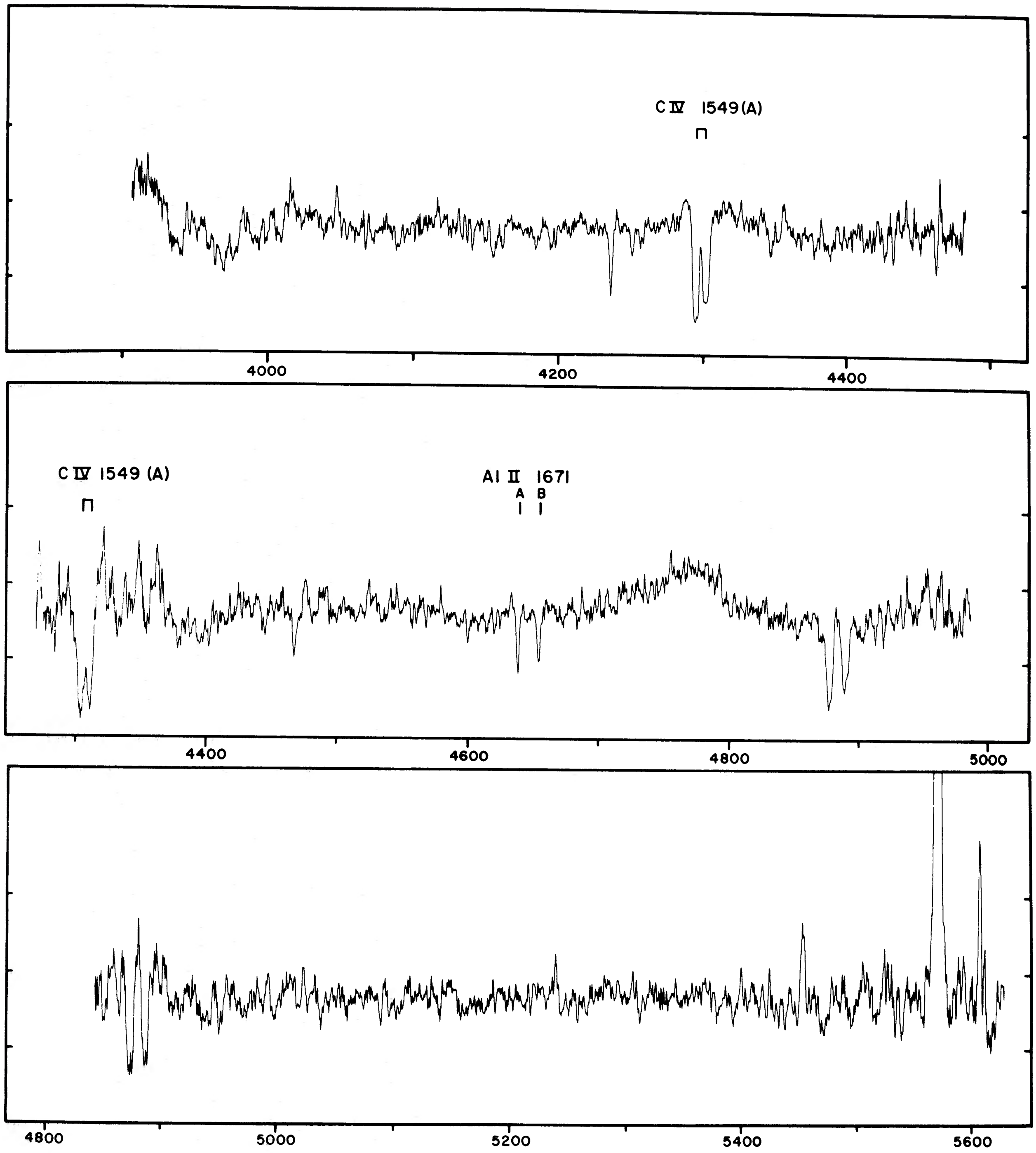

FIG. 3*b*.—PDS microdensitometer tracings of the 10th or 8th orders on a corrected relative intensity scale

TABLE 3

ABSORPTION LINE REDSHIFT SYSTEMS

Line	EqW	Identification	f	1+z	Comments
	System A: $\langle z \rangle = 1.7755$			Certain	
3172.5	1.7	FeII 1143.2	0.02	(2.7751)	Doubtful-too strong.
3179.4	---	FeII 1144.9	0.15	(2.7770)	Poss. line. Poor wavelength agreement
3263.2	0.7:	CIII 1175.6	---	(2.7758)	Doubtful: probably entirely SiIV 1403, system C
3303.5	1.2:	SiII 1190.4	0.31	2.7751	Too strong
3311.4	0.9:	SiII 1193.3	0.61	2.7750	Possibly blended with NI 1199 system E
3347.7	---	SiIII1206.5	1.70	(2.7747)	In wing broad Lα absorption - equivalent width not measured
3370:	---	Lα	0.42	---	Blend with Lα systems B and E
3497.2	1.8:	SiII 1260.4	1.20	2.7747	Possibly blended with FeII 1260.5
3614.7	1.2:	OI 1302.2	0.03	2.7758	
3620.7	1.1	SiII 1304.4	0.09	2.7758	
3704.1	2.4	CII 1334.5	0.26	2.7756	
3868.1	1.6	SiIV 1393.8	0.54	2.7752	
3893.2	0.8:	SiIV 1402.8	0.27	2.7753	
4237.5	1.5	SiII 1526.7	0.13	2.7756	
4296.4	3.6	CIV 1548.2	0.19	2.7751	
4303.5	2.9	CIV 1550.8	0.10	2.7750	
4464.5	0.8	FeII 1608.5	---	2.7756	
4637.6	1.6	AlII 1670.8	1.84	2.7757	
6507.6	5.1	FeII 2343.5	0.11	(2.7760)	Blend with MgII 2795, system C
(6575.5)	---	FeII 2366.7		(2.7775)	
6591.7	1.7	FeII 2373.7	0.04	2.7762	
6614.1	2.4	FeII 2382.0	0.33	2.7759	
7179.6	1.8	FeII 2585.9	0.06	2.7757	Blend with FeII 2599, system E
7217.3	1.5	FeII 2599.4	0.20	2.7758	
7761.7	3.6	MgII 2795.4	0.60	2.7757	
7786.9	6.0	MgII 2802.7	0.30	(2.7776)	Blend with MgII 2795, system B
	System B: $\langle z \rangle = 1.7852$			Certain	
3189.3	0.7:	FeII 1144.9	0.15	2.7857	
3274.6	0.4:	CIII 1175.6	---	2.7855	Possible line
3315.1	0.7	SiII 1190.4	0.31	2.7849	
3322.5	1.7:	SiII 1193.3	0.61	2.7843	
3340.1	---	NI 1199.9	0.35	(2.7836)	Possible line
3370:	---	Lα	0.42	---	Blend with Lα, systems A and E
3510.2	0.7	SiII 1260.4	1.20	2.7850	Possibly blended with FeII 1260.5
3627.3	1.1	OI 1302.7	0.03	2.7844	
3633.4	0.4:	SiII 1304.4	0.09	2.7855	
3717.3	1.4	CII 1334.5	0.26	2.7855	
4252.4	0.5	SiII 1526.7	0.13	2.7854	
4653.6	1.3	AlII 1670.8	1.84	2.7853	
6526.4	2.4	FeII 2343.5	0.11	(2.7841)	Blend with MgII 2802, system C
	System B: $\langle z \rangle = 1.7852$				Certain (continued)
6637.3	1.8	FeII 2382.0	0.33	2.7856	
7245.5	1.3	FeII 2599.4	0.20	2.7866	
7786.9	6.0	MgII 2795.4	0.60	(2.7847)	Blend with MgII 2802, system A
7805.8	2.9	MgII 2802.7	0.30	2.7843	
	System C: $\langle z \rangle = 1.3273$				Probable
3244.1	1.5	SiIV 1393.8	0.54	2.3275	
3263.2	0.7:	SiIV 1402.8	0.27	2.3262	Coincides with CIII 1175.6 in system A, but SiIV 1403 major (or only) contributor
3602.9	5.4:	CIV 1548.2	0.19	2.3272	Possible blend with SiII 1304, system E
3610.7	2.8:	CIV 1550.8	0.19	2.3283	
3888.9	0.4:	AlII 1670.8	1.84	2.3276	
5545	1.5	FeII 2382.0	0.33	2.3272	Probably too strong
6507.1	5.1	MgII 2795.4	0.60	(2.3278)	Blend with FeII 2366, system A
6526.4	2.4	MgII 2802.7	0.30	(2.3279)	Blend with FeII 2366, system B
	System D: $\langle z \rangle = 0.7441$				Possible
4141.3	---	FeII 2373.7	0.04	1.7441	Too strong, doubtful line
4155.9	---	FeII 2382.0	0.33	1.7442	Possible line
4877.1	3.3	MgII 2795.4	0.60	1.7441	
4889.4	2.5	MgII 2802.7	0.30	1.7440	
	System E: $\langle z \rangle = 1.7605$				Possible
3152.2	---	FeII 1142.3	0.01	2.7595	Near atmospheric cutoff
3244.1	1.5	CIII 1175.6	---	2.7595	Metastable lower level
3286.1	1.2	SiII 1190.4	0.31	2.7605	Too strong
3294.7	0.3	SiII 1193.3	0.61	2.7610	
3311.4	0.9:	NI 1199.9	0.35	(2.7597)	Blend SiII 1193, system A
3331.6	1:	SiIII1206.5	1.70	2.7614	
3370:	~50	Lα	0.42	---	Blend Lα, systems A and B
3478.9	1.6	SiII 1260.4	1.20	2.7602	
3602.9	5.4:	SiII 1304.4	0.09	(2.7621)	Blend CIV 1548, system C
3686.0	0.9:	CII 1334.5	0.26	2.7621	
6575.5	---	FeII 2382.0	0.33	2.7597	Possible line
7179.6	1.8	FeII 2599.4	0.20	(2.7620)	Blend FeII 2585, system A

line center. However, there is no sign of O I λ1306.0 in system A, and at best marginal evidence for a feature at 3638.0 Å which could correspond to this line in system B. The search for fine-structure lines of Si II in system A is made difficult by the presence of the absorption lines of Si II in system B at almost exactly the expected wavelengths. The only exception to this is the Si II λ1533.4 line, which should fall at 4255.8 Å, but there is no convincing evidence for a feature at this wavelength. The situation for system B is clearer, since there are no confusing lines from another redshift system. Again no convincing candidates could be found. The Si II λλ1264.7, 1265.0 lines should fall at 3522.3 and 3523.2 Å, respectively, and while there is a possible feature at 3524.3 Å, the rather poor wavelength agreement, and the absence of any other Si II fine-structure lines, make this identification difficult to believe. The C II λ1335.7 fine-structure line would be barely resolvable, if present, on our spectrum. There is, however, a hint in the 12th order spectrum of an extended red wing in the 3704.1 Å feature corresponding to C II λ1334.5 in system A (cf. fig. 2). In the 11th order, on the other hand, there is no sign of this structure, so its reality remains in doubt. We note, however, that the resolution is less in this order and the plate density is very high in the region of interest due to Lα emission. If the C II λ1335.7 line is present in this system, its equivalent width is almost certainly less than about one-third of the ground-state line. For system B no evidence of the fine-structure line could be found.

Despite the improvement in resolution, the extended high-resolution coverage in the ultraviolet, and the consequent increase in the number of absorption lines compared with those listed by Strittmatter *et al.* (1973), only one further probable absorption system could be identified. The new data also suggest that system C ($z = 1.964$) of Strittmatter *et al.*, which was based on Lα and the N V λ1240 doublet, should be rejected. We now identify the strong line at 3602.9 Å with C IV λ1548.2 (instead of Lα) in a new system C with $\langle z \rangle = 1.3273$. This identification is supported by the resolution of a second component at 3610.7 Å corresponding to the other line in the C IV doublet, and by the identification of the 3244.1, 3263.2 Å pair with the Si IV λλ1393.8, 1402.8 doublet. The presence of the Mg II λλ2795, 2802 doublet in this system deserves some comment, since with the observed wavelengths of 6507.6 and 6526.4 Å, respectively, this coincides with the relatively strong Fe II 2343.5 line in systems A and B. Strittmatter *et al.* quote equivalent widths for these lines based on the Lick scanner data, as being 5.1 and 2.4 Å, respectively, sufficiently close to the ratio (2:1) expected for a weak Mg II doublet to make one suspect that this is the main contributor. Examination of the equivalent widths of the Fe II lines λλ2382, 2599 in both systems reinforces this view. If the line optical depth is low, then Fe II λλ2343, 2382, 2599 should have relative equivalent widths 1:3:2 (Morton and Smith 1973) in each absorption system, while in system A these lines have approximate ratios 6:3:2, and in system B, 4:3:2. Thus if the oscillator strengths are approximately correct, an interpretation of the lines at 6507.6 and 6526.4 Å as being due solely to Fe II λ2343 seems untenable. The observations are, however, consistent with their being blends of the Fe II line and the relevant Mg II lines from system C.

Two further possible systems were suggested by Strittmatter *et al.* (1973). The first with $z_{\text{abs}} = 0.744$ was based solely on identification of the pair at 4877.9 and 4889.4 Å with the Mg II λ2798 doublet. We note that the measured line strengths are consistent with this hypothesis and that a weaker feature at 4155.9 Å could be identified with the strong Fe II λ2382 line. If this is correct, the other Fe II lines would probably not be detectable on the present spectrogram (Fe II λ2374.5 may contribute to a feature at 4141.3 Å). Confirmation or otherwise of this redshift system must await further observational material. A second possible system in which the strong line at 3765 Å was identified with Lα at a redshift of 2.094 could likewise not be confirmed, although the line at 3172.5 Å may be identified with Lβ. While no other plausible identifications could be found in either system, there are equally no strong reasons for rejecting them since both Mg II λ2798 and the Lα, Lβ combination are each known to appear alone: examples are 0735+178 (Carswell *et al.* 1974) and 4C 05.34 (Lynds 1971).

Finally, we note weak evidence for a possible redshift system with $z = 1.761$ for which Lα again lies in the large absorption trough but in which the Si II lines are all present if not precisely with the correct intensity ratios. Si III λ1206.5 and N I λ1199.9 are present. C II λ1334.5 may contribute to the feature at 3686 Å, and there may be some features corresponding to Fe II lines. The major weakness of this system is, however, the apparent absence of the Mg II λ2798 doublet. This system is also given in table 3 but is considered marginal at best.

V. DISCUSSION

Despite the improved spectral coverage and resolution compared with that of Strittmatter *et al.* (1973), only one additional probable absorption system and two marginal ones could be identified in 1331+170. Of the seven "definite" lines with wavelengths greater than that of Lα in the emission system and which could not be identified by Strittmatter *et al.* (1973), four (λλ4464.5, 6559, 5353, and 5545) still could not be made to fit into any reasonable redshift system. (The wavelength ratio of 5339 and 5353 is consistent with the Mg II λ2798 doublet, but the line strengths are not.) The large number of unidentified lines at wavelengths shortward of the emission Lα may well be due to Lα in clouds with sufficiently low column density that other elements are not seen, as suggested by Lynds (1971) in the case of 4C 05.34.

The possibility that the absorption systems A and B may be an example of the line-locking mechanism that may operate if radiation pressure is driving material from the central QSO (Lucy and Solomon 1968; Scargle, Caroff, and Noerdlinger 1970; Mushotzky, Solomon, and Strittmatter 1972; Scargle

1973; Weymann 1973) has already been discussed by Strittmatter *et al.* (1973). The evidence for locking between the two systems is based mainly on the apparent near coincidence of Mg II $\lambda 2802$ in system A with Mg II $\lambda 2795$ in system B and similar lockings in several Fe II features. It is interesting in this respect that the doublet ratio for the Mg II lines, at 1.00258, is only marginally greater than that for the Si II $\lambda\lambda 1190$, 1193 doublet at 1.00244. We might, therefore, expect to see the Si II $\lambda 1193$ line of system A blended with the Si II $\lambda 1190$ line in system B. There is, however, some suggestion in figure 3 that these two lines, which are identified with features at 3311.4 and 3315.1 Å, respectively, are in fact separated and might remain so even if the splitting were as large as that for Mg II. If this is correct and if the Mg II lines have the same profile, then this would imply that the apparently locked Mg II lines may well be separated also, thus removing the evidence for line locking. Under these circumstances the relative redshifts of systems A and B may be (*a*) an unfortunate coincidence, (*b*) due to some other strong line pair, or (*c*) the result of line locking at an earlier stage, followed by decoupling of the two systems as the incident flux varied. It might be useful, with reference to this last possibility, to monitor 1331+170 for spectroscopic and photometric changes. We should emphasize, however, that the present evidence certainly does not exclude the possibility of line locking in the Mg II $\lambda 2798$ doublet since (i) the Si II lines are in a comparatively noisy and highly blended region of the spectrum where some question already exists in regard to the wavelength and/or intensity ratios and (ii) the Mg II lines are very strong and may have rather wider profiles than the Si II lines, especially if they are on the radiation-damping part of the curve of growth. Clearly, higher-resolution spectra of the Mg II line region in 1331+170 are needed to settle this issue.

The possibility that the redshift of system A is a result of the coincidence of Lβ in that system with the Lyman limit in the emission system receives some support from the presence of system C at redshift 1.3273. In this case, $(1 + z_{\rm em})/(1 + z_{\rm abs}) = 1.324$, with the L$\alpha$ absorption line then close to the emission system Lyman limit. This suggests that the continuum flux below the Lyman limit in the emission system should be substantially smaller than that above, in contrast to the behavior seen at the hydrogen limit in, for example, OQ 172 (Wampler *et al.* 1973). OQ 172, however, with an absorption system at $z_{\rm abs} = 3.066$ (Baldwin *et al.* 1974), shares with PHL 957 (Lowrance *et al.* 1972), 4C 05.34 (Lynds 1971), and 1331+170 a well-established absorption system such that

$$(1 + z_{\rm em})/(1 + z_{\rm abs}) = 1.11 ,$$

suggestive of Lβ locking on the Lyman continuum. Since this cannot be due to the hydrogen continuum edge, at least in the case of OQ 172, the locking phenomenon, if real, would have to be ascribed to He II Lβ and the He II Lyman limit, implying that helium is the main driving element. This possibility is currently being investigated in more detail.

Finally we should comment on the similarity of the strong absorption Lα feature at 3370 Å to Lα in system A ($z = 2.309$) in PHL 957 (Lowrance *et al.* 1972; Beaver *et al.* 1972). Both features are extremely broad and imply column densities of neutral hydrogen $N_{\rm H} \sim 10^{21}$ cm^{-2} if the velocity dispersion of material contributing to the line is the same as for other lines in the respective redshift systems. Both systems A in 1331+170 and PHL 957 are at the same blueshift relative to their respective emission systems, and system B is very close. Also, the overall character of system B in 1331+170 resembles system A in PHL 957, in that both contain only H I region lines (cf. Grewing and Strittmatter 1973) and thus appear similar to absorption spectra expected from cool interstellar material. System A in 1331+170, however, contains both H I region lines and lines of higher ionization states. It is therefore especially important to obtain higher-resolution spectra of 1331+170 in the near-infrared (i.e., the Mg II line region) to ascertain whether or not line locking is taking place and hence to establish whether absorption systems A and B arise in material associated with the quasar or whether the intervening galaxy hypothesis (Bahcall 1971) remains tenable in the case of 1331+170.

VI. SUMMARY

A cross-dispersed echelette spectrograph is described which has considerable astronomical power as a means of obtaining spectra of objects where moderate dispersion is required over a large wavelength range. Spectral coverage is limited only by the atmosphere and the image tube response.

The main results of our echelette observations of 1331+170 are as follows:

i) Two well-established absorption systems ($z_{\rm abs} = 1.7754, 1.7851$) and one probable system ($z_{\rm abs} = 1.3273$) have been found in the 91 absorption lines listed. Other possible systems have been suggested but require confirmation.

ii) There is no strong evidence for fine structure lines of O I or Si II in either of the redshift systems A or B, though in the former case the presence of system B complicates the search for Si II lines. In system A the 0.01-eV C II $\lambda 1335.7$ line may be present at about one-third of the strength of the ground state line.

iii) The broad Lα absorption is similar to that seen in PHL 957. Also, the character of system A ($z = 2.039$) in PHL 957 is very similar to system B in 1331+170, in that the only absorption lines are those expected to arise in an H I region.

iv) The near coincidence of Lβ in system A and Lα in system C with the emission Lyman limit may be construed as evidence of line locking between the emission and absorption systems. This process may also occur between absorption lines in systems A and B, though higher-resolution spectra in the Mg II line region are needed to settle this issue. If line locking can be shown to be operating, then clearly the suggestion that intervening galaxies are responsible for the absorption lines is incorrect, at least for this object.

We are indebted to R. E. Williams for helpful discussions. This work has been supported by NATO (grant N0647) and the NSF (grant GP-32450). One of us (R. F. C.) wishes to thank E. M. Burbidge for hospitality at the Royal Greenwich Observatory where part of this work was carried out.

REFERENCES

Bahcall, J. N. 1971, *A.J.*, **76**, 283.

Baldwin, J. A., Burbidge, E. M., Hazard, C., Murdoch, H. S., Robinson, L. B., and Wampler, E. J. 1973, *Ap. J.*, **185**, 739.

Baldwin, J. A., Burbidge, E. M., Burbidge, G. R., Hazard, C., Robinson, L. B., and Wampler, E. J. 1974, submitted to *Ap. J.*

Beaver, E. A., Burbidge, E. M., McIlwain, C. E., Epps, H. W., and Strittmatter, P. A. 1972, *Ap. J.*, **178**, 95.

Carswell, R. F., Strittmatter, P. A., Williams, R. E., Kinman, T. D., and Serkowski, K. 1974, *Ap. J. (Letters)*, **190**, L101.

De Boer, K. S., Morton, D. C., Pottasch, S. R., and York, D. E. 1974, *Astr. and Ap.*, **31**, 405.

Grewing, M., and Strittmatter, P. A. 1973, *Astr. and Ap.*, **28**, 39.

Lowrance, J. L., Morton, D. C., Zucchino, P., Oke, J. B., and Schmidt, M. 1972, *Ap. J.*, **171**, 233.

Lucy, L. B., and Solomon, P. M. 1970, *Ap. J.*, **159**, 879.

Lynds, R. 1971, *Ap. J. (Letters)*, **164**, L73.

Morton, D. C., and Smith, W. H. 1973, *Ap. J. Suppl.*, **26**, 333.

Mushotzky, R. F., Solomon, P. M., and Strittmatter, P. A. 1972, *Ap. J.*, **174**, 7.

Scargle, J. D. 1973, *Ap. J.*, **179**, 705.

Scargle, J. D., Caroff, L. J., and Noerdlinger, P. D. 1970, *Ap. J. (Letters)*, **161**, L115.

Smith, A. M. 1972, *Ap. J.*, **176**, 405.

Strittmatter, P. A., Carswell, R. F., Burbidge, E. M., Hazard, C., Baldwin, J. A., Robinson, L., and Wampler, E. J. 1973, *Ap. J.*, **183**, 767.

Wampler, E. J., Robinson, L. B., Baldwin, J. A., and Burbidge, E. M. 1973, *Nature*, **243**, 336.

Wiese, W. L., Smith, M. W., and Glennon, B. M. 1966, NSRDS–NBS 4.

Wiese, W. L., Smith, M. W., and Miles, B. M. 1969, NSRDS–NBS 22.

Weymann, R. J. 1973, *Comments Ap. and Space Sci.*, **5**, 139.

R. F. CARSWELL: Dept. of Physics & Astronomy, University College, Gower Street, London, England

R. L. HILLIARD, P. A. STRITTMATTER, and R. J. WEYMANN: Steward Observatory, University of Arizona, Tucson, AZ 85721

D. J. TAYLOR: Behlen Laboratory of Physics, University of Nebraska, Lincoln, NE 68508

THE ASTROPHYSICAL JOURNAL, 196:363–368, 1975 March 1

FLUX DENSITY MEASUREMENTS OF RADIO SOURCES AT 2.14 MILLIMETER WAVELENGTH

J. R. COGDELL AND J. H. DAVIS
Electrical Engineering Research Laboratory, The University of Texas at Austin
B. T. ULRICH
Departments of Astronomy and of Physics, The University of Texas at Austin
AND
BEVERLEY J. WILLS
Department of Astronomy, The University of Texas at Austin

Received 1974 July 11

ABSTRACT

Flux densities of galactic and extragalactic sources, and planetary temperatures, have been measured at 2.14 mm wavelength (140 GHz). Results are presented for OJ 287; the galactic sources DR 21, W3, and Orion A; the extragalactic sources PKS 0106+01, 3C 84, 3C 120, BL Lac, 3C 216, 3C 273, 3C 279, and NGC 4151; and the Sun, Venus, Mars, and Jupiter. Also presented is the first measurement of the 2.14-mm temperature of Uranus. The spectra of some of these sources are discussed. The flux density scale was calibrated absolutely. The measurements were made with a new continuum receiver on the 4.88-m radio telescope of The University of Texas.

Subject headings: galaxies — infrared sources — planets — quasi-stellar sources or objects — radio sources — spectra, radio — spectra, infrared

I. INTRODUCTION

Few continuum observations of astronomical objects have been made in the region of 2 mm wavelength. Yet in this region we can hope to learn more about the nature of violent events in objects like OJ 287, in extragalactic objects, and in galactic objects like Cygnus X-3, because theoretical work and observations at longer radio wavelengths lead us to expect that the observed flux density variations at short radio wavelengths should more directly reflect the variations in energy of the emitting relativistic electrons, and of the magnetic field strengths. We may also learn more about the infrared "excess" radiation in both extra galactic and galactic objects by attempting to detect a corresponding millimeter "excess."

We present here the first measurements of flux density at 140 GHz (2.14 mm wavelength) with an improved receiver system on the 4.88-m radio telescope of the Millimeter Wave Observatory of The University of Texas. We compare our results with previous measurements at longer (radio) wavelengths and shorter (infrared) wavelengths.

II. INSTRUMENTATION

The observations were made with the 4.88-m equatorially mounted radio telescope (Cogdell *et al.* 1970) of the Millimeter Wave Observatory,[1] Mount Locke, Texas, using a dual-beam radiometer. The antenna pointing has been evaluated by Davis and Cogdell (1969) who derive tracking and pointing errors of $\sim \pm 12''$ rms. The antenna gain calibration is based upon a comparison of the antenna effective area with that of a standard gain horn which is calculated theoretically (see, e.g., Cogdell 1969 and Davis and Cogdell 1971). The measured efficiency and half-power beamwidths for the equally off-axis beams at 139.7 GHz were 49 ± 4 percent and $1'.83$, respectively, and their separation was $4'.92$ in the east–west direction. The measured feed loss in the west beam was 7 percent, and the east beam had a gain of 0.944 of that of the west beam, as determined by single-beam observations of Jupiter. The feeds were oriented with the electric vector east–west. The standard Dicke radiometer switched between east and west beams at 500 Hz and had an intermediate-frequency passband of 1–2 GHz with no image rejection. Sensitivity was $\delta T_{\rm rms} \approx 0.4°$ K for 1-s integration time under good sky conditions.

Receiver gain calibrations were derived from a neon noise tube and were made at 30-minute intervals during observations. The primary thermal calibration of the signal from the neon noise tube was accomplished by placing a matched termination on the west beam input and cycling its temperature between that of ice slush (0.1° C) and boiling water (92.8° C at the site). This calibration was confirmed within 5 percent by comparing the ambient temperature with that of a liquid-nitrogen–saturated absorber in front of the feed; and a further confirmation is afforded by the measurements of the Sun and planets, which agree well within the error quoted in the independently calibrated measurements by Ulich (1974). The receiver back-end consisted of a standard lock-in amplifier followed by an analog

---

[1] The Millimeter Wave Observatory is operated by the Electrical Engineering Research Laboratory, The University of Texas at Austin, with support from the National Aeronautics and Space Administration, the National Science Foundation, and McDonald Observatory.

1975ApJ...196..351C

integrator, the output of which was converted to digital form and stored in a small computer. The computer received calibrations prior to observations and so converted data to antenna temperatures, and also initiated the movement of the antenna between the east and west beams.

III. OBSERVATIONS AND ANALYSIS

The observations were made between 1973 May 30 and June 4. Ephemerides were prepared prior to the observations in the manner described in Ulich, Cogdell, and Davis (1973). Pointing was checked daily by observing Jupiter at the half-power points on the beam with consistent results from day to day within ±8″, which is negligible in comparison with the half-power beamwidth. During observations, the antenna was positioned so that the source was alternately in the east and west beam, and the signals were subtracted in the computer. Each position was observed for 15 s during each cycle, with 3 s dead time between for repositioning of the antenna. The resulting signal represents a value of twice (actually 1.944 times) the antenna temperature. A typical integration time for a single source observation was about 1 hour.

Several times daily the atmospheric absorption was measured by observing the difference, $\Delta T_{\rm AM}$, between the sky temperature at one and two air masses. The opacity was then computed according to the relationship:

$$\tau = \frac{\Delta T_{\rm AM}}{T_A} + 1.5\left(\frac{\Delta T_{\rm AM}}{T_A}\right)^2 ,$$

where $T_A = 238°$ K was taken to be the effective temperature of the atmosphere. This relationship was derived from a model based upon a constant thermal lapse rate and an exponential density profile for oxygen and water vapor with scale heights appropriate to Mount Locke. The antenna coupling to the atmosphere (88%) is included in the formula. The opacity varied smoothly between 0.11 and 0.25 nepers during the observing run and reflected the general weather patterns. Opacity corrections in the data averaged 22 percent.

IV. RESULTS

The 2.14-mm temperatures of planets, and the flux densities of galactic and extragalactic objects, are

TABLE 1

Solar System Objects

Object	Disk Temperature* (° K)	Comment
Sun.......	6190 ± 300	Coupling coefficient = 0.784; cf. Ulich *et al.* (1973)
Venus....	308 ± 4.8	Phase 265°
Mars.....	223 ± 7.5	
Jupiter....	178 ± 1	
Uranus...	122 ± 8	Assuming $34\overset{''}{.}49$ semidiameter at 1 a.u. given by Newburn and Gulkis (1971).

* Errors quoted are standard deviations determined from the scatter of data internal to a given source (see text). These errors do not include an overall system calibration error of 10%.

TABLE 2

Galactic and Extragalactic Objects

Source Name	Set Coordinates (1950.0) R.A.	Set Coordinates (1950.0) Decl.	Date (UT)	Flux Density (Jy) Peak	Flux Density (Jy) Total
PKS 0106+01....	$01^{h}06^{m}04\overset{s}{.}5$	+01°19′01″	June 1	0.4±2.5	
W3.............	02 21 56.0	+61 52 35	June 3	19.7 2.4	24*±4
3C 84............	03 16 29.6	+41 19 52	May 30	21.6 2.4	
3C 120...........	04 30 31.6	+05 15 00	June 2	7.5 3.2	
			June 3	10.0 2.3	
			weighted mean	9.1 1.9	
Orion A..........	05 32 46.8	−05 24 25	June 3	57.3 3.7	270*±50
OJ 287...........	08 51 57.3	+20 17 58	May 30	2.9 3.5	
3C 216...........	09 06 17.3	+43 05 59	May 31	2.2 2.4	
NGC 4151.......	12 08 02.0	+39 40 48	June 2	5.0 2.1	
3C 273...........	12 26 33.2	+02 19 43	May 30	33.7 7.2	
			June 1	16.0 6.4	
			June 2	24.9 2.3	
			weighted mean	24.7 2.1	
3C 279...........	12 53 35.8	−05 31 08	May 31	1.5 7.1	
DR 21†..........	20 37 14.3	+42 08 55	June 1	9.7 3.5	
			June 3	16.1 5.1	
			weighted mean	11.7 2.9	12.2±3.0
BL Lac..........	22 00 38.9	+42 02 09	June 1	9.4 3.5	
			June 3	15.7 5.6	
			weighted mean	11.2 3.0	
3C 454.3.........	22 51 29.6	+15 52 54	June 1	0.5 1.7	

* See the text for a discussion of these estimated total flux densities.

† Based upon the DR 21 spectrum reported by Dent (1972) as modified by Ulich *et al.* (1973) and the measurements of this source by Ulich (1974), we would judge our June 1 measurement of DR 21 low by about a factor of 2. Our observations of DR 21 were made near sunrise, and the resulting thermal effect on the receiver caused excessive drift on both days. The quoted errors include the uncertainty in the drift correction.

presented in tables 1 and 2. Our observed brightness temperatures for the Sun, Venus, Mars, and Jupiter listed in table 1 are in good agreement with previous values measured by Ulich (1974). Our temperature, 122° ± 8°, for Uranus is a new result, whose relation to measurements at other frequencies can be seen in the spectrum plotted by Ulich (1974). This temperature differs from our preliminary result quoted by Ulich because we have revised our determination of the overall system calibration. Measured peak flux densities for galactic and extragalactic objects, together with dates of observation, are given in table 2. In cases where we measured an object on more than one day, each day's value is listed separately, together with a weighted average of all the data. Since the errors due to receiver noise and occasionally atmospheric noise dominate over errors due to atmospheric extinction, pointing, receiver gain drift, and tracking, the errors listed with the observations are standard errors found from the scatter of data internal to a given source. The overall system calibration error of 10 percent is not included. The last column contains estimated total flux densities for the sources DR 21, W3, and Ori A, for which the angular sizes are significant compared with the 1'.83 half-power total beamwidth.

V. DISCUSSION

a) *Galactic Objects*

i) *W3*

The total flux density has been estimated from the flux density measured at the position given in table 2 by using a size correction determined from the 5-GHz map of this H II region given by Wynn-Williams (1971). Components were approximated by elliptical Gaussian brightness distributions. The estimated total flux density represents the sum from components A and B; contributions from components C and D are negligible (Wynn-Williams's notation). In using this structure to derive a correction, the components have been assumed to have similar spectral indices between 5 and 140 GHz, an assumption which is suggested by the similar spectra of the components as shown by Wynn-Williams. If large-scale structure has been missed in his map (which was made with a high-resolution interferometer), our size correction will be underestimated; but our errors allow for the possibility that the effective Gaussian half-widths of this region could be as large as 1'.3 × 1'.4 (as measured by Hobbs, Modali, and Maran (1971) at 85 GHz). Figure 1 shows the combined spectrum of components A and B. The millimeter wavelength measurements are seen to be consistent with the thermal model assumed, and there is no evidence for significant contributions from components which become optically thin at frequencies near 10^{11} Hz; nor is there any evidence of an increase of flux density with increasing frequency associated with the infrared excess.

ii) *Orion A*

A size correction has been found assuming Gaussian half-width of 3'.1 × 3'.7, as determined from the map at 15 GHz given by Schraml and Mezger (1969). Since their beam size is similar to ours, their map should represent well our observed brightness distribution, provided of course that the structure is not significantly different at 140 GHz. In addition, a small correction has been made for flux density included in the offset

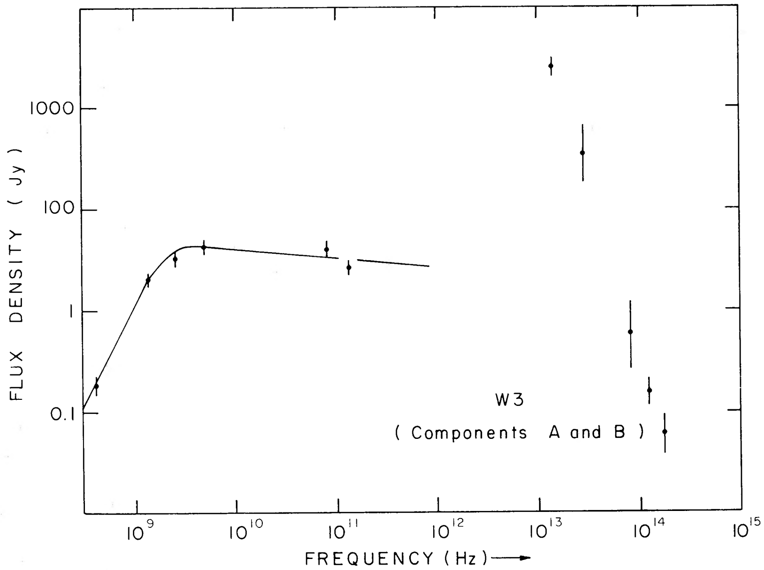

FIG. 1.—The combined radio and infrared spectrum of components A and B of the galactic H II region W3. The infrared sources IRS 1 and 3 are assumed to be the only infrared sources physically associated with the radio components, on the basis of position agreement. The new data are shown at 1.4×10^{11} Hz. Other data are from Wynn-Williams *et al.* (1972) and Hobbs *et al.* (1971) (8.5×10^{10} Hz). In the 8.6 to 133×10^{11} Hz (40–350 μ) range, flux densities are near the upper border of the figure as roughly estimated from the integrated flux density over this interval, reducing them by a factor of 2 to exclude the contribution of other infrared sources not associated with radio sources (Emerson *et al.* 1973).

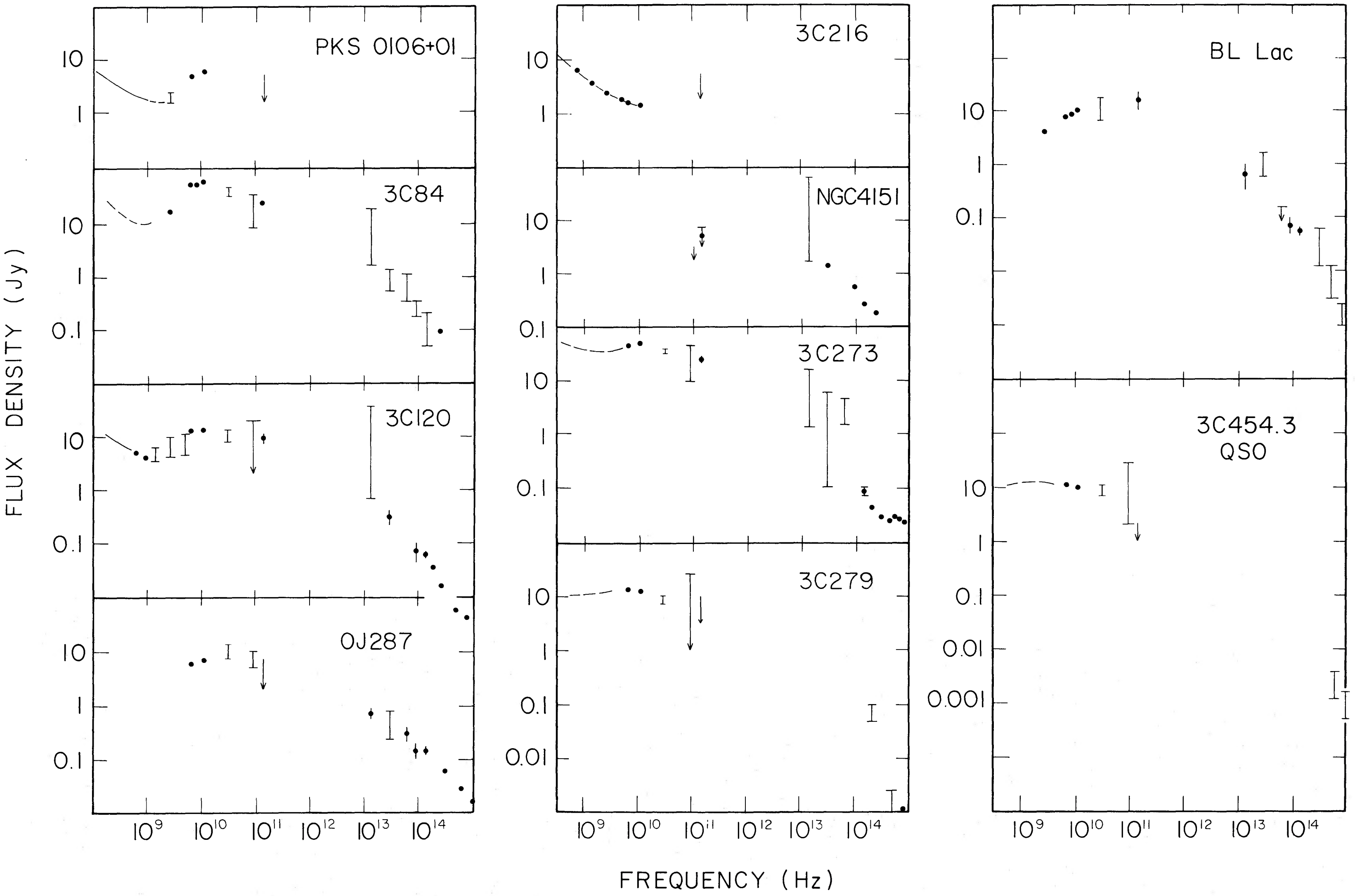

FIG. 2.—Radio and infrared spectra of extragalactic objects. The horizontal bars represent the range of observed flux densities at a given frequency. The present data are shown at 1.40×10^{11} Hz. Data at 6.5 and 10.6×10^9 Hz were kindly supplied by Dr. B. H. Andrew of the National Research Council of Canada; those at 2.695 and 8.085×10^9 Hz, by D. Wills. At 31.4×10^9 Hz, data are from Dent and Hobbs (1973). Data at 9×10^{10} Hz have been taken from Fogarty *et al.* (1971), at infrared wavelengths from Kleinmann and Low (1970*a*, *b*), Rieke and Low (1972*a*, *b*), Stein and Gillet (1971), Low and Johnson (1965), Oke *et al.* (1970), Visvanathan (1973*a*, *b*), Shields *et al.* (1972), and Neugebauer *et al.* (1971). At centimeter and millimeter wavelengths, individual points have been plotted if measurements were made at or near the time of the 140-GHz observations; however, at infrared wavelengths either representative flux densities or a range of flux densities at representative frequencies have been plotted.

beam. This total flux density is consistent with a predominantly thermal overall spectrum in agreement with the value of 284 ± 36 Jy[2] measured at 85 GHz by Brown and Broderick (1972).

b) *Extragalactic Objects*

In figure 2 our observations at 140 GHz are plotted along with other data to show the spectra of extragalactic objects and of OJ 287. For sources with time-variable flux density at other frequencies, horizontal bars show the range of observed variation unless a measurement made near the time of our observations was available. For variable sources, the astronomical potential of these 140-GHz data will be realized when they are combined with continuing measurements by us and by groups working at other frequencies. In the descriptions which follow, unpublished flux densities at 6.5 and 10.6 GHz have been used (B. H. Andrew, private communication).

i) *3C 84* (*NGC 1275*)

Since the first observations of this Seyfert galaxy in 1966, the flux density at 10.6 GHz has shown an overall increase (Medd *et al.* 1972) until the present time. Comparison with our observation, and with those near 90 GHz by Fogarty *et al.* (1971), shows that the spectral index has been positive[3] at millimeter wavelengths since monitoring was begun—i.e., most of the radiation is probably from optically thin regions.

ii) *3C 120*

Because the 6.5- and 10.6-GHz flux densities were declining during and for many weeks after our observations from two of the largest peaks ever observed in this Seyfert galaxy, the spectral index, α, of 0.2 between 10.6 and 140 GHz may be that of radiation from an expanding optically thin region—supporting previous indirect evidence from studies of time-variability of this source, that the energy distribution of the relativistic particles is flat compared with those of known nonvariable sources.

iii) *3C 216*

The spectrum of this QSO is of interest because of the slight increase in flux density above 1 GHz over that expected from an extrapolation of lower frequency data. Unfortunately, we cannot claim to have detected it.

iv) *NGC 4151*

It would be interesting if we have detected a long wavelength tail of the infrared "excess" in this infrared galaxy. However, our signal-to-noise ratio is only 2.5, which is insufficient to establish detection.

v) *BL Lacertae*

The 140-GHz flux density could lie on a smooth spectrum defined by the lower-frequency radio and high-frequency infrared flux densities, so the entire spectrum may arise from the same mechanism. Thus it will be of interest to search for correlations between time-variable flux densities at optical, infrared, and radio frequencies. Unlike the other sources observed here, the radio data suggest that this source of synchrotron radiation was optically thick at the time of observation, implying component sizes of the order of $0.0001 B^{1/4}$ arcsecond, where B is the magnetic field strength in gauss. For a model of this region which is homogeneous and isotropic, a temperature upper limit of 5×10^{10} ° K can be set (Kellermann and Pauliny-Toth 1969) by the requirement that electrons do not lose energy too rapidly by inverse Compton scattering. This maximum temperature implies an angular size $\geqslant 10^{-5}$ arcsecond or $B \geqslant 10^{-3}$ gauss, for components contributing to the flux density near 140 GHz.

VI. CONCLUSIONS

These first results have demonstrated the astronomical potential of a new system operating at 140 GHz. With this or an improved system we plan to monitor variable objects, observe active nuclei of galaxies, extend radio source spectra to 140 GHz (a higher frequency than those at which most radio sources have been observed), and also to investigate galactic infrared objects such as planetary nebulae and H II regions.

We acknowledge the contributions made to this series of measurements by Bobby L. Ulich of NRAO, who with J. H. Davis designed the basic receiver and generally developed many of the techniques and procedures used in this work. Various radiofrequency components and helpful suggestions were provided by A. A. Penzias of Bell Laboratories. The improved mixer diodes which made these measurements possible were the work of G. Wrixon and M. V. Schneider, also of Bell Laboratories. D. Dempsey, C. Tin, Guy Blair, and C. Garza helped in the observations or data reduction.

We are grateful to B. H. Andrew and his associates of the National Research Council of Canada for supplying us with unpublished data.

Thanks are due to Harlan J. Smith for the use of the facilities of McDonald Observatory at Mount Locke.

---

[2] 1 jansky (Jy) = 10^{-26} W m^{-2} Hz^{-1}.

[3] The spectral index, α, is defined by flux density $\propto$ (frequency)$^{-\alpha}$.

REFERENCES

Brown, R. L., and Broderick, J. J. 1973, *Ap. J.*, **181**, 125.

Cogdell, J. R. 1969, Electrical Engineering Res. Lab., Tech. Rept. NGL-006-69-1, University of Texas, Austin.

Cogdell, J. R., McCue, J. J., Kalachev, P. D., Salomonovitch, A. E., Moiseev, I. G., Stacey, J. M., Epstein, E. E., Altshuler, E. E., Feix, G., Day, J. W., Hvatum, H., Welch, W. J., and Barath, F. T. 1970, *IEEE Trans.*, **AP-18**, 515.

Davis, J. H., and Cogdell, J. R. 1969, Electrical Engineering Res. Lab., Tech. Memo., No. NGL-006-69-3, University of Texas, Austin.

———. 1971, *IEEE Trans.*, **AP-19**, 58.

Dent, W. A. 1972, *Ap. J.*, **177**, 93.

Dent, W. A., and Hobbs, R. W. 1973, *A.J.*, **78**, 163.

Emerson, J. P., Jennings, R. E., and Moorwood, A. F. M. 1973, *Ap. J.*, **184**, 401.

Fogarty, W. G., Epstein, E. E., Montgomery, J. W., and Dworetsky, M. M. 1971, *Ap. J.*, **76**, 537.
Hobbs, R. W., Modali, S. B., and Maran, S. P. 1971, *Ap. J.* (*Letters*), **165**, L87.
Kellermann, K. I., and Pauliny-Toth, I. I. K. 1969, *Ap. J.* (*Letters*), **155**, L71.
Kleinmann, D. E., and Low, F. J. 1970*a*, *Ap. J.* (*Letters*), **159**, L165.
———. 1970*b*, *ibid.*, **161**, L203.
Low, F. J., and Johnson, H. L. 1965, *Ap. J.*, **141**, 336.
Medd, W. J., Andrew, B. H., Harvey, G. A., and Locke, J. L. 1972, *Mem. R.A.S.*, **77**, 109.
Neugebauer, G., Becklin, E. E., and Hyland, A. R. 1971, *Ann. Rev. Astr. and Ap.*, **9**, 67.
Newburn, R. L., Jr., and Gulkis, S. 1971, JPL Tech. Rept., No. 32-1529.
Oke, J. B., Neugebauer, G., and Becklin, E. E. 1970, *Ap. J.*, **159**, 341.
Rieke, G. H., and Low, F. J. 1972*a*, *Ap. J.* (*Letters*), **176**, L95.
———. 1972*b*, *ibid.*, **177**, L115.
Schraml, J. and Mezger, P. G. 1969, *Ap. J.*, **156**, 269.
Shields, G. A., Oke, J. B., and Sargent, W. L. W. 1972, *Ap. J.*, **175**, 75.
Stein, W. A., and Gillet, F. C. 1971, *Nature Phys. Sci.*, **233**, 16.
Ulich, B. L. 1974, *Icarus*, **21**, 254.
Ulich, B. L., Cogdell, J. R., and Davis, J. H. 1973, *Icarus*, **19**, 59.
Visvanathan, N. 1973*a*, *Ap. J.*, **179**, 1.
———. 1973*b*, *ibid.*, **185**, 145.
Wynn-Williams, C. G. 1971, *M.N.R.A.S.*, **151**, 397.
Wynn-Williams, C. G., Becklin, E. E., and Neugebauer, G. 1972, *M.N.R.A.S.*, **160**, 1.

J. R. Cogdell and J. H. Davis: Electrical Engineering Research Laboratory, The University of Texas, Austin, TX 78712

B. T. Ulrich: Department of Physics, The University of Texas at Austin, Austin, TX 78712

B. J. Wills: Department of Astronomy, The University of Texas at Austin, Austin, TX 78712

THE ASTROPHYSICAL JOURNAL, 196:369–380, 1975 March 1

COLOR-MAGNITUDE DIAGRAMS FOR FOUR RICH CLUSTERS OF THE LARGE MAGELLANIC CLOUD

PHILIP J. FLOWER AND PAUL W. HODGE*
Astronomy Department, University of Washington, Seattle

Received 1974 August 5; revised 1974 September 9

ABSTRACT

Color-magnitude diagrams are presented for four very rich clusters of the Large Magellanic Cloud. Comparisons with theoretical color-magnitude diagrams show good agreement in the location and distribution of stars in the giant regions. All four have nearly identical ages of approximately 5×10^7 years. Each cluster has at least one anomalously luminous giant of intermediate color and $M_v \simeq -5.7$, over a magnitude brighter than both the observed and predicted giant branch.

Subject headings: globular clusters — Magellanic Clouds — stellar evolution

I. INTRODUCTION

A previous paper (hereafter called Paper I, Hodge and Flower 1973) discussed a color-magnitude diagram for the large and populous LMC cluster NGC 2164, for which observations were obtained with the 60-inch (1.5 m) telescope of the Cerro Tololo Inter-American Observatory. This paper presents similar data on the colors and magnitudes for members of three other clusters, NGC 2156, NGC 2159, and NGC 2172. These objects, sometimes called blue globular clusters, are important because, unlike most young clusters studied in our Galaxy, they are rich in giant stars, making it possible to carry out comparisons with theoretical evolutionary calculations for the giant phases of evolution. Improved photometry of NGC 2164 is also included in this paper.

II. MEASUREMENTS

The plates used are all described in Paper I, and all measures were made in a way identical to that for Paper I. Depending on their distance from the plate center, some clusters could not be measured on certain plate pairs because of field effects, and some were measurable only in the outer regions on specific plate pairs. Table 1 lists and describes the clusters and gives information on the number of plates that were usable in each case.

TABLE 1

CLUSTERS AND MEASUREMENTS

Cluster	No. of Stars Measured	No. of Plates
NGC 2156....	65	22
NGC 2159....	60	24
NGC 2164....	68	22
NGC 2172....	41	22

Reductions of the astrophotometer measures were carried out in the same manner as in Paper I. The measures of plates with exposure times of 10 minutes or less were used if the average V magnitude was brighter than 17.0. Magnitudes fainter than 17.0 from these short-exposure plates were found to be unreliable because of background effects. Each of the long-exposure plates, with exposures of 30 minutes or more, were considered individually for the effects of background and crowding. These long exposure plates were compared with each other to check for systematic effects. We found that the measures from plate pair 5–6

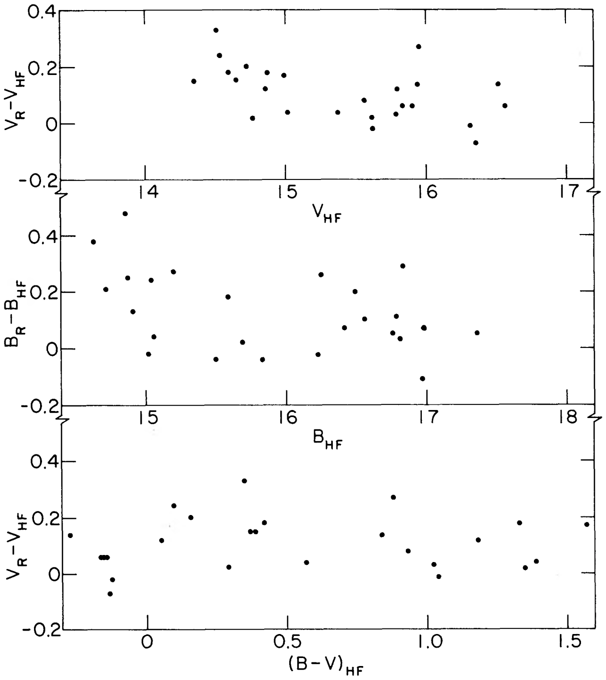

FIG. 1.—Comparison between measures of stars in common in NGC 2164 from Hodge and Flower (1973) and from Robertson (1974*b*).

---

* Visiting Astronomer, Cerro Tololo Inter-American Observatory, operated by Associated Universities for Research in Astronomy, Inc., under contract to the National Science Foundation.

TABLE 2

Star	V	N	σ(v)	B-V	N	σ(B-V)
NGC 2156						
1	14.71	10	0.12	0.07	10	0.12
2	17.29	3	0.09	-0.13	2	0.09
3	16.77	5	0.06	-0.03	5	0.19
4	16.75	5	0.06	1.24	5	0.07
5	17.16	3	0.07	-0.16	3	0.11
6	16.64	7	0.09	-0.06	7	0.09
7	18.25	2	0.08	-0.26	2	0.04
8	17.86	3	0.13	1.27	2	0.08
9	16.66	7	0.08	-0.02	7	0.08
10	16.88	1	--	-0.22	1	--
11	16.62	3	0.11	-0.02	3	0.17
12	16.91	3	0.15	0.03	2	0.12
13	17.91	3	0.13	-0.08	3	0.15
14	17.81	3	0.08	-0.13	3	0.10
15	18.33	2	0.14	-0.24	2	0.08
16	17.57	2	0.06	-0.21	2	0.07
17	16.07	7	0.06	0.03	6	0.03
18	16.88	3	0.06	0.00	3	0.18
19	16.92	1	--	0.24	1	--
20	16.53	3	0.06	-0.15	3	0.13
21	16.78	1	--	0.00	1	--
22	17.56	3	0.09	-0.12	3	0.12
23	17.44	2	0.06	-0.09	2	0.04
24	17.95	3	0.14	-0.07	3	0.13
25	16.79	5	0.08	-0.04	5	0.13
26	16.69	2	0.15	-0.27	2	0.27
27	16.61	2	0.02	-0.08	1	--
28	17.08	3	0.12	-0.08	3	0.12
29	17.34	3	0.08	-0.06	3	0.14
30	14.76	9	0.16	0.15	7	0.10
31	17.28	3	0.11	-0.19	3	0.14
32	17.98	3	0.12	-0.03	2	0.06
33	16.54	3	0.05	-0.03	3	0.10
34	16.76	2	0.03	-0.11	2	0.03
35	16.84	3	0.16	-0.14	3	0.17
36	15.98	8	0.07	1.03	6	0.06
37	16.80	5	0.08	-0.06	5	0.14
38	17.96	2	0.11	-0.04	1	--
39	17.41	2	0.10	-0.08	1	--
40	17.54	3	0.07	-0.11	2	0.05
41	16.99	5	0.08	1.45	3	0.09
42	18.17	2	0.07	-0.31	1	--
43	16.57	3	0.29	-0.26	3	0.18
44	16.72	3	0.09	-0.07	3	0.19
45	16.60	2	0.06	-0.16	2	0.04
46	16.66	3	0.12	-0.12	3	0.04
47	17.30	3	0.09	-0.23	3	0.24
48	15.65	8	0.14	0.83	6	0.07
49	17.63	2	0.11	1.62	2	0.04
50	18.15	2	0.07	1.12	1	--
51	16.52	5	0.12	-0.06	4	0.10
52	16.62	3	0.07	-0.03	2	0.19
53	16.84	1	--	0.00	1	--
54	16.59	3	0.06	-0.06	3	0.11
55	14.93	6	0.07	0.27	3	0.05
56	15.43	4	0.07	0.39	3	0.02
57*	14.92	-	--	0.21	-	--
58	14.84	-	--	0.29	-	--
59	14.48	3	0.11	0.52	3	0.10
60*	13.63	-	--	0.49	-	--
61	15.37	6	0.08	0.96	4	0.18
62	15.86	5	0.11	-0.22	4	0.11
63	16.35	2	0.03	-0.40	2	0.03
64	16.58	1	--	-0.40	1	--
65	16.47	2	0.04	-0.24	1	--
NGC 2159						
1	16.77	7	0.13	0.07	6	0.06
2	18.50	2	0.09	0.93	1	--
3	16.61	7	0.07	-0.07	7	0.07
4	18.83	2	0.13	-0.19	2	0.05
5	17.67	3	0.08	-0.10	3	0.10
6	18.42	2	0.17	-0.16	2	0.09
7	16.74	4	0.15	-0.16	3	0.22
8	17.25	3	0.08	-0.13	3	0.13
9	15.29	10	0.09		10	0.13
10	16.87	1	--	--	-	--
11	18.60	1	--	--	-	--
12	17.95	2	0.08	-0.34	1	--
13	18.82	2	0.15	-0.32	2	0.02
14	18.94	2	0.04	-0.03	2	0.07
15	18.74	2	0.05	-0.11	2	0.08
16	18.71	2	0.11	-0.14	2	0.06
17	16.52	7	0.09	0.49	7	0.13
18	18.91	2	0.07	-0.25	1	--
19	18.57	2	0.14	-0.38	2	0.09
20	18.15	3	0.07	-0.09	3	0.11
21	18.21	3	0.14	-0.25	3	0.26
22	18.66	2	0.12	-0.19	2	0.03
23	17.69	3	0.10	-0.25	3	0.19
24	16.96	3	0.14	-0.15	2	0.15
25	17.69	3	0.07	-0.13	2	0.06
26	17.66	3	0.08	-0.20	2	0.06
27	18.49	2	0.09	-0.19	1	--
28	17.32	2	0.19	-0.34	1	0.07
29	17.48	2	0.21	-0.19	2	0.22
30	17.64	3	0.06	-0.04	3	0.08
31	18.46	2	0.07	-0.19	2	0.01
32	17.50	3	0.07	-0.05	3	0.08
33	17.74	3	0.07	-0.12	3	0.06
34	18.49	2	0.05	-0.11	2	0.06
35	17.28	3	0.06	-0.12	3	0.10
36	17.34	3	0.05	-0.05	3	0.09
37	18.83	2	0.14	-0.24	1	--
38	16.59	6	0.07	0.63	6	0.11
39	16.24	6	0.12	1.09	6	0.15
40	16.56	7	0.05	0.87	7	0.11
41	16.75	5	0.10	1.65	3	0.11
42	16.74	5	0.11	1.66	3	0.13
43	16.37	6	0.08	0.92	6	0.17
44	17.16	3	0.07	-0.06	3	0.13
45	16.82	5	0.10	-0.06	4	0.14
46	17.68	3	0.08	-0.18	2	0.05
47	17.87	3	0.10	-0.16	3	0.10
48	18.48	2	0.11	-0.25	1	--
49	14.65	7	0.12	0.39	7	0.09
50	13.31	5	0.05	0.91	5	0.12
51	15.84	3	0.16	1.02	3	0.17
52*	15.62	2	--	--	2	--
53*	15.77	3	--	0.39	3	--
54*	14.76	3	--	0.94	3	--
55*	15.31	2	--	1.15	2	--
56	15.77	2	0.24	-0.11	2	0.33
57*	14.61	3	--	0.82	3	--
58*	14.62	6	0.17	1.05	3	0.19
59	16.68	2	0.05	-0.13	1	--
60	16.38	4	0.21	-0.27	3	0.13
NGC 2164						
1	15.02	8	0.15	1.30	6	0.28
2	14.88	9	0.13	0.21	10	0.09
3	14.77	10	0.16	0.46	9	0.04
4	14.68	6	0.17	0.39	4	0.17
5	15.13	6	0.12	1.53	3	0.17
6*	13.14	5	0.13	0.28	4	0.09
7	15.48	7	0.14	1.36	5	0.08
8	15.72	9	0.08	1.32	7	0.06
9	14.70	9	0.15	0.16	9	0.16
10	14.54	10	0.07	0.41	10	0.07
11	15.66	3	0.06	0.93	2	0.24
12	14.67	3	0.19	0.11	3	0.06
13*	16.03	2	0.01	-0.32	2	0.18
14[c]	15.14	3	0.14	0.74	2	0.15
15*	15.12	3	0.07	0.02	2	0.03
16	14.49	3	0.12	0.07	3	0.14
17*	15.72	3	0.09	-0.04	3	0.22
18*	14.83	3	0.17	0.66	3	0.10
19	14.58	3	0.14	0.34	3	0.05
20*	14.39	3	0.15	0.57	3	0.02
21	15.87	5	0.09	1.01	4	0.10
22	16.02	5	0.19	0.88	4	0.07
23	15.01	6	0.08	0.11	6	0.06
24	15.56	8	0.20	0.16	6	0.05
25	15.34	3	0.17	--	-	--
26*	15.52	4	0.14	0.49	2	0.05
27	15.31	3	0.13	1.24	3	0.20
28[c]	14.38	4	0.14	0.01	2	0.12
29*	14.56	2	0.16	0.02	2	0.08
30*	13.26	3	0.27	1.30	2	0.04
31*	13.38	2	0.28	0.99	2	0.45
32*	13.38	2	0.13	0.99	1	--
33*	15.40	2	0.26	0.00	2	0.18
34	16.67	2	0.06	-0.27	2	0.12
35	16.77	2	0.03	-0.04	2	0.07
36	16.75	2	0.04	-0.19	1	--
37	15.86	2	0.01	-0.10	1	--
38	16.63	2	0.02	-0.25	1.5	0.11
39	16.20	4	0.22	-0.23	4	0.03
40	17.11	3	0.07	-0.09	4	0.10
41	17.41	3	0.07	0.99	4	0.06
42	18.00	3	0.14	-0.06	4	0.16
43	16.55	6	0.15	-0.18	6	0.17
44	17.40	3	0.08	-0.14	4	0.11
45	17.44	3	0.08	-0.12	4	0.10
46	15.88	6	0.13	1.16	5	0.05
47	16.60	4	0.07	-0.06	4	0.10
48	16.02	5	0.05	0.85	5	0.07
49	16.78	4	0.04	1.63	4	0.17
50	16.53	5	0.14	0.92	4	0.08
51	16.97	2	0.05	-0.01	1	--
52	14.79	6	0.14	0.43	7	0.17
53	16.81	3	0.01	-0.03	3	0.13
54	16.80	3	0.19	-0.28	4	0.11
55	17.07	3	0.04	1.53	4	0.13
56	16.45	2	0.01	-0.90	2	0.13
58	16.55	2	0.01	-0.44	2	0.11
59	17.00	4	0.09	1.30	3	0.05
60	16.40	5	0.07	-0.05	5	0.09
61	15.98	5	0.11	-0.07	5	0.08
62	17.05	3	0.11	-0.32	4	0.16
63	16.69	3	0.08	-0.10	3	0.22
64	16.37	5	0.17	1.03	5	0.18
65	17.39	3	0.06	-0.18	4	0.12
66	16.43	4	0.33	-0.22	3	0.12
67	17.52	3	0.07	-0.14	4	0.12
68	15.91	6	0.09	-0.06	6	0.05
NGC 2172						
1	16.45	6	0.09	0.31	5	0.06
2	17.27	2	0.04	-0.01	1	--
3	16.87	3	0.11	0.03	2	0.01
4	16.67	3	0.05	-0.12	2	0.02
5	17.79	2	0.05	-0.19	2	0.08
6	17.41	1	--	-0.19	1	--
7	17.79	1	--	-0.21	1	--
8	17.11	2	0.00	-0.15	1	--
9	17.25	1	--	-0.21	1	--
10	16.66	2	0.17	--	-	--
11	16.83	2	0.03	-0.16	2	0.25
12	17.78	1	--	0.39	1	--
13	16.23	6	0.20	-0.19	5	0.11
14	16.19	6	0.15	-0.12	5	0.05
15	17.84	3	0.04	-0.18	4	0.04
16	17.52	2	0.03	-0.05	2	0.06
17	13.52	6	0.04	0.39	4	0.06
18	15.47	10	0.09	1.07	7	0.04
19	15.68	3	0.11	0.51	2	0.12
20	15.79	5	0.03	1.06	4	0.05
21	15.52	1	--	1.11	1	--
22	15.19	10	0.07	0.42	10	0.10
23	17.50	1	--	-0.17	1	--
24	17.53	1	--	-0.31	2	0.01
25	17.24	1	--	--	-	--
26	16.27	2	0.20	--	-	--
27	16.66	3	0.19	-0.19	3	0.20
28	17.45	2	0.05	0.05	1	0.13
29	17.52	2	0.05	-0.34	1	0.02
30	16.52	4	0.30	-0.23	4	0.25
31	17.42	1	--	-0.05	1	--
32	17.44	1	--	-0.16	1	--
33	15.66	4	0.12	1.19	4	0.05
34	16.67	1	--	0.90	1	--
35	16.80	1	--	0.32	1	--
36	14.54	6	0.09	0.22	4	0.05
37	15.69	2	0.03	-0.41	2	0.24
38	16.04	2	0.04	-0.12	2	0.04
39	16.18	2	0.14	0.56	2	0.14
40	15.71	1	--	--	-	--
41	16.04	1	--	--	-	--

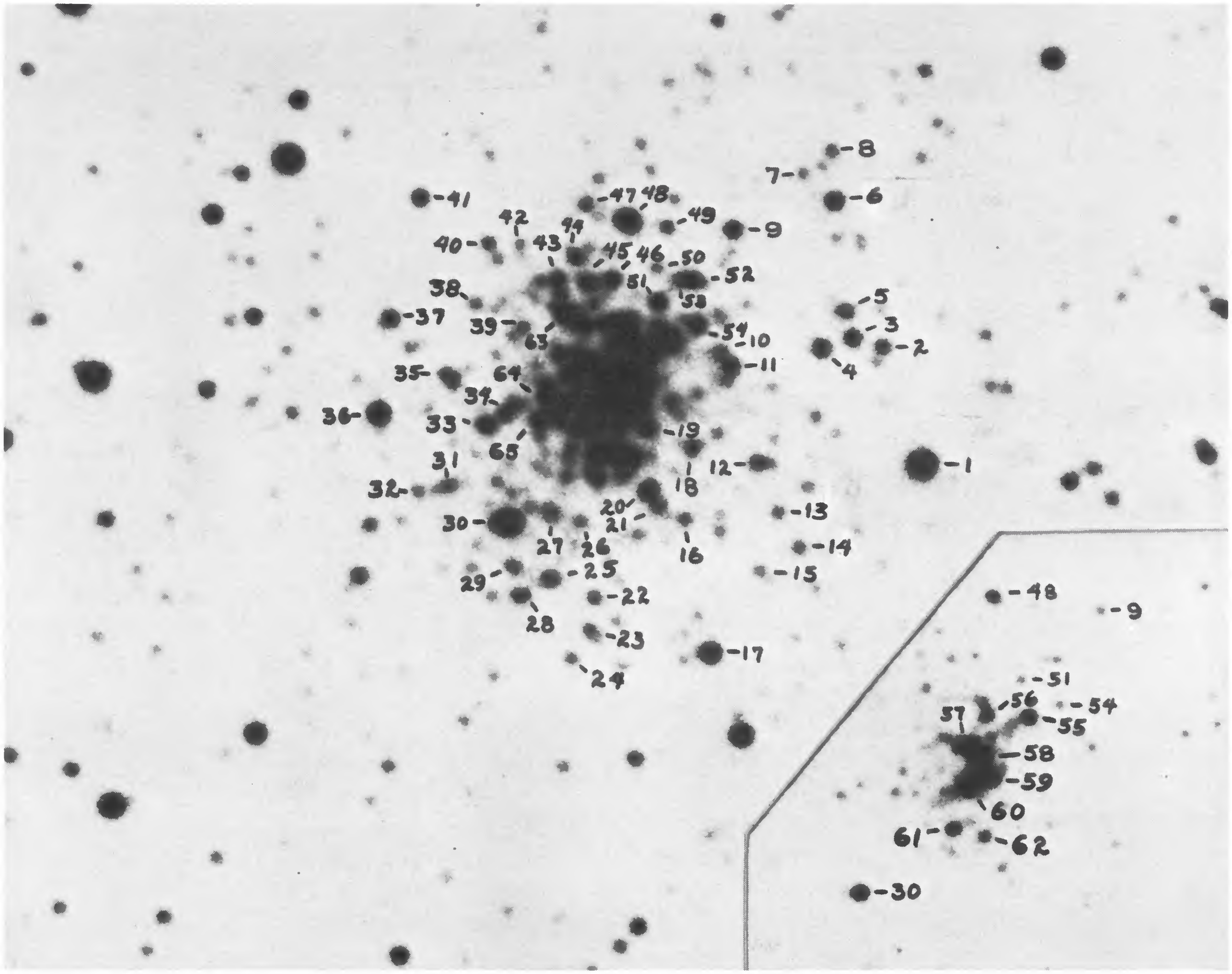

FIG. 2.—NGC 2156 from a *V* plate taken with the Cerro Tololo 60-inch telescope

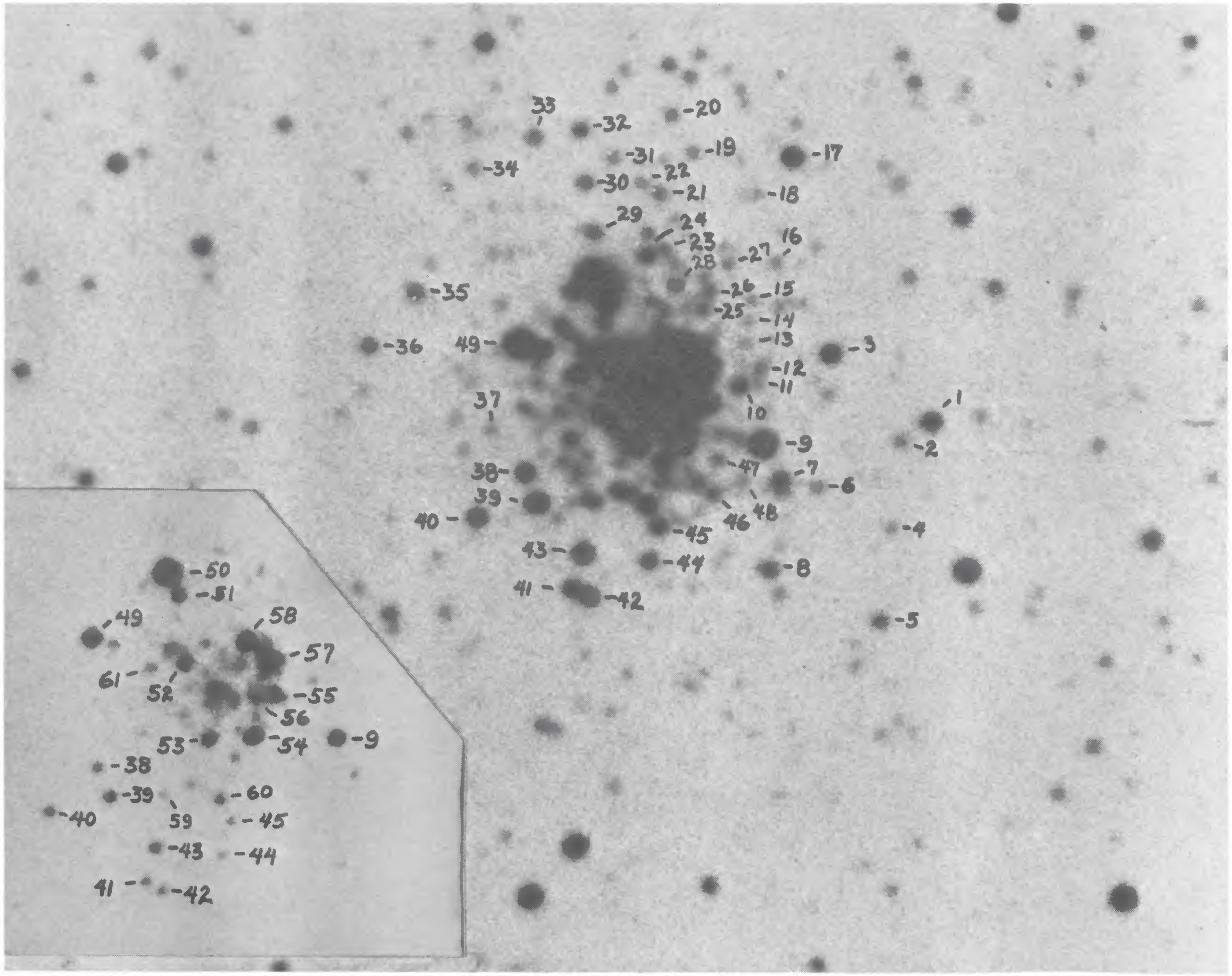

FIG. 3.—NGC 2159 from a *V* plate taken with the Cerro Tololo 60-inch telescope

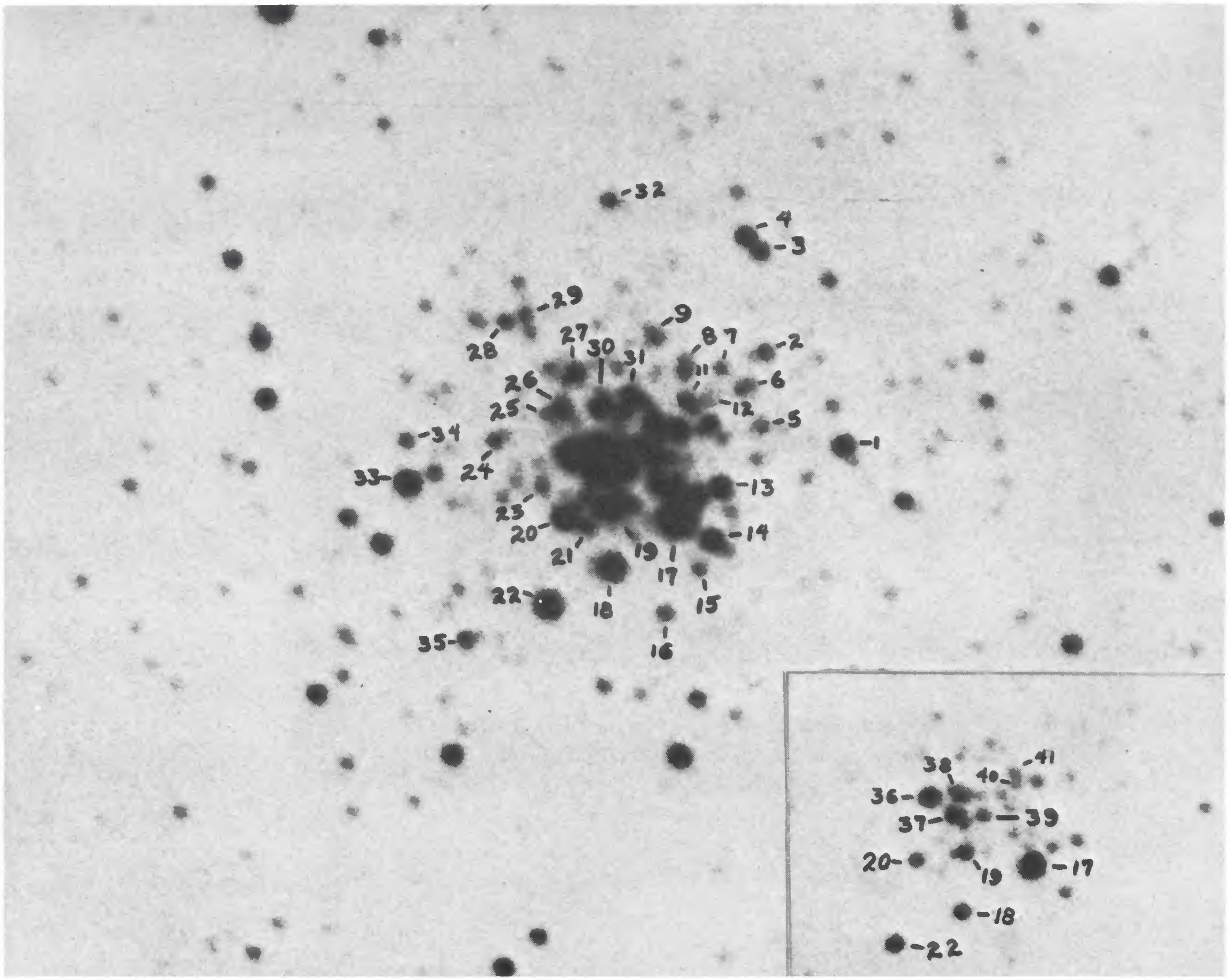

FIG. 4.—NGC 2172 from a *V* plate taken with the Cerro Tololo 60-inch telescope

were not reliable for NGC 2172, and for the inner portion of NGC 2156.

The data for NGC 2164, given in Paper I, are rediscussed here after being adjusted for color and magnitude equations. Least-squares solutions for the second set of plates, taken with the field corrector, give

$$B_{\mathrm{pe}} = B_{\mathrm{pg}} - 0.07(B - V)_{\mathrm{pg}} + 0.06$$

and

$$V_{\mathrm{pe}} = V_{\mathrm{pg}} = 0.06(B - V)_{\mathrm{pg}} - 0.03\,,$$

for color equations. This least-squares solution excluded plates with exposure times of 2 minutes or less, since on these plates there were too few standards brighter than the plate limit usable for a good determination. Application of these corrections to the data of Paper I for NGC 2164 improves agreement with the theoretical models and largely resolves the discrepancy of the main-sequence colors. With these corrections, we have compared our data with that of Robertson (1974*b*), kindly sent to us in advance of publication. His C-M diagram of NGC 2164 has 25 stars that are common to both programs, compared in figure 1. The comparison shows that there are systematic differences between the two sets of magnitudes and that they are not correlated with color. These differences are greatest at brighter magnitudes and nearly zero at the magnitude limit. To bring the data into better agreement, we have included his magnitudes for NGC 2164 stars in our final analysis of the data for the clusters of this paper. The resulting final magnitude equations are:

$$V' = V + 0.07(17.0 - V)\,,$$

$$B' = B + 0.07(18.0 - B)\,,$$

approximately valid over the interval $14 < V < 17$; $15 < B < 18$.

For all clusters the average V and $B - V$ and their standard deviation were calculated for each star. If a magnitude or color was found to be greater than 3 times the standard deviation, it was not included in the averages. Table 2 gives the magnitudes and colors, and figures 2 to 4 identify the measured stars in NGC 2156, 2159, and 2172.

Tests have shown that vignetting effects on plates taken with this telescope are less than 0.1 mag at the edges (Graham 1972). Field effects, however, due to uneven emulsion sensitivity or to the uneven unresolved LMC background can amount to as much as 0.1 mag. Therefore, the astrophotometer measures for these clusters are expected to be mutually consistent within a given cluster, but may be systematically off by perhaps 0.1 mag.

III. RESULTS

Figures 5 to 8 give the color-magnitude diagrams for the clusters, which are all four remarkably similar. Comparisons with theoretical models using Schlesinger's (1969) theoretical cluster color-magnitude diagrams give essentially identical estimates of turnoff masses and ages for the clusters, 7 $M_\odot$ and 5×10^7 years, respectively. The solid lines in the figures are based on Iben's (1967) calculations, after interpolation to 7 $M_\odot$, as in Paper I. Discussions of the individual clusters follow.

a) *NGC 2156* (Fig. 5)

This diagram is quite similar to that for NGC 2164, although it has fewer giants (~25 for NGC 2164, ~10 for NGC 2156). It has a concentration at the blue end of the helium-burning track, consisting of six stars with colors that agree well with the theoretical tracks, which also show a concentration at this location (Schlesinger 1969). At the red turnaround point there is, however, no conspicuous concentration. Three of the faint red stars are at some distance from the cluster center, and are possibly field stars. The open box at the top of the diagram represents a star at absolute magnitude of approximately −5.6, a magnitude brighter than any other of the giants. It was measurable on only one plate pair, so uncertainties in its magnitude and color are unknown, probably large, on the order of 0.3 mag or so. It is located right at the center of the cluster. It might be considered a field star, but the presence of similarly anomalous giants, occurring at the centers of the other clusters (table 3), makes it much more reasonable to accept that these stars are members and that they are in some superluminous stage of evolution, not yet reached in the theoretical calculations. Alternatively, they may be stragglers, which formed more recently than the cluster as a whole.

b) *NGC 2159* (Fig. 6)

This cluster's C-M diagram is also similar to that of NGC 2164. There are four stars near the red tip of the branch (and two somewhat beyond the theoretical tip), two stars at the blue tip, and four that lie near the end of the theoretical tracks as plotted.

c) *NGC 2164* (Fig. 7)

The newly plotted diagram is nearly identical to that given in Paper I, except that the color and magnitude equations have led to better detailed agreement with the theoretical curves, especially on the main sequence and at the blue turnaround on the giant branch.

TABLE 3

SUPERLUMINOUS GIANTS

Cluster	Star No.	M_v*	$B - V$
2156..........	60	−5.4	+1.0
2159..........	50	−5.7	+0.9
2164..........	6	−5.9	+0.2
	30	−5.9	+1.4
	31	−5.7	+1.0
	32	−5.7	+1.0
2172..........	17	−5.5	+0.4

* An apparent modulus of 19.05 was assumed.

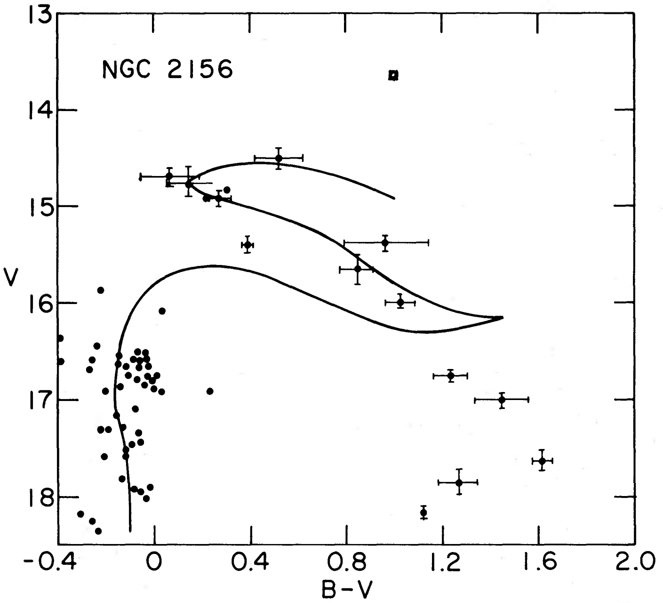

FIG. 5.—C-M diagram for NGC 2156. Error bars of main-sequence stars were omitted due to crowding of the diagram. Three of the faint red stars and two of the stars at the second turnoff are distant from the cluster and thus are possibly field stars. The line is a 5 × 10^7 yr isochrone from Schlesinger's (1969) curves, based on Iben's (1967) model calculations, adjusted as in Paper I.

d) *NGC 2172* (Fig. 8)

This cluster's C-M diagram is similar to the above, though the data show more scatter and larger measured errors for the main-sequence stars, apparently because of crowding of the fainter stars. There are fewer giants than in NGC 2164, probably nine among the plotted stars. Four are near the red tip, making up an accumulation there, as predicted by the theoretical models. The blue turnaround area of the giant branch has only two stars. There is a superluminous star above the giant branch, as found in the other clusters (table 3).

The theoretical evolutionary C-M diagrams used

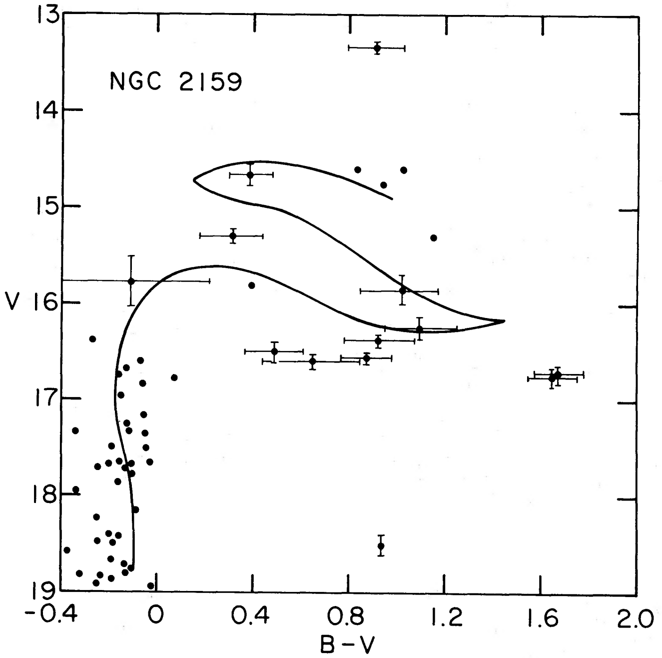

FIG. 6.—C-M diagram for NGC 2159. Isochrone is same as in fig. 5.

1975ApJ...196..351C

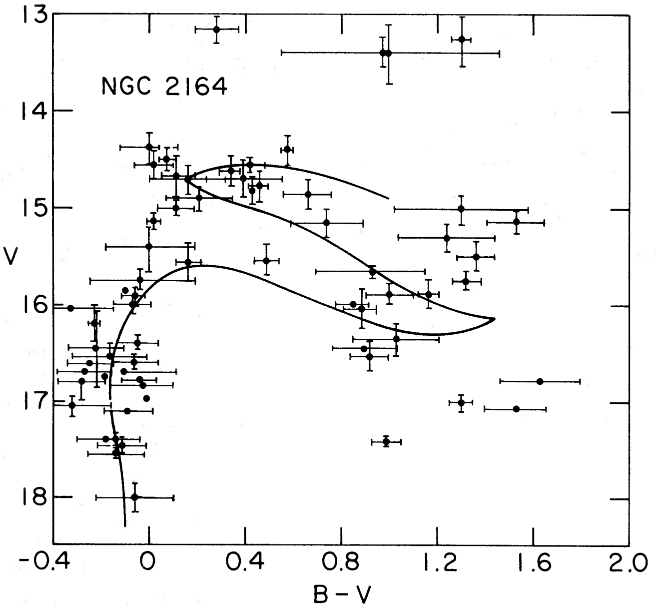

FIG. 7.—C-M diagram for NGC 2164. Isochrone is same as in fig. 5.

here (Schlesinger 1969) show accumulations of giants at the red end of the giant branch and at the blue, helium-burning turnaround. Schlesinger's cluster model B, for example, has six stars grouped between $B - V = +1.0$ and $+1.4$ at the red end and eight stars grouped between $B - V = +0.1$ and $+0.5$ at the blue turnaround. In general the observed clusters also show this tendency, with some interesting deviations in detail. NGC 2164 and NGC 2172 seem to agree with the model, but NGC 2156 and NGC 2159 seem to have significant differences from the model, in opposite sense. The giant branch of NGC 2156 is relatively depleted at the red turnaround, while that of NGC 2159 is depleted at the blue.

Robertson (1974*a*) has discussed the ratio, t_{br}, of the number of blue giants to the number of red giants for the clusters in his study. Having pointed out (Robertson 1972) the sensitivity of this ratio to abundances, he makes tentative conclusions about Y and Z for some of the clusters. The average for his clusters is $t_{br} = 0.7$.

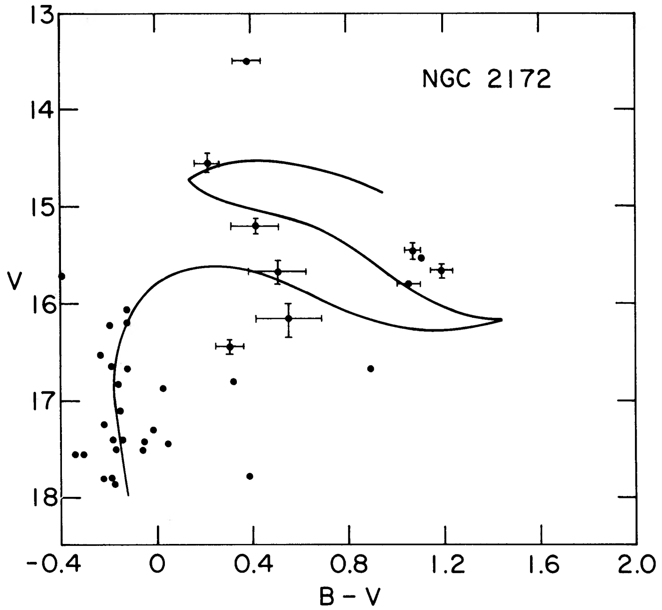

FIG. 8.—C-M diagram for NGC 2172. Isochrone is same as in fig. 5.

This shows better agreement with Cox-Stewart opacities than with Keller-Meyerott opacities, although the dependency of t_{br} on both abundances and opacities makes interpretation uncertain. We derive values for t_{br} of 2.0 ± 0.3 for NGC 2156, 0.3 ± 0.2 for NGC 2159, 1.0 ± 0.4 for NGC 2164, and 0.5 ± 0.4 for NGC 2172. Those for NGC 2164 and NGC 2172 are not significantly different from Robertson's average value, but those for NGC 2156 and NGC 2159 seem to show real differences. If these differences are ascribed to different Z values for the clusters, the qualitative conclusion is that NGC 2156 has unusually high Z while for NGC 2159, Z is unusually low. These conclusions must remain tentative until a more complete array of models is available (we are calculating these with Paczynski's program), and until more accurate photometry is possible, using the larger telescopes soon to be available in the southern hemisphere.

In summary, we have obtained color-magnitude diagrams for four "blue globular" clusters of the LMC. Comparisons with Iben's models indicate good agreement, both in shape and in distribution of stars on the giant branch. There are, however, superluminous, intermediate-color giants lying considerably above the giant branch in all of the clusters. All four clusters are of very nearly the same age (5×10^7 yr). This is significant in light of the results presented in another paper (Baird *et al.* 1974), which shows that many of the smaller, "open" clusters in this area of the Cloud also have this age.

We are grateful to the Cerro Tololo Inter-American Observatory for making these observations possible and to the National Science Foundation for its essential role in supporting part of this research through grants GP-16581 and GP-38490.

REFERENCES

Baird, S., Flower, P., Hodge, P. and Szkody, P. 1974, submitted for publication.
Graham, J. A. 1972, *IAU Colloquium No. 21, Toronto* (in press).
Hodge, P. W., and Flower, P. J. 1973, *Ap. J.*, **185**, 829.
Iben, I. 1967, *Ann. Rev. Astr. and Ap.*, **5**, 571.
Robertson, J. W. 1972, *Ap. J.*, **177**, 473.
———. 1974*a*, *ibid.*, **191**, 67.
———. 1974*b*, *Astr. and Ap. Suppl.*, **15**, 261.
Schlesinger, B. 1969, *Ap. J.*, **157**, 533.

Note added in proof.—Since writing this paper, one of us has computed new models from Paczynski's programs and has derived a series of isochrones intermediate in age between those of Schlesinger (1969). Comparison with the C-M diagrams indicates: (1) the main sequence fits better if Robertson's (1974*b*) magnitudes are *not* included with ours in the photometric reductions, and (2) the ages are probably somewhat smaller than derived above, more nearly 3×10^7 years.

PHILIP J. FLOWER and PAUL W. HODGE: Astronomy Department, FM-20, University of Washington, Seattle, WA 98195

THE ASTROPHYSICAL JOURNAL, **196**:381–405, 1975 March 1

DENSITY WAVE THEORY AND THE CLASSIFICATION OF SPIRAL GALAXIES

WILLIAM W. ROBERTS, JR.*
University of Virginia
MORTON S. ROBERTS
National Radio Astronomy Observatory†
AND
FRANK H. SHU‡
University of California at Berkeley

Received 1974 June 27; revised 1974 September 20

ABSTRACT

Axisymmetric models of disk galaxies taken together with the density wave theory allow us to distinguish and categorize spiral galaxies by means of two fundamental galactic parameters: the total mass of the galaxy, divided by a characteristic dimension; and the degree of concentration of mass toward the galactic center. These two parameters govern the strength of the galactic shocks in the interstellar gas and the geometry of the spiral wave pattern. In turn, the shock strength and the theoretical pitch angle of the spiral arms play a major role in determining the degree of development of spiral structure in a galaxy and its Hubble type. The application of these results to 24 external galaxies demonstrates that the categorization of galaxies according to this theoretical framework correlates well with the accepted classification of these galaxies within the observed sequences of luminosity class and Hubble type.

Subject headings: galactic structure — galaxies — shock waves — star formation

I. INTRODUCTION

From his extensive studies of the morphology of galaxies, Reynolds (1927) suggested a refinement to Hubble's (1926) classification which would take into account the bulkiness of the arms of spiral galaxies of similar Hubble type. He uses the terminology of "filamentary" and "massive" to distinguish the extremes. Examples are M101 (NGC 5457) for the former and M33 (NGC 598) for the latter type; both are Sc's in the Hubble system. This suggestion went essentially unnoticed in later discussions of the apparent structure of spirals (but see Hubble 1936, p. 44) until van den Bergh (1960*a*, *b*) found a correlation between the intrinsic luminosity of a spiral galaxy and the "degree to which spiral structure is developed...." Using criteria similar to Reynolds's "filamentary" and "massive" arms (and including the surface brightness), van den Bergh assigned luminosity classes to many of the galaxies in the Shapley–Ames (1932) catalog on the basis of their photographic image on the Palomar Sky Survey prints. The notation he adopts is similar to that used in stellar spectral classification: the roman numeral I denotes the intrinsically bright spiral galaxies with well-developed, "filamentary" spiral arms; and successive roman numerals denote intrinsically fainter spiral galaxies with less well-developed, "massive" spiral arms. His class V corresponds to a "dwarf" spiral some 4 mag fainter than class I. In his notation the two examples noted above are Sc I for M101 and Sc II–III for M33.

Any complete theory of spiral structure must be able to account for this remarkable variety in a natural way. A viable candidate at the present time is the density wave theory (see the review by Lin 1971) which addresses itself primarily to the dilemma of the persistence of spiral structure in a field of differential rotation and to the mechanism of formation of the stars which delineate spiral arms. In this theory, the enhanced luminosity of a spiral arm is believed to originate in the very young, newly formed stars whose births from interstellar clouds have been triggered by the passage of the crest of a spiral density wave. One wonders if this same wave mechanism can also account for the ordering of spirals into luminosity class and Hubble type. This is the issue which motivates the present work.

Within the context of the density wave theory, we show that a categorization of disk-shaped galaxies with spiral structure is possible by means of two fundamental parameters. These two parameters are: the total mass divided by the characteristic dimension of the galaxy, and the degree of concentration of mass toward the galactic center. The latter determines the pitch angle i of the spiral arms; and taken together, the two parameters determine $w_{\perp 0}$, the velocity component of basic rotation normal to the spiral arms. It is $w_{\perp 0}$ which so strongly influences the strength of the galactic shock wave. These results are applied to 24 extragalactic systems, and clear correlations between these theoretical quantities and the observed sequences of luminosity class and Hubble type are found.

---

* On sabbatical leave at the Kapteyn Institute, University of Groningen, The Netherlands.

† Operated by Associated Universities, Inc., under contract with the National Science Foundation.

‡ Alfred P. Sloan Foundation Fellow, 1972–1974.

II. THE CONSTRUCTION OF GALACTIC MODELS

We model a spiral galaxy to consist of two components, gas and stars, which are in gravitational interaction with one another. In disk galaxies, the gas is known to be concentrated in a very thin layer whose thickness is only a few percent of the diameter of the disk. Until recently, it was commonly accepted that the major portion of the mass of the stellar component is also confined to a fairly thin disk; however, recent work on the susceptibility of such configurations to barlike instabilities (see esp. Ostriker and Peebles 1973) has raised the possibility that spiral galaxies might have very massive halos.

In our work, we have retained the conventional view that most of the mass is distributed in a disk plus a central bulge. The inclusion of a stellar halo with mass comparable to that of the disk would influence our main results only in an indirect way since a more or less spheroidal halo exerts no direct influence on the dynamics of the spiral structure in the disk. However, its presence would affect the basic surface density σ_0 which one would deduce to be present in the disk on the basis of an examination of the *observed* rotation curve inasmuch as only a fraction of the source of the axisymmetric gravitational field would then be associated with the distribution of mass in the disk. The net effect would be to lower the length scale, $k_T^{-1} = 2\pi G\sigma_0/\kappa^2$, (Toomre 1964) which characterizes the collective gravitational interactions of a differentially rotating disk whose local epicyclic frequency is κ. Since the radial spacing of consecutive spiral arms would then be lowered proportionally, it would be necessary, in order to obtain the *same* fit for an observed spiral pattern, to raise either the pattern speed Ω_p or the stability parameter Q (see also § VI) or both. We have not felt such a course of action to be warranted at the present state of our knowledge of the role of stellar halos. In any case, since this correction would need to be applied to every galaxy in our sample, the main trends (§§ IV and V) revealed by our analysis would probably remain unchanged.

a) *Mass Models*

Various kinds of self-consistent axisymmetric mass models have been considered for the stellar populations of galaxies based upon their observed rotation curves (Schmidt 1956, 1965; Burbidge, Burbidge, and Prendergast 1959; Brandt 1960; Toomre 1963; Freeman 1970). In the present investigation, an overall mass model is taken to consist of a flattened disk (Toomre 1963) to represent the disk population, and a superposition of one or two inhomogeneous spheroids to cover the central bulge, where necessary. Our procedure follows that described by Shu, Stachnik, and Yost (1971) except that it has been standardized and automated to provide the best least-squares fit to the rotation curve data. In particular, this procedure automatically selects the number of spheroidal components (zero, one, or two) to be superposed on the Toomre component, as well as providing the best values for the length scales A and angular velocity scales B, once the model numbers (n_T and n_S) and eccentricities (e_S) of the various components have been chosen.

For each model component, the model number is a measure of the relative degree of central concentration. For example, the flat Toomre component always plays the most important role, and the radius, $\varpi_{0.5M}$, at which half its mass lies inside and half outside, can be found to be

$$\varpi_{0.5M} = A_T(2^{2/(2n+1)} - 1)^{1/2}, \tag{1}$$

where $n = n_T - 1$, and n_T is the Toomre model number. We shall find the half-mass radius, $\varpi_{0.5M}$, to be a useful concept, and we shall generalize its definition to include a superposition of component models. (The formula relating $\varpi_{0.5M}$ to the A's and B's is then no longer so simple as eq. [1].)

Figure 1 shows the rotation velocity data for the sample galaxy, NGC 157.[1] Superposed is the rotation curve corresponding to the mass model that provides the best least-squares fit to the rotation velocity data for each of several values of the model number, n_T. NGC 157 is one sample galaxy in which no spheroidal components are found to be necessary, and the Toomre component alone is sufficient. This galaxy is typical of most of the galaxies to be considered in § IV in the sense that the H II regions, constituting the rotation velocity data, and the visible spiral structure extend from the inner regions to the edge of the "easily visible" disk,[2] which itself generally lies well within the Holmberg radius.[3] In this galaxy as well as in many of the others, the rotation velocity data appear to reach a peak very close to the outermost data point, and this in turn lends uncertainty to the exact location of the real peak and to the value of n_T that allows for the best fit. However, it is important to note that the rotation curves for all these models spanning a large range of n_T values are all rather similar, particularly inside the region covering the "easily visible" disk where the spiral structure is prominent. For this reason the results herein do not depend in a sensitive manner on the choice of n_T. Therefore, a typical value of 5 is adopted for n_T in the Toomre component here as well as for n_S in each spheroidal component necessary for other galaxies considered in § IV.[4]

b) *Velocity Dispersions*

Following Shu *et al.* (1971), the overall mass model is adopted to have a finite but small disk thickness with a Schwarzschild distribution of peculiar velocities at each point. In this approach the velocity dispersion in the radial direction, $\langle c_\varpi^2\rangle^{1/2}$, and the velocity dispersion in the vertical direction, $\langle c_z^2\rangle^{1/2}$, can be arbitrarily specified. With regard to the ratio, $\langle c_z^2\rangle^{1/2}/$

---

[1] Rotation velocity data for NGC 157 and the estimate of its distance of 24.0 Mpc, based on a Hubble constant of $H = 75$, are taken from Burbidge *et al.* (1961*b*).

[2] "Easily visible" refers to eye estimates made by the authors.

[3] The Holmberg radius is based on the angular measurements of Holmberg (1958).

[4] The entire sequence of values for n_T is also considered later in §§ IV and VI.

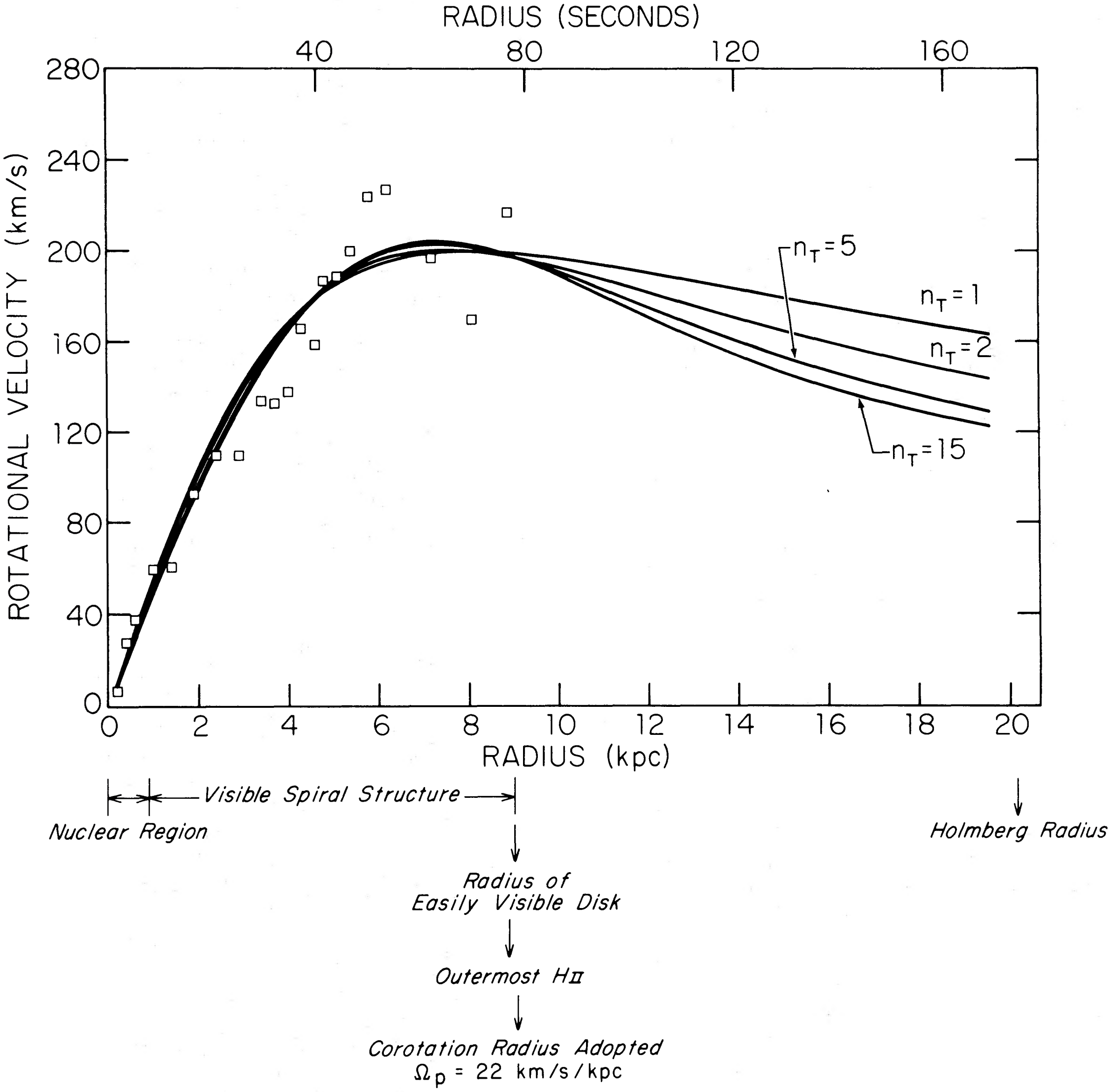

FIG. 1.—Rotation velocity data for the sample galaxy NGC 157, derived from H II regions, □, observed by Burbidge *et al.* 1961*b*. Superposed is the rotation curve corresponding to the mass model for the equilibrium disk which provides the best least-squares fit to the rotation velocity data for each of several values of the model number, n_T (no spheroidal components are necessary). The radial extent of the observed distribution of H II regions coincides with the radial extent of the visible spiral structure and the edge of the "easily visible" disk. Over the radial extent of these three tracers of spiral structure and recent star formation, the rotation curve is relatively insensitive to n_T.

$\langle c_\varpi^2\rangle^{1/2}$, Shu *et al.* suggest that it should have a value near unity in the central regions where a well-mixed state of equilibrium might be expected to prevail, and it probably reaches a value substantially less than unity in the outer regions where the motions perpendicular to the galactic plane are substantially decoupled from those parallel to it. For definiteness, we thus adopt the following relation:

$$\langle c_z^2\rangle^{1/2}/\langle c_\varpi^2\rangle^{1/2} = 1.0 - 0.5(\varpi/\varpi_{\text{edge}}), \qquad (2)$$

where ϖ_{edge} is taken to correspond to the observed Holmberg radius of the galaxy.

To determine $\langle c_\varpi^2\rangle^{1/2}$, we specify it as a ratio of the actual radial velocity dispersion to the minimum required to suppress all axisymmetric gravitational instabilities, $Q = \langle c_\varpi^2\rangle^{1/2}/\langle c_\varpi^2\rangle_{\min}^{1/2}$. Toomre (1964) showed how $\langle c_\varpi^2\rangle_{\min}^{1/2}$ could be determined for a stellar disk of infinitesimal thickness, and Shu *et al.* (1971) summarized the generalization given by Shu (1968) and Vandervoort (1970) for stellar disks of finite thickness. The results applied to the solar neighborhood show Q to be close to unity, but it may be substantially larger in the central regions of the Galaxy if the barlike instability is to be suppressed (see, e.g., Kalnajs 1972; also Toomre 1974; Wielen 1974). On the other hand, if we allow ourselves the freedom to vary Q arbitrarily with ϖ, we could fit almost any observed spiral pattern with arbitrary accuracy. To eliminate this degree of freedom, we adopt in this paper the hypothesis

$$Q = 1.0 \tag{3}$$

throughout the disk. We have examined the effect of varying Q and have found that better fits can often be obtained by allowing Q to be somewhat larger than unity in the inner portions of a galaxy where our computed spiral patterns tend sometimes to be too tightly wound. However, the determination of Q is such a vexing question, both theoretically and observationally, that it would be well beyond the scope of the present paper to settle the issue here. We merely remark that by adopting hypothesis (3), our fits for the spiral pattern contain only one free parameter, the pattern speed Ω_p (or, equivalently, ϖ_c, the radius where the matter corotates with the spiral wave).

c) *Corotation Radius of Spiral Density Waves*

With an equilibrium model of the type just discussed, the theoretical pattern of density waves in the stellar disk can be computed from the known dispersion relationship once an estimate of the pattern speed Ω_p is made. The radius where corotation occurs, and consequently the speed Ω_p at which the pattern rotates, are expected to influence the radial extents of at least three easily observable tracers: (1) the prominent spiral structure, (2) the "easily visible" disk, and (3) the distribution of H II regions in the original rotation curve study. In this paper the pattern speed Ω_p is adopted so that the radius of corotation, ϖ_c, lies nearly coincident with the radial extents of all three tracers, or with some representative median when the tracers differ substantially in extent (as indicated in tables 1 and 2). For NGC 157, shown in figure 1, the radial extents of these three tracers of spiral structure and recent and current star formation are about the same, and a natural choice for the corotation radius is one coincident with the edges of all three. This criterion to estimate corotation is the standard applied in § IV to each of the 24 external galaxies.

d) *Shock Waves in the Interstellar Gas*

Galactic shock waves are found to form in the gaseous component of a galaxy as a necessary consequence of the theory for forced spiral waves of sufficiently large amplitude (W. W. Roberts 1969; Shu, Milione, and Roberts 1973; Woodward 1973). In our view galactic shocks provide the triggering mechanism for the gravitational collapse of gas clouds, eventually leading to the formation of stars along a spiral arm. For a given wave amplitude, the *strength of the shock and the degree of compression of the gas vary as the square of the ratio*, $w_\perp/a$, where $w_\perp$ is the total (unperturbed plus perturbed) velocity component of the gas normal to a spiral arm and a is the effective acoustic speed of the interstellar gas. If the two-component model of the interstellar medium is adopted, a is unlikely to be very different from the sound speed associated with the intercloud medium, 7–12 km s^{-1}, and a mean value of a in this range might be dictated by the atomic physics of all spiral galaxies.

On the other hand, $w_\perp$ oscillates along a streamline about its unperturbed value $w_{\perp 0}$ because of the forcing of the spiral gravitational field of fractional amplitude, F. Shocks form if F is sufficiently large to force $w_\perp$ to achieve transonic values. For $w_{\perp 0} > a$, most of the gas on the streamline is moving at supersonic speeds while only a small portion is moving subsonically. The shocks that form in this situation tend to be *strong* and give rise to *narrow* regions of *high* gas compression. For $w_{\perp 0} < a$, most of the gas on the streamline is moving subsonically while only a small portion travels supersonically. In this situation the shocks tend to be *weak* and yield rather *broad* regions of relatively *low* gas compression (Shu *et al.* 1973). Therefore, the strength of the shock and compression of the gas and the consequent theoretical differentiation between spiral structure with *narrow* "filamentary" arms and *broad* "massive" arms seem to be critically dependent on the quantity

$$w_{\perp 0} = \varpi(\Omega - \Omega_p) \sin i\,, \tag{4}$$

where i is the pitch angle of the wave pattern which is to be obtained from the dispersion relationship once Ω_p is given.

Figure 2 shows the theoretical curves of $w_{\perp 0}$, i, and F in the sample galaxy NGC 157 for several different choices of the pattern speed Ω_p. The two-headed arrows indicate the range of radii for which the asymptotic calculations are considered numerically reliable (in accordance with the criteria adopted by Shu *et al.* 1971). The corresponding curves of each set appear to be rather similar and are relatively insensitive to the choice of pattern speed. Each of the curves of $w_{\perp 0}$, for example, attains a peak of moderate to large magnitude in the range of 15–20 km s^{-1}, and this indicates that moderately strong shocks are possible. NGC 157 is therefore one sample galaxy in which moderately well developed spiral structure would be predicted to be possible. The value of $w_{\perp 0}$ at about one-half the corotation radius appears to be a rather typical value representative of the magnitude of $w_{\perp 0}$ over a substantial portion of the "easily visible" disk, and for future comparison of a number of galaxies with one another this value of $w_{\perp 0}$ at one-half corotation in each galaxy is frequently used. Fortunately, the quantity $w_{\perp 0}$ is independent of the assumed distance, and therefore any uncertainty stemming from the estimates of distances of various galaxies will not enter here. Partly for this reason and partly for the reason that $w_{\perp 0}$ is relatively insensitive to the choice of corotation radius, $w_{\perp 0}$ will be one of the most important parameters to be used in comparing various galaxies in later sections.

Contained in figure 3 is a photograph of the sample galaxy NGC 157 with its moderately well developed spiral arms taken from the Hubble Atlas (Sandage 1961). The moderately well developed spiral structure is thought to be a consequence of the moderately strong shocks possible in this galaxy. For the purpose

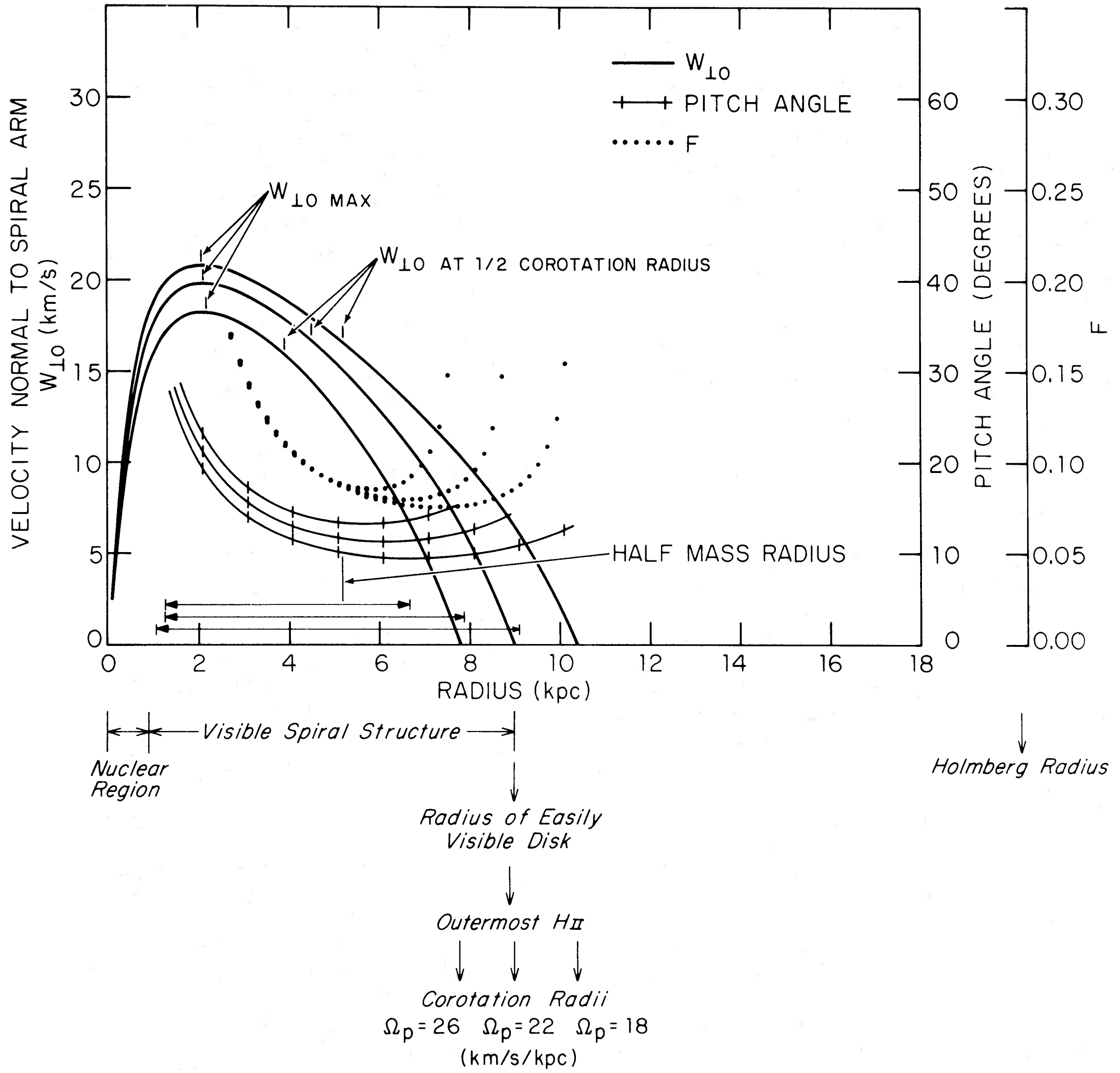

FIG. 2.—Characteristics of the wave pattern in the density wave model of the sample galaxy NGC 157. The quantity $w_{\perp 0}$ measures the velocity component of basic rotation normal to a spiral arm; i, the theoretical pitch angle of the same wave arm; and F, the ratio of the magnitude of the spiral gravitational field of the wave pattern to that of the central axisymmetric field. To show their dependence on the pattern speed, $w_{\perp 0}$, i, and F are sketched for each of three values of pattern speed Ω_p. The corresponding curves of the three sets are all rather similar and actually rather insensitive to the value of Ω_p. The galactic shock wave is viewed as a possible triggering mechanism for star formation along a spiral arm, and the strength of the shock can be estimated by the square of $w_{\perp 0}$. Since $w_{\perp 0}$ attains a substantial level for all cases in the range, 15–20 km s^{-1}, over a large region of the disk, moderately strong shocks are possible; and NGC 157 is capable of exhibiting moderately well-developed spiral structure over its disk.

of illustrating the sensitivity of the theoretical pattern to choice of pattern speed, this photograph has superposed on it the theoretical patterns calculated for two of the possible choices of pattern speed, $\Omega_p = 22$ and 26 km s^{-1} kpc^{-1}, illustrated in figure 2. Each pattern is sketched over a radial extent equivalent to its range of validity. Both patterns coincide well with the observed spiral structure; however, the more extensive pattern for $\Omega_p = 22$ km s^{-1} kpc^{-1} seems to satisfy better the criterion for corotation and to cover the radial extents of the prominent spiral structure and "easily visible" disk (and distribution of H II regions) a little more completely. For this reason, this pattern with corotation at 9 kpc is adopted for NGC 157. Since it is sketched only over its range of validity, 1.2–7.8 kpc, the adopted pattern is somewhat more extensive than the sketch might appear to indicate. Corotation at 9 kpc therefore lies about 15 percent farther out in the disk than the outermost point of the sketch at 7.8 kpc.[5]

---

[5] The theoretical behavior of spiral density waves near corotation is more complicated, even in the linear regime, than has been previously assumed. Mark (1974*b*; see also in Lin 1970, Feldman and Lin 1973) has shown that the trailing free-wave configuration near corotation cannot be represented as a single continuous wave, but must comprise three waves—

III. THEORETICAL CATEGORIZATION OF SPIRAL GALAXIES

In the preceding section the synthesis of axisymmetric models of disk galaxies with the density wave theory provides the theoretical framework for a deeper understanding of the important quantities $w_{\perp 0}/a$ and i, which are suggested to characterize wave phenomena among spiral galaxies. The quantity $w_{\perp 0}/a$ measures the tendency for the production of *strong* shocks with *narrow* regions of *high* gas compression. However, since we have already reasoned that a may have very similar values for all spiral galaxies, we will thus regard $w_{\perp 0}$ and i as the two important quantities which characterize wave phenomena in spiral galaxies. Dimensional analysis shows that typical values of $w_{\perp 0}$ and i (say, at half the corotation radius) can be expressed as

$$w_{\perp 0} = (GM/\varpi_c)^{1/2} f(\varpi_{0.5M}/\varpi_c) , \tag{5a}$$

$$\sin i = g(\varpi_{0.5M}/\varpi_c) , \tag{5b}$$

where f and g are functions whose forms are specified once the equilibrium disk has been specified except for scale factors. In equation (5a), G is the universal gravitational constant and M is the total mass of the galaxy. The combination GM/ϖ_c is a measure of the potential energy divided by the mass of the galaxy. Thus, we arrive at the fundamental conclusion of this paper: *The two critical and fundamental parameters which underlie the determination of the characteristics and the geometric form of normal spirals are M/ϖ_c (or, equivalently, $M/\varpi_{0.5M}$) and $\varpi_{0.5M}/\varpi_c$.*[6] In §§ IV and V we shall show that the categorization of galaxies by these two parameters correlates well with the accepted classification of galaxies within the observed sequences of luminosity class and Hubble type.

Figure 4 illustrates a practical application of these ideas. Plotted on the vertical axis is $w_{\perp 0}$ evaluated at half-corotation for an ensemble of hypothetical galaxies whose basic mass distribution is given by Toomre's model 5. The corresponding surface generated by computing $w_{\perp 0}$ for different values of $M/\varpi_{0.5M}$ and $\varpi_{0.5M}/\varpi_c$ will be referred to as the $w_{\perp 0}$ surface. In this figure, it has been calculated by considering a grid at equal intervals of $M/\varpi_{0.5M}$ and $(\varpi_{0.5M}/\varpi_c)^{-1}$.

The value of $w_{\perp 0}(0.5\varpi_c)$ for a given galaxy with specified mass M and specified half-mass radius $\varpi_{0.5M}$ can be determined along this surface for each of several different choices of the galaxy's pattern speed. The sequence of locations will follow a given curve of constant $M/\varpi_{0.5M}$. As an example, the black dots indicate the values of $w_{\perp 0}(0.5\varpi_c)$ for the sample galaxy NGC 157 for six different pattern speeds (so indicated in parentheses). For Ω_p small, the radius at half corotation is near inner Lindblad resonance and the value of $w_{\perp 0}$ is small. As Ω_p is increased, ϖ_c decreases and both $\varpi_{0.5M}/\varpi_c$ and i increase. At first, $w_{\perp 0}$ increases with $\sin i$ until a maximum is reached on the ridge of the $w_{\perp 0}$ surface. Here the rate of decrease of $(\Omega - \Omega_p)\varpi$ overtakes the rate of increase of $\sin i$ as Ω_p is further increased, and $w_{\perp 0}$ decreases slowly thereafter with increasing Ω_p and $\varpi_{0.5M}/\varpi_c$. All six cases of pattern speed are sketched here for the purpose of illustration only, since the criterion adopted for determining corotation has already been applied to NGC 157 in the previous section to yield the selection of $\Omega_p = 22$ km s^{-1} kpc^{-1} as the best estimate. For NGC 157, as for all galaxies to be considered later, ϖ_{edge} is taken as the observed Holmberg radius. On the other hand, the ensemble spanning the surface consists of cases in which ϖ_{edge} is taken as the typical scale A_T for each case. For this reason, NGC 157 is actually displaced slightly from the surface in several of the cases (as indicated by the very short vertical lines above several of the black dots). The three coordinates in this representation are ideal in the sense that they are distance-independent parameters, and any uncertainty that may be present in the estimate of distance of a galaxy does not enter here.

IV. RESULTS FOR TWENTY-FOUR EXTERNAL GALAXIES AND OUR OWN GALAXY

From the sample of galaxies with published rotation curves (except those for the Magellanic Clouds), 24 galaxies are selected on the basis of the following criteria: (1) The galaxy has a luminosity class assigned by van den Bergh (1960*a*, *b*) and, (2) the rotation curve extends, and is complete in its coverage, over a significant fraction of the photometric radius of the galaxy. When more than one rotation curve is available, the one chosen is indicated in the references to table 1. Specific comments regarding the radial velocity data for individual galaxies are noted in the Remarks column in table 1. Other entries in this table include van den Bergh's (1960*a*, *b*) type classification (col. [2]), and luminosity class (col. [3]). Because these type classifications are based on the small scale (and often dense images) of the Palomar Sky Survey, column (4) is added to give the classifications of the *Reference Catalogue of Bright Galaxies* (de Vaucouleurs 1964). With two exceptions, NGC 972 and NGC 3593, these two type classifications agree to within one class; most, to within half a class. The adopted distance, column (5), and inclination, angle between the principal plane of the galaxy and the plane of the sky, column (6), are taken from the original reference for the rotation curve data, column (10): Burbidge and Burbidge (BB); Burbidge *et al.* (1964) (BBCRP); Burbidge, Burbidge, and Prendergast (BBP); van Damme (1966) (van D); Demoulin (1969) (D); Fish (1961) (F); Gordon (1971)

---

two short waves which propagate radially in opposite directions and one long wave which propagates from the interior. Our modelings do not attempt to incorporate these effects, nor do they attempt to give an accurate representation of the behavior near the Lindblad resonance along the lines developed by Mark (1974*a*). Thus, our sketches of the spiral patterns show only the ranges of radii where the inwardly propagating short waves are expected to predominate in their usual simple form.

[6] Ostriker and Peebles (1973) point out that the dimensionless quantity, the ratio of a galaxy's rotational kinetic energy and its gravitational potential energy, determines its basic shape (i.e., flatness). This third dimensionless parameter plays no role in our work because we restrict our attention to galaxies of one basic shape, namely, disk galaxies.

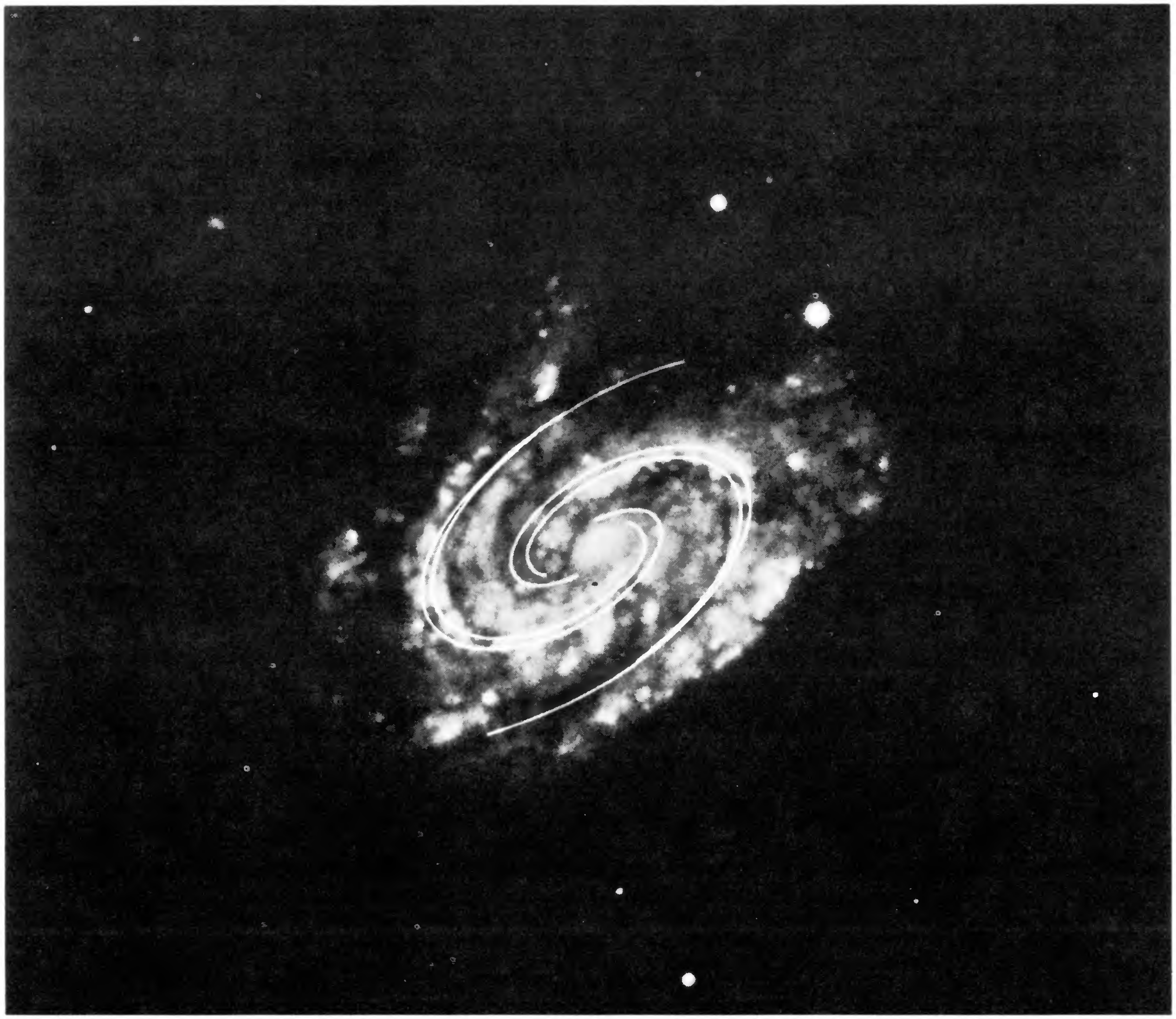

FIG. 3.—Photograph of the sample galaxy NGC 157 with its moderately well developed spiral arms taken from the Hubble Atlas. The wave patterns for two values of the pattern speed Ω_p (22 and 26 km s^{-1} kpc^{-1}) are superposed to illustrate the sensitivity to Ω_p. The more extensive pattern for $\Omega_p = 22$ km s^{-1} kpc^{-1} is adopted since it better satisfies the criterion for corotation and covers more adequately the radial extent of the observed spiral structure and "easily visible" disk. This pattern is sketched only over its range of validity, 1.2–7.8 kpc, and corotation at 9 kpc actually lies about 15% farther out in the disk from the edge of the sketch (at 7.8 kpc).

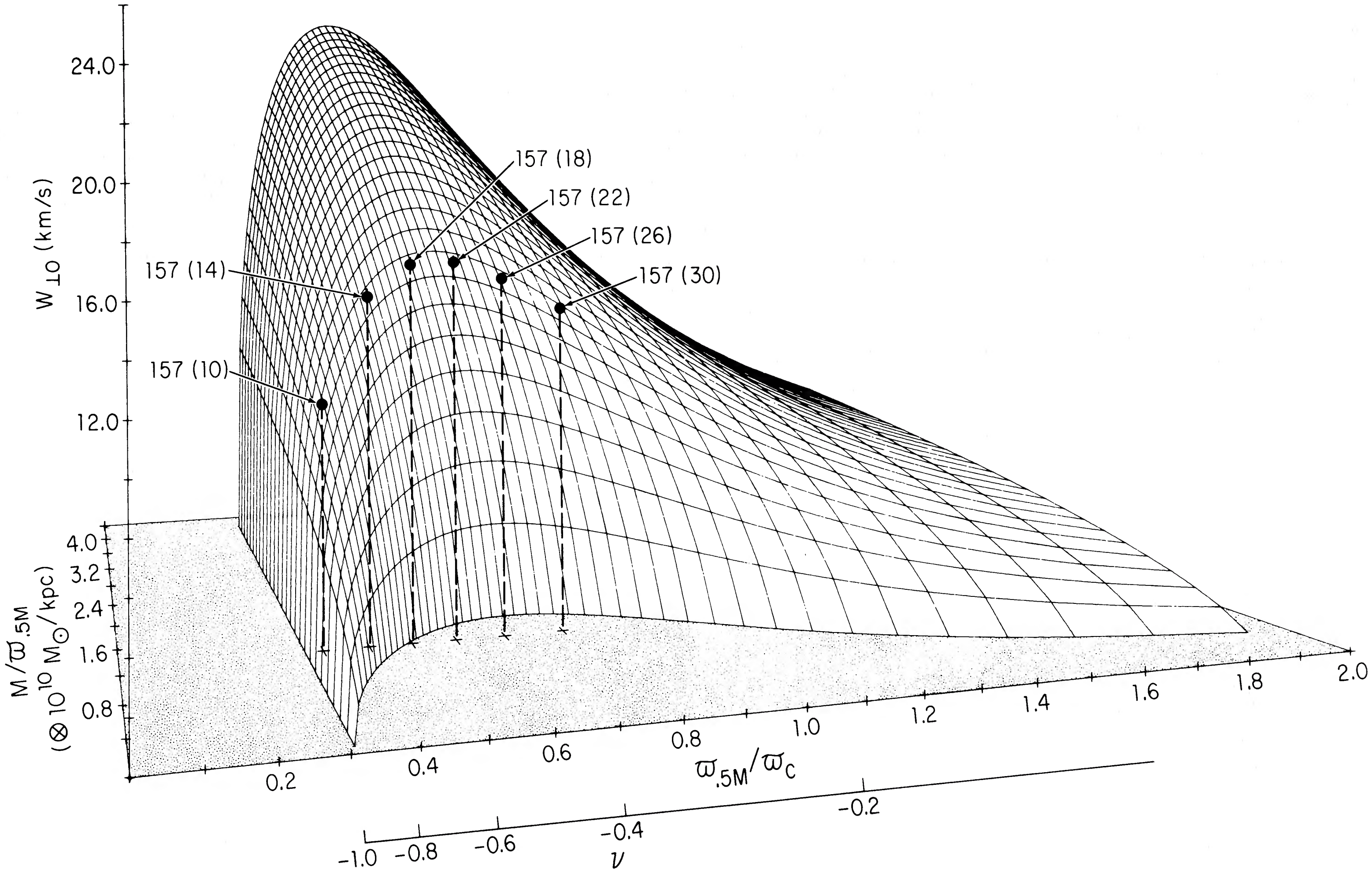

FIG. 4.—Theoretical categorization of disk-shaped galaxies; a representation of an ensemble of cases, spanning the two dimensional parameter space: $M/\varpi_{0.5M}$, $\varpi_{0.5M}/\varpi_c$. The mass model simulating the equilibrium state for each case in the ensemble is one of Toomre type, with no spheroidal components superposed, and ϖ_{edge} is taken as the typical scale A_T for each case. The quantity $w_{\perp 0}$ is evaluated at half-corotation for all cases, and the $w_{\perp 0}$ surface so generated is a measure of the strength of the galactic shock possible over this ensemble. The sample galaxy NGC 157 is sketched in this representation for each of six different values of pattern speed to illustrate how the values for $w_{\perp 0}$ at half-corotation in a given galaxy might vary over this surface with Ω_p. For reasonable values within the earlier adopted neighborhood of Ω_p = 22 km s^{-1} kpc^{-1}, the variation of $w_{\perp 0}$ is not great.

TABLE 1

OBSERVATIONAL DATA

NGC (1)	Type (van den Bergh) (2)	Luminosity Class (van den Bergh) (3)	Type (de Vaucouleurs) (4)	Distance (Mpc) (5)	Inclination (degrees) (6)	Radius of Easily Visible Disk (kpc) (7)	Radius of Outermost H II Region (kpc) (8)	Holmberg Radius (kpc) (9)	References (10)	Remarks (11)
157........	Sc(*)	I	SAB(rs)bc	24.0	58.6	9.0	8.9	20.2	BBP 1961*b*	
224........	Sb	I–II	SA(s)b	0.69	77.0	13.0	22.5	19.8	RF 1970	
598........	Sc	II–III	SA(s)cd	0.72	55.0	4.8	5.2	8.7	G 1971, RS 1972	
925........	S(B)c	II–III	SAB(s)d	6.8	53.0	7.7	9.0	13.8	RBB 1964, RRW 1967	7
972........	Sc(n)	II:	I0	22.1	66.3	4.7	4.0	(15.4)	BBP 1965	1
1084........	Sc	I–II	SA(s)c	19.2	65.0	5.2	5.2	(12.9)	BBP 1963	1
1832........	Sc	II	SB(r)bc	25.3	60.0	6.0	6.1	(16.2)	BB 1968	1
2403........	Sc	III	SAB(s)cd	3.25	60.0	4.6	6.7	13.7	RS 1972	
2903........	Sb$^+$	I–II	SAB(rs)bc	7.9	70.0	12.6	5.3	16.1	BBP 1960*b*	3
3031........	Sb	I–II	SA(s)ab	3.2	55.0	8.9	16.2	16.3	M 1959	
3109........	Ir$^-$	IV–V	Im sp	2.2	90.0	6.0	3.1	(5.9)	van D 1966	1
3389........	Sc*	III:	SA(s)c	15.0	62.0	3.2	2.6	(8.7)	RF 1967	1
3521........	Sb$^+$	II	SAB(rs)bc	8.5	65.5	6.2	7.3	16.8	BBCRP 1964	
3593........	Sb	III	SA(s)0/a:	7.0	75.0	1.2	4.1	(7.0)	D 1969	1
4236........	SB$^+$ or Ir$^+$	IV	SB(s)dm	3.25	75.0	9.6	. . .	12.3	S 1973	
4631........	Sc*	III?	SB(s)dsp	4.4	85.0	7.3	7.0	12.2	de V, de V 1963	
5005........	Sb$^-$	II	SAB(rs)bc	14.4	66.0	8.0	5.7	16.8	BBP 1961*a*	
5055........	Sb$^+$	II	SA(rs)bc	7.3	58.6	6.5	7.3	17.0	BBP 1960*a*, F 1961	
5194........	Sc(t)	I	SA(s)bcp	4.0	35.0	5.0	5.5	8.3	BB 1964, T 1972	6
5457........	Sc	I	SAB(rs)cd	6.9	22.0	15.5	15.3	28.1	RS 1972	
6946........	Sc	I (or II)	SAB(rs)cd	10.1	30.0	12.3	11.9	(27.9)	RS 1972	2
7331........	Sb	I–II	SA(s)bc	14.4	69.1	18.4	(10.4)	28.5	RBBCP 1965	4
7479........	SBb$^+$	I	SB(s)c	35.2	44.5	15.6	(11.6)	(31.3)	BBP 1960*c*	1, 5
IC342.......	Sc	I	SAB(rs)cd	4.5	25.0	11.0	. . .	(26.1)	RS 1972	2

REMARKS TO TABLE 1

1. Holmberg radius from M. S. Roberts (1969), eq. (2).
2. Holmberg radius from Rogstad and Shostak (1972).
3. Corotation radius adopted as radius of outermost H II region.
4. Five outermost velocity data points are assigned low weight and are not used in the determination of the rotation curve because of their large scatter. Upon exclusion of these five H II regions, the next outermost H II region at 10.4 kpc is adopted as the corotation radius.
5. Four outermost velocity data points are assigned low weight and are not used in the determination of the rotation curve because of their large scatter. The radius of the "easily visible" disk is adopted as the corotation radius.
6. Two sources of velocity data are considered from the published literature. First, the velocity data from Burbidge and Burbidge (1964) is adopted to determine a rotation curve; and a corresponding density wave pattern is computed with $\Omega_p = 42$ km s^{-1} kpc^{-1}. Second, the velocity data from Tully (1972) is adopted to determine a rotation curve; and a corresponding density wave pattern is computed with $\Omega_p = 90$ km s^{-1} kpc^{-1} (later referred to as 5194$_T$ or 5194*).
7. To extend the range in radius, one data point at 7 kpc from 21-cm measurements by Rogstad *et al.* (1967) is added to the optically measured data.

TABLE 2

Theoretical Results

NGC (1)	Components of Equilibrium Model			Mass M ($\times 10^{10}\ M_\odot$) (5)	Half-Mass Radius $\varpi_{0.5M}$ (kpc) (6)	Pattern Speed Ω_p (km s^{-1} kpc^{-1}) (7)	Corotation Radius ϖ_c (kpc) (8)	Central Mass Concentration $\varpi_{0.5M}/\varpi_c$ (9)	Velocity $(\Omega-\Omega_p)\varpi$ (km s^{-1}) (10)	Pitch Angle i ($0.5\varpi_c$) (degrees) (11)	Velocity $w_{\perp 0}(0.5\varpi_c)$ (km s^{-1}) (12)
	$n_T = 5$ (2)	$n_s = 5$, $e_s = 0.8661$ (3)	$n_s = 5$, $e_s = 0.9880$ (4)								
157......	T			6.8	5.2	22.0	9.0	0.58	78.1	12.3	16.7
224......	T	*S*	*S*	17.8	7.0	18.0	14.0	0.50	129.7	9.5	21.5
598......	T	*S*		1.3	3.5	32.0	2.8	1.24	24.8	19.6	8.3
				(1.9)	(4.7)	(32.0)	(2.8)	(1.67)	(31.3)	(16.0)	(8.7)
925......	T			1.8	4.9	14.0	7.7	0.64	35.1	14.4	8.7
972......	T			1.0	1.8	29.0	4.0	0.46	67.1	8.8	10.2
1084......	T	*S*		1.9	2.4	27.0	5.2	0.45	80.6	8.6	12.1
1832......	T	*S*		4.1	3.2	31.0	6.0	0.53	86.4	10.5	15.7
2403......	T	*S*		2.3	4.5	25.0	4.8	0.93	26.8	19.9	9.1
				(3.5)	(6.1)	(24.0)	(4.8)	(1.26)	(36.2)	(17.4)	(10.8)
2903......	T			4.3	2.7	38.0	5.4	0.51	101.9	10.2	18.0
3031......	T	*S*		12.5	5.5	26.0	9.7	0.57	103.1	11.8	21.0
3109......	T			0.5	6.3	8.0	6.0	1.04	6.2	26.1	2.7
3389......	T			2.2	2.3	65.0	2.6	0.87	31.6	20.8	11.2
3521......	T	*S*		8.1	3.2	33.0	7.3	0.44	137.3	8.4	20.2
3593......	T	*S*		0.2	0.4	80.0	1.2	0.37	73.7	5.4	6.9
4236......	T	*S*		1.7	6.9	9.0	9.6	0.72	25.1	16.0	6.9
4631......	T	*S*		2.5	6.2	15.0	7.3	0.84	23.1	19.9	7.9
5005......	T	*S*		7.3	2.4	27.0	8.0	0.31	180.8	3.9	12.2
5055......	T	*S*		5.8	2.1	32.0	6.6	0.31	177.6	4.0	12.4
5194*.....	T	*S*		3.3	2.6	42.0	4.5	0.58	77.7	11.7	15.7
				[2.4]	[1.2]	[90.0]	[2.4]	[0.51]	[106.9]	[9.6]	[17.9]
5457......	T	*S*		14.5	10.9	13.0	15.5	0.70	58.9	15.7	15.9
				(19.4)	(13.5)	(13.0)	(15.5)	(0.87)	(58.0)	(16.8)	(16.7)
6946......	T	*S*		11.5	8.1	17.0	12.3	0.66	68.4	14.2	16.7
				(19.7)	(12.0)	(16.0)	(12.3)	(0.98)	(74.8)	(14.2)	(18.3)
7331......	T	*S*		7.8	3.4	19.0	10.4	0.32	152.3	4.9	13.0
7479......	T			10.5	9.0	12.0	15.6	0.58	73.3	12.4	15.8
IC342.....	T	*S*		8.8	7.0	15.0	12.5	0.56	78.5	11.6	15.8
				(16.0)	(11.3)	(15.0)	(12.5)	(0.90)	(71.3)	(13.8)	(17.0)
Our Galaxy..	T	*S*		13.1	6.0	13.5	15.7	0.38	148.1	6.9	17.7

* Two extensive and independent rotation curve studies are available for this galaxy, NGC 5194. These are treated separately here. The first is from Burbidge and Burbidge (1964); the second is from Tully (1972).

1975ApJ...196..351C

(G); Münch (1959) (M); Rogstad, Rougoor, and Whiteoak (RRW); Rogstad and Shostak (1972) (RS); Rubin, Burbidge, and Burbidge (1964) (RBB); Rubin *et al.* (1965) (RBBCP); Rubin and Ford (RF); Shostak (1973) (S); Tully (T); and de Vaucouleurs and de Vaucouleurs (de V, de V). The radius of the easily visible disk, column (7), is based on eye estimates made by the authors. Column (8) gives the radius of the outermost H II region, which is taken from either Hodge (1967) or the furthermost H II region measured in the long-slit spectroscopic studies of these galaxies. The Holmberg radius, column (9), in kpc is either taken from the angular measurements by Holmberg (1958) or converted to his system from diameters given in the *Reference Catalogue of Bright Galaxies* through the relation given by M. S. Roberts (1969; those converted are indicated by parentheses).

Table 2 summarizes the theoretical results of the analysis described in § II as applied to 24 extragalactic systems plus our own Galaxy. Columns (2)–(4) indicate the number of components required in the mass model to fit the observed rotation curve data. Here T indicates a flat Toomre-type model and *S* refers to one or more spheroidal components. Column (5) contains the derived total mass. For several of the galaxies the rotation curve data is from 21-cm observations. Two masses are given in most of these cases: the value in parentheses represents the mass appro-

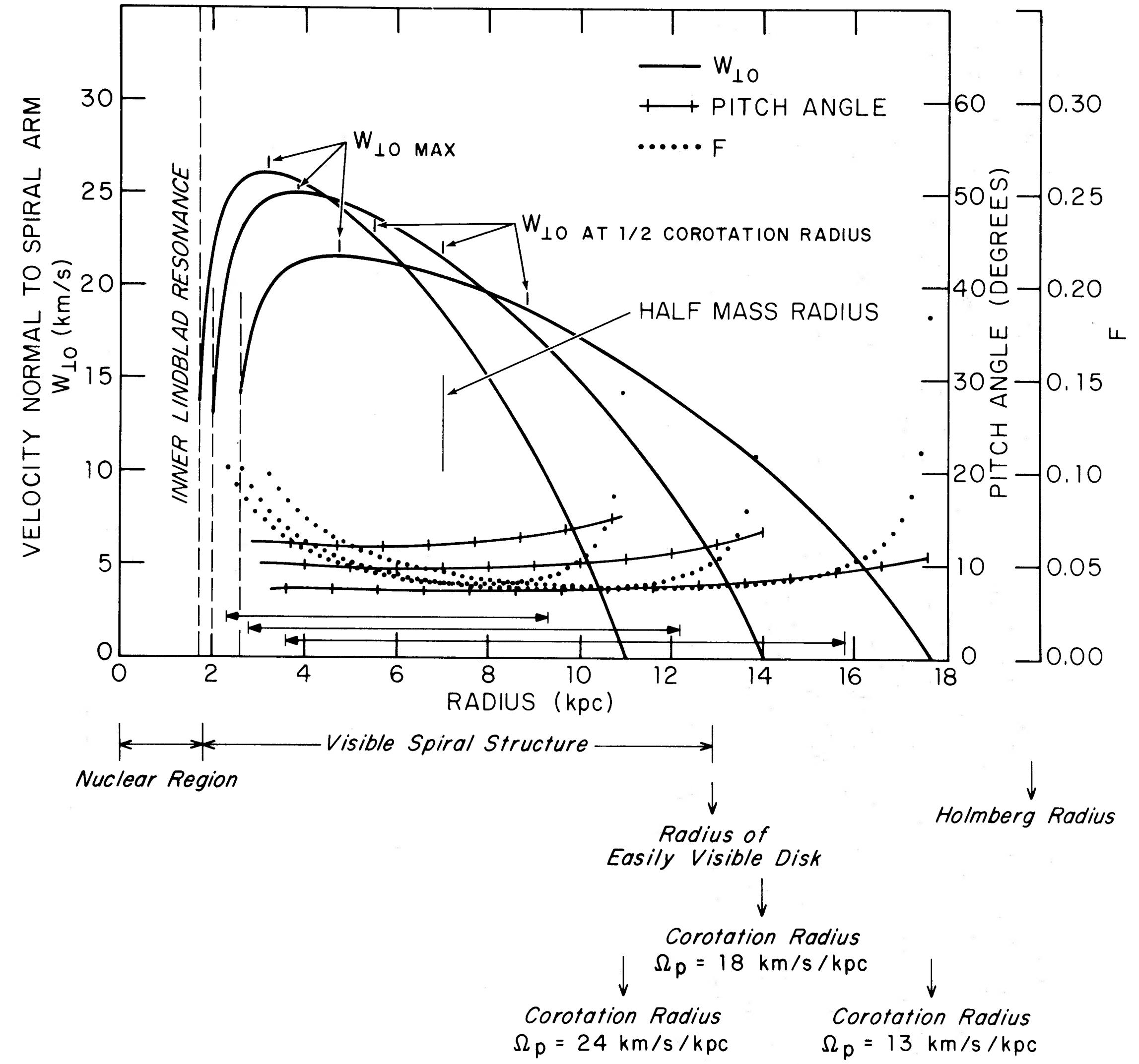

FIG. 5.—Characteristics of the density wave model of the sample galaxy NGC 224 (M31). The quantities $w_{\perp 0}$, i, and F are sketched for each of three values of the pattern speed Ω_p. Although the wide range of pattern speed spanned by these values almost doubles the possible radial extent of the pattern over the disk, the levels attained by $w_{\perp 0}$ are all rather similar and quite high, in the range 20–25 km s^{-1}. Since the distribution of H II regions extends well beyond everything else, corotation is thought to be more closely coincident with the radial extent of the visible spiral structure and the edge of the "easily visible" disk; and the pattern with Ω_p = 18 km s^{-1} kpc^{-1} is therefore adopted. Since $w_{\perp 0}$ is so large, strong shocks are possible.

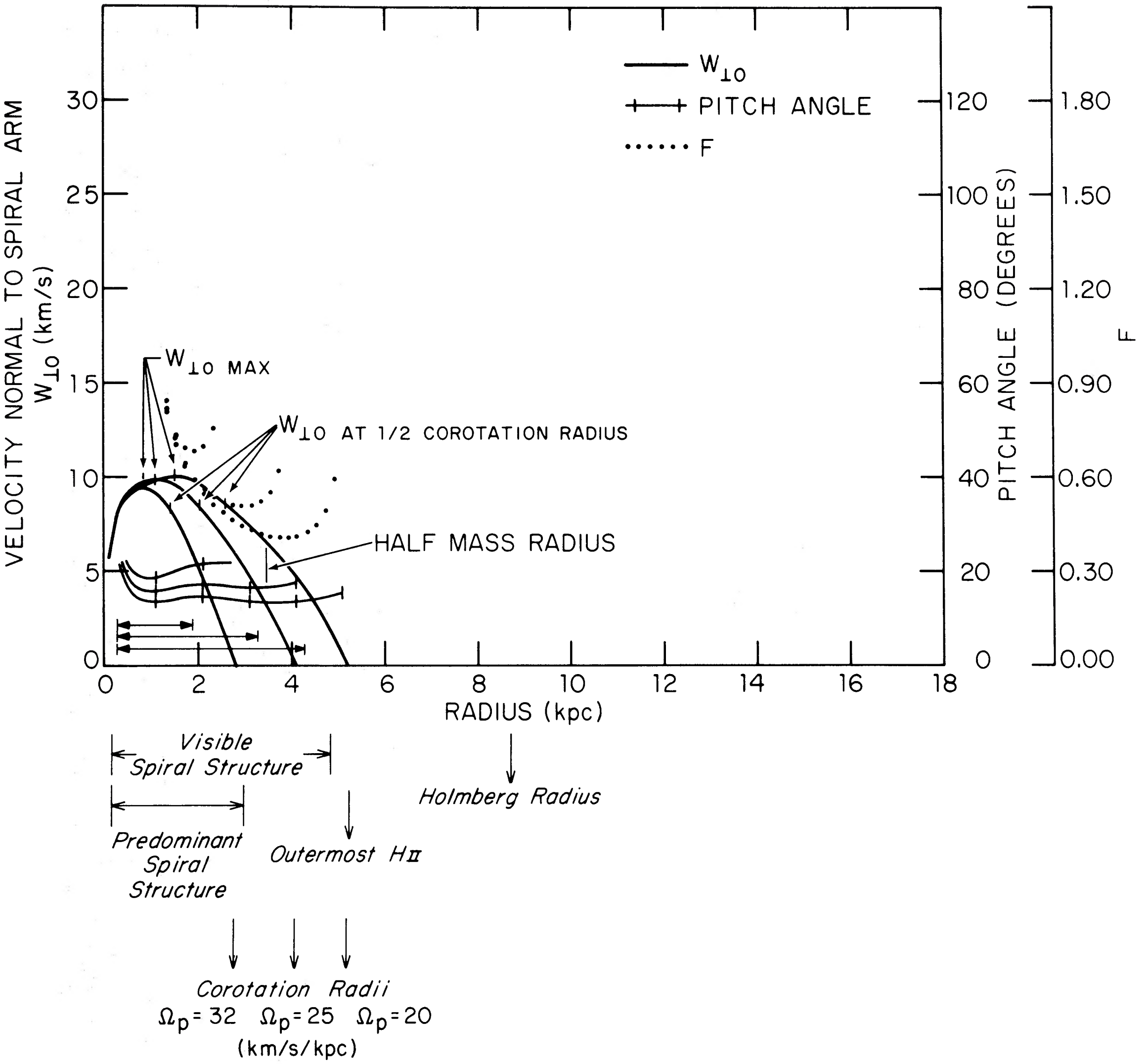

FIG. 6.—Characteristics of the density wave model of the sample galaxy NGC 598 (M33). The quantities $w_{\perp 0}$, i, and F are sketched for each of three values of Ω_p. In all three cases the levels attained by $w_{\perp 0}$ are quite low; and $w_{\perp 0}$, particularly at half corotation, remains insensitive to Ω_p. Although the distribution of H II regions and the visible spiral structure, with multiple arms in the outer parts, extend to about 5 kpc, the predominant spiral structure terminates about 2.8 kpc. For this reason the pattern with Ω_p = 32 km s^{-1} kpc^{-1} is adopted. Since $w_{\perp 0}$ is so small, only weak shocks, if any at all, are probable, and only patchy, "massive" spiral arms would be expected to be triggered.

priate to a model derived by fitting all the observed rotation curve data; the other value represents the mass appropriate to a model derived by fitting the observed rotation curve data only to a distance comparable to that covered by the optically derived data. This procedure is followed to show the uncertainty that arises from the differing observed limits in the various data available on rotation curves. For later discussion the first tabulated mass without parentheses is used. Column (6) lists the radius containing one-half the total mass. The following tabular entries relate to the application of the density wave theory. Column (7) contains the pattern speed Ω_p adopted according to the criterion for corotation discussed in § II*c*; column (8), the corresponding corotation radius ϖ_c; and column (9), the ratio of half-mass radius to corotation radius, $\varpi_{0.5M}/\varpi_c$. Column (10) gives the velocity of basic rotation relative to the pattern frame, evaluated at half-corotation, $(\Omega - \Omega_p)\varpi$. The theoretical pitch angle of the wave pattern, i, evaluated at half-corotation, is in column (11); and $w_{\perp 0}$, the velocity component of basic rotation normal to a spiral arm, also at half-corotation, is contained in column (12).

Shown in figures 5, 6, 7, and 8 are theoretical curves characterizing the density wave patterns determined for four sample galaxies: NGC 224 (M31), NGC 598 (M33); NGC 2403, and NGC 3031 (M81), respectively. The curves of $w_{\perp 0}$, i, and F are sketched for a number of possible choices of the pattern speed for each

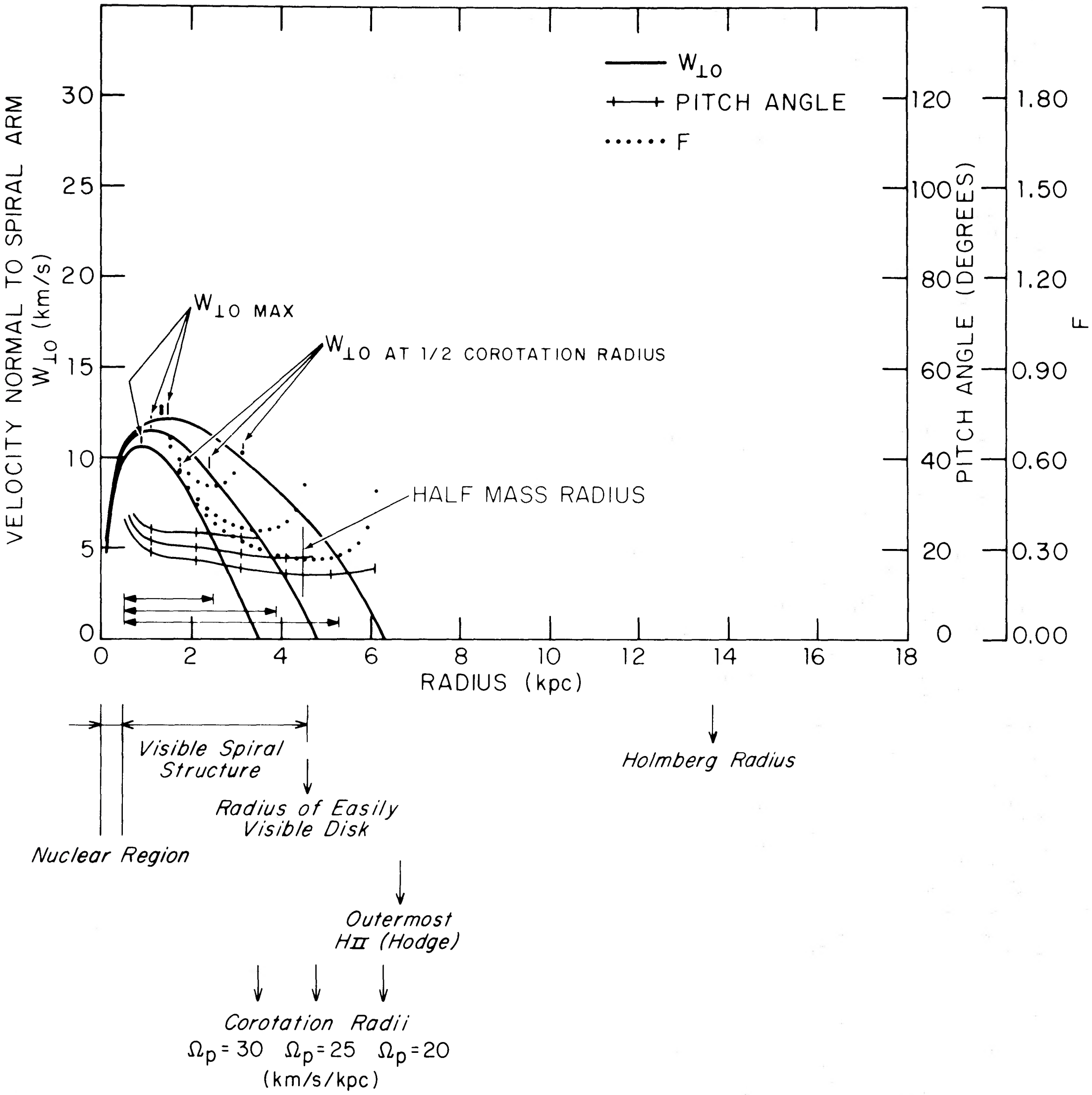

FIG. 7.—Characteristics of the density wave model for the sample galaxy NGC 2403. The quantities $w_{\perp 0}$, i, and F are sketched for each of three values of Ω_p. In all three cases the $w_{\perp 0}$ levels are low; and there is very little sensitivity of $w_{\perp 0}$ to Ω_p. In view of the radial extents of the visible spiral structure, the "easily visible" disk, and the distribution of H II regions, the pattern with Ω_p = 25 km s^{-1} kpc^{-1} appears to be a very reasonable choice; and this one is adopted. Because of the low level of $w_{\perp 0}$ here as in NGC 598 (M33), only weak shocks, if any at all, together with correspondingly patchy, "massive" spiral arms, would be probable.

galaxy. These curves for these galaxies exhibit rather well the general nature of the theoretical curves computed for all the galaxies in the sample. For example, the $w_{\perp 0}$ curves here, as for all galaxies considered, attain maxima coincident with the region of the visible spiral structure in the inner half of the disk. The superposition of three sets of curves for each galaxy illustrates that the magnitude of $w_{\perp 0}$ over its extent, and particularly at half-corotation, is very insensitive to different choices of pattern speed. The most striking case of this insensitivity is NGC 598, for which $w_{\perp 0}$ at half-corotation attains the nearly identical values of 8.3, 8.4, and 8.6 km s^{-1} although the possible choice of corotation radius is varied over a wide range. In accordance with the criterion for determining corotation discussed in § II*c*, corotation is adopted at 14.0, 2.8, 4.8, and 9.7 kpc corresponding to pattern speeds of 18, 32, 25, and 26 km s^{-1} kpc^{-1} for NGC 224, NGC 598, NGC 2403, NGC 3031, respectively. In comparing these four galaxies with one another, the most striking feature of comparison is reflected in the very high levels reached by $w_{\perp 0}$ in NGC 224 and NGC 3031 and the very low levels reached in NGC 598 and NGC 2403. Consequently, strong galactic shocks are possible in NGC 224 and NGC 3031, and for this reason these galaxies are thought to be capable of exhibiting well-developed spiral structure with *narrow*, "filamentary" spiral arms. On the other hand, in NGC 598 and NGC 2403 only very weak shocks, if any at all, would be probable,

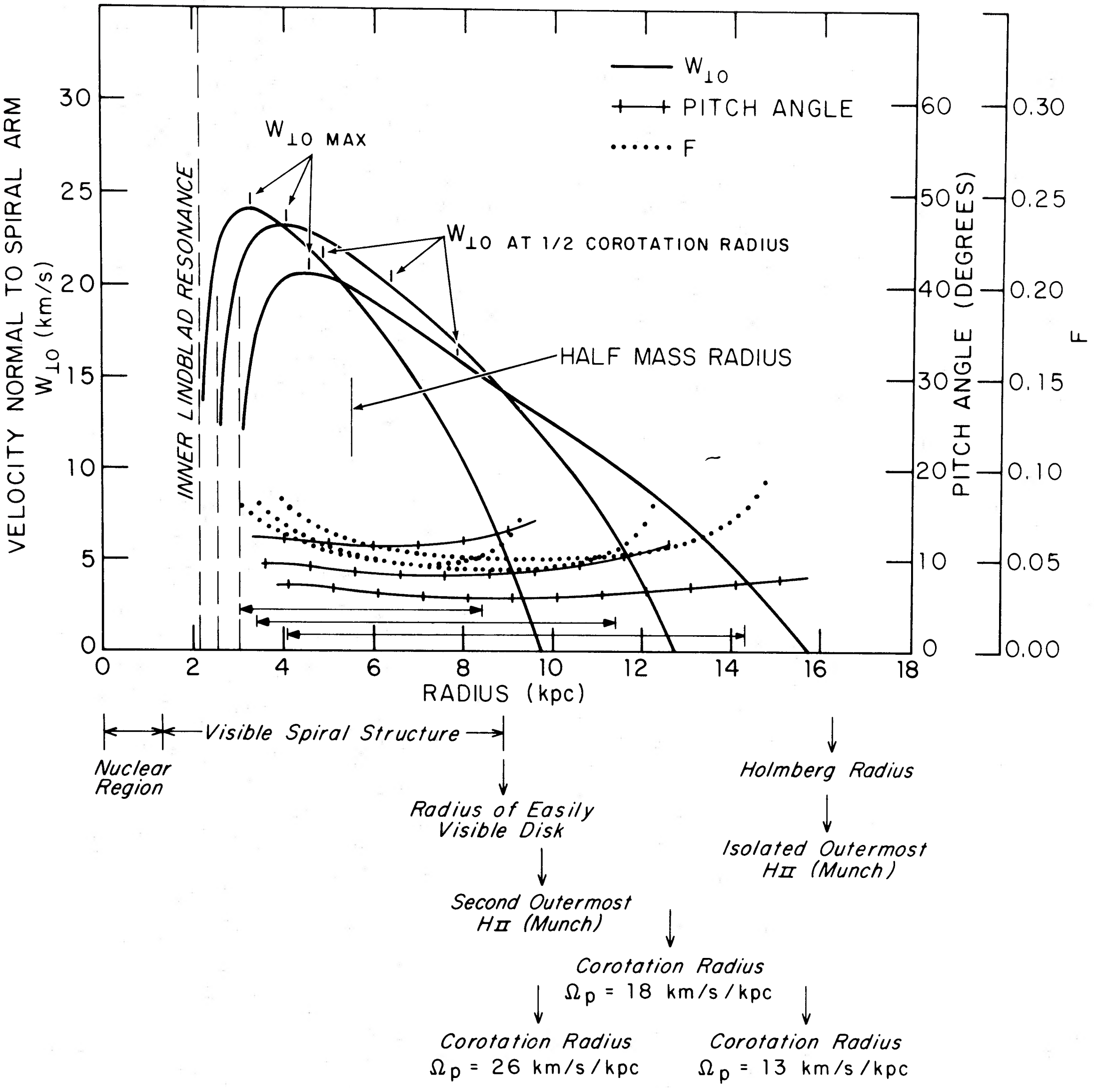

FIG. 8.—Characteristics of the density wave model for the sample galaxy NGC 3031 (M81). The quantities $w_{\perp 0}$, i, and F are sketched for each of three values of Ω_p. Here as in NGC 224 (M31), the levels attained by $w_{\perp 0}$ are quite high—in the range 20–25 km s^{-1}. The outermost H II region is an isolated one, and corotation is thought to be near the second outermost H II region which closely coincides with the radial extent of the visible spiral structure and the edge of the "easily visible" disk. The pattern with Ω_p = 26 km s^{-1} kpc^{-1} is therefore adopted. Since $w_{\perp 0}$ is so large, strong shocks and correspondingly well-developed "filamentary" spiral arms are possible.

and the corresponding spiral structure would be expected to be less well developed with *broad,* "massive" arms of a more fuzzy and patchy nature.

A photograph of the sample galaxy NGC 598 (M33), with its characteristically "massive" spiral arms taken from the Hubble Atlas, is shown in figure 9. This poorly developed spiral structure with rather broad, "massive" spiral arms is thought to be a consequence of the result that only very weak shocks, if any at all, are possible in this galaxy. Superposed is the computed wave pattern. The value of 2.8 kpc for the corotation radius coincides with that estimated by Dixon (1971) through his study of the age progression of stars across the southern spiral arm of M33 for radii greater than 3 kpc. The value of 32 km s^{-1} kpc^{-1} for the corresponding pattern speed is also within the bounds determined by Courtes and Dubout-Crillon (1971) through their study of the distribution of H II regions along the same arm of M33 for radii less than 2 kpc.

Figure 10 contains a photograph of the sample galaxy, NGC 3031 (M81), with its typically "filamentary" spiral arms taken from the Hubble Atlas. This well-developed spiral structure with narrow, "filamentary" spiral arms is thought to be a consequence of the rather strong shocks possible in this galaxy. Superposed is the computed wave pattern.

These sample galaxies, M33 and M81, shown in figures 9 and 10, are two of the three galaxies considered in Shu *et al.* (1971). It is advantageous to show these here, because the computed wave patterns appear somewhat different, primarily because of the different choices of corotation radius. The criterion for determining corotation adopted by Shu *et al.* (1971) is based solely upon the location of the outermost H II region, whereas the criterion adopted here is based upon a representative median of the radial extents of three tracers: the prominent spiral structure, the "easily visible" disk, and the distribution of H II regions. These two galaxies are prime examples of several galaxies in the sample in which the outermost patches of H II regions extend well beyond the prominent spiral structure; and it is primarily for this reason that the corotation radii adopted for M33 and M81 by Shu *et al.* (1971) are substantially greater than those adopted according to the criterion here.[7]

The theoretical wave patterns for 24 external galaxies plus our own Galaxy have been computed based upon the procedures followed and described for the sample galaxies: NGC 157 in § II; and NGC 224 (M31), NGC 598 (M33), NGC 2403, and NGC 3031 (M81) in this section. In order to compare these galaxies with each other, the fundamental parameters of total mass divided by the characteristic visible dimension of each galaxy, M/ϖ_c, and the degree of central mass concentration, $\varpi_{0.5M}/\varpi_c$, are considered together with their influence on $w_{\perp 0}$ and i. Figure 11 illustrates the $w_{\perp 0}$ surface generated by evaluating $w_{\perp 0}$ at half-corotation for the ensemble of hypothetical galaxies whose basic mass distribution is given by Toomre's model 5. The black dots indicate the locations of the 24 galaxies of the sample plus our own Galaxy with respect to this surface. All tend to lie along the general contour of the surface, although some are displaced somewhat above or below. For example, a galaxy such as NGC 224 or NGC 598, in which one or two spheroidal components are required in addition to a flat Toomre-type component, is displaced somewhat, primarily because of the additional mass of the spheroids.

The general nature of this surface is expected to be significant in determining the identity of a galaxy within the classification of galaxies. A galaxy with a mass distribution of moderate central concentration, as evidenced by the parameter $\varpi_{0.5M}/\varpi_c$ being near the value of 0.5, is found to lie near the ridge of the $w_{\perp 0}$ surface. Such a galaxy is capable of forming rather strong shock waves and is therefore predicted to have the capability of exhibiting well-developed "filamentary" spiral structure. The larger the mass of the galaxy, the higher along the ridge it can manifest itself, and the stronger the shocks to be predicted. NGC 157, NGC 224, and NGC 3031 are three prime examples where strong shocks would be predicted. On the other hand, a galaxy with a mass distribution of either very high or very low central concentration, as evidenced by the parameter $\varpi_{0.5M}/\varpi_c$ being substantially smaller or larger than 0.5, would lie along the surface at a level well below the ridge. A galaxy in this range would form only weak shocks, if any at all; and the corresponding spiral structure is expected to be less well developed and with "massive" spiral arms. Examples in which only weak shocks would be predicted are NGC 598, NGC 2403, and NGC 3109.

This $w_{\perp 0}$ surface represents an ensemble in which a value of 5 is assigned to the model number, n_T. Actually the entire sequence of values for n_T has been considered, as indicated in figure 1. Each such n_T value gives rise to a $w_{\perp 0}$ surface of the type sketched in figure 11. As n_T is assigned successive values along the sequence from large to small, the ridge of the corresponding $w_{\perp 0}$ surface shifts somewhat toward more positive $\varpi_{0.5M}/\varpi_c$. However, the overall nature of the surface and the relative locations of the galaxies lying along it remain unchanged; and for this reason the major characteristics illustrated here for $n_T = 5$ remain valid and invariant and apply over the entire sequence of n_T values (also see § VI and table 3).

V. CORRELATIONS WITH LUMINOSITY CLASS AND HUBBLE TYPE

This section investigates whether or not the concepts developed in the previous section correlate well with the observations.

a) Luminosity Class

Plotted in figure 12 along the vertical axis is the value of $w_{\perp 0}$ evaluated for each galaxy in our sample at half the radius of corotation. The galactic shock is expected to be strong in galaxies with high values of $w_{\perp 0}$ and weak in galaxies with low values of $w_{\perp 0}$. Plotted on the horizontal axis is the luminosity classification of van den Bergh (1960*a*, *b*). Figure 12 displays the predicted correlation between $w_{\perp 0}$ and the degree of development of spiral structure. Strong shocks with narrow regions of high gas compression are associated with galaxies with long, well-developed spiral arms; weak shocks with broad regions of relatively low gas compression are associated with galaxies with short, patchy spiral arms.[8]

The compressions reached in the spiral arms of 11 of the galaxies in our sample have been inferred observationally by van der Kruit (1973) from radio-continuum studies carried out using the Westerbork synthesis radio telescope. Comparison of our results with his for his subsample shows general agreement.

Strong shocks are expected not only to trigger well-developed "filamentary" arms but also to induce a high rate of star formation in a galaxy, if the gas content is sufficient; and this in turn should be reflected through a high surface brightness. This expectation seems to be consistent with the correlation found by van den Bergh between the intrinsic luminosity of a spiral galaxy and the "degree to which spiral structure is developed." Indeed, in figure 12 the galaxies with possible strong shocks are also the galaxies with high surface brightness.

---

[7] To be sure, the choice of corotation radius by our criterion provides a pattern speed for each of these galaxies in accord with the reasoning of Shu *et al.* (1971, p. 477): "If our determinations of the pattern speeds are to be revised at all, they should probably be revised upward."

[8] This correlation is found to be relatively insensitive to the choice of radius for evaluating $w_{\perp 0}$ in each galaxy; other radii which have been considered are quarter-corotation radius, half-mass radius, and the radius where $w_{\perp 0}$ takes on its maximum value (see, e.g., Roberts, Roberts, and Shu 1974 and Roberts 1974).

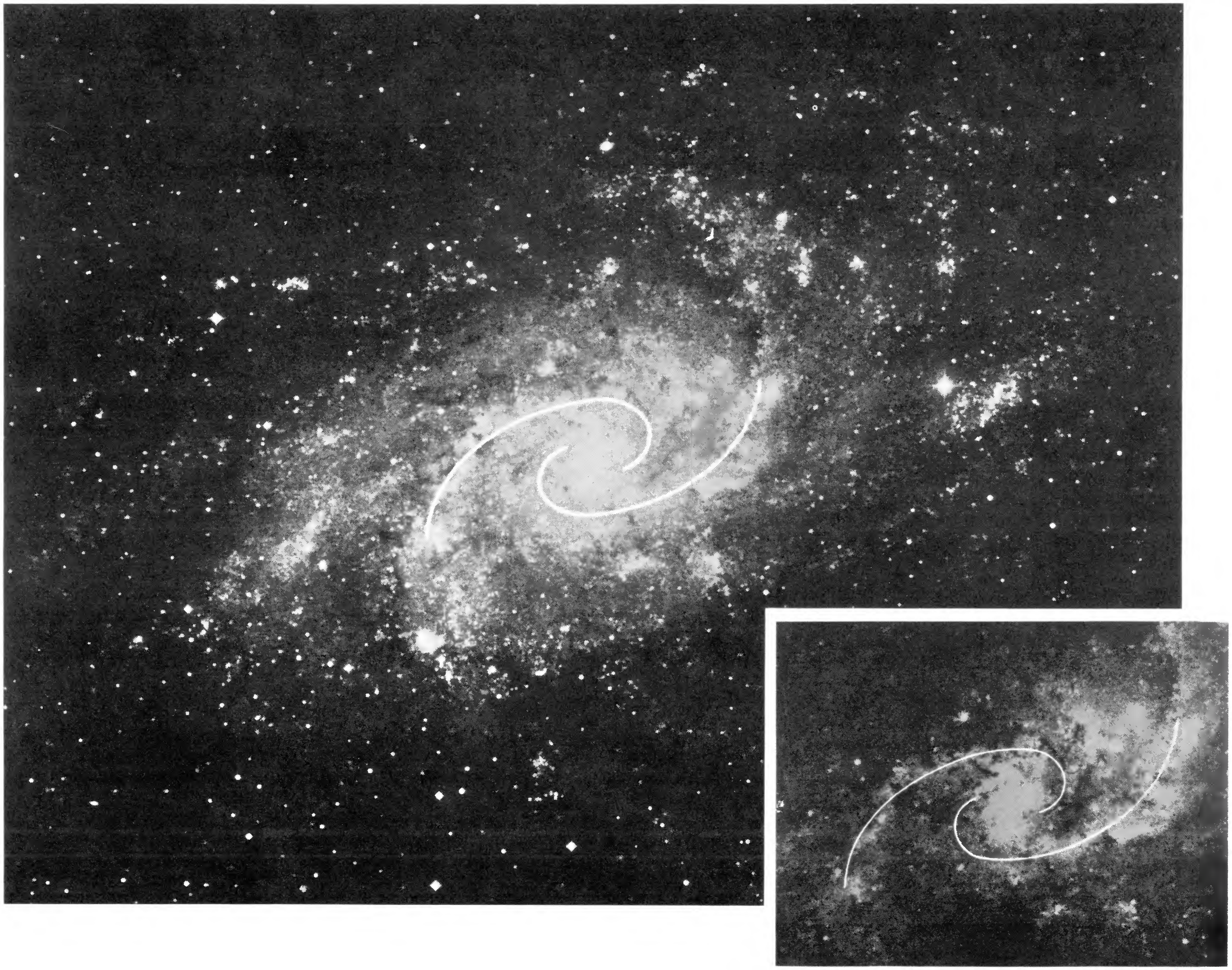

FIG. 9.—Photograph of the sample galaxy NGC 598 (M33) with its characteristically patchy, "massive" spiral arms, taken from the Hubble Atlas. The inserted photograph is one of the same scale but with less exposure. Superposed is the adopted wave pattern with $\Omega_p = 32 \text{ km s}^{-1} \text{ kpc}^{-1}$ in which only weak shocks, if any at all, are probable. The pattern is sketched over a radial extent equivalent to its range of validity: 0.4–1.8 kpc. Corotation at 2.8 kpc therefore lies about 56% farther out in the disk from the edge of the sketch (at 1.8 kpc).

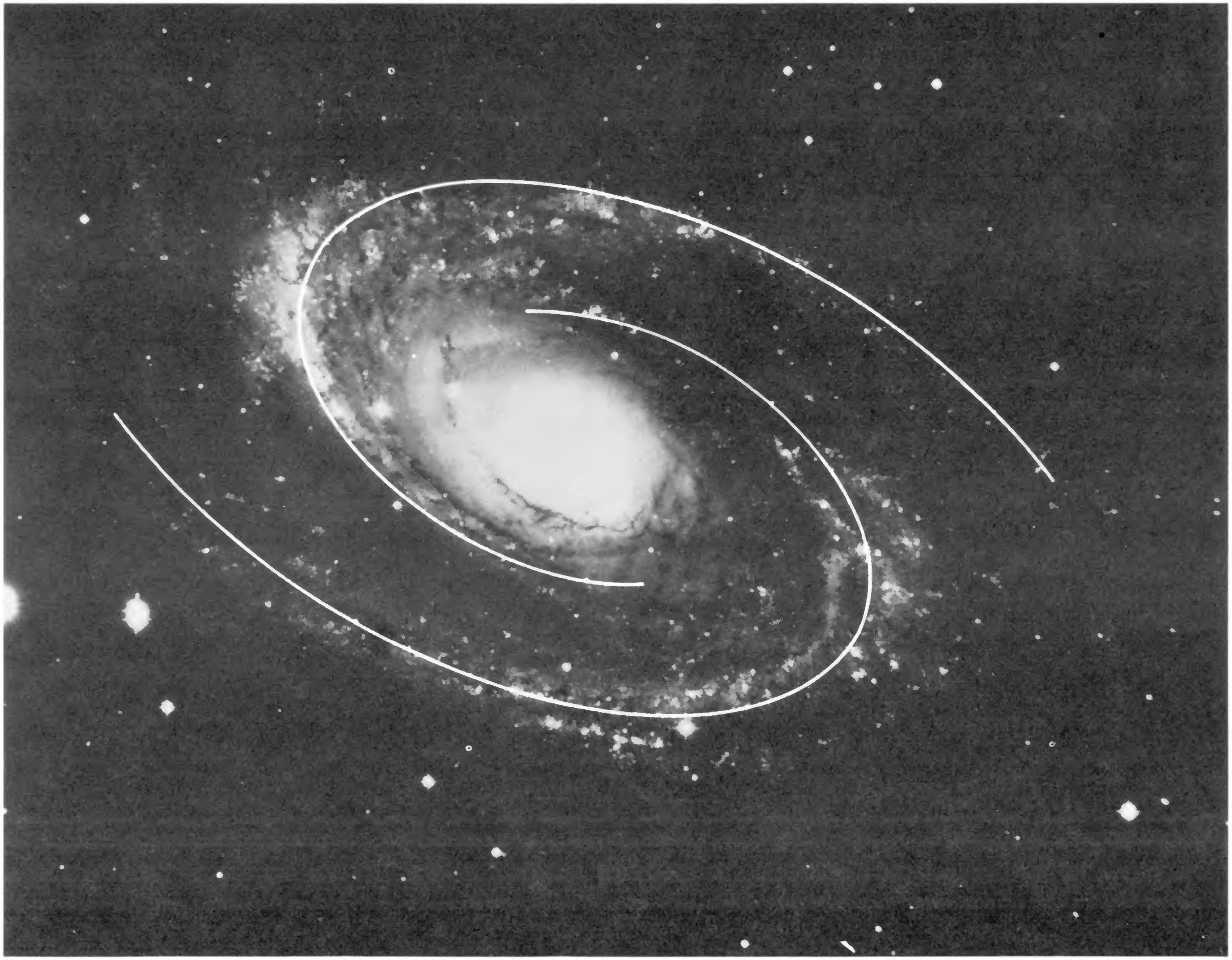

FIG. 10.—Photograph of the sample galaxy NGC 3031 (M81) with its characteristically "filamentary" spiral arms, taken from the Hubble Atlas. Superposed is the adopted wave pattern with $\Omega_p = 26$ km s^{-1} kpc^{-1} in which strong shocks are possible. The pattern is sketched over a radial extent equivalent to its range of validity: 3.1–8.3 kpc. Corotation at 9.7 kpc therefore lies about 17% farther out in the disk from the edge of the sketch (at 8.3 kpc).

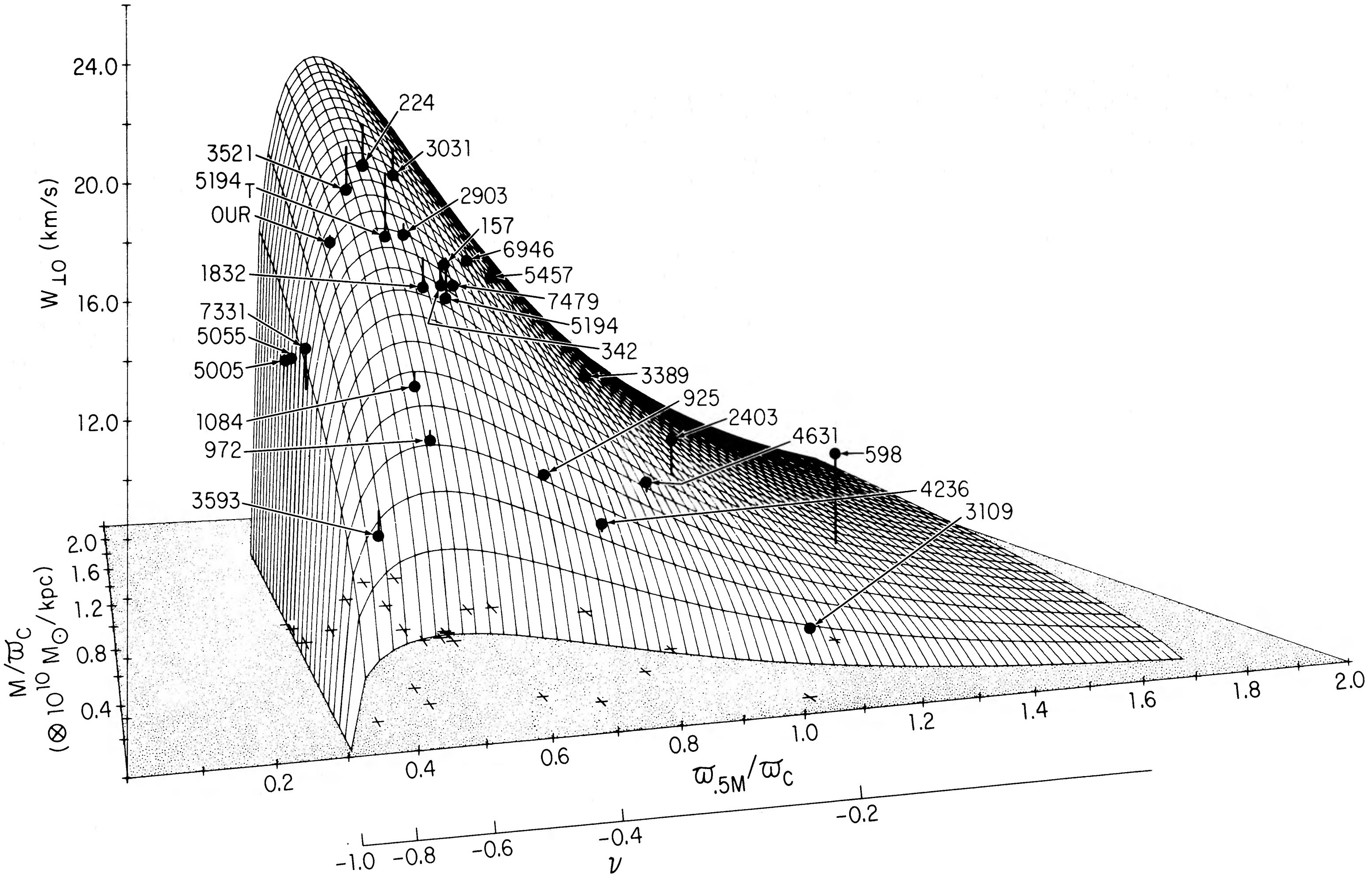

FIG. 11.—Theoretical categorization of disk-shaped galaxies; a representation of an ensemble of cases spanning the two-dimensional parameter space: M/ϖ_c, $\varpi_{0.5M}/\varpi_c$. The mass model simulating the equilibrium state for each case in the ensemble is one of Toomre type, with no spheroidal components superposed; and ϖ_{edge} is taken as the typical scale A_T for each case. The quantity $w_{\perp 0}$, evaluated at half-corotation, generates a $w_{\perp 0}$ surface which provides an estimate of the strength of the galactic shock possible over all cases of the ensemble. Superposed are 24 external galaxies plus our own. Galaxies whose models are of the Toomre type lie nearly coincident with the surface, whereas galaxies whose models have spheroidal components may lie displaced somewhat from the surface. Those galaxies with a moderate concentration of central mass $\varpi_{0.5M}/\varpi_c$ lie near the ridge of the $w_{\perp 0}$ surface; these galaxies for any fixed M/ϖ_c band are predicted to have the strongest shocks (e.g., NGC 3031 [M81]). Those galaxies with a central mass concentration either too great or too small lie well below the ridge and are predicted for any fixed M/ϖ_c band to have only relatively weak shocks, if any at all (e.g., NGC 598 [M33]). (The two entries for NGC 5194 with and without subscript T correspond to two sources of observed rotation velocity data: Tully 1972 and Burbidge and Burbidge 1964, respectively.)

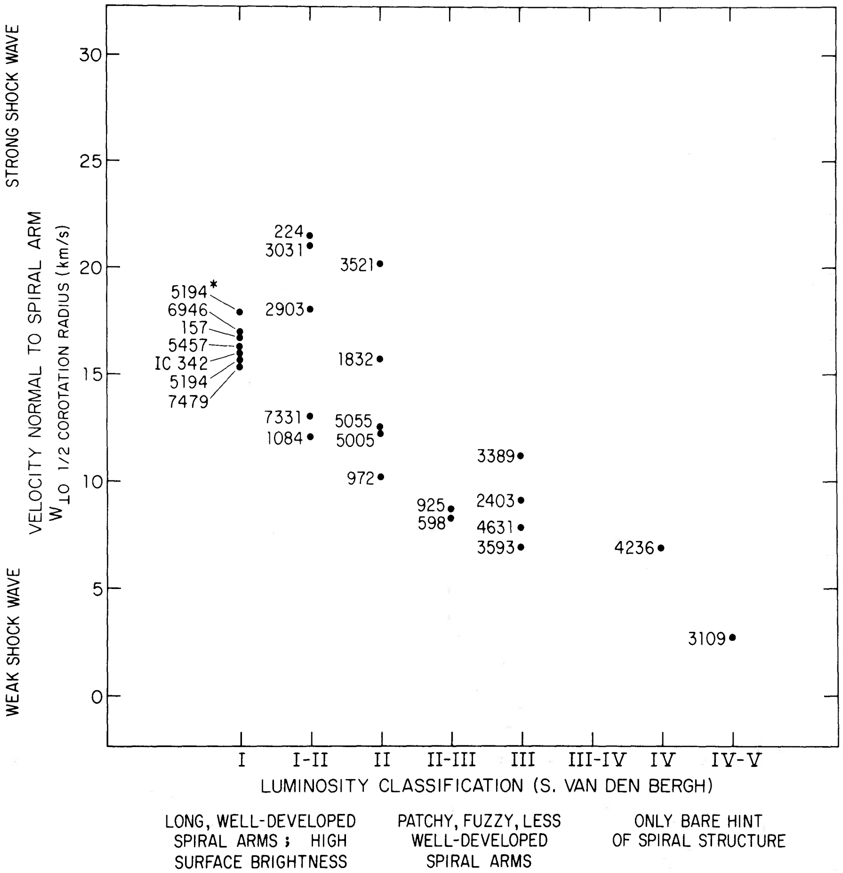

FIG. 12.—$w_{\perp 0}$ and luminosity class. Trend for a sample of 24 external galaxies indicative of the correlation between $w_{\perp 0}$—the velocity component of basic rotation normal to a spiral arm—and shock strength on the one hand, and luminosity classification and degree of development of spiral structure on the other. Those galaxies, in which strong shock waves are predicted, are found to exhibit long, well-developed spiral arms; and those galaxies in which weak shock waves are predicted are found to exhibit less-developed spiral structure. (The two entries for NGC 5194 with and without an asterisk correspond to two sources of observed rotation velocity data: Tully 1972 and Burbidge and Burbidge 1964 respectively.)

Analogous expectations on the surface brightness of spiral arms alone are not as clear. If all galaxies had the same relative gas content, those galaxies with the strongest shocks could probably trigger and exhibit the spiral arms of highest surface brightness. However, the gas content varies from galaxy to galaxy, and indeed a high rate of star formation during the evolution of a galaxy possessing strong shocks may lead to a high depletion of the original supply of gas in which the stars have been born, making the present-day formation of stars more difficult. If this is the case, then the present-day triggering of star formation and the corresponding present-day surface brightness of the spiral arms, in which the most recent births of stars are triggered, may not be as great as might otherwise be expected. Too great a depletion of gas in some galaxies with strong shocks could even conceivably lead to a situation in which the surface brightness of the arms in these galaxies might be lower than that of the arms of some galaxies with weak shocks. Further observational work on the photometry of the spiral arms in various galaxies could prove quite interesting in this respect.

b) *Hubble Type*

The typical pitch angle, *i*, of the theoretical wave pattern is governed (via eq. [5b]) by the more fundamental galactic parameter, $\varpi_{0.5M}/\varpi_c$, which measures the degree of central mass concentration toward the galactic center. Also governed by the degree of central mass concentration is the degree of nonuniform rotation characteristic of the disk of a galaxy. For a galaxy with a small value of $\varpi_{0.5M}/\varpi_c$, the major proportion of the mass is distributed with relatively high central concentration inside its visible radial extent, the galaxy possesses relatively strong differential rotation, and the theoretical pitch angle, *i*, of its wave pattern is small. Such a galaxy would then be expected to exhibit tightly wound spiral structure. For a galaxy with a large value of $\varpi_{0.5M}/\varpi_c$, a substantial portion of the total mass is outside its easily visible radial extent, the galaxy departs relatively little from nearly uniform rotation, and the theoretical pitch angle *i* of the wave pattern is large. Such a galaxy would be expected to exhibit loosely wound, open spiral structure.

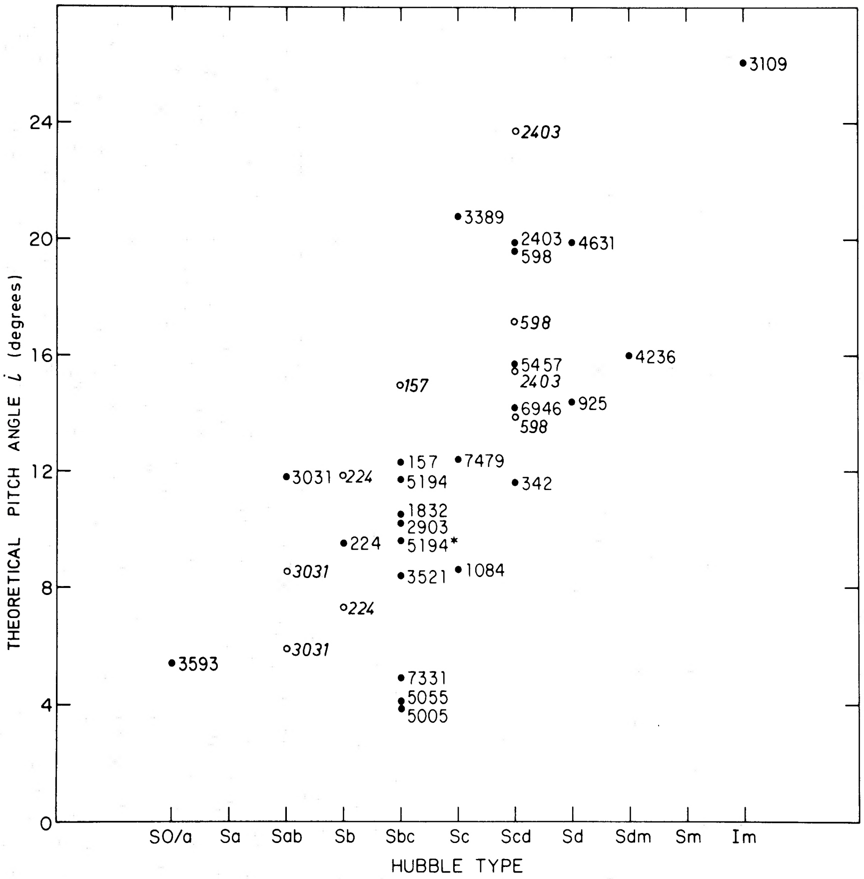

FIG. 13.—*Theoretical* pitch angle i, and Hubble Type. Trend for a sample of external galaxies indicative of the correlation between *theoretical* pitch angle i of the density wave pattern and Hubble type. Those galaxies whose models predict wave patterns with tightly wound arms of small i are the galaxies observed to be of relatively early type, S0/a–Sbc; and those galaxies whose models predict more open and loosely wound arms with large i are the galaxies observed to be of relatively late type, Sc–Im. The dark dots indicate the cases adopted. The open circles represent other possible cases for the other possible choices of the corotation radius shown in figs. 3, 5, 6, 7, and 8. (The two entries for NGC 5194 with and without an asterisk correspond to two sources of observed rotation velocity data: Tully 1972 and Burbidge and Burbidge 1964 respectively.)

Plotted in figure 13 on the vertical axis is the typical value of the *theoretical* pitch angle, i, evaluated for each galaxy at half-corotation. On the horizontal axis is plotted the Hubble type taken from de Vaucouleurs (1964). Figure 13 displays the predicted correlation between $\varpi_{0.5M}/\varpi_c$, *theoretical* pitch angle i, and geometry of the theoretical wave pattern on the one hand and Hubble type on the other. This correlation is equivalent to saying that the theoretical pattern obtained by choosing the corotation radius in the manner described in § II*c* agrees reasonably well with the observed spiral pattern for each galaxy in our sample. Statistically, then, galaxies with low values of $\varpi_{0.5M}/\varpi_c$ and small *theoretical* pitch angle i correspond to relatively early Hubble types, S0/a–Sbc; whereas galaxies with relatively high values of $\varpi_{0.5M}/\varpi_c$ and large *theoretical* pitch angle i correspond to relatively late Hubble types, Sc–Im. Admittedly, the correlation diagram shows some scatter, perhaps indicating that the self-gravity of the gas is not entirely negligible. In this respect, the ratio $M_{\text{gas}}/M_{\text{stars}}$ may be another important dynamical parameter. Alternatively, the scatter may reflect variations in the stability index Q (see §§ II and VI).

VI. CONCLUSIONS AND DISCUSSION

We have demonstrated that a theoretical characterization of spiral galaxies within the context of the density wave theory is possible by means of two fundamental galactic parameters. These two parameters are the total mass divided by the corotation radius, M/ϖ_c, and the degree of mass concentration toward the galactic center, $\varpi_{0.5M}/\varpi_c$. Both of these parameters are distance invariant; in addition, they correspond to ratios of the most basic of galaxy parameters.

Our semiempirical study has shown that the characteristic properties of the density wave patterns in models of 24 external spiral galaxies are correlated well with luminosity class and Hubble type. Moreover, the theoretical viewpoint sheds light on the physical mechanisms underlying the two-dimensional classification scheme of luminosity class and Hubble type.

1975ApJ...196..351C

TABLE 3

THEORETICAL RESULTS OVER THE RANGE OF MODEL NUMBER n_T FOR SEVERAL SAMPLE GALAXIES

NGC	MASS $M(\times 10^{10} M_\odot)$ $n_T =$			HALF-MASS RADIUS $\varpi_{0.5M}$ (kpc) $n_T =$			VELOCITY $W_{\perp 0}(0.5\varpi_c)$ (km s^{-1}) $n_T =$			THEORETICAL PITCH ANGLE $i\,(0.5\varpi_c)$ (degrees) $n_T =$		
	1	5	15	1	5	15	1	5	15	1	5	15
157.......	13.8	6.8	6.3	9.9	5.2	4.9	18.0	16.7	16.4	13.4	12.3	12.3
224.......	24.7	17.8	17.3	9.6	7.0	6.9	21.6	21.5	21.3	8.5	9.5	9.7
598.......	2.4	1.3	1.2	6.3	3.5	3.3	8.1	8.3	8.4	22.2	19.6	18.8
	(3.0)	(1.9)	(1.8)	(7.7)	(4.7)	(4.5)	(9.0)	(8.7)	(8.6)	(18.7)	(16.0)	(15.3)
2403.......	4.8	2.3	2.1	8.7	4.5	4.2	9.8	9.1	9.0	20.5	19.9	19.8
	(5.8)	(3.5)	(3.4)	(10.0)	(6.1)	(5.8)	(10.3)	(10.8)	(10.8)	(20.8)	(17.4)	(16.7)
3031.......	17.0	12.5	12.4	7.7	5.5	5.4	21.5	21.0	20.4	9.8	11.8	11.7

We have tested the sensitivity of our results on the details of the approach adopted in § II. We found the major results of the paper to be relatively insensitive to the procedure used to obtain mass models from observed rotation curves. Of course, the possibility exists that the observed rotation curve data for some galaxies may provide only a partial view of the overall rotation of the system, particularly at radii beyond the cutoff point of the data. Evidence to support this possibility is contained in the work of Roberts and Rots (1973), who find substantially more mass in the outer parts of three galaxies than was heretofore expected. Thus, a check was made for each galaxy of our sample by fitting it with a number of mass models with different Toomre model numbers, n_T, spanning the range from 1 to 15. Low values of n_T allow for substantially more mass in the outer parts. Table 3 illustrates the variation of the various physical quantities with n_T for several of the galaxies. These results are typical of all the galaxies considered and show the total mass and mass distribution can vary substantially with n_T but that $w_{\perp 0}$ and i, which constitute the major results of this paper, remain relatively insensitive to n_T. Thus the correlations found between $w_{\perp 0}$ and luminosity class and between i and Hubble type as illustrated for the case of $n_T = 5$ in § V actually hold and remain valid for all n_T, thereby ensuring their approximate invariance, in general.

The criterion adopted in this paper for the determination of corotation in a galaxy is based on the radial extent of three tracers: the prominent spiral structure, the "easily visible" disk, and the distribution of H II regions. All three are young tracers representative of recent and current dynamics. This criterion is expected to be valid in each galaxy in which the wave pattern is strongest and most coherent in the region inside corotation; for in this case, the spiral distribution of young stars and H II regions, whose formation has been triggered by galactic shocks, would be expected to be most prominent in the region inside corotation as well. Consequently, the radial extent of these tracers is probably a reasonable estimate for corotation.

In our view spiral dust lanes coincide with the region of maximum gas compression (W. W. Roberts 1969; Roberts and Yuan 1970; see also Mathewson *et al.* 1972). Thus, since the temporal sequence is gas compression followed by star formation, the relative displacement of dust lanes and young stars yields the relative sense of the motion of the matter with respect to the wave. For trailing spiral arms, whenever we see dust lanes on the inside edge of the optical spiral arms, we can deduce that the pattern rotates more slowly than the material speed at that radius. If we should see dust lanes on the outside edge, we would deduce that the pattern rotates faster than the material speed at that point. Corotation would occur near the radius where the crossover appears. According to Lynds (1970), the principal dust lanes generally lie on the inside edges of spiral arms throughout the face of a spiral galaxy; this is consistent with our assumption that corotation lies at the edge of the "easily visible" optical disk.[9]

The primary uncertainty present in our analysis is the correct value for the stability index Q. We have already remarked in § II that it is possible to improve our spiral fits if Q is allowed to be somewhat larger than unity in the interior of the disk. Conversely, if Q is substantially larger than unity everywhere in the disk, an annular region exists in the neighborhood of the corotation radius where spiral density waves cannot propagate (Shu 1968; Toomre 1969). Thus, apart from the question of the origin of spiral structure, the greatest uncertainty in the entire theoretical picture is the exact distribution of values for Q (Toomre 1974). Unfortunately, no immediate resolution of this fundamental uncertainty lies in sight.

Many workers have suggested a variety of excitation mechanisms to account for the origin and continued maintenance of spiral density waves (e.g., Lin 1970; Toomre and Toomre 1972; Lynden-Bell and Kalnajs 1972, van der Kruit, Oort, and Mathewson 1972; Mark 1974*b*). The significance of the present paper for this problem is the implication that, whatever the mechanism for the excitation of waves, a galaxy itself

---

[9] Of course, the possibility exists that some galaxies may have leading spiral arms. For leading spirals, we would expect the dust lanes on the outside edges of the optical spiral arms at radii inside corotation where the pattern rotates slower than the material speed, and the dust lanes on the inside edges of the optical spiral arms at radii outside of corotation where the pattern rotates faster than the material speed.

must be capable of playing a dominant role in prescribing the character of the wave phenomena which can persist to the degree of being able to order itself within the sequences of luminosity class and Hubble type and thereby govern its own identity within the classification of galaxies. Alternatively, the excitation mechanism of waves (or combination of such mechanisms) must be fairly well tuned to the basic structure and dynamics of the galaxy. Otherwise, the deduced correlations between $w_{\perp 0}$ and luminosity class, and between i and Hubble type, would be wholly fortuitous.

We acknowledge with pleasure many fruitful discussions with Drs. S. van den Bergh, P. C. van der Kruit, C. C. Lin, J. H. Oort, W. C. Saslaw, and A. Toomre.

This work has been supported in part by the National Science Foundation through grant GP-38126. The computations and numerical calculations were performed at the computer centers of the University of Virginia and the National Radio Astronomy Observatory in Charlottesville, Virginia.

REFERENCES

Brandt, J. C. 1960, *Ap. J.*, **131**, 293.
Burbidge, E. M., and Burbidge, G. R. 1964, *Ap. J.*, **140**, 1445.
———. 1968, *ibid.*, **154**, 857.
Burbidge, E. M., Burbidge, G. R., Crampin, D. J., Rubin, V. C., and Prendergast, K. H. 1964, *Ap. J.*, **139**, 1058.
Burbidge, E. M., Burbidge, G. R., and Prendergast, K. H., 1959, *Ap. J.*, **130**, 739.
———. 1960*a*, *ibid.*, **131**, 282.
———. 1960*b*, *ibid.*, **132**, 640.
———. 1960*c*, *ibid.*, p. 654.
———. 1961*a*, *ibid.*, **133**, 814.
———. 1961*b*, *ibid.*, **134**, 874.
———. 1963, *ibid.*, **137**, 376.
———. 1965, *ibid.*, **142**, 649.
Courtes, G., and Dubout-Crillon, R., 1971, *Astr. and Ap.*, **11**, 468.
Demoulin, M.-H. 1969, *Ap. J.*, **157**, 75.
de Vaucouleurs, G. 1964, *Reference Catalogue of Bright Galaxies* (Austin: University of Texas Press).
de Vaucouleurs, G., and de Vaucouleurs, A. 1963, *Ap. J.*, **137**, 363.
Dixon, M. E. 1971, *Ap. J.*, **164**, 411.
Feldman, S. I., and Lin, C. C. 1973, *Stud. Appl. Math.*, **3**, 1.
Fish, R. A. 1961, *Ap. J.*, **134**, 880.
Freeman, K. C. 1970, *Ap. J.*, **160**, 811.
Gordon, K. J. 1971, *Ap. J.*, **169**, 235.
Hodge, P. W. 1967, *An Atlas and Catalog of* H II *Regions in Galaxies* (Seattle: Astr. Dept., Univ. Washington).
Holmberg, E. 1958, *Medd. Lund.* Ser. II, No. 136.
Hubble, E. 1926, *Ap. J.*, **64**, 321.
———. 1936, *The Realm of the Nebulae* (New York: Dover).
Kalnajs, A. J. 1972, *Ap. J.*, **175**, 63.
Lin, C. C. 1970, in *Proc. IAU Symposium No. 38*, p. 377.
———. 1971, *Highlights of Astr.*, **2**, 81.
Lynden-Bell, D., and Kalnajs, A. J., 1972, *M.N.R.A.S.*, **157**, 1.
Lynds, B. T. 1970, in *Proc. IAU Symposium No. 38*, p. 26.
Mark, J. W. K. 1974*a*, *Ap. J.*, in press.
———. 1974*b*, *ibid.*, in press.
Mathewson, D. S., van der Kruit, P. C., and Brouw, W. N. 1972, *Astr. and Ap.*, **17**, 468.
Münch, G. 1959, *Pub. A.S.P.*, **71**, 101.
Ostriker, J. P., and Peebles, P. J. E., 1973, *Ap. J.*, **186**, 467.
Reynolds, J. H. 1927, *Observatory*, **50**, 185.
Roberts, M. S. 1969, *A.J.*, **74**, 859.
Roberts, M. S., and Rots, A. H. 1973, *Astr. and Ap.*, **26**, 483.
Roberts, W. W. 1969, *Ap. J.*, **158**, 123.
Roberts, W. W. 1974, *Vistas in Astronomy*, Vol. **19**.
Roberts, W. W., and Yuan, C. 1970, *Ap. J.*, **161**, 887.
Roberts, W. W., Roberts, M. S., and Shu, F. H. 1974, in *Proc. IAU Symposium No. 58*, in press.
Rogstad, D. H., Rougoor, G. W., and Whiteoak, J. B., 1967, *Ap. J.*, **150**, 9.
Rogstad, D. H., and Shostak, G. S. 1972, *Ap. J.*, **176**, 315.
Rubin, V. C., Burbidge, E. M., and Burbidge, G. R. 1964, *Ap. J.*, **140**, 94.
Rubin, V. C., Burbidge, E. M., Burbidge, G. R., Crampin, D. J., and Prendergast, K. H. 1965, *Ap. J.*, **141**, 759.
Rubin, V. C., and Ford, W. K. 1967, *Pub. A.S.P.*, **79**, 322.
———. 1970, *Ap. J.*, **159**, 379.
Sandage, A. 1961, *The Hubble Atlas of Galaxies* (Washington: Carnegie Institution of Washington).
Schmidt, M. 1956, *B.A.N.*, **13**, 15.
———. 1965, in *Galactic Structure* (Chicago: University of Chicago Press), p. 513.
Shapley, H., and Ames, A. 1932, *Ann. Harvard College Obs.*, **88**, 43.
Shostak, G. S., 1973, *Astr. and Ap.*, **24**, 411.
Shu, F. H. 1968, Ph.D. dissertation, Harvard University.
Shu, F. H., Milione, V., Gebel, W., Yuan, C., Goldsmith, D. W., and Roberts, W. W. 1972, *Ap. J.*, **173**, 557.
Shu, F. H., Milione, V., and Roberts, W. W. 1973, *Ap. J.*, **183**, 819.
Shu, F. H., Stachnik, R. V., and Yost, J. C. 1971, *Ap. J.*, **166**, 465.
Toomre, A. 1963, *Ap. J.*, **138**, 385.
———. 1964, *ibid.*, **139**, 1217.
———. 1969, *ibid.*, **158**, 899.
———. 1974, in *Highlights in Astronomy*, Gen. Assem. IAU, Sydney (in press).
Toomre, A., and Toomre, J. 1972, *Ap. J.*, **178**, 623.
Tully, R. B. 1972, Ph.D. Dissertation, Univ. of Maryland.
van Damme, K. J. 1966, *Australian J. Phys.*, **19**, 687.
van den Bergh, S. 1960*a*, *Ap. J.*, **131**, 215.
———. 1960*b*, *ibid.*, p. 558.
van der Kruit, P. C. 1973, *Astr. and Ap.*, **29**, 263.
van der Kruit, P. C., Oort, J. H., and Mathewson, D. S. 1972, *Astr. and Ap.*, **21**, 169.
Vandervoort, P. O. 1970, *Ap. J.*, **161**, 87.
Wielen, R. 1974, in *Highlights in Astronomy*, Gen. Assem. IAU, Sydney (in press).
Woodward, P. R. 1973, Ph.D. thesis, Berkeley.

William W. Roberts, Jr.: Department of Applied Mathematics and Computer Science, Thornton Hall, University of Virginia, Charlottesville, VA 22901

Morton S. Roberts: National Radio Astronomy Observatory, Edgemont Road, Charlottesville, VA 22901

Frank H. Shu: Department of Astronomy, Campbell Hall, University of California, Berkeley, CA 94720

1975ApJ...196..351C

THE ASTROPHYSICAL JOURNAL, **196**:407–411, 1975 March 1

THE FORMATION OF THE NUCLEI OF GALAXIES. I. M31

SCOTT D. TREMAINE
Joseph Henry Laboratories, Physics Department, Princeton University
AND
J. P. OSTRIKER AND LYMAN SPITZER, JR.
Princeton University Observatory
Received 1974 July 29

ABSTRACT

Globular clusters passing near the center of M31 interact with the background stars through dynamical friction and spiral in to the center of the galaxy, where they are tidally disrupted by interactions with the growing nucleus. By this process a distinct high-density central nucleus of mass $\sim 5 \times 10^7 M_\odot$ will be formed in 10^{10} years. These predictions are consistent with recent Stratoscope balloon observations of the nucleus of M31.

Subject headings: galactic nuclei — globular clusters — stellar dynamics — M31

I. INTRODUCTION

Several of the galaxies in the Local Group have distinct central nuclei of diameter $\leqslant 10$ pc, and similar structures presumably exist in more distant galaxies. We propose that such nuclei are naturally and inevitably formed as globular clusters spiral in to the center of their galaxy in the process of attempting to reach equipartition of energy with the field stars of the galaxy. Here we show that this hypothesis predicts many of the observed properties of the nucleus of M31, reserving for a subsequent paper details and applications to other galaxies.

II. THEORY

We consider a globular cluster of mass m and core radius $a_{\rm cl}$ moving with speed v in a galaxy represented locally by a Maxwellian distribution of stars of mass m_f, density ρ, and mean square velocity $\langle v^2 \rangle \equiv 3/2j^2$. Its motion is dominated by the large-scale, time-independent potential field of the galaxy, but it also experiences random perturbations in its velocity due to encounters with individual field stars, which cause it to evolve toward equipartition of energy with the stars. For $jv \sim 1$ and $m \gg m_f$, only the perturbations of the velocity vector parallel to itself (dynamical friction) are important (Spitzer 1962), and the diffusion coefficient is

$$\left(\frac{dv_\parallel}{dt}\right)_{\rm fr} \equiv \langle \Delta v_\parallel \rangle$$
$$= -4\pi G^2 m\rho \ln \Lambda \frac{[\varphi(jv) - jv\varphi'(jv)]}{v^2}\,, \quad (1)$$

where φ is the error function. The exact diffusion coefficient for impact parameters between $r_{\rm min}$ and $r_{\rm max}$ (Chandrasekhar 1943) can be evaluated numerically; we find that the approximation $\Lambda = r_{\rm max}/r_{\rm min}$ is adequate for the conditions occurring in the model described below. We take $r_{\rm min} = 1$ pc $(\sim a_{\rm cl})$ and $r_{\rm max} = \max(a, r)$, where a is the core radius of the galaxy (see below) and r is the distance of the cluster from the center of the galaxy. The results depend only weakly on the choices for $r_{\rm max}$ and $r_{\rm min}$.

We show below that the spheroidal component of M31 may be represented adequately by an isothermal sphere (Zwicky 1957), characterized by a central density ρ_0 and a structural length α, or core radius $a = 3\alpha$. The velocity distribution is Maxwellian, so that equation (1) applies with line-of-sight dispersion,

$$\sigma^2 = \tfrac{1}{3}\langle v^2 \rangle = \frac{1}{2j^2} = 4\pi G\rho_0\alpha^2\,. \quad (2)$$

As a globular cluster orbits in the galactic potential field $U(r)$ [where $U(0) \equiv 0$], dynamical friction produces relatively slow changes in its orbital parameters; i.e., the energy and angular momentum per unit mass (E, J) are approximate integrals of the motion, which decrease slowly as the cluster settles into the center over many orbits.

With these approximations, the evolution of the cluster orbit is represented by a track on a Lindblad (1933) diagram—the (E, J)-plane, shown in figure 1. A cluster moves along a track in a direction determined only by the instantaneous values of (E, J), at a rate proportional to its mass. We have calculated vectors $[\dot{E}(E, J), \dot{J}(E, J)]$ for some standard mass cluster at grid points in the allowed region of the Lindblad diagram $(E \geq 0,\ E - J^2/2r^2 - U(r) \geq 0)$. Then the orbital evolution of any cluster at any point (E, J) can be found by interpolating among calculated values of $\dot{E}$ and $\dot{J}$. We assume that initially the globular clusters had the same, isothermal distribution in phase space as the field stars. This is not an entirely ad hoc assumption since some processes of galaxy formation such as violent relaxation (Lynden-Bell 1967) could produce a phase-space distribution independent of mass. Since most of the clusters in the galaxy have not yet entered the nucleus, we may assume that the initial distribution of cluster masses is similar to the mass distribution seen presently in M31.

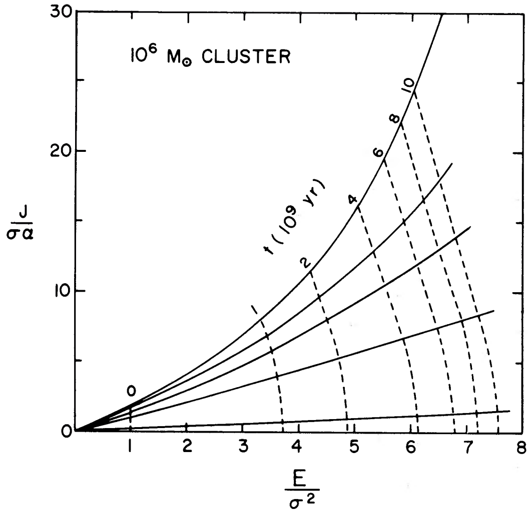

FIG. 1.—Lindblad diagram for an isothermal sphere. The abscissa is energy per unit mass, and the ordinate is angular momentum per unit mass, both in units of the line-of-sight velocity dispersion σ and the structural length α. Typical evolutionary tracks have been drawn. Dashed lines mark points from which a given time is required for a $10^6\ M_\odot$ cluster to reach $E/\sigma^2 = 1$; this is very nearly the time required for it to enter the nucleus. To scale the times to other cases, note that the time unit $\tau \equiv \alpha^2/\sigma G m$ has the value $\tau = 1.70 \times 10^8$ yr in the figure.

We then choose clusters both from the isothermal phase-space distribution and from an assumed mass distribution with maximum cluster mass $m_{\max}$ by a Monte Carlo technique. More massive clusters can be dragged in from a greater distance and from more energetic initial orbits. There is thus an energy per unit mass $E_{\max}$ such that clusters with $E \geq E_{\max}$ will not enter the nucleus in 10^{10} years if $m < m_{\max}$. In estimating the nuclear mass we thus need choose clusters only from the finite region of phase space with $E < E_{\max}$, rather than from the entire infinite isothermal distribution. Values of $E_{\max}$ are listed in table 1. The clusters are then placed on the Lindblad diagram and their evolution followed numerically. A cluster is considered to have entered the nucleus when $E < \sigma^2$, since beyond this point the cluster is in the core of the galaxy and orbits very rapidly toward the center.

TABLE 1

RESULTS OF CALCULATIONS

$m_{\max}$	$5.2 \times 10^6\ M_\odot$	$1 \times 10^8\ M_\odot$
$L_{\max}$	$2.6 \times 10^6\ L_\odot$	$5 \times 10^7\ L_\odot$
$\langle r\rangle$* (kpc)	0.8	1.1
$\langle mr\rangle/\langle m\rangle$* (kpc)........	1.3	3.8
$E_{\max}/\sigma^2$†	10.1	15.0
Nuclear mass ($M_\odot$)......	$(2.4 \pm 0.7) \times 10^7$	$(8 \pm 4) \times 10^7$
Mean number of clusters composing nucleus....	24	26

* $\langle r\rangle$ is the mean initial radius of the clusters which enter the nucleus. $\langle mr\rangle/\langle m\rangle$ is the mass-weighted mean initial radius of the clusters entering the nucleus.

† See § II.

III. SCALING ARGUMENTS

Before presenting our numerical calculations, we show how the results may be scaled to other cases of interest.

For most galaxies, the mass of the nucleus will be dominated by clusters which were initially in orbits far outside the core of the galaxy ($r \gg \alpha$) where most of the evolutionary time will be spent. In this region $\rho(r) = 2\rho_0\alpha^2/r^2$ in an isothermal sphere, and the mass interior to r is thus $M(r) = 8\pi\rho_0\alpha^2 r$. It is easy to show that the velocity v_c in a circular orbit remains constant as the orbit decays inward:

$$v_c{}^2 = \frac{GM(r)}{r} = 8\pi G\rho_0\alpha^2 = 2\sigma^2 . \tag{3}$$

Then, if $E(r)$ is the energy per unit mass on a circular orbit of radius r, we have

$$\frac{dE(r)}{dr} = \frac{dU(r)}{dr} = \frac{GM(r)}{r^2} = \frac{8\pi G\rho_0\alpha^2}{r} = \frac{2\sigma^2}{r} . \tag{4}$$

But from equation (1), neglecting changes in ln Λ,

$$\begin{aligned}\frac{dE}{dt} &= v_c\langle\Delta v_\|\rangle \\ &\propto -\frac{G^2 m\rho(r)}{v_c}\,[\varphi(jv_c) - jv_c\varphi'(jv_c)] . \end{aligned}\tag{5}$$

Since jv_c remains a constant ($=1$), the function in square brackets is constant and

$$\frac{dE}{dt} \propto -\frac{G^2 m\rho(r)}{\sigma} \propto \frac{Gm\sigma}{r^2} . \tag{6}$$

Dividing equation (6) by equation (4) yields

$$dr/dt \propto Gm/\sigma r \quad \text{or} \quad r^2(t) \propto Gmt/\sigma . \tag{7}$$

Clusters initially inside of $r(t)$ reach the center in time $\leqslant t$.

The mass of the nucleus $M_n(t)$ at time t equals the mass of all the clusters initially within $r(t)$ given by equation (7). If the number density of field stars (of mass m_f) at any radius is $1/f$ times the initial number density of clusters at that radius, then we obtain

$$M_n(t) \propto (m_f{}^{-1}fG^{-1/2})\sigma^{3/2}m^{3/2}t^{1/2} . \tag{8}$$

Note that the mass of the nucleus does not depend on the "size" α of the parent galaxy. If there is a distribution in cluster masses, the mean value of $m^{3/2}$ must be used in equation (8). In the more realistic case examined in the numerical calculations, the clusters do not all follow circular orbits; rather, their initial velocity distribution is isothermal and Maxwellian. It can be shown that equation (8) is valid in this case as well.

1975ApJ...196..351C

IV. APPLICATION TO M31

The distribution of light in M31 may be represented as the sum of a nucleus, a disk, and a spheroidal component, or bulge. We model the nuclear component (for all r) as an isothermal sphere whose central 1″ has the properties observed by Stratoscope II (Light, Danielson, and Schwarzschild 1975): central blue surface brightness of $B = (13.7 \pm 0.3$ mag) sec^{-2} and structural lengths along the major and minor axes of (0″.16, 0″.12). De Vaucouleurs (1958) has shown that the disk has a constant surface brightness $B = 22.8$ mag sec^{-2} inside 1800″ from the center. The distribution of light in the inner 1000″ of the major axis of M31 is then reproduced well by assuming that the bulge contribution is an isothermal sphere with central surface brightness $B = 18.3$ mag sec^{-2} and structural length 23″ (see fig. 2). We neglect the fact that the isophotes are ellipses of axial ratio ~0.7 and assume a spherical bulge. At a distance of 0.69 Mpc (van den Bergh 1968), 23″ is 77 pc.

The line-of-sight velocity dispersion in the bulge has been measured to be 225 km s^{-1} 10″ from the nucleus (Minkowski 1962) and 120 ± 30 km s^{-1} 13″ from the nucleus (Morton and Thuan 1973). We will use Morton and Thuan's value since it is roughly consistent with the rotational velocities observed by Rubin and Ford (1970) within 1 kpc of the nucleus, and also with the dispersion of 104 km s^{-1} found for 20 globular clusters in M31 within 20′ of the nucleus whose velocities have been measured by van den Bergh (1969). We adopt $\rho_0 = 50\ M_\odot$ pc^{-3}, $\alpha = 77$ pc, which from equation (2) gives $\sigma = 127$ km s^{-1}.

Between ~100 pc and ~1 kpc most of the mass lies in the bulge, and we therefore neglect the effect of the disk on the relaxation process. Between ~1 kpc and 30 kpc a large fraction of the mass of M31 lies in the disk. However, we believe that the isothermal sphere used to represent the bulge still provides a rough approximation to the relaxation rate in this region, since the rotation curve in this region resembles the flat rotation curve of an isothermal sphere (Roberts and Rots 1973), and neither the rotation curve nor the relaxation rate is strongly dependent on whether the mass lies in a disk or a sphere.

For the visual mass-to-light ratio of the globular clusters in M31 we adopt $(M/L)_v = 2$ in solar units. Illingworth and Freeman (1974) obtained a ratio of 1.7 ± 0.4 for the globular cluster NGC 6388 in our Galaxy. Scaling to other values of M/L is possible using equation (8).

The luminosity distribution $n(L)$ of the globular clusters in M31 has been determined by van den Bergh (1969). It may be represented by

$$\begin{aligned} \frac{dn(L)}{dL} &\propto \frac{(L/L_0)^a}{[1+(L/L_0)^{a+1}]^b}\,, \quad && L < L_{\max}\,, \\ &= 0\,, && L > L_{\max}\,, \qquad (9) \end{aligned}$$

where $a = 1.2$, $b = 1.6$, and L_0 corresponds to $M_v = -8.3$ (see fig. 3). The brightest observed cluster in M31 has $M_v = -11.2$ (van den Bergh 1969), so $L_{\max} \geq 2.6 \times 10^6 L_\odot$; however, beyond this limit we have no information on $L_{\max}$. Yet the choice of $L_{\max}$ is critical, since for $L \gg L_0$,

$$dn/dL(L) \propto (L/L_0)^{a-(1+a)b} = (L/L_0)^{-2.3}\,,$$

so that as $L_{\max} \to \infty$, $\langle m^{3/2} \rangle$ diverges (assuming M/L is constant), and the nuclear mass predicted by equation (8) also diverges. The divergence is purely formal, since the mass of all of the clusters in the galaxy yields a finite upper bound on the nuclear mass, but it does indicate a dependence of the nuclear mass on $L_{\max}$. Accordingly, we will examine two models: with $L_{\max} = 2.6 \times 10^6 L_\odot$ and with $L_{\max} = 5 \times 10^7 L_\odot$.

Finally we must normalize the results of the Monte Carlo calculations to the actual number of clusters in M31. We estimate that the 108 clusters with $B-V > 0.5$ listed by Kinman (1963) within 20′ of the nucleus are a reasonably complete sample. We therefore choose the initial central number density of clusters in our model so that the number remaining within 20′ (projected distance) of the nucleus after 10^{10} years is 108.

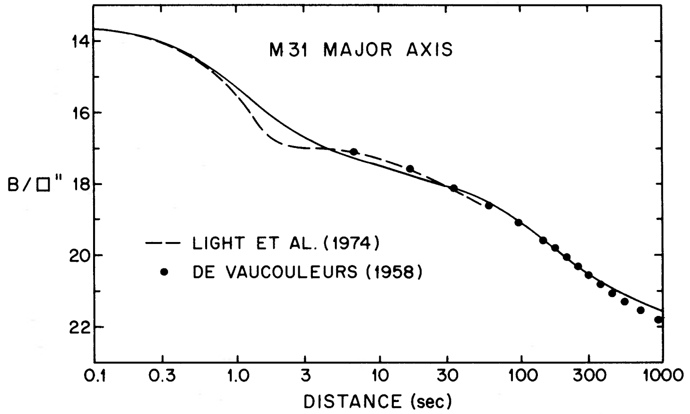

FIG. 2.—Surface brightness of the inner 1000″ of the major axis of M31. The solid curve is calculated from the model discussed in the text.

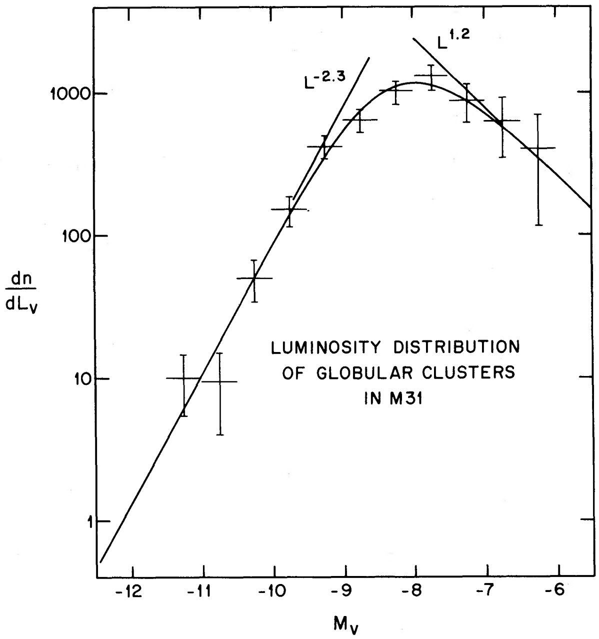

FIG. 3.—The luminosity of the globular clusters in M31 (van den Bergh 1969). The vertical scale is arbitrary. For an interval containing n clusters the error bars represent populations of $n \pm \sqrt{n}$. The solid curve is a fit to the data described in § IV of the text.

The results of the calculations, which incidentally verify the $M_n \propto t^{1/2}$ dependence predicted by equation (8), appear in table 1. The quoted uncertainty in the nuclear masses is an intrinsic statistical uncertainty (determined from the Monte Carlo simulation) due to the small number of clusters which compose the nucleus and neglects the uncertainties in the parameters chosen to define the calculation.

As expected, the nuclear mass depends on whether or not the mass distribution function had a tail of massive globular clusters which are not now seen because most of them have been dragged into the nucleus. We may use equation (8) to estimate the effects of changes in the model parameters. If we had chosen $(M/L)_v = 1$, the nuclear masses would be reduced by $2^{3/2} = 2.83$. Choosing Minkowski's (1962) velocity dispersion of 225 km s^{-1} would increase the masses by $(225/127)^{3/2} = 2.36$.

We have glossed over the physical processes which occur as the clusters approach the growing nucleus. Dynamical friction tends to circularize the orbits so that most clusters enter the inner ~100 pc on nearly circular orbits. The density distribution in this region will not be that of an isothermal sphere after the nucleus has begun to form, since its mass will distort the distribution, enhancing the density and speeding up the relaxation. Clusters will spiral in, gradually being stripped of their outer parts by the tidal forces from the nucleus. A cluster will completely dissociate at the Roche limit, when the mean density interior to it is roughly its own central density. Some clusters may dissociate before this point as a result of tidal heating by the bulge or by the growing nucleus. The component cluster stars will then be relatively unaffected by dynamical friction, although they will achieve some evolution toward equipartition of energy among themselves; using Light *et al.*'s (1975) estimates of the nuclear parameters and Spitzer's (1969) definition of the equipartition time t_{eq}, we find $t_{\text{eq}} = (1.8 - 3.1) \times 10^9$ yr $\times\ m_*^{-1}$, where m_* is a typical star mass in solar units. We do not have a detailed dynamical model capable of explaining the density in the nucleus of M31, although, as we show in the next section, our calculation of the nuclear mass is in reasonable agreement with observations.

V. COMPARISON WITH OBSERVATIONS

Light *et al.* (1975) find that M31 has a distinct nucleus with mass $M_n = (0.45\text{–}1.6) \times 10^8\ M_\odot$, consistent with the predictions made in table 1. They find $(M/L)_v$ between 8 and 30, assuming no absorption within M31. However, dust has been noted within 6″ of the nucleus (Johnson and Hanna 1972), and it is reasonable to assume that the high M/L is due to absorption. The lower values of mass and M/L follow from Morton and Thuan's (1973) measurement of the velocity dispersion of the nucleus, and the upper values from Minkowski's (1962) measurement. Although both authors assert that the velocity dispersion in the bulge is the same as the dispersion in the nucleus, we stress that there is no *a priori* reason why this should be so if the nucleus is indeed a distinct dynamical structure.

While the agreement in mass is the most striking evidence in favor of the model, there is other, indirect, evidence as well. Einasto (1972) has pointed out that the system of globular clusters in M31 has a much larger mean radius than the bulge. This result follows naturally from the much greater dynamical friction in the high-density central region, which will depopulate it of clusters without greatly affecting the outer regions.

Also, Spinrad, Smith, and Taylor (1972) have observed an increase in metallicity (as measured by the cyanogen band index) between 15 pc and 5 pc from the center of M31, followed by a dip in metallicity in the inner 5 pc, where the light is dominated by the nucleus. Such a dip is to be expected if the nucleus is composed of relatively metal-poor globular clusters.

VI. CONCLUSIONS

The action of dynamical friction on the globular clusters in M31 will cause the formation of a compact nucleus with mass 10^7–$10^8\ M_\odot$. Further measurements of the velocity dispersion, color, metallicity, and stellar content of the nucleus would provide important tests of the theory proposed here, as would a measurement of the absorption within M31 at the nucleus. With more complete information on the distribution and kinematics of globular clusters in M31, it might be possible to see the effect of dynamical friction on the distribution of their orbits.

Scaling arguments indicate that galaxies similar to M31 should have distinct stellar nuclei with masses

$\sim 10^{7.5}\sigma_{100}{}^{3/2} M_\odot$, where σ_{100} is the line-of-sight velocity dispersion in the nuclear bulge, in units of 100 km s^{-1}. Thus "hot" enough galaxies or galaxies rich enough in globular clusters, should, by the mechanism outlined in this paper, develop massive nuclei within which stellar collisions and other exotic phenomena might possibly occur.

We thank E. S. Light, R. E. Danielson, and M. Schwarzschild for the use of unpublished Stratoscope data, and we acknowledge very useful discussions with S. van den Bergh and J. E. Gunn. This work was supported financially by National Science Foundation grant MPS 74-18970, and one of us (S. D. T.) was supported by a fellowship from Imperial Oil Ltd.

REFERENCES

Chandrasekhar, S. 1943, *Ap. J.*, **97**, 255.
de Vaucouleurs, G. 1958, *Ap. J.*, **128**, 465.
Einasto, J. 1972, in *External Galaxies and Quasi Stellar Objects*, ed. D. S. Evans (Dordrecht: Reidel), p. 37.
Illingworth, G., and Freeman, K. C. 1974, *Ap. J. (Letters)*, **188**, L83.
Johnson, H. M., and Hanna, M. M. 1972, *Ap. J. (Letters)*, **174**, L71.
Kinman, T. D. 1963, *Ap. J.*, **137**, 213.
Light, E. S., Danielson, R. E., and Schwarzschild, M. 1975, submitted to *Ap. J.*
Lindblad, B. 1933, in *Handbuch der Astrophysik*, ed. G. Eberhard, A. Kohlschütter, and H. Ludendorff (Berlin: Springer), **5**, 937.
Lynden-Bell, D. 1967, *M.N.R.A.S.*, **136**, 101.
Minkowski, R. 1962, in *Problems of Extragalactic Research*, ed. G. C. McVittie (New York: Macmillan), p. 112.
Morton, D. C., and Thuan, T. X. 1973, *Ap. J.*, **180**, 705.
Roberts, M. S., and Rots, A. H. 1973, *Astr. and Ap.*, **26**, 483.
Rubin, V. C., and Ford, W. K. 1970, *Ap. J.*, **159**, 379.
Spinrad, H., Smith, H. E., and Taylor, D. J. 1972, *Ap. J.*, **175**, 649.
Spitzer, L. 1962, *Physics of Fully Ionized Gases* (2d ed; New York: Interscience).
———. 1969, *Ap. J. (Letters)*, **158**, L139.
van den Bergh, S. 1968, *J.R.A.S. Canada*, **62**, 219.
———. 1969, *Ap. J. Suppl.*, **19**, 145.
Zwicky, F. 1957, *Morphological Astronomy* (Berlin: Springer), p. 135.

J. P. OSTRIKER and LYMAN SPITZER, JR.: Princeton University Observatory, Peyton Hall, Princeton, NJ 08540

SCOTT D. TREMAINE: Department of Physics, Jadwin Hall, Princeton University, Princeton, NJ 08540

THE ASTROPHYSICAL JOURNAL, 196:413–432, 1975 March 1

A PHOTOMETRIC STUDY OF NGC 2419

RENÉ RACINE* AND WILLIAM E. HARRIS†
David Dunlap Observatory, Richmond Hill, Ontario; and Erindale College, University of Toronto

Received 1974 July 11

ABSTRACT

Photometry to $V = 22.2$ and $B = 23.7$ is reported for the outer-halo globular cluster NGC 2419. The color-magnitude diagram of the cluster is similar to that of the classic metal-poor cluster M92, and indicates a very low metallicity $Z \simeq 1.5 \times 10^{-4}$. The reddening $E(B - V)$ is 0.03 ± 0.01 mag, and the apparent distance modulus is $(m - M)_V = 19.87 \pm 0.09$, leading to a galactocentric distance of $R_g = 100 \pm 5$ kpc. The RR Lyrae nature of the numerous short-period variables discovered by Baade is confirmed; of the five known brighter variables, one appears to be a Population II Cepheid, while the others fall near the tip of the red giant branch. Attention is drawn to a significant gap in the giant branch. The cluster's age is estimated as $T = 11.0 \pm 0.5 \times 10^9$ yr from its HB morphology, or $T = 11.9 \pm 0.3 \times 10^9$ yr from a discussion of its galactic orbit.

The galactic orbit of NGC 2419 is determined. The cluster is gravitationally bound to the Galaxy, traveling on an orbit of eccentricity 0.62 with a period of 3.4×10^9 yr, and is presently near its apogalacticon. It is argued that the cluster was born close to its perigalacticon distance of 24 kpc. A possible gravitational encounter between NGC 2419 and the Magellanic Clouds is mentioned briefly. Finally it is shown that NGC 2419, like many metal-poor halo clusters, possesses an orbit of large angular momentum per unit mass h, and that globular clusters with the largest h are among the metal poorest.

Subject headings: galactic structure — globular clusters

I. INTRODUCTION

The northern cluster NGC 2419 (α: 7^h35^m; δ: $+39°00'$ (1950); $l = 180\overset{\circ}{.}4$, $b = +25\overset{\circ}{.}6$) is of interest simply because of its enormous distance. Drifting in intergalactic space at 100 kpc from the center of the Galaxy, this object marks one of the last detectable outposts of our Galactic system. Along with a very few Palomar clusters, NGC 2419 is the most distant globular cluster for which the color-magnitude (C-M) diagram can still be studied in detail.

The C-M diagrams already obtained for "intergalactic" globular clusters like NGC 7006 (Sandage and Wildey 1967) and Pal 3 and 4 (Burbidge and Sandage 1958), and for the dwarf spheroidal galaxies in Draco (Baade and Swope 1961) and Ursa Minor (van Agt 1967), have shown unusual features whose interpretation in terms of abundance peculiarities (Hartwick 1968; Hartwick and McClure 1972) or age differences (Rood 1973) remains problematic. Furthermore, all the known clusters and dwarf spheroidals farther than ~40 kpc from the Galactic center *except* for NGC 2419 are diffuse, low-density objects which could not survive close tidal encounters with the Galaxy. By contrast NGC 2419 is a populous and compact (class II) object similar to the "nearby" common halo globular clusters. Thus an investigation of its stellar population could help to disentangle the effects of galactocentric distance and of space density on the evolutionary characteristics of Population II systems.

II. OBSERVATIONS

NGC 2419 is difficult to observe. Visual inspection under good seeing at the prime focus of the 200-inch telescope shows the brightest cluster stars barely resolved, and crowding problems impose severe limitations on photometric measurements except in the outer regions. The only previously published photometry of the cluster stars in the last 40 years is the work by Baade (1935) on the variables, an eloquent testimony to the observational difficulty presented by this outstanding object.

A local sequence of photoelectric *UBV* standards around the cluster down to $V = 17.1$ was measured with the No. 1 36-inch (91 cm) telescope at the Kitt Peak National Observatory in 1973 January. These standards are identified in figure 1, and their photoelectric and photographically smoothed magnitudes and colors are listed in table 1. For the photoelectric measurements, standard *UBV* filters were used with a 1P21 phototube and single-channel pulse counting equipment. Standard and extinction stars used to transform the instrumental measures to the *UBV* system were taken from Johnson *et al.* (1966), Crawford *et al.* (1971), and the Cerro Tololo list of standards compiled by Demers and Kunkel.

Average values of the standard deviation of a single photoelectric measurement, as judged from the night-to-night scatter of the individual measures, are listed in table 2 as a function of the magnitude level V. The entries in this table should be divided by $\sqrt{n}$ to give the internal standard errors of the photoelectric values in table 1.

---

* Guest investigator at the Hale Observatories.

† Visiting astronomer 1973, Kitt Peak National Observatory, operated by the Association of Universities for Research in Astronomy, Inc., under contract with the National Science Foundation.

TABLE 1

Photometric Data for Standard Stars

Star	V	$B-V$	n	$U-B$	n	V_{pg}	$(B-V)_{pg}$
+39°1979....	7.19	0.27	5	0.07	4	...	...
+39°1978....	7.94	0.15	5	0.07	4	...	...
+39°1976....	9.32	0.34	5	0.08	4	...	...
A...........	11.12	0.87	5	0.47	4	...	...
B...........	11.94	1.09	5	0.95	4	...	...
C...........	12.29	0.59	5	0.08	3	...	...
D...........	13.00	0.50	4	0.02	3	...	...
E...........	13.40	0.51	4	−0.04	3	13.41	0.49
F...........	13.47	0.58	4	−0.01	3	13.46	0.55
G...........	13.51	0.63	5	0.04	3	13.48	0.62
H...........	13.57	1.22	5	1.14	4	13.65	1.19
I...........	13.75	0.67	4	0.17	3	13.73	0.67
J...........	14.33	0.63	4	0.14	3	14.27	0.67
K...........	15.19	0.50	2	−0.06	1	15.31	0.34
L...........	15.24	0.78	5	0.43	4	15.30	0.78
M...........	15.37	0.89	5	0.67	3	15.31	1.02
N...........	15.55	0.59	4	−0.05	3	15.47	0.76
P...........	15.55	0.55	4	0.04	3	15.47	0.63
Q...........	15.74	0.71	2	0.23	1	15.87	0.55
R...........	15.81	0.81	2	0.31:	1	15.69	0.98
S...........	15.82	0.64	5	−0.08	4	15.79	0.64
T...........	15.87	0.78	4	0.23:	2	15.86	0.79
U...........	16.00	0.78	3	0.19	2	16.09	0.66
V...........	16.03	1.03	2	0.76	1	16.16	0.93
W...........	16.13	1.20	4	0.69	2	16.09	1.27
X...........	16.69	0.99	2	0.45:	1	16.70	0.93
Y...........	16.91	0.88	2	0.25:	1	16.92	0.92
Z...........	17.14	1.35	1	...	...	17.10	1.27

TABLE 2

Random Errors of Single Photoelectric Measures

V	σ_v	σ_{B-V}	σ_{U-B}
<13.0........	0.015	0.014	0.019
13.0–16.0......	0.022	0.034	0.035
>16.0........	0.06	0.06	(0.05)

A series of B and V plates of the cluster was obtained with the 200-inch telescope as described in table 3. These were taken at the prime focus with the f/3.67 Ross corrector, and with an auxiliary calibration wedge described by Racine (1969, 1971). This wedge produces artificial secondary images of each star which are fainter than their primaries by $\Delta m = 5.00$ mag, and which are used to extend the photometric calibration to the plate limit ($V_{\text{lim}} \approx 22.2$, $B_{\text{lim}} \approx 23.7$).

On the six photographic plates, all uncrowded stars within two annular regions north and south of the cluster center (rings A and B, as shown in fig. 1) were measured with a Cuffey-type iris photometer at the David Dunlap Observatory. The east and west sectors containing the bright field star BD+39°1979 and its ghost image were excluded because of obvious background problems. In addition to rings A and B, a few brighter stars were measured within the inner boundary of ring A (called the "inner region") in order to help delineate the upper part of the giant branch of the cluster. All the stars measured photographically are identified in figure 1 (ring B and outer ring A) and figure 2 (inner ring A and inner region).

The color equations for the plate-filter combinations used were known from previous work on M67 (Racine 1971) and were verified from the NGC 2419 standard sequence. The relations between the photographic and photoelectric magnitudes used were

$$V = y + 0.118\,(b - y)\,, \tag{1a}$$

$$B = b - 0.064\,(b - y)\,. \tag{1b}$$

TABLE 3

Journal of Photographic Observations

Plate No.	Date	PST	Emulsion + Filter	Exposure (minutes)
PH-5461-R....	1970 Apr. 4	07:20	103aO+GG13	20
PH-6167-R....	1972 Mar. 9	07:41	103aD+GG11	30
PH-6168-R....	1972 Mar. 9	08:14	103aD+GG11	30
PH-6169-R....	1972 Mar. 9	08:43	103aO+GG13	20
PH-6170-R....	1972 Mar. 10	07:20	103aO+GG13	20
PH-6175-R....	1972 Mar. 10	09:09	103aO+GG13	20

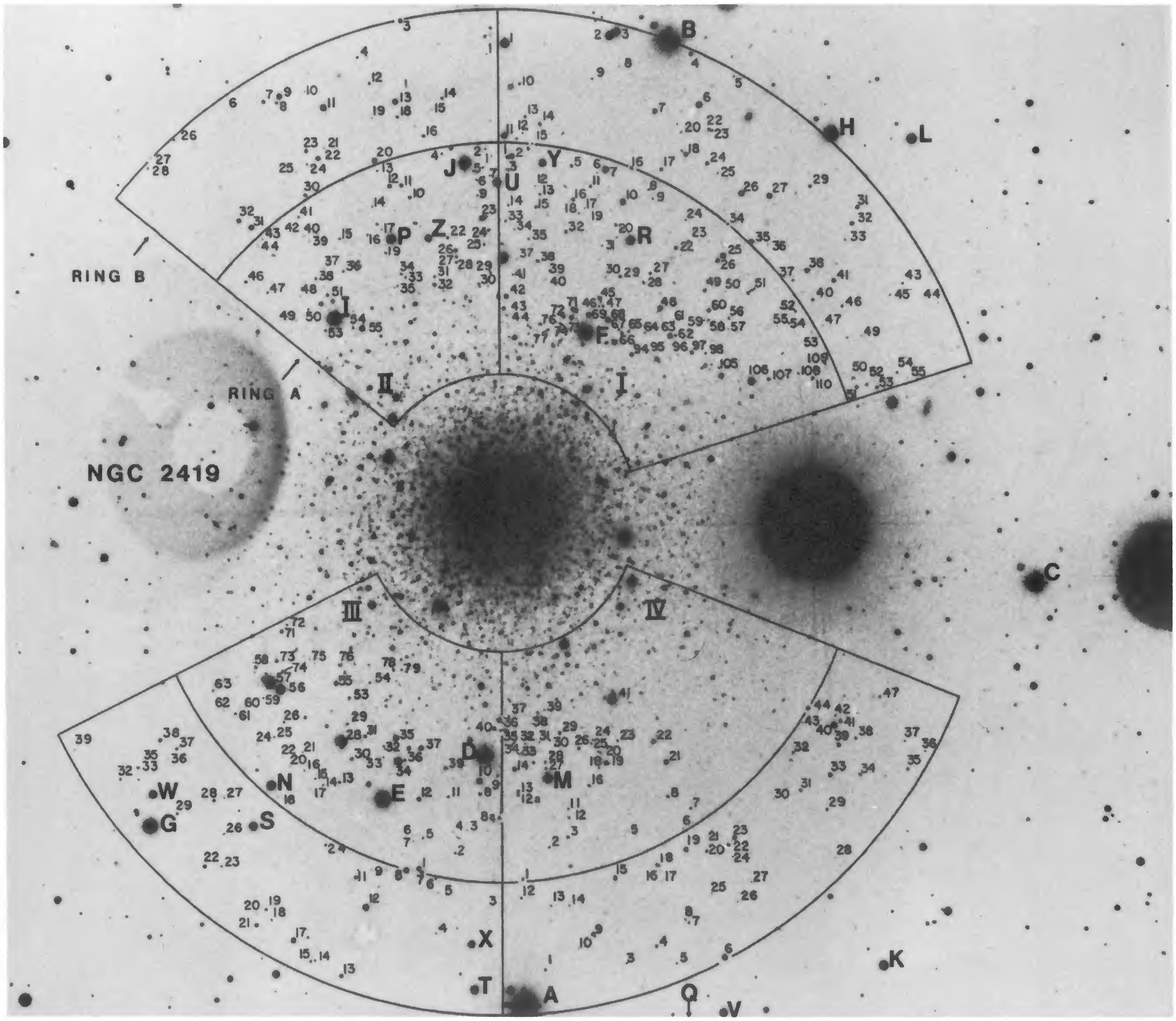

FIG. 1.—Finder chart for the photometric survey of NGC 2419, made from a 30-min *V* exposure at the prime focus of the 200-inch. North is at the top and east at left. The photoelectrically measured standard stars are marked by capital letters, and their secondary images appear 15″ NE of each one. The region measured photographically is divided into two annular rings, A and B, and four sectors I–IV as shown. The three concentric circles defining rings A and B have radii of 1′.69, 4′.50, and 6′.13. The photographically measured program stars are shown for ring B and the outer part of ring A; wherever possible, the number is placed to the right of the star. At left, the shadows of the "auxiliary wedge" and its holder can be seen in the out-of-focus ghost image of the bright star BD + 39°1979.

1975ApJ...196..351C

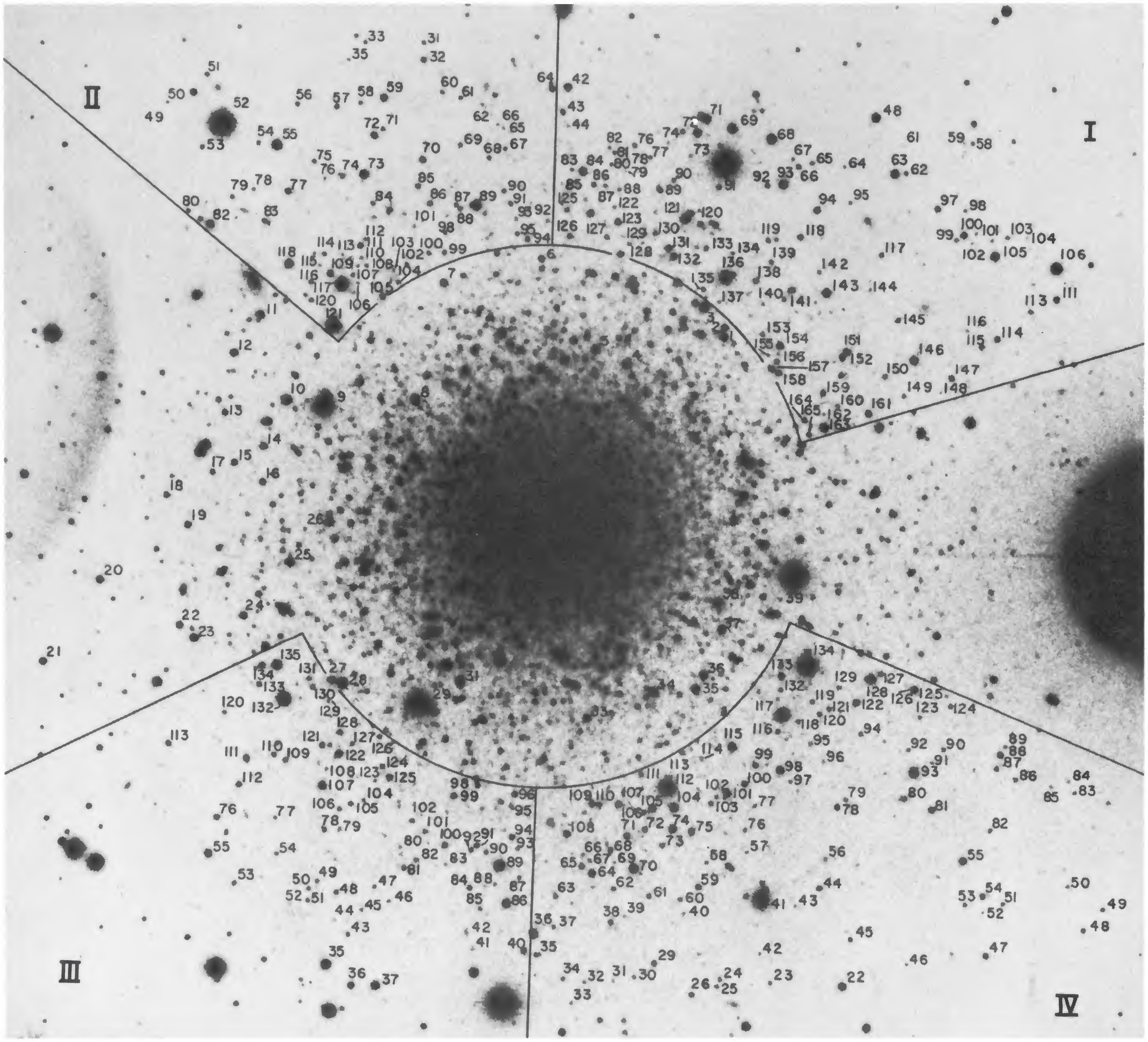

FIG. 2.—Finder chart for the program stars in the inner part of ring A and in the "inner region" around the cluster center

TABLE 4

NGC 2419—PROGRAM STARS RING A

STAR	V	B−V	STAR	V	B−V	STAR	V	B−V	STAR	V	B−V	STAR	V	B−V	STAR	V	B−V
I 1	19.44	0.54	54	21.42	0.44	107	19.87	0.72	159	19.87	0.12	50	21.13	0.72	105	20.55	0.15
2	17.88	0.44	55	22.25	0.59	108	21.31	0.21	160	20.81	0.47	51	20.12	0.90	106	21.43	0.90
3	20.52	0.21	56	20.76	0.58	109	20.68	0.56	161	19.02	0.90	53	20.23	0.30	107	20.50	0.19
5	20.36	0.71	57	22.05	0.26	110	20.19	0.71	162	21.39	0.56	54	20.53	0.81	108	20.93	0.88
6	22.00	0.64	58	20.86	−0.08	111	19.52	1.21	163	18.07	0.96	55	17.58	0.58	109	21.30	0.93
7	17.26	0.89	59	21.97	0.26	113	20.35	0.19	164	19.76	0.69	56	20.47	0.11	110	21.16	0.93
8	21.35	0.64	60	19.61	0.82	114	19.59	0.80	165	20.13	0.70	57	20.07	0.82	111	19.51	0.85
9	21.78	0.46	61	21.86	0.63	115	20.06	0.44	II 1	21.78	−0.13	58	20.83	0.77	112	20.86	0.57
10	17.81	1.09	62	20.48	0.07	116	21.51	0.40	2	21.56	1.74	59	18.81	0.97	113	21.48	0.53
11	20.86	1.64	63	18.39	0.94	117	20.40	1.60	4	21.11	1.04	60	20.74	0.69	114	20.42	0.34
12	21.76	0.51	64	21.38	0.71	118	19.76	0.80	5	21.28	0.50	61	20.86	0.94	115	21.55	0.70
13	20.67	−0.05	65	20.87	1.01	119	20.08	0.48	6	21.07	0.91	62	21.35	0.91	116	19.19	0.96
14	21.49	0.62	66	19.96	0.76	120	19.65	0.77	7	21.46	0.90	64	19.40	0.93	117	16.48	1.43
15	20.65	0.82	67	21.52	0.45	121	17.58	1.21	9	21.66	−0.09	65	21.71	1.39	118	18.13	1.07
16	20.02	0.75	68	17.90	1.10	122	21.53	0.75	10	20.22	0.87	66	21.73	1.25	120	20.49	0.74
17	22.06	0.51	69	17.89	1.10	123	19.28	0.93	11	19.13	0.46	67	20.66	0.11	121	15.93	0.93
18	21.75	0.49	71	18.16	0.51	125	20.49	0.16	12	19.02	0.95	68	20.54	0.12	III 1	18.44	0.85
19	22.31	0.10	72	19.98	0.59	126	19.68	0.86	13	21.48	0.61	69	20.70	0.78	2	21.36	2.14
20	21.81	0.83	73	21.38	0.65	127	20.57	0.74	14	21.73	0.07	70	19.43	0.86	3	21.77	0.67
22	19.58	0.88	74	21.89	0.48	128	19.29	0.84	15	21.26	0.75	71	20.43	0.11	4	21.59	1.04
23	21.00	0.77	76	20.35	0.19	129	21.05	0.84	16	21.66	1.58	72	19.07	0.93	5	21.58	0.43
24	21.70	1.08	77	20.83	0.82	130	20.36	0.90	17	21.85	0.48	73	18.18	0.51	6	22.47	1.25
25	17.76	1.16	78	22.04	1.07	131	18.96	0.92	19	20.77	0.69	74	20.35	0.73	7	22.09	0.73
26	19.36	1.51	79	22.03	0.81	132	18.81	0.91	22	20.38	0.33	75	20.48	0.19	8	19.82	0.52
27	20.53	0.83	80	21.14	0.83	133	20.40	0.64	23	18.05	1.11	76	21.50	1.22	8A	19.80	0.73
28	20.60	0.79	81	20.63	0.04	134	20.95	0.77	24	20.36	0.53	77	19.38	0.99	9	20.58	0.80
29	20.44	0.80	82	21.15	0.59	135	20.45	0.21	25	20.66	0.16	78	21.07	0.79	10	17.54	1.29
30	22.06	0.41	83	21.08	0.76	136	16.30	0.91	26	19.36	0.85	79	20.53	0.07	11	20.94	0.81
31	21.77	0.62	84	18.52	0.97	137	21.19	0.77	27	20.22	0.79	80	20.21	0.89	12	18.97	0.87
32	20.56	0.79	85	21.83	0.64	138	20.15	1.06	28	20.71	0.17	82	19.22	1.75	13	20.42	1.56
33	21.19	0.28	86	20.13	0.70	139	20.34	0.21	29	20.61	0.14	83	20.02	0.53	14	21.23	0.58
34	21.92	0.29	87	20.59	0.05	140	21.56	0.58	30	20.65	0.10	84	20.57	0.81	15	21.13	0.89
35	21.35	0.87	88	21.22	0.79	141	20.58	0.08	31	20.70	0.06	85	20.11	0.84	16	21.86	0.41
37	22.05	1.31	89	19.59	0.86	142	20.87	0.79	32	19.81	0.94	86	20.07	0.89	17	22.47	0.59
38	19.82	0.80	90	20.60	0.67	143	18.38	1.33	33	20.59	0.19	87	20.56	0.65	18	22.04	1.04
39	20.42	0.19	91	19.81	0.63	144	21.25	0.73	34	20.41	0.18	88	20.40	0.16	20	22.06	0.07
40	22.04	0.28	92	20.04	0.74	145	20.29	0.10	35	21.48	0.77	89	17.56	0.61	21	21.62	0.74
41	21.78	0.37	93	18.15	1.38	146	18.31	0.93	36	20.59	0.20	90	20.60	0.81	22	22.38	−0.37
42	18.92	0.90	94	19.25	1.27	147	19.56	0.71	37	22.60	0.87	91	20.60	0.22	24	22.21	1.35
43	19.95	0.85	95	21.03	−0.03	148	21.75	0.56	38	20.78	0.14	92	21.35	0.87	25	21.35	0.95
44	21.69	0.55	97	19.57	0.79	149	20.66	0.02	39	22.06	0.29	93	21.45	0.84	26	20.92	1.27
45	19.08	0.92	98	21.48	0.39	150	20.33	0.00	40	22.24	0.67	94	20.23	0.40	28	14.84	0.39
46	21.07	0.00	99	20.89	0.70	151	18.73	0.93	41	21.79	0.80	95	20.64	0.14	29	20.88	0.78
47	20.43	0.14	100	19.19	0.92	152	19.15	0.77	42	22.08	0.51	98	20.72	0.16	30	19.86	0.71
48	18.19	1.01	101	21.41	0.70	153	20.42	0.20	43	21.67	1.65	99	20.59	0.65	31	19.93	0.86
49	19.91	0.59	102	21.93	0.25	154	18.70	0.93	44	22.39	0.60	100	20.61	0.14	32	21.55	0.68
50	22.07	0.57	103	21.33	0.68	155	21.11	0.59	46	20.43	0.88	101	21.54	0.56	33	21.27	0.68
51	20.50	0.65	104	20.86	0.84	156	19.79	0.68	47	21.03	0.73	102	20.75	0.70	34	16.20	0.82
52	20.84	0.79	105	18.23	1.04	157	19.37	0.76	48	22.19	0.87	103	21.45	0.71	35	17.66	0.56
53	22.22	0.55	106	17.05	0.60	158	19.06	0.83	49	21.99	0.94	104	20.59	0.61	36	19.06	1.01

TABLE 4—*Continued*

STAR	V	B−V	STAR	V	B−V	STAR	V	B−V	STAR	V	B−V	STAR	V	B−V	STAR	V	B−V
37	18.36	1.01	96	19.98	0.64	23	20.94	0.86	73	20.53	0.81	93	17.86	1.13	113	20.56	0.12
39	19.62	0.85	98	19.96	0.61	24	20.87	0.04	74	18.72	0.95	94	20.70	0.60	114	21.61	0.70
40	19.44	0.82	99	19.63	0.83	25	20.76	-0.01	75	19.55	0.44	95	21.01	0.68	115	18.50	0.95
41	21.64	-0.20	100	19.71	0.82	26	19.96	0.82	76	20.99	0.13	96	21.71	0.56	116	20.29	0.32
42	21.25	0.67	101	20.50	0.18	27	20.63	0.04	77	21.18	0.84	97	21.28	0.81	117	16.46	1.04
43	20.74	0.00	102	20.69	0.71	28	20.75	0.69	78	19.82	0.78	98	18.69	0.93	118	20.51	0.09
44	22.00	0.62	104	21.10	0.78	29	20.18	0.78	79	20.96	0.78	99	19.68	1.47	119	20.46	0.16
45	21.54	0.71	105	20.18	0.13	30	21.24	0.45	80	20.32	1.49	100	19.74	0.79	120	20.27	0.62
46	21.35	0.51	106	20.58	0.18	31	21.97	0.34	81	19.44	0.81	101	18.54	0.93	121	20.18	0.25
47	21.08	0.70	107	18.37	1.04	32	21.42	0.70	82	20.81	0.68	102	20.98	0.76	122	19.09	0.91
48	20.45	0.74	108	21.19	0.80	33	21.67	0.65	83	21.40	0.59	103	20.42	0.19	123	21.02	0.62
49	20.80	0.76	109	20.17	0.79	34	20.79	0.10	84	21.50	0.86	104	18.25	1.00	124	20.23	0.44
50	20.60	0.11	110	20.03	0.85	35	20.32	0.48	85	21.58	0.27	105	19.05	0.94	125	21.39	0.70
51	20.82	1.40	111	19.16	0.93	36	18.47	1.10	86	20.49	0.01	106	20.52	0.15	126	18.78	0.88
53	20.47	0.78	112	19.65	1.52	37	20.78	0.14	87	20.31	0.06	107	19.29	0.90	127	19.90	0.71
54	21.22	0.80	113	19.83	0.78	38	20.25	0.72	88	19.26	0.84	108	19.33	0.92	128	17.84	1.12
55	18.60	1.02	120	20.75	0.37	39	22.00	0.25	89	20.95	0.39	109	19.24	0.86	129	20.66	0.75
56	15.32	0.65	121	19.53	0.78	40	21.80	0.71	90	20.60	0.04	110	20.03	0.82	132	20.57	0.14
57	14.65	0.90	122	18.70	0.98	41	15.60	0.64	91	21.36	0.51	111	20.45	0.79	133	19.10	0.91
58	21.76	0.52	123	21.38	0.63	42	21.76	0.71	92	20.91	0.73	112	15.60	0.87	134	14.73	1.01
59	21.23	1.02	124	20.01	0.76	43	21.89	0.44									
60	22.24	1.60	125	19.28	0.93	44	19.99	0.75									
61	20.78	0.08	126	20.33	0.31	45	20.39	0.68									
62	22.37	1.53	127	20.55	0.16	46	21.50	0.62									
63	20.87	0.64	128	19.89	0.79	47	19.75	0.76									
71	19.45	0.60	129	21.07	0.69	48	20.51	0.60									
72	20.63	0.19	130	20.03	0.76	49	20.70	1.37									
73	19.50	0.78	131	20.68	0.62	50	21.43	0.68									
74	20.60	0.02	132	16.27	0.74	51	20.94	0.63									
75	21.55	0.86	133	19.94	0.81	52	21.92	0.39									
76	19.73	0.82	134	19.18	0.89	53	20.78	0.00									
77	21.30	0.75	135	17.72	0.47	54	19.92	0.74									
78	20.27	0.21	IV 1	20.82	0.02	55	19.02	0.88									
79	20.99	0.54	2	20.90	0.76	56	21.11	-0.09									
80	21.63	0.73	3	20.53	0.15	57	21.56	0.61									
81	19.97	0.35	5	22.28	0.92	58	21.32	0.92									
82	20.61	0.85	6	23.09	0.85	59	19.89	1.63									
83	21.60	0.68	7	20.67	0.60	60	20.66	0.12									
84	19.98	0.84	8	20.57	0.70	61	20.44	0.11									
85	20.93	0.84	11	21.91	0.87	62	20.61	0.72									
86	18.29	1.02	12	20.95	0.63	63	20.71	0.80									
87	20.78	0.06	12A	20.67	0.72	64	19.09	0.92									
88	21.49	0.67	13	19.80	0.69	65	19.70	0.80									
89	17.33	1.34	14	18.96	0.95	66	21.56	0.53									
90	20.53	0.10	16	20.43	0.13	67	20.92	0.62									
91	20.16	0.68	18	21.70	0.71	68	20.12	0.51									
92	20.49	0.16	19	18.34	1.43	69	21.60	0.76									
93	21.43	0.69	20	21.62	0.84	70	18.07	1.24									
94	19.95	0.85	21	18.44	0.98	71	19.64	0.79									
95	20.91	0.06	22	18.67	0.81	72	20.07	0.76									

NGC 2419 - PROGRAM STARS   INNER REGION

STAR	V	B−V	STAR	V	B−V	STAR	V	B−V
1	18.35	1.05	13	19.33	0.93	25	18.05	1.08
2	18.70	1.04	14	18.93	1.00	26	17.81	1.11
3	17.54	1.36	15	19.28	0.80	27	18.62	0.76
4	17.76	1.21	16	19.23	0.88	28	17.30	1.38
5	17.68	1.23	17	20.00	0.53	29	13.85	1.00
6	19.14	1.01	18	19.48	0.77	31	17.78	1.22
7	18.84	1.03	19	18.99	0.92	33	18.32	1.03
8	17.43	1.40	20	18.64	1.07	34	17.45	1.11
9	14.50	0.59	21	18.64	0.96	35	18.25	1.06
10	17.59	1.28	22	18.92	0.94	36	18.14	1.13
11	18.25	1.09	23	18.14	0.54	37	18.16	1.13
12	18.63	0.99	24	18.63	0.91	38	17.43	1.33
						39	13.45	0.79

TABLE 4—*Continued*

NGC 2419—PROGRAM STARS RING B

STAR	V	B−V	STAR	V	B−V	STAR	V	B−V
I 1	15.74	0.76	4	20.89	0.86	32	20.76	0.10
2	16.01	0.89	6	21.99	0.51	33	20.30	0.87
3	16.02	1.03	7	19.68	1.44	35	22.09	0.18
4	19.21	0.92	8	20.58	0.12	36	21.86	0.62
5	21.64	0.19	9	17.61	0.36	37	20.34	0.68
6	17.52	0.64	10	21.77	0.72	38	19.36	0.77
7	18.72	1.32	11	16.95	0.51	39	21.38	-0.07
8	21.76	-0.34	12	20.72	0.18	IV 1	20.92	0.74
9	21.48	0.16	13	17.80	1.07	3	21.51	0.90
10	20.70	0.13	14	20.72	0.06	4	20.76	1.71
11	17.31	0.93	15	22.19	1.48	5	21.41	0.82
12	21.07	0.80	16	20.28	0.82	6	17.69	1.25
13	20.77	1.14	18	20.54	0.17	7	20.89	0.70
14	19.99	1.52	19	21.82	1.18	8	21.21	0.84
15	21.26	0.67	20	18.16	1.57	9	18.94	1.46
16	20.14	0.96	21	21.80	1.46	10	21.88	0.62
17	20.29	1.70	22	18.55	1.04	12	20.83	0.76
18	18.78	0.49	23	19.55	0.63	13	21.17	-0.14
20	21.39	0.26	24	21.38	-0.07	14	21.38	0.30
22	20.79	-0.03	25	21.81	1.33	15	19.12	1.19
23	20.75	0.02	26	20.86	1.58	16	22.19	0.29
24	19.83	0.85	27	21.52	-0.36	17	22.03	0.47
25	21.41	0.27	28	20.94	-0.08	18	19.64	1.28
26	17.87	0.92	30	19.76	0.60	19	18.82	0.58
27	18.06	1.07	31	18.06	1.10	20	20.67	1.63
29	20.13	0.53	32	18.75	1.06	21	22.19	0.21
31	19.64	1.54	III 3	22.20	0.27	22	19.93	0.75
32	19.27	0.79	4	21.29	0.95	23	18.93	0.51
33	21.20	-0.01	5	21.73	0.72	24	21.38	0.88
34	20.55	0.80	6	20.59	0.40	25	21.92	0.57
35	18.62	1.06	7	19.29	0.84	26	21.91	0.45
36	21.54	-0.19	8	17.68	0.37	27	21.86	0.60
37	21.28	0.84	9	21.72	0.75	28	21.84	0.51
38	18.57	1.45	11	19.70	1.21	29	20.62	0.84
40	20.56	1.33	12	17.10	0.49	30	21.95	0.54
41	19.05	1.39	13	19.22	0.84	31	20.55	1.33
43	21.15	0.12	14	21.09	1.61	32	20.68	0.70
44	21.83	0.13	15	20.71	1.13	33	19.12	0.33
45	21.54	0.23	17	18.04	0.70	34	21.06	0.94
46	20.83	0.76	18	21.37	0.97	35	20.63	0.68
47	21.84	0.12	19	20.67	0.67	36	21.70	0.75
49	21.26	0.49	20	22.11	0.03	37	21.64	0.80
50	21.05	0.76	21	19.20	1.52	38	20.39	0.14
51	19.93	0.76	22	19.23	1.30	39	19.32	0.89
52	20.82	1.09	23	20.78	0.00	40	17.33	1.42
53	19.94	0.66	24	20.56	0.62	41	19.39	0.80
54	21.16	0.45	26	21.15	1.08	42	21.18	1.19
55	21.43	-0.22	27	21.15	0.80	43	21.57	0.80
II 1	21.80	0.58	28	19.91	0.88	44	19.24	0.78
3	18.73	0.65	29	20.50	0.14	47	21.08	1.41

Table 4 presents the final list of V and $B - V$ values for the 700 photographically measured program stars. The internal random errors of the tabulated values, determined from the plate-to-plate residuals, are listed in table 5.

Plate-to-plate comparison of the faint-magnitude scales indicates that the final magnitude calibration should have a *systematic* error of less than ±0.07 mag at $V \simeq 21$. Systematic errors in the *colors* of faint stars should be ±0.05 mag or less; this is achieved by ensuring that the photographically determined colors of each primary-secondary image pair are the same (as they should be, since the "wedge" itself is achromatic).

TABLE 5

RANDOM ERRORS OF PHOTOGRAPHIC MAGNITUDES

V	σ_V	σ_B	σ_{B-V}
≤19..........	0.05	0.02	0.05
20..........	0.04	0.05	0.06
21..........	0.10	0.09	0.14
22..........	0.18	0.13	0.22

Radial field errors were also investigated, by comparing the C-M arrays at varying distances from the cluster center. Corrections were found to be negligible except for faint stars ($V > 20$) within 5ʹ.2 of the cluster center. Corrections (reaching 0.20 mag in the innermost region at $V \simeq 21$) were applied to the magnitudes of these stars, but no *color* corrections were found necessary.

The final C-M diagrams for rings A and B and for all data combined are presented separately in figures 5*a*, 5*b*, and 6; these will be discussed in § V below.

III. COMPARISON WITH BAADE'S $m_{\rm pg}$ SCALE

The photometric scale in NGC 2419 used in the previous work by Baade (1935) was established by three closely consistent photographic transfers to a faint standard sequence in SA 51. In SA 51, Baade himself had used the exposure ratio technique to extend a bright sequence, which was itself transferred from the North Polar Sequence (Seares, Kapteyn, and van Rhijn 1930).

In order to transform Baade's observations of the variables in NGC 2419 to the present B magnitude scale, his $m_{\rm pg}$ values and our B magnitudes for a number of his standard stars were compared. In addition, the bright Mount Wilson magnitudes in SA 51 were compared with Baum's (unpublished) photoelectric measurements, since Baade did not publish his extended faint sequence in SA 51. The results are shown in figure 3 and indicate that for faint stars the Mount Wilson scale is compressed with respect to the present B scale, and that the trend in SA 51 continues in NGC 2419 without a perceptible break. This shows that Baade's transfers were correct and that the error lay with the SA 51 photographic scale. For the magnitude range of interest in NGC 2419 ($17 < B < 22$) the two scales are adequately transformed by the linear relation

$$B = 1.35\, m_{\rm pg} - 5.36\,. \qquad (2)$$

In figure 3, the random scatter of ± 0.09 mag (A.D.) in $m_{\rm pg}$ is gratifyingly small. Baade's photometry has an internal probable error of ± 0.06 mag; this implies an external probable error of ± 0.07 mag for the present B magnitudes for $18 < B < 23$, in reasonable agreement with the random errors of ± 0.08 mag mentioned previously (table 5).

IV. REDDENING DETERMINATION

Six methods can be used to determine the foreground reddening of NGC 2419. These are discussed below in approximate order of decreasing accuracy.

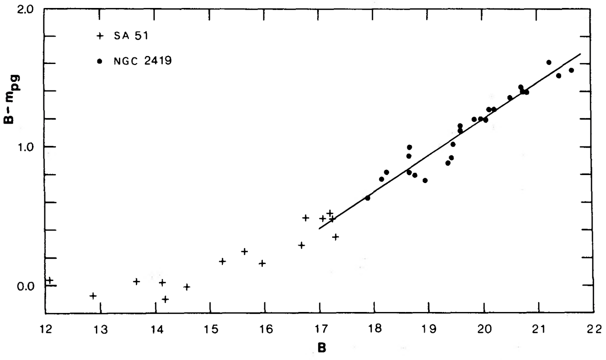

FIG. 3.—Comparison of the present B magnitude scale in NGC 2419 and in SA 51 with Baade's $m_{\rm pg}$ scale. The difference between the two scales, $B - m_{\rm pg}$, is plotted as a function of B. For $B < 17$, Baum's photoelectric measures of stars in SA 51 are compared with the old $m_{\rm pg}$ values for these stars (Seares *et al.* 1918), and for $B > 17$, the plotted points are for Baade's (1935) standard stars in NGC 2419. The adopted relation between the two scales is given by eq. (2) in the text.

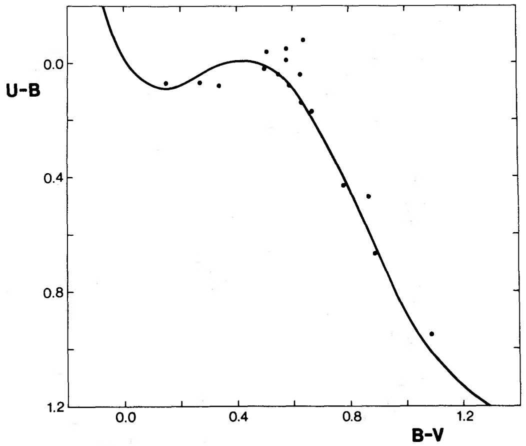

FIG. 4.—Two-color diagram for the photoelectric standard stars in table 1. All stars with at least three measurements in each color are plotted, along with the unreddened ZAMS line. A low foreground reddening of $E(B - V) \lesssim 0.04$ is indicated for NGC 2419.

a) *Integrated Color of Cluster*

Racine (1973) has calibrated the integrated color $(B - V)_0$ of a globular cluster in terms of its integrated spectral type (Kinman 1959*b*). The spectral type of F5 and integrated color $B - V = 0.68$ (Harris and van den Bergh 1974) lead to $E_{(B-V)} = 0.03$.

b) *UBV Photometry of Field Stars*

The two-color diagram for all the photoelectric standards in table 1 with at least three measurements in each color is shown in figure 4, together with the unreddened main sequence line. Neglecting the stars near $B - V = 0.6$ showing obvious ultraviolet excess, a reddening of $E_{(B-V)} \lesssim 0.04$ is derived.

c) *Blue Edge of RR Lyrae Gap*

The heavily populated blue horizontal branch seen in figure 5*a* stops abruptly at $B - V = 0.20 \pm 0.01$. The intrinsic color of this blue edge is assumed to be $(B - V)_0 = 0.17 \pm 0.01$ (Sandage 1969*a*), which implies $E_{(B-V)} = 0.03 \pm 0.02$. This method acts only as a check on the others, since it depends critically on the systematic accuracy of the photographic color determinations.

d) *Fitting to M92*

The C-M diagram for NGC 2419 is closely similar to that for the classical halo cluster M92 (Sandage 1970). Fitting the M92 ridge lines to the NGC 2419 diagram in figure 5*a* shows the latter to be redder by 0.02 ± 0.02 mag. Since M92 itself is reddened by 0.02 mag (Sandage 1969*a*), this implies $E_{(B-V)} = 0.04 \pm 0.02$ for NGC 2419.

e) *Reddening of NGC 2420*

The old open cluster NGC 2420 lies within 18° of NGC 2419 and at the same galactic latitude. An

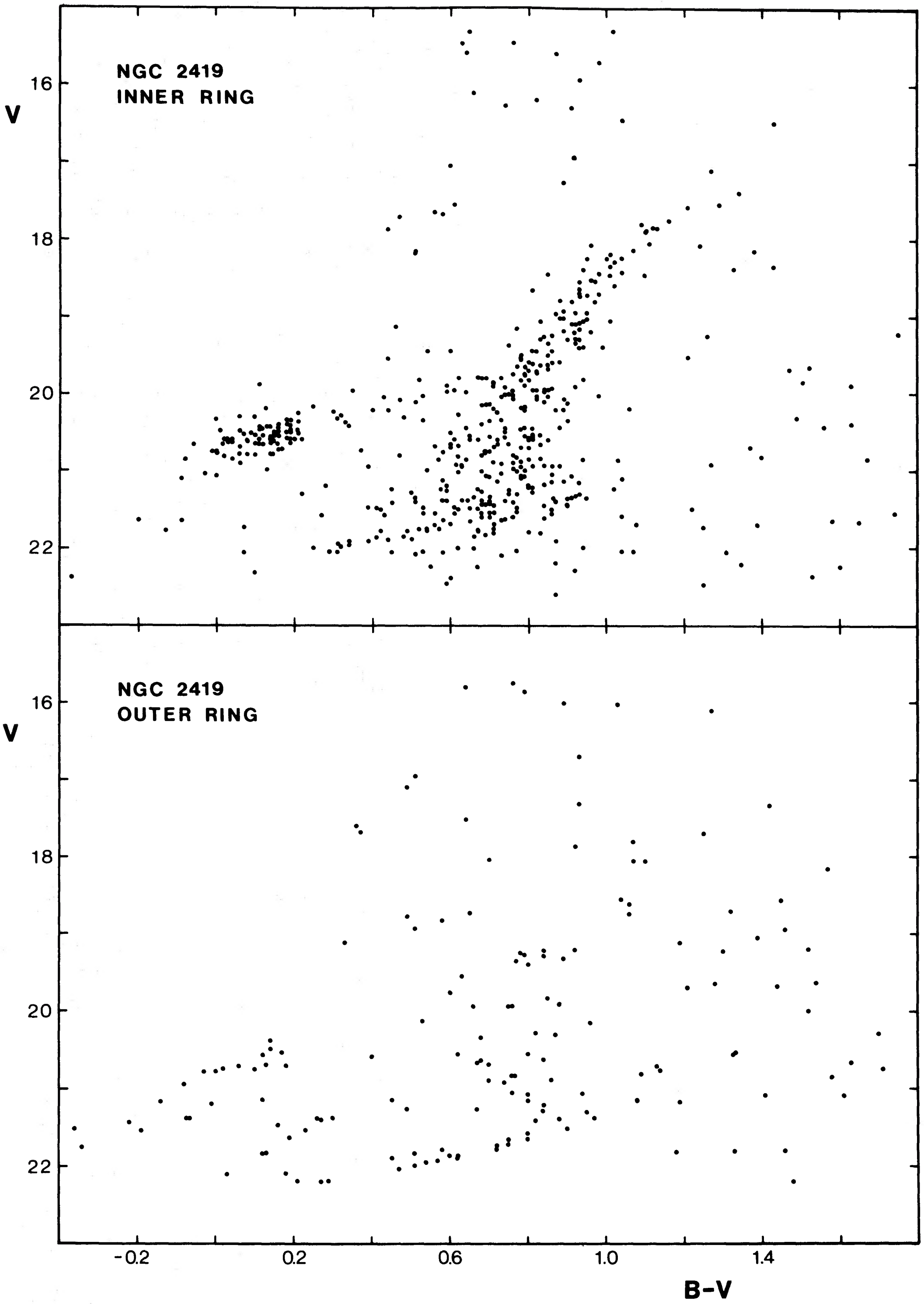

FIG. 5.—(*a*) C-M diagram for all measured stars in ring A, is listed in tables 1 and 4. (*b*) Same for the outer ring B. The population of foreground field stars should be the same for both rings since they have the same area.

TABLE 6

REDDENING DETERMINATIONS FOR NGC 2419

Method	$E(B-V)$
Integrated color..........	0.03
Field stars...............	0.04
RR Lyrae blue edge......	0.03
Fitting to M92...........	0.04
NGC 2420...............	0.02
Cosecant law............	0.04
Adopted mean	0.033 ± 0.01

intermediate-band and BV photometric study by McClure, Forrester, and Gibson (1974) yields $E_{(B-V)} = 0.02, \pm 0.01$ for NGC 2420.

f) *Cosecant Law*

The newly modified cosecant absorption law by Sandage (1973) predicts $E_{(B-V)} = 0.04$ at the galactic latitude of NGC 2419.

The various reddening estimates—which are remarkably consistent—are summarized in table 6. A final mean of $E_{(B-V)} = 0.033 \pm 0.01$ is adopted, corresponding to $A_V = 3.2E_{(B-V)} = 0.10 \pm 0.03$.

V. THE C-M DIAGRAM

a) *Morphology*

The C-M diagram displayed in figure 5*a* shows immediately that NGC 2419 has the characteristics of a "normal" halo globular cluster. The giant branch (GB), which sets in at $V \simeq 17.4$, $B-V \simeq 1.4$, has the steepness and color typical of metal-poor clusters, and a heavily populated blue horizontal branch (BHB) appears at $V \simeq 20.5$. A thin line of stars at $V \simeq 20.1$, $B-V \gtrsim 0.4$, may represent an incipient red horizontal branch, or the lower part of an asymptotic giant branch (AGB). Unfortunately the random errors in $B-V$ are too large to trace a possible AGB much higher than this.

The GB continues downward to the plate limit past $V \sim 22.3$. The data become incomplete below $V = 21.0$ in the inner part of ring A, where radial field errors also become noticeable. Foreground field stars appear to contribute about half the total population of the outer ring B, but these do not present a problem in ring A where the principal cluster sequences are well populated.

Figure 6 displays the combined C-M data for *all* stars in tables 1 and 4, along with some of the known variables (see § V*f* below); the mean ridge lines for this graph are given in table 7. It should be emphasized that figure 6 does *not* represent a homogeneous sample of data (as do figs. 5*a* and 5*b*), since the upper part of the giant branch has been reinforced by including the extra "inner region" stars.

b) *Metallicity*

Comparison with a number of other halo clusters shows that the NGC 2419 C-M diagram closely resembles those of the two classic very-metal-poor

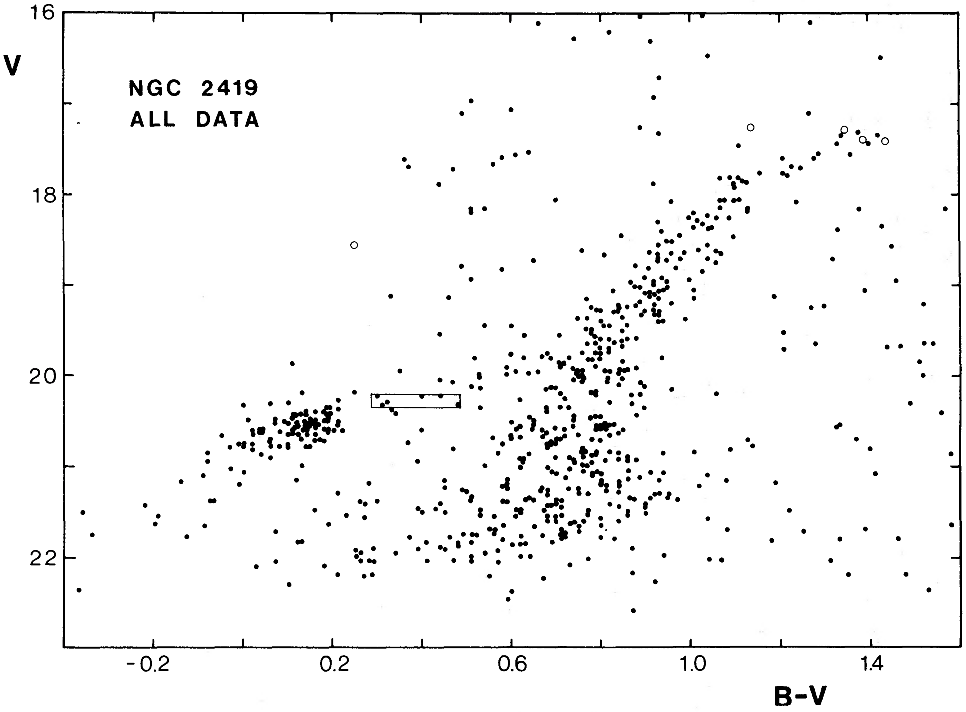

FIG. 6.—Combined C-M diagram for *all* measured stars, including the "inner region" as listed in table 4. The approximate mean positions of the five bright variables are shown by open circles, and the rectangular error box at $V \simeq 20.3$ denotes the mean position of the 12 short-period (RR Lyrae) variables measured in the present study.

TABLE 7

RIDGE LINES FOR COLOR-MAGNITUDE DIAGRAM

GIANT BRANCH		AGB + HB	
V	$B - V$	V	$B - V$
17.33	1.42	19.00	0.85
17.36	1.40	19.22	0.80
17.52	1.30	19.48	0.75
17.71	1.20	19.70	0.70
18.00	1.10	19.88	0.65
18.45	1.00	19.95	0.60
19.03	0.90	20.10	0.50
19.33	0.85	20.20	0.44
19.72	0.80	20.50	0.20
20.28	0.75	20.60	0.10
21.10	0.70	20.70	0.05
22.00	0.65	20.87	0.00
		21.00	−0.04
		(21.30	−0.10)
		(21.55	−0.15)

clusters M92 and M15 (Sandage 1970). The giant branch (GB) and blue horizontal branch (BHB) match extremely well with M92 in particular.

The low metallicity of NGC 2419 is further established by three well-known parameters describing the height and slope of the giant branch: the height ΔV at $(B - V)_0 = 1.4$ (Sandage and Wallerstein 1960), the intrinsic color at the level of the horizontal branch $(B - V)_{0,g}$ (Sandage and Smith 1966) and the slope S (Hartwick 1968). These are listed for NGC 2419 in table 8, in comparison with M92 and M15 (Sandage 1970).

One other notable feature in the C-M diagram of figure 6 is the way that the BHB cuts off abruptly at $V = 20.9$ with only a thin scattering of stars below this—again, resembling a similar phenomenon in M15 (Sandage, Katem, and Kristian 1968). This cannot be a result of incompleteness or selection effects, since it occurs even in the outer parts of ring A where these problems do not appear until $V > 21.5$. This cutoff may possibly be related to the "gap" discussed by Newell (1973), at $(B - V)_0 = -0.13$, $(U - B)_0 = -0.40$, in the distribution of field BHB stars.

c) Distance

The distance modulus of NGC 2419 can be estimated either from the level of the BHB and RR Lyrae variables, or by fitting to the M92 C-M diagram. For the latter method, NGC 2419 is 5.32 mag fainter than M92 as shown in § IV above. Combining this with $(m - M)_v(\text{M92}) = 14.63$ (Sandage 1970) then gives $(m - M)_V = 19.95$ for NGC 2419.

TABLE 8

PARAMETERS OF THREE METAL-POOR CLUSTERS

Parameter	M15	M92	NGC 2419
ΔV	3.2	3.2	3.15 ± 0.1
$(B - V)_{0,g}$	0.68	0.68	0.70
S	6.9	5.7	6.8 ± 0.5

For the horizontal branch, the stars in figure 6 at the blue edge of the RR Lyrae gap $(0.1 < B - V < 0.2)$ fall at a mean level $\langle V \rangle_{\text{HB}} = 20.54 \pm 0.40$ (s.e.). This gives $(m - M)_V = 19.94$, assuming $M_V(\text{HB}) = 0.6$ (Sandage 1970).

Finally, the mean magnitude of the RR Lyrae variables can be used. Transforming Baade's mean m_{pg} for his 31 variables by equation (2) gives $\langle B \rangle_{RR} = 20.62 \pm 0.02$, or $\langle V \rangle_{RR} = 20.32 \pm 0.05$ assuming $\langle B - V \rangle_{RR} = 0.3 \pm 0.05$. By comparison, our own measurements of 12 of these stars from the B and V plates taken in a single 2-hour period, yield $\langle V \rangle_{RR} = 20.28 \pm 0.10$ (s.e.) and $\langle B - V \rangle_{RR} = 0.39 \pm 0.13$. This reinforces Baade's result and supports the identification of these stars as RR Lyrae types.

The difference of 0.22 ± 0.06 mag between the levels of the blue edge and of the RR Lyrae themselves is significant and suggests that the "horizontal branch" of NGC 2419 in fact slopes upward as $B - V$ increases. The thinly populated *red* horizontal branch noted previously in figure 6 thus seems to be a direct natural continuation of this slope; at $B - V = 0.6$ the HB is 0.5 mag higher than at the blue edge. This somewhat unusual feature of NGC 2419 will be rediscussed in the next section.

The distance modulus estimates are summarized in table 9, and lead to the adopted result $(m - M)_V = 19.87 \pm 0.09$ m.e., or $(m - M)_0 = 19.77 \pm 0.1$ with the adopted reddening (§ IV). [The quoted errors neglect the uncertainty in $M_V(\text{HB})$.] The result places NGC 2419 a distance of 90 ± 5 kpc from the Sun and 100 kpc from the Galactic center, more distant than any other known cluster. The immensity of this distance can be emphasized by noting that the brightest giant-branch stars in NGC 2419 are almost a full magnitude *fainter* than the main-sequence turnoff stars in the *closest* known globular cluster, NGC 6397 (Woolley *et al.* 1961)!

d) Age

A detailed comparison of the C-M diagram of NGC 2419 with theoretical models would be premature in view of the work in progress by a number of authors on the advanced evolution of globular-cluster stars. Nevertheless, a few brief comments can be made here on the age and abundance characteristics of NGC 2419 by referring to recent work by Rood (1973, 1974), who has been able to show how the morphology of the HB depends on cluster metallicity and age. Especially relevant to the case of NGC 2419 is Rood's finding that for very metal-poor clusters $(Z \sim 10^{-4})$ the HB indeed slopes up toward its red end. (For example, compare our fig. 6 with Rood's 1973 fig. 4*b*.) Since the HB slope (at constant Z) is nearly independent of age, this criterion can be used to estimate Z. Comparing Rood's models with the NGC 2419 C-M diagram, we estimate $Z \simeq 1.5 \times 10^{-4}$ for NGC 2419, confirming quantitatively our earlier conclusion about its very low metallicity. The age itself follows from the relative number of stars at the blue and red sides of the RR Lyrae region and from the way that the BHB extends to fainter magnitudes.

TABLE 9

DISTANCE MODULUS OF NGC 2419

Method	Assumptions	$(m-M)_v$
Blue edge of HB........	M_v (blue edge) = +0.6	19.94
Median B_{RR}............	M_v(RR) = +0.6	19.72
Fit to M92.............	Identical ridge lines; $(m-M)_{v,M92} = 14.63$	19.95
Adopted mean........		19.87 ± 0.09 m.e.
$(m-M)_0$............		19.77 ± 0.10
Distance.............		90 ± 5 kpc

Again comparing NGC 2419 with Rood's models, we find $T = 11 \pm 0.5 \times 10^9$ yr. Note, however, that the *luminosity* of the HB in Rood's models is a sensitive function of the arbitrarily adopted mean mass loss in the pre-HB phases, and that his HB's are from 0.3 to 0.8 mag brighter than the "canonical" observational value $M_v = 0.6$ which we preferred to adopt for our distance estimate.

The age of NGC 2419 will be discussed again from a completely independent viewpoint in § VI, in relation to its galactic orbit.

e) Luminosity Function of the Giant Branch

Interest in the luminosity function of giant-branch stars in globular clusters was given new impetus by the work of Sandage *et al.* (1968), who pointed out the possible existence of "gaps" in the giant branch of M15 and other clusters. A similar analysis can effectively be carried out here for NGC 2419 because of the large number of stars measured. Visual inspection of figures 5*a* and 6 indicates a rather obvious "gap" at $V \simeq 20.3$, and two other noticeable ones at $V = 19.5$ and $V = 18.9$.

A simple statistical test of the significance of these possible gaps can be carried out in the manner employed by Hawarden (1971) and Newell (1973). Figure 7 shows the cumulative luminosity function for the giant branch of NGC 2419, where $N(V)$ is the total number of giants brighter than magnitude V. In this graph, a "gap" will appear as a horizontal break or flattening of the integral curve. The statistical significance can then be estimated by averaging the mean slopes of the curve on either side of the chosen gap, and using this average slope to predict the number N_0 of stars that would be expected to fall in the gap. Comparing N_0 with the actual number of stars N in the gap then gives the statistic $\chi^2 = (N_0 - N)^2/N_0$, from which the probability P of its chance occurrence can be evaluated (cf. the discussion by Newell 1973).

For the luminosity function in figure 8, the "gaps" at $V = 18.9$ and 19.5 prove to be not statistically significant ($P = 0.07$ and 0.12, respectively). The feature centered at $V = 20.3$ and 0.3 mag wide has $\chi^2 = 7.04$, from which $P = 0.008$. This gap must therefore be considered likely to be a physically significant feature, in the sense that it represents a temporary speeding up of stellar evolution through this region.

Another possible but more prosaic explanation of this feature might be that the C-M diagram has a well-populated asymptotic giant branch (AGB) which stops at $V \simeq 20.1$ just at the red horizontal branch, thus creating the illusion of a gap immediately below. For example, if we assume that one-third of the stars above the HB are part of a populous AGB, the gap would be significant at the 93 percent confidence level; but in this case, the *change* in slope at $V = 20.3$ in figure 8 would become significant.

It is notable that this gap is $\lesssim 0.2$ mag above the horizontal branch, whereas in the M15 data of Sandage *et al.* the principal gap is 0.9 mag above the horizontal branch. Theoretical suggestions made to explain the existence of a gap include the effects of interior rotation on the outward movement of the hydrogen-burning shell of a giant star (Demarque, Mengel, and Sweigart 1972), or simply fluctuations in the cluster's initial mass function (Iben 1971). In neither case is it clear whether any gap would be expected to occur always at the same point. Further work of this type on other clusters will be essential if the gap position is to be related to other cluster properties.

f) The Bright Variables

In addition to 31 short-period variables, Baade discovered five brighter variables which he believed to be irregular and to "probably belong to spectral types G to K." All but one of these are too close to the cluster's center to be measured by iris photometry. Their colors were therefore estimated visually on the two V and three B plates taken on 1972 March 9 and 10. The results are given in table 10 where $\langle V \rangle$ has been obtained by transforming Baade's median m_{pg} into $\langle B \rangle$, then applying the mean $\langle B - V \rangle$ estimates. These variables are shown as open circles in the C-M diagram of figure 6. V1, V8, and V20 are seen to fall at the tip of the GB. Notably, they occur at somewhat

TABLE 10

OBSERVATIONS OF BRIGHT VARIABLES

Variable	$\langle V \rangle$	$\langle B - V \rangle$
V1........	17.41	+1.44
V8........	17.30	+1.35
V10........	17.27	+1.14
V18........	18.57	+0.25
V20........	17.39	+1.39

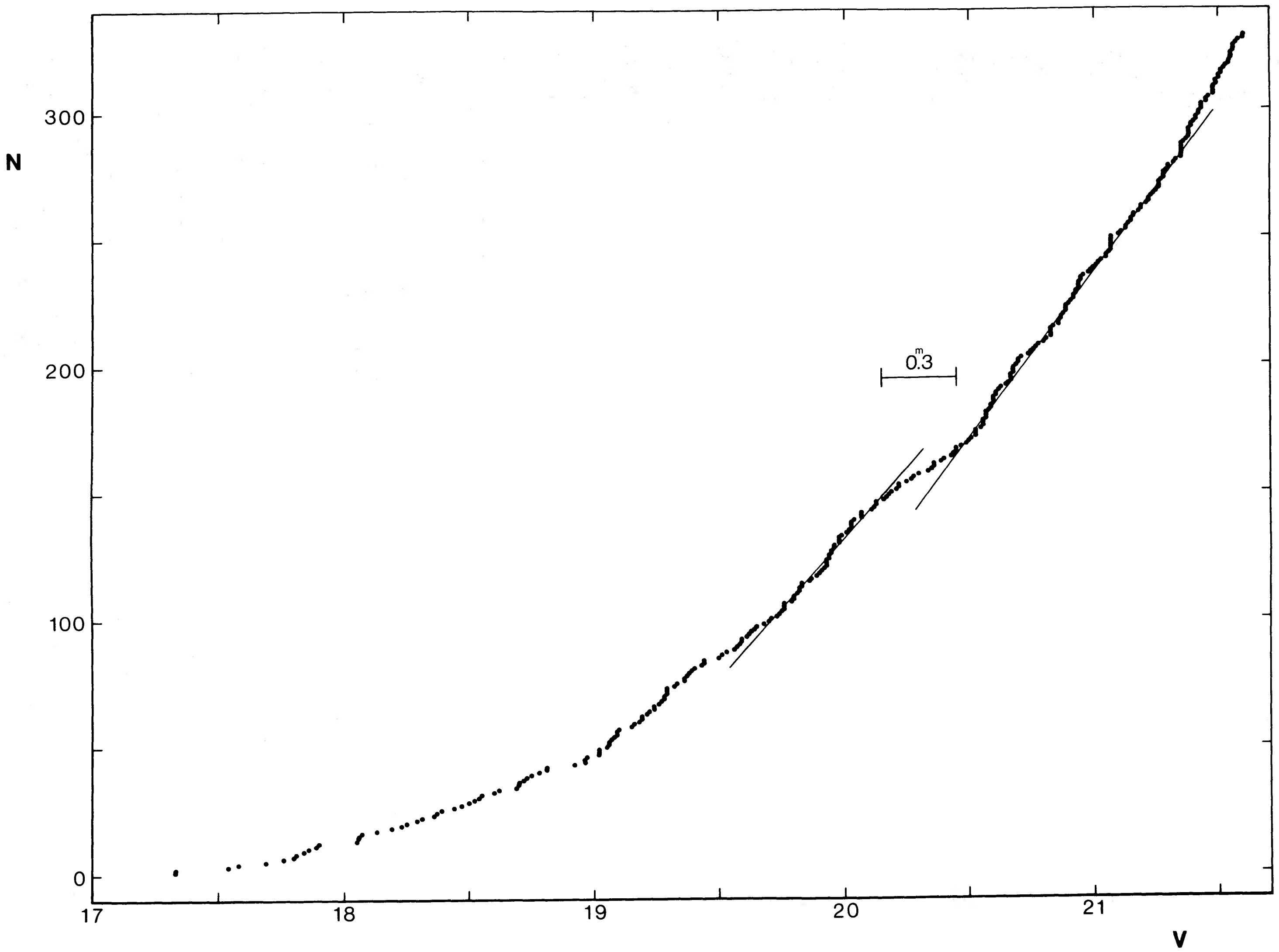

FIG. 7.—Cumulative luminosity function for the giant branch down to $V \simeq 21.5$. Here N is the total number of giant stars brighter than magnitude V, plotted as a function of V. All stars in rings A and B which fall on the giant branch are used.

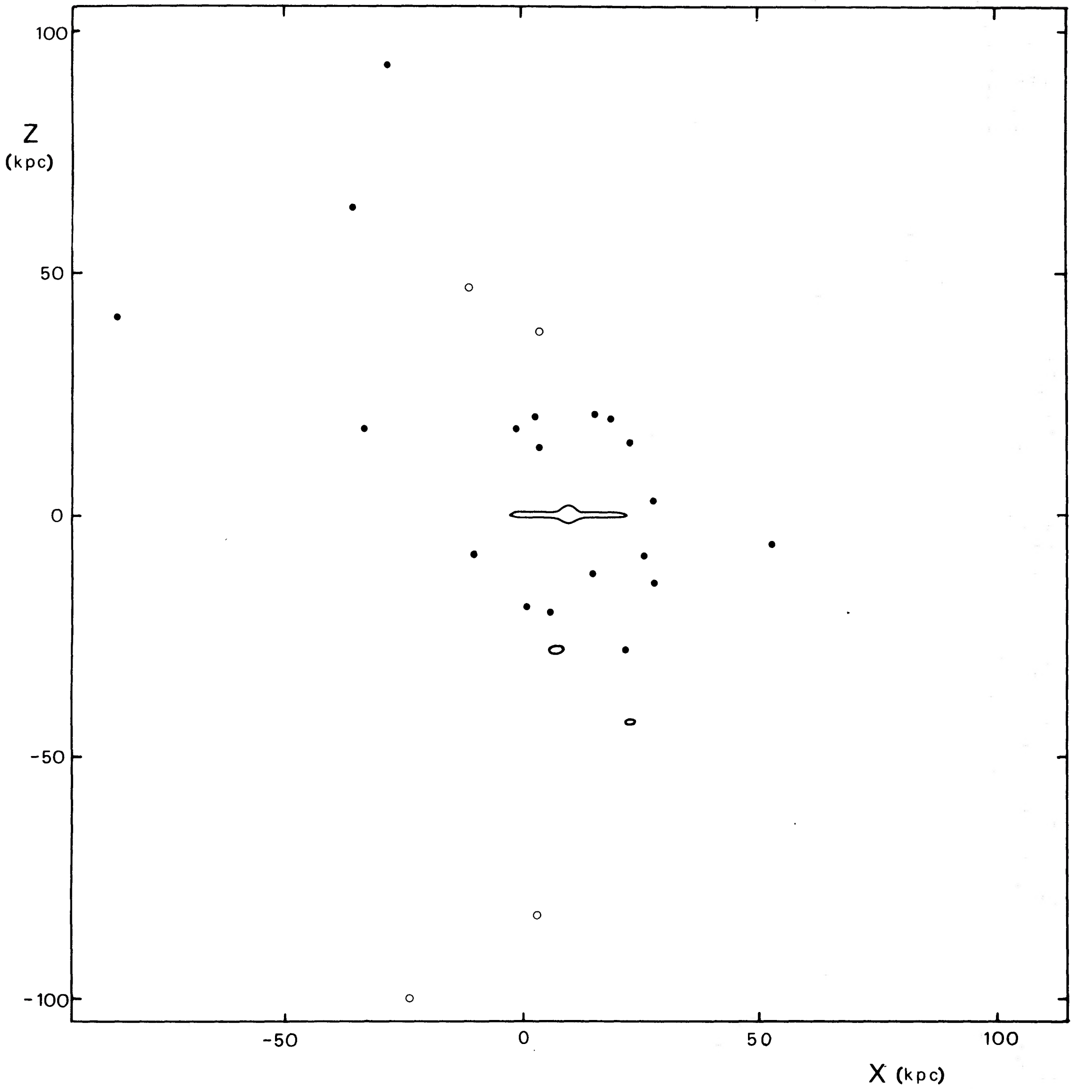

FIG. 8.—The distribution of "outer halo" objects, projected in the (X, Z)-plane. The diagram includes all objects with known galactocentric distances larger than 20 kpc. The Galactic disk is seen at center. Globular clusters are plotted as dots; dwarf spheroidal galaxies, as open circles; and the Magellanic Clouds, as the two small ellipses below the Galactic plane. NGC 2419 is the cluster at farthest left; this emphasizes its extreme distance and its present position at the fringe of the outer halo.

higher effective temperatures than the M-type variables found in later type globular clusters. Stothers (1963) points out that clusters rich in RR Lyrae variables tend to have shorter period and bluer late-type variables and the F3- to F5-type globulars produce RV Tauri variables. This appears to be confirmed in NGC 2419 whose integrated spectral type is F5 (Kinman 1959*b*). V10, slightly to the blue of the GB, is possibly an RV Tauri type.

The nature of the blue bright variable V18 is uncertain. Its position in the C-M diagram is too blue to be consistent with the location of the Population II Cepheid instability strip (Demers and Harris 1974); but its photometry is very uncertain, and a final conclusion must await a study of its light and color curves.

VI. ORBITAL KINEMATICS

a) The Outer Galactic Halo

Figure 8 shows the distribution of objects in the outer galactic halo (those with galactocentric distances greater than 20 kpc), projected on the (X, Z)-plane. NGC 2419 is seen to belong to the outermost fringes of our stellar system, comparable with the dwarf spheroidals and more distant than the Magellanic Clouds. In a forthcoming paper (Racine 1975) it will be shown that the galactic halo has an outer limiting radius R_t (imposed by tidal encounters with M31 ?) which falls in the range $8R_0 < R_t < 15R_0$, where the solar galactocentric distance is $R_0 =$ 9 kpc (van den Bergh 1971). Hence the outlying systems in figure 8 may all be within R_t. Whether they are all actually gravitationally bound to the Galaxy might only be decided on the basis of their generally unavailable radial velocities.

A number of statistical investigations of the orbits of globular clusters have been published. Edmondson (1935) and Kurth (1960) found that the orbits (assumed to be ellipses) have axial ratios close to unity ($b/a > 0.8$), whereas von Hoerner (1955) and Kinman (1959*c*) concluded that the orbital eccentricities are high ($e > 0.8$). Because of the uncertainties involved in such studies, these two conclusions need not be incompatible; for an elliptical orbit, we have $b/a = (1 - e^2)^{1/2}$, and so $b/a \sim 1$ even for large eccentricities.

The picture of halo objects having highly eccentric orbits gained considerable substance from the classical study of the kinematics of nearby stars by Eggen, Lynden-Bell, and Sandage (1962, denoted ELS). They concluded, by studying a large sample of stars of different velocities and abundances, that the metal-poor galactic halo collapsed on a time scale comparable to the present rotation period of the disk ($\simeq 2 \times 10^8$ yr at the Sun). More recently this view has been challenged, particularly by Rood and Iben (1968) and Bond (1970) (but see footnote in Sandage 1970). In addition, Larson (1974) has provided strong evidence that the collapse phase and star-formation period of a large galaxy can be 10^9 years or longer even for the halo.

Conclusive evidence on the kinematics prevailing during the formation period of the present halo objects would be better obtained from a study of objects *now* in the halo, rather than from a sample of nearby stars selected on kinematical grounds. In practice, this approach is extremely difficult since the orbital parameters of these distant objects must be determined without knowledge of their tangential velocities. Large uncertainties may also be introduced by a possible error in our estimate of the circular velocity at the Sun. In the case of NGC 2419, however, the orbit *can* be uniquely determined.

b) Orbital Parameters of NGC 2419

Because NGC 2419 is so distant and lies in the anticenter direction, the angular separation between the Sun and the galactic center is only 2°.5 as seen from the cluster. Its radial velocity with respect to the Sun can thus be taken as the radial component V_R of its orbital velocity about the galactic center. Its measured radial velocity is $+14 \pm 20$ km s^{-1} (Kinman 1959*a*); after correcting to the local standard of rest (Delhaye 1965), this gives $V_R = +4 \pm 20$ km s^{-1}. Since V_R is essentially zero compared with the circular velocity at its present distance ($\Theta_c = 85$ km s^{-1} at 100 kpc, from Schmidt 1965), the cluster can therefore be assumed to be at either apogalacticon or perigalacticon.

Star counts in NGC 2419 (Peterson and King 1973) show that the cluster possesses a well-defined tidal radius of 10′. From this, Peterson (1974) deduces that the cluster must have a perigalacticon of $R_p =$ 22.5 kpc, using $R_g = 80$ kpc for its present galactocentric distance, and assuming a mass-to-light ratio within the cluster of unity. The new distance of $R_g = 100$ kpc determined here leads to $R_p = 24$ kpc. This then implies that NGC 2419 is gravitationally bound to the Galaxy, and is now very close to its apogalacticon.

TABLE 11

ORBITAL PARAMETERS FOR NGC 2419*

Semimajor axis	62 kpc
Eccentricity	0.62
Period	3.4×10^9 yr
Time of perigalacticon passage	1.7×10^9 yr ago

* Adopted galactic mass: $1.8 \times 10^{11} M_\odot$ (Schmidt 1965).

The orbital parameters, derived under the assumption of an elliptical orbit, are summarized in table 11. The orbit is completely determined *except* for inclination and sense of rotation; for no other cluster is it possible to do this, either because the geometry is ambiguous or the radial velocities are unknown. It should be emphasized that the parameters in table 11 are rather insensitive to the detailed mass model of the Galaxy and (except for the eccentricity) depend only weakly on the value of R_p derived from the tidal radius. This is so because, for most or all of its orbit, NGC 2419 is at such a huge galactocentric distance that only the *total* mass M_g of the Galaxy affects its motion. In particular, the time elements in table 11 scale as $M_g^{-1/2}$.

c) Angular Momentum of Halo Clusters

Although the present orbit of NGC 2419 may not be its original one (§ VI*d* below), it must at present possess a high angular momentum h per unit mass, since it moves on such a large orbit of axial ratio $b/a = 0.8$. This is contrary to the ELS picture of old halo objects moving in "nearly rectilinear orbits" of low h, and suggests that it would be worthwhile to compare this feature of NGC 2419 with the other globular clusters.

Peterson's (1974) recent determination of perigalacticon distances R_p for 41 clusters can be used to compute *minimum* values of h for these clusters, from the general relation

$$h^2 = GMR_p(1 + e) . \qquad (3)$$

On the other hand, the *maximum* possible value of h for each cluster can be found by assuming $e = 1$. The frequency distributions of $h_{\min}$ and $h_{\max}$ are shown in figure 9, where h has been normalized to the mass-weighted mean angular momentum for the Galaxy according to the Schmidt (1965) mass model. For the Sun, $h \simeq \langle hg \rangle = 2500$ km kpc s^{-1}. It is apparent from the figure that the *outer halo* clusters possess orbital angular momenta which are generally *larger* than those of the clusters close to the galactic disk. Furthermore, figure 10 shows how h correlates with the metallicity parameter Q (van den Bergh

1975ApJ...196..351C

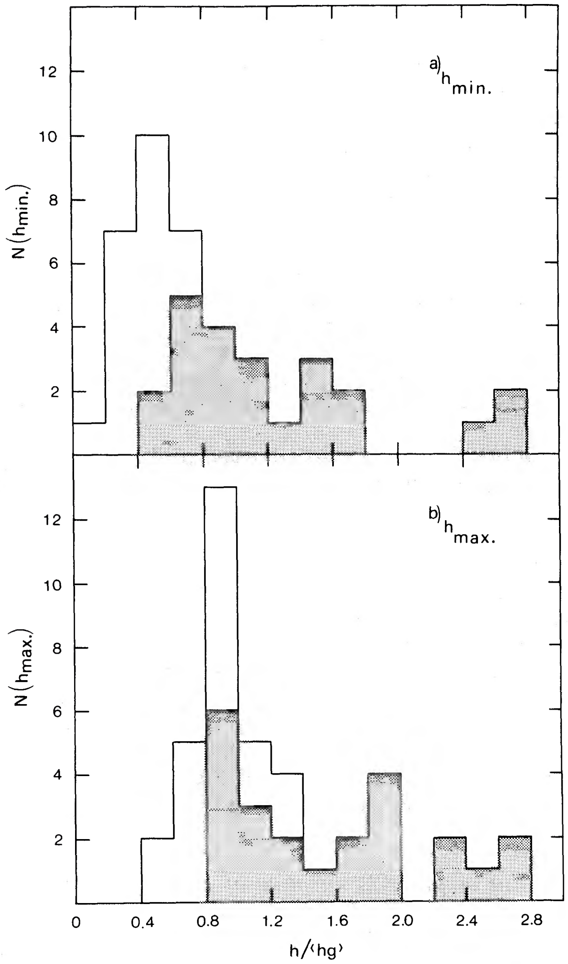

FIG. 9.—(*a*) Frequency distribution of the angular momentum per unit mass *h* for globular clusters, assuming minimum orbital eccentricity. The group of halo clusters (R_g > 10 kpc) are plotted as grey strips. (*b*) Same distribution assuming maximum possible orbital eccentricity, $e = 1$. The figure shows that the halo clusters tend to have more angular momentum than the inner "disk" clusters.

1967) for globular clusters. This reveals that the clusters with the largest angular momenta are among the metal-poorest.

The statement made by ELS—namely, that the old, metal-poor halo objects have orbits of high eccentricity and low angular momentum—clearly differs from the conclusion drawn here. Figures 9 and 10 demonstrate that those objects *in the halo now* were born from protogalactic material, which, at their formation time, *already* had a substantial amount of angular momentum. Furthermore, since so many extremely metal-poor clusters have high *h*, this proto-cluster material possessed this angular momentum *before* metal enrichment took place.

It should be stressed that our conclusions modify those of ELS because the objects used here differ fundamentally from theirs. The sample analyzed by ELS consisted of stars of all *different* ages, abundances, and velocities, but was inevitably restricted to stars now in the local solar neighborhood. The old metal-poor stars in this selected sample thus have orbits of predominantly *low* angular momentum with apogalactica near the Sun, and few stars are seen with large orbits taking them well beyond the Sun. By contrast, the globular clusters discussed here are *all* extremely old objects in the sense that they belong to the earliest phase of the Galaxy, and they are spread out in a vast region throughout the halo. Not surprisingly, many of these have large orbits of *high* angular momentum and small or moderate eccentricity, and represent a kinematic class of extremely old objects not seen by ELS in their sample. Notably, later work by Sandage (1969*b*) showed that indeed, old stars with these characteristics can be found even near the Sun. The principal conclusion here is that objects in the halo, which were formed during the initial collapse phase of the Galaxy, could be formed in orbits of *any* shape and angular momentum.

It should be pointed out that in the angular momentum statistics discussed here, as in ELS, the sign of *h* is neglected. For globular clusters, nothing else can be done since the sense of the orbits is generally unknown. For nearby high-velocity stars with accurate astrometric data, Eggen and Freeman (private communication) find that direct and retrograde orbits have significantly different distributions of angular momenta. It would be very exciting if a similar analysis for globular clusters could be carried out! (We are indebted to Professor Eggen for bringing this point to our attention.)

d) *The Origin of NGC 2419*

Since NGC 2419 is by its morphology and its C-M diagram so similar to the "inner" halo objects (R_g < 20 kpc), and so different from objects in its own spatial "neighborhood" at $R_g \sim 100$ kpc, it may therefore be logical to suggest that the cluster was formed while close to its perigalacticon distance, at a time and place where the other inner halo objects were born. If the cluster's orbit has remained essentially unperturbed since its birth, an unorthodox but amusing estimate of its age could be based on the times of perigalacticon passages computed from the orbital data of table 11. And since the cluster *remains* near its perigalacticon in the inner halo (R_g < 50 kpc) for less than 0.6×10^9 yr, the birth date thus found would be accurate to $\pm 0.3 \times 10^9$ yr if the correct passage were identified. Tracing the orbit backward suggests that possible epochs of formation are 8.5, 11.9, and 15.3×10^9 yr ago. Current estimates of the absolute ages of globular clusters (Iben and Rood 1970*a*, *b*; Rood 1970, 1973; Sandage 1970; Demarque, Mengel, and Aizenman 1971; Demarque *et al.* 1972) range between 10×10^9 yr and 13×10^9 yr. This would favor $T = 11.9 \pm 0.3 \times 10^9$ yr for NGC 2419. The agreement between this value and $T = 11 \times 10^9$ yr found in § V from the HB morphology is comforting but probably fortuitous.

The weakness of the above argument stems from the assumption of an unperturbed orbit. The very fact

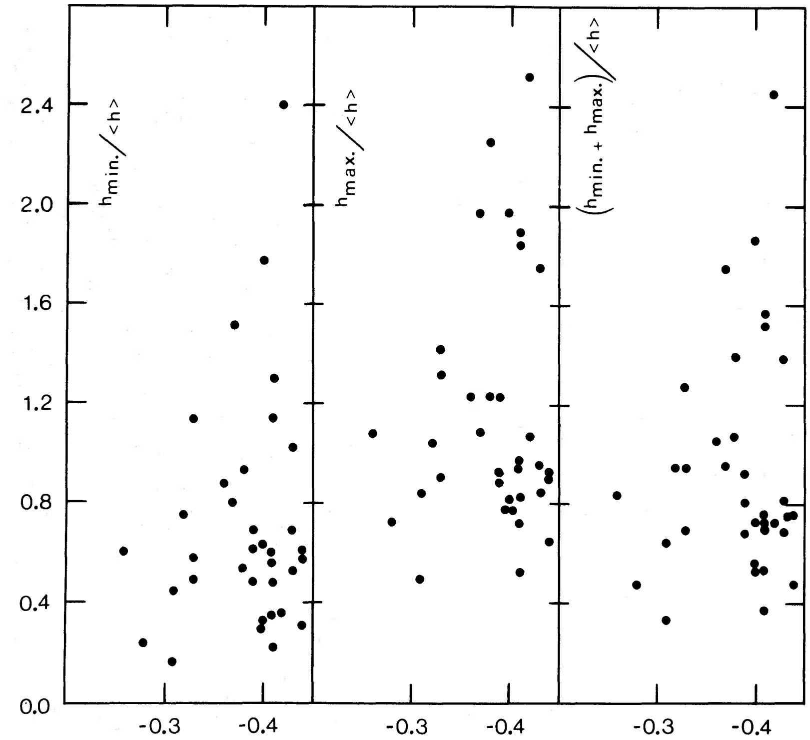

FIG. 10.—Relation between the metallicity parameter Q and the (a) minimum, (b) maximum, and (c) median angular momentum per unit mass, for 35 globular clusters. Clusters with the largest values of h tend to have low metallicity.

that NGC 2419 has so many family traits of the inner halo objects might be taken to mean that the cluster was "launched" from a lower initial orbit by a gravitational encounter with a more massive object, possibly one of the Magellanic Clouds. Rough calculations show that the probability of at least one halo cluster being significantly perturbed by a Magellanic Cloud passage (as proposed by Toomre 1972) is relatively high. In this event our results on the orbit of NGC 2419 could help to define further constraints on the geometry of such a Cloud-Galaxy encounter. In particular, if such an encounter is responsible for the present orbit of NGC 2419, the Magellanic Cloud(s) must be gravitationally bound to the Galaxy, because the last perigalacticon passage of NGC 2419 ($T \sim 1.7 \times 10^9$ yr ago) occurred long before the last passage of the Cloud(s) through the inner halo ($T \sim 0.5 = 10^9$ yr ago). This means that any encounter must have taken place on a previous passage of the Clouds.

VII. CONCLUSION

NGC 2419 is a normal, low-metallicity globular cluster presumably formed in the inner galactic halo. The cluster is gravitationally bound to the Galaxy, and its extremely large apogalactic distance and moderately low orbital eccentricity may be the result of the initial conditions at formation, but might also be due to an encounter with the Magellanic Clouds. Further studies of the Clouds' orbits guided by the present findings are needed to clarify this point.

The 31 short-period variables discovered by Baade are RR Lyrae-type from their position in the C-M diagram, and three of the five bright variables are red giants whereas the other two may be Cepheid or RV Tauri types. It is hoped that the magnitude sequences defined here in NGC 2419 will prove useful to the study of these variables.

A significant gap is observed in the red giant branch 0.2 mag above the HB. The gap position is different from that observed in other clusters.

Finally it is pointed out that the angular momentum per unit mass of the outer-halo globular clusters is generally large and that the conventional picture of very elongated plunging orbits for globular clusters may need revision.

We are greatly indebted to Dr. H. W. Babcock, Director, Hale Observatories and Dr. L. Goldberg, Director, KPNO, for the privilege of using the Palomar and Kitt Peak facilities and for generous allocations of observing time, without which this project could not have been completed. Correspondence with Dr. T. D. Kinman during the 4-year period since our first contact with NGC 2419 was instrumental in stimulating this research. Numerous discussions with and objections from Dr. S. van den Bergh and Dr. D. A. MacRae helped to put this paper into reasonable form.

Financial support through the National Research Council of Canada is gratefully acknowledged.

REFERENCES

Baade, W. 1935, *Ap. J.*, **82**, 396.
Baade, W., and Swope, H. 1961, *A.J.*, **66**, 300.
Bond, H. E. 1970, *Ap. J. Suppl.*, **22**, 117.
Burbidge, E. M., and Sandage, A. R. 1958, *Ap. J.*, **127**, 527.
Crawford, D. L., Golson, J. C., and Landolt, A. U. 1971, *Pub. A.S.P.*, **83**, 652.
Delhaye, J. 1965, in *Galactic Structure*, ed. A. Blaauw and M. Schmidt (Chicago: University of Chicago Press), p. 61.
Demarque, P., Mengel, J. G., and Aizenman, M. 1971, *Ap. J.*, **163**, 37.
Demarque, P., Mengel, J. G., and Sweigart, A. V. 1972, *Ap. J.* (*Letters*), **173**, L27.
Demers, S., and Harris, W. E. 1974, *A.J.*, **79**, 627.
Edmondson, F. K. 1935, *A.J.*, **45**, 1.
Eggen, O. J., Lynden-Bell, D., and Sandage, A. R. 1962, *Ap. J.*, **136**, 748 (ELS).
Harris, W. E., and van den Bergh, 1974, *A.J.*, **79**, 31.
Hartwick, F. D. A. 1968, *Ap. J.*, **154**, 475.
Hartwick, F. D. A., and McClure, R. D. 1972, *Ap. J.* (*Letters*), **176**, L57.
Hawarden, T. G. 1971, *Observatory*, **91**, 78.
Iben, I. 1971, *Pub. A.S.P.*, **83**, 697.
Iben, I., and Rood, E. T. 1970*a*, *Ap. J.*, **159**, 605.
———. 1970*b*, *ibid.*, **161**, 587.
Johnson, H. L., Mitchell, R. I., Iriarte, B., and Wisniewski, W. Z. 1966, *Comm. Lunar and Planet. Lab.*, **4**, 99.
Kinman, T. D. 1959*a*, *M.N.R.A.S.*, **119**, 157.
———. 1959*b*, *ibid.*, **119**, 538.
———. 1959*c*, *ibid.*, p. 558.
Kurth, R. 1960, *Zs. f. Ap.*, **50**, 215.
Larson, R. B. 1974, *M.N.R.A.S.*, **166**, 585.
McClure, R. D., Forrester, W. T., and Gibson, J. 1974, *Ap. J.*, **189**, 409.
Newell, E. B. 1973, *Ap. J. Suppl.*, **26**, 37.
Peterson, C. J. 1974, *Ap. J.* (*Letters*), **190**, L17.
Peterson, C. J., and King, I. R. 1973, *Bull. AAS*, **4**, 385.
Racine, R. 1969, *A.J.*, **74**, 1073.
———. 1971, *Ap. J.*, **168**, 393.
———. 1973, *A.J.*, **78**, 180.
———. 1975, in preparation.
Rood, R. 1970, *Ap. J.*, **161**, 145.
———. 1973, *ibid.*, **184**, 815.
———. 1974, preprint.
Rood, R., and Iben, I. 1968, *Ap. J.*, **154**, 215.
Sandage, A. R. 1969*a*, *Ap. J.*, **157**, 515.
———. 1969*b*, *ibid.*, **158**, 115.
———. 1970, *ibid.*, **162**, 841.
———. 1973, *ibid.*, **183**, 711.
Sandage, A. R., and Smith, L. L. 1966, *Ap. J.*, **144**, 886.
Sandage, A. R., and Wallerstein, G. 1960, *Ap. J.*, **131**, 598.
Sandage, A. R., and Wildey, R. 1967, *Ap. J.*, **150**, 469.
Sandage, A. R., Katem, B., and Kristian, J. 1968, *Ap. J.* (*Letters*), **153**, L129.
Schmidt, M. 1965, in *Galactic Structure*, ed. A. Blaauw and M. Schmidt (Chicago: University of Chicago Press), p. 513.
Seares, F. H., Kapteyn, J. C., and van Rhijn, P. J. 1930, *Carnegie Pub.*, No. 402.
Stothers, R. 1963, *A.J.*, **68**, 242.
Toomre, A. 1972, *Quart. J.R.A.S.*, **19**, 266.
van Agt, S. L. T. J. 1967, *B.A.N.*, **19**, 275.
van den Bergh, S. 1967, *A.J.*, **72**, 70.
———. 1971, *ibid.*, **76**, 1082.
von Hoerner, S. 1955, *Zs. f. Ap.*, **35**, 255.
Woolley, R. v. d. R., Alexander, J. B., Mather, L., and Epps, E. 1961, *R.O.B.*, No. 43, E303.

William E. Harris: Yale University Observatory, P.O. Box 2023, Yale Station, New Haven, CT 06520

René Racine: David Dunlap Observatory, Richmond Hill, Ontario, Canada, L4C 4Y6

THE ASTROPHYSICAL JOURNAL, **196**:433–456, 1975 March 1

INTERSTELLAR H_2CO. I. ABSORPTION STUDIES, DARK CLOUDS, AND THE COSMIC BACKGROUND RADIATION

N. J. EVANS II*
University of California, Berkeley
B. ZUCKERMAN†
University of California, Berkeley and University of Maryland
AND
G. MORRIS AND T. SATO
Jet Propulsion Laboratory, California Institute of Technology

Received 1974 May 14; revised 1974 September 10

ABSTRACT

The $2_{11} \leftarrow 2_{12}$ transition at 2-cm wavelength of interstellar formaldehyde has been observed in absorption against galactic continuum sources and the 2.7° K cosmic background radiation. In addition, the $1_{10} \leftarrow 1_{11}$ transition at 6-cm wavelength of the rare isotopic species $H_2{}^{13}C^{16}O$ has been detected in absorption against the cosmic background radiation in at least two clouds. These observations are used to distinguish among the various models for cooling the 6-cm doublet of $H_2{}^{12}C^{16}O$ below 2.7° K, and a collisional pumping model is found to be in the best agreement with the observations. In the dark clouds that display this cooling, calculations indicate that the H_2 densities are between 10^3 and 10^4 cm^{-3}, $n_e/n_{H_2} \lesssim 10^{-5}$, and the value of $H_2{}^{13}C^{16}O/H_2{}^{12}C^{16}O$ is similar to the terrestrial $^{12}C/^{13}C$ ratio. Estimates of the H_2CO/H_2 ratio in several diverse clouds indicate values of the order of $2\text{–}4 \times 10^{-9}$. Observations toward Cas A indicate that the temperature of the cosmic background radiation at 2-mm wavelength is $\lesssim 2.9°$ K.

Subject headings: cosmic background radiation — molecules, interstellar — nebulae

I. INTRODUCTION

The $1_{10} \leftarrow 1_{11}$ transition of interstellar H_2CO is observed in absorption against many galactic continuum sources. More strikingly, it is also seen in absorption toward many dark clouds where the molecules are absorbing the cosmic background radiation at 6-cm wavelength. This "anomalous" absorption implies that the excitation temperature characterizing the populations in the levels 1_{10} and 1_{11} (see fig. 1) is less than the temperature of the cosmic background radiation at 6 cm. A number of pumping models have been proposed for lowering the excitation temperature of the 6-cm doublet; the models make different predictions about the excitation temperature of the 2_{12} and 2_{11} levels. Thus observations in dark clouds of the 2_{11}–2_{12} transition at 2-cm wavelength have offered the promise of discriminating among some of the models. In the first study of the 2-cm transition, the line was detected in absorption against a few strong continuum sources (Evans, Cheung, and Sloanaker 1970). However, that study was not able to detect a 2-cm line from dark clouds. A very sensitive maser radiometer, used in conjunction with the NASA/JPL Deep Space Network[1] 64-m antenna at Goldstone, has made possible detection of 2-cm absorption lines from dark clouds.

Another feature of the present study is the high spatial resolution obtained with the $1'.2$ beam of the 64-m antenna. Previous single antenna maps of H, OH, and H_2CO absorption lines were hampered by poor spatial resolution. High-resolution maps of 6-cm H_2CO absorption in a few sources have been obtained through interferometry (Fomalont and Weliachew 1973). The present results can be compared directly with these interferometer maps, as well as with millimeter wavelength emission maps of H_2CO and other molecules, obtained with similar resolution. Such comparisons are discussed in §§ III and IV.

For reliable comparison of absorption at 6 cm and 2 cm, regions of similar size should be observed at both wavelengths. For this purpose, the 140-foot (43 m) telescope of the National Radio Astronomy Observatory[2] was used to map 2-cm absorption in L134 N and a dark cloud in Taurus. In §§ IV*a* and IV*d* the results of these maps, as well as the dark cloud observations made at Goldstone, are used in conjunction with 6-cm observations to examine pumping models and conditions in the dark clouds.

Detailed comparison of 2- and 6-cm absorption in dark clouds also requires a knowledge of the 6-cm optical depth. This can sometimes be deduced from careful studies of the 6-cm hyperfine pattern (e.g., Heiles 1973). An alternative method is a search for

---

* Present address: Owens Valley Radio Observatory, Caltech.

† Alfred P. Sloan Foundation Fellow.

[1] The NASA/JPL Deep Space Network is operated by the Jet Propulsion Laboratory, California Institute of Technology, under contract NAS 7–100 sponsored by the National Aeronautics and Space Administration.

[2] The National Radio Astronomy Observatory is operated by Associated Universities, Inc., under contract with the National Science Foundation.

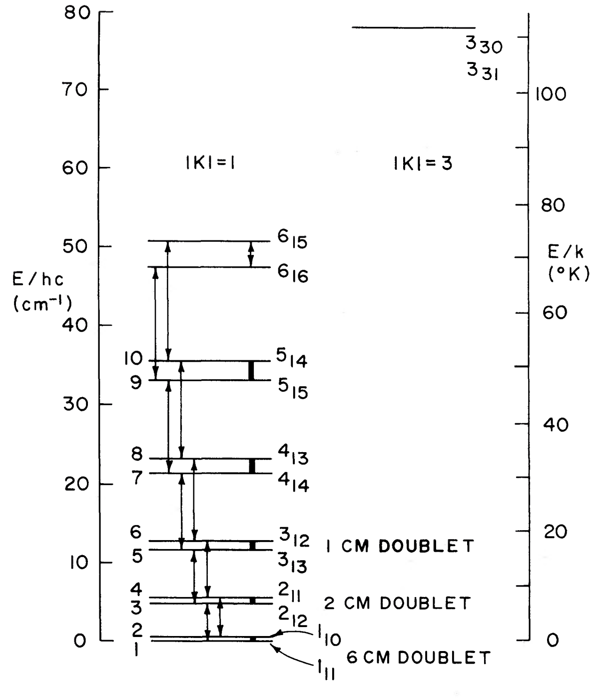

FIG. 1.—Part of the energy level diagram for orthoformaldehyde, courtesy of P. Thaddeus. The simplified numbering scheme to the left of the energy levels is used in most of the text.

the 6-cm transition of $H_2{}^{13}C^{16}O$. We discuss observations of this transition, undertaken with the Hat Creek 85-foot (26 m) telescope, in § III. Information on the 6-cm optical depth, pumping models (§ IV*a*), and isotopic abundances (§ IV*e*) may be obtained from these observations.

In a low-density cloud, the populations in the 2_{12} and 2_{11} levels will be determined primarily by the cosmic background radiation, and hence comparison of 2- and 6-cm optical depths allow measurement of the cosmic background intensity at 2-mm wavelength. Very weak 2-cm absorption lines were observed with the 140-foot telescope in the direction of Cas A; they are discussed in connection with the background spectrum in § IV*g*.

II. EQUIPMENT AND OBSERVING TECHNIQUES

A more detailed discussion of the equipment and techniques described below is given by Evans (1973). The primary source for the data reported here was the NASA/JPL Deep Space Network 64-m antenna at Goldstone, California. At 2-cm wavelength, the antenna is equipped with a circularly polarized feed and has a half-power beamwidth of about 1′.2. The beam efficiency was estimated by observing the center of the Moon. Measurements in 1972 June gave a beam efficiency of 0.57; a nominal value of 0.6 was used with data reduction. Although most of the data were accumulated in 1972, some points on the Orion, W3(OH), and NGC 2024 maps were obtained in 1973, after some changes occurred in the subreflector. The beam efficiency was then measured to be 0.5 over a wide range of hour angles; antenna temperatures for that data were scaled to account for the change. The traveling wave maser receiver, constructed at the Jet Propulsion Laboratory, typically produced total system temperatures at zenith near 30° K. The 64-channel autocorrelator had a variable bandwidth up to 3.0 MHz or a fixed bandwidth of 4.8 MHz. All observations at Goldstone were made in the total-power mode. The spectra were calibrated by measuring the total system temperature with a noise adding radiometer (NAR). The use of the NAR eliminates the need for a switch which would increase the system temperature (Ohm and Snell 1963); it works by adding modulated noise from a calibrated noise diode through a directional coupler.

The beamwidth at 2-cm wavelength of the 140-foot antenna of the National Radio Astronomy Observatory was measured to be 2′.0 × 2′.1. The beam efficiency was determined to be 0.70 from five measurements at the center of the Moon; there was no apparent dependence on hour angle. The cooled parametric amplifier gave system temperatures between 90° and 100° K. Frequency switching was arranged to produce the lines in both signal and reference spectra. The 384-channel autocorrelator was used in the parallel observing mode, except for observations of Cas A, which were obtained in the series mode.

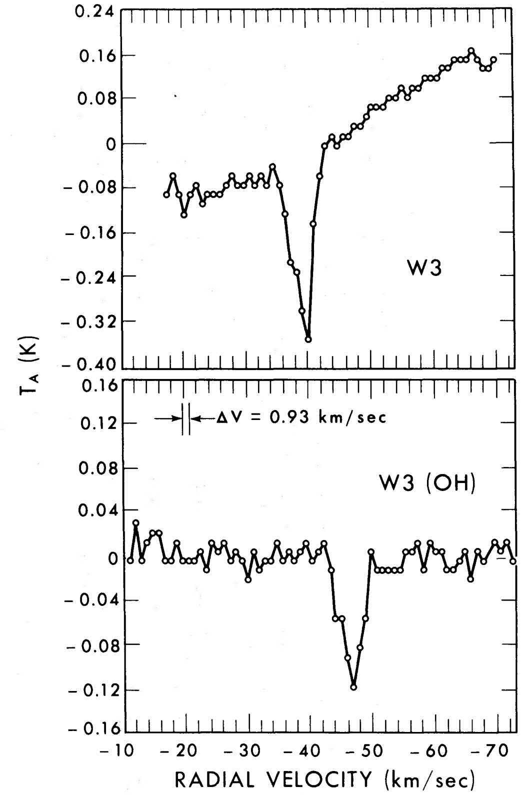

FIG. 2.—Spectra from the continuum maximum of W3 and from 35″ north of the W3 (OH) continuum maximum.

1975ApJ...196..351C

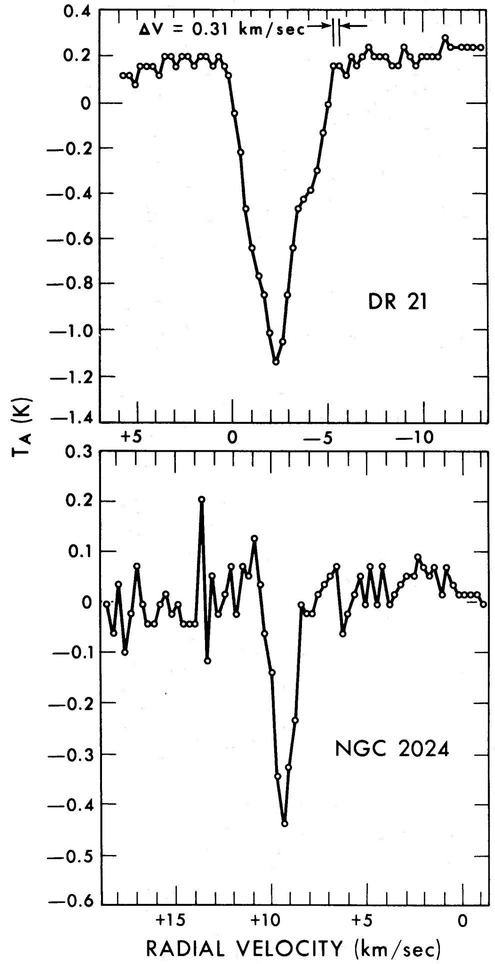

FIG. 3.—Spectra from the continuum maximum position in DR 21 and NGC 2024.

The 6-cm observations of $H_2{}^{13}C^{16}O$ were made with the 85-foot antenna at the Hat Creek Radio Observatory. The beamwidth is roughly 10′ at 6 cm, and a beam efficiency of 0.79 was measured by observations of the Moon. A cooled parametric amplifier gave a system noise temperature of 60° K, and the 100-channel filter bank was used with 10 kHz filters. As at NRAO, frequency switching was arranged to produce lines in both signal and reference spectra.

III. THE OBSERVATIONS

a) *Formaldehyde Absorption at 2 Centimeters*

The observations of H_2CO absorption at 2 cm obtained at JPL and NRAO are presented in tables 1 and 2 and figures 2–8. Observations of 2-cm emission from Orion will be presented in Paper II (Evans *et al.* 1975). In tables 1 and 2, column (1) gives the source name. For continuum sources that were mapped, the positional offsets from the first position listed are given in minutes and seconds of arc. Columns (4)–(9) are the following: integration time on source; spectral resolution used; peak antenna temperature in the line, or upper limit when appropriate; radial velocity with respect to the local standard of rest (but see following sentences); full line width at half-maximum intensity, uncorrected for broadening by the spectrometer; and antenna temperature of the background continuum source above 2.7° K. One difference between tables 1 and 2 is in column (7). When only an upper limit to antenna temperature is given in table 1, the tabulated velocity refers to the center of the spectral window, and the upper limits to ΔT_A refer to the whole spectral window. In table 2 the upper limits to ΔT_A given for Cas A apply only at the specific velocities listed in column (7); these velocities correspond to features at 6 cm.

The rest frequencies used at 6 and 2 cm are those of Tucker, Tomasevich, and Thaddeus (1971, 1972). Thus, when comparing the 6-cm survey of Zuckerman *et al.* (1970) with the present survey, we always add 0.7 km s^{-1} to their radial velocities to correct them to a rest frequency of 4829.660 MHz.

For some of the continuum sources, maps were made of the 2-cm absorption. These are presented in figures 5–8. The line antenna temperatures and velocity widths in the maps differ from those given in the tables because they have been corrected for broadening by the filters. The apparent optical depth, $\tau' = \Delta T_A/T_c$, is also given for positions where the continuum antenna temperature, T_c, was sufficiently strong.

b) *Observations of* $H_2{}^{13}C^{16}O$ *in Anomalous Absorption*

Observations of the $H_2{}^{13}C^{16}O$ line at 4593.089 MHz are summarized in figure 9 and table 3. We regard the features in L134 N and Taurus as definite detections, the Orion and NGC 2264 features as probable detections, and the L134 feature as a possible detection. The center velocities, given in column (8) of table 3, have been corrected, for both $H_2{}^{12}CO$ and $H_2{}^{13}CO$, for shifts due to hyperfine effects (Tucker *et al.* 1971). The antenna temperatures (col. [7]) and line widths (col. [9]) have not been corrected for filter or hyperfine broadening.

We believe that the $H_2{}^{13}CO$ absorption is "anomalous" in the sense that the molecules are absorbing the cosmic background radiation, rather than the weaker diffuse galactic continuum radiation. Unlike $H_2{}^{12}CO$ lines observed in dust clouds, $H_2{}^{13}CO$ lines are weak enough so that, in principle, the absorption could be of the galactic continuum provided that the $H_2{}^{13}CO$ optical depth at 6 cm was quite large and that the $H_2{}^{13}CO$ excitation temperature was essentially exactly equal to the temperature of the cosmic background. Quantitative analysis shows this to be an extremely unlikely solution.

c) *Individual Sources*

i) *W3* (*continuum*)

A map of this source is presented in figure 5. The radial velocity of the line appears to vary across the

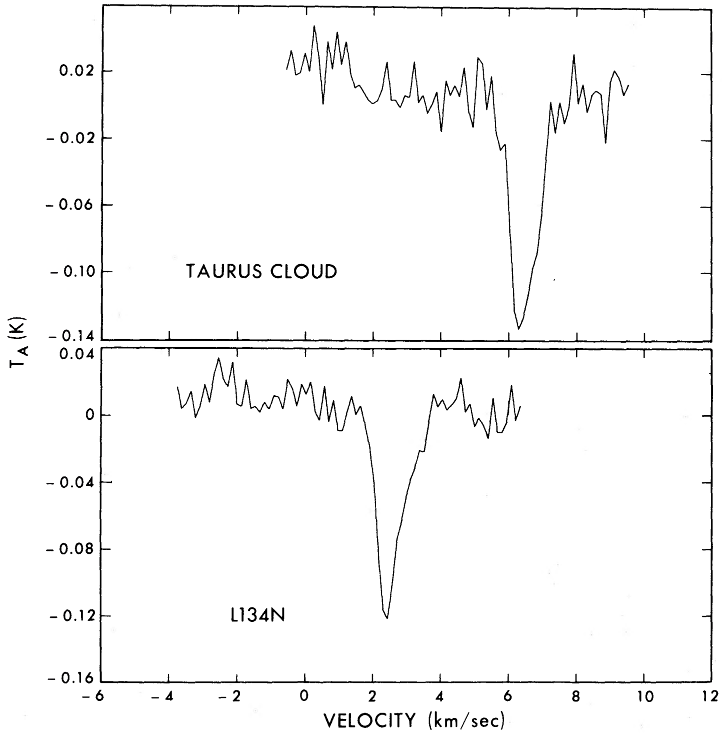

FIG. 4.—Spectra of the Taurus cloud and L134 N, formed by averaging over a map made with the 140-foot telescope

source in the E–W direction. The radial velocity and line widths of the 2- and 6-cm lines agree within the noise. The 2-cm line is stronger than expected for an optically thin cloud with low hydrogen densities (see § IV*b*). Based on the 6-cm interferometric observations of Fomalont and Weliachew (1973) and the observation that $H_2{}^{12}CO/H_2{}^{13}CO > 71$ (Zuckerman *et al.* 1974), the 6-cm lines do indeed appear to be optically thin. Although Fomalont and Weliachew estimate an upper limit to the H_2 density of 3×10^3 cm^{-3}, it would be difficult to understand the observed ratio of 2- and 6-cm line intensities under such conditions.

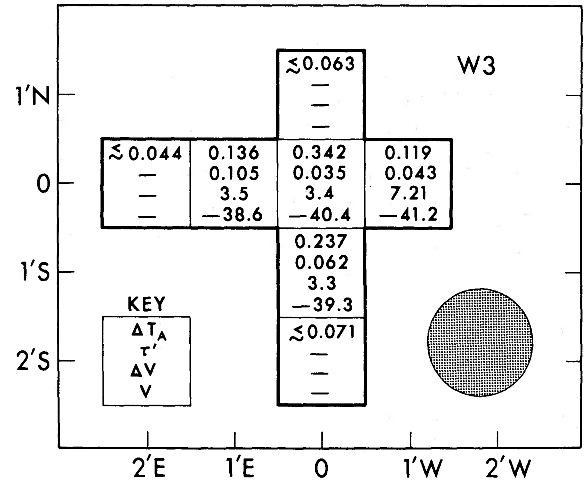

FIG. 5.—Map of the 2-cm absorption against W3. Beam size is indicated in the lower right-hand corner. Line antenna temperature, apparent optical depth, line width, and center velocity are indicated when appropriate.

ii) *W3(OH)*

A map of this source is given in figure 6. No systematic trends in radial velocity are apparent, and both the radial velocity and line width agree with the 6-cm line. Surprisingly, the peak antenna temperatures in the 2- and 6-cm absorption lines are approximately equal. The absorption appears to be mostly of the very small W3(OH) continuum source (Wynn-Williams 1971; Wink, Altenhoff, and Webster 1973) rather than, for example, the cosmic background. The radial velocity of the W3(OH) H II region is −45.1 km s^{-1}, based on the 109α recombination line (Palmer and Zuckerman 1969). The good agreement with the H_2CO velocity suggests that the cloud containing H_2CO is associated with the H II region.

iii) *NGC 2024*

A map of this source is shown in figure 7. The radial velocities of the 6-cm, 2-cm, and 2-mm lines are in reasonable agreement. The 6-cm line appears to be somewhat broader than the 2-cm line; this might be due to the larger area included in the 6-cm beam. However, the 2-mm line, observed at a position 1′ north of the continuum maximum, is considerably broader (4 km s^{-1}) than either centimeter line. An analysis of the cloud responsible for the 6-cm line

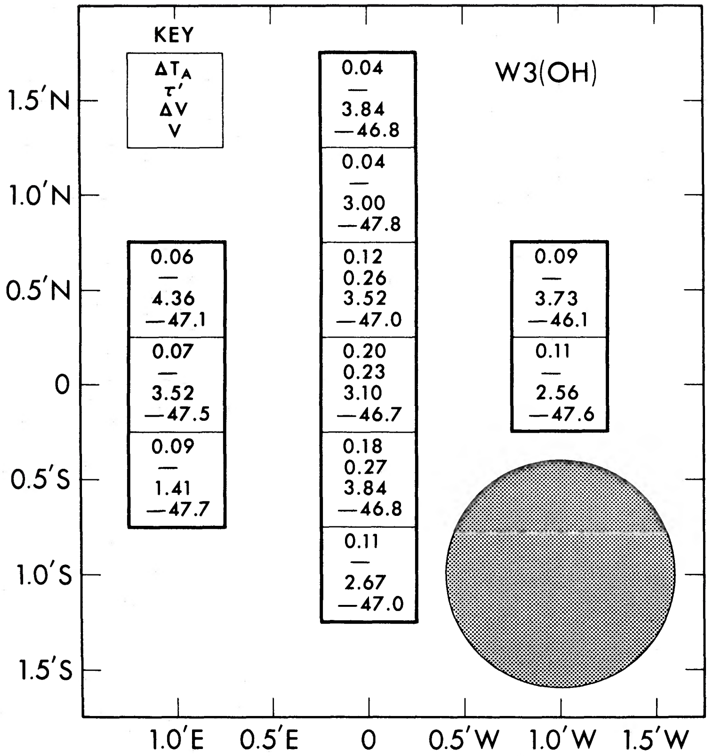

FIG. 6.—Map of 2-cm absorption in direction of W3(OH). Key is as in fig. 5, but the scale is expanded.

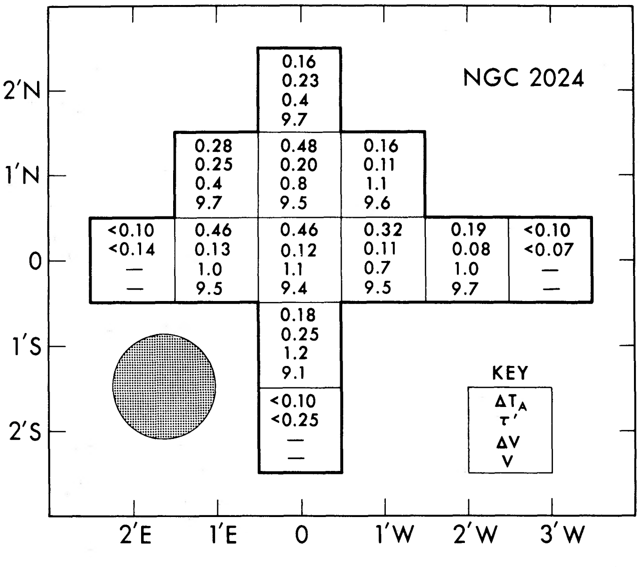

FIG. 7.—Map of 2-cm absorption in direction of NGC 2024. Key and scale are as in fig. 5.

TABLE 1

2-CENTIMETER H_2CO OBSERVATIONS FROM THE 64-METER GOLDSTONE ANTENNA

Source (1)	α(1950) (2)	δ(1950) (3)	Integration Time (min) (4)	Spectral Resolution (km s^{-1}) (5)	ΔT_A(° K)* (6)	v_{LSR}† (km s^{-1}) (7)	Δv (km s^{-1}) (8)	T_c(° K) (9)
NGC 604	$1^h31^m42^s.0$	30°31′48″	20	1.13	< 0.03	−237.2	. . .	0
W3‡ (cont. max.)	2 21 55.0	61 52 35	40	1.13	0.33	−40.4	3.6	9.8
1′ W	2 21 46.5	61 52 35	20	1.13	0.12	−41.2	7.3	2.8
1′ N	2 21 55.0	61 53 35	5	1.13	0.063?	−39.3?	0.93?	1.8
1′ S	2 21 55.0	61 51 35	5	1.13	0.22	−39.3	3.5	3.8
2′ S	2 21 55.0	61 50 35	5	1.13	0.071?	−38.5?	0.93?	0
1′ E	2 22 03.5	61 52 35	5	1.13	0.13	−38.6	3.7	1.3
2′ E	2 22 12.0	61 52 35	5	1.13	0.044?	−38.5?	0.93?	0
W3 (OH)‡	2 23 16.8	61 38 54	15	1.13	0.186	−46.7	3.3	0.87
1′ W, 35″ N	2 23 08.8	61 39 29	10	1.13	0.089	−46.1	3.9	0.39
1′ W	2 23 08.8	61 38 54	10	1.13	0.10	−47.6	2.8	0.24
1′ 35″ N	2 23 16.8	61 40 29	10	1.13	0.043	−46.8	4.0	0.13
1′ N	2 23 16.8	61 39 54	10	1.13	0.042	−47.8	3.2	0.04
35″ N	2 23 16.8	61 39 29	20	1.13	0.11	−47.0	3.7	0.45
25″ S	2 23 16.8	61 38 29	5	1.13	0.17	−46.8	4.0	0.66
1′ S	2 23 16.8	61 37 54	10	1.13	0.104	−47.0	2.9	0.25
1′ E, 35″ N	2 23 24.8	61 39 29	10	1.13	0.054	−47.1	4.5	0.13
1′ E	2 23 24.8	61 38 54	10	1.13	0.07	−47.5	3.7	0
1′ E 25″ S	2 23 24.8	61 38 29	10	1.13	0.071	−47.7	1.8	0.13
Taurus (dark cloud)	4 29 28.1	24 15 42	15	0.38	0.071	6.35	0.71	0
	4 29 32.5	24 15 42	10	0.38	0.078	6.2	0.68	0
	4 29 36.9	24 15 42	10	0.38	0.083	6.1	1.15	0
	4 29 40.0	24 15 18	70	0.38	0.082	6.2	0.96	0
	4 29 41.3	24 14 05	15	0.38	0.145	6.4	0.56	0
	4 29 41.3	24 13 05	30	0.19	0.116	6.3	0.31	0
	4 29 41.8	24 19 17	15	0.38	0.093	6.25	0.99	0
	4 29 41.8	24 18 17	10	0.38	0.124	6.3	1.03	0
	4 29 41.8	24 17 17	10	0.38	0.147	6.1	0.81	0
	4 29 43.4	24 15 55	25	0.38	0.136	6.15	0.72	0
	4 29 47.2	24 15 30	10	0.38	0.158	6.4	0.96	0
	4 29 51.6	24 15 30	15	0.38	0.087	6.2	0.59	0
Cloud 2 (dark cloud)	4 36 30.0	25 32 00	25	0.38	< 0.05	4.7	. . .	0
	4 38 30.0	25 18 00	55	0.38	0.076	5.25	0.47	0
L1436 (dark cloud)	4 50 00.0	51 40 00	10	0.38	< 0.07	1.3	. . .	0
HK Ori	5 28 39.8	12 07 01	10	1.17	< 0.05	31	. . .	0
			10	1.17	< 0.05	−31.2	. . .	0
Orion (dark cloud)	5 31 36.0	−5 48 00	5	1.13	< 0.05	8.0	. . .	0
	5 32 00.0	−5 42 00	5	1.13	0.055?	8.0?	0.93?	0
	5 32 00.0	−5 48 00	5	1.13	0.052	9.5	3.2	0
	5 32 00.0	−5 54 00	10	1.13	< 0.03	8.1	. . .	0
	5 32 24.0	−5 42 00	5	1.13	< 0.04	8.1	. . .	0
	5 32 24.0	−5 46 00	5	1.13	0.11	8.6	1.4	0
	5 32 24.0	−5 48 00	10	1.13	0.17	8.9	1.6	0
	5 32 24.0	−5 50 00	5	1.13	0.078	8.6	1.6	0
	5 32 24.0	−5 54 00	5	1.13	< 0.05	8.0	. . .	0
	5 32 32.0	−5 48 00	5	1.13	0.09	7.1	1.5	0
RR Tau	5 36 23.5	26 20 50	10	1.17	< 0.05	−31.1	. . .	0
			10	1.17	< 0.03	31	. . .	0
NGC 2024‡	5 39 12.0	−1 56 42	10	0.38	0.44	9.4	1.2	3.8
3′ W	5 39 00.0	−1 56 42	5	0.38	< 0.10	8.5	. . .	1.4
2′ W	5 39 04.0	−1 56 42	5	0.38	0.18	9.7	1.1	2.4
1′ W, 1′ N	5 39 08.0	−1 55 42	5	0.38	0.15	9.6	1.2	1.4
1′ W	5 39 08.0	−1 55 42	5	0.38	0.28	9.5	0.78	2.8
2′ N	5 39 12.0	−1 54 42	5	0.38	0.12	9.7	0.55	0.7
1′ N	5 39 12.0	−1 55 42	5	0.38	0.43	9.5	0.84	2.4
1′ S	5 39 12.0	−1 57 42	5	0.38	0.17	9.1	1.3	0.7
2′ S	5 39 12.0	−1 58 42	5	0.38	< 0.10	8.6	. . .	0.4
1′ E, 1′ N	5 39 16.0	−1 55 42	5	0.38	0.20	9.7	0.54	1.1
1′ E	5 39 16.0	−1 56 42	5	0.38	0.43	9.5	1.0	3.6
2′ E	5 39 20.0	−1 56 42	5	0.38	< 0.10	8.6	. . .	0.7
FU Ori	5 42 38.2	9 03 02	5	1.88	< 0.04	−0.1	. . .	0
HD 250550	5 59 06.5	16 31 06	5	1.88	< 0.04	0	. . .	0
LkHα 208	6 04 53.2	18 39 55	10	1.88	< 0.03	0	. . .	0
R Mon	6 36 25.9	8 46 57	15	1.13	< 0.04	8	. . .	0
NGC 2264 (mm)	6 38 28.4	9 32 12	15	1.13	0.095	7.1	4	0
	6 38 28.4	9 52 12	5	1.13	< 0.05	4.7	. . .	0
Bok globule	6 38 28.4	9 28 12	10	1.13	0.03?	7.1?	1.9?	0
	6 38 28.4	9 24 12	10	1.13	< 0.03	4.8	. . .	0
	6 38 44.4	9 24 12	15	1.13	0.05	8.2	1.7	0
	6 38 44.4	9 20 12	5	1.13	< 0.03	4.7	. . .	0

TABLE 1—*Continued*

Source (1)	α(1950) (2)	δ(1950) (3)	Integration Time (min) (4)	Spectral Resolution (km s^{-1}) (5)	ΔT_A(° K)* (6)	v_{LSR}† (km s^{-1}) (7)	Δv (km s^{-1}) (8)	T_c(° K) (9)
Z CMa	$7^h01^m22^s.6$	−11°28′36″	8.3	1.88	< 0.03	0	...	0
IRC+10216	9 45 14.8	13 30 41	30	1.13	$\lesssim$0.012	−23.5	...	0
L134	15 50 50.0	−4 39 00	14	0.38	< 0.06	2.3	...	0
	15 50 54.0	−4 31 00	25	0.38	0.136	2.5	0.6	0
	15 51 00.0	−4 26 56	21	0.38	0.057	2.6	0.6	0
L134 N	15 51 26.0	−2 45 31	20	0.38	0.11	3.1	1.2	0
Cloud 4 (dark cloud)	16 23 18.5	−24 18 02	17	1.13	< 0.15	3.4	...	0
	16 23 52.0	−24 27 40	21	0.38	< 0.06	3.2	...	0
	16 24 48.0	−24 33 01	29	0.38	0.057	3.4	1.5	0
W43	18 45 00.0	−2 00 00	15	0.38	0.13	92.4	3.1	3.6
G35.4+0.1 (dark cloud)	18 53 07.0	2 09 49	60	0.38	< 0.03	12.5	...	0
B335 (dark cloud)	19 34 29.0	7 27 37	60	0.38	0.065	8.4	0.43	0
DR21‡ (cont. max)	20 37 14.0	42 09 00	20	0.38	1.3	−2.34	2.8	7.2
3′ W	20 36 57.8	42 09 00	10	0.38	< 0.07	−3.3	...	0
2′ W	20 37 03.2	42 09 00	10	0.38	< 0.04	−3.25	...	0
1′ W	20 37 08.6	42 09 00	10	0.38	0.384	−2.5	2.6	2.0
0′.5 W, 3′ N	20 37 11.3	42 12 00	5	0.38	< 0.04	−3.3	...	0
DR 21 (OH)	20 37 14.0	42 12 00	15	0.38	< 0.03	−3.3	...	0
2′ N	20 37 14.0	42 11 00	5	0.38	0.117	−2.1	0.62	0.4
1′ N	20 37 14.0	42 10 00	5	0.38	0.167	−2.7	2.8	1.6
1′ S	20 37 14.0	42 08 00	5	0.38	0.53	−2.4	2.5	2.5
2′ S	20 37 14.0	42 07 00	5	0.38	0.125	−2.6	1.2	0
3′ S	20 37 14.0	42 06 00	5	0.38	0.065	−2.6	1.2	0
1′ E	20 37 19.4	42 09 00	10	0.38	0.31	−2.6	2.5	1.9
2′ E	20 37 24.8	42 09 00	10	0.38	< 0.07	−3.3	...	0.15
3′ E	20 37 30.2	42 09 00	5	0.38	< 0.05	−3.4	...	0
L896 (dark cloud)	20 40 00.0	39 30 00	20	0.38	< 0.05	−1.5	...	0
Cloud 1 (dark cloud)	22 35 47.0	74 58 28	17	0.38	< 0.06	−3.5	...	0
NGC 7538 (OH position)	22 11 23.0	61 13 48	10	0.38	< 0.07	−57.0	...	1.8
	23 11 30.0	61 12 48	5	0.38	< 0.10	−57.0	...	0.8
	23 11 37.0	61 11 48	15	0.38	< 0.05	−57.0	...	0.9
	23 11 37.0	61 10 48	5	0.38	< 0.07	−57.0	...	0.6
	23 11 48.0	61 11 48	5	0.38	< 0.10	−57.0	...	0.6
Cas A	23 21 11.0	58 32 48	10	1.13	< 0.16	−42.7	...	19.7
			65	0.38	$\lesssim$0.074	−2.3	...	20.5

* Antenna temperatures are for absorption.

† If only upper limit to ΔT_A is given, v is the central radial velocity of the spectral window.

‡ Positional offsets are with respect to the 2-cm continuum maximum.

suggests that it is similar to optically dark nebulae (Zuckerman and Ball 1973). If so, it is probably not dense enough to produce the observed 2-mm emission line. Thus the H_2CO lines observed in this direction may originate in two distinct regions both having a radial velocity near 9 km s^{-1}.

Based on the 6-cm interferometric observations of Fomalont and Weliachew (1973) and the fact that $H_2{}^{12}CO/H_2{}^{13}CO > 67$ (Zuckerman *et al.* 1974), the 6-cm lines are optically thin. The apparent optical depths at 2-cm vary across the source in a fashion somewhat similar to the 6-cm optical depths, observed by Fomalont and Weliachew, except in the north where the 2-cm optical depth seems to increase.

The coordinates of the continuum peak given in table 1 differ from those given by Zuckerman *et al.* (1970). Although Zuckerman *et al.* were also pointed at the continuum peak, the coordinates of the peak listed in their table 1, which come from Reifenstein *et al.* (1970), appear to be incorrect (cf. Schraml and Mezger 1969; Fomalont and Weliachew 1973).

iv) *NGC 2264*

There appear to be two extended clouds in this general direction. A high-density one is responsible for millimeter wavelength emission lines (Zuckerman *et al.* 1972). This same cloud might also be responsible for the component of the H_2CO absorption line (Rickard *et al.* 1975) observed at nearly the same radial velocity (~8 km s^{-1}). Another cloud, presumably with lower density, is seen at $v_R \sim 5$ km s^{-1} in 6-cm H_2CO absorption and 18-cm OH emission. The radial velocity and line width of the 2-cm absorption line (table 1) agree to within the noise with the radial velocity (7.7 km s^{-1}) and line width (~3 km s^{-1}) of the 0_{00}–1_{01} H_2CO emission line observed by Morris *et al.* (1975) in the direction of the millimeter source. Thus the 2-cm absorption appears to be associated with the denser of the two clouds.

v) *DR 21*

A map of this source is shown in figure 8. The radial velocities of the 2- and 6-cm absorption lines

1975ApJ...196..351C

TABLE 2

2-Centimeter H$_2$CO Observations from the NRAO 140-Foot Antenna

Source (1)	α(1950) (2)	δ(1950) (3)	Integration Time (min) (4)	Spectral Resolution (km s^{-1}) (5)	ΔT_A(° K)* (6)	v_{LSR} (km s^{-1}) (7)	Δv (km s^{-1}) (8)	T_c(° K) (9)
Taurus								
(dark cloud)........	4^{h}29^{m}34^{s}6	24°17′55″	240	0.16	0.16	6.1	0.78	0
	4 29 34.6	24 15 55	240	0.16	0.14	6.2	0.41	0
	4 29 34.6	24 13 55	240	0.16	0.11	5.6	0.68	0
	4 29 43.4	24 17 55	194	0.16	0.22	6.1	0.93	0
	4 29 43.4	24 15 55	216	0.16	0.22	6.1	0.78	0
	4 29 43.4	24 13 55	240	0.16	0.19	6.2	0.46	0
	4 29 52.2	24 17 55	118	0.16	0.17	6.3	0.96	0
	4 29 52.2	24 15 55	120	0.16	0.18	6.3	0.81	0
	4 29 52.2	24 13 55	240	0.16	0.11	6.3	1.25	0
L134 N								
(dark cloud)........	15 51 10	−2 45 31	328	0.16	0.10	2.6	0.55	0
	15 51 18	−2 43 31	120	0.16	0.14	2.5	0.80	0
	15 51 18	−2 45 31	236	0.16	0.15	2.2	0.52	0
	15 51 18	−2 47 31	220	0.16	0.12	2.5	0.68	0
	15 51 26	−2 41 31	240	0.16	0.10	2.6	0.99	0
	15 51 26	−2 43 31	236	0.16	0.19	2.4	0.70	0
	15 51 26	−2 45 31	232	0.16	0.13	2.7	1.11	0
	15 51 26	−2 47 31	240	0.16	0.14	2.5	0.81	0
	15 51 26	−2 49 31	248	0.16	0.14	2.2	0.41	0
	15 51 34	−2 43 31	120	0.16	0.19	2.3	0.34	0
	15 51 34	−2 45 31	240	0.16	0.13	2.4	0.71	0
	15 51 34	−2 47 31	240	0.16	0.17	2.3	0.56	0
	15 51 42	−2 45 31	240	0.16	0.12	2.3	0.67	0
DR 21 (cont. peak)....	20 37 14	42 09 00	91.7	0.33	0.94	−2.4	3.12	3.9
Cas A†..............	23 21 11	58 32 48	406	0.33	0.07	−1.5	0.46	21.8
					< 0.04	−0.2		
					≲0.045	−39		
					< 0.025	−47		

* Antenna temperatures are for absorption.

† The upper limits to ΔT_A are at the velocities given in column (7). This format differs from that used in table 1 (see footnote).

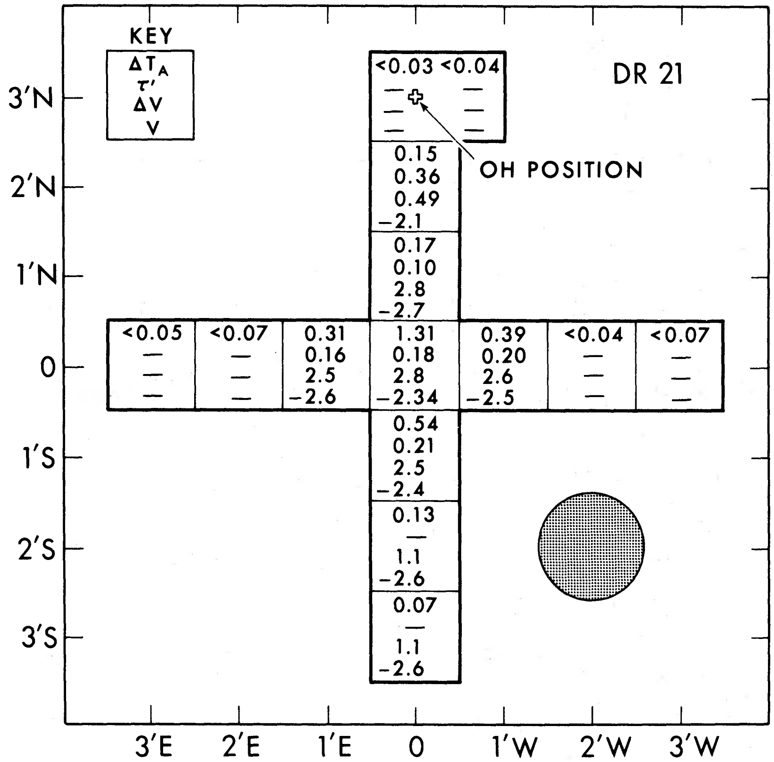

Fig. 8.—Map of 2-cm absorption in direction of DR 21. The OH position is indicated. Key and scale are as in fig. 5.

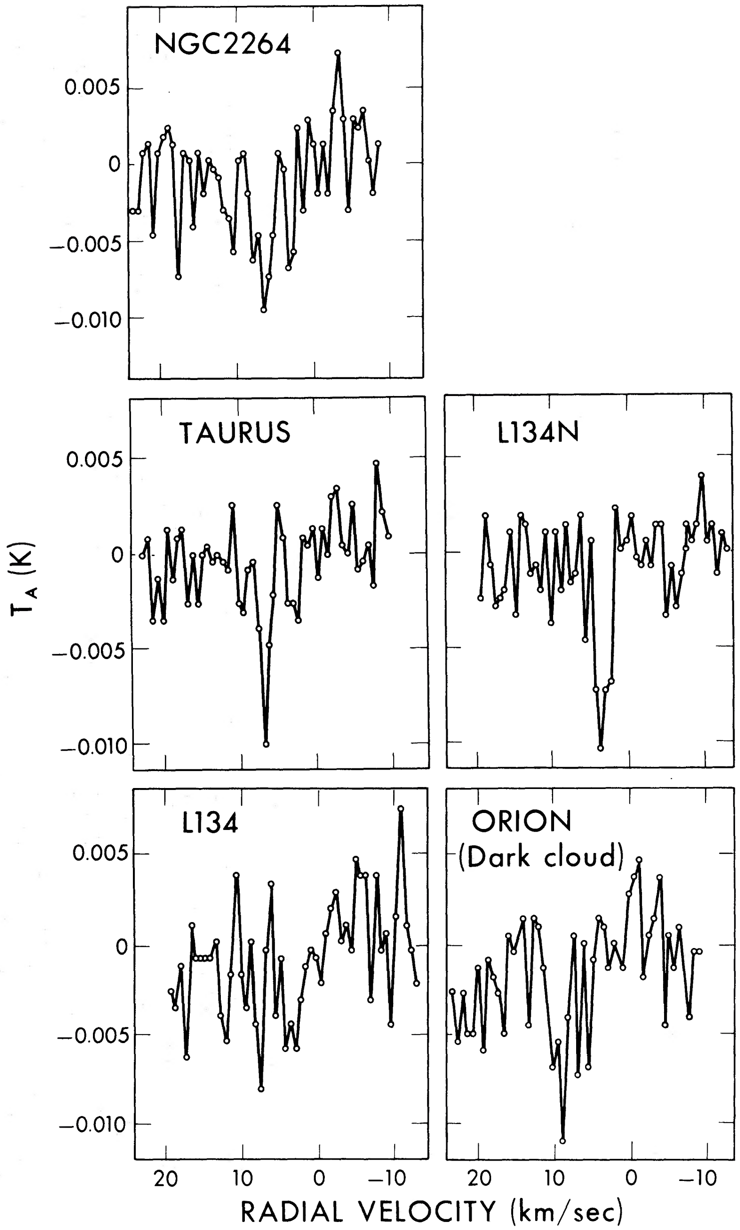

FIG. 9.—Spectra of the 6-cm line of $H_2{}^{13}C^{16}O$ from five dark clouds

are in good agreement, but the 6-cm line appears to be somewhat broader. The 2-cm line source appears to be more extended in the north–south than in the east–west direction. Qualitatively this picture agrees with that obtained by Morris *et al.* (1974) from a map of DR 21 in the $J = 1 \rightarrow 0$ transition of HCN.

Although the cloud responsible for the 2-cm absorption appears to be associated with the continuum source, there is probably anomalous absorption of the cosmic background radiation 2′ and 3′ south of the continuum peak. Our continuum observations and those of Schraml and Mezger (1969) indicate that the antenna temperature due to DR 21 at these positions is less than the observed antenna temperature in the 2-cm H_2CO lines. There is a diffuse continuum background at 2 cm (e.g., Downes and Rinehart 1966; Dent 1972) that probably contributes ~0.1°–0.2° K near the position of DR 21. Thus, in principle, it is possible that at the southern positions the 2-cm doublet of H_2CO has a large optical depth ($\gtrsim 1$) and an excitation temperature equal to 2.7° K, and it is absorbing this diffuse background radiation. Because of the much lower optical depths measured at the position of DR 21, we believe that a more plausible explanation of the H_2CO lines observed 2′ and 3′ south of the continuum peak is that the excitation

1975ApJ...196..351C

TABLE 3

6-CENTIMETER $H_2{}^{13}CO$ OBSERVATIONS FROM THE HAT CREEK 85-FOOT ANTENNA

Source (1)	α(1950) (2)	δ(1950) (3)	Isotope (4)	Integration Time (hr) (5)	Spectral Resolution (km s^{-1}) (6)	ΔT_A(° K) (7)	v_{LSR} (km s^{-1}) (8)	Δv (km s^{-1}) (9)	$H_2{}^{12}CO$*/ $H_2{}^{13}CO$ (10)
Taurus (dark cloud)..	$4^h29^m43^s.4$	24°15′55″	$H_2{}^{12}CO$	5.0	0.62	0.326	6.2	1.7	33
			$H_2{}^{13}CO$	74.9	0.65	0.0098	6.6	1.14	
Orion (dark cloud)..	5 32 12.0	−5 51 00	$H_2{}^{12}CO$	1.4	0.62	0.299	8.83	3.32	≥28
			$H_2{}^{13}CO$	57.2	0.65	≤0.007	8.37	3.92	
NGC 2264 (dark cloud)..	6 38 28.4	9 31 12	$H_2{}^{12}CO$	1.1	0.62	0.232	6.12	4.28	≥32
			$H_2{}^{13}CO$	33.9	0.65	≤0.0094	6.37	2.42	
L134 (dark cloud)..	15 50 54.0	−4 31 00	$H_2{}^{12}CO$	3.9	0.62	0.306	2.75	1.61	≥31
			$H_2{}^{13}CO$	42.9	0.65	≤0.0053	3.3	2.28	
L134 N (dark cloud)..	15 51 26.0	−2 45 31	$H_2{}^{12}CO$	7.6	0.62	0.311	2.6	1.83	20
			$H_2{}^{13}CO$	95.6	0.65	0.0098	2.6	2.28	
Cas A.........	23 21 11.0	58 32 48	$H_2{}^{12}CO$	1.4	0.62	0.982	−0.65	3.16	
			$H_2{}^{13}CO$	22.8	0.65	< 0.015	−0.65	...	> 50
			$H_2{}^{12}CO$	1.4	0.62	1.135 1.3	$\left.\begin{matrix}-36.9\\-39.4\end{matrix}\right\}$.	~2.5 ~3.7	≥44
			$H_2{}^{13}CO$	22.8	0.65	≤0.022	−38.1	~4.6	
			$H_2{}^{12}CO$	1.4	0.62	1.22	−46.57	~3.7	≥63
			$H_2{}^{13}CO$	22.8	0.65	≤0.02	−45.33	~2.6	

* Ratio of equivalent widths (defined as $T_A\Delta v$) calculated by assuming that both the 6-cm and 2-mm lines are optically thin in both isotopic species. See § IV*e* for a discussion of correction factors which must be applied to these ratios.

temperature at those positions is less than 2.7° K; that is, the 2-cm doublet is seen in anomalous absorption.

The apparent 2-cm optical depths in figure 8 are large when compared with the optical depth at 6 cm (0.32). Both the relatively low value for the $H_2{}^{12}CO$/$H_2{}^{13}CO$ ratio obtained from the 6-cm lines (Zuckerman *et al.* 1974) and the slightly broader 6-cm, as compared with 2-cm, line suggests that the 6-cm line may be somewhat optically thick. If so, the absorbing material must be clumpy.

vi) *Cas A*

In the case of Cas A our primary concern is a study of the intensity of the cosmic background radiation at 2-mm wavelength. The 2-cm absorption lines seen in front of other continuum sources are generally strong; collisional excitation to the 2-cm levels and trapping of 2-mm photons (see § IV) make it difficult to use these sources to study the cosmic background. In contrast, provided that the H_2CO is fairly uniformly distributed across the continuum source, the small apparent optical depths in the Cas A absorption features at 6 cm make it likely that the 2-mm lines are optically thin, so that trapping is unimportant. The hydrogen densities might also be low enough so that collisional excitation is negligible. The weakness of the features detected at 2 cm and the low upper limits on undetected features (see table 2) tend to bear out these expectations. The entries for velocities at −39 and −47 km s^{-1} are meant to refer to the two broad Perseus arm absorption features seen at 6 cm.

The greatest uncertainty in interpreting the Cas A data is the lack of firm evidence that the H_2CO molecules, or the H_2 molecules that might collisionally excite them, are distributed uniformly across the source. The H atoms in the Orion arm clouds seem to be quite uniform in 21-cm absorption studies (Clark 1965), but the Perseus arm clouds show considerable spatial structure (Clark 1965; Greisen 1973). Because the molecules are likely to be more concentrated than the atoms, clumpiness in the H_2CO is certainly possible even in the Orion arm clouds. The Cas A continuum source is smaller than the 6′.6 beam used by Zuckerman *et al.* (1970), but it is much larger (Mayer and Hollinger 1968) than the 2′ beam used in the present study. Thus, if the H_2CO is clumped, it is possible that we were pointed at a "hole," where the column densities are less than average. This would make the 2-cm line appear too weak compared with the 6-cm line. Only a H_2CO map of the whole source at 2 cm—a difficult project due to the weakness of the line—or an interferometric observation of the 6-cm line can decide the issue.

vii) *Dark Clouds*

The Taurus dark cloud was studied at 6 cm with the 6′.6 beam of the NRAO 140-foot telescope (Kutner 1973). Maps were made, both at JPL and NRAO, of the 2-cm absorption in a region ~6′.6 in diameter. This region has a deep 6-cm absorption line which appears to be very similar to that at several nearby 6-cm positions. The NRAO map covered nearly all the area inside a 6′.6 diameter, but the JPL map did not. L134 N, located about 2° north of L134, was studied at 6 cm with the 10′ beam of the 85-foot Hat Creek telescope (Heiles 1973). The 2-cm absorption map, made at NRAO, covers almost all the area inside the Hat Creek half-power beam.

Significant variations in ΔT_A, and probably in Δv, exist in all three maps on a scale of a few minutes of arc. This variation suggests that molecular observations with larger beams may average over a considerable amount of structure. To compare 6-cm and 2-cm results, we averaged the 2-cm spectra obtained at each point of a map to produce an average spectrum; the spectra resulting from the two NRAO maps are shown in figure 4. The JPL map of the Taurus cloud gave an average spectrum in reasonable concordance with the NRAO data. The velocity widths at individual points in the 2-cm map of the Taurus cloud are systematically less than those in the averaged spectrum; this fact may be due to the broadening effect of adding many narrower components with slightly different center velocities. The radial velocities and line widths from the averaged NRAO spectra (6.11 and 1.0 km s^{-1} for Taurus; 2.49 and 0.76 km s^{-1} for L134 N) agree quite well with the 6-cm observations. These results suggest that observations of other molecules with high spatial resolution might show narrower lines, and that comparison of line widths in observations taken with different beam sizes may be expected to show larger line widths in the lines observed with the larger beam (cf. Crutcher 1973*a*).

viii) *Negative Results*

We searched, at JPL, for the 2-cm line in the direction of the cometary nebulae R Mon, LkHα 208, Z CMa, HK Ori, RR Tau, FU Ori, and HD 250550, all of which have been studied in the infrared by Cohen (1973). Our upper limit in IRC + 10216 suggests that H_2CO is less abundant relative to HCN, CN, and CS in IRC + 10216 than it is in clouds near H II regions. The first of the three positions given for cloud 4 in table 1 is a strong CO source and also a source of other millimeter wavelength molecular emission (Encrenaz 1973), as well as 350-μ radiation (Simon *et al.* 1973). We searched for 2-cm emission in this direction without success, although the limits that were achieved were not especially sensitive.

IV. DISCUSSION

The data presented here afford insight into a variety of physical and astronomical problems. Besides the information provided on the structure of individual sources in space and velocity, which has been discussed in § III, the 2- and 6-cm observations are relevant to the spectrum of the cosmic background radiation, to densities of hydrogen molecules and electrons in interstellar clouds, and to isotopic abundances. We begin by discussing the implication of these results for the various pumping models that have been proposed to explain anomalous absorption at 6 cm.

a) *Pumping Models*

A large number of dark nebulae have now been shown to contain formaldehyde with a 6-cm excitation temperature, T_{12}, less than 2.7° K (Palmer *et al.* 1969; Dieter 1973; Minn and Greenberg 1973). Proposals for producing this low T_{12} have employed a number of pumping cycles, all of which involve excitation to higher states and subsequent radiative decay. The excitation has been produced in one model by collisions (Townes and Cheung 1969) and, in a second class of models, by radiation at millimeter (Solomon and Thaddeus 1970; Thaddeus 1972*a*), infrared (Litvak 1970), and ultraviolet wavelengths (Oka 1970).

Any pumping model must satisfy a number of general constraints. The pump rate must be at least comparable with the rate of transitions between the two levels of the doublet. At low densities, the latter is just the rate of transitions stimulated by the 2.7° K background, 4.2×10^{-8} s^{-1}. The ultraviolet pumping model encounters a serious obstacle here because, to produce a steady-state cooling, it requires that the molecules be dissociated and recombined at high temperatures. Oka found that the rate for the dissociation process is about 10^{-10} s^{-1} in unshielded regions. Subsequent laboratory studies of ultraviolet absorption in H_2CO suggest that the photodissociation rate may be about 10^{-9} s^{-1} (Stieff *et al.* 1972). However, since H_2CO seems to be cooled in dark clouds, where the ultraviolet radiation will be attenuated substantially, the rates are still too slow to effectively cool T_{12}. In addition, formation rates are unlikely to be sufficiently rapid for this mechanism to work. If this constraint on the pump rate is applied to collisional models with typical cross sections of 10^{-15} cm^2, it implies that densities on the order of 10^3 cm^{-3} are required to produce appreciable cooling of T_{12}.

A second constraint results from the widespread occurrence of anomalous absorption. A pumping model which requires very specialized conditions must be regarded with considerable skepticism. In the absence of the required special conditions, collisions would heat the 6-cm doublet above 2.7° K (unless one assumed that collisions also cool the doublet but are nevertheless not responsible for the observed absorption). Since 6-cm emission has never been seen, with the possible exception of the extremely dense Orion molecular cloud, the conditions required for the pump to operate must be nearly the same as the conditions for the existence of formaldehyde. This ubiquitous presence of anomalous absorption argues against a complicated model like the infrared pumping model. It is hard to imagine that the rather special conditions, involving shock waves and resonance radiation, are as universal as is required by observations.

A stronger test of the infrared model can be made by searching for anomalous absorption of $H_2{}^{13}CO$. Because the pump radiation, produced by hot formaldehyde, is unlikely to be very optically thick for $H_2{}^{12}CO$, the infrared lines of $H_2{}^{13}CO$ should be quite weak and the pumping ineffective. The $H_2{}^{13}CO$ observations discussed in § III indicate that anomalous absorption from the rare isotopic form exists and is probably quite common. This fact provides strong evidence against pumping by infrared resonance radiation and against any other pumping model employing enhanced radiation at molecular resonances peculiar to a given isotopic species. To retain the infrared pumping model, in light of these results, would require altering the original model to make the infrared lines of $H_2{}^{12}CO$ very optically thick in these sources. Then one might expect to see broad 6-cm and 2-cm emission from the hot $H_2{}^{12}CO$, but there is no evidence for broad emission lines in our spectra. One way to produce pumping of both isotopic species is to use continuum, rather than line, infrared radiation. This model gains some plausibility from the discovery of 2-μ sources in the Ophiuchus cloud (Grasdalen, Strom, and Strom 1973); but similar sources would have to be distributed throughout every cloud displaying anomalous absorption, since 6-cm emission from dark clouds has never been observed. In fact, near-infrared observations of other dark clouds revealed only a few sources (Strom 1974), in sharp contrast to the Ophiuchus cloud.

The two other pumping models, one involving collisions and the other proposing deviations of the cosmic background radiation from a blackbody spectrum at 2 mm, satisfy the general constraints quite well, but they make qualitatively different predictions about the 2-cm doublet. The millimeter pumping model assumes excess radiation from the cosmic background, either at both frequencies ν_{13} and ν_{24} or at ν_{24} only. (We number the states of ortho–H_2CO in fig. 1 by 1, 2, 3, etc.) The effect of excess radiation at ν_{24} will be a net transfer of molecules from level 2 to level 4, cooling the 6-cm doublet and heating the 2-cm doublet. Excess radiation at both ν_{13} and ν_{24}, though less effective, produces the same results. Such a model cannot make both T_{12} and T_{34} less than 2.7° K, and thus the observation of anomalous absorption at 2 cm conclusively eliminates this model.

The collisional pumping model asserts that collisions from either level of the 6-cm doublet to level 3 are favored over those to level 4; thus T_{34} is cooled. The very fast radiative rates between levels 1 and 3 then produces excess population in level 1, cooling T_{12}. Hence this model predicts anomalous absorption at both 6 cm and 2 cm. A classical calculation (Townes and Cheung 1969) of these cross sections using small hard spheres for the atoms in the molecule and the projectile and rigid molecular bonds gave $\sigma_{31} = \sigma_{32} = 1.25\sigma_{41}$, where σ_{ij} is the cross section for a collision with a neutral particle to cause a transition from level i to level j. On the other hand, the Born approximation for the same model gives $\sigma_{32} \sim \frac{1}{3}\sigma_{41}$, and a sudden approximation calculation (Thaddeus 1972*b*) also gives σ_{32} less than σ_{41}. The classical calculation is questionable because classical mechanics fails for small quantum numbers. However, neither the Born nor the sudden approximation is valid when the kinetic energy involved in the collision is close to the transition energy, as is the case for H_2CO being struck by hydrogen molecules at temperatures near 10° K. Hence, none of the currently available calculations can be considered adequate. Recent calculations using the semiclassical approximation (Augustin and Miller 1974) indicate that $\sigma_{32} > \sigma_{41}$, and Evans (1975) has shown that the effect of including coupling of molecular states in a quantum-mechanical calculation is to enhance σ_{32} relative to σ_{41}.

Although the theoretical situation remains unclear (see Evans 1973 for further discussion), the observations clearly favor a collisional model. Because the cross sections between the $J = 1$ and $J = 2$ doublets are still uncertain, and because those cross sections are the most effective in cooling the 6-cm doublet, we have chosen to deal with collisional models in which transitions with $\Delta J > 1$ have zero cross section. For simplicity, we have taken cross sections with $\Delta J \leq 1$ to be equal to $\sigma_0 = 10^{-15}$ cm^2, with the exception of certain cross sections between the $J = 1$ and $J = 2$ doublets (e.g., σ_{32}). The equations of statistical equilibrium were solved for the lowest 24 levels of ortho–H_2CO in the presence of the 2.7° K background and collisions. By enhancing σ_{32} by various amounts compared with σ_{41}, sufficient cooling of T_{12} can be produced over a large range of densities. In figure 10, we show the excitation temperature versus density for $\sigma_{32} = 1.4 \times \sigma_{41}$. T_{12} is cooled to 1.7° K, which appears to be a common temperature in dark clouds (Heiles 1973), at $T_K = 10°$ and 20° K; the cooling is somewhat less effective at $T_K = 5°$ K. Several points should be noted. One is that the cross sections between the $J = 2$ and $J = 3$ doublets may also have a cooling effect; neglecting these may lead us to overestimate the required enhancement of σ_{32} over σ_{41}. The second point is that one might choose so-called "hard" collisions, in which all ΔJ are allowed; such collisions produce some differences in the details of the excitation; but the enhancement of σ_{32} over σ_{41} will still produce cooling over hydrogen densities from 10^3 cm^{-3} to 10^5 cm^{-3}. The third point is that collisions causing transitions between levels 1 and 2 and collisions with electrons will heat T_{12} (see § IV*f*). Finally, the choice of $\sigma_0 = 10^{-15}$ cm^2, while unimportant from the point of view of cooling mechanisms, will affect the determination of densities, since rates are proportional to $n\sigma_0 v$, where n is the density of colliding particles and v is the velocity. We have used $v = (8kT_K/\pi m)^{1/2}$, where m is the mass of a hydrogen *atom* and T_K is the kinetic temperature. Thus to achieve the same rates, the hydrogen *molecule* cross sections would have to be 1.4×10^{-15} cm^2. Such differences are negligible compared with present uncertainties in the cross sections, but we mention them for the sake of clarity. Data from pressure-broadening experiments with H_2CO and H_2 at room temperature indicate total cross sections for disturbance of a given state to be 3–10 × 10^{-15} cm^2 (Rogers and Roberts 1973), with the larger values having been measured for the 6- and 2-cm doublets. Assuming some of this

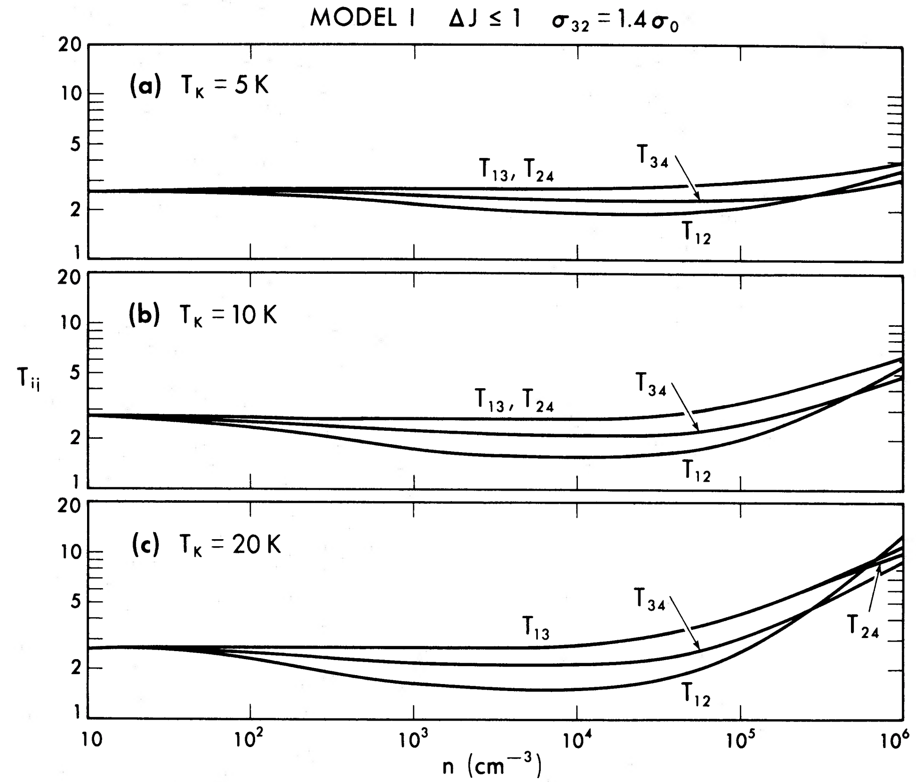

FIG. 10.—Excitation temperatures as a function of density, resulting from solution of the equations of statistical equilibrium at various kinetic temperatures. Density scale is appropriate for H atoms if $\sigma_0 = 1.0 \times 10^{-15}$ cm^2 and for H_2 molecules if $\sigma_0 = 1.4 \times 10^{-15}$ cm^2.

is due to elastic collisions and noting that five transitions are allowed from any given state by our selection rule of $\Delta J \leq 1$, our choice of σ_0 is consistent with the available laboratory data.

As we shall discuss in § IV*e*, the isotopic abundance ratios in table 3 will depend on the excitation temperature and hence the pumping mechanism. Although present knowledge of collision cross sections is poor, it seems unlikely that the cross sections would be different for $H_2{}^{13}CO$, as compared with $H_2{}^{12}CO$. A collisional pumping model would then give equal cooling in the two isotopic forms, neglecting the possible effect of radiative trapping.

b) *Definitions*

A few definitions and relations will be useful in the following discussion. If I_ν is the intensity of the radiation, the radiation temperature will be defined as

$$T_R = c^2 I_\nu / 2\nu^2 k \,,$$

and ΔT_{Rij} represents the difference in radiation temperature on and off a line at frequency ν_{ij}. The brightness temperatures, T_B and ΔT_{Bij}, are equal to T_R and ΔT_{Rij} in the Rayleigh-Jeans limit. In this convention we can represent ΔT_{Rij} in terms of the excitation temperature T_{ij}, optical depth τ_{ij}, reduced energy difference $\epsilon_{ij} = h\nu_{ij}/k$, and background temperature $T_{\rm bg}$ as follows:

$$\Delta T_{Rij} = \frac{\epsilon_{ij}}{\exp(\epsilon_{ij}/\Delta T_{Bij}) - 1} = \left[\frac{\epsilon_{ij}}{\exp(\epsilon_{ij}/T_{ij}) - 1} - \frac{\epsilon_{ij}}{\exp(\epsilon_{ij}/T_{\rm bg}) - 1}\right] \times [1 - \exp(-\tau_{ij})] \,. \tag{1}$$

Equation (1) is the solution for radiative transport through a uniform cloud and reduces to the more familiar

$$\Delta T_{Bij} = (T_{ij} - T_{\rm bg})[1 - \exp(-\tau_{ij})] \tag{1a}$$

in the Rayleigh-Jeans limit. The radiation temperature as used here is related to the measured antenna temperature, T_A, by $T_A = \eta F T_R$, where η is the beam efficiency and F is approximated by the fraction of the main beam covered by the source.

In subsequent discussion we will compare 2-cm results with data on the H_2CO 6-cm transition. The ratio of the optical depth at 6 cm to that at 2 cm is

$$\frac{\tau_{12}}{\tau_{34}} = \frac{g_1|\mu_{12}|^2}{g_3|\mu_{34}|^2} \exp(\epsilon_{13}/T_{13}) \frac{1 - \exp(-\epsilon_{12}/T_{12})}{1 - \exp(-\epsilon_{34}/T_{34})} \,, \tag{2}$$

where g_i is the degeneracy of state i and $|\mu_{ij}|^2$ is the square of the dipole moment matrix element for the transition from i to j. A common approximation, valid unless the doublet temperatures T_{12} and T_{34} are very low, is to replace the last factor in equation (2) by $\epsilon_{12}T_{34}/\epsilon_{34}T_{12}$. Then

$$\frac{\tau_{12}}{\tau_{34}} = \frac{3}{5}\exp(6.76/T_{13})\frac{T_{34}}{T_{12}} \sim 7.33\frac{T_{34}}{T_{12}}, \qquad (2a)$$

where the last expression comes from setting $T_{13} = 2.7°$ K. For rotational transitions with $\Delta J = 1$, excitation temperatures, such as T_{13}, will be close to equilibrium with the 2.7° K background in clouds of low density.

Another useful equation relates the excitation temperatures of the lowest four levels. Using only the definition of excitation temperature, one can show that

$$T_{34} = \epsilon_{34}\left(\frac{\epsilon_{12}}{T_{12}} + \frac{\epsilon_{24}}{T_{24}} - \frac{\epsilon_{13}}{T_{13}}\right)^{-1}. \qquad (3)$$

Equation (3) may be used to illustrate a number of effects. Any pumping model that cools T_{12} while keeping $T_{13} = T_{24} = 2.7°$ K will also cool T_{34}; but because $\epsilon_{34} = 3\epsilon_{12}$, T_{34} is cooled less than T_{12}. In the limit that $T_{13} = T_{24} \to \infty$, T_{34} will approach $3T_{12}$. On the other hand, if $T_{13} \neq T_{24}$, as in the millimeter pumping model, one doublet will be heated if the other is cooled. This is true because removing population from the upper level of one doublet (cooling) requires that the population be increased in the upper level of the other doublet (heating). For example, $T_{24} > T_{13}$ will heat T_{34} relative to T_{12}. Because ϵ_{24} and ϵ_{13} are much larger than ϵ_{12} and ϵ_{34}, slight differences in T_{13} and T_{24} can have a large effect on the doublet temperatures.

c) Absorption in Front of Continuum Sources

In absorption against discrete continuum sources, the expected relative strength of the 2- and 6-cm lines can depend on a variety of possible effects. Some of these are observational effects, and others concern the excitation conditions of the molecular states in the clouds being studied. In the simplest case, where the absorbing cloud uniformly covers a strong source and H_2 densities in the cloud are low enough that $T_{13} = 2.7°$ K, equation (2a) should be applicable. Then with reasonable assumptions concerning T_{12} and T_{34}, one consistently finds that the 2-cm line is stronger than one would predict based on the 6-cm line intensity. This tendency was observed in Sgr A, Sgr B2, and W51 (Evans *et al.* 1970), as well as in most of the sources in the present study (see § III). The single exception, Cas A, will be used in § IV*g* to discuss the cosmic background radiation.

Let us first consider observational effects that might account for the strong 2-cm lines. We define an apparent optical depth $\tau_{ij}' = \Delta T_{Aij}/T_c$, calculated from the observed antenna temperatures of the line (corrected for filter broadening) and the continuum. The apparent optical depths at 6 and 2 cm and the ratio τ_{12}'/τ_{34}' are given in table 4. The τ_{12}' were taken from Zuckerman *et al.* (1970), except for W3 and NGC 2024, for which interferometric data (Fomalont and Weliachew 1973) were used to correct for structure in the absorbing cloud. The τ_{34}' refer to the position centered on the continuum maximum, with the exception of NGC 2024 where comparisons at a number of positions are given.

Because beam efficiency and calibration errors cancel in τ_{ij}', we also have $\tau_{ij}' = \Delta T_{Rij}/T_s$ (where T_s is the continuum source radiation temperature), provided that the absorbing cloud uniformly covers the continuum source (assumption *a*). The observations of Fomalont and Weliachew (1973) indicate that the absorption at 6 cm is indeed fairly uniform across most of the continuum sources that they studied. From figures 5–8, it may be seen that while the apparent 2-cm optical depths may vary, the absorbing cloud is clearly extended over the whole continuum source. If assumption *a* is valid and the

TABLE 4

ABSORPTION OF CONTINUUM SOURCES

Source (1)	τ_{12}' (2)	τ_{34}' (3)	τ_{12}'/τ_{34}' (4)	T_{13}(° K)* (5)	T_{13}(° K)† (6)	nL/T_{12} (cm^{-2} deg-K^{-1}) (7)
W3	0.11	0.035	3.1	4.0		1.4×10^{13}
W3 (OH)	0.22	0.23	0.96	14.7		
NGC 2024 (cont. max.)	0.46	0.12	3.8	3.2		2.5×10^{13}
1′ S	0.69	0.25	2.8	3.5		
1′ N	0.35	0.20	1.8	5.8		
1′ E	0.35	0.13	2.7	4.1		
1′ W	0.46	0.11	4.2	3.1		
2′ W	0.23	0.080	2.9	4.1		
DR 21	0.32	0.18	1.77	5.8		4.9×10^{13}
Cas A						
-1.6 km s^{-1}	0.023	0.0032	7.2	2.7	3.3	
-0.2 km s^{-1}	0.017	< 0.0018	> 9.3	< 2.5	< 2.9	
-39 km s^{-1}	0.0165	$\lesssim 0.0021$	$\gtrsim 8.0$	$\lesssim 2.7$	$\lesssim 3.1$	
-47 km s^{-1}	0.0155	< 0.0011	> 13.6	< 2.2	< 2.3	

* Excitation temperatures were derived by assuming $T_{34} = T_{12}$.

† Excitation temperatures were derived using equation (5) to relate T_{34} to T_{12}, and assuming $T_{12} = 1.7°$ K and $T_{13} = T_{24}$.

continuum source is bright, so that $T_s \gg T_{ij} - 2.7°$ K, then

$$\tau_{ij}' = 1 - \exp(-\tau_{ij}) . \qquad (4)$$

This approximation is quite good for all the sources in question here; for example, even W3(OH) with a low continuum antenna temperature has a very high T_s (Wynn-Williams 1971).

Although the molecules absorbing radiation at both 6 and 2 cm are clearly extended over many 1'.2 beamwidths, they might, in principle, be clumped on a very small scale. For example, the ratio τ_{12}'/τ_{34}' observed in DR 21 could be produced by many clumps of molecules, each with $\tau_{12} = 6$, which are distributed fairly uniformly across the continuum source but which cover only 0.32 of it. Such large optical depths would be expected to produce much stronger 6-cm lines of $H_2{}^{13}CO$ than are observed (Zuckerman *et al.* 1974). In particular $\tau_{12} > 2$ seems unlikely in DR 21, while τ_{12} is probably less than 1 in NGC 2024 and W3.

If the true optical depths are small, then equation (4) reduces to $\tau_{ij}' = \tau_{ij}$, and τ_{12}'/τ_{34}' can be related to excitation temperatures by equation (2a). If $T_{13} = T_{24} = 2.7°$ K (assumption *b*) and $T_{12} = T_{34}$ (assumption *c*), τ_{12}'/τ_{34}' should equal 7.33; but it is clear from table 4 that only Cas A is consistent with assumptions *a*, *b*, and *c*. Allowing for the small, but finite, optical depth in the sources is not sufficient to resolve the discrepancy, except possibly at a few positions in NGC 2024.

Since no observational effects appear to be important enough to explain the low values of τ_{12}'/τ_{34}', it is necessary to abandon either assumption *b* or assumption *c*. We will show that, in any case, assumption *b* must be abandoned, and that there must be significant excitation to the $J = 2$ doublet. Column (5) of table 4 shows the solutions for T_{13}, using equations (4) and (2a), if assumption *c* is retained. The relatively large values of T_{13} presumably imply regions of rather high density, where some combination of collisional excitation and trapping of the 2-mm photons produce an appreciable population in the levels of the 2-cm doublet. For example, if $T_{13} = 5.0°$ K, then approximately 40 percent of the H_2CO will be in levels 3 and 4. These processes will be considered in greater detail in § IV*d*, but first we show that assumption *b* cannot be retained by dropping assumption *c*. The ratio τ_{12}/τ_{34} in equation (2a) would be decreased if T_{12} were larger than T_{34}. But if $T_{13} = T_{24} = 2.7°$ K (assumption *b*), then T_{12} must be greater than 2.7° K, in order for $T_{12} > T_{34}$, as a result of equation (3). Thus, if we attempted to explain the observed low ratios τ_{12}'/τ_{34}' by varying *only* T_{12} and T_{34}, we would require that the doublets are not cooled, and in fact rather large T_{12} would be required in most cases. However, based on 6-cm observations of Whiteoak and Gardner (1970), the 2-cm results on DR 21 described in § III, and the absence of 6-cm emission in the hundreds of clouds that have been surveyed, it is probable that T_{12} is not heated significantly above 2.7° K in clouds absorbing continuum sources. If in fact, $T_{12} < 2.7°$ K, and if $T_{13} = T_{24}$, then $T_{34} > T_{12}$, as discussed in § IV*b*; thus the observations would require T_{13} even larger than those in column (5). In conclusion then, while variations in T_{12} and T_{34} introduce some uncertainty into the values of T_{13} derived by comparing 6- and 2-cm absorption, the evidence is strong that considerable excitation to the 2-cm doublet levels must be occurring. The T_{13} that we derive in W3 and DR 21 indicate that they are likely sources of 2-mm H_2CO emission.

These results allow reconsideration of the column density of H_2CO derived from 6-cm observations. Zuckerman *et al.* (1970) and Fomalont and Weliachew (1973) assumed that only the 0_{00}, 1_{11}, and 1_{10} levels were populated and that 90 percent of the H_2CO was in the ortho form. Taking an ortho-para ratio of 3:1 and noting that $T_{13} \sim 5.0°$ K, we find the column densities in column (7) of table 4, which represent an increase of ~60 percent over earlier estimates. Appreciable population in other levels would raise these values still more.

To derive the fractional H_2CO abundance requires knowledge of $n_{H_2}L$ between the observer and the continuum source. It is difficult to estimate $n_{H_2}L$ reliably for most H II regions that are highly obscured. However, for W3, Wynn-Williams, Becklin, and Neugebauer (1972) have estimated the visual extinction in front of the strongest 6-cm continuum component as 14 ± 3 mag. With this value of A_v, we find $n/n_{H_2} \sim 3 \times 10^{-9}$ toward W3 (assuming 1 mag corresponds to $n_{H_2}L = 10^{21}$ cm^{-2}). If $A_v = 50$ mag in front of DR 21 (Sibille, Bergeat, and Lunel 1974; Wynn-Williams, Becklin, and Neugebauer 1974), we find $n/n_{H_2} \sim 3 \times 10^{-9}$ in that source as well.

d) Dark Clouds

Analysis of H_2CO absorption in dark clouds presents a set of difficulties and uncertainties different from those encountered in analyzing the continuum source absorption. However, the general conclusion that emerges is the same—namely, that the strong 2-cm lines imply appreciable excitation to the 2-cm doublet by collisions and trapping. Since the H_2CO in the dark clouds absorbs the cosmic background at 6 and 2 cm, problems concerning size and structure in a continuum source do not arise and we know that T_{12} and T_{34} are less than 2.7° K. On the other hand, little information on optical depth is available in dark clouds, unlike continuum sources. Studies of hyperfine structure in the 6-cm line (Heiles 1973) supply τ_{12} for a few of the clouds studied at 6 cm, and these are listed in column (5) of table 5. The $H_2{}^{13}CO$ data discussed earlier may also be used to constrain τ_{12}. If $H_2{}^{13}CO$ is no less abundant than 1/89 of $H_2{}^{12}CO$, then the ratios of the line radiation temperatures imply that τ_{12} is less than 4.5 in L134 N, 2.5 in Taurus, 3.1 in Orion, and 2.8 in L134, where we have assumed that the 6-cm excitation temperatures are equal in the two isotopic species. As we shall see, trapping of 2-mm photons will probably cause $T_{12}(^{12}C)$ to differ from $T_{12}(^{13}C)$. If $T_{12}(^{12}C) < T_{12}(^{13}C)$, then our estimates of τ_{12} will be too low. If, as is more likely in the higher-density clouds, $T_{12}(^{12}\mathrm{C}) > T_{12}(^{13}\mathrm{C})$, then we have overestimated τ_{12}.

Another serious difficulty in comparison of 6- and 2-cm observations arises from the very different beam sizes at the two wavelengths. Cloud conditions derived from the observations could be meaningless if the cloud is not uniform over a region defined by the size of the beam at 6 cm. The maps of L134 N and the Taurus cloud, discussed in § III, show that variations in antenna temperature up to a factor of 2 do exist on scales of a few minutes of arc. For these two clouds a direct comparison to the 6-cm data can be made by using the spectra averaged over the 2-cm map (fig. 4). The agreement in v and Δv of these average spectra with the 6-cm values supports such a comparison. For the other clouds, which were not mapped at 2 cm, the conclusions of this section will apply only in a statistical sense; i.e., it is likely that we will average over spatial structure by observing many clouds.

If again we use assumption c, $T_{34} = T_{12}$, and assumption b, $T_{13} = T_{24} = 2.7°$ K, and in addition assume that $\tau_{12} \ll 1$, equations (1) and (2a) predict $\Delta T_{R12}/\Delta T_{R34} = 7.33$. The 6-cm radiation temperatures, obtained by dividing the antenna temperatures from various references by η, are given in table 5. The 2-cm antenna temperatures from tables 1 and 2, also divided by the appropriate η, and the ratio of radiation temperatures are also given in table 5. No correction for filter broadening has been applied. Since we have also somewhat overestimated η, the true ΔT_{R34} may be slightly larger than those given in table 5. The range of entries illustrates the variability of the relative intensities of the two lines. Some of the variation in the unmapped clouds is probably due to spatial structure. However, there is evidence for variation from cloud to cloud because none of the positions in L134 N or the Taurus cloud give values of $\Delta T_{R12}/\Delta T_{R34}$ as large as are seen in some of the other clouds. Even more striking than the variation among clouds is the existence of small $\Delta T_{R12}/\Delta T_{R34}$ (e.g., L134, L134 N, and Taurus). Retaining assumptions b and c, the 6- and 2-cm radiation temperatures may be used to solve for τ_{12} and T_{12} in equation (1); equation (2) removes τ_{34} as a variable. The results are given in columns (6) and (7) of table 5. For L134 and L134 N,

TABLE 5

ABSORPTION IN DARK CLOUDS

Source (1)	ΔT_{R12}(° K) (2)	ΔT_{R34}(° K) (3)	$\frac{\Delta T_{R12}(°\,\mathrm{K})}{\Delta T_{R34}(°\,\mathrm{K})}$ (4)	τ_{12} observed (5)	τ_{12}* (6)	T_{12}(° K)* (7)	τ_{12}† (8)	T_{12}(° K)† (9)	ζ(%) T_{24} = 2.7° K (10)	ζ(%) T_{24} = 5.0° K (11)
Taurus..............	0.66[a]	0.16[b]	4.1	...	1.9	1.93	9.3	2.04	6.2	7.6
	0.66[a]	0.20[c]	3.3	...	2.8	2.00	14.5	2.04	8.2	8.8
Cloud 2.............	0.61[d]	< 0.08	> 7.6	...	< 0.5	< 1.15	< 3.9	< 2.08	...	...
	0.88[d]	0.127	6.9	...	0.7	0.95	4.3	1.81	4.8	4.1
L1436...............	0.10[e]	< 0.12	> 0.8	...	...	...	...	...	...	...
Orion (dark cloud)...	0.15[f]	< 0.08	...	...	...	...	...	...	...	...
	0.35[f]	0.09?	3.9	...	2.1	2.31	12.0	2.35	2.8	6.7
	0.36	0.087	4.1	...	1.9	2.28	10.5	2.34	2.8	6.6
	0.50[f]	< 0.05	> 10.0	...	< 0.3	< 0.77	< 2.7	< 2.17	...	...
	0.48[f]	< 0.07	> 6.9	...	< 0.5	< 1.48	< 4.5	< 2.22	...	...
	0.50[f]	0.18[g]	2.8	...	3.5	2.19	35.0	2.20	7.0	8.5
NGC 2264 (mm).....	0.56[h]	0.16	3.5	...	2.5	2.09	13.5	2.14	6.0	7.8
	0.25[h]	< 0.08	> 3.1	...	< 3.0	< 2.44	...	...	...	...
Bok globule.........	0.35[h]	0.05?	7.0	...	0.5	1.81	4.7	2.35	...	...
	0.26[h]	< 0.05	> 5.2	...	< 1.2	< 2.31	< 7.5	< 2.44	...	...
	0.35[h]	0.08	4.4	...	1.7	2.28	9.5	2.35	2.3	6.6
	0.21[h]	< 0.05	> 4.2	...	< 1.9	< 2.46	< 11.5	< 2.49	...	...
L134................	...	< 0.10	...	...	...	...	...	...	...	...
	0.58[i]	0.227	2.6	0.9	4.0	2.11	No solution		11.0	10.7
	0.58[j]	0.095	6.1	...	0.8	1.60	5.3	2.12	3.5	5.6
L134 N.............	0.53[i]	0.18[b]	2.9	1.4	3.3	2.15	23.0	2.17	4.5	7.8
	0.53[i]	0.18[c]	2.9	1.4	3.3	2.15	23.0	2.17	4.5	7.8
Cloud 4.............	[k]	<0.25	...	...	...	...	...	...	...	...
	0.68[j]	< 0.10	> 6.8	...	< 0.7	< 1.35	< 4.5	< 2.02	...	...
	0.67[i]	0.095	7.1	...	0.5	1.15	4.3	2.02	2.8	4.8
G35.4+0.1..........	0.53[j]	< 0.05	> 10.6	...	< 0.3	< 0.65	< 2.5	< 2.13	...	...
B335...............	0.17[l]	0.11	1.5	...	8.7	2.53	No solution		3.7	8.1
L896................	0.20[e]	< 0.08	> 2.5	...	< 4.1	< 2.50	...	...	...	...
Cloud 1.............	0.30[j]	< 0.10	> 3.0	...	<3.1	< 2.39	...	...	...	...

* Optical depths and excitation temperatures based on $T_{34} = T_{12}$.

† Optical depths and excitation temperatures based on T_{34} given by T_{12} and equation (3), with $T_{13} = T_{24} = 2.7°$ K.

SOURCE.—[a] Kutner 1973. [b] 2-cm data taken at Goldstone unless otherwise noted; Taurus cloud refers to spectrum formed by averaging over a map. [c] NRAO data; spectra for the Taurus cloud and L134 N resulting from maps. [d] Palmer *et al.* 1969. [e] Dieter 1973. [f] Kutner and Thaddeus 1971. [g] Partial map made at Goldstone. [h] Rickard *et al.* 1975; ΔT_{R34} refers to 8 km s^{-1} feature. [i] Heiles 1973, and private communication; note that τ_{12} used here include all the hyperfine components. [j] Palmer *et al.* 1975. [k] Encrenaz 1973. [l] Rickard *et al.* 1975; note that ΔT_{R12} may be underestimated due to beam dilution.

the τ_{12} derived in this manner are considerably larger than those measured by Heiles.

In fact, the discrepancy becomes more striking if we consider assumption *b* in light of equation (3). Because $T_{12} < 2.7°$ K in the dark clouds, equation (3) with assumption *b* implies that $2.7° \text{ K} > T_{34} > T_{12}$, as pointed out in § IV*b*. Hence assumptions *b* and *c* are incompatible in dark clouds. Furthermore, the line radiation temperatures in dark clouds are especially sensitive to the excitation temperatures T_{12} and T_{34}, because the molecules absorb only the cosmic background, and thus the factor $T_{ij} - 2.7°$ K, or its equivalent in equation (1), is critical to ΔT_{Rij}. This factor is roughly twice as large for the 6-cm doublet as for the 2-cm doublet under assumption *b*. Thus, the value of $\Delta T_{R12}/\Delta T_{R34}$ expected for $\tau_{12} \ll 1$ is ~ 16—much larger than any of the observed ratios. We can try to retain assumption *b* by dropping assumption *c* and instead using equation (3) to relate T_{12} and T_{34}. The resulting solutions for τ_{12} and T_{12} are given in columns (8) and (9) of table 5; they represent a *reductio ad absurdum* to retaining assumption *b*.

Clearly there must be a mechanism that disturbs T_{13} and T_{24} away from 2.7° K. If the mechanism heats T_{13} and T_{24} equally, equation (3) shows that T_{34} will be even higher relative to T_{12} than if $T_{13} = T_{24} = 2.7°$ K. Because of the strong dependence of ΔT_{R34} on $T_{34} - 2.7°$ K, the heating of T_{34} outweighs the increase in τ_{34} associated with increasing T_{13}, and the predicted 2-cm radiation temperature actually declines as one increases $T_{13} = T_{24}$. This argument suggests that $T_{13} > T_{24}$ in dark clouds.

Based on the following discussion, we conclude that the most natural way to explain all the H_2CO observations in dark clouds lies in a collisional model with σ_{32} and σ_{31} enhanced over σ_{41} and σ_{42}, respectively. Because radiative transitions are not allowed between levels 2 and 3, the enhancement of σ_{32} acts to cool T_{12} and T_{34} even at rather low densities. At higher densities, the fact that $\sigma_{31} > \sigma_{42}$ causes T_{13} to heat faster than T_{24}, cooling T_{34} relative to T_{12} and increasing the absorption in the 2-cm line. With such a model, variations in density provide a natural means of explaining the variation from cloud to cloud of the ratio of 2-cm to 6-cm absorption. Before presenting the detailed arguments that lead to this conclusion, we remark that we have investigated the effects of changing other cross sections. The critical ratio of $T_{12} - 2.7°$ K to $T_{34} - 2.7°$ K is hardly affected either by including cooling cross sections at higher *J* (e.g., $\sigma_{54} > \sigma_{63}$) or by allowing $\Delta J > 1$ transitions.

The crux of the matter is this: the doublet excitation temperatures, T_{12} and T_{34}, are extremely sensitive to different excitation temperatures at the two $\Delta J = 1$ transitions ($T_{13} \neq T_{24}$). Because $T_{34} > T_{12}$ makes the dark cloud results very difficult to explain, there must be some physical effect which makes $T_{13} > T_{24}$ and thus cools T_{34} relative to T_{12}, according to equation (3). By itself, this effect, henceforth called the "second pump," would cause T_{12} to be greater than 2.7° K, so that the following picture emerges. There is a primary pump, which we have argued is due to collisions, that cools T_{12}; it also cools T_{34} but not as much as it cools T_{12}. At least in some clouds, there is also a second pump that further cools T_{34} *relative* to T_{12} by making $T_{13} > T_{24}$. (The separation into first and second pumps is made only for convenience in discussion; in fact, we will show that both effects are best explained by collisions.) For the moment, the discussion will remain model independent by using equation (3) to calculate from any given T_{12}, the values of T_{13} and T_{24} required to produce the desired T_{34}. For example, figure 11 shows the fractional excess $\zeta = (T_{13} - T_{24})/T_{24}$, as a function of T_{24}, that is required to produce $T_{34} = T_{12}$ in the case of the two best studied clouds, L134 N and Taurus. T_{12} has been determined from ΔT_{R12} and τ_{12} through the use of equation (1), and $\tau_{12} = 1.0$ was assumed for the Taurus cloud, while the measured value of $\tau_{12} = 1.4$ was used for L134 N. Because increasing T_{13} and T_{24} above 2.7° K increases the population in the 2-cm doublet and hence τ_{34}, the ζ required to produce the observed ΔT_{R34} (fig. 11, *dotted lines*) has a different dependence on T_{24} from the ζ required for $T_{12} = T_{34}$. Columns (10) and (11) in table 5 give the fractional excess at $T_{24} = 2.7°$ and 5.0° K required to give the observed ΔT_{R34}, ΔT_{R12}, and τ_{12}. In clouds where τ_{12} has not been measured, $\tau_{12} = 1$ was assumed.

The above considerations have been quite general, involving only observed quantities and equations which are independent of the specific processes that cool T_{12} and T_{34}. In order to affect T_{13} and T_{24}, the second pump must compete with the fast radiative rates at 2 mm. The rate of spontaneous decay from level 3 to level 1 is $\sim 5 \times 10^{-5}\ \text{s}^{-1}$. If the second pump is due to collisions (for other possibilities, see Evans 1973), this condition suggests hydrogen densities $n_{H_2} \sim 10^5\ \text{cm}^{-3}$. However, trapping of the 2-mm photons generated by these collisions will tend to lower the densities required, and this will be considered below in greater detail. Because the radiative rates are slower at the lower frequency of ν_{13} than at ν_{24}, collisions will tend to heat T_{13} faster than T_{24}. However, model I, the model discussed in § IV*a*, with only σ_{32} enhanced, does not produce an appreciable ζ until the densities become very large. At $T_K = 10°$ K, T_{13} reaches 3.4° K at $n_{H_2} = 10^5\ \text{cm}^{-3}$, but ζ is only 1.4 percent. Figure 10 shows that T_{34} remains larger than T_{12} throughout the range of densities where both are cooled below 2.7° K, which is but an illustration of the general constraint implied by equation (3).

Because the optical depths in the 2-mm lines are likely to be large, trapping of the photons in those lines must be considered. The radiative transport was calculated by Dr. M. M. Litvak, using a modified version of the technique described by him recently (Litvak 1972). A uniform-density cloud was assumed, and solutions for the excitation temperatures were found at a grid of points spaced through the cloud. The combined effects of the 2.7° K background, collisions, and trapping of photons generated by

1975ApJ...196..351C

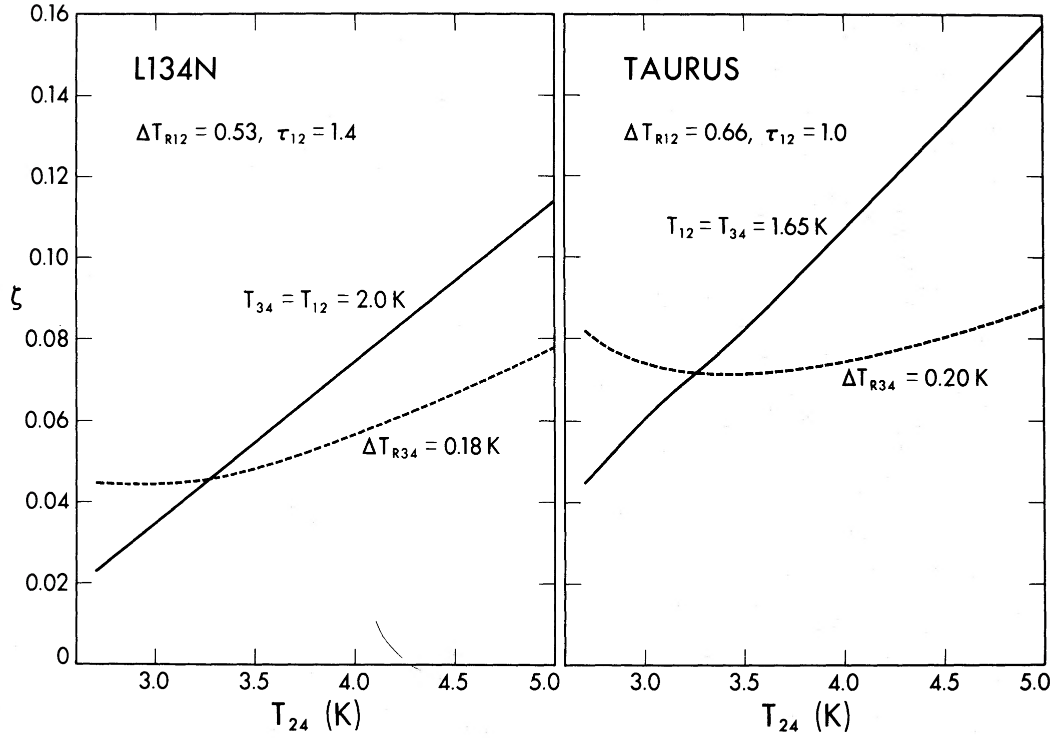

FIG. 11.—The solid lines give the fractional excess, ζ, as a function of T_{24}, required to give $T_{34} = T_{12}$, where T_{12} has been determined from ΔT_{R12} and τ_{12}. The dotted lines give ζ, as a function of T_{24}, required to give the observed ΔT_{R34}.

collisions generally produced a variation in excitation temperature through the cloud. Calculations were done for model I cross sections and ortho-H_2CO projected densities nL such that $nLc/\Delta v = 1.3 \times 10^{19}$ cm^{-2}. This column density gave $\tau_{12} = 0.95$ without trapping, and 0.7 with trapping; the tendency of trapping to lower τ_{12} is fairly general. Rather than try to model a particular cloud, we chose to do all calculations with the above value of $nLc/\Delta v$; hence trapping may be more or less important than we indicate, depending on the cloud in question. For model I, the effect of trapping was to create considerably larger T_{13}, T_{24}, and ζ in the center of the cloud than at the edges. At $n_{H_2} = 10^4$ cm^{-3}, $T_{13} = 3.86°$ K and $\zeta = 8$ percent

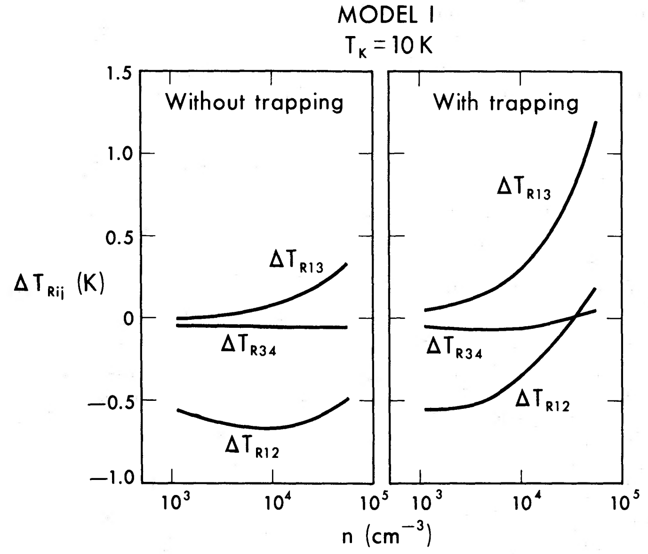

FIG. 12.—Line radiation temperatures as a function of density for Model I cross sections at a kinetic temperature of 10° K. The density scale is as described for fig. 10.

1975ApJ...196..351C

at the center of the cloud; but because T_{13} and ζ decrease away from the center, the net effect is lessened. Because of the gradients in excitation temperature, the results of the trapping calculations are more clearly presented as graphs of the line radiation temperatures, ΔT_{Rij}, calculated by integrating through the cloud. Figure 12 shows these for model I. At $n_{H_2} = 1.2 \times 10^4\ \mathrm{cm}^{-3}$, $\Delta T_{R12}/\Delta T_{R34} = 6.4$, which is still larger than many of the values in table 5, particularly the well-studied cases of L134 N and the Taurus cloud. In addition, the predicted absorption is quite weak at both 6 and 2 cm because of the heating of T_{12}. The latter problem could be solved by taking $\sigma_{32} = 1.7\sigma_0$. Such a model (Ia) gives $\Delta T_{R12} = -0.86°\ \mathrm{K}$ and $\Delta T_{R34} = -0.125°\ \mathrm{K}$ at $n_{H_2} = 10^4\ \mathrm{cm}^{-3}$; the ratio of 6-cm and 2-cm lines is still rather high (6.9). At the column density used, $nLc/\Delta v = 1.3 \times 10^{19}\ \mathrm{cm}^{-2}$, $\tau_{12} \sim 1.0$, so that using much larger column densities with this model would be questionable.

Because model I cross sections, even with trapping, are not very successful in producing the observed ΔT_{R12} and ΔT_{R34}, other models were considered. Because the observations indicate that $T_{13} > T_{24}$, a model with $\sigma_{31} > \sigma_{42}$ is suggested. As mentioned in § IV*a*, the classical calculations of Townes and Cheung did result in both σ_{31} and σ_{32} being enhanced over σ_{41} and σ_{42}. Although the size of σ_{31} relative to σ_{42} is not important in low-density clouds, it does become relevant when higher densities and trapping are involved. Hence we consider model II, with $\sigma_{31} = \sigma_{32} = 1.7\sigma_0$. A related model was suggested by a calculation that $\sigma_{42} = 2.0\sigma_{41}$ for a hard sphere plus van der Waals interaction (Litvak 1972). We took $\sigma_{42} = 2.0\sigma_{41}$ and $\sigma_{31} = 2.0\sigma_{32}$, in addition to $\sigma_{32} = 1.7\sigma_{41}$; to keep the total cross section consistent with laboratory data (see § IV*a*), we renormalized, so that $\sigma_{41} = 0.6\sigma_0$, $\sigma_{42} = 1.2\sigma_0$, and $\sigma_{31} = 2.0\sigma_0$ (model III). Both model II and model III produce considerable cooling of T_{12} at densities between 10^3 and $10^4\ \mathrm{cm}^{-3}$, and then a rapid rise in T_{12} while T_{34} remains quite constant (figs. 13 and 14). At $T_K = 10°$ K, $T_{12} = T_{34}$ at $n_{H_2} = 10^5\ \mathrm{cm}^{-3}$ in model II, and at $n_{H_2} = 4 \times 10^4\ \mathrm{cm}^{-3}$ in the more extreme model III. Although these densities are still quite high for dark clouds (Turner *et al.* 1973), trapping will lower the required densities.

Figures 15 and 16 show the ΔT_{Rij} resulting from trapping calculations with models II and III. The same column density was used as for model I. The strong tendency of these models to raise T_{12} relative to T_{34} at high densities is accentuated by trapping, and the densities required are lowered by about one order of magnitude. For example, line temperatures near those seen in the Taurus cloud and L134 N are predicted at $n_{H_2} \sim 10^4\ \mathrm{cm}^{-3}$ for model II. Because the true column densities and cross sections are uncertain, a solution for n_{H_2} in a particular cloud is

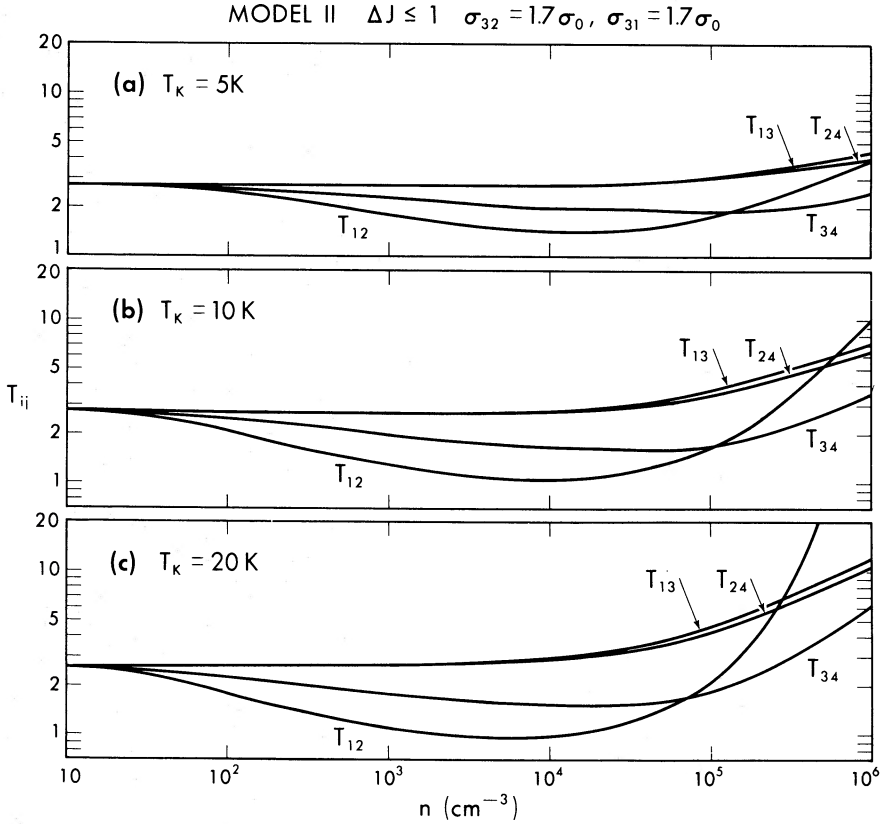

FIG. 13.—Excitation temperatures as a function of density for Model II cross sections at various kinetic temperatures

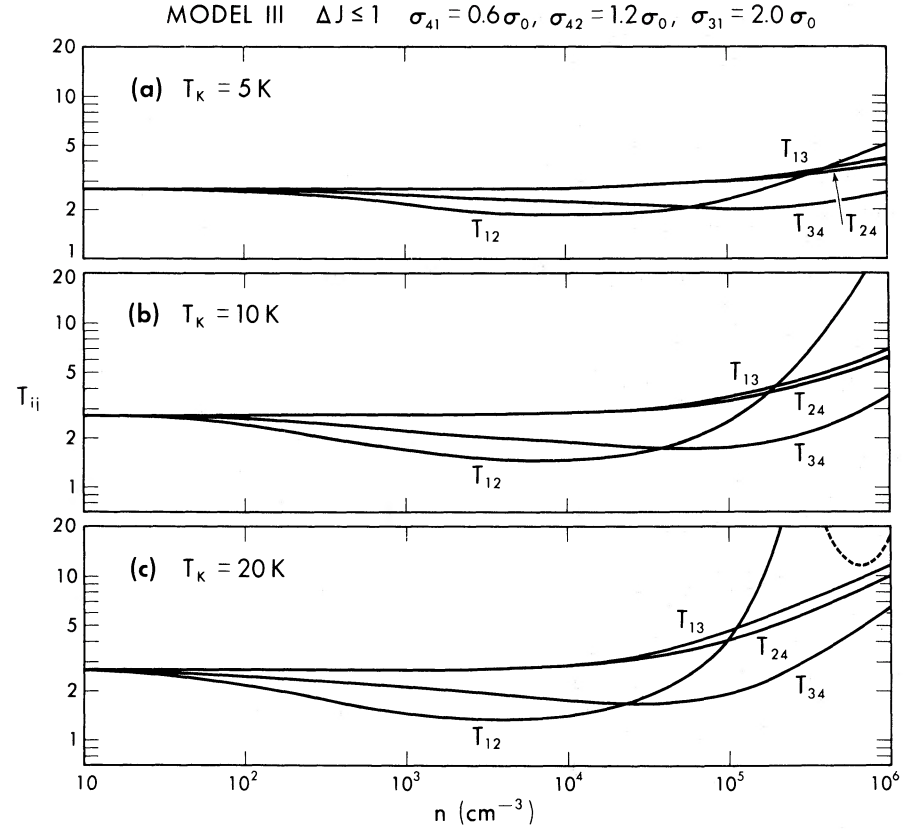

FIG. 14.—Excitation temperatures as a function of density for Model III cross sections at various kinetic temperatures

uncertain. However, it is clear that the data are best explained by models with both σ_{32} and σ_{31} enhanced. The large variations in $\Delta T_{R12}/\Delta T_{R34}$, seen both in dark clouds and in front of continuum sources, are probably caused by variations in n_{H_2} and nL from cloud to cloud, since models II and III produce a wide range in predicted $\Delta T_{R12}/\Delta T_{R34}$. We also note that the rapid changes in $\Delta T_{R12}/\Delta T_{R34}$ with increasing density shown in figures 15 and 16 imply that these lines provide a very sensitive measure of relative density fluctuations. For the σ_0 that we assumed, densities $\sim 10^3$ cm^{-3} are required for the primary pump, which seems to operate in most dark clouds. The clouds where the second pump operates must have densities $\sim 10^4$ cm^{-3}. At these densities, a weak 2-mm emission line might be detectable, as indicated in figures 15 and 16.

At the beginning of this section we remarked that the $H_2{}^{12}CO$ optical depths derived from $H_2{}^{13}CO$ measurements might be overestimates; this is true for all models at densities above 10^3 cm^{-3} because T_{12} is raised by trapping, as reflected in figures 12, 15, and 16, where the ΔT_{R12} are less for the case with trapping. Besides its consequences for the optical depths, this effect must be considered in deriving the isotopic abundance ratios in § IV*e*.

To derive the H_2CO fractional abundance, n/n_{H_2}, from these data, we must evaluate the range of values likely for nL and $n_{H_2}L$. While $nL = 4.4 \times 10^{13}$ cm^{-3} and $n_{H_2} = 10^4$ cm^{-3} give good agreement with observations, nL could easily be larger (and n_{H_2} smaller), because τ_{12} increases somewhat more slowly than nL, the effect of trapping being to heat T_{12} and to put more molecules in higher states. Indeed the $H_2{}^{13}CO$ observations of the Taurus cloud suggest $nL \sim 9 \times 10^{13}$ cm^{-2}, if the $H_2{}^{12}CO/H_2{}^{13}CO$ ratio is terrestrial. Kutner (1974) finds a blue extinction of 6.0 mag in this part of the cloud; since the extinction could well be larger, this provides a lower limit to $n_{H_2}L$ of 4.8×10^{21} cm^{-2}, yielding $n/n_{H_2} \lesssim 2 \times 10^{-8}$. An upper limit to $n_{H_2}L$ may be obtained by assuming $n_{H_2} = 10^4$ cm^{-3} and L equal to the long transverse dimension of ~ 4 pc (see Crutcher 1973*b* for the suggestion that this cloud is a rotating disk). Since n_{H_2} is unlikely to be 10^4 cm^{-3} over the whole line of sight, $n_{H_2}L \lesssim 1.2 \times 10^{23}$ yielding $n/n_{H_2} \gtrsim 7.5 \times 10^{-10}$. Note that the much larger $n_{H_2}L$ derived in this way implies that $n_{H_2} \neq 10^4$ cm^{-3} over 4 pc, unless the optical extinction is much greater. Taking the geometrical mean of the upper and lower limits to the fractional abundance yields $n/n_{H_2} = 4 \times 10^{-9}$. If similar extinction and distance apply for L134 N (the cloud appears

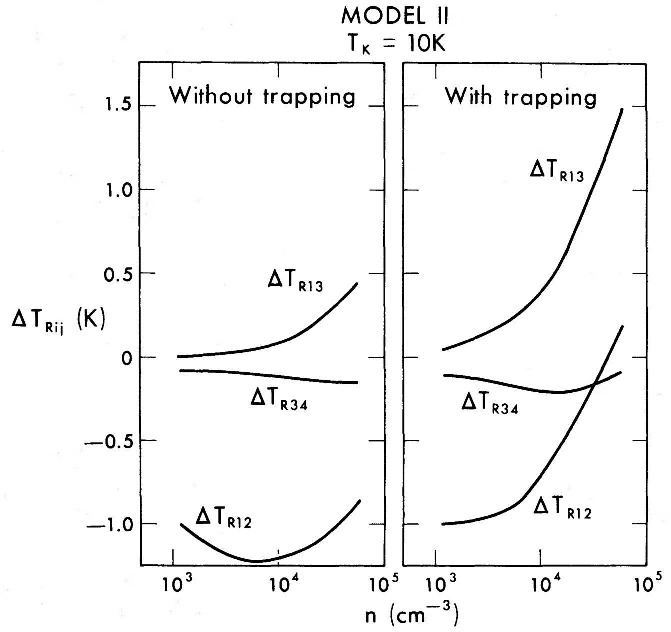

FIG. 15.—Line radiation temperatures as a function of density for Model II cross sections at a kinetic temperature of 10° K

opaque), then a similar abundance would be derived for that cloud.

e) $H_2{}^{12}C^{16}O/H_2{}^{13}C^{16}O$ *in Dark Clouds*

To derive the abundance ratio of $H_2{}^{12}C^{16}O$ to $H_2{}^{13}C^{16}O$, (col. [10] of table 3), we have used the equivalent width, defined by $\Delta T_A \Delta v$, and corrected for the fraction of the total intensity contained in hyperfine components within the line width (Tucker *et al.* 1971). In the case of L134 N a correction for the $H_2{}^{12}C^{16}O$ optical depth as measured by hyperfine studies (Heiles 1973) gives $H_2{}^{12}CO/H_2{}^{13}CO \sim 37$. Another source of uncertainty in the abundance ratios is the possibility of differences in excitation. Although a collisional model would probably give equal cooling in $H_2{}^{12}C^{16}O$ and $H_2{}^{13}C^{16}O$, differences cannot be ruled out completely. Furthermore, trapping of 2-mm photons in $H_2{}^{12}C^{16}O$ will raise the 6-cm excitation temperature and also increase the population in the $J = 2$ levels of $H_2{}^{12}C^{16}O$, whereas such

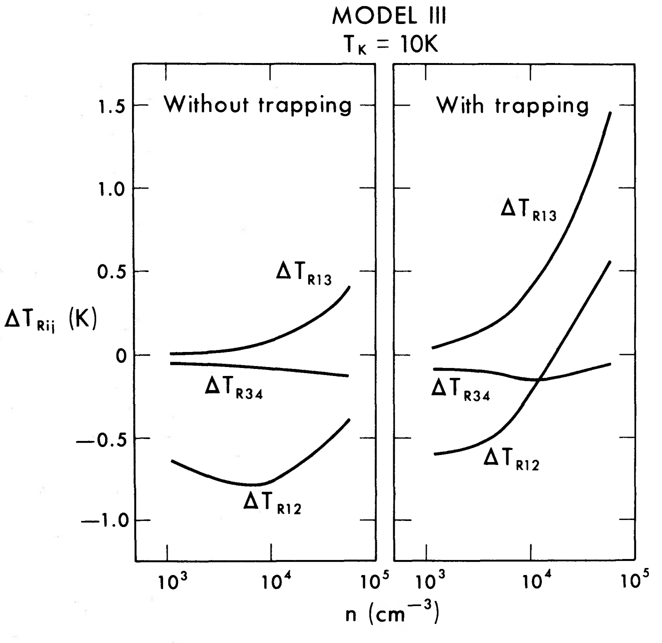

FIG. 16.—Line radiation temperatures as a function of density for Model III cross sections at a kinetic temperature of 10° K

effects would be absent in the optically thin 2-mm resonance lines of $H_2{}^{13}C^{16}O$. A radiative trapping calculation similar to those described in § IV*d* was carried out for L134 N. Compared with the case where trapping is ignored, the 6-cm $H_2{}^{12}CO$ line is weakened by a factor of 2. Taking this factor and the optical depth into account results in an isotope ratio close to the terrestrial value. While we lack information on τ_{12} in the other dark clouds, we expect similar correction factors.

The ratios of $H_2{}^{12}CO$ to $H_2{}^{13}CO$ in dark clouds thus appear to be similar to the ratios obtained by Zuckerman *et al.* (1974) in the direction of seven H II regions. Because the H_2CO optical depths in the clouds in front of the H II regions appear to be smaller than those in dark clouds, the effects of trapping may also be less important. This should be particularly true for Cas A, where the 2-cm data suggest that trapping is negligible. Thus, Cas A is the best source for measuring the true ratio, $H_2{}^{12}CO/H_2{}^{13}CO$; confirmation of the marginal detections in table 3 would suggest nonterrestrial abundances. Additional data with ~ 2 km s^{-1} resolution, which is not given in table 3, again suggest the presence of $H_2{}^{13}CO$ features near -38 and -45 km s^{-1} at approximately the same level as in table 3.

f) *Collisions across Doublets and the Effect of Electrons*

In the collisional models discussed in § IV*a*, all cross sections with $\Delta J \leq 1$ were chosen to be equal, except for a few cross sections with $\Delta J = 1$, which were adjusted to give the desired pumping. The cross sections for $\Delta J = 0$, corresponding to transitions across the doublets, can have an important effect on the efficacy of the cooling mechanism (Oka 1972). Collisions with H_2 molecules may have a larger cross section for transitions with $\Delta J = 0$ than for transitions with $\Delta J = 1$. In addition, electron collisions at low kinetic temperature will primarily produce $\Delta J = 0$ transitions. Thus we can evaluate both these effects by considering an enhancement of $\Delta J = 0$ transitions. If we denote by r_{ij} the rate of transitions from level i to level j induced by either electrons or neutrals, and use r_β to represent all $\Delta J = 0$ transitions and r_ξ to represent transitions from the $K = 1$ ladder to the $K = 3$ ladder, we can obtain the following approximate equation:

$$\frac{\sigma_{32}}{\sigma_{41}} = \frac{r_{32}}{r_{41}} \geq 1 + 0.20 \times \left(\frac{r_{41} + r_\beta + r_\xi}{r_{41}}\right) . \quad (5)$$

The form of this equation comes from Oka (1972). The coefficient of 0.20 gives the enhancement of σ_{32} over σ_{41} required to cool T_{12} to about 1.7° K, based on the solution of the statistical equilibrium equations. We can assume $r_\xi = 0$ in dark clouds since the lowest level with $K = 3$ lies $\sim 100°$ K above the ground state (see fig. 1). Then if $r_\beta = 2.0 r_{41}$, $\sigma_{32}/\sigma_{41} \geq 1.6$; if $r_\beta = 3.0 r_{41}$, $\sigma_{32}/\sigma_{41} \geq 2.0$ would be required.

Equation (3) of Kutner *et al.* (1971) may be evaluated at $T_K = 10°$ K to give the rate of electron collisions across the 6-cm doublet; given a cross section for neutral particle collisions, σ_0, of 10^{-15} cm^2 (1.4×10^{-15} for H_2), the electron collision rate would equal the neutral collision rate if $n_e \sim 5 \times 10^{-6}$ times the neutral particle density. Electron collision rates calculated recently (Itikawa 1972) are somewhat larger than those used above. Knowledge of neutral particle collisions is not yet sufficient to rule out large enhancements of σ_{32} over σ_{41}; but if we assume that $\sigma_{32} < 2.0 \times \sigma_{41}$ and $\sigma_{21} = \sigma_{41} = \sigma_0$, then $n_e/n_H < 10^{-5}$ in dark clouds.

g) *The Cosmic Background Radiation*

One of the primary motivations of original studies of the 2-cm transition was to extend the spectral measurements of the cosmic background to higher frequencies. This method has the advantage that the molecules respond to the brightness temperature, whereas a radiometer measures radiation temperature. Direct spectral measurements at wavelengths near 2 mm are very difficult.

The excitation temperature T_{13} represents an upper limit to the brightness temperature of the cosmic background radiation at $\nu_{13} \sim 141$ GHz, since collisional excitation to the 2-cm doublet can only increase T_{13}. Unfortunately, only for Cas A are the derived T_{13} in table 4 low enough to suggest that collisional excitation is unimportant. As we pointed out in § III, the possibility that the H_2CO is not distributed uniformly over the Cas A continuum source makes the determination of T_{13} for any single feature uncertain; but an average over the four features should be more reliable.

If the densities in the clouds in front of Cas A are so low ($< 10^2$ cm^{-3}) that even the first pump fails to operate, then $T_{12} = T_{34} = 2.7°$ K. Then the values for T_{13} in column (5) are applicable. Counting the upper limits equally with the detections, the average T_{13} is $\sim 2.5°$ K. If densities are less than 10^4 cm^{-3} and if trapping of the 2-mm photons is negligible, the second pump discussed in § IV*d* will not operate, and $T_{13} = T_{24}$. However, the densities may well be sufficient for the first pump to operate; if so, $T_{12} < 2.7°$ K. Under these conditions $T_{34} > T_{12}$, and the T_{13} would have to be somewhat larger than the values of column (5) to explain the observations. If we assume $T_{12} = 1.7°$ K and use equation (3) with $T_{13} = T_{24}$ to find T_{34}, we find the solutions for T_{13} that are given in column (6) of table 4. The average over the four Cas A features is 2.9° K. Thus, the uncertainties in T_{13} due to variations in T_{12} and T_{34} are probably small compared with the potential uncertainties due to possible source structure in the absorbing clouds.

Interpretation of dark-cloud observations in terms of the cosmic background temperature at 2 mm are hampered by the different spatial resolution available at the two wavelengths. In the two cases where 2-cm maps allow correction for this problem, the strong

2-cm lines suggest that T_{13} is raised above the background temperature, most likely by collisions and trapping according to the picture presented earlier. The large value of $\Delta T_{R12}/\Delta T_{R34} = 16$ predicted by solely 2.7° K background excitation to the 2-cm levels is not attained in any of the clouds observed. Such weak 2-cm lines would be difficult to detect. The observations of 2-cm anomalous absorption can place some constraints on the cosmic background, however; as noted earlier, an increase in $T_{13} = T_{24}$ will heat T_{34} (see eq. [3]). If the cosmic background were much hotter than 2.7° K at both $\nu_{13} = 141$ GHz and $\nu_{24} = 150$ GHz, the mechanism cooling T_{34} would be overcome, T_{34} would be raised above 2.7° K, and the 2-cm line would be driven into emission. If $T_{12} = 1.7°$ K, T_{34} would exceed 2.7° K if $T_{13} = T_{24} > 4.3°$ K. The fact that no emission is seen suggests that the background temperature is less than $\sim 5°$ K at both ν_{13} and ν_{24}.

We now consider the possibility that the brightness temperature of the cosmic background is different at ν_{13} than at ν_{24} $[T_{CB}(\nu_{13}) \neq T_{CB}(\nu_{24})]$. Very tight limits may be placed on the extent to which T_{24} can exceed T_{13}, or how negative ζ can be (see § IV*d*). If $T_{12} = 1.0°$ K, equation (3) shows that T_{34} would be heated above 2.7° K if $\zeta < -6$ percent. For the more commonly accepted value of $T_{12} = 1.7°$ K, the limit is $\zeta < -2$ percent. Of course, these limits are on the excitation temperatures, and they are applicable to the cosmic background only if the excitation temperatures T_{13} and T_{24} are equal to $T_{CB}(\nu_{13})$ and $T_{CB}(\nu_{24})$, respectively. Since there appear to be processes in at least some clouds that increase T_{13} over T_{24}, it is only in low-density clouds that one could test these limits. Presumably, the clouds with a large $\Delta T_{R12}/\Delta T_{R34}$ (e.g., G35.4+0.1) are clouds in which the collisions and trapping do not affect T_{13} and T_{24} very much, and we do not detect 2-cm emission in any of these clouds. Finally, we consider the possibility that the enhancement of T_{13} over T_{24} (positive ζ), the second pump which seems to be required in many clouds, is due to the cosmic background being brighter at ν_{13} than at ν_{24}. Because of the range of observed $\Delta T_{R12}/\Delta T_{R34}$ and, in particular, the high values of this ratio in clouds like G35.4+0.1, we believe that the second pump must be a local phenomenon, rather than a universal one. In addition, if the second pump were due to $T_{CB}(\nu_{13}) > T_{CB}(\nu_{24})$, then the 6-cm doublet would be heated in low-density clouds, where the first pump is weak. Solution of the equations of statistical equilibrium show that, for the collisional models we have used, T_{12} will be greater than 2.7° K at $n_{H_2} = 10^2$ cm^{-3} if $T_{CB}(\nu_{13}) > 1.04\, T_{CB}(\nu_{24})$ and at $n_{H_2} = 10^3$ cm^{-3} if $T_{CB}(\nu_{13}) > 1.17 T_{CB}(\nu_{24})$. Hence the cosmic background does not seem suitable as a second pump.

Although the 2-cm observations clearly rule out 2-mm pumping to cool the formaldehyde doublets, other deviations from a blackbody spectrum could affect the doublet temperatures. For instance, excess radiation at ν_{35} and ν_{46} or just at ν_{46} (see fig. 1) would cool both T_{12} and T_{34} but heat T_{56}, in a manner completely analogous to the way that 2-mm excess radiation cooled T_{12} but heated T_{34}. However, this process is very inefficient, partly because the population in the 2-cm levels is generally less than that in the 6-cm levels, so that the pump operates on a small fraction of the molecules. To examine this pumping scheme, the equations of statistical equilibrium were solved with equal cross sections for all transitions with $\Delta J \leq 1$, at $T_K = 10°$ K. Brightness temperatures as high as 7° K at both ν_{46} and ν_{35} could not cool T_{12} and T_{34} at densities of 10^3 cm^{-3}. A temperature of 5° K at ν_{46} alone cooled T_{12} fairly effectively at very low densities, but it also failed at densities greater than $\sim 10^3$ cm^{-3}.

Another interesting possibility for explaining anomalous absorption is that excess radiation exists at 6 cm and 2 cm, but not at shorter wavelengths. In this picture no pumping model is needed; the formaldehyde doublets are at 2.7° K because of the fast 2-mm rates, and they absorb the background radiation, which is hotter than 2.7° K at 6 cm and 2 cm. This would occur if the spectrum were not truly blackbody, but was characterized by somewhat higher temperatures at longer wavelengths. Actually, long-wavelength observations of the background spectrum do not rule this out (Thaddeus 1972*a*). The equations of statistical equilibrium were solved at $T_K = 10°$ K with cross sections all equal to σ_0 (see § IV*a*) if $J \leq 1$, assuming brightness temperatures of the background at 6 cm, 2 cm, and 2 mm of 3.7°, 3.2°, and 2.7° K, respectively. At all densities the excitation temperatures T_{12} and T_{34} were larger than the background temperature, and thus H_2CO would not display anomalous absorption. Because of this heating effect, a nonblackbody spectrum with an excess of centimeter wavelength radiation would actually make anomalous absorption harder to explain.

V. SUMMARY

In a number of dark clouds, the 2-cm transition of $H_2{}^{12}CO$ and the 6-cm transition of $H_2{}^{13}CO$ are seen in absorption against the cosmic background radiation. These observations, together with considerations of the rates required for cooling the 6-cm levels and the widespread occurrence of this cooling, lead to the conclusion that only the collisional cooling model of Townes and Cheung agrees with all the existing observations.

Such a model requires that $n_{H_2} \lesssim 10^3$ in dark clouds where substantial cooling of the H_2CO doublets exists. Because collisions with electrons heat the doublets, $n_e/n_{H_2} \lesssim 10^{-5}$ is required for a collisional model. A similar limit would apply to other proposed models because their rates are comparable to the neutral collision rates. Strong 2-cm absorption lines observed in some dark clouds require $n_{H_2} \sim 10^4$ cm^{-3}, even when favorable cross sections are used and trapping of the 2-mm H_2CO resonance radiation is considered. Significant structure in density and velocity appears to exist in dark clouds on a scale of a few minutes of arc.

The strong 2-cm lines observed toward continuum sources imply that ~40 percent of the H_2CO molecules are in the 2-cm doublet, indicating that considerable collisional excitation and possibly trapping of 2-mm photons exists. Determinations of the H_2CO abundance toward W3 and DR 21, in a dark cloud in Taurus, and in the Orion molecular cloud (Paper II) lead to consistent estimates with $n_{\mathrm{H_2CO}}/n_{\mathrm{H_2}} \sim 2$–$4 \times 10^{-9}$.

The 6-cm observations of $H_2{}^{13}CO$ indicate that the $H_2{}^{12}CO/H_2{}^{13}CO$ ratio in dark clouds is similar to that obtained from studies of 6-cm absorption against galactic continuum sources. The ratio is not very different from the terrestrial $^{12}C/^{13}C$ ratio; but if any real difference exists, the ^{13}C form is slightly overabundant.

Observations of the 2-cm line in the direction of Cas A can be used to study the intensity of the cosmic background radiation near the peak of a 2.7° K blackbody spectrum. The data indicate that the brightness temperature at 141 GHz of the cosmic background is less than ~2.9° K, subject to uncertainties due to possible structure in the absorbing clouds. The dark cloud observations suggest that differences in the background temperatures at 141 and 150 GHz, in the sense of higher temperatures at 150 GHz, are less than 6 percent of the average background temperature. The data also suggest that background temperatures are not larger at centimeter wavelengths than at millimeter wavelengths.

We are grateful to Messrs. D. Spitzmesser, L. Skjerve, and R. Gardner for their very important assistance with the observations at Goldstone; Mr. T. Cram for assistance with the reduction of data from NRAO; Mr. W. T. Lum for assistance with the Hat Creek observations; and the observing crews at Goldstone, NRAO, and Hat Creek. We thank Dr. C. Heiles for the use of his computer programs and his generous help with reducing the Hat Creek data. We are very grateful to Dr. M. Litvak for calculating the effects of radiative trapping on the H_2CO line intensities. We thank Dr. C. H. Townes for helpful discussions. Partial financial support for this work came from NSF grant GP-26218 to the University of Maryland and from the Alfred P. Sloan Foundation. The work of N. Evans was supported in part by NSF grant GP-3042X and NASA grant NGL05-003-272.

REFERENCES

Augustin, S. D., and Miller, W. H. 1974, *J. Chem. Phys.*, in press.
Clark, B. G. 1965, *Ap. J.*, **142**, 1398–1422.
Cohen, M. 1973, *M.N.R.A.S.*, **161**, 105–111.
Crutcher, R. M. 1973*a*, *Ap. J.*, **185**, 857.
———. 1973*b*, *Ap. Letters*, **14**, 147.
Dieter, N. H. 1973, *Ap. J.*, **183**, 449–468.
Dent, W. A. 1972, *Ap. J.*, **177**, 93–99.
Downes, D., and Rinehart, R. 1966, *Ap. J.*, **144**, 937–942.
Encrenaz, P. 1973, private communication.
Evans, N. J., II. 1973, unpublished dissertation, University of California, Berkeley.
———. 1975, in preparation.
Evans, N. J., II, Cheung, A. C., and Sloanaker, R. M. 1970, *Ap. J.* (*Letters*), **159**, L9–L14.
Evans, N. J., II, Zuckerman, B., Sato, T., and Morris, G. 1975, *Ap. J.*, submitted.
Fomalont, E. B., and Weliachew, L. 1973, *Ap. J.*, **181**, 781.
Grasdalen, G. L., Strom, K. M., and Strom, S. E. 1973, *Ap. J.* (*Letters*), **184**, L53.
Greisen, E. W. 1973, *Ap. J.*, **184**, 363–377.
Heiles, C. 1973, *Ap. J.*, **183**, 441–448.
Itikawa, Y. 1972, *J. Phys. Soc. Japan*, **32**, 217–226.
Kutner, M. L. 1973, in *Molecules in the Galactic Environment*, ed. M. A. Gordon and L. E. Snyder (New York: Wiley).
———. 1974, private communication.
Kutner, M., and Thaddeus, P. 1971, *Ap. J.* (*Letters*), **168**, L67–L71.
Kutner, M., Thaddeus, P., Jefferts, K. B., Penzias, A. A., and Wilson, R. W. 1971, *Ap. J.* (*Letters*), **164**, L49–L54.
Litvak, M. M. 1970, *Ap. J.* (*Letters*), **160**, L133–L138.
———. 1972, in *Atoms and Molecules in Astrophysics*, ed. T. R. Carson and M. J. Roberts (London: Academic Press), pp. 201–275.
Mayer, C. H., and Hollinger J. P. 1968, *Ap. J.*, **151**, 53–63.
Minn, Y. K., and Greenberg, J. M. 1973, *Astr. and Ap.*, **22**, 13.
Morris, M., Palmer, P., Turner, B. E., and Zuckerman, B. 1974, *Ap. J.*, **191**, 349.
———. 1975, *ibid.*, in preparation.
Ohm, E. A., and Snell, W. W. 1963, *Bell System Tech. J.*, **42**, 2047.
Oka, T. 1970, *Ap. J.* (*Letters*), **160**, L69.
———. 1972, *Mém. Soc. R. Sci. Liège*, Ser. 6, **3**, 61–81.
Palmer, P., Buhl, D., Snyder, L. E., and Zuckerman, B. 1975, in preparation.
Palmer, P., and Zuckerman, B. 1969, unpublished.
Palmer, P., Zuckerman, B., Buhl, D., and Snyder, L. E. 1969, *Ap. J.* (*Letters*), **156**, L147–L150.
Reifenstein, E. C., III, Wilson, T. L., Burke, B. F., Mezger, P. G., and Altenhoff, W. J. 1970, *Astr. and Ap.*, **4**, 357.
Rickard, L. J., Buhl, D., Palmer, P., and Zuckerman, B. 1975, in preparation.
Rogers, D. V., and Roberts, J. A. 1973, *J. Mol. Spectrosc.*, **46**, 200.
Schraml, J., and Mezger, P. G. 1969, *Ap. J.*, **156**, 269–301.
Sibille, F., Bergeat, J., and Lunel, M. 1974, *Astr. and Ap.*, **30**, 181.
Simon, M., Righini, G., Joyce, R. R., and Gezari, D. Y. 1973, *Ap. J.*, **186**, L127.
Solomon, P. M., and Thaddeus, P. 1970, *Bull. AAS*, **2**, 218–219 (abstract of paper delivered at 131st meeting of AAS, New York City).
Stieff, L. J., Donn, B., Glicker, S., Gentieu, E. P., and Mentall, J. E. 1972, *Ap. J.*, **171**, 21–30.
Strom, S. E. 1974, private communication.
Thaddeus, P. 1972*a*, *Ann. Rev. Astr. and Ap.*, **10**, 305.
———. 1972*b*, *Ap. J.*, **173**, 317–342.
Townes, C. H., and Cheung, A. C. 1969, *Ap. J.* (*Letters*), **157**, L103.
Tucker, K. D., Tomasevich, G. R., and Thaddeus, P. 1971, *Ap. J.*, **169**, 429–440.
———. 1972, *ibid.*, **174**, 463–466.
Turner, B. E., Zuckerman, B., Palmer, P., and Morris, M. 1973, *Ap. J.*, **186**, 123.
Whiteoak, J. B., and Gardner, F. F. 1970, *Ap. Letters*, **5**, 5.
Wink, J. E., Altenhoff, W. J., and Webster, W. J., Jr. 1973, *Astr. and Ap.*, **22**, 251–255.
Wynn-Williams, C. G. 1971, *M.N.R.A.S.*, **151**, 397–420.
Wynn-Williams, C. G., Becklin, E. E., and Neugebauer, G. 1972, *M.N.R.A.S.*, **160**, 1–14.
———. 1974, *Ap. J.*, **187**, 473.
Zuckerman, B., and Ball, J. A. 1973, *Ap. J.*, **190**, 35.
Zuckerman, B., Buhl, D., Palmer, P., and Snyder, L. E., 1970, *Ap. J.*, **160**, 485–506.
———. 1974, *ibid.*, **189**, 217.
Zuckerman, B., Morris, M., Palmer, P., and Turner, B. E. 1972, *Ap. J.* (*Letters*), **173**, L125–L129.

THE ASTROPHYSICAL JOURNAL, **196**:457–463, 1975 March 1

THE NUCLEATION AND EXPULSION OF CARBON PARTICLES FORMED IN STELLAR ATMOSPHERES

RONALD G. TABAK,* JOHN P. HIRTH,† GLYN MEYRICK,† AND TERRY P. ROARK*
The Ohio State University

Received 1974 July 16

ABSTRACT

The conditions for significant nucleation of carbon particles to occur in several late-type stellar atmospheres are considered. The theoretical treatment includes the contributions from the translational, rotational, and vibrational degrees of freedom of the nuclei which have been omitted in previous considerations. It is shown that the range of possible surface free energies of the particles, for which nucleation can be achieved in these atmospheres, is small. The effects of electrostatic drag on escaping particles are discussed. Under the conditions considered here, these effects are shown to be of secondary importance to those of viscous drag.

Subject heading: interstellar matter

I. INTRODUCTION

The existence of small solid particles in interstellar space has been widely accepted for over 40 years. General acceptance of the chemical composition and sites of origin has been much more elusive. It does seem reasonable, however, to consider the atmospheres of cool, high-luminosity stars as one likely site for the nucleation, growth, and subsequent expulsion of such particles.

The question of whether or not carbon particles can nucleate within carbon and Mira variable stars has been considered by Donn *et al.* (1968) and by Fix (1969). Those authors concluded that nucleation was quite likely early in the cooling cycle of such stars so that nucleation, itself, would provide no constraint to the formation of carbon grains which might then be expelled to form one component of the interstellar medium. There are three aspects of these investigations that we wish to consider further. The first two concern the proper formulation of the nucleation rate equation and the adoption of a value for the surface free energy of the material considered. The third problem arises when one considers electrostatic drag effects in discussions of the possibility of particle ejection.

II. THE NUCLEATION PROBLEM

The studies by Donn *et al.* (1968) and by Fix (1969) employed the classical nucleation theory of Volmer (1939), corrected to include the Zel'dovich (1942) non-equilibrium factor cited in Hirth and Pound (1963). However, this theory has been further modified by Lothe and Pound (1962), who included rotational and translational partition functions in the description of the vapor-phase nuclei: these modifications were also presented in Hirth and Pound (1963) and treated more extensively by Feder *et al.* (1966). The latter form of the theory is sufficiently general to treat in terms of statistical mechanics any system for which the particle partition function is known. Generally, however, the partition function for small particles is not known, and the small nuclei or embryos are treated in an approximation as having bulk volume and surface free energies, with activated rotational and translational degrees of freedom and a compensating loss of six degrees of vibrational freedom. The uncertainties in removal of vibrational modes appear formally in the theory in the so-called replacement factor, for which values ranging from 10^4 to 10^{20} have been suggested.

Specific criticisms of the Lothe-Pound theory, focusing on the replacement factor, have been presented by Reiss and Katz (1967), Reiss, Katz, and Cohen (1968), Dunning (1969), Kikuchi (1969, 1971), and Blander and Katz (1972), with rebuttals being given by Lothe and Pound (1966, 1968), Nishioka, Pound, and Abraham (1970), Pound, Nishioka, and Lothe (1972), and Nishioka and Pound (1974). Both points of view are discussed in the compendium by Abraham (1974). However, even for liquid droplet nucleation, where the Lothe-Pound assumptions are most severely tested, atomic calculations by Burton (1973) and experiments on nonpolar liquids (but not polar ones) by Dawson *et al.* (1969) support the Lothe-Pound theory.

For solids such as graphite, most of the controversial questions do not apply, and the Lothe-Pound formalism is expected to apply with a replacement factor near the smaller end of the range mentioned above. This is so because of the highly localized nature of the atomic binding in graphite so that the free energy of a cluster can rather accurately be divided into volume and surface terms equivalent to those for bulk graphite. It should be noted that there is reason to doubt that carbon particles formed in cool star atmospheres will necessarily have the specific crystalline structure of graphite (Czyzak and Santiago 1973). The effect of other possible carbon structures on the replacement factor has not been examined in

---

* Department of Astronomy.

† Department of Metallurgical Engineering.

detail, and we will adopt the Lothe-Pound value of this factor for subsequent computations. Because the inclusion of the Lothe-Pound correction can cause an enormous change, of the order of a factor of 10^{20} in the predicted nucleation rate, the consequences of such corrections should be considered for the carbon nucleation problem.

A second uncertain aspect of the earlier treatments of carbon nucleation is the adoption of a value for the surface energy, γ, of 1000 ergs cm^{-2}. While this is a reasonable median value, there is a large variation in the values reported for the surface energy of various forms of graphite and other carbon solids. This variation is shown in table 1. In part, the variation arises from anisotropy in surface energy with orientation and in part from possible adsorption effects. Since adsorption can be excluded at the temperatures of interest in nucleation, the lower adsorption-affected values need not be considered. The best values for crystalline graphite would then appear to be (Abrahamson 1973) 40 to 170 ergs cm^{-2} for the basal surface and 4000 to 4800 ergs cm^{-2} for the prism surface. What then should one choose for a nucleus? Graphite fragments observed in evaporation experiments are disk-shaped crystals (Whittaker and Kintner 1969) with an area ratio of basal to prism-type surfaces of about 8:1 which, using the surface energy values of Abrahamson, would give an average surface energy of 500 ergs cm^{-2}, or, normalized to a hypothetical spherical shape of the same mass and of the same total surface energy, 1410 ergs cm^{-2}. On the other hand (Walker 1972), soot particles or graphite particles formed by carbonization can have shapes varying among polyhedral, bounded by basal planes but containing internal voids of an atomic size scale; scroll-like glassy carbon; and spherulitic carbon. For the latter, the higher values of 2400 ergs cm^{-2} (Munson 1967) to 4400 ergs cm^{-2} (Abrahamson 1973) would be more appropriate. Any deviation from bulk surface energies, as discussed previously, would be expected to be in a similar manner toward larger values on the basis of a dangling bond model. In the absence of astronomical or other data defining the form of the nucleus, we take the value of 1000 ergs cm^{-2} used previously as a typical value at the lower end of the distribution of values appropriate for graphite and 3000 ergs cm^{-2} as a typical value at the upper end. As shown in the following, this variation in γ also produces an enormous change in the nucleation rate.

Third, we consider the bulk free energy term. In addition to the assumptions discussed above, we follow the other treatments of the nucleation problem in considering the nucleus to be pure graphite aside from a possible central foreign ion. In the actual case, other elements may be present, in particular hydrogen arising from hydrocarbon intermediate forms (Salpeter 1974). However, desorption should be rapid at the temperatures in question; and in the absence of data to the contrary, we suppose the particles to consist of graphite. The other aspect of the bulk free energy is the assumption of quasi-equilibrium between polymers and monomer. Dorfeld and Hudson (1973) have considered the possibility of a kinetic constraint additional to those in the Lothe-Pound theory in the step of formation of carbon dimer from monomer, an effect which should be important at relatively low temperatures and monomer pressures. In the cases we consider, however, preexisting dimer and trimer would suffice to produce nucleation at essentially the same critical supersaturation as for the monomer case. Thus, we follow Fix (1969) and Donn *et al.* (1968) in assuming quasi-equilibrium in the vapor.

Including the Lothe-Pound factor Γ in the nucleation rate equations developed by Fix (1969), as well as the (Katz, Saltsburg, and Reiss 1966) modification for associated vapors, we find for the homogeneous nucleation rate

$$J_1 = n_1 \Omega \Gamma (4\gamma / kT)^{1/2} \times \sum_1^3 (\beta_j \alpha_j j^2) \exp(-A_1^*/kT)\,, \quad (1)$$

and for the heterogeneous nucleation rate on ions

$$J_2 = n_1 \Omega \Gamma [(4\gamma - e^2/\pi r^{*3})/kT]^{1/2} \times \sum_1^3 (\beta_j \alpha_j j^2) \exp(-A_2^*/kT)\,, \quad (2)$$

where $\beta_j = P_j/(2\pi jmkT)^{1/2}$, P_j is the partial pressure of the j-mer, m is the atomic mass of carbon, k is

TABLE 1

FREE SURFACE ENERGY, γ, OF VARIOUS CARBON SOLIDS

	γ(ergs cm^{-2})	Material	Reference
1)	40–170	Crystalline graphite—basal surface	Abrahamson 1973
2)	4000–4800	Crystalline graphite—prism surface	Abrahamson 1973
3)	65–126	Graphitized channel black—basal surface	Good *et al.* 1958
4)	100–380	Pyrolytic graphite—basal surface	Elyutin *et al.* 1968, as corrected by Abrahamson 1973
5)	500	Graphite evaporation fragments—Disk-shaped 8:1 basal to prism-type surface areas	Calculated by authors from entries 1 and 2
6)	1410	Same as above but normalized to hypothetical spherical shape	Calculated by authors from entries 1 and 2
7)	3760	Diamond	Beloguriov 1960
8)	1700–2700	Graphite	Munson 1967
9)	690–2830	Polycrystalline graphite carbon	Mortimer and Nicholas 1970

Boltzmann's constant, T is absolute temperature, $n_1 = P_1/kT$ is the concentration of monomer, $n_i = P_i/kT$ is the concentration of ions, Ω is the atomic volume of carbon, e is the unit charge in esu, r^* is the size of the critical nucleus, α_j is the condensation coefficient for the j-mer, and A^* is the free energy of formation of the critical sized nucleus. When the nucleus is phenomenologically taken to be spherical in shape, the free energies of formation in the two cases are

$$A_1^* = 4\pi\gamma r^{*2}/3\,, \tag{3}$$

$$A^*_2 = (4\pi\gamma r^{*2} - e^2/r^*)/3\,. \tag{4}$$

The Lothe-Pound factor is given by

$$\Gamma = \frac{kT}{P_1}\frac{F_T F_R}{F_v^6}\,, \tag{5}$$

with the translational, rotational, and vibrational partition functions given by

$$F_T = (2\pi m i^* kT)^{3/2}/h^3\,, \tag{6}$$

$$F_R = (8\pi^2 IkT)^{3/2}/h^3\,, \tag{7}$$

$$F_v = [1 - \exp(-h\nu/kT)]^{-1} \approx kT/h\nu\,, \tag{8}$$

where $I = 8\pi m r^{*5}/15\Omega$ the moment of inertia, i^* is the number of carbon atoms in a critical nucleus, h is Planck's constant, and ν is the Debye frequency.

Data from five typical cases of nucleation in carbon-producing stars are presented in table 2. P_g is the total pressure of the atmosphere (dynes cm^{-2}); C/O is the carbon-oxygen ratio; O/H is the oxygen/hydrogen ratio; T the temperature (° K); P_1, P_2, and P_3, respectively, the monomer, dimer, and trimer partial pressures (dynes cm^{-2}); S the supersaturation ratio, and P_i (dynes cm^{-2}) the partial pressure of ions. All ion pressures were calculated from the equation of Fix (1969). For cases A, D, and E, the general data and the vapor pressure data for the carbon dimer and trimer molecules are taken directly from Morris and Wyller (1967) while the data for monomer vapor pressure are calculated from their dissociation constants. The vapor pressure of monomer for cases B and C is calculated from the supersaturation ratios listed by Fix (1969): in the absence of direct data, the dimer and trimer vapor pressures are calculated for these cases by using the same supersaturation ratio. As seen in the following, the nucleation rates are quite insensitive to minor changes in the pre-exponential terms so the latter approximation should introduce a negligible error. The monomer vapor pressures are plotted in figure 1 together with the equilibrium vapor pressure, P_1^e, over graphite (Masser 1967). Values of the supersaturation ratio $S = P_1/P_1^e$ computed from these data are included in table 2. Values used for the condensation coefficients are those given by Thorn and Winslow (1957), $\alpha_1 = 0.37$, $\alpha_2 = 0.34$, and $\alpha_3 = 0.08$. Salpeter (1973) has recently suggested that supercritical particles near the critical size can be heated to temperatures well above the ambient because of the release of the heat of condensation. If present, such an effect would markedly reduce the effective value of α_1. However, for the cases considered in the present work, computation of the thermal effect from the equations (40′) and (42) of Feder *et al.* (1966) reveal that the heating effect is completely negligible, corresponding to a change in α_1 by an increment of 10^{-4} percent. Physically, this is so because of the relatively high population of hydrogen which serves to maintain near-isothermal conditions.

In order to examine limiting cases of nucleation behavior, tests were conducted for both $\gamma = 1000$ and $\gamma = 3000$ ergs cm^{-2}, using 1600°, 1800°, and 1960° K as the temperatures for nucleation. The nucleation rate varies so strongly with supersaturation that the rate changes from effectively zero to an enormously

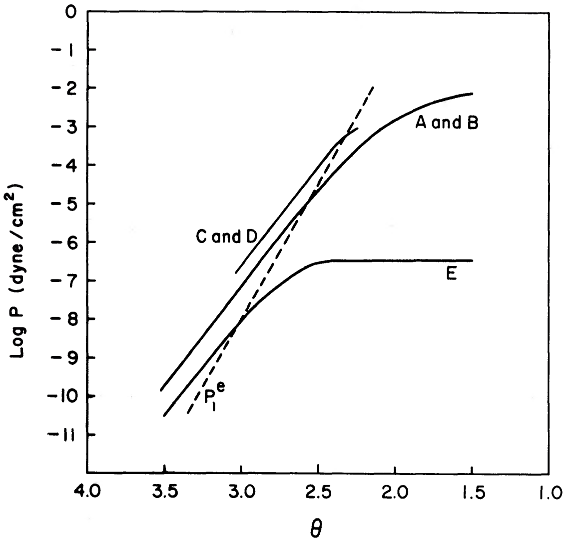

FIG. 1.—Partial pressures of carbon monomer for cases given in table 1 (*solid lines*) and equilibrium pressure over graphite, p_1^e (*dashed line*) as a function of $\theta = 5040/T$(° K).

TABLE 2

ATMOSPHERIC AND ABUNDANCE PARAMETERS

	P_g	C/O	O/H	T	P_1	P_2	P_3	S	P_i
A	10^2	2.3	2×10^{-5}	1600	1.0×10^{-8}	1.6×10^{-9}	2.5×10^{-7}	10.0	3.2×10^{-6}
B	10^2	2.3	2×10^{-5}	1800	7.9×10^{-7}	1.0×10^{-8}	4.0×10^{-7}	3.3	1.9×10^{-5}
C	10	3.0	10^{-3}	1800	2.4×10^{-6}	1.8×10^{-9}	1.5×10^{-8}	10.0	3.2×10^{-6}
D	10	3.0	10^{-3}	1970	5.0×10^{-5}	5.0×10^{-6}	2.0×10^{-5}	2.7	9.3×10^{-6}
E	10^{-2}	2.3	2×10^{-5}	1600	1.0×10^{-9}	5.0×10^{-12}	6.0×10^{-9}	1.6	

TABLE 3

VALUES OF CRITICAL SUPERSATURATION RATIO FOR FOUR TYPICAL CASES WITH TWO VALUES OF SURFACE ENERGY, γ

			HOMOGENEOUS			HETEROGENEOUS		
	T	S	J_{Cl}	J_m	$J_{m'}$	J_{Cl}	J_m	$J_{m'}$
$\gamma = 1000$ ergs cm^{-2}								
A	1600	10.0	4.7×10^7	(4.27)*	(2.99)	(8)	(3.42)	(2.76)
B	1800	3.3	249	(3.15)	(2.43)	5.7	(2.8)	(2.3)
C	1800	10.0	132	(3.09)	(2.42)	(6)	(3)	(2.33)
D	1970	2.7	25.5	(2.56)	(2.11)	4.55	(2.43)	(2.1)
$\gamma = 3000$ ergs cm^{-2}								
A	1600	10.0	1.3×10^{33}	3.0×10^3	353	1×10^4	558	183
B	1800	3.3	1.2×10^{12}	549	118	2.8×10^3	204	53
C	1800	10.0	5.1×10^{10}	493	113	2.78×10^3	209	79
D	1970	2.7	1.5×10^7	165	54	980	99	48

* Values in parentheses indicate that nucleation will occur for the imposed supersaturation ratios, S.

rapid rate with a small variation of the supersaturation ratio around a critical value. Hence, the value of this critical ratio is a measure of the propensity of the system for nucleation. The value S^* of the critical supersaturation ratio for a chosen critical nucleation flux J was determined numerically. Three separate cases of nucleation were examined, and the results are shown in table 3. In the first the flux $J_{\mathrm{Cl}} = 1$ cm^{-3} s^{-1} was assumed and S^* values were calculated using the classical theory as considered by Donn *et al.* (1968) and Fix (1969). In the second case a flux $J_m = 1$ cm^{-3} s^{-1} was assumed, and in the third case $J_m' = 10^{-18}$ cm^{-3} s^{-1}. The second and third cases employ the modified flux rate equations (1) and (2) with Γ as given by equation (5). The range in J_m of 10^{18} between the second and third cases must surely bracket any actual nucleation rates that may occur in real stars.

The supersaturation for case E was insufficient to produce nucleation. Results for the other cases, given in table 3, are of interest not only with regard to the interstellar dust question but also with respect to nucleation in general. In particular the results illustrate the points in the above discussion of the critical supersaturation ratio. We note the small change in this ratio between cases J_m and J_m', corresponding to a change by a factor of 10^{18} in nucleation rates. The inverse of this, of course, also applies: a small change in supersaturation ratio near the critical value produces a large change in nucleation rate J.

There are several other implications of the results in table 3. First, we note that in no case does nucleation occur with $\gamma = 300$ ergs cm^{-2}. Continuing the calculations to lower temperatures would not change this situation, in contrast to the usual expectation of nucleation theory. This seeming anomaly occurs because for the standard nucleation cases (e.g., water) at or near room temperature, the surface energies are an order of magnitude smaller and the equilibrium vapor pressure less temperature dependent. In the present case, the decrease in the pre-exponential factor with temperature leads to a requirement for a smaller exponential factor, and in turn the high surface energy means that the supersaturation ratio S must increase very rapidly to achieve that smaller factor. This trend offsets the increase of the actual supersaturation with the decrease in P_i^e, and means that nucleation cannot occur at lower temperatures.

Second, we see that the Lothe-Pound modification is significant in deciding whether nucleation is possible: even if $\gamma = 1000$ ergs cm^{-2}, the classical theory does not give nucleation at all in the homogeneous case and only marginally does so for the heterogeneous case A. However, the corrected theory containing the partition function terms does indicate nucleation for all cases with $\gamma = 1000$ ergs cm^{-2}. It is very clear that the role played by the surface energy is most dramatic and that the boundary between γ-S regimes where nucleation does or does not occur is rather sharp. The plausibility of the hypothesis that carbon particles can be a major constituent of the interstellar medium is crucially dependent upon the value of the surface energy. In this respect it is worth noting that if carbon particles of imperfect or otherwise unusual metastable modifications of graphite are invoked, it is to be expected that the relevant surface energies in these instances would fall in the same range as that described previously. However, in such cases the volume free energy terms should be smaller in magnitude than those for normal graphite and consequently the corresponding nucleation fluxes would be smaller than for graphite.

The $\gamma = 1000$ ergs cm^{-2} data are also of interest in illustrating the insensitivity of S^* to the pre-exponential factor. The difference between cases B and C is a difference of about one order of magnitude in the pre-exponential factor. As can be seen, this difference has a minimal effect on S^* in the range where nucleation is likely. The difference between the J_m and J_m' cases is a factor of 10^{18} in the pre-exponential factor. Even with this huge difference, the values of S^* differ by less than 50 percent in all cases for $\gamma = 1000$ ergs cm^{-2}. Because of this steep functional dependence it is clear that the prediction of meaningful nucleation rates awaits a more accurate knowledge of the pertinent surface energy and of the actual supersaturation ratios in a given stellar atmosphere. At present the supersaturation ratios are poorly known for actual carbon and Mira stars at temperatures below 2000° K (Wallerstein 1973).

III. THE GRAIN EJECTION PROBLEM

Assuming that the difficulties and uncertainties described above can be overcome and that nucleation with subsequent growth of carbon particles does occur, these particles must be ejected from the stellar atmosphere if they are to become a part of the interstellar medium. Particles in stellar atmospheres are influenced by at least eight different effects: (*a*) radiation pressure, (*b*) gravitation, (*c*) viscous drag, (*d*) electrostatic interactions, (*e*) sputtering, (*f*) accretion, (*g*) radiation damage to structure, and (*h*) magnetic fields. From what is known of the conditions in carbon-star atmospheres, the last four items are of secondary importance for the time interval of 10^7 s in which escape must occur (approximately one-third of the light variation period for such stars).

Detailed discussions of the relative contribution of the first three mechanisms to the ejection or retention of particles have been undertaken by Wickramasinghe (1967, 1972). To within an order of magnitude, we have confirmed his results that grains will escape if the overall density of the photosphere can be made low enough ($n_{\mathrm{H}} = 10^{12}$–10^{11}). His analysis, however, does not include possible effects of electrostatic drag.

If the grain is electrically charged, there arises a Coulomb-type drag force (F_{C}) that, like the viscous drag force, is directly proportional to the relative grain velocity, viz.,

$$F_{\mathrm{C}} = \zeta v\,, \tag{9}$$

where ζ is the mass of the grain divided by t_s, the slowing-down time as defined by Spitzer (1963), p. 134, i.e.,

$$t_s = \frac{11.7 A_g T^{3/2}}{A^{1/2} n Z_g^{2} Z^{2} \Lambda}\,, \tag{10}$$

where A_g and A are the grain and ion masses, respectively, in atomic mass units, T is the temperature in degrees K, n is the number density of the field particles, Z_g and Z are the charges on the grain and ion, and Λ is a cutoff factor which arises because shielding reduces the effectiveness of encounters beyond a certain critical distance. In the temperature and density region under consideration, Spitzer (1968) gives

$$\Lambda = \frac{3}{2 Z_g Z e^3}\,(k^3 T^3/\pi n_e)^{1/2}\,, \tag{11}$$

where n_e is the number density of electrons. If n_e can be obtained from models of carbon star atmospheres, the only uncertain quantity in finding ζ is the value for the charge on the grain, Z_g.

The surface of the grain can become charged in two ways: (1) photoemission of ions by ultraviolet radiation and (2) accretion of ions. At temperatures of the order of 2000° K, the charge due to photoemission off graphite should be much smaller than that due to accretion. Also, because of equipartition of energy, the velocity of the electron is at least 43 times greater than the velocity of an ion. Therefore the electron collision frequency will greatly exceed that of the ions. Taking the condensation coefficient of electrons as unity, one would thus expect to find the grain with a net negative charge. The procedure followed to find Z_g is basically the same as that used by Spitzer (1968), except that we consider the case of a mixture of single ionized atoms instead of only one species. The main assumption made in both instances is that every ion which strikes the grain is neutralized before it leaves. Thus, we will get an upper bound on the rate of charge accumulation.

Suppose that the spherical grain is at rest and that its mass, M_g is much greater than the mass of the ion, M_i. If r is the radius of the grain and the ion path is just tangent to the grain surface, conservation of angular momentum and energy yields the following collisional cross sections for an electron and an ion with a grain carrying Z_g units of charge:

$$\sigma_e = \pi r^2\left(1 - \frac{2 Z_g e^2}{M_e v_e^{2} r}\right),$$

$$\sigma_i = \pi r^2\left(1 + \frac{2 Z_g e^2}{M_i v_i^{2} r}\right). \tag{12}$$

Assuming steady-state conditions, the grains will not continually accumulate negative charge. When equilibrium is established, the number of electrons striking the grain and being neutralized will equal the number of positive ions being captured, even though $v_e \geqslant 43 v_i$. If a Maxwellian velocity distribution holds, we can write:

$$\int_{v_0}^{\infty} n_e \sigma_e v_e f(v_e)\,dv_e = \sum_i \int_0^{\infty} n_i \sigma_i v_i f(v_i)\,dv_i\,, \tag{13}$$

where

$$f(v) = 4\pi^{-1/2}(m/2kT)^{3/2} v^2 \exp\left(-mv^2/2kT\right) \tag{14}$$

and v_0 is the electron velocity that makes $\sigma_e = 0$ in equation (12). If all of the ions are singly ionized, equation (13) can be integrated to yield

$$e^{-y} = \frac{(1 + y)}{n_e} M_e^{1/2} \sum_i (n_i/M_i^{1/2})\,, \tag{15}$$

where $y = Z_g e^2/rkT$. Equation (15) is a transcendental equation that can be solved numerically for y once we know the kinds of ions we are dealing with and their amounts. This in turn requires knowledge of the electron density.

Using the model atmospheres calculated by Johnson (1973), we found that potassium, sodium, calcium, and aluminum were the primary sources of

TABLE 4

COEFFICIENTS FOR VISCOUS DRAG ξ, COULOMB DRAG ζ, AND GRAIN CHARGE Z_g

	2000° K			2500° K		
a (μ)	Z_g	ζ	ξ	Z_g	ζ	ξ
0.001	0.5	...*	$4.5 \times 10^{-32} n_{\mathrm{H}}$	0.6	...*	$5.1 \times 10^{-32} n_{\mathrm{H}}$
0.01	5.0	$8.6 \times 10^{-35} n_{\mathrm{H}}$	$4.5 \times 10^{-30} n_{\mathrm{H}}$	6.0	$5.5 \times 10^{-34} n_{\mathrm{H}}$	$5.1 \times 10^{-30} n_{\mathrm{H}}$
0.05	25.	$1.8 \times 10^{-33} n_{\mathrm{H}}$	$1.1 \times 10^{-28} n_{\mathrm{H}}$	30.	$1.1 \times 10^{-32} n_{\mathrm{H}}$	$1.3 \times 10^{-28} n_{\mathrm{H}}$

* Statistical fluctuation of surface charge too great for determination of ζ.

electrons. The cosmic abundances quoted by Allen (1963) yield a mean mass of $39 m_p$ for the ions, where m_p is the mass of a proton. With $n_e = \sum n_i$, equation (15) becomes

$$f(y) = 1 + y - 268 e^{-y} = 0 \,,$$

which yields $y \approx 4$. Thus,

$$Z_g = 4 r k T / e^2 \,. \tag{16}$$

Some values for Z_g are tabulated in table 4. We note that for typical critical condensation nuclei with radii of 10 Å or less, the particle will have no more than one unit charge. Hence, multiply charged particles need not be included in considerations of heterogeneous nucleation in these cool atmospheres.

At τ (optical depth at 1 μ) = 1, Johnson (1973) gives (1) $n_e = 1.77 \times 10^8$ cm^{-3} and $P = 3.15 \times 10^2$ dynes cm^{-2} at $T_{\mathrm{eff}} = 2000°$ K and (2) $n_e = 5.73 \times 10^8$ cm^{-3} and $P = 1.03 \times 10^2$ dynes cm^{-2} at $T_{\mathrm{eff}} = 2500°$ K. This yields for $n = n_e$ in equation (10) the following:

$$n = 2 \times 10^{-7} n_{\mathrm{H}} (T_{\mathrm{eff}} = 2000° \mathrm{K})$$

and

$$n = 1.4 \times 10^{-6} n_{\mathrm{H}} (T_{\mathrm{eff}} = 2500° \mathrm{K}) \,.$$

The Coulomb drag coefficients (ζ) can now be computed; they are tabulated in table 4 where it is assumed that $Z = 1$; $A = 39$; $g = 1$ cm s^{-2}; C/O = 5.

The time required for a grain to escape is inversely proportional to its terminal velocity, v_t. The terminal velocity is given by

$$v_t = \frac{F_r - F_g}{\chi} \,,$$

where F_r is the radiation force and F_g is the gravitational force, both assumed constant, and χ is the drag coefficient. The coefficient χ is the sum of the viscous (particle) drag coefficient, ξ, and the Coulomb drag coefficient, ζ, since both retarding forces are directly proportional to velocity. As shown in table 4, ζ is much less than ξ (by a factor of $\sim 10^4$) in every case. Thus, the electrostatic drag mechanism is insufficient by itself to hinder a possible escape of grains.

IV. CONCLUSIONS

In the foregoing discussion of whether or not carbon particles can nucleate within the atmospheres of cool carbon-rich stars it has been demonstrated that a reliable answer depends crucially on two parameters. These are the surface energy of the particles and the supersaturation ratio that exists in the atmosphere. It can be concluded that investigations designed to obtain more accurate knowledge of these would be worthwhile. Furthermore, it has been shown that Coulomb drag forces would provide a negligible hindrance to the subsequent escape of the particles in comparison to the effects previously considered by Wickramasinghe (1967, 1972). More reliable data to evaluate the latter effects would be desirable.

REFERENCES

Abraham, F. F. 1974, *Homogeneous Nucleation Theory* (New York: Academic Press).

Abrahamson, J. 1973, *Carbon*, **11**, 337.

Allen, C. W. 1963, *Astrophysical Quantities* (London: Athlone Press).

Beloguriov, B. V. 1960, *Zh. Fiz. Khim.*, **34**, 440.

Blander, M., and Katz, J. L. 1972, *J. Stat. Phys.*, **4**, 55.

Burton, J. J. 1973, *Acta Metall.*, **21**, 1225.

Czyzak, S. J., and Santiago, J. J. 1973, *Ap. and Space Sci.*, **23**, 443.

Dawson, D. B., Willson, E. J., Hill, P. G., and Russell, K. C. 1969, *J. Chem. Phys.*, **51**, 5389.

Donn, B., Wickramasinghe, N. C., Hudson, J. B., and Stecher, T. P. 1968, *Ap. J.*, **153**, 451.

Dorfeld, W. G., and Hudson, J. B. 1973, *Ap. J.*, **186**, 715.

Dunning, W. J. 1969, in *Nucleation*, ed. A. C. Zettlemoyer (New York: Dekker).

Elyutin, V. P., Kostikov, V. I., and Charitonov, A. B. 1968, *Dokl. Akad. Nauk. SSSR*, **182**, 376.

Feder, J., Russell, K. C., Lothe, J., and Pound, G. M. 1966, *Adv. Phys.*, **15**, 111.

Fix, J. D. 1969, *M.N.R.A.S.*, **146**, 37.

Good, R. J., Girifalco, L. A., and Kraus, G. 1958, *J. Phys. Chem.*, **62**, 1418.

Hirth, J. P., and Pound, G. M. 1963, *Condensation and Evaporation* (New York: Macmillan).

Johnson, H. R. 1973, private communication.

Katz, J., Saltsburg, H., and Reiss, H. 1966, *J. Colloid. Sci.*, **21**, 560.

Kikuchi, R. 1969, *J. Stat. Phys.*, **1**, 351.

———. 1971, *ibid.*, **3**, 331.

Lothe, J., and Pound, G. M. 1962, *J. Chem. Phys.*, **36**, 2080.

———. 1966, *ibid.*, **45**, 630.

———. 1968, *ibid.*, **48**, 1849.

Masser, C. 1967, NASA TN D-4147.

Morris, S., and Wyller, A. A. 1967, *Ap. J.*, **150**, 877.

Mortimer, D. A., and Nicholas, M. 1970, *J. Materials Sci.*, **5**, 149.

Munson, R. A. 1967, *Carbon*, **5**, 471.
Nishioka, K., Pound, G. M., and Abraham, F. F. 1970, *Phys. Rev. A*, **1**, 1542.
Nishioka, K., and Pound, G. M. 1974, *Surf. Colloid Sci.*, **8**, in press.
Pound, G. M., Nishioka, K., and Lothe, J. 1972, *NTP Int. Rev. Sci.: Surface Chem. and Colloid.*, **7**, 147.
Reiss, H., and Katz, J. L. 1967, *J. Chem. Phys.*, **46**, 2496.
Reiss, H., Katz, J. L., and Cohen, E. R. 1968, *J. Chem. Phys.*, **48**, 5553.
Salpeter, E. E. 1973, *J. Chem. Phys.*, **58**, 4331.
———. 1974, *Ap. J.*, **193**, 579.
Spitzer, L. 1963, *Physics of Fully Ionized Gases* (New York: Interscience).
Spitzer, L. 1968, *Diffuse Matter in Space* (New York: Interscience).
Thorn, R., and Winslow, G. 1957, *J. Chem. Phys.*, **26**, 186.
Volmer, M. 1939, *Kinetik der Phasenbildung* (Dresden: Steinkopff).
Walker, P. L., Jr. 1972, *Carbon*, **10**, 369.
Wallerstein, G. 1973, *Ann. Rev. Astr. and Ap.*, **11**, 115.
Whittaker, A. G., and Kintner, P. 1969, *Carbon*, **7**, 414.
Wickramasinghe, N. C. 1967, *Interstellar Grains* (London: Chapman & Hall).
———. 1972, *M.N.R.A.S.*, **159**, 269.
Zel'dovich, J. 1942, *J. Exp. Theor. Phys.*, **12**, 525.

John P. Hirth and Glen Meyrick: Ohio State University, Columbus, OH 43210

Terry P. Roark and Ronald G. Tabak: Department of Astronomy, Ohio State University, Columbus, OH 43210

THE ASTROPHYSICAL JOURNAL, **196**: 465–472, 1975 March 1

STARLIGHT EXCITATION OF PERMITTED LINES IN THE ORION NEBULA

STEVEN A. GRANDI
Steward Observatory, University of Arizona

Received 1974 July 25; revised 1974 September 3

ABSTRACT

From an idealized model of the Orion Nebula and from an analysis of line ratios it is shown that direct starlight excitation of the permitted O I lines dominates over recombination and Lyman line fluorescence. The line strengths predicted by this mechanism agree reasonably well with those observed in the Orion Nebula. The application of direct starlight excitation to other ions is also discussed.

Subject headings: line formation — Orion Nebula

I. INTRODUCTION

Permitted lines of O I (primarily λ8446) have been seen in the Orion Nebula and in several planetary nebulae (Morgan 1971; Andrillat and Houziaux 1968; Danziger and Aaronson 1974). In this paper we will investigate possible excitation mechanisms for these lines. The observed triplet lines (from Morgan 1971) are shown on the energy level diagram in figure 1 with the observed line strengths (corrected for reddening and normalized to Hβ). The line at λ5555 is an uncertain identification, according to Morgan, while the line at λ5958 is assumed to be part of a blend with Si II $4p\ ^2P_{1/2}$–$5s\ ^2S$. The λ4368 line was not actually observed by Morgan, but she included it from the work of Kaler, Aller, and Bowen (1965). This line was also observed by Chopinet and Fehrenbach (1961), where it was identified as a line of C II. λ7254 and λ6046 were also listed (but not identified) by Flather and Osterbrock (1960).

The usual explanation for permitted lines in the spectra of nebulae is recombination from higher ionization states. However, the recombination process is not sufficient to explain the strength of the λ8446 line, as we will show in § II. Two other possible excitation mechanisms, Lyman line fluorescence and direct excitation by starlight, have been suggested (Morgan 1971), and will be discussed in §§ III and IV, respectively.

To explicitly calculate the strength of the λ8446 and other permitted lines of O I arising from each of these three mechanisms, we have constructed a very idealized model of the Orion Nebula consisting of an O7 V star (Conti 1973) surrounded by a spherical, uniform density nebula containing 4000 hydrogen atoms per cubic centimeter. The star is modeled by a 37,500° K, $\log g = 4.0$, non-LTE stellar atmosphere (Mihalas 1972). Immediately beyond the edge of the H II region, the density drops to the normal interstellar value. In figure 2, we show the oxygen ionization structure of this model where we have utilized an $N_{\rm O}/N_{\rm H}$ number ratio of 6×10^{-4}. This idealized Orion Nebula model is based on work by S. Grandi, E. Jensen, J. Scott, J. Stocke, and R. Williams which will be reported on elsewhere. Although the actual physical conditions in the Orion Nebula are quite a bit more complicated than described in this model (Simpson 1973), the normalized line strengths of the prominent forbidden and recombination lines predicted by this model are in order-of-magnitude agreement with the observations (from Johnson 1968) as listed in table 1. While we do not pretend that this model adequately represents the Orion Nebula, it should be sufficient to delineate the relative effects of the physical processes under consideration. Since the other parameters needed for our calculations—the atomic constants for O I and Morgan's (1971) visually determined line ratios—are also somewhat uncertain, a detailed model is not truly justified. However, we shall also note the model-independent O I line ratios in our discussion of each process.

II. RECOMBINATION

We first predict the ratio of O I λ8446 flux to Hβ flux assuming that all of the λ8446 flux is due to recombination from O II. Since only the total recombination coefficient and the coefficient to the ground state have been determined for O I, we will follow Andrillat and Houziaux (1968) and assume that all recombinations not to the ground state go to the $3p\ ^3P$ term and decay via λ8446. Using the recombination coefficients given by Aldrovandi and Pequignot (1973), we obtain the following for the volume emission coefficients for λ8446:

$$j_{8446} = N_e N_{\rm O\,II} \frac{h\nu_{8446}}{4\pi} 2.1 \times 10^{-13} t_e^{-0.68}\,, \qquad (1)$$

where N_e and $N_{\rm O\,II}$ are the electron and O II densities, respectively, and t_e is the electron temperature in units of 10^4 ° K. Similarly, the volume emission coefficient for Hβ is

$$j_{\rm H\beta} = N_e N_{\rm H\,II} \frac{h\nu_{\rm H\beta}}{4\pi} 3.07 \times 10^{-14} t_e^{-0.90} \qquad (2)$$

using the recombination coefficient from Seaton

TABLE 1

LINE STRENGTHS FROM IDEALIZED ORION NEBULA MODEL

Line	Observed Strength	Predicted Strength
Hβ...............	1.0	1.0
He I 5876.........	0.25	0.14
He I 4471.........	0.051	0.048
[O III] 5007........	3.32	9.0
[O II] 3727........	1.83	0.84
[O I] 6300.........	0.046	0.010
[N II] 6584........	0.36	0.66
[N I] 5199.........	0.007	0.021
[Ne III] 3869.......	0.27	0.35

(1968*a*). The λ8446/Hβ flux ratio is

$$\frac{F_{8446}}{F_{\mathrm{H}\beta}} = \int_0^R j_{8446} r^2 dr \Big/ \int_0^R j_{\mathrm{H}\beta} r^2 dr \,, \tag{3}$$

where R is the radius of the nebula. Using the idealized Orion Nebula model, we obtain from these expressions a flux ratio of 1.7×10^{-4}, which is over two orders of magnitude below the observed ratio of 0.015.

Also, the lack of quintet lines of comparable strength to the triplet lines would seem to rule out recombination as an excitation mechanism. One would expect, if recombination were exciting the O I lines, that the quintet lines and triplet lines should be present

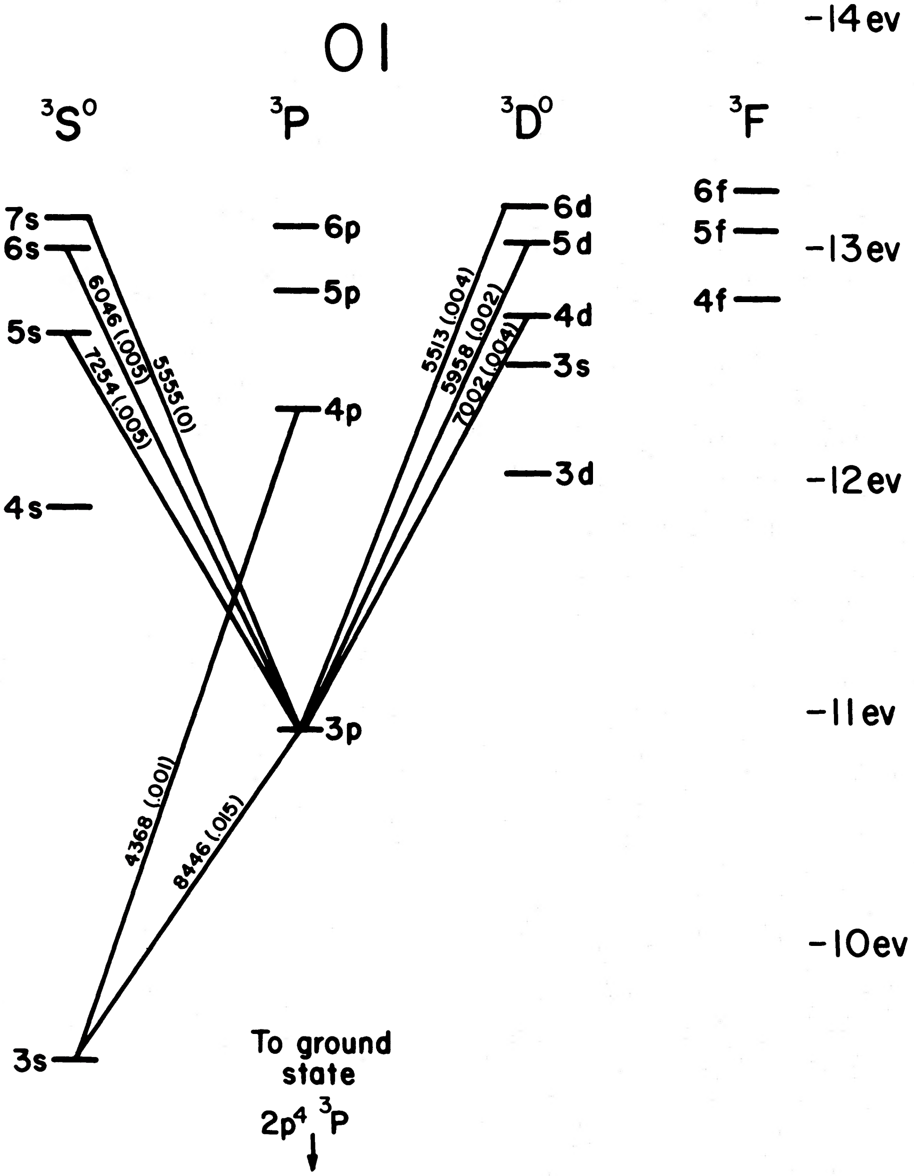

FIG. 1.—Energy level diagram of the triplets of O I showing transitions seen in the Orion Nebula. Line strengths (normalized to Hβ = 1) are shown in parentheses.

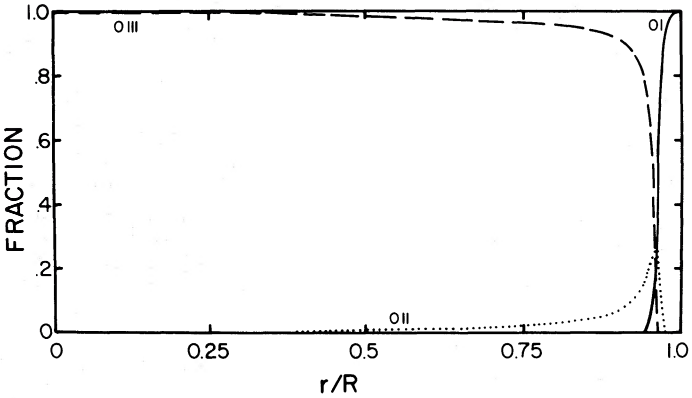

FIG. 2.—Oxygen ionization structure of the idealized Orion Nebula model. The fractional ionization is plotted versus the fractional radius.

in ratios corresponding to the ratio of their statistical weights. However, instead of being slightly stronger the only observed quintet line (λ7774, $3s\,{}^5S$–$3p\,{}^5P$) is a full order of magnitude weaker than its triplet equivalent (λ8446).

III. FLUORESCENCE

Since the ionization potential of O I and H I are almost exactly the same, their upper energy levels are quite similar. Many of the transitions from the ground state of O I are within a few angstroms of a Lyman line, and some are virtually coincident. It happens that the strongest component of the ground-state transition to $3d\,{}^3D$ in O I is λ1025.77, while Lβ is at 1025.72 Å. This close coincidence in line frequency makes the fluorescence mechanism an attractive candidate to explain the strength of the λ8446 line (Swings 1955).

To calculate the ratio $F_{8446}/F_{\mathrm{H}\beta}$ expected from this process, we will follow Morgan (1971) and provisionally assume that Lβ fluorescence of the $3d\,{}^3D$ term accounts for all the λ8446 line emission. We obtain for the volume emission coefficient of λ8446 from fluorescence:

$$j_{8446} = N_{\mathrm{O\,I}}\langle J_{\mathrm{L}\beta}\rangle B_{1027}\,\frac{A_{11287}}{A_{11287}+A_{1027}}\,\frac{h\nu_{8446}}{4\pi}\,, \qquad (4)$$

where the subscript 1027 refers to the $2p^4\,{}^3P$–$3d\,{}^3D$ transition and the subscript 11287 refers to the $3p\,{}^3P$–$3d\,{}^4D$ transition. $\langle J\rangle$ is an appropriate average over frequency of the mean intensity of radiation, and A and B are the Einstein coefficients.

If we now assume that all of the Hα photons we see from the nebula are generated by the degradation of Lβ, we obtain

$$j_{\mathrm{H}\alpha} = N_{\mathrm{H\,I}}\langle J_{\mathrm{L}\beta}\rangle B_{\mathrm{L}\beta}\,\frac{A_{\mathrm{H}\alpha}}{A_{\mathrm{H}\alpha}+A_{\mathrm{L}\beta}}\,\frac{h\nu_{\mathrm{H}\alpha}}{4\pi}\,, \qquad (5)$$

where $A_{\mathrm{H}\alpha}$ refers to the $2s$–$3p$ transition only. We will assume that the value of $\langle J_{\mathrm{L}\beta}\rangle$ in equations (4) and (5) are equal even though $\langle J_{\mathrm{L}\beta}\rangle$ corresponding to the O I λ1027 line is likely to be smaller than the value in equation (5) due to the 0.05 Å offset between Lβ and O I λ1027. Also, some Hα photons will not be produced by Lβ degradation, hence equation (5) is a lower limit to $j_{\mathrm{H}\alpha}$. Therefore, because of these two effects, the λ8446/Hα flux ratio we will derive will be an upper limit. Finally, if we ignore any possible temperature dependence and if we assume that the mean intensity of Lβ as seen at a particular point in the nebula is representative only of the physical conditions at that point (i.e., a Lβ photon will not travel into regions of differing physical conditions before it is converted into Lα and Hα photons by collisions with neutral hydrogen), then the mean intensity of Lβ will be proportional to

$$\langle J_{\mathrm{L}\beta}\rangle \propto \frac{N_e N_{\mathrm{H\,II}}}{N_{\mathrm{H\,I}}}\,, \qquad (6)$$

where the numerator represents the production and the denominator represents the loss of Lβ photons.

By combining equations (3), (4), (5), and (6) we obtain for the λ8446/Hα flux ratio:

$$\frac{F_{8446}}{F_{\mathrm{H}\alpha}} = \frac{\int_0^R (N_{\mathrm{O\,I}} N_e N_{\mathrm{H\,II}}/N_{\mathrm{H\,I}}) r^2 dr}{\int_0^R N_e N_{\mathrm{H\,II}} r^2 dr} \times \left(\frac{B_{1027}A_{11287}h\nu_{8446}}{A_{11287}+A_{1027}}\right)\bigg/\left(\frac{B_{\mathrm{L}\beta}A_{\mathrm{H}\alpha}h\nu_{\mathrm{H}\alpha}}{A_{\mathrm{H}\alpha}+A_{\mathrm{L}\beta}}\right). \qquad (7)$$

We use a calculation of the Balmer decrement (Brocklehurst 1971) to obtain the ratio of Hα to Hβ flux, which leads to a value of 3.0×10^{-5} for the λ8446 to Hβ flux ratio for our model, as compared with the observed flux ratio of 1.5×10^{-2}. A nearly model independent result can be obtained from equation (7) by considering the fact that, due to charge exchange (Williams 1973), the number ratios $N_{\mathrm{O\,II}^*}/N_{\mathrm{O\,I}}$ and $N_{\mathrm{H\,II}}/N_{\mathrm{H\,I}}$ are approximately equal throughout the nebula (O II* here refers to all the ionized forms of oxygen). Since in most of the nebular region, all of the hydrogen and oxygen atoms are ionized, we can substitute $N_{\mathrm{O}}/N_{\mathrm{H}}$, the number ratio of oxygen to hydrogen nuclei, for $N_{\mathrm{O\,II}^*}/N_{\mathrm{H\,II}}$ which is equal to $N_{\mathrm{O\,I}}/N_{\mathrm{H\,I}}$ due to charge exchange throughout the nebula. Thus equation (7) becomes

$$\frac{F_{8446}}{F_{\mathrm{H}\alpha}} = \frac{N_{\mathrm{O}}}{N_{\mathrm{H}}} \frac{B_{1027}A_{11287}h\nu_{8446}}{A_{11287} + A_{1027}} \bigg/ \frac{B_{\mathrm{L}\beta}A_{\mathrm{H}\alpha}h\nu_{\mathrm{H}\alpha}}{A_{\mathrm{H}\alpha} + A_{\mathrm{L}\beta}}, \qquad (7a)$$

which leads to a value of 5.5×10^{-4} for the λ8446 to Hβ flux ratio assuming a value for $N_{\mathrm{O}}/N_{\mathrm{H}}$ of 6×10^{-4}.

Even if Lβ fluorescence could account for the strength of the λ8446 line, the observed strengths of the other permitted O I lines must still be explained. Direct fluorescent excitation cannot account for most of the lines. For example, the resonance lines to $7s\,^3S$, which excite λ5555, are located at λλ976.45, 977.96, and 978.62 which are far outside the Lγ line at λ972.54. Morgan (1971) points out that there is a coincidence between Lϵ at λ937.80 and a component of the resonance multiplet to $7s\,^3S$ at λ937.84. Also, Lζ at λ930.75 corresponds to a component of the resonance multiplet to $7d\,^3D$ at λ930.90. However, cascades from these terms cannot explain the strengths of the other lines. For example, let us assume that a cascade from $7s\,^3S$ through $6p\,^3P$ accounts for Morgan's (1971) observed strength of λ6046. Using Einstein A values derived from Kelly (1964) we find that the observed λ6046/Hβ line ratio of 0.005 implies a λ5555/Hβ line ratio of 0.645 (43 times stronger than the observed strength of λ8446). In reality, Morgan (1971) calls her identification of λ5555 uncertain.

Column (3) of table 3 lists the O I/O I λ8446 line ratios predicted by a calculation of Lyman line fluorescence of the $3d\,^3D$, $7s\,^3S$, and $7d\,^3D$ levels in O I by Lβ, Lϵ, and Lζ, respectively. These line ratios are expected to be essentially model-independent, since they depend only on the relative strengths of these Lyman lines, which are given by the solution to the hydrogen capture-cascade equations (Pengelly 1964) which depend only weakly on temperature and density in the nebula.

IV. STARLIGHT EXCITATION

Seaton (1968*b*) has invoked the excitation of permitted lines by starlight to account for the presence of these lines in the spectra of planetary nebulae. Morgan (1971) has suggested that this mechanism might account for the O I line strengths in the Orion Nebula.

A difficulty in calculating line strengths due to this excitation mechanism occurs because of the nonuniformity of the spectral energy distribution of the central star due to the presence of absorption lines, which when combined with the absorption of these line photons by the nebular gas will prevent certain O I terms from being excited. For example, the coincidence of Lβ with the ground state to $3d\,^3D$ transition in O I mentioned in § III will prevent this term from being significantly excited by starlight. Also, the ground-state transition to the $3s\,^3D$ term corresponds to the N III resonance line at λ990 which is prominent in O star spectra (Smith 1970). N III is also present in large quantities in the nebula. Consequently, if direct starlight excitation is the principal excitation mechanism, lines resulting from cascades from these two terms should be practically nonexistent (except for contributions from cascades from still higher terms) compared with lines resulting from other cascades. Therefore, λ7990 ($3p\,^3P$–$3s\,^3D$) should be much weaker than corresponding lines such as λ7002; in fact, this line was not found by Morgan (1971) in her spectral survey. Also the line at λ11287 ($3p\,^3P$–$3d\,^3D$) should be much weaker than the corresponding line at λ13165 ($3p\,^3P$–$4s\,^3S$). If Lyman fluorescence were the dominant source of excitation, however, the reverse would be true: λ11287 should be much stronger than λ13165 since the ground-state transition to $4s\,^3S$ (at λ1040) does not correspond to a Lyman line; similarly, λ7990 should be of comparable strength with the other lines that would all presumably be cascades from $7s\,^3S$ and $7d\,^3D$.

Now let us assume that all the λ8446 photons produced come from the direct starlight excitation of the $4s\,^3S$, $5s\,^3S$, $6s\,^3S$, $7s\,^3S$, $4d\,^3D$, $5d\,^3D$, and $6d\,^3D$ terms followed by decays to $3p\,^3P$ and then a decay via λ8446. Consequently, the volume emission coefficient for λ8446 at a radial distance r from the central star becomes

$$j_{8446}{}^{(r)} = \frac{h\nu_{8446}}{4\pi} N_{\mathrm{O\,I}} \sum_i J_i{}^*(r) B_i \frac{A_i}{\sum A_i}, \qquad (8)$$

where the first sum is over all the above mentioned terms, $J_i{}^*(r)$ is the mean intensity due to starlight at r at the proper excitation frequency, A_i is the Einstein A coefficient connecting this particular term to $3p\,^3P$, and $\sum A_i$ is the sum of the Einstein A's for all the downward transitions from this term.

When available, the transition probabilities were obtained from Wiese, Smith, and Glennon (1966); and, if necessary, the coefficients were derived from the line strengths of Kelly (1964). The mean intensity due to starlight is equal to

$$J^*(r) = H_{\mathrm{SURFACE}}{}^* R_*{}^2/r^2, \qquad (9)$$

where R_* is the radius of the central star and $H_{\mathrm{SURFACE}}{}^*$ is the Eddington flux obtained from the stellar model (Mihalas 1972) used in the idealized Orion Nebula model. We have assumed that there is no opacity inside the nebula at these wavelengths, which are all longward of λ912. Extinction due to dust is also not considered. Over the wavelengths of interest, the stellar flux is approximately constant, so J^* has been taken outside the sum in equation (8).

The resulting λ8446 to Hβ flux ratio calculated due to this mechanism for the idealized Orion Nebula model is 0.009, while the observed value is 0.015. Cascades from the $4s\,^3S$ term generate 47 percent of the line strength, and cascades from $4d\,^3D$ supply 35 percent of the line strength. Similarly, we can derive line strengths for the other observed O I lines, and these are listed in table 2 (normalized to Hβ), along with predictions for some lines that have not been investigated. (The observed line strengths are from Morgan 1971 and Johnson 1968.) The λ5555 and λ5513

TABLE 2

NORMALIZED LINE STRENGTHS FROM STARLIGHT EXCITATION OF O I

Wavelength of O I Line (1)	Observed (2)	Predicted (3)	Normalized (4)
3692	...*	0.002	0.009
4368	0.001	0.001	0.006
5513	0.004	0.00002*	0.0001
5555	0*	0.0002*	0.0008
5958	0.002	0.0004	0.002
6046	0.005	0.0005	0.002
7002	0.004	0.004*	0.02
7254	0.005	0.001	0.005
7774	0.001	...*	...
8446	0.015	0.009	0.032
11287	...	0.0002*	0.001
13150	...	0.003	0.01

* See text.

lines come from terms whose excitation wavelengths are close to Lϵ, so the line strengths predicted here may be overestimated because of absorption lines and nebular opacity (λ5555 is called an uncertain identification by Morgan). The line at λ7002 is a similar case in that its excitation wavelength is close to Cl IV λ973 and Lγ so that the stellar flux exciting this line will be depressed. The coincidence is not exact enough for nebular opacity to be important, however. The line at λ7774 ($3s\,^5S$–$3p\,^5P$) is the quintet counterpart of λ8446 and is presumably due to intercombination transitions among the excitations or the cascades. The presence of λ3692 ($3s\,^3S$–$5p\,^3P$) is masked by H16 which is 10 times stronger and only 1 Å away. As can be seen, the predictions are in order-of-magnitude agreement with the observations except for λ5513. The predicted line strengths are in general smaller than the observed line strengths, but the predicted [O I] λ6300 line strength is also smaller than observed (see table 1). Column (4) of table 2, therefore, contains the O I/Hβ line ratios normalized so that the observed and predicted line strengths of [O I] λ6300 agree. It should be noted, however, that the regions emitting O I radiation are not in general the same regions emitting [O I] radiation due to the requirement of free electrons to excite the forbidden lines.

TABLE 3

O I LINE RATIOS

Line Ratio (1)	Observed (2)	Lyman Fluorescence (3)	Direct Starlight Excitation (4)
4368/8446.....	0.07	1×10^{-4}	0.2
7254/8446.....	0.3	1×10^{-5}	0.1
6046/8446.....	0.3	6×10^{-6}	0.06
5555/8446.....	0*	6×10^{-4}	0.02
7002/8446.....	0.3	1×10^{-6}	0.4
5958/8446.....	0.1	8×10^{-8}	0.06
5513/8446.....	0.3†	2×10^{-9}	0.003

* Uncertain identification.

† See text.

Table 3 contains the O I/O I λ8446 line ratios predicted by direct starlight excitation, which should be almost entirely model independent, since the ratios depend only on the spectrum of the exciting star.

V. CONCLUSIONS

Comparing the results of the previous three sections, we find that, based on our model, direct starlight excitation dominates the excitation of λ8446 over recombination and Lyman line fluorescence by several orders of magnitude. The line strengths (when normalized so that the observed and predicted strength of [O I] λ6300 agree) predicted by direct starlight excitation are in reasonable agreement with observations (see table 2). Also, the lack of quintet lines as predicted by recombination and the large disagreements between the line ratios predicted by Lyman fluorescence and the observed ratios provide model-independent reasons for discounting these processes in favor of direct starlight excitation, which predicts O I line ratios in fair agreement with observation (see table 3). Therefore, we conclude that direct starlight excitation is the correct mechanism for exciting the permitted O I lines in the Orion Nebula.

The large discrepancy between the observed and the predicted line strength of λ5513 leads us to believe that Morgan's (1971) identification of the line observed at λ5513 as O I $3p\,^3P$–$6d\,^3D$ is incorrect. If, however, the calculations of Kelly (1964) which lead to an Einstein A for the λ5513 line of 1.9×10^4 (the smallest of any downward permitted transition from $6d\,^3D$) are in error and the Einstein A for this transition is actually greater than Kelly's value, then the predicted strength of the line would accordingly be larger, perhaps enough larger to account for the discrepancy with the observed λ5513 strength. Assuming that Kelly's results are correct, however, a line strength for O I λ5513 as large as reported by Morgan would result in an even stronger line at λ14114 ($4p\,^3P$–$6d\,^3D$) because the Einstein A for this line is 18 times larger than that for λ5513. This would, in turn, result in an enhanced λ4368 line ($3s\,^3S$–$4p\,^3P$). If we assume that all levels are excited by direct starlight excitation except for $6d\,^3D$ which somehow is excited 50 times more strongly than by the starlight in order to produce the observed λ5513 strength, we obtain a λ4368/λ8446 line ratio of 0.7, which is an order of magnitude larger than the observed ratio of 0.07. In other words, if the Einstein A for λ5513 transition taken from Kelly is correct, there is no mechanism that can produce the observed λ5513 line strength without also producing a λ4368 line strength 10 times that which is observed. Therefore, we conclude that the observed line at λ5513 is not the O I λ5513 line.

VI. DISCUSSION

The fact that the presence of O I is confined to the transition region of the nebula is a crucial one in the dominance of starlight excitation over excitation by Lyman line fluorescence. It turns out that over the whole nebula, about 100 times more Lβ photons are

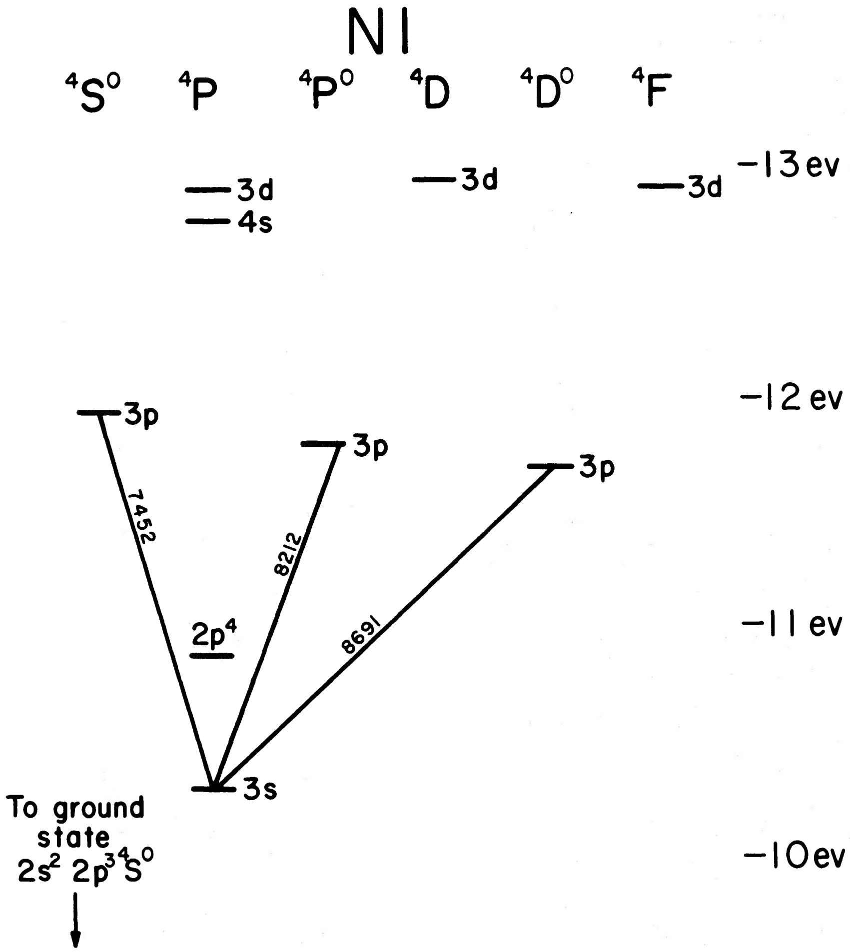

FIG. 3.—Energy level diagram of the quartets of N I showing the three transitions discussed in the text

generated per second than stellar photons capable of exciting the O I lines. However, the vast majority of the Lβ photons exist in the inner parts of the nebula where $(N_{\text{H II}}/N_{\text{H I}})N_e$ is large. Since these Lβ photons cannot travel into the outer regions of the nebula without being degraded by scatterings with neutral hydrogen, the Lβ density in the regions where O I exists will reflect the low $(N_{\text{H II}}/N_{\text{H I}})N_e$ ratio present there. Consequently, since the Lβ photons are confined to the interior while the O I is confined to the exterior, Lβ fluorescence is not important. One way to circumvent this difficulty would be to postulate a sufficient optical depth in the Balmer lines in the transition region of the nebula which might allow enough Lβ photons to be generated in the O I region to account for the observed λ8446 strength by fluorescence. However, the fact that the other observed O I lines could not be produced by Lβ fluorescence would seem to exclude this possibility.

As we mentioned in § IV, the relative strengths of λ11287 and λ13150 will provide a test of the excitation mechanism present in the Orion Nebula. We predict, on the basis of direct starlight excitation, that λ13150 should have a normalized strength of 0.01 relative to Hβ (see table 2). Based on the hydrogen recombination-line calculations of Brocklehurst (1971), this line strength corresponds to a λ13150/Paschen β flux ratio of 0.06. Since λ11287 cannot be excited directly by starlight, we consider its excitation by cascades from the $4d\,{}^3D$, $5d\,{}^3D$, $5s\,{}^3S$, and $6s\,{}^3S$ terms via the $4p\,{}^3P$ and $5p\,{}^3P$ terms. Based on the idealized Orion Nebula model, this process results in a normalized λ11287/Hβ flux ratio of 0.001 which is an order of magnitude fainter than λ13150. The contribution to the λ11287 line strength from Lβ fluorescence as calculated in § III is more than an order of magnitude below the contribution of starlight excitation.

Danziger and Aaronson (1972) remark on the large spatial variation of λ8446 in the Orion Nebula, and they note that it increases in strength dramatically on the bright arc near θ^2 Ori. However, the spatial variations are different from those of the forbidden lines or recombination lines. One might expect such variations in starlight-excited lines in the actual Orion Nebula near another source of starlight excitation; and since the mechanisms involved are distinct, the mode of

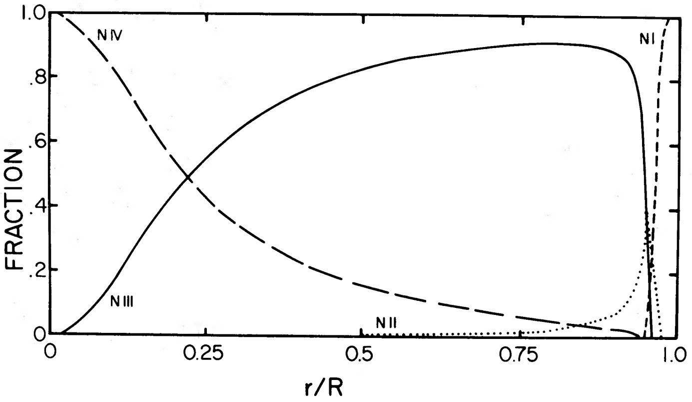

FIG. 4.—Nitrogen ionization structure of the idealized Orion Nebula model. The fractional ionization is plotted versus the fractional radius.

spatial variation should be different from that for recombination or collisionally excited lines.

VII. APPLICATION TO OTHER IONS

The effect of the starlight excitation mechanism on ions other than O I in H II regions is limited by several factors. First, for higher ionization states, the presence of absorption lines in the stellar spectrum (due to the same ionization states) will tend to eliminate any excitation. For example, the lines of the N III and N IV ions are prominent in O-star spectra (Smith 1970). This would presumably rule out starlight-excited lines from these ions. If the wavelengths needed to excite the ionic lines lie shortward of 912 Å, both the opacity inside the nebula and the dropoff of the stellar continuum flux will largely degrade the excitation. The O III ion is in this category since the wavelength of the resonance transition to the first excited term is λ374. Finally, in some cases recombination will clearly dominate all other processes (the permitted O II lines, for example). From these arguments, it appears that among the abundant ions besides O I, only the N I ion should be significantly excited by this mechanism.

Accordingly, we have considered the excitation of the $3d\ ^4P$ and $4s\ ^4P$ terms in N I by starlight and calculated the line strengths from the permitted decays leading to λ7468, λ8216, and λ8680 (the strongest members of their respective multiplets), following the techniques of § IV. In figure 3 we show the quartet energy levels of N I and the three transitions we have investigated. We present in figure 4 the nitrogen ionization structure of the idealized Orion Nebula as calculated from our model. We have assumed a $N_{\mathrm{N}}/N_{\mathrm{H}}$ number ratio of 2×10^{-4}, and intercombination lines have been ignored. The resulting flux ratios to Hβ are 0.003, 0.003, and 0.004 for λ7468, λ8216, and λ8680, respectively. If we adjust these ratios to reflect the fact that our model overestimates the strength of the [N I] λ5199 line, we must reduce these ratios by a factor of 3. Even though lines of these predicted strengths should have been observed by Morgan (1971), the uncertainties involved in our calculations make this lack of detection not surprising.

Offhand, it may seem likely that if starlight excitation is dominant in exciting the permitted lines of O I, the same mechanism should be just as dominant in exciting the H I lines since the ionization potential and nebular ionization structures for these two ions are so similar. However, for the most part, the stellar radiation that excites the O I line is not subject to absorption lines in the stellar spectrum or opacity in the nebula. The Lyman line radiation required to excite the neutral hydrogen lines, on the other hand, is reduced by both the presence of Lyman absorption lines in the stellar spectrum and a great deal of opacity due to neutral hydrogen in the nebula. In essence, for the same reasons as discussed in § VI for Lβ fluorescence, the starlight Lyman line photons are largely confined to the inner parts of the nebula, while the neutral hydrogen is present in quantity only in the transition region. Therefore, recombination easily dominates over direct starlight excitation in the production of the Balmer lines.

We have calculated with our idealized Orion Nebula model the ratio of the Hβ flux produced by direct starlight excitation by Lγ to that produced by recombination. Assuming that the stellar Lγ line is depressed from the surrounding continuum by a factor of 10, we arrive at a ratio of 5×10^{-4}. As we showed in § II, the corresponding ratio for O I λ8446 is over 100.

We are grateful to E. B. Jensen, R. J. Weymann, and R. E. Williams for very useful discussions.

REFERENCES

Aldrovandi, S. M. V., and Pequignot, D. 1972, *Astr. and Ap.*, **25**, 137.
Andrillat, J., and Houziaux, L. 1968, in *IAU Symposium 34, Planetary Nebulae*, ed. D. E. Osterbrock and C. R. O'Dell (New York: Springer-Verlag), p. 68.
Brocklehurst, M. 1971, *M.N.R.A.S.*, **153**, 471.
Chopinet, M., and Fehrenbach, C. 1961, *J. d'Obs.*, **44**, 141.
Conti, P. S. 1973, *Ap. J.*, **179**, 181.
Danziger, I. J., and Aaronson, M. 1974, *Pub. A.S.P.*, **86**, 208.
Flather, E., and Osterbrock, D. E. 1960, *Ap. J.*, **132**, 18.

Johnson, H. M. 1968, in *Nebulae and Interstellar Matter*, ed. B. M. Middlehurst and L. H. Aller (Chicago: University of Chicago Press), p. 65.
Kaler, J. B., Aller, L. H., and Bowen, I. R. 1965, *Ap. J.*, **141**, 912.
Kelly, P. S. 1964, *J. Quant. Spectrosc. and Rad. Transf.*, **4**, 117.
Mihalas, D. 1972, *NCAR Tech. Note*, No. STR-76.
Morgan, L. A. 1971, *M.N.R.A.S.*, **153**, 393.
Pengelly, R. M. 1964, *M.N.R.A.S.*, **127**, 145.
Seaton, M. J. 1968*a*, in *IAU Symposium 34*, *Planetary Nebulae*, ed. D. E. Osterbrock and C. R. O'Dell (New York: Springer-Verlag), p. 129.
Seaton, M. J. 1968*b*, *M.N.R.A.S.*, **139**, 129.
Simpson, J. P. 1973, *Pub. A.S.P.*, **85**, 479.
Smith, A. M. 1970, in *IAU Symposium 36*, *Ultraviolet Stellar Spectra and Related Ground-Based Observations*, ed. L. Houziaux and H. E. Butler (Dordrecht: Reidel), p. 164.
Swings, P. 1955, in *Aurorae and the Airglow*, ed. E. B. Armstrong and A. Dalgarno (Oxford: Pergamon Press), p. 249.
Wiese, W. L., Smith, M. W., and Glennon, B. M. 1966, *Atomic Transition Probabilities, Hydrogen through Neon*, (NSRDS–NBS 4).
Williams, R. E. 1973, *M.N.R.A.S.*, **164**, 111.

Note added in proof.—A recent far-red spectrum of the bright inner region of the Orion Nebula shows the strongest member of the N I multiplet near 7468 Å and the five strongest members of the N I multiplet near 8216 Å. The observed line strengths are in fair agreement with the predictions of § VII.

STEVEN A. GRANDI: Steward Observatory, University of Arizona, Tucson, AZ 85721

THE ASTROPHYSICAL JOURNAL, 196:473–478, 1975 March 1

THE STRUCTURE OF THE ORION A MOLECULAR CLOUD

HUMBERTO GEROLA AND SABATINO SOFIA*
Joint Institute for Laboratory Astrophysics, University of Colorado and National Bureau of Standards

Received 1974 April 17; revised 1974 June 7

ABSTRACT

A consistent model of the Orion A molecular cloud is obtained by making use of the observed brightness temperature distributions of the $J = 2 \rightarrow 1$ and the $J = 1 \rightarrow 0$ transitions of the CO molecule, and the central component ($F = 2 \rightarrow 1$) of the $J = 1 \rightarrow 0$ transition of HCN, as well as the observed line profiles of the $J = 2 \rightarrow 1$ transition of CO, and the $J = 1 \rightarrow 0$ transition of HCN. The modeling is accomplished by fitting simultaneously all of these observations through solutions of the coupled equations of statistical equilibrium and radiative transfer for a spherical cloud having a kinetic temperature gradient, and different density and velocity distributions. We find that Orion A is strongly gravitationally bound and contracting, and that it can maintain the observed temperature distribution only by virtue of internal energy sources other than the contraction. This last conclusion is reached by computing the radiative losses due to the CO and HD cooling, as well as the losses due to inelastic collisions between the gas and the dust. Our results show that while the contraction rate is just about sufficient to balance the rate of radiation by CO, it is less than one-tenth of the rate at which energy is radiated by HD, and less than 0.001 of that at which energy could be lost to cool grains through totally inelastic collisions.

Subject headings: molecules, interstellar — nebulae

I. INTRODUCTION

Observations carried out in recent years have led to the discovery of a host of molecular spectral lines originating within dense interstellar clouds. In addition to revealing the presence of these particular molecules in the interstellar medium, these observations have already provided valuable information about isotopic abundances in different regions of our Galaxy. They have also yielded reliable estimates on the densities and temperatures of the cloud, indicating that, unless other mechanisms such as turbulent pressure or rotation are very important, they must be contracting. Thus, the cloud constitutes an important link between the diffuse interstellar gas and the stars or stellar systems (cf. Snyder 1973). A most exciting potential of the molecular line observations, then, is their use in determining the structure and kinematics of these dense clouds, a feat that has so far escaped other methods of attack.

Until quite recently, there had been no attempts to tackle the structure problem, mainly because, in its most general form, it is extremely complicated. In particular, since many of the lines are optically thick, the coupled equations of radiative transfer and statistical equilibrium must be solved for media having eventually complicated velocity structures. This situation is further complicated by the fact that most of the clouds do not present a simple geometry (e.g., spherical), so that it is doubtful whether many of the available techniques of radiative transfer theory are applicable at all.

Scoville and Solomon (1974), and Goldreich and Kwan (1974) have shown that for the case of spherical clouds in which a velocity field, increasing outward in absolute value, exists, the problem can be solved by applying the method of escape probabilities first introduced by Sobolev (1960) for the case of expanding atmospheres. In this case, the observed radiation originates in the interior regions as well as from the near boundary, even for optically thick lines. This provides a means of exploring the clouds throughout. The above authors, however, only derived the central brightness temperature arising from an idealized cloud of constant density and temperature and did not attempt to derive the parameters of real clouds. The Sobolev technique is valid when a photon emitted at a certain point P either is absorbed in the immediate surroundings or escapes so that the transfer of radiation depends only on local properties. It is easy to see that if the absolute value of the radial velocity field increases inward there exists a family of surfaces with zero relative velocity with respect to P; therefore, the transfer problem is no longer local, and Sobolev's technique is invalid.

Clark, Buhl, and Snyder (1974), on the other hand, did attempt to model the innermost portion of the Orion A cloud by using HCN mappings. They considered only a static cloud, although it can be seen that the velocity fields constitute a crucial feature of the transfer problem. This restriction, and the fact that they considered lines from only one molecule, introduces serious uncertainties into their results.

In the case of the molecular cloud Orion A, we will see that most probably a macroscopic velocity field increasing outward exists. Therefore, in this paper we extend the discussion of Goldreich and Kwan (1974) and Scoville and Solomon (1974), applying it to selected multimolecular observations. By fitting brightness temperature distributions and line profiles, we are able to obtain detailed information on the structure and kinematics of this cloud. In §§ II and III

---

* 1973–1974 Visiting Fellow, on leave from the Department of Astronomy, University of South Florida, Tampa.

we describe the observations we wish to account for, and the method of analysis. Results are in § IV, and in § V we discuss the meaning of these results, with particular regard to the state of evolution of this cloud.

II. THE ORION A MOLECULAR CLOUD

Detailed mappings of Orion exist in the lines of CO (Phillips, Jefferts, and Wannier 1973) and HCN (Snyder and Buhl 1974). The brightness temperature maps show secondary enhancements in many directions. These enhancements are evidence of the departures from spherical symmetry which, as mentioned earlier, seriously complicate the transfer problem. However, in the east–west direction, a roughly symmetrical distribution in $T(r)$ appears in the lines of both molecules centered on the Kleinmann-Low nebula. We assume that this particular direction represents the undisturbed cloud, even though smaller secondary enhancements are still present.

The CO emitting region extends much farther out than the HCN emission. Since CO is much more abundant than HCN and has a lower dipole moment, this difference in distribution implies the existence of a density gradient, with a maximum at the center of the cloud. Because of its low dipole moment (0.1 debye) and high abundance, the CO molecule thermalizes at low densities. The observations by Phillips *et al.* (1973) which show that the $J = 1 \rightarrow 0$ and the $J = 2 \rightarrow 1$ transitions have equal brightness temperatures in the inner regions of the cloud imply that both transitions are thermalized within this region (up to about $\Delta\alpha = 10'$). Thus, both lines are optically thick and the kinetic temperature $T_k(\alpha)$ equals the observed brightness temperature $T_b(\alpha)$. The T_k values found for this region have a linear decrease on α. Since the $J = 1 \rightarrow 0$ transition of CO remains thermalized to lower densities than the $J = 2 \rightarrow 1$ transition, we make a linear fit to the average of the T_b values measured beyond $10'$ east and west of the cloud center, and assume that this represents the T_k in the outer region of the cloud. This outer region fit, made on somewhat weaker grounds than that in the inner region, is post factum supported by our results.

The widths of the lines of both CO and HCN are much larger than the Doppler widths at the observed temperatures, and this indicates the existence of other broadening mechanisms within the cloud. Among the mechanisms so far proposed, we count turbulence, or macroscopic velocity fields. However, the widths of the HCN profiles in the E–W direction decrease outward, suggesting large-scale systematic effects related to the position in the cloud. Moreover, Heiles (1973) has pointed out a correlation between the widths of the lines of H_2CO, CS, and CH_3OH and the minimum densities required to excite these molecules in Orion A. The molecules that require higher minimum densities in order to be excited have smaller line widths. This effect, and the fact that the density decreases outward, indicates the existence of a macroscopic velocity field increasing with the radius. Consequently, in agreement with what has been argued by Goldreich and Kwan (1974), we consider this velocity field rather than turbulence to be responsible for the widening of the lines. This systematic velocity could, in principle, be contraction or expansion.

Summarizing, the observations allow us to say the following about the Orion A molecular cloud: (1) the density decreases monotonically outward according to a relation to be determined; (2) a linear kinetic temperature distribution (given in table 1) describes the cloud; and (3) the cloud possesses a systematic, macroscopic velocity field that increases with r according to a relation also to be determined.

III. METHOD

The transfer of radiation for the case of spherical symmetry with a macroscopic velocity field much larger than the thermal velocity field and increasing outward has been treated by Sobolev (1960) and extended by Castor (1970) and by Lucy (1971). Goldreich and Kwan (1974) present an interesting detailed discussion of the application of these methods to the case of molecular transitions; we refer to this and to Castor's paper for more specific details. To make the present paper self-contained, we present the basic relations in this section.

The populations of the levels at each point in the cloud satisfy the equations of statistical equilibrium

$$\frac{dN_J}{dt} = R_J + C_J = 0\,. \qquad (1)$$

The radiative terms for a pair of levels

$$R_J = (N_u A_{u,l} + N_u B_{u,l}\langle J_{u,l}\rangle - N_l B_{l,u}\langle J_{u,l}\rangle) \qquad (2)$$

can be written (Castor 1970)

$$R_J = N_u A_{u,l}\beta(\sigma, \tau) \qquad (3)$$

where $\beta(\sigma, \tau)$ is the probability that a photon escapes from the cloud. The universal blackbody radiation at 3° K was also included in the rate equations.

In general,

$$\beta(\sigma, \tau) = \int_0^1 \frac{1 + \sigma x^2}{\tau}\left[1 - \exp\left(\frac{-\tau}{1 + \sigma x^2}\right)\right] dx \qquad (4)$$

where, besides an angular factor of the order of unity,

$$\tau(r) = \frac{\Pi e^2}{mc}(gf)_{l,u}[(N_l/g_l) - (N_u/g_u)/\nu_0 V(r)/c]r\,. \qquad (5)$$

The subscripts l and u refer to the lower and upper levels, respectively, and r is the distance from the center of the cloud. Also

$$\sigma \equiv \frac{d \ln V}{d \ln r} - 1\,. \qquad (6)$$

Complete redistribution in frequency is assumed in all these developments.

Notice that τ can be very large, but because of the velocity field we may be able to detect photons coming from the regions of high local opacity.

A severe limitation is the lack of information on collisional-excitation cross sections. Most probably only collisions with H_2 and with electrons have to be considered. Electrons have greater collisional-excitation cross sections (cf. Goldsmith 1972). However, because of its large extent and density, the Orion molecular cloud should be shielded over most of its volume from external ionization agents such as the diffuse interstellar ultraviolet background, the soft X-ray background, and the low-energy cosmic rays, so that the electron content can be assumed negligible. In this case H_2 molecules cause the dominant collisional excitation of CO and HCN.

In outer parts of the Orion cloud and in smaller clouds, the electron content should be calculated and taken into account for the excitation of different molecules. Another class of processes capable of producing electrons in a dense interstellar cloud are the chemiionization processes suggested by Dalgarno, Oppenheimer, and Berry (1973). For simplicity, we have ignored these processes.

Neither the absolute value of the cross section nor the form of the selection rules for the collisions is known. We assume the de-excitation cross sections to be of the order of the geometrical cross section, 10^{-15} cm^{-2}, and we have calculated models with different selection rules for the de-excitation cross sections $\sigma(\Delta J)$. We have found that with no selection rule, $\sigma(\Delta J) = \sigma$, $\Delta J = 1, 2, \ldots$, the model clouds always show limb brightening, in conflict with the observations of $T_b(r)$. On the other hand, there were no great differences between the cases $\sigma(\Delta J) = 0$, if $\Delta J > 1$, up to $\sigma(\Delta J) = 0$, if $\Delta J > 4$.

The calculation follows an iterative scheme. The cloud is divided into a grid of concentric shells. For the case of CO which thermalizes at lower densities, the convergence is very fast and a rather coarse grid can be used. For the case of HCN, even the center of Orion A is not thermalized and a much more narrow mesh of points is required; in particular, we ran cases for HCN with up to 100 shells.

Once the population distribution is determined throughout the cloud, it is possible to calculate the absolute line profiles observed at different angular distances from the center.

The absolute intensity is given by

$$I_\nu = S[(\rho^2 + z_0{}^2)^{1/2}]\{1 - \exp[-\tau(\nu, \rho)]\}, \quad (7)$$

where $S(r)$ is the source function at a distance $r = (\rho^2 + z_0{}^2)^{1/2}$ from the center; ρ is the impact parameter which gives the position in the cloud that we are looking at, and z_0 satisfies the relation

$$\frac{\nu_0}{c}\,\frac{V[(\rho^2 + z_0{}^2)^{1/2}]}{(\rho^2 + z_0{}^2)^{1/2}}\, z_0 = -(\nu - \nu_0), \quad (8)$$

where ν_0 is the central frequency of the line. The angular factor in τ was taken into account.

IV. RESULTS

We emphasize that all the considerations described up to now do not depend on the sign of the velocity fields, i.e., on whether the cloud expands or contracts. Here, however, we shall assume that contraction is taking place, since it will be later shown that this is clearly the case.

We did not attempt to solve the hyperfine-structure components of the $J = 1 \to 0$ transition of HCN; we fitted the peak brightness temperature of the central, most intense, component ($F = 2 \to 1$). The widths of this central component, given by Snyder and Buhl (1974), also are much larger than the thermal width; therefore, they should be broadened by the macroscopic velocity field, and in determining the model we used as an additional constraint the widths of this line.

We transform $T_A{}^*(\alpha)$ of CO of Phillips *et al.* (1973) to $T_b(r)$ by taking the distance to Orion to be equal to 500 pc, and $T_A{}^*(\alpha) = T_b(\alpha)$. These quantities differ from each other by amounts smaller than the uncertainties in the beam efficiency factors used in the conversion. Then we derive $T_k(r)$ in the manner indicated in § II, and this is given in table 1.

Since the $T_k(\alpha)$ profile we obtain cannot be modified appreciably without failing to fit the CO observations, we use it without variations in all of our calculations.

As was discussed earlier, the observations of different molecules require a cloud density with a monotonic decrease from the center. Because of the results obtained by theoretical models of contracting clouds (cf. Hunter 1969), we first attempt the case in which the molecular density $\rho = \omega_1/r^2$. Then, as a limiting case representing slower dependences of ρ on r, we try $\rho = \omega_2$. The values of ω_1 and ω_2 can be obtained from the condition that at the center of the cloud both the $J = 1 \to 0$ and the $J = 2 \to 1$ transitions of CO are thermalized, whereas the $J = 1 \to 0$ transition of HCN is not thermalized. Here we can see the need of a multimolecule solution to the problem of modeling a cloud. We also see that the choice of CO and HCN is a good one, since while the former is a good thermometer, the latter is a good densitometer.

The last feature of the problem to be determined is the velocity field. Initially, we try the velocity fields that are consistent with a pressure-free contraction for each of the considered density profiles. It can be easily shown that in a pressure-free contraction of a cloud whose $\rho \propto r^{-x}$, $x \geq 0$, the resulting velocity field is $V \propto (r^{2-x})^{1/2}$. Consequently, for the homogeneous cloud $V(r) = V_0 r$, whereas for the centrally condensed cloud $V(r) = V_1$. The coefficients V_0 and V_1 can be derived from characteristics of the cloud, but since they are themselves model-dependent, we find them by

TABLE 1

THE ORION A MOLECULAR CLOUD MODEL

$T_k(r) = -2.00 \times 10^{-17}\, r + 70$ for $r \leq 2 \times 10^{18}$ cm
$\quad\;\; = -2.44 \times 10^{-18}\, r + 33$ for $r > 2 \times 10^{18}$ cm
$V(r) = 10^{-13}\, r$
$\rho(r) = 2 \times 10^{41}/r^2$ hydrogen molecules cm^{-3}
$R = 1.2 \times 10^{19}$ cm
$M(R) = 10^{38}$ g
$\eta_{\text{CO}}/\eta_{\text{H}_2} = 3 \times 10^{-5}$
$\eta_{\text{HCN}}/\eta_{\text{H}_2} = 10^{-8}$

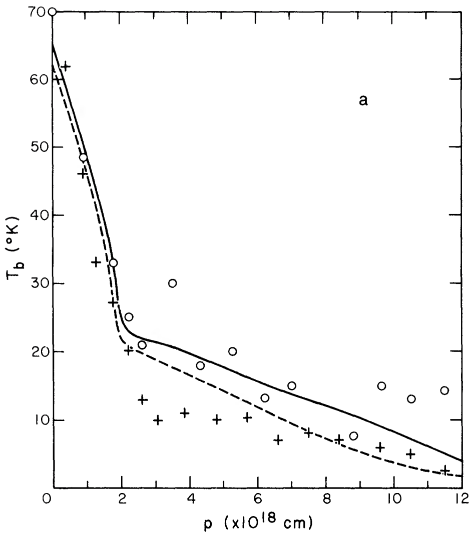

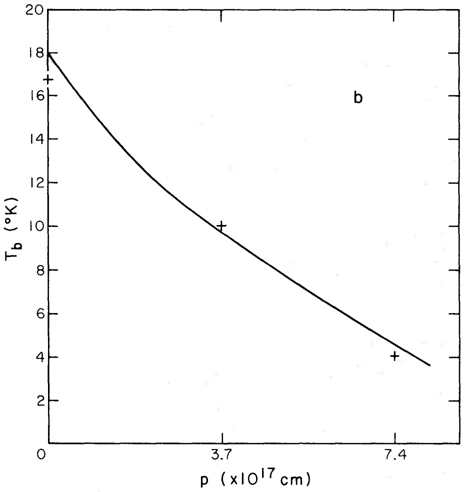

FIG. 1*a*.—A comparison between the brightness temperatures of CO as a function of the impact parameter obtained for our model, and the corresponding observations for the east side of the Orion A cloud, obtained by Phillips *et al.* The solid line shows the theoretical $J = 1 \rightarrow 0$ transition values for a collisional selection rule which makes $\sigma = 0$ for $\Delta J > 4$, whereas the broken line represents the $J = 2 \rightarrow 1$ transition with the same selection rule. The crosses give the observations for the $J = 1 \rightarrow 0$ transitions, and the circles give those for the $J = 2 \rightarrow 1$.

FIG. 1*b*.—A comparison between the brightness temperature distribution of the HCN $J = 1 \rightarrow 0$ lines as a function of the impact parameter (*solid line*) with the observations by Snyder and Buhl of the central component of the hyperfine structure of this molecule (*crosses*).

trial and error, seeing which one, if any, produces the observed line shapes. We find that for $V(r) = V_1$, all the resulting line profiles are broad and flat, totally incompatible with the observed line profiles. We also fail to obtain profiles similar to those observed when we try the case $V = V_0 r$ and $\rho = \omega_2$. This time we also obtain a broad, shallow profile, again incompatible with the observations. Consequently, we abandon the simplest assumption of pressure-free (and/or rotation-free) contraction, which is clearly not obeyed by the inner portion of the more realistic cloud models (cf. Hunter 1969), and try to fit a case with independently chosen density and velocity gradients. After several trials, we find that the best agreement with the CO and HCN observations is obtained with a model with $\rho = \omega_1/r^2$, $V(R) = V_0 r$, $\omega_1 = 2 \times 10^{41}$, and $V(R) = 12 \text{ km s}^{-1}$. In figures 1*a* and 1*b*, respectively, we show the brightness temperature distributions for CO and HCN. Figure 2 shows the $J = 2 \rightarrow 1$ profile of CO derived here, together with the observations of the same line by Phillips *et al.* (1973) near the center of the cloud. This model also produces the line widths of the $J = 1 \rightarrow 0$ ($F = 2 \rightarrow 1$) transition of HCN with values similar to those observed by Snyder and Buhl (1974) (about 4 km s^{-1}). We do not show these lines, which cannot be easily compared with the observations, because we did not treat the fine structure, which they resolved. However, our line widths are of the right values, and also decrease outward (although somewhat more slowly) in the same sense as seen in the observations.

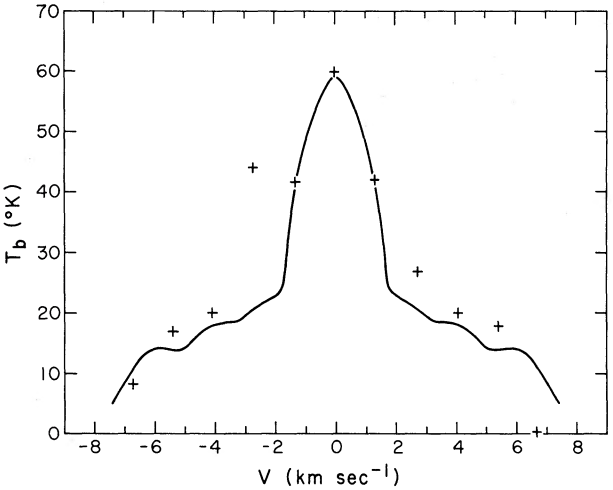

FIG. 2.—The line profile of the $J = 2 \rightarrow 1$ transition of CO obtained near the center of our Orion A model (*solid line*) compared with the corresponding observation (*crosses*) by Phillips *et al.*

For HCN, the conversion from T_A to T_b is made by dividing T_A by 0.6, the beam efficiency of the Kitt Peak NRAO telescope at the HCN line frequency.

In discussing the quality of the fitting of our model with the observations, we begin with the CO molecule. We consider the fitting very good, since we are applying a very simple model to a real case containing inhomogeneities and asymmetries which we are not considering in the model. In the inner (denser) region of the cloud, where both the $J = 2 \rightarrow 1$ and the $J = 1 \rightarrow 0$ transitions are thermalized and are therefore less sensitive to density fluctuations, the fitting is much better than in the outer region. In this outer region it can be seen from figure 1*a* that the calculated $T_b(2 \rightarrow 1)$ values correspond to the lower envelope of the observed (east half) distribution. The observations indicate that inhomogeneities may be rather prominent in this region.

As can be seen from figure 1*a*, we fail to reproduce the observed differences between $T_b(2 \rightarrow 1)$ and the $T_b(1 \rightarrow 0)$ in CO. We always find $T_b(2 \rightarrow 1) < T_b(1 \rightarrow 0)$, whereas the observations show the opposite. This problem could not be resolved by any of the manipulations that we attempted with our model. We feel that this difficulty arises as a consequence of the specific law of collisional excitation that we used. In view of the poor knowledge we have regarding this factor, we have not attempted to make any additional manipulations for the sole purpose of fitting this particular effect.

Despite these difficulties, our calculations reproduce the observed CO profile very well near the cloud center, which is very encouraging since these profiles are sensitive to both velocity and density distributions.

The HCN fittings are less striking in $T_b(\alpha)$ because the extent of the emitting region is only a few beamwidths wide. However, the use of the HCN observations was crucial in finding the cloud density profile.

The ratios of the components of the hyperfine structure of the $J = 1 \rightarrow 0$ transition of this molecule as observed by Snyder and Buhl (1974) change with position in the cloud and therefore should contain additional redundant information on the structure of the innermost portion of Orion A. Because of the particular nature of this problem we did not attempt to solve it here, and we hope to present details in a forthcoming paper.

After many trials varying the dependence laws and/or the constant involved in the model, we never came close to fitting all of the observations used here with a significantly different model. These trials give us confidence in the uniqueness of the solution. We find, however, that any single set of observations can be fitted in a variety of ways, so that any modeling based on the observations of only one molecule should be suspect. In particular, Clark *et al.* (1974), by analyzing observations of different isotopes of HCN only, give a temperature distribution for the region $r < 2 \times 10^{18}$ cm of the form $T = a/\sqrt{r} + b$, which in their static approximation fits the HCN distribution but, as we have discussed, fails to explain the brightness temperature distribution of CO in the same region.

A very important point to keep in mind is the possibility that the abundance of HCN may be dependent on the density, as it appears in the theory of formation of molecules of Herbst and Klemperer (1973); this, of course, would affect our method of diagnostics. However, given the fact that in their paper these authors have used only an estimate for the rates of formation for HCN, which subsequent measurements have shown incorrect by an order of magnitude (Herbst, private communication), it is not clear whether this effect is real. Therefore, we adopted a constant abundance for HCN.

V. DISCUSSION

We have already remarked that the observations cannot differentiate whether the cloud is expanding or contracting (in which case it would likely be in the process of star formation). Let us first consider the material near the boundary of the cloud. There we find the kinetic energy per gram of the systematic motion to be $E_k = 7 \times 10^{11}$ cm^2 s^{-2}, whereas the potential energy per gram $E_p = -5.5 \times 10^{11}$ in the same units. These numbers, which within their uncertainties are equal to each other, indicate either free fall or, if the velocity were expansion, that the boundary material could expand to infinity. As we move inward, however, $E_p(r) \propto M(r)/r$ = constant, whereas $E_k(r) \propto (r/R)^2$, which decreases. Very soon we reach values for E_p much larger than E_k, an inequality that will grow as we near the center of the cloud. Since the second derivative of the moment of inertia $\ddot{I} < 0$, the virial theorem tells us that the motion must be a contraction. This shows beyond question that Orion A is gravitationally bound and that the systematic velocities are negative.

It is of interest to see whether the rate of contraction of the cloud is sufficient to balance the rate at which energy is radiated away by different processes. Goldreich and Kwan (1974) have addressed themselves to this question, and conclude that in their idealized cloud model the contraction would not be sufficient to provide the energy at the rate radiated by the CO alone. Thus, they postulate the existence of an energy source other than the contraction to maintain in their cloud a temperature in the range of values observed.

We examine this question, following Goldreich and Kwan (1974), by defining a factor S which compares the rate of cooling to the rate of heating provided by an adiabatic contraction as:

$$S = (R/V) \sum_{\text{shells}} (dE/dt)/E\,,$$

where R is the radius of the cloud, $V = V(R)$, E is the thermal energy, and dE/dt is the cooling rate. The most important processes contributing to the cooling of dense molecular clouds are radiative emission by molecules and collisions of the gas particles with dust grains. The most abundant molecules are H_2, HD, and CO, and the contribution from the other much less abundant molecules can be neglected. In the particular case of Orion, H_2 can also be neglected, since it does not radiate appreciably for temperatures below 70° K (Dalgarno and Wright 1972), which is the maximum temperature in this cloud. In our model for Orion A we find that the CO contribution to the cooling rate of 4.5×10^{33} ergs s^{-1} gives a value of $S = 0.9$, which within the uncertainties of these numbers means that the contraction is just capable of providing the energy radiated by the CO. In computing the HD losses, we assume an abundance ratio of this molecule to H_2 equal to 5×10^{-5} (Dalgarno and Wright 1972). By using our code, which takes into account the effect of opacity, we find that $S = 15$. Now, for the Orion molecular cloud, Wilson *et al.* (1973) have found a ratio DCN/HCN 6×10^{-3}. Following the ideas of Watson (1973), however, we assume that this ratio does not reflect isotopic abundances but that it reflects chemical fractionation, and that the D/H ratio is a factor 10^2 smaller.

The cooling by collisions of the gas particles with the grains is estimated by assuming the dust-to-gas ratio in the cloud to be equal to that measured in the interstellar medium and totally inelastic collisions. Then we have (Dalgarno and McCray 1972):

$$C_g = 2 \times 10^{-33} n_{\mathrm{H}_2}{}^2 T^{1/2}(T - T_g) \text{ ergs cm}^{-3}\text{ s}^{-1} ,$$

where n_{H_2} is the density of the hydrogen molecule, T is the kinetic temperature of the gas, and T_g is the temperature of the grains. We calculate the total grain cooling by integrating C_g throughout the cloud. For the Orion model, with $T_g = 4°$, $10°$, and $20°$ K, we find the cooling rates to be 8.3×10^{36}, 7.4×10^{36}, and 5.8×10^{36} ergs s^{-1}, respectively. By contrast, the cooling rate by CO amounts to only 4.5×10^{33} ergs s^{-1}, and that by HD to 7×10^{34} ergs s^{-1}. So, while $S \approx 1$ if we only consider the CO, it becomes 15 when we include HD, and $\geq 10^3$ if we include the grain cooling. Of course, this estimate of the grain cooling is an upper limit corresponding to perfectly inelastic collisions, whereas the lower limit corresponding to totally elastic collisions is zero. The true value is difficult to assess. However, despite the uncertainties in the abundance of HD, as well as in the efficiency of the dust cooling, we believe that for the Orion A cloud it can be concluded that additional sources of energy are required to maintain the observed temperature structure.

The requirement of this extra energy source makes it difficult to compare this model with theoretical models of contracting clouds which are all source-free. This is particularly true for the temperature distribution. However, if as shown by Disney, McNalley, and Wright (1969) the temperature distribution does not seriously affect the velocity and density distributions, then we find it difficult to reconcile the extent of the linear regime of the velocity flow obtained for Orion with all of the calculated models. The results of Hunter (1969) show, for example, that when the density distribution approaches $1/r^2$, the velocity increases linearly from the center to about 10 percent of the cloud, and then it becomes essentially flat, approximating in that way the asymptotic similarity solutions. The existence of such an extended region of rather constant velocity in the cloud is at odds with the observed profile of the $J = 2 \rightarrow 1$ transition of CO near the center of Orion.

In this paper we were limited by the available observations, and it is clear that an observational plan designed primarily to deduce the structure of clouds, for comparison with theoretical predictions, could yield more decisive results.

Recent observations by Liszt *et al.* (1974) show an elongation of the cloud in the north–south direction; this is an important fact to be taken into account when discussing the evolutionary state of this cloud. However, for the reasons stated at the beginning of § II we did not attempt to derive the structure of the Orion cloud in that direction.

We hope that this paper will be taken as an example that with available methods of diagnostics and a careful selection of observations of molecular transition, it is possible to analyze observationally the initial stages of star formation.

We wish to thank J. Castor for numerous extended discussions of this problem, L. Snyder for his encouragement and ideas on the meaning of the observations, D. Hummer and R. McCray for their constant interest and encouragement, and U. Palmer for superb assistance in programming and computing. Part of the computer time was generously provided by the Computing Center of the University of Colorado. H. G. was partly supported by NSF grant GP-38736, S. S. acknowledges the support of a JILA Visiting Fellowship.

REFERENCES

Castor, J. I. 1970, *M.N.R.A.S.*, **149**, 111.
Clark, F. O., Buhl, D., and Snyder, L. 1974, *Ap. J.*, **190**, 545.
Dalgarno, A., and McCray, R. 1972, *Ann. Rev. Astr. and Ap.*, **10**, 375.
Dalgarno, A., Oppenheimer, M., and Berry, R. S. 1973, *Ap. J.* (*Letters*), **183**, L21.
Dalgarno, A., and Wright, E. L. 1972, *Ap. J.* (*Letters*), **174**, L49.
Disney, M. J., McNalley, D., and Wright, A. E. 1969, *M.N.R.A.S.*, **146**, 123.
Goldreich, P., and Kwan, J. 1974, *Ap. J.*, **189**, 441.
Goldsmith, P. F. 1972, *Ap. J.*, **176**, 597.
Heiles, C. 1973, *Ap. J.* (*Letters*), **179**, L17.
Herbst, E., and Klemperer, W. 1973, *Ap. J.*, **185**, 505.
Hunter, J. H. 1969, *M.N.R.A.S.*, **142**, 473.
Liszt, H. S., Wilson, R. W., Penzias, A. A., Jefferts, K. B., and Wannier, P. G. 1974, *Ap. J.*, **190**, 557.
Lucy, L. B. 1971, *Ap. J.*, **163**, 95.
Phillips, T. G., Jefferts, K. B., and Wannier, P. G. 1973, *Ap. J.* (*Letters*), **186**, L19.
Scoville, N. Z., and Solomon, P. M. 1974, *Ap. J.* (*Letters*), **187**, L67.
Snyder, L. 1973, in *Interstellar Dust and Related Topics*, ed. J. M. Greenberg and H. C. van de Hulst (Dordrecht: Reidel), pp. 351–361.
Snyder, L., and Buhl, D. 1974, to be published.
Sobolev, V. V. 1960, *Moving Envelopes of Stars* (Cambridge, Mass.: Harvard University Press).
Watson, W. 1973, *Ap. J.* (*Letters*), **181**, L129.
Wilson, R. W., Penzias, A. A., Jefferts, K. B., and Solomon, P. M. 1973, *Ap. J.* (*Letters*), **179**, L107.

H. Gerola: Physics Department, New York University, 4 Washington Place, New York, NY 10003

S. Sofia: Department of Astronomy, University of South Florida, Tampa, FL 33612

1975ApJ...196..351C

THE ASTROPHYSICAL JOURNAL, **196**:479–487, 1975 March 1

NEUTRAL HYDROGEN ASSOCIATED WITH SUPERNOVA REMNANTS.
I. THE CYGNUS LOOP

L. K. DENOYER
University of Illinois

Received 1974 June 17; revised 1974 September 13

ABSTRACT

Observations of H I near the Cygnus Loop show that (1) the remnant is encountering interstellar clouds with densities 5–10 cm^{-3} adjacent to its optical filaments, and (2) the remnant does not contain the cool H I shell as predicted by current evolution theories which equate the present shock velocity with the optical expansion velocity. It is suggested that the remnant is adiabatically expanding into a two-phase medium, and the original energy of the explosion was 10^{51} ergs.

Subject headings: supernova remnants — 21-cm radiation

I. INTRODUCTION

Theoretical models of the evolution of supernova remnants (SNRs) predict that massive thin shells of neutral hydrogen will be formed behind the shock front of old remnants, due to the high cooling rates in plasmas excited by low-velocity (< 200 km s^{-1}) shock waves (Chevalier 1974; Mansfield and Salpeter 1973; Straka 1973). Furthermore, it is generally believed that the optical filaments of old remnants are formed near the shock front at those positions where the expanding remnant encounters denser clouds of the interstellar medium (Cox 1972*b*). Thus, old SNRs are expected to show (*a*) denser H I clouds in the interstellar medium adjacent to their optical filaments, and (*b*) an expanding shell of neutral hydrogen interior to the filaments. Observations of the 21-cm line of H I near six large-diameter SNRs with visible optical filaments were made to look for such features. The results for the Cygnus Loop are reported here; three further papers in this series will discuss IC 443, HB 9, OA 184, VRO 42.05.01, and CTA 1.

II. OBSERVATIONS

The data were obtained with the NRAO[1] 91-m telescope which was equipped with four 21-cm parametric amplifiers fed by four linearly polarized horns. System temperatures were approximately 150° K. A 400-channel autocorrelator was used as four separate 96-channel correlators for the Cygnus Loop mapping operations. A frequency-switched signal, with 90 percent of the time spent at the signal frequency, was fed into each autocorrelator. The spectra have 16 kHz per channel resolution and 13 kHz separation between channels.

The data for the Cygnus Loop were taken as scans in galactic longitude, separated by 0°.16 in galactic latitude. (The antenna beamwidth was 0°.16.) Intercalibration of the gain of the four receivers was achieved by comparing the frequency-integrated spectra of four scans in galactic latitude with all the longitude scans. Postdetection smoothing in the frequency domain with a Hanning function resulted in a final resolution of 32 kHz, or 6.7 km s^{-1}. Linear baselines were fitted to all spectra. All data discussed in this paper will be in units of antenna temperature; the conversion from antenna to brightness temperature, calibrated by continuum observations of 3C 59, 3C 62, 3C 68.1, 4C 35.03, 0214+10, 0222−00, 0223+34, and NRAO 1000, is $T_b = 1.5T_a$ at the declinations covered in the observations presented here. All velocities are measured with respect to a standard of rest defined by a solar motion of 20 km s^{-1} toward 18^{h}, 30° (1900).

III. THE FEATURES OF H I NEAR THE CYGNUS LOOP

Five of the 34 scans across the region containing the Cygnus Loop are shown in figure 1. A sketch of the optical filaments has been added to each profile to show the position of the antenna beam relative to the SNR during each scan. The general features of H I which will be discussed below are (*a*) the absence of a hydrogen shell expanding at 100 km s^{-1}, (*b*) a correlation between low-velocity hydrogen clouds and the optical filaments of the SNR, and (*c*) a complex of clouds with velocities between −30 and −60 km s^{-1} which appear to be at the same distance as the SNR.

a) *Absence of Predicted Expanding Shell*

The models of Mansfield and Salpeter (1973) (hereafter called MS) and Chevalier (1974) (called C) for the evolution of a supernova remnant which is expanding into a homogeneous medium, predict that a cool ($T \leq 10°$ K) shell of neutral hydrogen will begin to form immediately after the shock velocity has slowed to ~ 200 km s^{-1}. The total mass (or H I surface density) of the shell is approximately determined by the density of the interstellar medium, and the volume swept out since shell formation began. Since the remnant's radius at the inception of shell

---

[1] Operated by Associated Universities, Inc., under contract with the National Science Foundation.

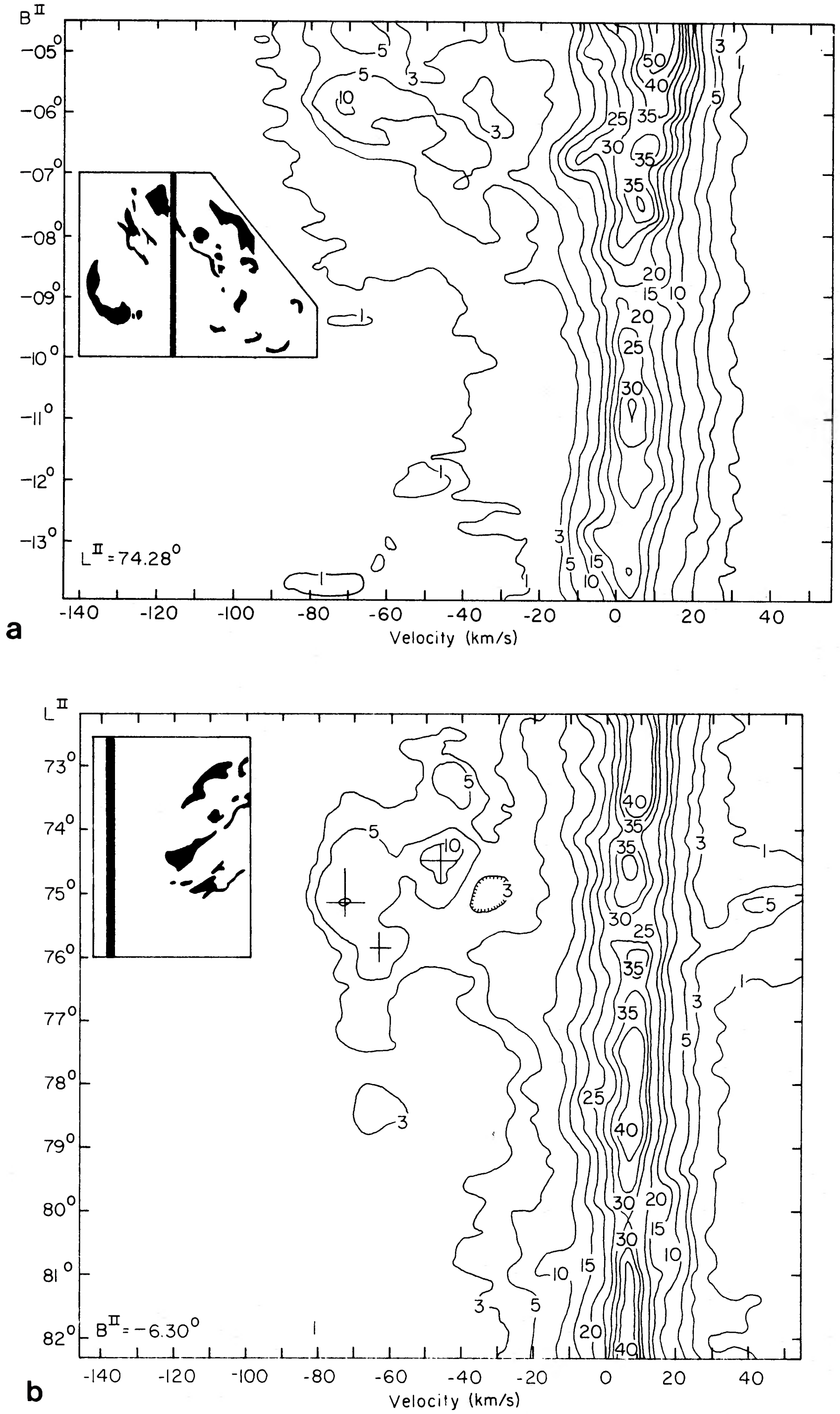

FIGS. 1*a*–*e*.—Contour maps of antenna temperature of H I, for one scan in galactic latitude and four scans in galactic longitude, displayed in velocity versus position coordinates. Inserts show the optical features on the same angular scale as the H I maps. The positions of the antenna beam during each scan are indicated by the solid line on each insert.

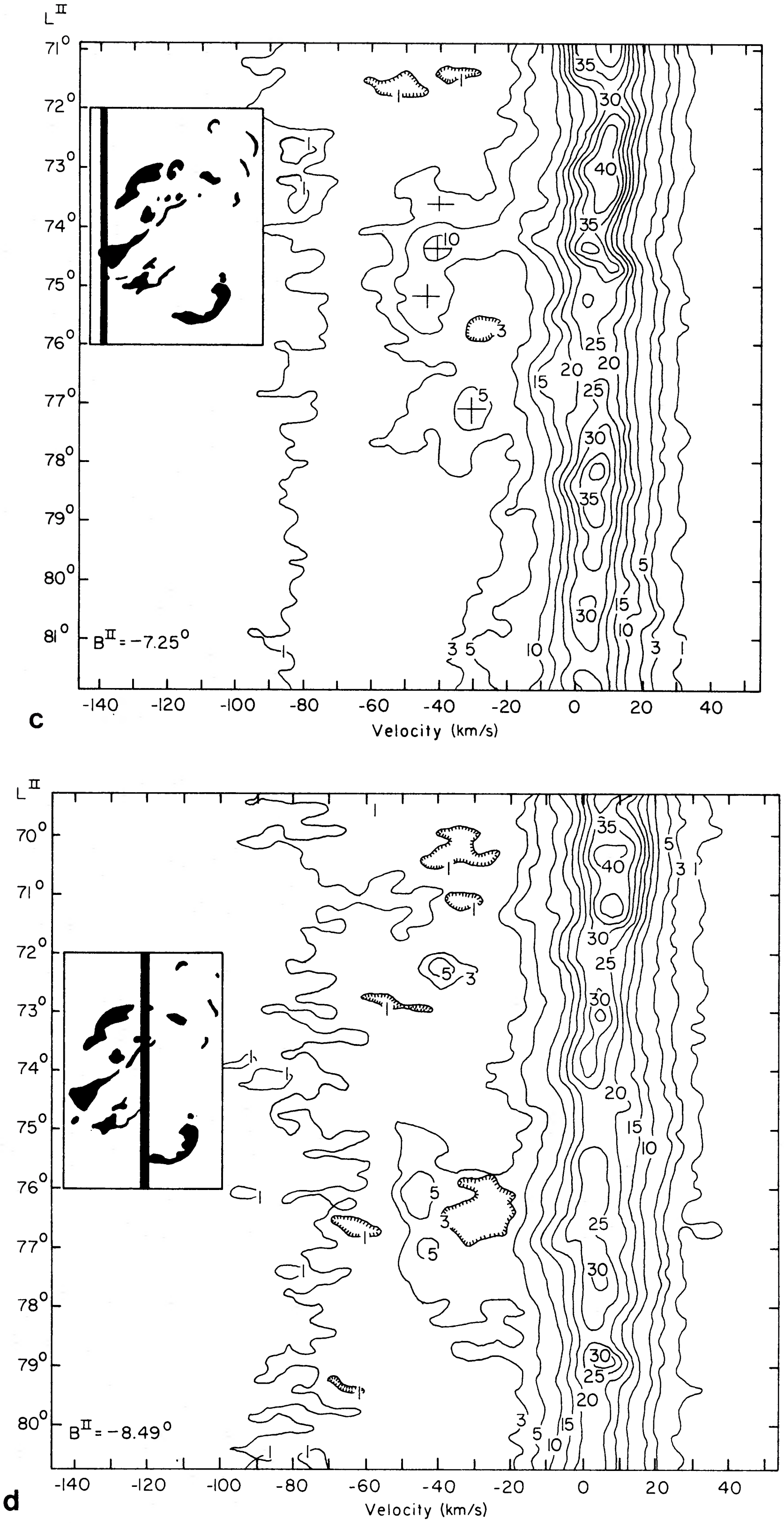

Fig. 1.—*Continued*

1975ApJ...196..351C

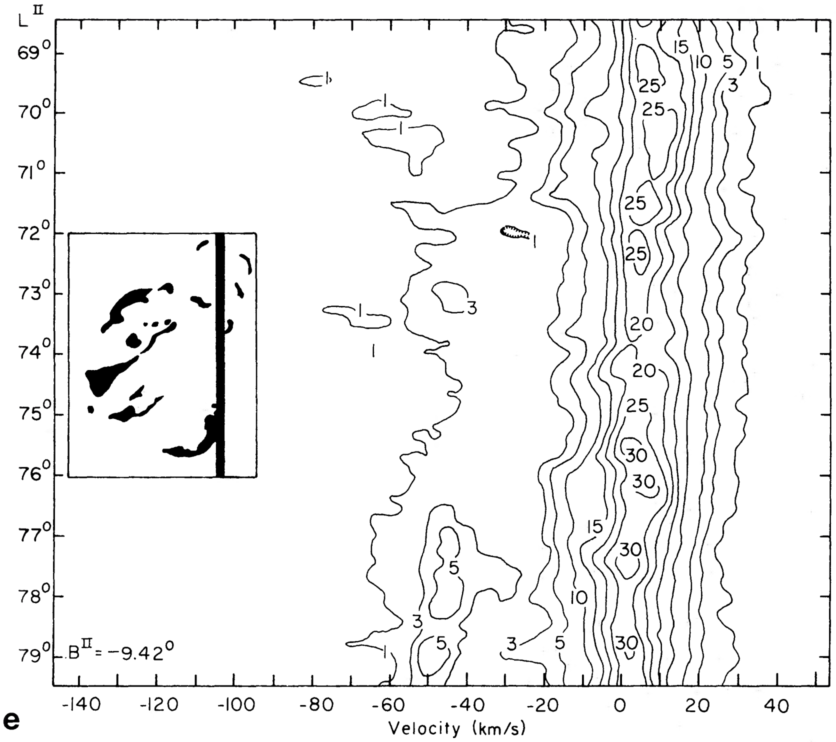

FIG. 1.—*Continued*

formation depends upon the initial energy E_0 of the remnant and upon the density n_0 of the surrounding medium, the predicted shell surface density will depend on E_0, n_0, and the present size of the remnant. We can use the X-ray luminosity of the Cygnus Loop to set limits on the permitted values of E_0 and n_0. Following Cox (1972*b*), we require that n_0 be 1 cm^{-3} in order to reproduce the X-ray luminosity of 10^{36} ergs s^{-1}. E_0 is then restricted to $\sim 3.9 \times 10^{50}$ ergs in order to produce a remnant with present radius 20 pc and expansion velocity 100 km s^{-1}, the usually accepted parameters for the Cygnus Loop. The detailed evolutionary models of MS and C for an initial energy $E_0 = 3 \times 10^{50}$ ergs and interstellar density $n_0 = 1$ cm^{-3} predict that a remnant with an optical radius ~ 20 pc would have a neutral shell with total hydrogen mass > 640 $M_\odot$. The H I surface density of such a shell would be $\sigma_{\text{sh}} \geq 1.7 \times 10^{19}$ atoms cm^{-2}.

The predicted shell thickness depends upon the magnitude of the interstellar magnetic field. Chevalier has included a field of 3×10^{-6} gauss in his models, which does not affect the shell's mass for interstellar densities greater than 1 cm^{-3}, but does produce a thicker shell than no magnetic field. The shell thickness for the Cygnus Loop, if $E_0 = 3 \times 10^{50}$ ergs and $n_0 = 1$ cm^{-3}, is 0.6 pc. This thickness corresponds to 3′ at the distance of 800 pc. Since we are unable to resolve this shell with a 10′ beam, the H I shell should appear coincident with the optical shell. The velocity characteristics of the neutral shell should match the optical remnant. Minkowski (1958) has estimated that the optical remnant of the Cygnus Loop is expanding at 116 km s^{-1}, centered at 33 km s^{-1} with respect to the local standard of rest.

Three wide-bandwidth scans were made across the nebula at galactic latitudes $-8.^\circ6$, $-8.^\circ8$, and $-9.^\circ2$, in order to look for the presence of an expanding shell of hydrogen. The velocity range covered in the scans at $-8.^\circ8$ and $-9.^\circ2$ was -180 to 70 km s^{-1}; the scan at $-8.^\circ6$ covered -300 to 200 km s^{-1}, all with a velocity resolution of 3.3 km s^{-1}. There was no evidence for an expanding shell with an antenna temperature greater than 1° K. The limit applies to a shell with expansion velocities greater than 20 km s^{-1} centered on 33 km s^{-1}, and to expansion velocities greater than 50 km s^{-1} centered at any velocity between -200 and 100 km s^{-1}. A shell with low expansion velocities could have been masked by foreground hydrogen between -30 and $+30$ km s^{-1}.

The upper limit on the surface density of neutral hydrogen within the Cygnus Loop which corresponds to $T_a \leq 1°$ K, is $\sigma_{\text{sh}} \leq 2.7 \times 10^{18} \Delta V$ (km s^{-1}) atoms cm^{-2}. ΔV is the larger of (1) the thermal or turbulent Doppler width of H I within the shell, and (2) the velocity resolution of the observations (3.3 km s^{-1}). For the predicted shell temperature of 10° K, $\sigma_{\text{sh}} \leq 9 \times 10^{18}$ atoms cm^{-2}. However, the shell may be hotter or more turbulent than expected. Since the hydrogen does not recombine until the temperature in the cooling region is less than 10^4 ° K, we do not expect to see a Doppler width greater than 16 km s^{-1} in the neutral shell. Consequently, an absolute limit on the surface density is $\sigma_{\text{sh}} \leq 4.3 \times 10^{19}$ atoms cm^{-2}. We conclude that a cool shell with hydrogen mass greater

1975ApJ...196..351C

than 340 $M_\odot$ is not present in the Cygnus Loop; the upper limit to a hot or turbulent shell is 1600 $M_\odot$.

b) *Relation to Interstellar Clouds*

The cloud features between 0 and 10 km s^{-1} of the hydrogen profiles of figure 1 border the brightest optical filaments of the SNR, and mimic the shape of an optical absorption lane west of the remnant. Figure 2, a contour map of antenna temperature integrated between 0 and 10 km s^{-1}, shows these features, and supports the idea that the optical filaments of old SNRs mark the positions of denser clouds in the adjacent interstellar medium. The column densities of atomic hydrogen in these clouds range from 5×10^{19} cm^{-2} for the small features east of NGC 6992–95 to $1\text{–}2 \times 10^{20}$ cm^{-2} for the elongated clouds adjacent to the western filaments. If we assume that the cloud depth along the line of sight is equal to the narrower dimension seen in figure 2, and use a distance of 770 pc, then the clouds are 5–10 pc in cross section and they have H I densities of 5–10 cm^{-3}. (Cox 1972*a* predicted a lower limit for the density of clouds adjacent to the optical filaments from the electron density derived from the [O II] lines. His value was 6 cm^{-3}.)

The optical absorption lane west of the SNR is seen in emission in figure 2. This result was unexpected, since Heiles (1969) found H I emission from only one of 48 dust clouds he surveyed. His conclusion was that a significant amount of the hydrogen was in molecular form. In the present case, X-ray or ultraviolet radiation from the SNR may be heating the cloud and destroying any H_2 molecules within. The excess antenna temperature at the position of the cloud is approximately 15° K; thus the H I excitation temperature within the cloud is ≥ 22° K. H I densities are 5–10 cm^{-3}. Observations of H_2 or other molecules in this cloud would be most interesting, since the existence of molecules with such a long formation time ($\tau_{H_2} \approx 10^{17} n^{-1}$ cm^{-3} s; Hollenbach and Salpeter 1971) would preclude the possibility that this cloud was ionized by an ultraviolet flash from the original SNR explosion.

The frequent association of nonthermal radio emission with bright optical filaments of SNRs has long been noted. However, most optically visible SNRs also have patches of radio emission which are not associated with optical filaments. The western hemisphere of the Cygnus Loop is a much stronger radio source than the eastern hemisphere, and although most of the optical filaments also occur in the western half, radio-optical correlations are not the rule. The radio emission is particularly intense in the southwestern quadrant and in the tail of the remnant, where the optical filaments are weak. Thus, it is appropriate to ask whether the extinction varies across the remnant, obscuring some optical filaments. Figure 2 shows that the adjoining interstellar medium is denser on the western side of the remnant, and H I clouds may obscure some optical filaments between NGC 6960 and the "carrot-top" nebulosity. In fact, the optical filaments which are seen in the area are more diffuse than those of NGC 6960 or NGC 6992–95. However, the H I column density between 0 and 10 km s^{-1} is not as large in the southwest quadrant as in the northwest where the optical filaments are brighter. The same conclusion follows from figure 3 also, which shows the column density of all H I in the line of sight. The paucity of optical filaments in the southwest is probably a real phenomenon.

The observed column density of H I in the direction of the Cygnus Loop varies between 1.5 and 3×10^{21} cm^{-2}. It is impossible to use the H I velocities to separate out the hydrogen which lies in front of the Loop because (1) most of the total hydrogen has a spatial structure which is correlated with the optical filaments, so that a front/behind choice cannot be made, and (2) even the negative-velocity hydrogen which should lie far beyond the remnant appears to be near the SNR (§ III*c*). Since the remnant lies 100 pc below the galactic plane, and since approximately one-half of galactic

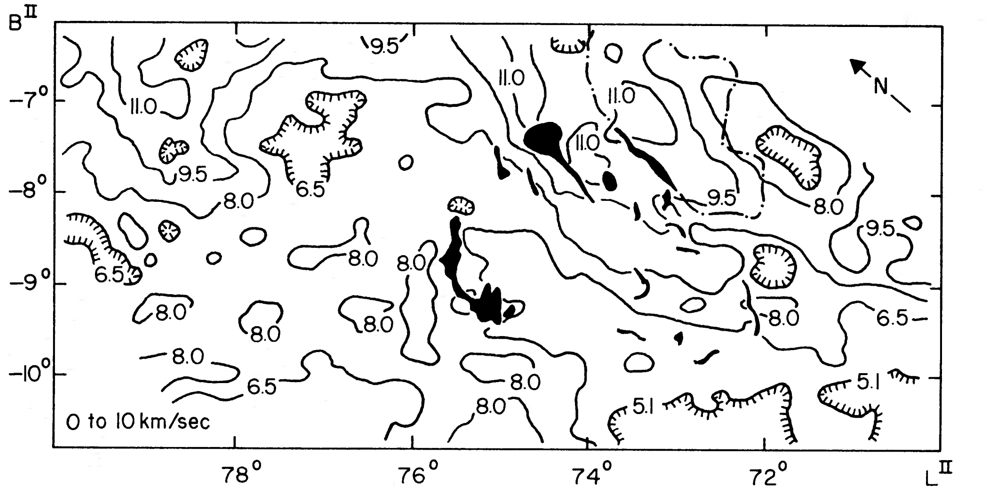

FIG. 2.—Antenna temperature of H I, integrated between 0 and 10 km s^{-1}. Contours are labeled in units of 10^{20} atoms cm^{-2}. Dark areas indicate optical filaments of the Cygnus Loop; the dashed line outlines an optical absorption lane.

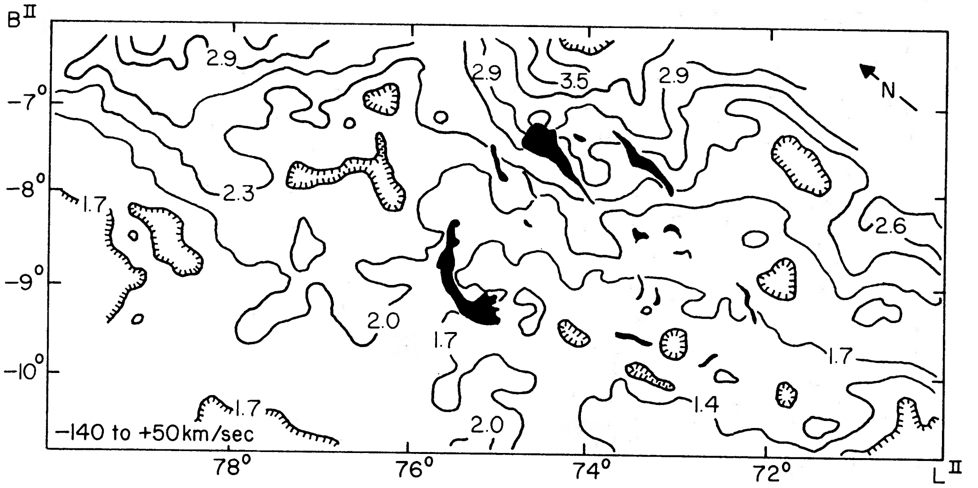

FIG. 3.—Antenna temperature of H I, integrated between −140 and 50 km s^{-1}. Contours are labeled in units of 10^{21} atoms cm^{-2}.

H I lies within 110 pc of the plane (Kerr and Westerhout 1965), it seems appropriate to assign a column density of 7–15 × 10^{20} cm^{-2} to the H I between the Sun and the Cygnus Loop. Borken (1974) reports that an H I column density of 5 ± 2 × 10^{20} cm^{-2} fits the X-ray spectrum.

c) *The Complex of Negative Velocity Clouds*

The second outstanding feature of the region of the sky near the Cygnus Loop is the complex of clouds with velocities between −30 and −60 km s^{-1}. The complex is extended beyond the outline of the SNR, but it is local to the region of the sky surveyed. The latitude-scans at 74° (fig. 1*a*) suggest that clouds at these velocities are confined to $b^{\text{II}} < -5°$. The H I profiles of Burton and Verschuur (1974) limit the extent to $l^{\text{II}} < 82°$ and $b^{\text{II}} > -12°$. The complex probably ends at cloud OXM 330 (Meng and Kraus 1970), which has a mean velocity of −64 km s^{-1} and is located at 81°.5 l^{II}, −10°.2 b^{II}. The mass of the complex within the area surveyed is 2.7 × 10^3 D^2 $M_\odot$ (*D* is the distance in kpc), and the total mass of the complex is probably 3–4 × 10^3 D^2 $M_\odot$.

i) *Velocity Structure*

Perhaps the most important characteristic of this complex is the correlation of the velocity structure of the material with the low-velocity clouds in the region. The velocity of the isolated cloud features changes from approximately −35 km s^{-1} at the western edge of the region, to −50 km s^{-1}, and then back to −35 km s^{-1} at the eastern edge. Dividing the velocity space into the intervals −30 to −40 km s^{-1} and −40 to −60 km s^{-1} as in figures 4 and 5, illustrates this. The hydrogen in the interval −30 to −40 km s^{-1} of figure 4 is more widely distributed than the material in figure 5, and there are long ridges of

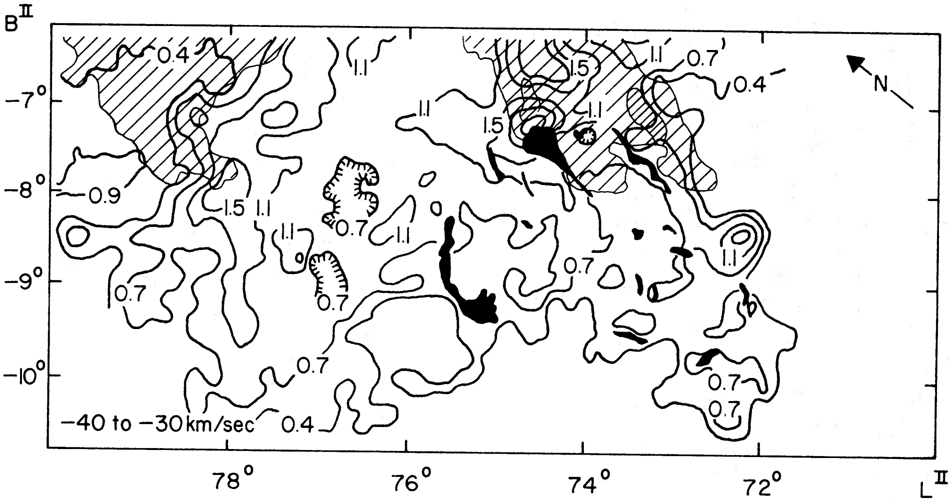

FIG. 4.—Antenna temperature of H I, integrated between −40 and −30 km s^{-1}. Contours are labeled in units of 10^{20} atoms cm^{-2}. Hatched areas show regions of H I emission at 0–10 km s^{-1}.

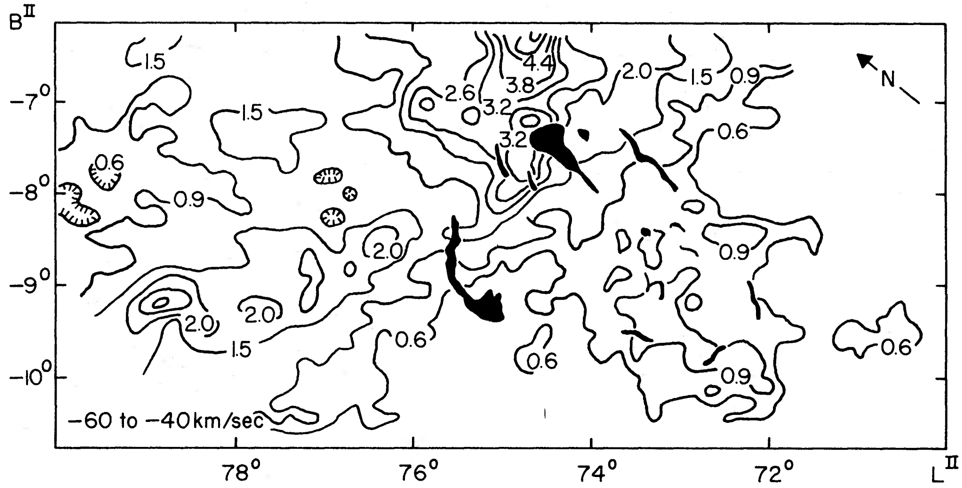

FIG. 5.—Antenna temperature of H I, integrated between −60 and −40 km s^{-1}. Contours are labeled in units of 10^{20} atoms cm^{-2}.

higher temperature at the eastern and western boundaries of the lower-velocity hydrogen. These ridges are not separate emission features, but are the result of a smooth decrease in the average velocity of the −30 to −60 km s^{-1} H I at the edges of the complex. The smoother velocity changes from −40 km s^{-1} to lower ridges lie along the edges of the 0 to 10 km s^{-1} clouds, as shown in figure 4. In the eastern half of the region, the 0–10 km s^{-1} clouds are located at latitudes $b^{\mathrm{II}} > -9°$, where the negative-velocity ridge is most prominent. Notice how the ridge bends around the edge of the low-velocity cloud at 78° l^{II}, −8° b^{II}. Thus, the complex of negative-velocity clouds shows (1) a spatial correlation with the 0–10 km s^{-1} hydrogen in this area of the sky and (2) a smooth velocity change toward smaller velocities at positions adjoining the 0–10 km s^{-1} clouds. On these bases, we conclude that the complex is interacting with the low-velocity clouds.

ii) *Filaments*

The H I between −30 and −60 km s^{-1} has a filamentary structure, a common feature for galactic hydrogen (Verschuur 1974). Much of the structure was probably unresolved by the 10′ beam, as the profiles of figure 1 suggest. However, some bright filaments, as shown by crosses in figure 1, could be traced in position and velocity over several degrees. These filaments are plotted in figure 6. The width of the filaments, approximately $0\overset{\circ}{.}5$, is not accurately represented in this figure, since filaments with different velocities often have similar positions. Nearly all the H I filaments have a velocity gradient along their axis,

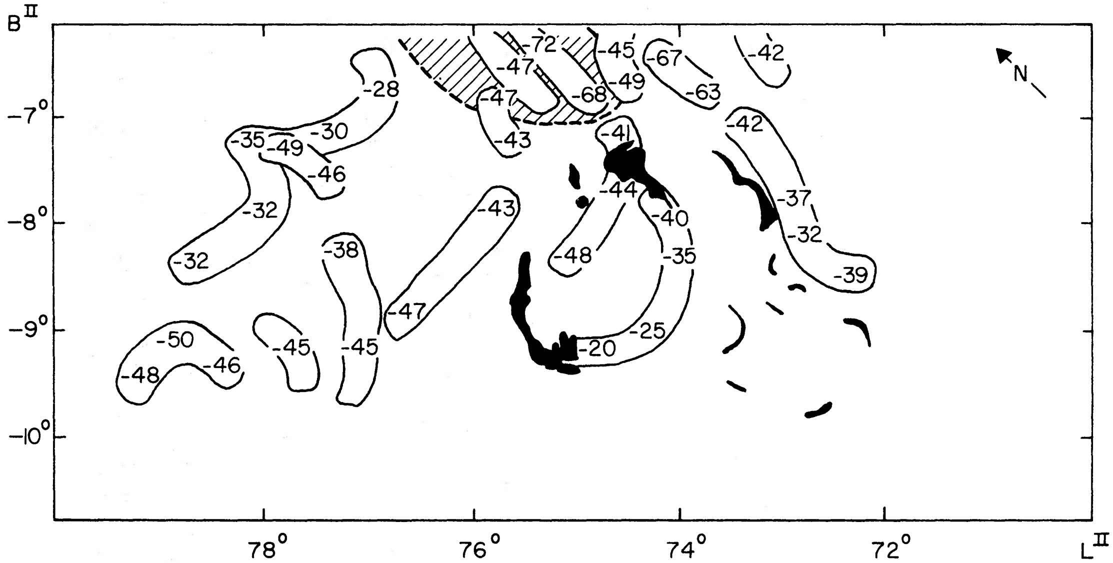

FIG. 6.—Filamentary structure of the negative velocity complex. Filament velocities (km s^{-1}) are labeled within schematic filament contours. Hatched region shows approximate position of positive velocity material.

suggesting either that acceleration occurs along the filaments or that Alfvén waves and turbulent motions are capable of producing velocity gradients ≥ 5 km s^{-1} perpendicular to the axes of the filaments. It is fascinating that the alignment of the H I filaments is nearly the same as the alignment of the optical filaments of the remnant; namely, north–south for those optical and H I filaments west of the remnant's center, and east–west for the filaments east of center. This strengthens the conclusion that the SNR and the negative-velocity complex are in the same vicinity.

Immediately north of the remnant, where the negative-velocity emission features are most intense, the most negative velocities (-70 km s^{-1}) in the complex are found. In this same area, there is also H I at positive velocities (≤ 60 km s^{-1}). Only an approximate position of this material could be drawn in figure 6, since the positive velocities were not well covered by the observations. This spatial coincidence between the most negative and most positive velocities has no obvious explanation, and further observations of the positive velocities are desirable.

iii) *Interaction with the SNR*

The H I in the interval -30 to -40 km s^{-1} which borders the complex of negative-velocity clouds on the north and west has probably been compressed by the supernova shock. Figure 7 shows contours of continuum radiation at 49 cm (DeNoyer 1974) superposed on the H I contours from figure 4, in a small region surrounding the remnant. The ridge of H I west of the remnant, adjacent to the optical filaments of NGC 6960, is definitely outside the optical remnant and yet lies within the contours of radio emission from the SNR. Careful examination of the Palomar red plate of this remnant reveals faint filaments west of NGC 6960 which follow the outermost radio contours shown in figure 6 and also enclose the H I ridge on the western side. These fainter filaments probably reside at the current shock position.

A similar H I emission feature at 74°.5 l^{II}, $-7°.6$ b^{II}, lies at the northern edge of the "carrot-top" filaments. This intense emission feature has a large velocity width, beginning at -50 km s^{-1} and blending into the foreground emission at -10 km s^{-1} (see fig. 1*c*). There are no faint optical filaments bordering this feature on the northern side, but its position in relation to the optical filaments suggests that it is part of the remnant also.

The two hydrogen emission features discussed above are not thought to be part of the predicted H I shell for the following reason. Similar emission features, with same velocity characteristics but without the accompanying radio and optical emission, can be seen 1° north of the remnant (fig. 1*b*) and 2° east (fig. 1*d*). It would be difficult to interpret the two SNR-associated features as part of a shell without including the entire negative-velocity complex, but the complex does not have the velocity characteristics of an expanding shell. Furthermore, it is not centered on either the optical or the X-ray remnant, as would be expected for a shell. Thus, these emission features appear to be clouds, or density inhomogeneities, which have been overtaken by the SNR shock (Sgro 1972).

IV. DISCUSSION

Theories which interpret the optical filaments of the Cygnus Loop as regions of rapid cooling behind a 100 km s^{-1} shock front also predict that a cool H I shell will be present, yet none was found. Neutral hydrogen shells have been found in HB 21 (Assousa and Erkes 1973), S147 (Assousa, Balick, and Erkes 1973), and W44 (Knapp and Kerr 1974). In each case,

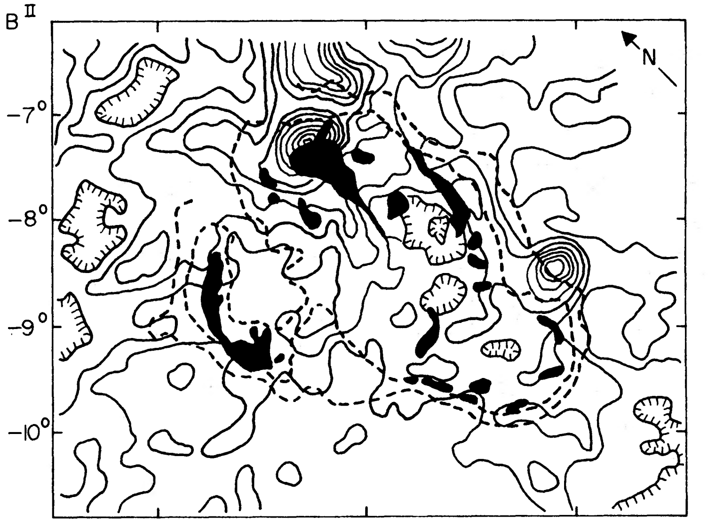

FIG. 7.—Optical (*dark areas*) and 49-cm continuum emission contours (*heavy dashed line*) from the Cygnus Loop superposed on contours of H I antenna temperature integrated between -40 and -30 km s^{-1}. The H I contour interval is 2.2×10^{19} atoms cm^{-2}.

the shell was exterior to the radio or optical remnant, and the shell diameter was several times as large as the radio diameter; the expansion velocities were low (≤ 25 km s^{-1}). H I in the vicinity of the Cygnus Loop does not show these features either.

It is possible that the SNR has not yet reached the shell formation stage; if so, the shock velocity is greater than 200 km s^{-1}. The X-ray temperature of 2.25×10^6 ° K (Borken 1974) requires a present shock velocity v_s of 390 km s^{-1} (postshock temperature $T_s = 1.45 \times 10^{-9} v_s^2$; Woltjer 1972), if the density in the postshock region is proportional to r^9 (the Sedov similarity solution). However, MS show that the density falls off more slowly behind the shock than r^9, resulting in an X-ray spectrum with characteristic temperature $2T_s$. In this case, we would deduce a shock velocity of 280 km s^{-1} from the X-ray spectrum. The optical expansion velocity may then represent a slower shock driven into denser clouds of a two-phase interstellar medium. The shock velocity into the clouds v_c is related to the intercloud shock velocity v_s by $(v_c/v_s)^2 = n_0/n_c$, where n_c is the cloud density. Cloud densities near the Cygnus Loop are $n_c \approx$ 5–10 cm^{-3}. With $v_c = 100$ km s^{-1} and $v_s = 280$ km s^{-1}, we deduce $n_0 \approx 1$ cm^{-3}, entirely consistent with the density required to reproduce the X-ray luminosity (Cox 1972*b*). These values of n_0 and v_s are consistent with a present size of 20 pc only if $E_0 \approx 10^{51}$ ergs ($E_0 = 5.7 \times 10^{-24} R^3 n_0 v_s^2$ for the Sedov phase of expansion).

In conclusion, the present H I observations show clouds with densities 5–10 cm^{-3} adjacent to the optical filaments of the Cygnus Loop, and place an upper limit of 340 $M_\odot$ on the mass of a cool H I shell. These data are best reconciled with the X-ray luminosity and optical expansion velocity if the SNR is adiabatically expanding into a two-phase medium.

I am grateful for financial support under an NSF grant.

REFERENCES

Assousa, G. A., Balick, B., and Erkes, J. W. 1973, *Bull. AAS*, **5**, 410.
Assousa, G. A., and Erkes, J. W. 1973, *A.J.*, **78**, 885.
Borken, R. 1974, private communication.
Burton, W. B., and Verschuur, G. L. 1973, *Astr. and Ap. Suppl.*, **12**, 145.
Chevalier, R. A. 1974, *Ap. J.*, **188**, 501 (C).
Cox, D. P. 1972*a*, *Ap. J.*, **178**, 143.
———. 1972*b*, *ibid.*, p. 169.
DeNoyer, L. K. 1974, *A.J.*, **79**, 1253.
Heiles, C. 1969, *Ap. J.*, **156**, 493.
Hollenbach, D., and Salpeter, E. E. 1971, *Ap. J.*, **163**, 155.
Kerr, F. J., and Westerhout, G. 1965, in *Galactic Structure*, ed. A. Blaauw and M. Schmidt (Chicago: University of Chicago Press), p. 167.
Knapp, G. R., and Kerr, F. J. 1974, preprint.
Mansfield, V. N., and Salpeter, E. E. 1973, CRSR 565, Cornell University, Ithaca (MS).
Meng, S. Y., and Kraus, J. D. 1970, *A.J.*, **75**, 535.
Minkowski, R. 1958, *Rev. Mod. Phys.*, **30**, 1058.
Sgro, A. G. 1972, Ph.D. thesis, Columbia University.
Straka, W. C. 1973, *Bull. AAS*, **5**, 392.
Verschuur, G. L. 1974, *Ap. J. Suppl.*, **27**, 65.
Woltjer, L. 1972, *Ann. Rev. Astr. and Ap.*, **10**, 129.

L. K. DeNoyer: Observatory, University of Illinois, Urbana, IL 61801

1975ApJ...196..351C

THE ASTROPHYSICAL JOURNAL, **196**:489–501, 1975 March 1

M78: AN ACTIVE REGION OF STAR FORMATION IN THE DARK CLOUD LYNDS 1630

K. M. STROM AND S. E. STROM
Kitt Peak National Observatory*
LUIS CARRASCO†
University of California, Berkeley; and Kitt Peak National Observatory*
AND
FREDERICK J. VRBA
Steward Observatory, University of Arizona; and Kitt Peak National Observatory*
Received 1974 August 1

ABSTRACT

Several luminous stars in the dark cloud (L1630) containing M78 (NGC 2068) are found to have ages as young as a few times 10^5 years. The properties of the stellar population apparently associated with this dark cloud are investigated; it appears that star formation has taken place over a period of several million years. A significant number of heavily obscured ($A_v \gtrsim 10$ mag) stars has been found in the course of a 2-μ survey of selected regions in the L1630 cloud complex. These objects appear best interpreted as stars of late B and early A spectral type embedded within the dense cloud material. The ratio of total to selective extinction achieves values as high as 5.8 in L1630; furthermore, the ratio of λ4430 band strength to visible extinction is anomalously low in this dense cloud complex.

Subject headings: infrared sources — interstellar extinction — nebulae, individual — pre-main-sequence stars — star formation

I. INTRODUCTION

The region centered on M42 and extending throughout the constellation of Orion has long been recognized as a complex containing a large number of recently formed stellar objects. A great deal of attention has been centered on studies of the Orion Nebula region itself and on more general studies of the larger OB association. Optical studies (Sharpless 1962) of early-type stars have shown that star formation has taken place over a wide range of ages; groups of mean ages 5×10^5 to 5×10^6 years have been isolated as a result of these studies.

More recent radio and infrared studies provide compelling reasons to believe that star formation is actively proceeding at present. Although detailed molecular line studies of the Orion region are far from complete, several areas of particular interest have been isolated. These include:

1. The two dense molecular clouds near the Orion Nebula, OMC 1 and OMC 2 (Gatley *et al.* 1974; Werner *et al.* 1974). The former is centered on the BN complex of point infrared sources and the more extended KL nebula. OMC 2 is centered on a cluster of infrared sources located 12′ northeast of OMC 1. In both cases, we appear to be observing heavily obscured clusters of recently formed stars. There is also reason to believe that the KL complex may contain one or more protostellar objects.

2. The dense molecular cloud associated with the "Orion B" radio continuum source, the obscured H II region NGC 2024 (Tucker, Kutner, and Thaddeus 1973). This region also contains point infrared sources, which probably represent the observable upper main sequence of a recently formed cluster (Grasdalen 1974).

3. The dense molecular cloud near NGC 1999 (Loren, Vanden Bout, and Davis 1973; Tucker *et al.* 1973; Turner, private communication). This reflection nebula, located in the dark cloud complex Lynds 1641, contains the unusual early-type emission variable star V380 Ori (Herbig 1960). If this object is similar to its spectroscopic counterparts, it is probably no older than several times 10^5 years. The cloud also contains a large number of Hα emission objects (Haro 1953) and several Herbig–Haro objects. Again, recent estimates of the age of this class of objects suggest an upper limit of several $\times 10^5$ years.

4. A complex of CO emission in the dark dust cloud Lynds 1630 (Lynds 1962). Low spatial resolution CO maps of this region suggest the presence of a large cloud of material of $n \sim 10^3\ \text{cm}^{-3}$, $M \sim 10^5\ M_\odot$ centered $\alpha = 5^h43^m$ (1950) at $\delta = -1°$ and with a projected size of 13×35 pc at the distance of the cloud. Within this very large molecular cloud are located several local condensations of considerably higher density. Strong CO emission has been found centered on the reflection nebulae NGC 2023 and NGC 2068 (see also Milman *et al.* 1974). Subsequent study of these "hot spots" suggests that they are

---

* Operated by the Association of Universities for Research in Astronomy, Inc., under contract with the National Science Foundation.

† Becario del Consejo Nacional de Ciencia y Tecnología, Mexico; presently at the Instituto Nacional de Astrofisica Optica y Electronica, Tonantzintla, Puebla, Mexico.

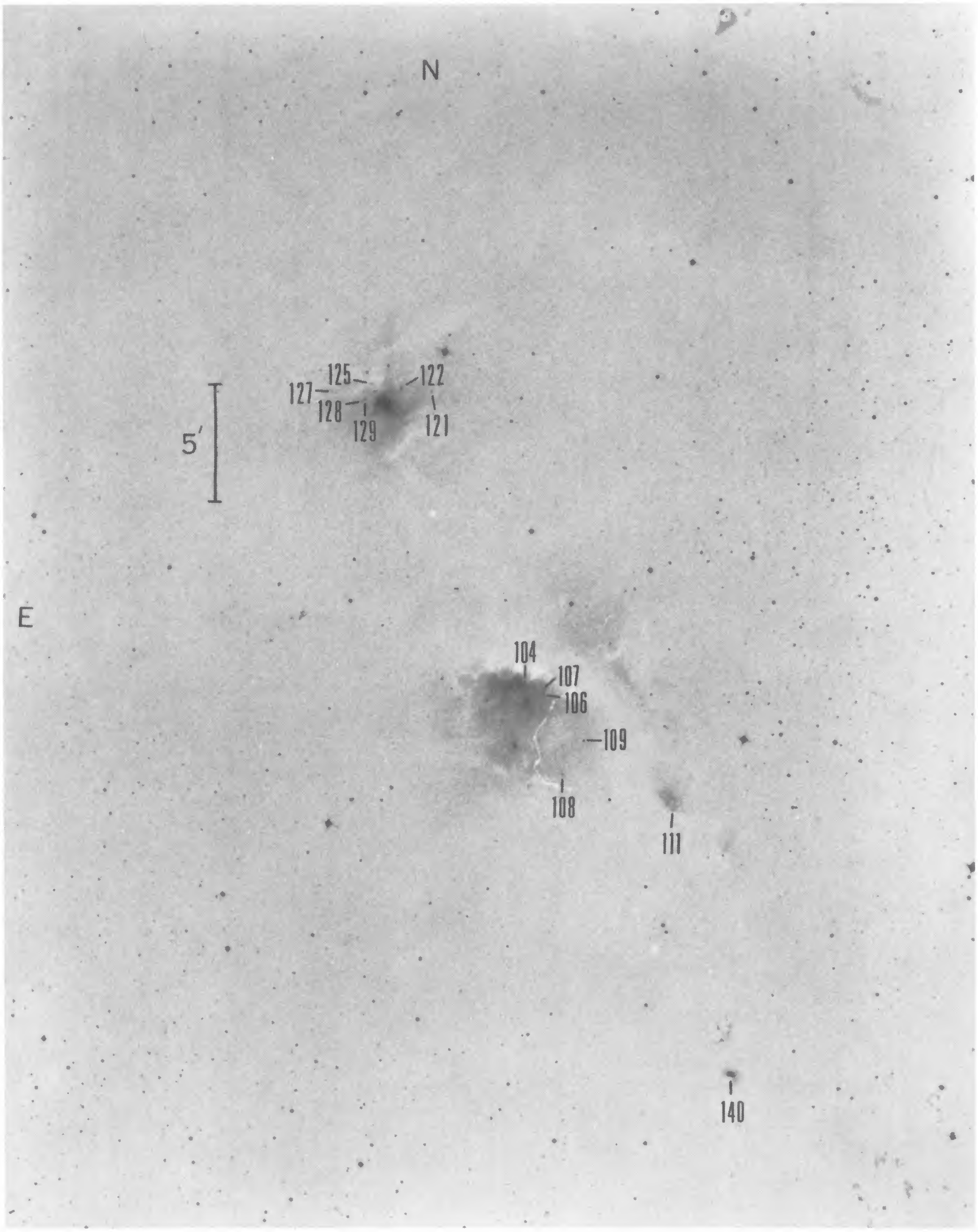

FIG. 1*a*.—A red photograph of the NGC 2068 and NGC 2071 region taken by G. L. Grasdalen of KPNO using the 24-inch Curtis–Schmidt telescope at CTIO; a water-hypersensitized 098-02 emulsion, and an RG-610 filter define the effective bandpass. The stars marked have been observed in the infrared (see text) and appear best interpreted as heavily obscured ($A_v \gtrsim 10$ mag) stars of late B- or early A-type.

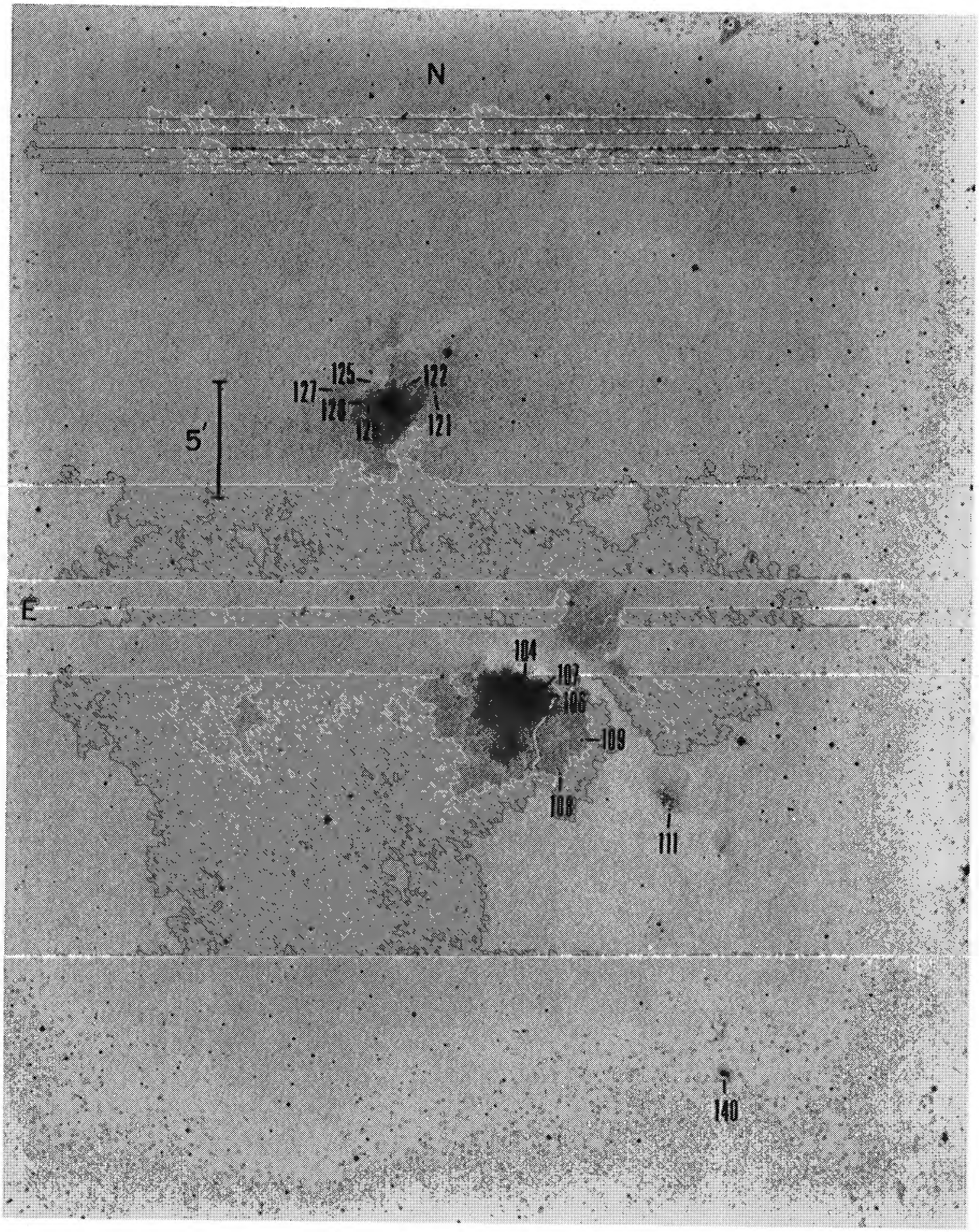

FIG. 1*a*.—A red photograph of the NGC 2068 and NGC 2071 region taken by G. L. Grasdalen of KPNO using the 24-inch Curtis–Schmidt telescope at CTIO; a water-hypersensitized 098-02 emulsion, and an RG-610 filter define the effective bandpass. The stars marked have been observed in the infrared (see text) and appear best interpreted as heavily obscured ($A_v \gtrsim 10$ mag) stars of late B- or early A-type.

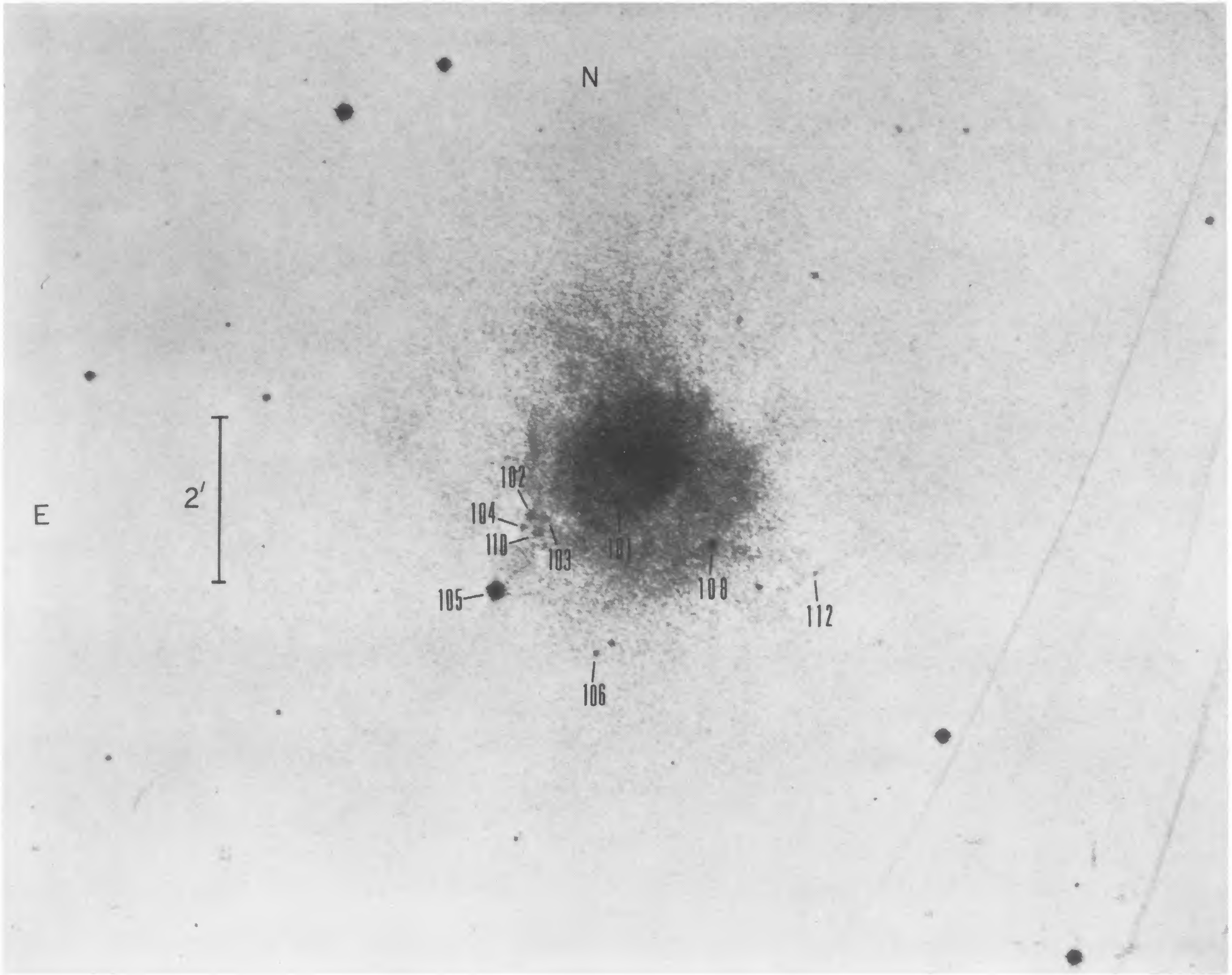

FIG. 1*b*.—The NGC 2023 region. Other remarks as in fig. 1*a*.

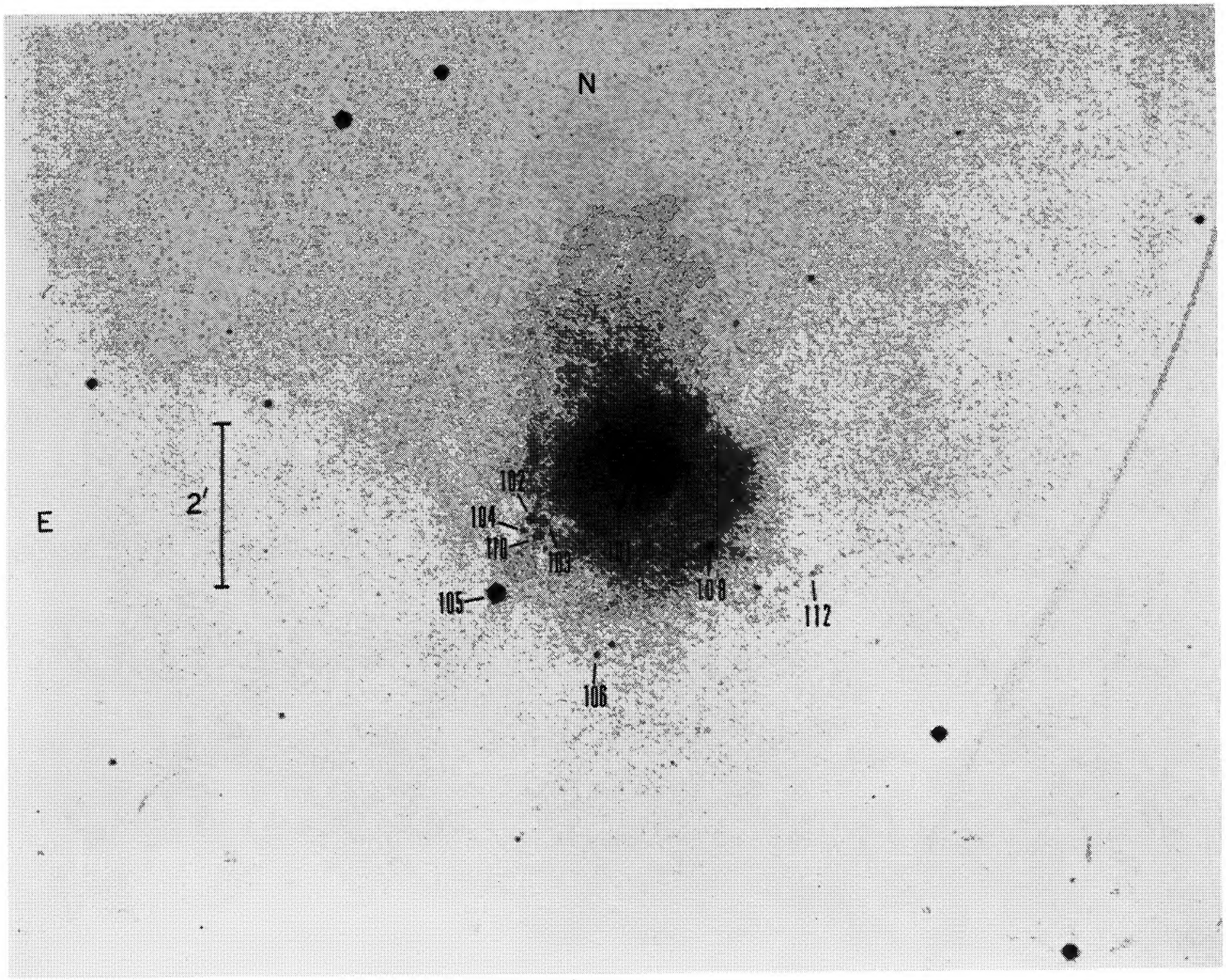

FIG. 1*b*.—The NGC 2023 region. Other remarks as in fig. 1*a*.

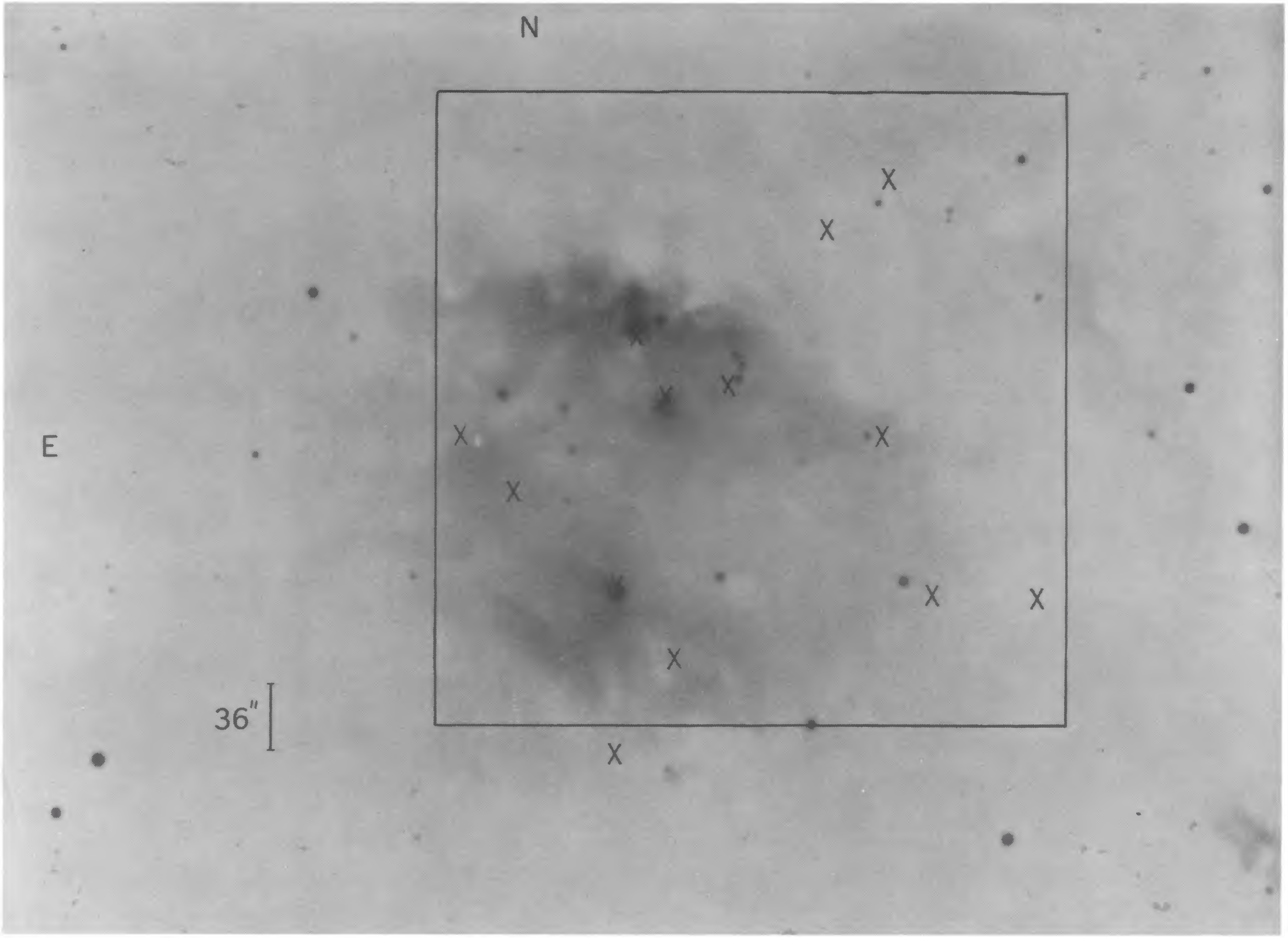

FIG. 2.—An enlargement of a red photograph of the M78 region taken with the 4-m telescope at prime focus, a water-hypersensitized 098-02 emulsion, and an RG-610 filter defined the effective bandpass. We indicate by the ×'s the location of the 2-μ sources found in the course of mapping the M78 region; the solid lines outline the boundaries of the mapped area.

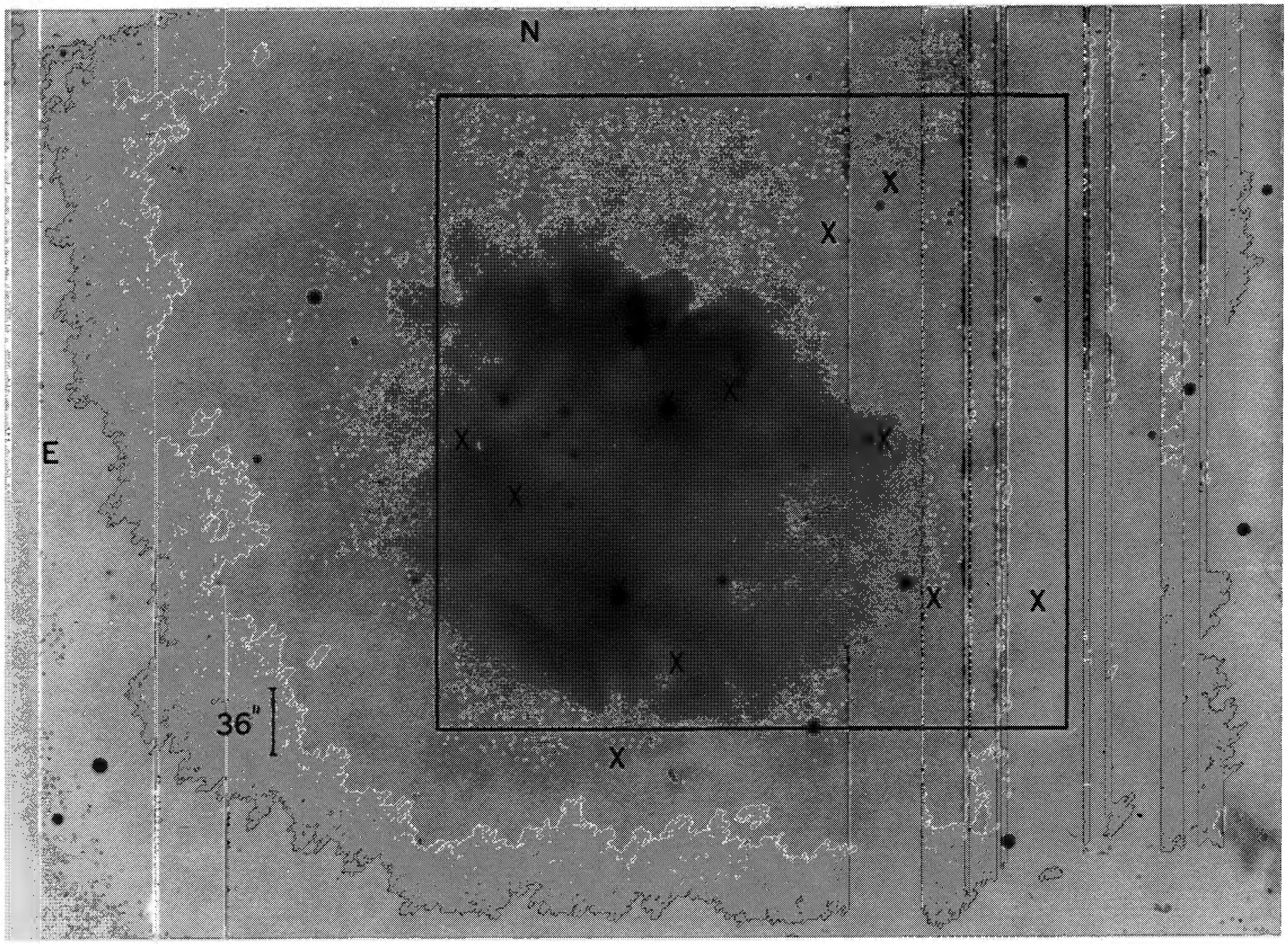

FIG. 2.—An enlargement of a red photograph of the M78 region taken with the 4-m telescope at prime focus, a water-hypersensitized 098-02 emulsion, and an RG-610 filter defined the effective bandpass. We indicate by the ×'s the location of the 2-μ sources found in the course of mapping the M78 region; the solid lines outline the boundaries of the mapped area.

TABLE 2

Photometric Observations of the Orion Population Stars

	m_{pg}	J	H	K	L	Hα Intensity	A_V
LkHα 295	19.0	5.94	4.46	3.90	3.44	m	
298	17.0			9.1	8.5	s	2.4
300	18.0			7.95	6.64	var	4.5
301	16.5			9.0	8.0	w	2.0
302	16.5			10.0		w	1.0
303	18.0			>11.0		s	<1.5
308	18.0			8.4	7.3	m	4.0
310	18.0			9.5	8.3	w	3.0

in M78 first appear at a luminosity almost 2 mag fainter than that observed for spectroscopically similar objects in the general Orion region. Infrared observations should allow us to determine the extent to which this observation results from differences in intrinsic luminosity, circumstellar envelope characteristics, or dark cloud reddening. Our observations of these stars are summarized in table 2 along with the Hα intensities and photographic magnitudes tabulated by Herbig and Kuhi (1963).

Both photographic and near-infrared (2.2 μ) mapping techniques were employed to select objects in category 3. In figures 1*a* and 1*b*, we reproduce a 098-02+RG-610 plate of the M78 region obtained by G. L. Grasdalen with the 24-inch University of Michigan Curtis-Schmidt at Cerro Tololo Inter-American Observatory. Faint objects in the vicinity of the reflection nebulae NGC 2023, 2068, and 2071 were selected for further infrared photometric study. They are identified in figure 1, and the photometry is summarized in table 3. The photometry strongly supports our belief that most of these objects are heavily obscured stars associated with the dark cloud (see § III).

A 2.2-μ map of a region 6′ × 6′ (0.8 × 0.8 pc) centered on NGC 2068 was made with the KPNO 1.3-m telescope and the InSb photometer developed recently by Richard Joyce. A 36″ beam and a 36″ "chopper throw" were used in observing the region; the integration time per mapped point was 60s. A source with $K = 10.5$ is detected at the 3 σ level under these conditions.

TABLE 3

Infrared Observations of Faint Red Stars in the L 1630 Cloud

Star	J	H	K	L	4.8 μ
M78/104			8.83±.07	8.90±.2	
106			9.60		
107			10.00		
108			8.90		
109		9.70	9.40		
111			10.50±.25	9.05±.2	
121			10.00		
122			9.96±.15	9.70±.4	
125			10.70		
127			10.50		
128-9			9.60		
140	9.26	8.62	8.36		
2023/101			9.55±.15	9.50±.5	
102-4			9.40		
105		8.03	7.40±.05	6.42±.05	5.5±.25
106			>10.1 (3σ)		
108			8.53±.10	6.90±.1	5.7±.25
110			9.40		
112			10.60		
HD 37903			7.20	6.96	

Notes: The magnitudes quoted generally have an internal accuracy of ± 0.2 mag. Somewhat larger systematic errors in scale may arise from the fact that many of these data were obtained at large air mass.

Star 140 was observed to have a 10 μ mag of > 7.0 (1 σ).

TABLE 4

Objects Detected in the 2.2 μ Survey

M78 No.	α (1950)	δ (1950)	K	Remarks
1	$5^{\rm h}43^{\rm m}54^{\rm s}.9$	+00°01′47″	9.80	
2	5 43 58.9	+00 01 47	9.40	M78/109
3	5 44 00.9	+00 03 17	9.70	visible star
4	5 44 00.9	+00 05 47	9.00	visible star
5	5 44 02.9	+00 05 17	9.20	H = 10.3
6	5 44 06.9	+00 03 47	8.80	M78/106-107
7	5 44 08.9	+00 01 17	9.80	
8	5 44 09.5	+00 03 33	8.29	HD 38563 S
9	5 44 10.9	+00 04 17	6.65	HD 38563 N
10	5 44 10.9	+00 00 17	8.60	
11	5 44 11.5	+00 01 38	8.68	HD 38563 C
12	5 44 14.9	+00 02 57	9.50	
13	5 44 16.9	+00 03 32	9.50	

Notes: These data were obtained at large air mass; the K magnitudes may be subject to a systematic error as large as 0.3 mag.

The notation "visible star" indicates a possible identification of the 2.2-μ source with a star visible on the 4-m plate.

The positions of the sources are accurate to ± $1^{\rm s}$ in RA and ± 15″ in declination. Accurate astrometric positions are given for HD 38563 N, HD 38563 S, and HD 38563 C.

In figure 2, we identify the point sources discovered in the course of our 2-μ survey. The underlying print is an enlargement of a 4-m telescope photograph of the M78 region obtained with a water-hypersensitized 098-02 plate and an RG-610 filter. The 2-μ source positions and estimated magnitudes are listed in table 4.

III. DISCUSSION

a) The Early-Type Population

The brightest stars associated with the reflection nebulae NGC 2023, NGC 2068 (M78), and NGC 2071 all appear to be extremely young, early-type stars.

HD 38563 N and S and star C, located 3′.3 south of the pair, illuminate NGC 2068 (M78). HD 38563 N is classified (B2(III)), while S is type B3–B5. The star HD 38563 C appears to be a heavily obscured star of high luminosity. Its spectral type, as deduced from a poor-quality spectrogram, is quite uncertain; we have tentatively assigned a type of A0 II. In the cases of HD 38563 N and S, we were able to derive surface gravities from our calibrated spectra; these values are $\log g = 3.4$ and 3.7, respectively. If, as seems likely, these are young stars, ages of $\sim 10^5$ years (N) and 3×10^5 years (S) are derived (Iben 1965).

HDE 290861 illuminates NGC 2071; it is of spectral type B2–B3 and has a surface gravity $\log g = 3.5$ (Strom, Grasdalen, and Strom 1974*b*). An age of 10^5 years is suggested from its location on the theoretical H-R diagram.

HD 37903 (B1.5 V) illuminates NGC 2023. Its location in the $[\beta, (U - B)_0]$-diagram (Crawford and Barnes 1966) suggests that it falls on the zero-age main sequence. If so, a minimum age of 1.5×10^5 years can be assigned to this star.

Our data suggest that the reflection nebulae represent three distinct centers of star formation which became active between 1 and 3 × 10^5 years ago.

The M78 region also appears to contain a probable analog to the Herbig Ae and Be stars associated with nebulosity (Herbig 1960): HD 38238 (A2). Its $K - L$ color suggests the presence of strong circumstellar infrared emission. It is noted as "variable" in the HD catalog, although no comments are available to suggest whether the variability is spectroscopic, photometric, or both. Unfortunately, no data, other than our photometric observations, are available as a further guide to its nature. The infrared magnitudes at longer wavelengths ($5\,\mu$: 5.3 ± 0.2; $8.4\,\mu$: 3.97 ± 0.10; $11.2\,\mu$: 3.76 ± 0.1; and $12.6\,\mu$: 3.55 ± 0.20) provide evidence which supports its membership in the Ae, Be class. Our blue spectrogram reveals no hydrogen or metallic-line emission; unfortunately, no Hα-region spectrograms are available. These characteristics suggest a similarity to AB Aur, although an Hα spectrogram would be necessary to confirm this speculation.

Several early-type stars show clear spectroscopic evidence of giant or subgiant characteristics. Infrared observations show no evidence for circumstellar envelopes; hence, we believe that they are probably analogous to the nonemission, nonvariable A and early F type stars found in NGC 2264 (Walker 1956) and in Orion OB 1 (Walker 1969), which appear to be approaching the main sequence along equilibrium radiative tracks. The reddening of these stars lies between 0.00 and 0.30, while that typical of the Orion cluster near the nebula is ~0.06 mag. It could be argued that the more heavily reddened stars in this group are associated with the dark cloud material in Lynds 1630. However, this argument provides only the most tentative case for identifying these objects as direct evolutionary counterparts to the extremely young stars illuminating the reflection nebulae. Perhaps the most conservative interpretation of the observed characteristics of the visible, early-type stellar population is that (*a*) all the stars are relatively young, having ages no greater than a few million years; and (*b*) a wide representation of stellar ages is found throughout the cloud suggesting either multiple episodes of star formation or continuous formation over several million years.

b) *The Orion Population*

The apparent visual faintness of the Hα-emission objects relative to similar objects in the Orion Nebula cluster (Herbig and Kuhi 1963) seems to arise from the extinction typical of the Lynds 1630 cloud. Typically, variables of the T Tauri type have intrinsic $V - K$ color indices of 4.0 (Mendoza 1966). In table 2, we list the visual extinction predicted from the assumption that $V - K = 4.0$ and $V - m_{\rm pg} \sim 1.5$. These extinction values are quite consistent with the range found throughout Lynds 1630. Moreover, the $K - L$ color indices appear to be consistent with the mean values of 0.8 characteristic of these objects. Hence, the shape of the infrared spectral energy distribution appears normal for stars of this type. Therefore, no strong case can be made to argue in favor of intrinsic luminosity differences between these objects and their unobscured counterparts near the Orion Nebula cluster.

c) *The Embedded Stellar Populations*

CO observations of the Lynds 1630 region suggest a characteristic minimum density of $n_{\rm H_2} \sim 10^3$ cm^{-3}. If the cloud depth is comparable to its projected size on the plane of the sky (15 pc), then the minimum extinction through the cloud is ~10 mag at V, if a standard interstellar gas/dust ratio is assumed. Unfortunately, Lynds 1630 has yet to be surveyed thoroughly in molecular transitions requiring higher densities for excitation. However, a region centered on the Herbig–Haro object (H-H 24) was recently found by Lada *et al.* (1974) to have a minimum density of ~10^4 cm^{-3}; hence, it is reasonable to assume that regions having densities higher than 10^3 and hence visual extinctions greater than 15 mag may be found elsewhere in the cloud.

Reference to table 4 reveals 13 sources brighter than $K = 10.0$ in a region $6' \times 6'$ centered on NGC 2068. Most of these sources cannot be identified with optically visible stars brighter than $R \sim 16.0$. Hence, we can rule out identifying these sources with late-type *foreground* stars since the brightest would have $K \sim 12.0$.

We next explore the possibility that the detected stars are background to Lynds 1630. Let us assume a mean cloud extinction of 10.0 mag at V, or 1.0 mag at K. We then compute (Allen 1963) the expected number of stars brighter than $K = 9.0$ (corresponding to an observed, obscured K magnitude of 10.0) in the direction of this cloud within a $6' \times 6'$ area to be smaller than 2. Hence, it is most likely that we are observing a group of heavily obscured stars embedded *within* Lynds 1630. These same arguments apply to the faint ($R \gtrsim 16.0$) visible stars selected in figures 1*a* and 1*b*; they too must be stars embedded in Lynds 1630. The few $H - K$ and $K - L$ color indices observed for the sources listed in tables 3 and 4 suggest extinction values of between 10 and 20 mag at V. If the sources listed in tables 3 and 4 are obscured by this amount, we conclude that their absolute K magnitudes range from ~1.0 to −1.0. These stars are therefore likely to be embedded objects of late B or early A type associated with the more luminous young stellar objects which illuminate NGC 2023, NGC 2068, and NGC 2071. These tight clusters are reminiscent of those young stellar groups associated with O stars (Sharpless 1954), and the infrared clusters found in OMC 1 and OMC 2. It is also possible that some of these objects are members of the Orion population. Unfortunately, we have not yet observed these sources at longer wavelengths and therefore cannot state how many of them possess infrared-emitting circumstellar envelopes.

Four embedded objects are worthy of further comment. The first is the infrared source associated with

H-H 24, which has been discussed recently by Strom *et al.* (1974*b*) and by Strom, Strom, and Kinman (1974*a*). A visual extinction of 20–30 mag seems plausible from the measurements reported by Strom *et al.* (1974*b*). If we assume this H-H star to be embedded in a cloud condensation of size ~1 pc (Lada *et al.* 1974), then the predicted minimum density is ~2000–3000 cm^{-3}, a value roughly consistent with the collision rates required to excite the observed molecular transitions. It would appear that this source is a very young object still closely associated with the subcondensation responsible for its formation.

The star labeled 140 in figure 1*a* is involved in an unusual reflection nebula and lies near the center of the apparent density peak in the Lada *et al.* 2-mm H_2CO map of the H-H 24 region. We classify the star as an M2–M4 giant; Hα and Hβ are weakly in emission. Star 140 is therefore most likely a late, T Tauri–like star. Its infrared colors are consistent with very small reddening and no discernible excess. If it is indeed unreddened, we predict $V \sim 12.5$ and $R \sim 11.0$ from Johnson's (1966) intrinsic colors for stars of this type. A Hubble-type relation between angular size for reflection nebulae and the apparent red magnitude of the illuminating stars has been derived by Dorschner and Gürtler (1966). From their relation, we predict a diameter of about 50″ for the reflection nebula around star 140; the maximum extent of the nebula is about 70″, which we regard as reasonable agreement. It is somewhat surprising that no infrared excess out to 2.2 μ is observed despite the presence of Hα and Hβ emission. However, we have noted (Strom, Strom, and Rydgren, unpublished) that late-type stars of the Orion population often have very weak infrared excesses.

LkHα 295 is an unusually strong infrared source, a fact noted first by D. Allen (private communication). Herbig and Kuhi (1963) note that it appears "very red." Because the absolute K magnitude is approximately -4.5, it is probably a reddened, early-type emission star analogous to the Herbig Ae and Be stars associated with nebulosity; if its colors are typical of stars of this type, A_v lies between 7 and 12 mag and $M_v \sim -1$ to -2.

Star 111 apparently illuminates a faint patch of reflection nebulosity and appears similar to Grasdalen, Strom, and Strom (1973) source 1 in Ophiuchus and to IC 2087 (Allen 1972). Its $K - L$ color suggests a formal value of extinction in excess of 30 mag; however, the error in this index is sufficiently large to render this determination very uncertain. The star illuminating the reflection nebula could be as early in type as B5 and as late as A0. On the other hand, S 111 may be an unrecognized member of the Orion population with larger intrinsic $K - L$ and consequent smaller extinction.

d) *The Dark Cloud Environment*

The density of the L1630 cloud, $n \gtrsim 10^3\ \text{cm}^{-3}$, suggests that an observable increase in grain size could take place as a consequence of accretion of heavy elements in the gas by the dust particles (Carrasco, Strom, and Strom 1973; Strom, Strom, and Carrasco 1974*c*). Some evidence (Grasdalen 1974; Vrba *et al.* 1975) suggests that ice mantles are produced on the grains in dense, dark cloud regions. Thus far, however, the observations serve only to support the idea that the mean particle size increases in dark cloud complexes. The nature of the mantle acquired by the particles in dark clouds is as yet not firmly established.

Grain growth results in an increase in the observed ratio of total to selective extinction and in the wavelength of maximum polarization. In table 1, we list stars in M78 for which we have estimated values of R from $R \sim 1.1\ E_{VK}/E_{BV}$. These values, given for the most heavily obscured stars, range from 3.6 to 5.8; the mean interstellar value is 3.1. Hence, our observations strongly suggest an increase in particle size in some regions of L1630. Polarimetric measurements by Coyne, Gehrels, and Serkowski (1974) for HD 38563 N, HD 38563 S, HD 38563 C, and HD 37093 yield $\lambda_{\max}$ values of 1.03, 0.63, 0.62, and 0.69 μ, respectively; the $\lambda_{\max}$ typical of the interstellar medium is 0.55 μ. Hence, these data lend additional support to the grain growth hypothesis.

e) *The λ4430 Diffuse Band*

Wampler (1966), Snow and Cohen (1974), and Strom *et al.* (1974*c*) have noted that the strength of the λ4430 diffuse interstellar band is unusually weak (per unit extinction) in dense, dark clouds. Since the agent responsible for this feature has yet to be identified, it is not clear what change in physical conditions is responsible for the observed weakness in dense regions. However, if the grains are carriers, we note that their increased size may affect the shape and/or strength of the λ4430 profile; moreover, the grain mantle may not contain the λ4430 "carrier." If a molecule is the responsible agent, the high density in these regions may shift the molecular equilibrium so that the species producing λ4430 is no longer sufficiently abundant.

We have derived λ4430 strengths from our Carnegie image-tube spectrograms of three of the most heavily

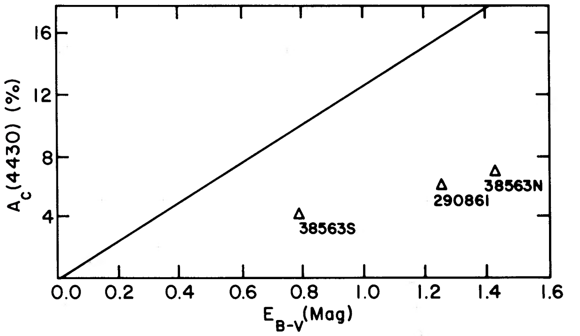

FIG. 3.—A plot of the mean relation between the central intensity of the diffuse interstellar feature at λ4430 and E_{BV} (see Snow and Cohen 1974). The observed locations in this plot of three heavily obscured stars in the M78 region are indicated by the open triangles.

1975ApJ...196..351C

obscured stars in the L1630 complex: HD 38563 N, HD 38563 S, and HDE 290861. In figure 3, we reproduce Snow and Cohen's mean relation between λ4430 central depth and E_{BV} for stars in the general interstellar medium. We have superposed our measurements for the three L1630 stars on this plot. Despite our estimated error of ±2 percent in A_c, it seems clear that the behavior of λ4430 in the dense L1630 complex is similar to that found in other dark clouds.

f) *The Reflection Nebulae*

We have noted already the presence of partially obscured clusters of early-type stars in the vicinity of the three reflection nebulae. It may be that these clusters are observed because the reflection nebulae represent the centers of these subclusterings in the L1630 region. However, it is also possible that the more luminous stars, responsible for producing the reflection nebulae, have also altered the dark cloud environment so that these clusters are partially visible; stellar winds may be responsible for driving out dark cloud material in the vicinity of these clusters. There is growing evidence that most, if not all, stars develop strong stellar winds sometime during their pre–main-sequence evolutionary phases. A typical value for mass loss rate for Orion population variables and Herbig Ae and Be stars associated with reflection nebulosity is $\sim 10^{-7}\ M_{\odot}\ \mathrm{yr}^{-1}$. The typical outflow velocities are $\sim 200\ \mathrm{km\ s}^{-1}$. This value applies during the phases of their evolution after they have emerged from their "cocoon" clouds. However, there is some evidence (Strom *et al.* 1974*b*) that values of mass loss a factor of 10 larger may be found at earlier stages of evolution such as the H-H phase. A crude static analysis suggests that in a cloud of density $10^3\ \mathrm{cm}^{-3}$ regions of order 0.1 pc in size can be swept clean by stellar winds of this magnitude. We note that this corresponds to $\sim 0\rlap{.}'7$ at the distance of L1630. It is noteworthy that multiple velocity systems have been observed (Tucker *et al.* 1973) in the direction of NGC 2023 and NGC 2068 suggesting, perhaps, recent interaction between the embedded stars and the cloud medium.

Radiation pressure may also be effective in clearing out small regions near the luminous stars. The radius at which radiation pressure from the embedded stars is balanced by the pressure of the dark cloud medium is

$$R_{\mathrm{RP}} = 2.0 \times 10^2 (L/Tn)^{1/2} ,$$

where L is in units of $L_{\odot}$. However, because the optical depth of the cloud medium is large, particularly in the ultraviolet, the dust and gas can be accelerated outward only after τ is reduced, probably by grain evaporation. Because the opacities and evaporation temperature of the grains are uncertain, we have not estimated the time scale for creating a transparent shell around the star.

Our main point is that stellar winds, for a wide range in stellar masses, and possibly radiation pressure for more luminous stars or stellar clusters, may play a significant role in affecting the dark cloud environment and in rendering recently formed clusters visible either optically or at near-infrared wavelengths.

The presence of recently formed stars or clusters embedded in dark clouds should also be noticeable in radio molecular surveys for the following reasons: (1) The embedded stars heat the grains which then, by collision with H_2 molecules, heat the gas (Loren *et al.* 1973). Hence, CO "hot spots," local regions of apparently elevated kinetic temperature, may well be indicators of embedded clusters. (2) The local velocity field may be affected by pre–main-sequence stars. High spatial resolution studies may show that regions surrounding objects having strong, observable stellar winds have higher velocity dispersions than is typical of the surrounding dark cloud environment. It is appealing to interpret the double velocity systems and increased velocity widths observed in CO by Loren *et al.* (1973) near several Herbig Ae and Be stars as resulting from the interaction of the stellar wind and the dark cloud medium. Certainly, it is possible that local increases in velocity dispersion observed in molecular transitions may be caused, in part, by stellar-wind/dark-cloud interactions.

III. CONCLUSIONS

The results of this study can be summarized as follows:

1. The Lynds 1630 cloud appears to be a region in which star formation has been active for several million years; the most recent episode of star formation may have taken place no more than a few times 10^5 years ago.
2. The visible Orion population variables presently located near the surface of the dark cloud seem to have normal optical and infrared properties, although further study of this point seems warranted.
3. The cloud appears to be similar to the Ophiuchus complex in that an extensive number of embedded stars have been found in the course of a 2-μ survey of the region. The embedded population seems to encompass the range of types from extremely young "H-H stars" to objects which are most likely heavily obscured stars of B to early A spectral type.
4. Several stars in L1630 are observed to have high values of R, the ratio of total to selective extinction. We regard this as evidence of grain growth, which results either from accretion of the heavy elements in the gas onto the grains, or growth of ice mantles on the grains. This behavior is enhanced in high-density, dark cloud environments because of the increased rate of grain-gas collisions.
5. The λ4430 diffuse band is anomalously weak compared with typical interstellar conditions for stars suffering a similar amount of visual extinction. This behavior is again typical of dense, dark cloud complexes.
6. The more luminous members of recently formed clusters of stars may significantly affect the dark cloud

environment by (*a*) heating the nearby grains and hence the gas, thereby producing local increases in the gas kinetic temperature, and (*b*) sweeping out the nearby dark cloud material by virtue of the strong stellar winds characterizing most pre–main-sequence objects, or possibly by the action of radiation pressure on the grains for the more luminous objects.

We wish to thank Drs. G. Grasdalen and R. Chevalier of Kitt Peak National Observatory for several stimulating and informative discussions. The contributions of Dr. R. Joyce of KPNO, who has developed a first-class InSb infrared system, are worthy of particular note. We thank him both for his generosity of spirit and his technical advice.

REFERENCES

Allen, C. W. 1963, *Astrophysical Quantities* (London: Athlone Press).
Allen, D. A. 1972, *Ap. J.* (*Letters*), **172**, L55.
Carrasco, L., Strom, S. E., and Strom, K. M. 1973, *Ap. J.*, **182**, 95.
Coyne, G. V., S.J., Gehrels, T., and Serkowski, K. 1974, *A.J.*, **79**, 581.
Crawford, D. L., and Barnes, J. V. 1966, *A.J.*, **71**, 610.
Dorschner, J., and Gürtler, J. 1966, *Astr. Nachr.*, **289**, 57.
Fedorovich, V. P. 1960, *Variable Stars*, **13**, 166.
Gatley, I., Becklin, E. E., Matthews, K., Neugebauer, G., Penston, M. V., and Scoville, N. 1974, *Ap. J.* (*Letters*), **191**, L121.
Grasdalen, G. L. 1973, *Ap. J.*, **182**, 781.
———. 1974, *ibid.*, **193**, 373.
Grasdalen, G. L., Strom, K. M., and Strom, S. E. 1973, *Ap. J.* (*Letters*), **184**, L53.
Haro, G. 1953, *Ap. J.*, **117**, 73.
Herbig, G. H. 1960, *Ap. J. Suppl.*, **4**, 337.
———. 1974, *Lick Obs. Bull.*, No. 658.
Herbig, G. H., and Kuhi, L. V. 1963, *Ap. J.*, **137**, 398.
Iben, I., Jr. 1965, *Ap. J.*, **141**, 993.
Johansson, L. E. B., Höglund, B., Winnberg, A., Nguyen-Q-Rieu, and Goss, W. M. 1974, *Ap. J.*, **189**, 455.
Johnson, H. L. 1966, *Ann. Rev. Astr. and Ap.*, **4**, 193.
Lada, C. J., Gottlieb, C. A., Litvak, M. M., and Lilley, A. E. 1974, *Ap. J.*, **194**, 609.
Loren, R. B., Vanden Bout, P. A., and Davis, J. H. 1973, *Ap. J.* (*Letters*), **185**, L67.
Lynds, B. T. 1962, *Ap. J. Suppl.*, **7**, 1.
Mendoza, E. E. 1966, *Ap. J.*, **143**, 1010.
Milman, A. S., Knapp, G. R., Kerr, F. J., Knapp, S. L., and Wilson, W. J. 1974, *Ap. J.*, in press.
Rosino, L. 1960, *Contr. Asiago*, No. 109.
Sharpless, S. 1954, *Ap. J.*, **119**, 334.
———. 1962, *ibid.*, **136**, 767.
Snow, T., and Cohen, J. G. 1974, *Ap. J.*, **194**, 313.
Strom, K. M., Strom, S. E., and Kinman, T. D. 1974*a*, *Ap. J.* (*Letters*), **191**, L93.
Strom, S. E., Grasdalen, G. L., and Strom, K. M. 1974*b*, *Ap. J.* **191**, 111.
Strom, S. E., Strom, K. M., and Carrasco, L. 1974*c*, *Pub. A.S.P.*, **86**, 798.
Tucker, K. D., Kutner, M. L., and Thaddeus, P. 1973, *Ap. J.* (*Letters*), **186**, L13.
Vrba, F. J., Strom, K. M., Strom, S. E., and Grasdalen, G. L. 1975, *Ap. J.*, in press.
Walker, M. F. 1956, *Ap. J. Suppl.*, **2**, 365.
Walker, M. F. 1969, *Ap. J.*, **155**, 447.
Wampler, E. J. 1966, *Ap. J.*, **144**, 921.
Werner, M. W., Elias, J. H., Gezari, D. Y., and Westbrook, W. E. 1974, *Ap. J.* (*Letters*), **192**, L31.

LUIS CARRASCO: Instituto Nacional de Astrofísica Optica y Electronica, Apartados Postales 51 y 216, Puebla, Puebla, Mexico

KAREN M. STROM and STEPHEN E. STROM: Kitt Peak National Observatory, P.O. Box 26732, Tucson, AZ 85726

FREDERICK J. VRBA: Steward Observatory, University of Arizona, Tucson, AZ 85721

1975ApJ...196..351C

THE ASTROPHYSICAL JOURNAL, **196**:503–513, 1975 March 1

THE BALMER DISCONTINUITIES OF O9–B2 SUPERGIANTS

R. E. SCHILD AND F. H. CHAFFEE
Center for Astrophysics, Harvard College Observatory and Smithsonian Astrophysical Observatory
Received 1974 July 19; revised 1974 September 9

ABSTRACT

New energy distributions of supergiants at 50 Å resolution from λλ3200–8000 show that the Balmer discontinuities are poorly correlated with spectral types. A particularly good example is ε Ori, whose Balmer discontinuity is 0.1 mag larger than other O9.5 Ia and B0.5 Ia supergiants. Analysis of available four-color and Hβ photometry shows that whereas Hβ correlates well with luminosity as indicated by MK luminosity class, the Balmer discontinuity does not.

Our energy distributions show that several O9.5–B0.5 Ia supergiants have Balmer discontinuities in emission on the Palomar system of absolute calibration. They appear to be continuous across the Balmer discontinuity on the calibration of Hayes.

Subject headings: atmospheres, stellar — early-type stars — luminous stars — spectrophotometry

I. INTRODUCTION

The hot supergiants are among the most poorly understood stars with respect to our knowledge of masses, effective temperatures, dimensions, and atmospheric surface effects. The reasons for this fact are well known: Most supergiants are very distant and reddened and are blowing off their atmospheres at high supersonic velocities. Thus, our ability to measure their intrinsic energy distributions or to compute stellar models for them is severely hampered.

We present observations of OB supergiants made in conjunction with a program for the synthesis of energy distributions of young clusters. In the course of dereddening the fluxes, we have found that the energy distributions are of sufficient intrinsic interest to be worthy of separate discussion.

II. OBSERVATIONS

Energy distributions of the OB supergiant standards of the MK system were measured with the Latham grating spectrometer on the Mount Hopkins 60-inch (1.5 m) Tillinghast reflector. A 50 Å bandpass was used throughout, and the blue and red portions of the spectra were measured on separate nights. Nightly extinction coefficients were computed and applied to our data. The data are reported on the absolute calibration system of Oke and Schild (1970) and are believed to be accurate to ±0.02 mag at all wavelengths except 8000 Å.

All energy distributions have been corrected for interstellar extinction by the use of the interstellar reddening law of Radick (1973) and Hayes *et al.* (1973). Because Hayes *et al.* and Radick based their results on Whiteoak's (1966) data, which extend only to λ3448, we have had to extend the reddening law for our data to shorter wavelengths with procedures similar to theirs. The observed and corrected fluxes are listed in table 1. We have made no corrections for blocking in our treatment of the data, because such corrections rarely exceed 2 percent for the hot stars and because we make no comparisons with unblanketed models.

III. BALMER DISCONTINUITIES OF THE SUPERGIANTS

In figure 1, we compare our dereddened energy distributions for the O9.5 Ia supergiants α Cam and HD 195592 to the blanketed model atmospheres (25,000, 3.5) of Kurucz, Peytremann, and Avrett (1974). Comparison with a lower surface-gravity model would be preferable, but such models do not exist, owing to the well-known radiation-pressure problem. Here, we do not propose to determine the effective temperatures and gravity of the supergiants; rather, we wish only to show that the Balmer discontinuity appears in *emission* in the two O9.5 Ia supergiants. This is made clear in figure 1 by the dashed line, a smooth extrapolation of the continuum for $\lambda > 4000$ Å with the same slope as the Balmer continuum of the model.

We caution that the appearance of a Balmer discontinuity in emission may be, at least in part, an artifact of the absolute calibration, which still must be considered uncertain across the Balmer discontinuity. Adoption of the calibration of Hayes (1970) gives energy distributions that are continuous across the Balmer jump. Recent calculations by Mihalas and Hummer (1974) of non–LTE spherically extended static atmospheres for $T_{\rm eff} \approx 39{,}500^\circ$ K and $\log g = 3.5$, with a variety of treatments to account for radiation pressure, all show a Balmer jump in absorption. While our stars are presumably cooler than the Mihalas and Hummer (1974) models, they are similarly far from LTE and we would expect to find Balmer jumps in absorption. It is of course well known that supergiants have expanding atmospheres and that the region below the Balmer discontinuity is formed in a relatively high atmospheric layer. These facts suggest that the atmospheric expansion affects the atmospheric structure and continuum formation, and we eagerly await the development of models that incorporate expansion.

TABLE 1

		HD 1383		HD 14143		HD 30614		HD 43818	
λ	1/λ	Observed	Dereddened	Observed	Dereddened	Observed	Dereddened	Observed	Dereddened
3200	3.13	0.34	-0.37	0.70	-0.26	-0.10	-0.44	0.26	-0.50
3250	3.08	0.31	-0.38	0.65	-0.28	-0.11	-0.44	0.22	-0.52
3300	3.03	0.21	-0.43	0.58	-0.29	-0.14	-0.45	0.17	-0.52
3350	2.99	0.25	-0.35	0.55	-0.27	-0.11	-0.40	0.18	-0.47
3400	2.94	0.18	-0.39	0.51	-0.26	-0.14	-0.41	0.15	-0.46
3450	2.90	0.16	-0.37	0.47	-0.25	-0.14	-0.40	0.12	-0.45
3500	2.86	0.15	-0.36	0.45	-0.24	-0.13	-0.37	0.13	-0.42
3571	2.80	0.18	-0.28	0.43	-0.19	-0.09	-0.31	0.14	-0.35
3636	2.75	0.16	-0.26	0.40	-0.17	-0.08	-0.28	0.13	-0.32
4036	2.48	0.05	-0.17	0.15	-0.14	-0.04	-0.14	0.05	-0.18
4167	2.40	0.04	-0.09	0.10	-0.08	-0.02	-0.08	0.04	-0.10
4255	2.35	0.03	-0.08	0.08	-0.07	-0.01	-0.06	0.03	-0.09
4464	2.24	0.00	0.00	0.00	0.00	0.00	0.00	0.00	0.00
4566	2.19	0.00	0.04	-0.01	0.04	0.02	0.04	-0.01	0.03
4780	2.09	-0.02	0.10	-0.09	0.07	0.07	0.13	-0.03	0.10
5000	2.00	-0.04	0.20	-0.15	0.17	0.09	0.20	-0.05	0.21
5263	1.90	-0.11	0.27	-0.29	0.22	0.12	0.30	-0.10	0.31
5556	1.80	-0.14	0.36	-0.37	0.31	0.14	0.38	-0.12	0.42
5840	1.71	-0.12	0.47	-0.41	0.39	0.18	0.46	-0.13	0.50
6050	1.65	-0.11	0.53	-0.43	0.44	0.21	0.52	-0.13	0.56
6430	1.56	-0.09	0.65	-0.46	0.54	0.27	0.63	-0.12	0.67
6821	1.47	-0.10	0.74	-0.51	0.63	0.31	0.72	-0.14	0.76
7102	1.41	-0.10	0.80	-0.54	0.68	0.36	0.79	-0.14	0.83
7530	1.33	-0.09	0.90	-0.59	0.75	0.40	0.88	-0.13	0.93
7780	1.29	-0.11	0.93	-0.57	0.83	0.41	0.91	-0.14	0.97
8060	1.24	-0.09	0.99	-0.60	0.86	0.45	0.97	-0.13	1.03

TABLE 1—*Continued*

		HD 190919		HD 192422		HD 194839		HD 195592	
λ	1/λ	Observed	Dereddened	Observed	Dereddened	Observed	Dereddened	Observed	Dereddened
3200	3.13	0.31	-0.28	0.69	-0.40	1.28	-0.41	1.10	-0.41
3250	3.08	0.28	-0.29	0.63	-0.42	1.20	-0.44	1.01	-0.45
3300	3.03	0.24	-0.30	0.57	-0.42	1.10	-0.44	0.92	-0.45
3350	2.99	0.24	-0.26	0.55	-0.38	1.05	-0.39	0.88	-0.41
3400	2.94	0.21	-0.26	0.48	-0.39	0.97	-0.38	0.80	-0.41
3450	2.90	0.18	-0.27	0.45	-0.37	0.90	-0.38	0.74	-0.40
3500	2.86	0.19	-0.23	0.43	-0.35	0.86	-0.35	0.70	-0.38
3571	2.80	0.20	-0.18	0.42	-0.29	0.81	-0.29	0.66	-0.32
3636	2.75	0.19	-0.16	0.39	-0.26	0.75	-0.26	0.61	-0.29
4036	2.48	0.04	-0.14	0.15	-0.18	0.35	-0.17	0.30	-0.16
4167	2.40	0.03	-0.08	0.10	-0.11	0.24	-0.08	0.21	-0.08
4255	2.35	0.01	-0.08	0.06	-0.11	0.17	-0.10	0.15	-0.09
4464	2.24	0.00	0.00	0.00	0.00	0.00	0.00	0.00	0.00
4566	2.19	-0.01	0.02	-0.02	0.04	-0.06	0.03	-0.06	0.02
4780	2.09	-0.05	0.05	-0.09	0.09	-0.24	0.04	-0.20	0.05
5000	2.00	-0.06	0.14	-0.14	0.23	-0.40	0.17	-0.36	0.15
5263	1.90	-0.10	0.21	-0.27	0.31	-0.65	0.25	-0.56	0.24
5556	1.80	-0.12	0.30	-0.38	0.39	-0.85	0.35	-0.75	0.32
5840	1.71	-0.10	0.39	-0.43	0.47	-1.00	0.41	-0.88	0.37
6050	1.65	-0.09	0.45	-0.45	0.54	-1.08	0.46	-0.95	0.42
6430	1.56	-0.07	0.55	-0.00	–	-1.21	0.56	-1.06	0.52
6821	1.47	-0.08	0.62	-0.51	0.78	-1.40	0.61	-1.23	0.56
7102	1.41	-0.08	0.67	-0.54	0.85	-1.47	0.68	-1.27	0.65
7530	1.33	-0.05	0.77	-0.55	0.97	-1.55	0.81	-1.37	0.73
7780	1.29	-0.04	0.82	-0.58	1.01	-1.61	0.87	-1.41	0.80
8060	1.24	-0.04	0.86	-0.60	1.06	-1.70	0.88	-1.49	0.81

TABLE 1—*Continued*

λ	1/λ	HD 199216		HD 204172		HD 209975		HD 216411	
		Observed	Dereddened	Observed	Dereddened	Observed	Dereddened	Observed	Dereddened
3200	3.13	0.70	-0.35	-0.17	-0.43	0.04	-0.42	0.79	-0.32
3250	3.08	0.62	-0.40	-0.18	-0.43	0.01	-0.43	0.72	-0.36
3300	3.03	0.55	-0.40	-0.20	-0.44	-0.04	-0.46	0.62	-0.39
3350	2.99	0.52	-0.38	-0.18	-0.40	-0.01	-0.40	0.63	-0.32
3400	2.94	0.47	-0.37	-0.19	-0.40	-0.04	-0.41	0.51	-0.38
3450	2.90	0.44	-0.35	-0.18	-0.38	-0.05	-0.40	0.48	-0.36
3500	2.86	0.42	-0.33	-0.16	-0.35	-0.03	-0.36	0.46	-0.34
3571	2.80	0.36	-0.32	-0.13	-0.30	0.00	-0.30	0.43	-0.29
3636	2.75	0.36	-0.26	-0.11	-0.27	0.00	-0.27	0.40	-0.26
4036	2.48	0.10	-0.22	-0.08	-0.16	-0.01	-0.15	0.21	-0.13
4167	2.40	0.06	-0.14	-0.04	-0.09	0.00	-0.09	0.13	-0.08
4255	2.35	0.04	-0.13	-0.03	-0.07	0.00	-0.07	0.09	-0.09
4464	2.24	0.00	0.00	0.00	0.00	0.00	0.00	0.00	0.00
4566	2.19	-0.03	0.03	0.03	0.04	0.01	0.03	-0.02	0.04
4780	2.09	-0.11	0.07	0.07	0.11	0.03	0.11	-0.14	0.05
5000	2.00	-0.17	0.18	0.12	0.21	0.04	0.19	-0.23	0.14
5263	1.90	-0.32	0.24	0.17	0.31	0.04	0.28	-0.37	0.22
5556	1.80	-0.39	0.35	0.21	0.40	0.05	0.38	-0.48	0.31
5840	1.71	-0.41	0.46	0.28	0.50	0.09	0.47	-0.53	0.40
6050	1.65	-0.47	0.48	0.32	0.56	0.12	0.54	-0.57	0.44
6430	1.56	-0.52	0.58	0.39	0.66	0.17	0.65	-0.63	0.53
6821	1.47	-0.54	0.71	0.44	0.75	0.18	0.73	-0.69	0.64
7102	1.41	-0.51	0.83	0.50	0.83	0.21	0.79	-0.75	0.67
7530	1.33	-0.54	0.92	0.58	0.95	0.27	0.91	-0.78	0.78
7780	1.29	-0.56	0.98	0.59	0.97	0.27	0.94	-0.80	0.83
8060	1.24	-0.56	1.04	0.66	1.06	0.32	1.02	-0.83	0.87

TABLE 1—*Continued*

		NGC 581 #3*		NGC 6913 #2		NGC 6913 #3		NGC 6913 #4	
λ	1/λ	Observed	Dereddened	Observed	Dereddened	Observed	Dereddened	Observed	Dereddened
3200	3.13	0.44	-0.25	1.23	-0.40	1.38	-0.33	1.11	-0.46
3250	3.08	0.42	-0.21	1.15	-0.33	1.27	-0.29	1.04	-0.38
3300	3.03	0.37	-0.20	1.05	-0.30	1.17	-0.26	0.92	-0.38
3350	2.99	0.37	-0.17	0.98	-0.32	1.10	-0.27	0.89	-0.35
3400	2.94	0.34	-0.17	0.92	-0.30	1.03	-0.25	0.82	-0.34
3450	2.90	0.33	-0.14	0.87	-0.29	0.95	-0.26	0.77	-0.33
3500	2.86	0.33	-0.11	0.81	-0.29	0.89	-0.25	0.72	-0.32
3571	2.80	0.35	-0.06	0.78	-0.21	0.83	-0.23	0.68	-0.29
3636	2.75	0.33	-0.05	0.70	-0.23	0.80	-0.17	0.63	-0.26
4036	2.48	0.02	-0.17	0.31	-0.16	0.33	-0.16	0.28	-0.16
4167	2.40	0.04	-0.10	0.20	-0.12	0.21	-0.11	0.18	-0.13
4255	2.35	0.01	-0.08	0.15	-0.06	0.16	-0.06	0.12	-0.09
4464	2.24	0.00	0.00	0.00	0.00	0.00	0.00	0.00	0.00
4566	2.19	0.00	0.05	-0.05	0.05	-0.04	0.08	-0.06	0.03
4780	2.09	-0.04	0.08	-0.18	0.10	-0.23	0.06	-0.19	0.08
5000	2.00	-0.05	0.15	-0.32	0.15	-0.37	0.13	-0.31	0.13
5263	1.90	-0.10	0.27	-0.54	0.30	-0.55	0.34	-0.50	0.31
5556	1.80	-0.14	0.32	-0.71	0.34	-0.73	0.38	-0.66	0.35
5840	1.71	-0.10	0.42	-0.79	0.40	-0.85	0.41	-0.74	0.41
6050	1.65	-0.09	0.50	-0.90	0.45	-0.92	0.52	-0.79	0.53
6430	1.56	-0.07	0.61	-0.94	0.64	-1.00	0.66	-0.86	0.67
6821	1.47	-0.06	0.72	-1.02	0.78	-1.12	0.77	-0.96	0.76
7102	1.41	-0.07	0.77	-1.10	0.84	-1.20	0.84	-1.01	0.85
7530	1.33	-0.05	0.86	-1.15	0.95	-1.27	0.94	-1.06	0.95
7780	1.29	-0.04	1.01	-1.20	1.00	-1.31	1.02	-1.09	1.03
8060	1.24	-0.08	1.09	-1.26	1.04	-1.38	1.06	-1.15	1.06

*Numbers are from Hoag et al. (1961).

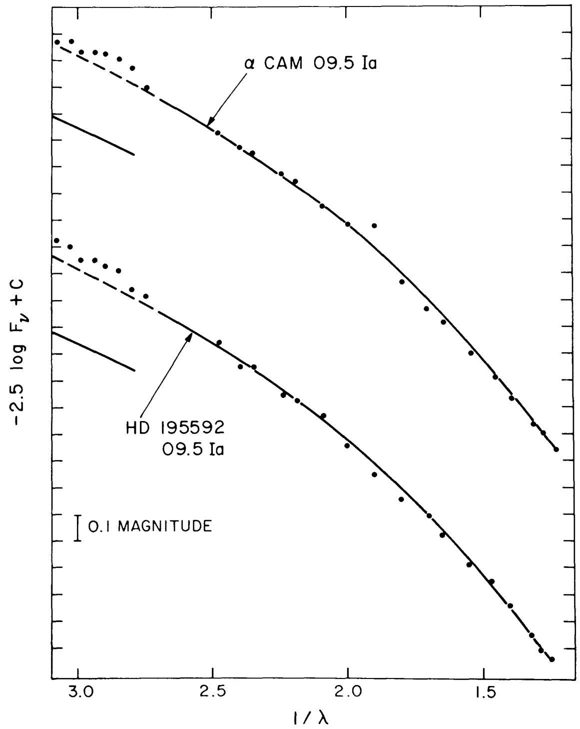

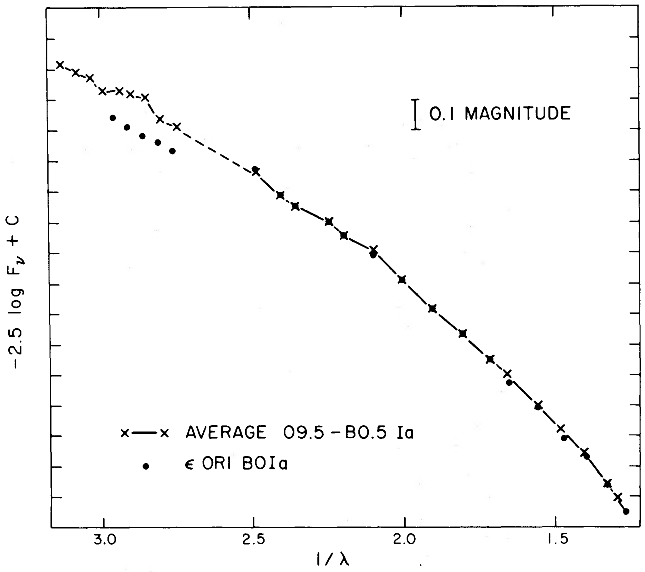

FIG. 1 (*left*).—Energy distribution λλ3200–8000 of two O9.5 Ia supergiants, showing the apparent negative (emission) Balmer discontinuities.

FIG. 2 (*right*).—Energy distribution of ε Ori (B0 Ia) compared with the average for O9.5 Ia–B0.5 Ia stars, showing the significantly more positive Balmer discontinuity.

In figure 2, we compare the energy distribution of ε Ori (B0 Ia) to a mean energy distribution of the three Ia supergiants, α Cam (O9.5 Ia), HD 195592 (O9.5 Ia), and HD 194839 (B0.5 Ia), which have comparable negative Balmer discontinuities and whose average curve is quite smooth. In the Paschen continuum, ε Ori agrees well with the mean curve for the three supergiants; in the Balmer continuum, however, ε Ori is fainter by 0.1 mag. We had expected to find the Balmer discontinuity to increase monotonically with advancing spectral type. We believe ε Ori is a clear exception and but one of several that could be shown to illustrate our general finding that *among the supergiant MK standards, the amounts of the Balmer discontinuities are poorly correlated with spectral type.*

We have chosen to illustrate our point with ε Ori because it is a reasonably certain yet exceptional case. All our Ia supergiants of spectral type B1 and earlier have negative Balmer discontinuities, except for ε Ori, which has a positive discontinuity of 0.06 mag. The data for ε Ori are quite certainly correct: It is one of the original Oke (1964) spectrophotometric standards and has been compared frequently with the others. There is no question of the spectral type of ε Ori, since it has always been a B0 Ia standard and is a fundamental (dagger) standard of the new classifications of Morgan and Keenan (1973). Furthermore, its absolute magnitude is known from its membership in the Ori Ib association; its absolute visual magnitude of −6.8 puts it definitely in the Ia luminosity class.

We list in table 2 the Balmer discontinuities for all the supergiants in table 1, given in order of increasing amount, so as to illustrate further the poor correlation with spectral type. These Balmer discontinuities were estimated by graphically fitting the extrapolated Paschen continuum of Kurucz *et al.*'s (1973) blanketing-corrected models to the dereddened observations of table 1. We used the (25,000, 3.5) model for all stars except the O9.5 and B2 stars, for which we used a (30,000, 3.5) model and a (20,000, 3.0) model, respectively. We have checked the Hayes *et al.* (1973) reddening law with our own data for highly reddened and little reddened supergiants, and we find good agreement. From successive fits to models with somewhat different reddening laws and reddening amounts, we believe that the Balmer discontinuities have been estimated self-consistently to 0.02 mag, although systematic errors, such as an error in the adopted Balmer jump of Vega, could necessitate a uniform revision of the entire scale. We note that adoption of the Hayes (1970) calibration of Vega would make all Balmer jumps 0.05 mag more positive and would thus eliminate the negative Balmer jumps in the Ia supergiants.

Only four of the stars for which we have determined Balmer jumps have previous determinations by Chalonge and Divan (1952). Our Balmer jumps cor-

1975ApJ...196..351C

TABLE 2

Name*	HD	Spectral Type	Balmer Discontinuity
	195592	O9.5 Ia	-0.05
α Cam	30614	O9.5 Ia	-0.04
	194839	B0.5 Ia	-0.02
	216411	B1 Ia	-0.03
	43818	B0 II	+0.02
69 Cyg	204172	B0 Ib	+0.02
19 Cep	209975	O9.5 Ib	+0.03
	1383	B1 II	+0.03
	192422	B0.5 Ib	+0.04
ε Ori	37128	B0 Ia	+0.06
6913 #4†	–	O9.5 III	+0.07
	190919	B1 Ib	+0.06
	14143	B2 Ia	+0.08
6913 #2	–	B0 II	+0.12
	199216	B1 II	+0.13
6913 #3	–	B0 Iab	+0.14
581 #3	–	B2 III	+0.24

*Stars lacking HD numbers are identified by their cluster NGC number, followed by the identifying number.

†Numbers are from Hoag et al. (1961).

relate with theirs and also with $[u - b]$ for three stars. The fourth, 19 Cep, is discrepant in the comparison of all the available photometry. We suggest that the Balmer jump of 19 Cep may have actually changed.

IV. FOUR-COLOR AND Hβ PHOTOMETRY OF SUPERGIANTS

To check our finding that the Balmer jumps are poorly correlated with MK spectral type, we have analyzed the published four-color and Hβ photometry of all luminosity class I and II supergiants of spectral types B2 and earlier. Using data taken from the published surveys of Crawford and associates (Crawford, Barnes, and Golson 1970, 1971*a*, *b*; Crawford, Glaspey, and Perry 1970; Crawford *et al.* 1971), we have derived $(b - y)_0$ and c_0 by conventional procedures. We recall that $(b - y)_0$ measures the slope of the Paschen continuum, whereas for early-type stars, c_0 primarily measures the Balmer jump. The spectral types of the supergiants are generally taken from Morgan, Whitford, and Code (1955) and Hiltner (1956). Stars with Hβ and four-color photometry are listed in table 3.

Figure 3 is a (c_0, Hβ)-diagram for the B1 supergiants; the different luminosity classes are shown separately. We have used spectral type B1 because published data are available for twice as many B1 stars as for other types. We recall that at spectral type B1, classification can be done with good accuracy because the lines of O II and Si III are strong and sensitive to luminosity.

The (c_0, Hβ)-diagram appears to show that the MK luminosity class is well correlated with Hβ but not with c_0. With only two exceptions, the Hβ photometry has completely separated the four luminosity classes and has even separated those of Ia+ from those of Ia. This result is surprising, since hydrogen-line strength is not a primary criterion of luminosity class in MK

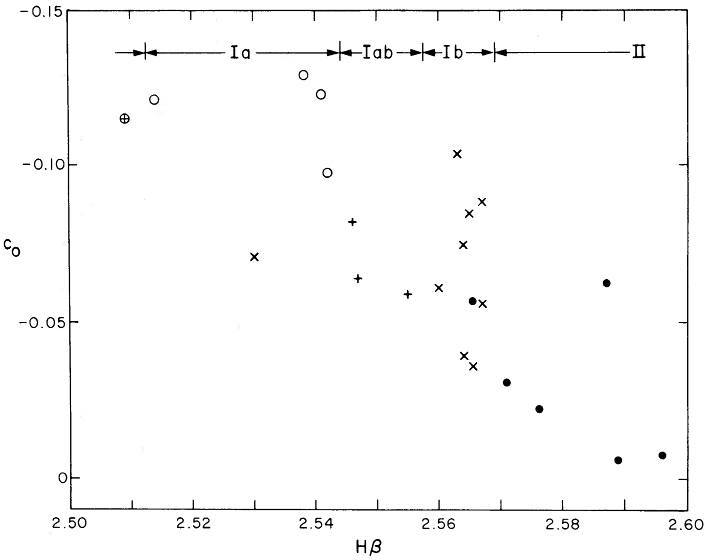

FIG. 3.—The c_0, Hβ diagram for B1 supergiants. Whereas Hβ appears to be well correlated with MK luminosity class, c_0 is evidently not. Symbols denote luminosity class as follows: (●) = II, (×) = Ib, (+) = Iab, (○) = Ia, and (⊕) = Ia+.

TABLE 3

Star HD	Spectral type	Hβ	m_1	c_1	(b - y)	c_0	$(b - y)_0$	[u - b]
290	B1 Ia	2.514	-0.042	-0.059	0.176	-0.121	-0.132	-0.115
13854	B1 Iab	2.546	-0.080	0.008	0.285	-0.082	-0.128	-0.106
14818	B2 Ia	2.526	-0.076	0.050	0.303	-0.035	-0.124	-0.054
24398	B1 Ib	2.564	-0.020	0.015	0.143	-0.039	-0.124	-0.002
30614	O9.5 Ia	2.530	0.014	-0.110	0.080	-0.153	-0.135	-0.069
37128	B0 Ia	2.557	0.026	-0.090	-0.032	-0.110	-0.131	-0.043
38771	B0.5 Ia	2.564	0.026	-0.084	-0.036	-0.103	-0.130	-0.038
40111	B1 Ib	2.565	0.018	-0.053	0.030	-0.085	-0.128	-0.012
41117	B2 Ia	2.513	-0.080	-0.022	0.292	-0.106	-0.131	-0.135
44743	B1 II	2.596	0.052	-0.002	-0.090	-0.008	-0.121	0.088
47432	O9.5 II	2.545	-0.042	-0.084	0.181	-0.147	-0.135	-0.139
52089	B2 II	2.577	0.078	-0.002	-0.081	-0.010	-0.121	0.141
52382	B1 Ib	2.530	-0.050	-0.001	0.222	-0.071	-0.127	-0.065
54764	B1 II	2.587	0.029	-0.016	0.107	-0.063	-0.126	0.059
57061	O9 Ib	2.564	0.054	-0.120	-0.048	-0.137	-0.134	-0.020
64760	B0.5 Ib	2.563	0.042	-0.086	-0.030	-0.106	-0.131	-0.007
68450	O9.5 II	2.556	0.018	-0.087	0.075	-0.129	-0.133	-0.039
86606	B1 Ib	2.567	0.061	-0.063	0.000	-0.089	-0.129	0.059
91316	B1 Iab	2.555	0.033	-0.039	-0.025	-0.059	-0.126	0.023
109867	B1 Ia	2.542	0.015	-0.051	0.104	-0.098	-0.130	-0.004
112244	O9 Ib	2.543	0.029	-0.142	0.079	-0.185	-0.139	-0.071
115842	B0.5 Ia	2.528	-0.037	-0.084	0.296	-0.171	-0.137	-0.111
122879	B0 Ia	2.559	-0.017	-0.088	0.164	-0.148	-0.135	-0.096
141318	B2 II	2.593	0.014	0.122	0.081	0.083	-0.112	0.163
148688	B1 Ia+	2.509	-0.090	-0.019	0.349	-0.115	-0.132	-0.143
149038	B0 Ia	2.551	-0.011	-0.074	0.130	-0.127	-0.133	-0.075
149404	O9 Ia	2.516	-0.010	-0.107	0.331	-0.201	-0.140	-0.074
150168	B1 III	2.565	-0.005	-0.018	0.067	-0.057	-0.126	-0.017
150898	B0.5 Ia	2.554	0.025	-0.100	0.019	-0.130	-0.133	-0.047
152003	O9.5 Ib	2.554	-0.093	-0.052	0.371	-0.152	-0.135	-0.179
152147	O9.5 Ib	2.562	-0.062	-0.071	0.371	-0.171	-0.137	-0.136
152234	B0.5 Ia	2.551	-0.033	-0.066	0.226	-0.138	-0.134	-0.096
152235	B1 Ia	2.541	-0.106	-0.003	0.468	-0.123	-0.132	-0.140
152236	B1.5 Iap+	2.499	-0.102	-0.049	0.440	-0.163	-0.136	-0.183
152249	O9.5 Ib	2.554	-0.016	-0.099	0.215	-0.169	-0.137	-0.097
152405	O9.5 Ib	2.566	-0.025	-0.089	0.178	-0.151	-0.135	-0.111

TABLE 3—*Continued*

Star HD	Spectral type	Hβ	m_1	c_1	(b - y)	c_0	$(b - y)_0$	[u - b]
152424	O9 Ia	2.547	-0.064	-0.068	0.369	-0.168	-0.137	-0.137
152667	B0.5 Ia	2.521	-0.060	-0.088	0.273	-0.170	-0.137	-0.164
154090	B1 Ia	2.538	-0.046	-0.010	0.265	-0.089	-0.129	-0.060
154368	O9 Ia	2.549	-0.109	-0.014	0.459	-0.132	-0.133	-0.159
155450	B1 II	2.576	-0.023	0.030	0.135	-0.021	-0.122	0.006
157426	B1 Ib	2.560	0.034	-0.040	-0.023	-0.061	-0.126	0.024
164402	B0 Ib	2.585	0.007	-0.070	0.074	-0.111	-0.131	-0.044
164637	B0 II	2.592	0.020	-0.067	0.056	-0.104	-0.130	-0.018
165024	B2 Ib	2.583	0.035	0.027	0.004	0.002	-0.120	0.098
165516	B0.5 Ib	2.575	0.010	-0.046	0.145	-0.101	-0.130	-0.003
165793	B1 II	2.571	0.011	0.004	0.054	-0.031	-0.123	0.035
167263	O9 II	2.578	-0.001	-0.086	0.089	-0.130	-0.133	-0.074
167264	B0 Ia	2.562	0.102	0.003	-0.080	-0.005	-0.121	0.194
167756	B0.5 Ia	2.554	0.021	-0.083	-0.015	-0.106	-0.131	-0.043
168021	B0 Ib	2.575	-0.055	-0.032	0.276	-0.113	-0.131	-0.098
185859	B0.5 Ia	2.562	-0.074	-0.059	0.343	-0.155	-0.135	-0.152
188209	O9.5 Ia	2.552	0.032	-0.102	0.006	-0.130	-0.133	-0.037
190603	B1.5 Ia	2.492	-0.105	0.009	0.470	-0.111	-0.131	-0.126
191877	B1 Ib	2.566	0.000	0.004	0.076	-0.036	-0.124	0.016
204172	B0 Ib	2.544	0.010	-0.077	0.016	-0.106	-0.131	-0.054
205139	B1 Ib	2.567	-0.028	0.004	0.175	-0.056	-0.126	-0.024
206165	B2 Ib	2.560	-0.051	0.135	0.275	0.057	-0.114	0.077
207198	O9 II	2.544	-0.016	-0.045	0.281	-0.128	-0.133	-0.032
209975	O9.5 Ib	2.547	-0.002	-0.083	0.127	-0.135	-0.134	-0.067
213087	B0.5 Ib	2.565	-0.081	0.008	0.341	-0.086	-0.129	-0.099
NGC 6871-2	B1 Ib	2.564	-0.02	0.00	0.25	-0.075	-0.128	0.0
NGC 6871-3	B1 Ib	2.563	-0.01	-0.03	0.24	-0.104	-0.130	-0.012
NGC 6871-5	B0 Ib	2.579	-0.02	-0.04	0.26	-0.038	-0.124	-0.038
h+χ Per 003	B2 Ib	2.568	-0.053	0.051	0.244	-0.021	-0.122	-0.016
h+χ Per 16	B1 Iab	2.547	-0.074	0.016	0.280	-0.064	-0.126	-0.087
h+χ Per 612	B1 II	2.589	-0.051	0.070	0.255	-0.006	-0.121	0.009
h+χ Per 1162	B2 Ia	2.546	-0.114	0.101	0.443	-0.012	-0.121	-0.056
h+χ Per 1899	B2 II	2.586	-0.045	0.138	0.289	0.057	-0.114	0.094
h+χ Per 2227	B2 II	2.584	-0.084	0.111	0.328	0.022	-0.118	-0.005
h+χ Per 2541	B2 II	2.610	-0.070	0.146	0.292	0.065	-0.114	0.053

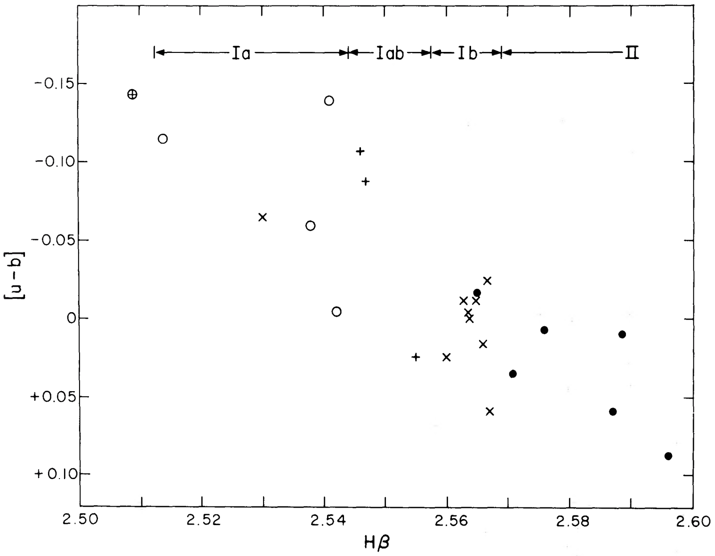

FIG. 4.—The ($[u - b]$, Hβ)-diagram for B1 supergiants. Symbols have the same meaning as in fig. 3. The poor correlation between $[u - b]$ and either Hβ or MK luminosity class is again evident.

classification. On the other hand, we find that the c_0 index is very poorly correlated with luminosity class and shows large variations at a given luminosity class. For example, we see that the B1 Ib stars have 0.07-mag scatter in c_0 and the B1 Iab stars are well within the range of the B1 Ib stars in c_0. We interpret this as confirmation of our finding from continuum energy distributions that the Balmer jumps are poorly correlated with spectral type (including luminosity class).

We note, however, two stars that differ from the Hβ–Sp relation (fig. 3), both of which have been classified by Morgan *et al.* (1955). HD 150168 is a luminosity class II bright giant with Ib Hβ. Its c_0 overlaps with both Ib and II, and the discrepancy is minor. On the other hand, HD 52382 has an Hβ that differs by two subclasses from its Ib luminosity class, also assigned by Morgan *et al.* We suggest that HD 52382 may have Hβ emission, which is common in Ia supergiants (Osmer 1973) but rarely seen in Ib supergiants.

Because c_0 measures not only the Balmer discontinuity but also line blocking in the λ4800 region, we present in figure 4 a ($[u - b]$, Hβ)-diagram for the stars in table 3. We have followed the procedures of Strömgren (1966) and computed $[u - b]$ from the reddening-free indices $[c_1]$ and $[m_1]$ through the relation $[u - b] = [c_1] + 2[m_1]$. The results in figure 4 appear to confirm the conclusion from figure 3—namely, that the Balmer discontinuity in B1 supergiants is poorly correlated with MK luminosity class or Hβ. There is some suggestion that $[u - b]$ shows the greatest variation in the Ia and Iab supergiants, but the number of stars available is too small for such a general statement. We note that the range in $[u - b]$ for Ia and Iab supergiants is almost 0.15 mag; this is slightly greater than the difference in Balmer discontinuities between ε Ori and the O9.5–B0.5 Ia supergiants.

V. THE INTRINSIC COLORS OF SUPERGIANTS

The intrinsic colors of the supergiants have not yet been calibrated on the four-color system, probably at least in part because of the problem of the variability of the Balmer jump. With our present empirical understanding of the origin of the problem, we attempt here a calibration of a limited portion of the H-R diagram. This is only a preliminary calibration; we are waiting for an observational program designed for this purpose to be carried out.

Table 4 lists the intrinsic $(b - y)_0$ colors of the O9–B2 supergiants. We note that all the entries for Iab are interpolations, which is not serious, because the luminosity dependence of $(b - y)_0$ is slight. From the agreement at spectral types where data for several

TABLE 4

Spectral Type	$(b - y)_0$					
	O9	O9.5	B0	B0.5	B1	B2
Ia	-0.137	-0.135	-0.133	-0.132	-0.131	-0.126
Iab	-0.136	-0.135	-0.132	-0.131	-0.128	-0.122
Ib	-0.136	-0.135	-0.131	-0.130	-0.126	-0.119
II	-0.135	-0.134	-0.130	-0.127	-0.121	-0.114

TABLE 5

Spectral Type	Hβ
B1 Ia	2.540
B1 Iab	2.552
B1 Ib	2.565
B1 II	2.584

stars are available, we estimate the uncertainty of our means to be 0.003 mag.

We had insufficient data to calibrate Hβ at all spectral types except B1. The scant data available suggested that the Hβ–luminosity-class correlation derived for B1 is applicable at B0 to B2, and the relation is given in table 5.

We thank Dr. C. Payne-Gaposchkin for delightful and stimulating discussions about supergiants and for her comments on the manuscript. We also thank S. Perrenod and J. Mariska for assistance with the reddening corrections and Dr. R. Kurucz for helpful discussions and unpublished blanketed models.

REFERENCES

Chalonge, D., and Divan, L. 1952, *Ann. der Ap.*, **15**, 201.
Crawford, D. L., Barnes, J. V., and Golson, J. C. 1970, *A.J.*, **75**, 624.
———. 1971*a*, *ibid.*, **76**, 621.
———. 1971*b*, *ibid.*, p. 1058.
Crawford, D. L., Barnes, J. V., Hill, G., and Perry, C. L. 1971, *A.J.*, **76**, 1048.
Crawford, D. L., Glaspey, J. W., and Perry, C. L. 1970, *A.J.*, **75**, 822.
Hayes, D. S. 1970, *Ap. J.*, **159**, 165.
Hayes, D. S., Mavko, G. E., Radick, R. R., Rex, K. H., and Greenberg, J. M. 1973, in *IAU Symposium No. 52*, ed. J. M. Greenberg and H. C. van de Hulst (Boston: Reidel), p. 83.
Hiltner, W. A. 1956, *Ap. J. Suppl.*, **2**, 389.
Hoag, A. A., Johnson, H. L., Iriarte, B., Mitchell, R. I., Hallam, K. L., and Sharpless, S. 1961, *Pub. U.S. Naval Obs.*, **17**, 349.
Kurucz, R. L., Peytremann, E., and Avrett, E. H. 1974, *Blanketed Model Atmospheres for Early-Type Stars* (Washington: Smithsonian Institution Press).
Mihalas, D., and Hummer, D. G. 1974, *Ap. J.* (*Letters*), **189**, L39.
Morgan, W. W., and Keenan, P. C. 1973, *Ann. Rev. Astr. and Ap.*, **11**, 29.
Morgan, W. W., Whitford, A. E., and Code, A. D. 1955, *Ap. J. Suppl.*, **2**, 41.
Oke, J. B. 1964, *Ap. J.*, **140**, 689.
Oke, J. B., and Schild, R. E. 1970, *Ap. J.*, **161**, 1015.
Osmer, P. S. 1973, *Ap. J.*, **186**, 459.
Radick, R. 1973, unpublished thesis, Rensselaer Polytechnic Institute.
Strömgren, B. 1966, *Ann. Rev. Astr. and Ap.*, **4**, 433.
Whiteoak, J. 1966, *Ap. J.*, **144**, 305.

Rudolph E. Schild and Frederic H. Chaffee: Smithsonian Astrophysical Observatory, 60 Garden Street, Cambridge, Ma 02138

THE ASTROPHYSICAL JOURNAL, **196**: 515–520, 1975 March 1

NEUTRAL HELIUM LINE STRENGTHS. VIII. LINE PROFILES IN THE WEAK-HELIUM-LINE STAR 3 SCORPII

JOHN NORRIS
Yale University Observatory

AND

P. A. STRITTMATTER
Steward Observatory, University of Arizona

Received 1974 May 23; revised 1974 September 17

ABSTRACT

It is shown that the profiles of the diffuse helium lines in the weak-helium-line star 3 Sco are anomalously broad and shallow in relation to results obtained for various metal lines. An explanation is proposed in terms of partial gravitational settling which gives rise to a nonuniform distribution of helium either in patches on the surface or in depth. Various constraints and consequences of these alternatives are considered, but neither could be ruled out on the basis of present observational data.

Subject headings: abundances, stellar — line profiles — stars, individual

I. INTRODUCTION

It has been known for some time that certain B stars have very weak helium lines for their color (or temperature). Michaud (1970) has suggested that this observation may be understood in terms of downward diffusion of helium from the visible layers of these stars. The hypothesis is, however, rather difficult to test, and little has so far been achieved in this regard. In view of the importance of understanding the weak-helium-line (WHL) phenomenon both in Population I, in which only a small percentage of B stars show the effect, and in Population II, in which *all* blue-horizontal-branch stars of globular clusters appear to be helium weak (Norris 1974, and references contained therein), we have considered it worthwhile to investigate in some detail the line profiles in the WHL stars to see if any relevant information is contained therein. (We note in this regard that Garrison 1973 has reported that both the hydrogen and the helium lines have a peculiar appearance in these stars.) In this paper we present observed profiles of several elements (§ II) in the WHL star 3 Sco (HD 142301) first noted as a star of this type by Garrison (1967). These profiles are interpreted in terms of model atmosphere computations (§ III). With the exception of He I, the profiles of all lines may be well represented by the computations. The wings of the He I lines, however, are observed to be somewhat broader than computed. Possible explanations of this result in terms of partial diffusion are considered in § IV.

II. OBSERVATIONS

The spectra of 3 Sco on which the present results are based have been described by Norris (1971*a*) in an investigation of 12 WHL stars. Profiles of the hydrogen lines Hγ and Hδ, together with the continuum in the range $\lambda\lambda$3400–5600 have already been published therein. These observations are shown graphically in figure 1 for Hγ (*filled circles*) and for the continuum (*open circles*).

Direct intensity tracings of three spectra have been averaged to yield profiles of the lines He I $\lambda\lambda$4026, 4471; C II λ4267; Mg II λ4481; and Si II $\lambda\lambda$4128–4130. These are shown in figure 2. The extent of the bars

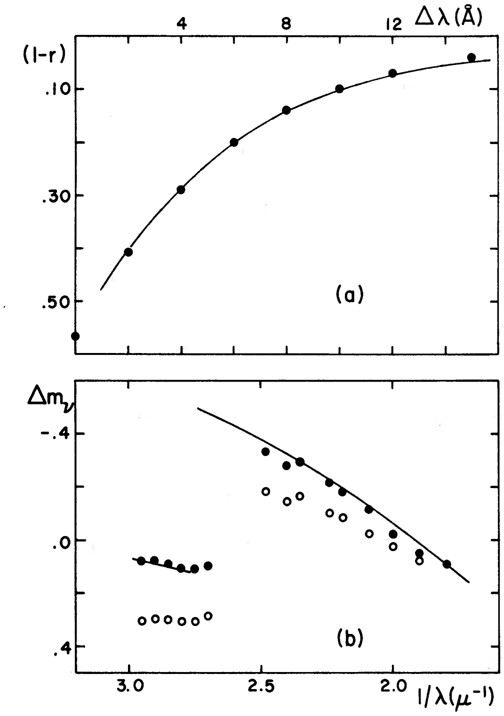

FIG. 1.—(*a*) Comparison of the observed profile of Hγ in 3 Sco (*filled circles*) with that computed for a model with T_e = 16,800°, log g = 4.0, and N(He)/N(H) = 0.11. (*b*) The observed continuum of 3 Sco (*open circles*) corrected for reddening of E_{B-V} = 0.12 (*filled circles*) as compared with that computed for the same model.

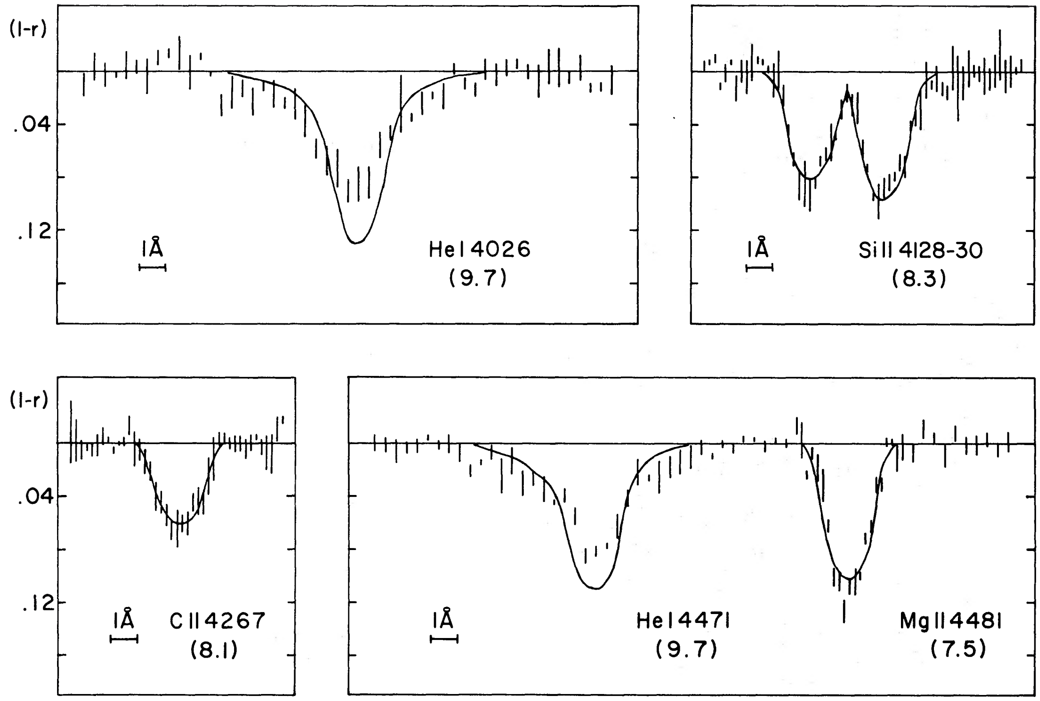

FIG. 2.—Comparison of observed profile (the bars represent 2 standard errors of the measurements) of He I λ4026, λ4471; C II λ4267; Mg II λ4481; Si II λλ4128–4130 with line profiles computed for a model with $T_e = 16{,}800°$, $\log g = 4.0$, and $N(\mathrm{He})/N(\mathrm{H}) = 0.11$. The adopted abundances were given in parentheses below the line identification; we have used $\zeta_t = 0$ km s^{-1} and $v_e \sin i = 80$ km s^{-1}.

represent twice the standard error in the measurements, where the standard error is computed according to small sample statistics (Keeping 1962) as $0.3R$ and R is the range in the three measurements at any wavelength. The choice of lines was determined by two factors. As may be seen from figure 2, the star has an appreciable rotational velocity; $v \sin i \sim 75$ km s^{-1} according to Norris (1971*a*). This restricts the choice to lines having strengths greater than ~ 100 mÅ. Second, the weakness of the helium lines allows only the two diffuse lines at λλ4026 and 4471 to be measured satisfactorily.

III. COMPARISON OF OBSERVATION WITH MODEL ATMOSPHERE COMPUTATIONS

One may compare these observations with LTE model atmosphere computations. In particular, the observed continuum and hydrogen line profile may be used to determine the effective temperature and surface gravity. According to Norris (1971*a*), 3 Sco has $T_{\mathrm{eff}} = 16{,}800°$ and $\log g = 3.9$. We show in figure 1 the fit of the observed Hγ and continuum to those computed for a model atmosphere with $T_{\mathrm{eff}} = 16{,}800°$, $\log g = 4$, and $N(\mathrm{He})/N(\mathrm{H}) = 0.11$. The model is similar to those used by Norris (1971*b*) and is based on the ultraviolet-line-blanketed model of Adams and Morton (1968). In the case of the continuum, the observations (*open circles*) must be corrected for a reddening $E_{B-V} = 0.12$ mag as indicated by the *UBV* colors (*filled circles*) before comparison with the computations. It is clear that a satisfactory fit between observation and computations can be obtained.

We should note that these conclusions are not strongly dependent on the assumed helium abundance since this element contributes essentially only to the mean molecular weight. For example, a change in $N(\mathrm{He})/N(\mathrm{H})$ to 0.01 would allow an equally good fit to be made to the observational data if $\log g$ were increased by only ~ 0.1.

We have also computed profiles for the lines given in figure 2 using the program of Baschek, Holweger, and Traving (1966) as modified by Schmitt, Scholz, and Traving (1971). For the helium lines the procedure described by Schmitt *et al.* has been adopted, while for the metallic lines we have employed the atomic data given by Kodaira and Scholz (1970). To fit the computations to the observations, we adopted the following procedure. Assuming a microturbulent velocity $\zeta_t = 0$ km s^{-1}, line profiles were computed to give the same equivalent widths as observed, with the element abundance as a free parameter. These profiles were then rotationally broadened using the procedure of Unsöld (1955) (with $\beta = 0.66$), until the best fit with the observations of the lines of C II, Mg II, and Si II was obtained. The results of this procedure are shown in figure 2, where the abundances ($\log [N(\mathrm{Element})/N(\mathrm{H})] + 12$) are given in parentheses below the line identification, and where the adopted rotational velocity is 80 km s^{-1}. A comparison of the derived abundances with those determined from the same lines by Kodaira and Scholz (1970) in the normal B3 V star ι Her shows that Mg and C have normal abundance, while Si is overabundant by a factor ~60. These results are of the same character as is found in many of the hotter Ap stars.

It is clear, however, that when the lines of C II, Mg II, and Si II are well fitted by this procedure, those of He I are still broader than computed. The discrepancy would become worse still if a nonzero microturbulent velocity were adopted. It appears unlikely that this phenomenon can be ascribed to observational error, especially in view of the close proximity of the He I λ4471 and Mg II λ4481 lines, which allows us to rule out the effects of calibration difficulties. The possibility that the wings of both helium lines may be blended with weaker metal lines seems implausible. In order to test the possibility of errors in effective temperature and gravity, we have repeated the procedure outlined above for models with ($T_{\rm eff}$, log g) values of (16,800°, 4.5) and (18,600°, 4.0). In both cases the essential result remained unchanged. Furthermore, the He I line profiles computed for normal He line stars (Norris 1971*b*) are in comparatively good agreement with the observations, so that errors in normal He line profile calculations cannot plausibly be blamed for the present difficulty.

There remains the possibility that the anomalous He I line profiles could arise from aspect effects or from differential rotation in a rapidly rotating star of uniform (albeit anomalous) surface composition. In either case it is required that the main contribution to the He I lines come from the most rapidly rotating regions. The law of gravity darkening, however, ensures that in the B star range both the He I line strength and the flux contribution should be at a relative minimum for such regions. The Mg II and Si II lines should, on the other hand, be stronger in such regions, and the effects in these lines should be correspondingly greater. Both expectations are in conflict with the observations. If, as suggested below, the Si II overabundance is confined to the same regions as the He I deficiency, significant effects due to differential rotation can be ruled out.

Finally, we note that, according to the work of Poland (1970), Kodaira and Scholz (1970), Leckrone (1971), and Auer and Mihalas (1973), both non-LTE calculations and the observed He I lines in normal stars yield profiles which are *deeper* than those derived from LTE models. This argues against an explanation of the present observations in terms of departures from LTE, and gives confidence that the phenomenon observed in 3 Sco does not result from the use of LTE computations.

It will be recalled that Garrison (1973) has reported that both the hydrogen and the helium lines have a peculiar appearance in the WHL stars. We have not found this to be the case for 3 Sco—while we concur with his result for helium, we find that hydrogen is normal. We suggest that further investigations are necessary to clarify this problem, which is of some consequence in our understanding of these stars.

Having accepted the peculiarity of the helium line profiles, we are then led to seek an explanation of the phenomenon in 3 Sco in terms of a nonuniform relative distribution of helium either in depth or in patches over the stellar surface. This could arise from either incomplete gravitational settling over the entire stellar disk or complete settling in certain areas defined perhaps by a magnetic field. The alternative hypothesis of selective magnetic accretion (cf. Havnes and Conti 1971) seems unlikely to lead to helium deficiencies in the hotter Ap (i.e., Bp) stars. We estimate that both the H II and He II regions around a star like 3 Sco extend past the magnetospheric distance suggested by Havnes and Conti (1971). Then, accepting their argument that further ionization after entering the magnetosphere favors accretion, the second ionization of helium, though rare, can only lead to an overabundance of helium relative to hydrogen, which cannot be further ionized. We will not consider this hypothesis further, but suggest that it might be relevant to the group of strong-helium-line early *B* stars described by Osmer and Peterson (1974).

IV. PARTIAL DIFFUSION

a) The Case of a Patchy Distribution

The profiles in figure 2 were computed on the assumption of an even distribution of helium over the stellar surface and $N({\rm He})/N({\rm H}) \sim 0.01$. Suppose, however, that a large surface region of the star contains no helium, while in the remaining area it is normal. The profile in the radiation of the second region will have a core not too much deeper than that in an atmosphere with $N({\rm He})/N({\rm H}) \sim 0.01$ (because of saturation), but it will have much stronger wings where the increase in strength is approximately linear with helium abundance. The result of averaging the radiation from such a region with that of one k times as large with zero helium abundance is a profile with absorption reduced by a constant factor $1 + k$; in the present case we estimate $k \sim 2$. In particular, the core will be shallower and the wings correspondingly stronger than a line of the same equivalent width computed on the basis of a uniform but lower helium abundance. This occurs only because, in the He abundance range of interest, the line center is saturated.

This effect may be seen in figure 3 where we compare our observed profiles of He I λλ4026 and 4471 with the non-LTE results of Stoeckley and Mihalas (1973),[1] reduced by a factor $1 + k = 3.3$, for the parameters $T_{\rm eff} = 17{,}500°$, $\log g = 4.0$, $N({\rm He})/N({\rm H}) = 0.10$, and $v \sin i = 80$ km s^{-1}. Compared with figure 1, we now have a considerably better fit.

---

[1] We realize that, strictly speaking, we should not average flux distributions in this manner; but since we have no knowledge of the surface distribution of helium, we feel the approximation to be a reasonable one. We note too that $T_{\rm eff} = 17{,}500°$ on the unblanketed scale of Stoeckley and Mihalas (1973) corresponds closely to $T_{\rm eff} = 16{,}800°$ on the blanketed scale used in the present work.

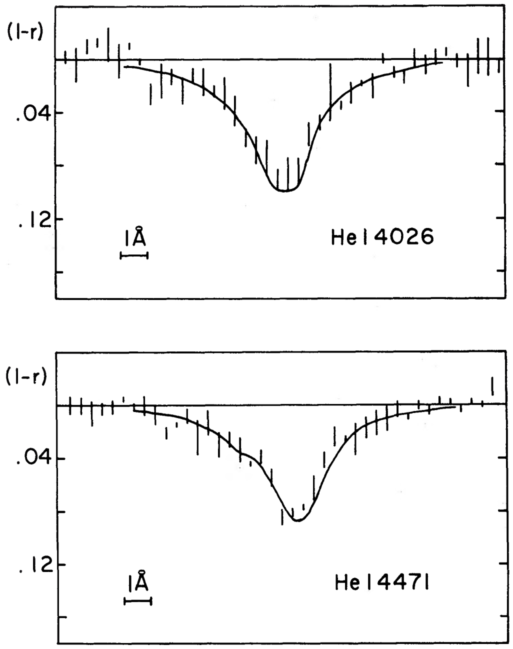

FIG. 3.—Comparison of the observed profile of He I λ4026 and He I λ4471 with approximate theoretical profiles representing a patchy helium distribution in which two-thirds of the surface have no helium and the remaining area has a normal abundance. See text for details.

The above interpretation receives additional support from the existence of spectrum variables among the Ap and Bp stars. The case of a Cen, which has been interpreted as possessing one or more helium-rich regions (Norris and Baschek 1972; Mihalas 1973), is of particular relevance. Also, of the eight definite WHL stars studied by Norris (1971*a*, three—ι Ori B (Conti and Loonen 1970), HD 144334, and HD 162374—are probably spectrum variables. There is, however, no evidence of spectrum variability in our data of 3 Sco, which, with a true rotational velocity of at least 80 km s^{-1}, would imply either that the zoning is longitude independent or of very small scale compared with the stellar radius. The former is perhaps more likely and would arise naturally if due to a magnetic field whose axis of symmetry coincided with the rotation axis. A magnetic field would indeed seem to be a requirement for either model if circulation currents are not to cause rapid atmospheric mixing (Smith 1970; Strittmatter and Norris 1971). Following the latter authors (their eq. [3.7]), we estimate that a field $\sim 10^3$ gauss is required in the present case. Unfortunately, direct evidence for such a field cannot be obtained because of the relatively high rotational velocity. From the metal lines we note that Mg and C are probably more or less uniformly distributed over the stellar surface. Silicon, on the other hand, is overabundant; and although this could in principle be a property of the entire stellar surface, it seems more likely that it should be confined to the helium-deficient zones. The anticorrelation of He and Si line strengths in, for example, the Si λ4200 stars 56 Ari and HD 124224 (Peterson 1966) would argue in favor of this. Further observations would clearly be useful in placing more precise limits on the variability.

b) The Case of Incomplete Settling with Depth

This situation is rather more difficult to analyze, and we shall confine ourselves here to a simplified discussion. In the case of 3 Sco, hydrogen should be virtually completely ionized throughout the photosphere; He is neutral in the upper atmosphere, but at optical depth $\tau \sim 1$ significant ionization sets in. Provided the atmosphere is completely stable, gravitational settling proceeds at a velocity given approximately by

$$W = \tfrac{1}{2} g t_{\rm coll} \,,$$

where $t_{\rm coll}$ is the time between collisions of helium with the ambient hydrogen. Using the collision cross section given by Loeb (1934), we have, for neutral helium,

$$W(\text{He I}) \sim 4 \times 10^{-6} g T^{1/2}/p_g \text{ cm s}^{-1} \,.$$

When He is once ionized, however, we have (Spitzer 1962)

$$W(\text{He II}) \sim 2 \times 10^{-24} g T^{3/2}/\rho \text{ cm s}^{-1} \,.$$

In the following we shall assume that if a proportion q of the He is neutral, the effective settling velocity is given by

$$W(\text{He}) = q W(\text{He I}) + (1 - q) W(\text{He II}) \,.$$

No significant amounts of He III should be present in the visible layers ($\tau < 10$) of 3 Sco. Values of τ (at $\lambda = 4000$ Å), T, p_g, ρ, q, and W(He) are listed in table 1 for the Mihalas (1965) model atmosphere with $T_{\rm eff} = 18{,}000°$ K and $\log g = 4.0$. When allowance is made for the fact that Mihalas's models do not include the effects of ultraviolet line blanketing, this model is quite similar to that adopted in the present study. Also listed is the time scale t (τ) for settling to occur over an interval $\Delta\tau = \tau$ at optical depth τ. It is immediately clear that, in the absence of magnetic effects, diffusion proceeds on a time scale very short compared with the evolutionary time scale ($\sim 10^7$ years) of a typical early B star. In these circumstances, it is necessary that a steady-state situation exist in which the gravitational settling rate is balanced by normal diffusion of He down a composition gradient. This gradient is approximately exponential with a scale height which is essentially independent of the collision cross section; for helium the scale height is $\sim$one-fourth the local pressure scale height. Clearly, this would allow a considerable range in relative He abundance across the photosphere. In order, however, to maintain an approximately normal He abundance at optical depths $\tau \sim 2$–5 with the diffusion times given in table 1, some source of normal He abundance material is required at approximately these depths.

TABLE 1

CALCULATED VALUES OF OPTICAL DEPTH (τ) FOR 3 SCORPII

τ	T (10^4 ° K)	p_g (10^3 dyn cm^{-2})	ρ (10^{-9} g cm^{-3})	q	W(He) (10^{-3} cm s^{-1})	$\log_{10}t$ (years)	$1/\rho W$(He) (10^{12} g^{-1} cm^2 s^1)
0.04.....	1.31	0.36	0.25	0.952	12.11	2.38	0.33
0.10.....	1.39	0.63	0.40	0.888	6.66	2.69	0.38
0.50.....	1.64	1.71	0.89	0.386	1.19	3.54	0.95
1.00.....	1.80	2.67	1.24	0.153	0.34	4.15	2.37
2.50.....	2.03	4.97	2.05	0.038	0.07	4.90	6.90
5.00.....	2.25	8.09	3.01	0.013	0.03	5.30	10.46
8.00.....	2.42	11.35	3.92	0.007	0.02	5.48	11.13

Rotationally driven circulation currents could in principle provide this material, but it is rather difficult to see why the upper atmosphere should not be strongly mixed (Smith 1970; Strittmatter and Norris 1971). Convection may also suffice, although the He ionization zones do not appear to be correctly located if the present model is appropriate to 3 Sco. An alternative presents itself if there is a strong magnetic field. The diffusion velocity of neutral helium will not be much affected thereby. The ionized component, on the other hand, would be strongly influenced if the gyration frequency is higher than the collision frequency (Michaud 1970). As seen from table 1, this would affect the flow at optical depths $\tau \gtrsim 1$ as suggested by the observations. A horizontal field strength in excess of 3×10^4 gauss would, however, be required. Although comparatively large, this value certainly cannot be ruled out by the observations. Indeed, in view of the need for an agency to overcome the destabilizing effects of meridional circulation, such a field is rather attractive.

A second possibility is that normal material is being accreted from the interstellar medium. In a steady state, we have at each depth

$$\rho_{\mathrm{He}} W(\mathrm{He}) = \mathrm{const.}\,,$$

which represents He conservation. The local He abundance is then given by

$$\frac{\rho_{\mathrm{He}}}{\rho} = \frac{\mathrm{const.}}{\rho W(\mathrm{He})}\,.$$

The quantity $1/\rho W(\mathrm{He})$ is also listed in table 1, and suggests that ρ_{He}/ρ indeed increases by a factor ~ 30 between $\tau = 0.04$ and $\tau = 8$. In order that the He abundance at $\tau \sim 2.5$ should satisfy $Y = 0.166$ ($n_{\mathrm{He}}/n_{\mathrm{H}} \sim 0.05$), the required accretion rate of normal composition material is given by

$$\frac{dM}{dt} = 4\pi r_0{}^2 \rho(\tau = 2.5) W_{\mathrm{He}}(\tau = 2.5)(Y/Y_i)\,,$$

where r_0 is the stellar radius and Y_i the mass fraction of He in the interstellar material. If we assume $r_0 = 3 \times 10^{11}$ cm and $Y_i = 0.30$, we obtain $dM/dt = 7 \times 10^{18}$ g yr^{-1}. The accretion rate to a star of mass M, moving with velocity v (km s^{-1}) relative to a medium of particle density N_i is given (Bondi and Hoyle 1944) by

$$\frac{dM}{dt} \sim 3 \times 10^{22} \left(\frac{M}{M_\odot}\right)^2 \frac{N_i}{v^3}\,.$$

For a star with $M = 5\,M_\odot$, $v \sim 20$ km s^{-1}, and $N_i \sim 1$ cm^{-3}, the accretion rate is accordingly 10^{20} g yr^{-1}. The rates are not so dissimilar as to rule out the possibility that such a balance exists.

A final possibility exists if the star possesses a poloidal magnetic field which has not decoupled from the ambient medium. In this case a centrifugal wind as described by Strittmatter and Norris (1971) may lead to mass loss from the extremely helium-deficient layers. It is then instructive to compare the time scale for the loss of an atmosphere with that for the diffusion of helium through the atmosphere. The mass loss rate is

$$dM/dt = 4\pi r^2 \rho v_p\,,$$

where r is the corotation radius, and ρ and v_p are the density and velocity of the outward flow, respectively, at this point. Since v_p is comparable to the tangential velocity at this point, it follows that

$$dM/dt \sim 4\pi r^2 \rho v_r \left(\frac{r}{r_0}\right)\,,$$

where v_r is the velocity at the stellar surface. Making use of equation (4.2) of Strittmatter and Norris (1971), one finally obtains

$$dM/dt \sim 4 r_0{}^2 \rho^{5/8} v_r{}^{1/4} B^{3/4}\,,$$

where B is the magnetic field at the surface. If we define the atmospheric mass ΔM as that down to $\tau \sim 5$, we have

$$\Delta M \sim 4\pi r_0{}^2 \bar{\rho} h \sim 20\pi r_0{}^2/\bar{\kappa}\,,$$

where h is the atmospheric depth and $\bar{\rho}$ and $\bar{\kappa}$ are the atmospheric mean density and opacity, respectively. The required time scale for mass loss is thus

$$t \sim 15 \rho^{-5/8} v_r{}^{-1/4} B^{-3/4} \kappa^{-1}\,.$$

Then, setting $\rho \sim 10^{-24}\,\mathrm{g\,cm^{-3}}$, $v \sim 100\,\mathrm{km\,s^{-1}}$. $B \sim 10^3$ gauss, and $\bar{\kappa} \sim 5\,\mathrm{cm^2\,g^{-1}}$, one obtains $t \sim 10^4$ years. Comparison with the diffusion time scales in column (7) of table 1 shows surprisingly good agreement.

There is a possible observational test which may distinguish between the hypothesis of a strong magnetic field on the one hand, and those of mass loss or accretion on the other. If the former obtains, one might expect that all WHL stars have considerably smaller helium abundances than normal. In the case of the latter mechanisms, one would expect all possible values of helium abundance from very low to normal. While the present observations appear to support the former possibility, this may be the result of a selection effect favoring the detection of very helium-weak objects. The question can only be satisfactorily answered by the analysis of a large sample of B stars.

It appears, then, that a case can be made that partial diffusion is responsible for the He I line profiles in 3 Sco, although it is not yet clear whether this occurs in surface patches or in depth. In either case, one remaining problem requires discussion. In view of the considerable overabundance of Si in 3 Sco, why are no strong distortions of the Si II λλ4128–4130 line profiles seen analogous to those found in the He I lines? The answer to this probably lies in the lower overall abundance of Si relative to He and the degree of intrinsic line broadening compared with that due to rotation. For Si, all lines are essentially Doppler broadened with an associated velocity which is substantially less than the rotational velocity. Rotation thus dominates the resultant profile, and a "good fit" to the profile will thus always be obtained for the abundance that gives the correct equivalent width. For He, however, the Stark wings are intrinsically broader than the rotational width so that profile information is retained. It is this additional information that can no longer be accommodated with a single abundance parameter.

V. SUMMARY

From high-dispersion spectrograms and scanner observations of the WHL star 3 Sco it has been shown that the diffuse He I lines λλ4026 and 4471 have anomalously broad wings and correspondingly shallow cores. The most promising interpretations appear to be in terms of partial gravitational settling. This could occur in patches over the stellar surface while other regions retain a normal He abundance; a ratio of approximately 2:1 between regions of zero and normal He is indicated by the observations. Alternatively it is possible that partial diffusion has occurred uniformly over the entire stellar surface, leading to an increase in relative helium abundance with optical depth. In this case, a source of normal composition material—perhaps from the stellar interior or from accretion—or mass loss from the upper atmosphere is required unless a very strong ($\gtrsim 3 \times 10^4$ gauss) horizontal magnetic field exists in the photospheric layers. It is not possible to decide from the present data which, if any, form of partial diffusion is taking place. A search for periodic spectrum variations would be particularly important in this regard. It would also be valuable to know whether helium abundances in the WHL group range from extremely low to normal. In any case, however, a magnetic field ($\gtrsim 10^3$ gauss) is probably required to ensure sufficient atmospheric stability for diffusion to occur in a star with a rotational velocity of $\sim 80\,\mathrm{km\,s^{-1}}$. Other abundance characteristics of 3 Sco, in particular an excess of Si, are typical of the hotter Ap stars.

One of us (J. N.) wishes to thank the Deutsche Forschungsgemeinschaft for financial support at the Lehrstuhl für Theortetische Astrophysik, University of Heidelberg, where part of this work was performed. A travel grant from IAU Commission No. 38 is also acknowledged. This research was supported, in part, by grant NSF 37926 from the National Science Foundation.

REFERENCES

Adams, T. F., and Morton, D. C. 1968, *Ap. J.*, **152**, 195.
Auer, L. H., and Mihalas, D. 1973, *Ap. J. Suppl.*, **25**, 433.
Baschek, B., Holweger, H., and Traving, G. 1966, *Abh. Hamburger Sternw.*, **8**, 26.
Bondi, H., and Hoyle, F. 1966, *M.N.R.A.S.*, **104**, 273.
Conti, P. S., and Loonen, J. P. 1970, *Astr. and Ap.*, **8**, 197.
Garrison, R. F. 1967, *Ap. J.*, **147**, 1003.
———. 1973, *Spectral Classification and Multicolor Photometry, IAU Symposium No. 50*, ed. Ch. Fehrenbach and B. E. Westerlund (Dordrecht: Reidel), p. 13.
Havnes, O., and Conti, P. S. 1971, *Astr. and Ap.*, **14**, 1.
Keeping, E. S. 1962, *Introduction to Statistical Inference* (Princeton: Van Nostrand).
Kodaira, K., and Scholz, M. 1970, *Astr. and Ap.*, **6**, 93.
Leckrone, D. S. 1971, *Astr. and Ap.*, **11**, 387.
Loeb, L. B. 1934, *The Kinetic Theory of Gases* (New York: McGraw-Hill).
Michaud, G. 1970, *Ap. J.*, **160**, 641.
Mihalas, D. 1965, *Ap. J. Suppl.*, **9**, 321.
———. 1973, *Ap. J.*, **184**, 851.
Norris, J. 1971*a*, *Ap. J. Suppl.*, **23**, 213.
———. 1971*b*, *ibid.*, p. 193.
———. 1974, submitted to *Ap. J.*
Norris, J., and Baschek, B. 1972, *Astr. and Ap.*, **21**, 385.
Osmer, P. S., and Peterson, D. M. 1974, *Ap. J.*, **187**, 117.
Peterson, B. A. 1966, *Ap. J.*, **145**, 735.
Poland, A. I. 1970, *Ap. J.*, **160**, 609.
Schmitt, A., Scholz, M., and Traving, G. 1971, *Astr. and Ap.*, **12**, 36.
Smith, R. E. 1970, *M.N.R.A.S.*, **148**, 275.
Spitzer, L. J. 1962, *Physics of Fully Ionized Gases* (2d ed.; New York, London: Interscience).
Stoeckley, T. R., and Mihalas, D. 1973, NCAR Tech. Note, NCAR-TN/STR-84 (Boulder: National Center for Atmospheric Research).
Strittmatter, P. A., and Norris, J. 1971, *Astr. and Ap.*, **15**, 239.
Unsöld, A. 1955, *Physik der Sternatmospharen* (Berlin, Göttingen, Heidelberg: Springer).

J. NORRIS: Mount Stromlo and Siding Spring Observatories, Woden, A.C.T., Australia

P. A. STRITTMATTER: Steward Observatory, University of Arizona, Tucson, AZ 85721

THE ASTROPHYSICAL JOURNAL, **196**:521–524, 1975 March 1

NUCLEAR AND NONNUCLEAR ABUNDANCE PATTERNS IN THE MANGANESE STARS*

CHARLES R. COWLEY AND G. CHRISTOPHER L. AIKMAN
Dominion Astrophysical Observatory
Received 1974 August 30

ABSTRACT

The manganese stars show abundance anomalies that are in conflict with the predictions of nuclear astrophysics. We stress the deviations from the odd-even effect that occur for phosphorus, gallium, and yttrium. The abundance anomalies (e.g., the Mn/Fe ratio) in the iron peak are less serious; within the uncertainties of the current determinations, they may be explained in terms of the same processes that predict the solar-system abundances.

Subject headings: abundances, stellar — nucleosynthesis — peculiar A stars

I. INTRODUCTION

In the past few years, promising nonnuclear hypotheses have been developed to explain abundance anomalies in early-type stars (cf. Michaud 1970; Havnes and Conti 1971). These ideas were developed in response to the difficulties of explaining the abundance anomalies within the context of nucleosynthesis in apparently unevolved stars.

The difficulties with nucleosynthesis are to a large extent a function of the "boundary conditions" that are imposed. These conditions are frequently more detailed than those applied in the case of the solar system, where the primary effort has been to find a sequence of temperatures and pressures that will explain the observed abundances. Much less thought has gone into the question of how the products of the *p*-, *r*-, *s*-, etc., processes come together to give the observed mixture.

By contrast, stellar abundance workers frequently demand a *connection* between the abundance anomalies of elements, such as silicon and the rare earths, which are usually thought to be due to quite distinct processes. There is, moreover, some compulsion to attempt a detailed, if qualitative, integration of the nucleosynthesis into the framework of stellar evolution.

We should like to call attention to a particular kind of abundance pattern that poses grave difficulties for any nuclear theory, quite independent of such "boundary conditions." Such a pattern occurs when an element of odd atomic number Z has an abundance that is greater than that of the adjacent elements with even Z.

The tendency of elements with even atomic number to be more abundant than their neighbors with odd Z is an extraordinarily marked characteristic of the solar system abundances. This odd-even effect owes its existence to the pairing energies of nucleons—a fundamental property of the atomic nucleus. It is to be expected whenever nuclear forces are primarily responsible for cosmic abundances. In this sense, it is more fundamental than the "peaks" of the theory of nucleosynthesis, which only appear with a particular process. Deviations from the odd-even effect may be taken as good evidence for nonnuclear processes.

The best examples of deviations from the odd-even effect occur in the manganese stars, and the best case is probably the yttrium to strontium and zirconium ratio. In what follows, we shall discuss abundances found by other workers, chiefly Aller and his colleagues, but we shall confine our discussion to stars that we have studied for element identifications using 2.4 Å mm^{-1} plates taken at the Dominion Astrophysical Observatory (DAO).

II. THE YTTRIUM ANOMALY

Abundances for strontium, yttrium, and zirconium are shown in table 1 for the manganese stars ϕ Her and ι CrB. The strontium abundance has been adjusted from the value reported in the references, since the experimental *gf*-values adopted there were affected by self-absorption. We adopt log $gf = 0.1$ and -0.2 for λλ4077 and 4215.

We are in the process of a detailed study of the abundances of "critical" elements in these and a number of other manganese stars, but preliminary work shows little likelihood that the yttrium abundance could be reduced to the point where the anomaly would no longer exist. Even a visual inspection of our plates of ϕ Her shows the Sr II resonance lines to be weak in comparison with a number of Y II lines. There can be no question of the identification of these lines, nor is there any possibility that chance blends could increase the strength of so many strong features. We have considered hyperfine structure, oscillator strengths, and the degree of ionization as possible

TABLE 1

LOGARITHMS OF Sr, Y, AND Zr ABUNDANCES

	Sr	Y	Zr	Reference
ϕ Her.......	3.5	5.3	4.1	Zimmerman *et al.* 1970
ι CrB.......	3.4	4.5	3.4	Ross and Aller 1970

---

* *Dominion Astrophysical Observatory Contribution* No. 243.

1975ApJ...196..351C

sources of error, and concluded that none of these factors could change the Y/Sr ratio by the large amount necessary to remove the discrepancy in ϕ Her.

The abundance of zirconium has possibly been underestimated—we say this simply because the *gf*-values are not as well known as those of strontium and yttrium. However, a nuclear process that would give the abundance pattern Sr < Y < Zr would almost certainly produce observable amounts of niobium and molybdenum, and these elements are not observed in the manganese stars.

III. THE PHOSPHORUS AND GALLIUM ANOMALIES

Two additional conflicts with the odd-even effect occur in the manganese stars at phosphorus and gallium. We shall report the results of our own statistical investigations of phosphorus and sulfur in five manganese stars, because the abundance data are exiguous. Our material has the advantage of completeness and uniformity, and is adequate for the present purposes, since it shows that it is possible to identify both phosphorus and sulfur in stars of similar temperatures and gravities. In the spectrum of ϕ Her, we can identify sulfur but not phosphorus, while in that of ι CrB the situation is reversed. In the spectrum of the hotter star κ Cnc, phosphorus lines are present in profusion, while the sulfur lines are weak or absent. The ionization potentials would lead us to expect sulfur rather than phosphorus in this spectrum. Aller (1970) found a very high abundance of phosphorus, while sulfur was not studied, presumably because its lines could not be found. In this case we clearly may conclude that phosphorus is more abundant than sulfur, and, with care, other qualitative conclusions concerning abundances may be drawn from the data in table 2.

The element-identification program was discussed by Hartoog, Cowley, and Cowley (1973) to whom we refer for details. The program investigates the statistical significance of *H* coincidences or "hits" within a tolerance window *w*, which is usually chosen to be ± 0.06 Å. The *N* strongest laboratory lines are selected, and the coincidences with them are compared with coincidences on (usually) 200 sets of *N* nonsense wavelengths. The result of this Monte Carlo procedure that has the most meaning is the fraction of times *f* that the number of coincidences obtained for the nonsense wavelengths was equal to or greater than those obtained for the laboratory wavelengths, since it is an approximation to the probability that the coincidences with the laboratory set are due to chance. However, when *f* is very small, a large number of trials with nonsense wavelength sets is necessary to determine it accurately. Consequently, we also compute a parameter *s* (we use a lower case *s* to avoid confusion with the chemical symbol for sulfur), which gives, roughly speaking, the "significance" of the result in standard deviations (cf. Hartoog *et al.* 1973). Some care must be used in interpreting this parameter, though, because the statistics are frequently far from Gaussian.

Four of the stars in table 2 were investigated on DAO plates. The results for HR 4072 are in press (Cowley *et al.* 1974). The stars are arranged in order of effective temperature, as determined in abundance studies: the reference for π^1 Boo is Montgomery and Aller (1969); for HR 4072, Guthrie (1966).

No nuclear reactions that even approach equilibrium will predict more phosphorus than sulfur. Aller's (1970) study of κ Cnc gives P $\geq$ Si, a completely perverse situation. It is as though the decay channels of the compound nucleus $^{32}S^*$, the intermediate result of $^{16}O + {}^{16}O$, were manifested in the Si, P, and S abundances in κ Cnc (cf. Spinka and Winkler 1972). The possibility that the *direct* products of $^{16}O + {}^{16}O$ might be related to stellar abundances does not seem to have been seriously considered. Silicon-28 is thought to be the dominant product of oxygen burning. Yet perhaps some consideration *should* be given to nonequilibrium processes. For this reason we feel that the odd-*Z* anomaly at phosphorus is not quite so incisive as at yttrium.

Certainly one of the most bizarre identifications in the entire domain of peculiar A stars is that of Ga II in the manganese stars (cf. Bidelman 1960). Although the importance of this discovery has long been known, it does not seem to have been discussed in the context of the odd-even effect.

The probability that gallium is misidentified is small. Our results for κ Cnc are as follows, based on measurements of 362 lines in the wavelength region 3780–4635 Å. All four Ga II lines listed by Bidelman and

TABLE 2

COINCIDENCE STATISTICS FOR PHOSPHORUS AND SULFUR*

	P II $(\chi_{I}, \chi_{II}) = 10.5, 19.7$			S II (10.4, 23.3)		
STAR	H/N	*f*	*s*	H/N	*f*	*s*
κ Cnc..........	19/26	< 0.005	+16.3	1/22	0.72	−0.02
π^1 Boo.........	6/28	< 0.005	+ 3.8	8/22	< 0.005	+6.1
ϕ Her..........	2/28	0.82	− 0.6	11/22	< 0.005	+5.5
ι CrB..........	10/28	< 0.005	+ 4.7†	2/22	0.55	+0.5
HR 4072.......	4/32	0.15	+ 1.4	7/24	0.03	+2.4

* First and Second ionization potentials are given.

† At $w = \pm 0.04$, $s = 6.5$.

1975ApJ...196..351C

Corliss (1962) were measured. With $w = \pm 0.06$, $f = 0.0012$; with $w = \pm 0.04$, $f = 0.0003$. These figures are based on 10,000 Monte Carlo trials.

Aller's (1970) values for the abundance of gallium in κ Cnc is comparable to that of iron! Although it is possible that this situation might arise under conditions of very high density, or by addition of neutrons to the iron peak nuclei there is no way that the odd-Z element gallium could be more abundant than zinc or germanium. There may be some possibility that our failure to detect these elements is due to their atomic properties, which are much less well known than those of strontium, yttrium, and zirconium. For this reason, we believe the yttrium anomaly to be more clearly demonstrated than that of gallium, but the latter is potentially a very strong case.

IV. SILICON AND THE IRON PEAK

It is interesting to examine the run of abundances in these stars from silicon through the iron peak. We do not feel that the manganese abundance presents a strong case against nucleosynthesis. Most of the abundances that can be found in the literature predate the revision of the f-value scale, which affected both Fe I and Fe II. Consequently, all of the iron abundances must be reconsidered. We cannot make revisions (as in the case of the Sr II lines) without a careful examination of a large number of iron lines in each spectrum, but certainly all of the iron abundances will increase, probably by factors between 2 and 10. Thus, there is no necessity to conclude that Mn/Fe > 1 in any star, although some of the stars (e.g., 53 Tau) showing very high values of this ratio should be carefully reexamined.

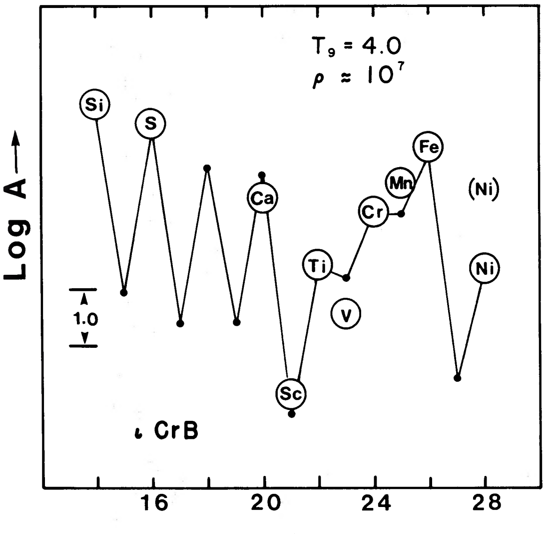

FIG. 1.—A comparison of quasi-equilibrium abundances with the determinations of Ross and Aller (1970). The stellar abundances are indicated by the chemical symbols inside the open circles. The filled circles connected by solid lines are the theoretical predictions. Logarithms of the proton and neutron densities are 27.787 and 19.815. The larger Ni abundance inside the parentheses is for Ni I. The lower point is for Ni II.

In ι CrB the abundances from silicon through the iron peak are quite similar to the predictions of silicon-burning quasi-equilibrium. Figure 1 shows a comparison of the observations with theoretical predictions that we have made following the method of Bodansky, Clayton, and Fowler (1967). With the possible exception of Ni, which we shall discuss below, the fit is promising, especially when we consider the uncertainties of the stellar determination. The theoretical calculations, incidentally, were not optimized for the ι CrB data, but were made in the course of exploratory calculations to see how sensitive *elemental* abundances were to the assumed physical conditions.

Our statistical program gives significance to the wavelength coincidences with Ni II lines in the spectrum of ι CrB, but not to those of Ni I: f(Ni I) = 1.0, f(Ni II) < 0.005. We therefore have some objective basis for rejecting the determination from Ni I, which gives a much less satisfactory fit, in figure 1 and ascribing the wavelength coincidences to chance. But even if a closer examination should show the higher Ni abundance to be more correct, we only have a conflict with *one specific prediction* of nucleosynthesis; we need not let one rotten apple spoil the barrel!

The fit for ϕ Her shown in figure 2 is also promising, with the exception of the point for scandium. This abundance is undoubtedly high, since the scandium lines are outstandingly strong in this star. The dynamic calculations (cf. Woosley, Arnett, and Clayton 1973) of nucleosynthesis show that scandium lies in a "bottleneck," which connects the flow of synthesis between two "clusters" of nuclides that tend to be in equilibrium among themselves. Its abundance is always very low, and consequently it could be easily increased by secondary processes which would hardly affect the relative positions of the more abundant elements.

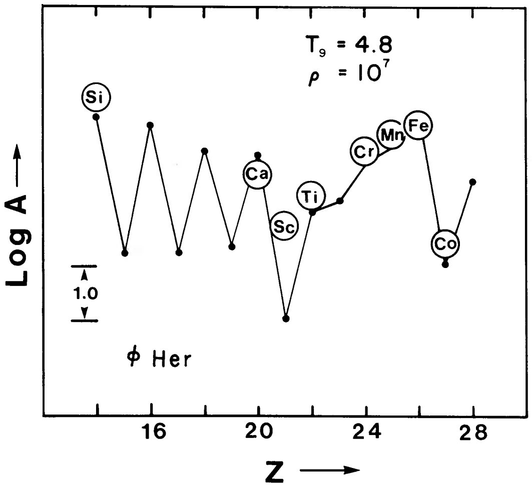

FIG. 2.—Same format as fig. 1. The stellar abundances are from Zimmerman *et al.* (1970). Logarithms of the proton and neutron densities are 28.704 and 22.875.

The three other manganese stars shown in table 2 show abundance patterns unlike any that we have obtained thus far. But we emphasize that we have by no means undertaken the complete multiparameter search that would enable us to say that *no* quasi-equilibrium fit could be obtained. It is also possible that the dynamic calculations of explosive silicon burning would be required.

Thus, it seems possible to say that the most formidable difficulties for nucleosynthesis are the deviations from the odd-even effect, rather than the peculiarities that occur near the iron peak.

V. SUMMARY

The manganese stars show three deviations from the odd-even effect that are in conflict with the predictions of nuclear astrophysics. We consider the yttrium anomaly to be the best indication of such a conflict. Consequently, it is a favorable problem for non-nuclear theories to attack. Michaud (1970) has made calculations that are highly promising for this particular case. We await their refinement.

We must remark, however, that manganese stars that are quite similar in effective temperature and surface gravities show different abundance patterns. Such differences inevitably call for an explanation in terms of a variety of processes with a variable relative mixture. Scientists may abhor theories with adjustable parameters, but nature may require them all the same.

C. R. C. wishes to acknowledge a very useful correspondence with Drs. J. B. Blake, Georges Michaud, Hans Suess, and Dieter Zeh; also, a conversation with Dr. David Bodansky was extremely helpful. He also wishes to thank director K. O. Wright and the staff of the Dominion Astrophysical Observatory for their hospitality.

REFERENCES

Aller, M. F. 1970, *Astr. and Ap.*, **6**, 67.
Bidelman, W. P. 1960, *Pub. A.S.P.*, **72**, 471.
Bidelman, W. P., and Corliss, C. H. 1962, *Ap. J.*, **135**, 968.
Bodansky, D., Clayton, D. D., and Fowler, W. A. 1967, *Ap. J. Suppl.*, **16**, 299.
Cowley, C. R., Hartoog, M. R., and Cowley, A. P. 1974, *Ap. J.*, **194**, 343.
Guthrie, B. G. N. 1966, *Pub. Roy. Obs. Edinburgh*, **6**, 1.
Hartoog, M. R., Cowley, C. R., and Cowley, A. P. 1973, *Ap. J.*, **182**, 847.
Havnes, O., and Conti, P. S. 1971, *Astr. and Ap.*, **14**, 1.
Michaud, G. 1970, *Ap. J.*, **160**, 641.
Montgomery, J. W., and Aller, L. H. 1969, *Proc. Nat. Acad. Sci. USA*, **63**, 1039.
Ross, J. E., and Aller, L. H. 1970, *Ap. J.*, **161**, 189.
Spinka, H., and Winkler, H. 1972, *Ap. J.*, **174**, 455.
Woosley, S. E., Arnett, W. D., and Clayton, D. D. 1973, *Ap. J. Suppl.*, **26**, 231.
Zimmerman, R. E., Aller, L. H., and Ross, J. E. 1970, *Ap. J.*, **161**, 179.

G. CHRISTOPHER AIKMAN: Dominion Astrophysical Observatory, Victoria, B.C., V8X 3X3, Canada

CHARLES R. COWLEY: Department of Astronomy, Physics-Astronomy Building, University of Michigan, Ann Arbor, MI 48104

1975ApJ...196..351C

The Astrophysical Journal, **196**:525–547, 1975 March 1

THERMAL PULSES; *p*-CAPTURE, α-CAPTURE, *s*-PROCESS NUCLEOSYNTHESIS; AND CONVECTIVE MIXING IN A STAR OF INTERMEDIATE MASS*

Icko Iben, Jr.
University of Illinois, Champaign-Urbana

Received 1974 June 17; revised 1974 September 16

ABSTRACT

After extrapolating from the characteristics of a model star of mass 7 $M_\odot$ during the course of 10 thermal relaxation oscillations, the following inferences are drawn: (1) The reaction ^{22}Ne (α, *n*)^{25}Mg serves as a major source of neutrons for *s*-process nucleosynthesis. (2) This nucleosynthesis takes place at the high temperature base of a convective shell of mass 0.002 $M_\odot$ at and near the peak of a thermal pulse which recurs at intervals of roughly 2500 yr. (3) At maximum size, the convective shell extends from the position of highest helium-burning rate to just below the hydrogen-helium discontinuity, and no further. (4) The ^{22}Ne that is the immediate precursor of neutrons owes its formation to the ^{14}N that has been left behind by the hydrogen-burning shell during the interpulse phase; after two α-captures and a β decay, ^{14}N is converted completely into ^{22}Ne within the convective shell. (5) Following the disappearance of the convective shell, the base of the convective envelope extends into the outer portion of the region previously contained in the convective shell; fresh products of *p*-capture, α-capture, and *s*-process nucleosynthesis are then convected to the surface; in particular, surface abundances of ^{4}He, ^{22}Ne, ^{25}Mg, and the *s*-process progeny of ^{25}Mg and ^{56}Fe are enhanced, and the abundance of ^{12}C may also be enhanced.

Adopting solar system abundances of ^{56}Fe and CNO elements, one may infer that roughly 42 neutrons will be released in the convective shell for every fresh ^{56}Fe nucleus. Neutron captures on ^{22}Ne, on ^{25}Mg, and on the progeny of these nuclei reduce the number of neutrons available for capture on ^{56}Fe and its progeny to about four or five, exactly the number required to establish a steady-state distribution of *s*-process elements that closely resembles the distribution in the solar system.

As a consequence of burning within the convective envelope during interpulse phases, the surface abundance of ^{14}N continues to increase at the expense of ^{12}C, and the number ratio ^{12}C/^{13}C approaches 3.4. Whether or not injections of fresh ^{12}C that occur immediately following each pulse can counteract the destruction of ^{12}C during the interpulse phases depends on the treatment of convection in surface layers. One may anticipate that the ratio ^{13}C/^{12}C will be correlated with the ratio ^{16}O/^{12}C at the surface of stars in which many pulses have occurred.

During the quiescent phase that follows each pulse, the hydrogen-burning shell converts CNO nuclei almost entirely into ^{14}N at an abundance that slowly increases after each pulse. Thus, the abundance of ^{22}Ne, the final source of neutrons, increases after each pulse. One may infer that the mass-weighted mean of *s*-process elements heavier than ^{56}Fe that appears at the stellar surface will be larger in stars with a lower initial iron abundance.

Subject headings: abundances, stellar — convection — interiors, stellar — nucleosynthesis — stellar evolution

I. INTRODUCTION

Schwarzschild and Härm (1967) together with Sanders (1967) first suggested that the synthesis of elements by slow neutron capture on iron and on elements heavier than iron may take place in stars undergoing thermal pulses. A key ingredient of their argument is the fact that, at the peak of any given pulse, a convective shell reaches from the region of peak energy production almost to the hydrogen-helium discontinuity that defines the base of the hydrogen-burning shell. If the convective shell were to actually reach into the hydrogen-rich region, the reactions $^{12}\mathrm{C}(p,\gamma)^{13}\mathrm{N}(\beta^+\nu)^{13}\mathrm{C}(\alpha,n)^{16}\mathrm{O}$ would release neutrons that could be captured by seed nuclei, beginning with iron, to form the so-called *s*-process elements (Cameron 1954, 1955; Burbidge *et al.* 1957; Clayton *et al.* 1961; Seeger, Fowler, and Clayton 1965).

Several variations and elaborations of this basic idea of bringing hydrogen, carbon, and helium into contact at high temperatures have recently appeared (e.g., Ulrich and Scalo 1972; Scalo and Ulrich 1973; Ulrich 1973; Smith, Sackmann, and Despain 1973; Sackmann, Smith, and Despain 1974). A review of the nucleosynthesis aspects of the various models is given by Truran (1973).

The Ulrich-Scalo mechanism supposes that the convective shell just reaches, but does not extend beyond, the hydrogen-rich region. It is supposed that some protons are capable of tunneling through the thin radiative region between the base of the hydrogen-rich region and the outer edge of the convective shell. On entering the convective shell, these cunning protons immediately initiate the reactions $^{12}\mathrm{C}(p,\gamma)^{13}\mathrm{N}(\beta^+\nu)^{13}\mathrm{C}$. The ^{13}C so formed is then presumably convected downward until it reaches temperatures high enough for the reaction $^{13}\mathrm{C}(\alpha,n)^{16}\mathrm{O}$ to occur. The resulting neutron flux then acts on ^{56}Fe to produce the heavy *s*-process elements. During the course

---

* Supported in part by the National Science Foundation grant GP-35863.

of the pulse, the dominant constituents of the convective shell—fresh ^{12}C produced in the shell and ^{4}He left behind by the hydrogen-burning shell—are conjectured to diffuse into the hydrogen-rich region, along with the freshly produced *s*-process elements. It is then postulated that "plumes" driven by the reactions $^{12}C(p, \gamma)^{13}N(\beta^{+}\nu)^{13}C$ are formed. The plumes are imagined to extend up to the base of the convective envelope and thus act as conduits for bringing the newly produced elements (most importantly ^{12}C, ^{13}C, and *s*-process elements) to the surface.

One disadvantage of this scheme is the necessity of very fine tuning: just the right number of protons must be injected into the convective shell region to achieve the desired distribution of *s*-process elements (3–4 neutrons for every ^{56}Fe seed nucleus). Further, the requisite attributes of the postulated plumes cannot be calculated from first principles. In particular, it has not yet been demonstrated that the shell convective zone can make repeated contact with the hydrogen-helium discontinuity so that ^{12}C can be injected into the hydrogen-rich region to initiate the process of plume formation. Nor can one calculate from first principles (even if contact is made) the amount of ^{12}C and ^{4}He that will be transported into the hydrogen-rich region to form plumes.

The Smith-Sackmann-Despain scheme supposes that the convective shell driven by helium burning physically merges with the convective envelope. Although the elemental abundances that emerge from this scheme appear to exhibit many attractive coincidences with "cosmic abundance" distributions, no model star yet made develops an unbroken convective region extending all the way from the helium-burning zone to the surface. In all models to date, the shell convective zone is precisely out of phase with the envelope convective zone. That is, as the outer edge of the shell convective zone moves outward in mass, so does the base of the convective envelope. Only after the shell convective zone disappears does the base of the convective envelope move inward again in mass.

Despite the drawbacks of the specific mechanisms that have been proposed, one common feature—many repeated neutron bursts separated by long periods of quiescence—seems to be a crucial element in obtaining a cosmic distribution of *s*-process elements (Ulrich 1973). Thus, the hope still remains that a quite straightforward and unambiguous scheme for producing repeated neutron bursts and bringing neutron-capture products to the surface can be demonstrated in realistic models of stars experiencing thermal pulses.

The scheme presented in this paper may meet the requirements. It is based on an extrapolation of the behavior of a model star of intermediate mass during the passage of 10 thermal pulses. At the peak of each of the last seven pulses, the convective shell which is formed below the base of the hydrogen-rich envelope contains about 0.002 $M_{\odot}$ of ^{12}C, ^{16}O, ^{4}He, and ^{22}Ne. The ^{22}Ne has as its progenitors ^{12}C, ^{14}N, and ^{16}O and is therefore equal in abundance (by number) to the sum of the original abundances of CNO elements. The separation between the outer edge of the convective shell (at its maximum size) and the location of the hydrogen-helium discontinuity appears to be reaching either a minimum or an asymptotic value somewhat smaller than 0.00009 $M_{\odot}$. Sweigart (1973, 1974) demonstrates that this separation does, under appropriate circumstances, reach a minimum.

With each succeeding pulse, the average temperature in the convective shell increases and the lifetime of ^{22}Ne against α-capture via the neutron-emitting channel $^{22}Ne(\alpha, n)^{25}Mg$ decreases. For example, the temperature at the base of the convective shell rises from 281 million degrees at the peak of the ninth pulse to 286 million degrees at the peak of the tenth pulse and the mean lifetime of ^{22}Ne in the shell drops from 100 yr to 70 yr. It is plausible to assume that this trend will continue until the lifetime of ^{22}Ne in the shell drops well below the duration time of the convective shell (about 15 years). For every initial ^{56}Fe seed nucleus, roughly 40 neutrons will then be released within the convective shell during each pulse. Most of these neutrons will be captured by ^{22}Ne and its progeny and by ^{25}Mg and its progeny. By a curious accident, the number of neutrons left over for capture on ^{56}Fe and its progeny leads to a distribution of heavier neutron-rich *s*-process elements that closely resembles the solar system distribution of these elements.

After the convective shell disappears, the *s*-process elements so produced will be brought to the surface as a consequence of the following chain of events. During each thermal pulse, the excess kinetic energy deposited by helium-burning causes matter within and beyond the helium-burning region to expand and to be propelled outward. As densities drop, the ratio of gas pressure to radiation pressure decreases and the adiabatic temperature gradient also drops until, in regions successively further inward *in mass*, matter becomes unstable against convection. Although the base of the convective envelope moves inward in mass, it remains at about the same spatial position. Hence, a more descriptive characterization of the phenomenon is that matter flows into a convective region whose base remains nearly fixed.

In the period following each of the last four pulses, matter left behind by the hydrogen-burning shell flows into the convective region. With each succeeding pulse, the amount of newly processed matter that passes into the convective region increases. Before moving outward again in mass following the eighth pulse, the base of the convective envelope reaches to within 5×10^{-5} $M_{\odot}$ of the carbon discontinuity left behind by the convective shell at its maximum extent. Following the ninth pulse, the base of the convective envelope and the carbon discontinuity reach to within 7×10^{-6} $M_{\odot}$ of one another. Following the tenth pulse, the base of the convective envelope extends past the carbon discontinuity formed by the preceding convective shell by 4×10^{-5} $M_{\odot}$. It is anticipated that, following succeeding pulses, significant quantities of freshly made carbon and *s*-process elements will flow into the convective region. A trace of ^{16}O will also be added. As it is probably not completely destroyed during the pulse, fresh ^{22}Ne will also reach the surface.

This, then, completes one cycle of production and mixing to the surface. With each successive cycle, the total surface abundance of CNO elements and the total abundance of *s*-process elements should increase slowly in step while the relative abundances of *s*-process elements should much more slowly adjust toward the heavy end of the periodic table.

The proposed scheme possesses several virtues: (1) all ingredients are straightforward consequences of realistic model calculations; (2) the number of neutrons per seed nucleus is determined, at least in stars of population I composition, primarily by the choice of the initial CNO abundances and of the abundances of seed nuclei, rather than by an ad hoc assumption regarding the amount of ^{12}C that produces neutrons following proton captures and α-particle captures; (3) the buildup of carbon and *s*-process elements in the stellar envelope can in principle be calculated quantitatively (given enough computer time and human patience).

In common with other schemes, the scheme proposed here suggests that, in the context of galactic nucleosynthesis, the formation of *s*-process elements is a second and third generation phenomenon. That is, all proposals for producing heavy neutron-rich elements during thermal pulses require the presence of initial iron-seed nuclei and therefore require an earlier generation of stars that produce iron and regurgitate it into the interstellar medium.

In contrast with other schemes, however, the scheme here advocated requires at first also a large initial abundance of CNO nuclei. Thus, all other things being equal, the production of *s*-process elements in a given star is at first quadratically, rather than linearly, dependent on the overall abundances of elements heavier than helium. One would therefore expect that, if *s*-process elements are made in and brought to the surface of both Population II and Population I stars via the process herein advocated, the abundance of such elements should be roughly correlated with the square of some metal abundance parameter (e.g., the Z popular among makers of models of the stellar interior). This contrast with the linear dependence predicted by other schemes should be susceptible to observational test.

In making the test, one must take care to recognize that the enhancement of surface abundances by any of the suggested processes will be a strong function of the mass of the envelope. All other things being equal, the smaller the envelope mass, the greater the enhancement. Furthermore, the extent to which convection penetrates into the region where nuclear processing has occurred may, through the opacity in surface layers, be sensitive to the abundance of heavy elements. The extent of penetration will also be sensitive to the mass of the envelope.

The inference that ^{22}Ne acts as a major source of neutrons for *s*-process nucleosynthesis during thermal pulses and the discovery that carbon and *s*-process elements are convected to the surface following thermal pulses were first presented in colloquia at Kitt Peak (1974 May 9) and Michigan State (1974 May 16), in a NATO conference "On the Origin of the Elements" (Cambridge, England, 1974 July) and at the 143rd meeting of the AAS (Iben 1974*b*).

II. THE VARIATION OF SEVERAL BULK STRUCTURAL CHARACTERISTICS DURING RELAXATION OSCILLATIONS

The general pattern of relaxation oscillations in a star of intermediate mass is described by Weigert (1966), who has followed six such oscillations in a 5 $M_\odot$ model with a carbon-oxygen core of mass about 0.8 $M_\odot$. The present paper focuses on relaxation oscillations in a model star of mass 7 $M_\odot$ with a carbon-oxygen core of mass about 0.95 $M_\odot$. Some of the properties of the model have already been published (Iben 1972, 1973*a*, *b*, 1974*a*). Radiative and conductive opacities used in the investigation are described in Appendices A and B. Nuclear reaction cross sections have been taken from Fowler, Caughlin, and Zimmerman (1975). The pressure contributed by electrons is approximated as in Eggleton, Faulkner, and Flannery (1974).

The temporal behavior of several bulk characteristics during and between the eighth and ninth thermal pulses is shown in figure 1. It is remarkable that the tremendous variations in power output by nuclear fuels in the two burning shells has such a minor influence on those surface characteristics that are in principle most readily observable. Although the power output by hydrogen-burning (L_H) and the power output by helium-burning (L_He) vary by factors of about 10,000 and the total power output by nuclear burning varies by a factor of 30, the surface luminosity varies by less than a factor of 2. The difference in nuclear power output and surface luminosity is, of course, made up by transfers to and from the gravitational potential energy content and thermal energy content of the star. At the peak of each pulse, almost all of the energy liberated by helium-burning is used up in raising temperatures and expanding matter in the vicinity of the burning region. The sudden loss of power from the hydrogen-burning shell is partially made good by the release of gravitational potential energy from contracting portions of the star. It is interesting that surface luminosity L_s and Radius R_s keep in step in such a way that surface temperature T_e varies almost imperceptibly.

From the standpoint of the influence of nuclear processing in the interior on surface abundance characteristics, of major interest is the variation in the location of the base of the convective envelope (M_CE) relative to the location of discontinuities in composition brought about by nuclear transformations in the interior. The curve labeled M_{XY} in figure 1 marks the boundary between hydrogen-rich matter and hydrogen-exhausted matter. Each line segment labeled "carbon discontinuity" marks the location of

1975ApJ...196..351C

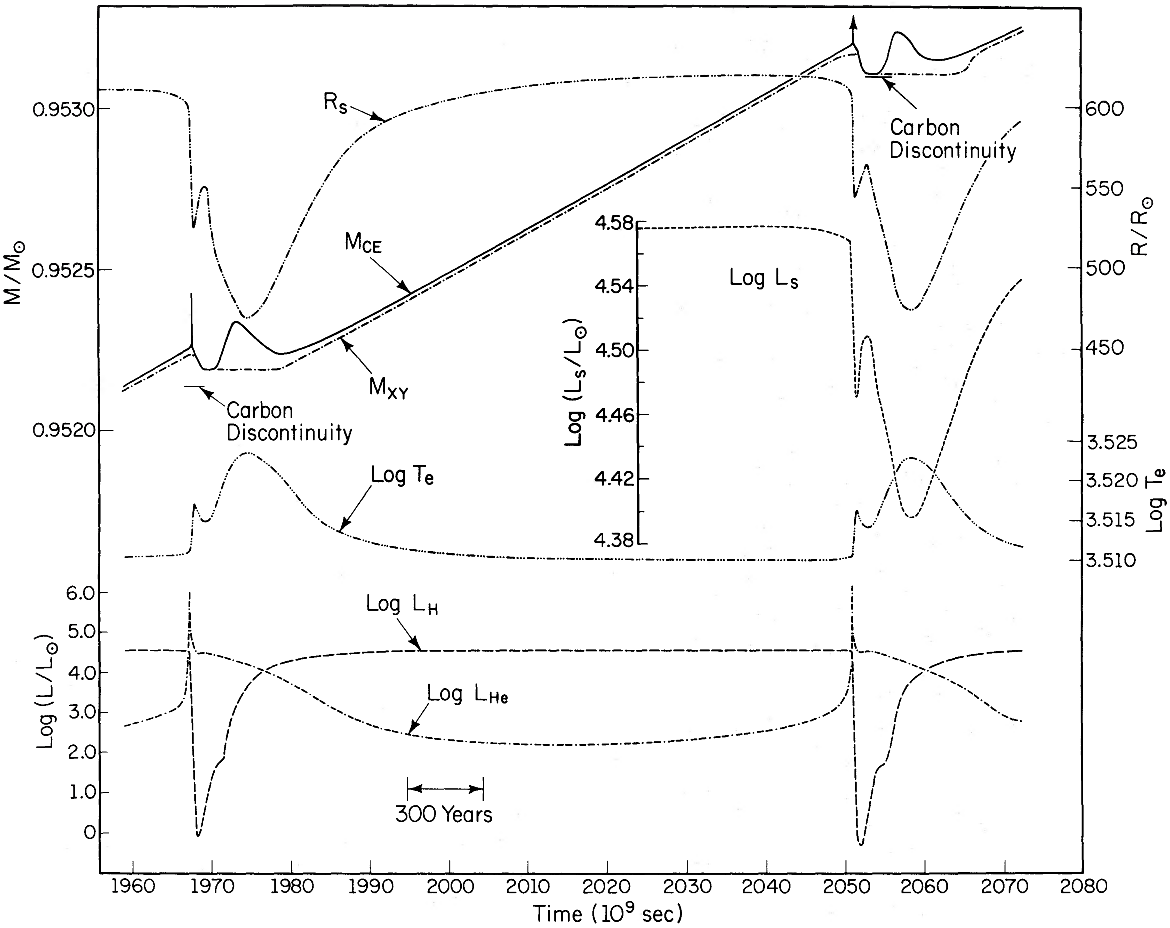

FIG. 1.—Time dependence of several model characteristics during and between the eighth and ninth thermal pulses. R_s = stellar radius, L_s = surface luminosity, T_e = surface temperature, $L_{\rm H}$ = power output from hydrogen-burning reactions, $L_{\rm He}$ = power output from helium-burning reactions, M_{XY} = mass at discontinuity in hydrogen and helium abundances (edge of hydrogen-exhausted core), $M_{\rm CE}$ = mass at base of convective envelope. The lines marked "carbon discontinuity" show the furthest outward reach (in mass) of the convective shell that appears briefly when $L_{\rm He}$ is at a relative maximum.

the maximum outward extent of the convective shell that is achieved when the power output by helium-burning is near a relative maximum.

Note that, during each pulse, the base of the convective envelope at first recedes outward in mass and then moves back inward. During the initial portion of the ensuing relaxation phase, when hydrogen-burning reactions are effectively inactive, the base of the convective envelope moves into the region previously exhausted of hydrogen. Thus, following the eighth and ninth pulses, freshly made ^{4}He and ^{14}N are convected toward the surface.

Note also that the maximum inward penetration of convection in the period immediately following a pulse is larger after the ninth pulse than it is after the eighth pulse. After the eighth pulse the base of the convective envelope and the carbon discontinuity are separated by only $5 \times 10^{-5}\, M_\odot$. After the ninth pulse, they are separated by $7 \times 10^{-6}\, M_\odot$. Following the tenth pulse the base of the convective envelope extends beyond the location of the carbon discontinuity established during the peak of the pulse by $4 \times 10^{-5}\, M_\odot$; products of helium-burning are therefore distributed throughout the envelope.

As is illustrated in figure 2, the amplitudes of other variations also increase with each successive pulse. The arrows in figure 2 mark the times at which the power output by helium-burning reactions reaches a relative maximum. All quantities other than $\log L_{\rm He}$ in figure 2 are characteristics of the model star at times when the power output by helium-burning reactions is at a relative minimum. They are therefore representative of the star during most of the interpulse period of evolution.

During the interpulse period, roughly 80 percent of the power output by hydrogen-burning reactions occurs in the region bounded by the hydrogen-helium (XY) discontinuity and the base of the convective envelope. In figure 2, the temperature at the XY discontinuity is denoted by T_{XY} and the temperature at the base of the convective envelope is denoted by $T_{\rm CEB}$. Burning at the base of the convective envelope

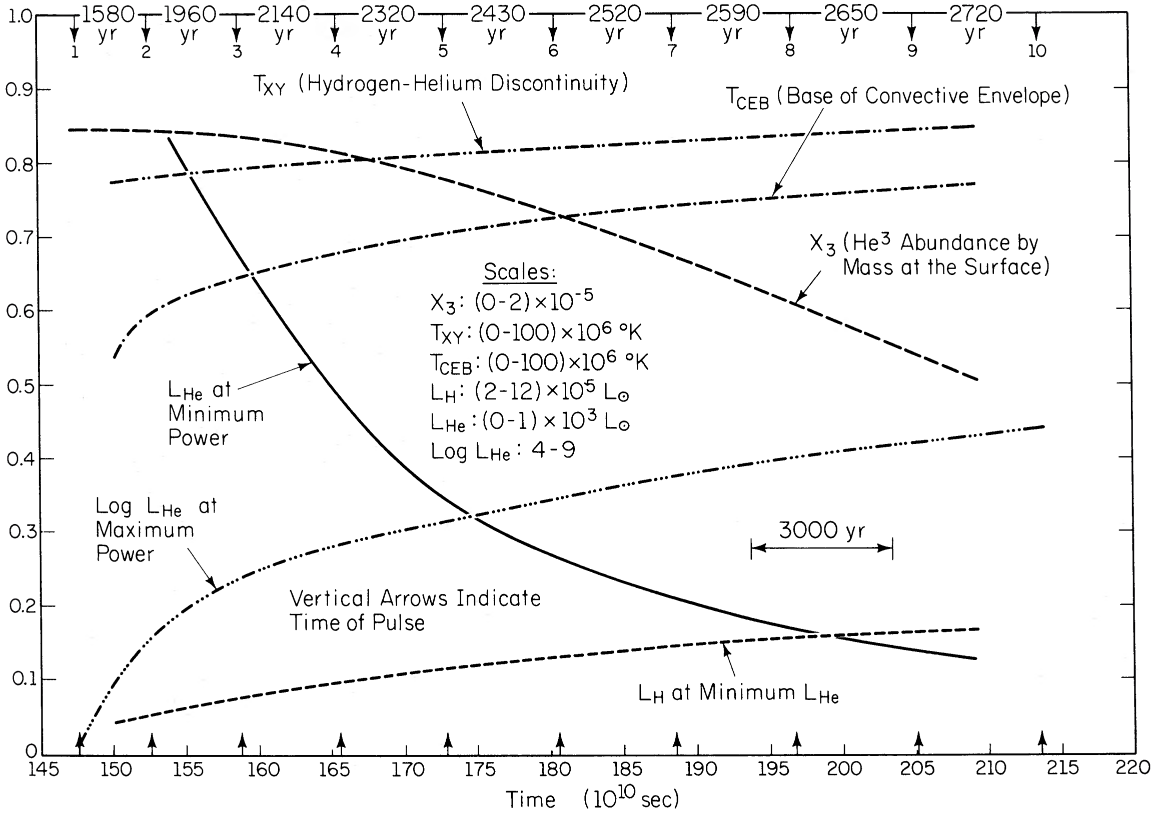

FIG. 2.—Characteristics at minimum L_{He}. L_{He} = power output from helium-burning reactions, L_{H} = power output from hydrogen-burning reactions, T_{XY} = temperature at base of hydrogen-burning shell, T_{CEB} = temperature at base of convective envelope, X_3 = surface abundance by mass of ^{3}He. Also shown is log L_{He} = the logarithm of the maximum power output from helium-burning reactions. The maxima in power output occur at times marked by arrows. All quantities other than log L_{He} are placed arbitrarily at time positions exactly midway between times of power maxima. The scale for L_{H} is (2–12) × $10^4 L_\odot$ rather than (2–12) × $10^5 L_\odot$.

steadily depletes the ^{3}He throughout the envelope. The abundance of ^{12}C also decreases with time during the first 10 relaxation oscillations (see fig. 12). The abundance of ^{13}C in the envelope relative to the abundance of ^{12}C there is essentially the inverse of the ratio of the cross sections for proton capture. That is, $^{12}\mathrm{C}/^{13}\mathrm{C} \approx 3.4$ (Truran 1973). The elements ^{3}He, ^{12}C, and ^{13}C will be discussed more fully in § VII.

Further consequences of significant burning at the base of the convective envelope in stars of intermediate mass have been explored by Uus (1970, 1971, 1973) and by Sugimoto and Nomoto (1974), who show that the properties of the envelope and the rates of burning there are sensitive to the treatment of surface convection.

As the mean temperature in the hydrogen-burning shell continues to rise with each successive relaxation cycle, the rate at which ^{13}N (the product of proton capture on ^{12}C) disappears via proton captures begins to become comparable to the rate at which it disappears via positron decay. This fact will eventually have to be taken explicitly into account in determining the overall rate of energy production by the CN cycle.

III. RADIAL MOTION AND TEMPERATURE EVOLUTION OF THE INTERIOR

Shown in figures 3 and 4 is the temporal variation of the radial position and temperature of matter in various mass shells in the star during and between the eighth and ninth pulses. Also indicated in figure 3 are the position of the hydrogen-helium discontinuity and the position of the base of the convective envelope.

During the long interpulse relaxation phase, perhaps the most dramatic occurrence is the infall of matter into the region of hydrogen-burning. This region, which is precisely bounded on the inward side by the XY discontinuity and is roughly bounded on the outward side by the base of the convective envelope, exhibits remarkable temperature and positional stability. Matter flows into this spatially (nearly) fixed region, is heated to a (nearly) fixed temperature, and has its hydrogen converted into helium, whereupon it passes out of the burning region to become a part of a relatively inert helium-rich shell.

Radial and temperature history during the eighth thermal pulse is shown with better temporal resolution in figures 5 and 6. During the course of the pulse all

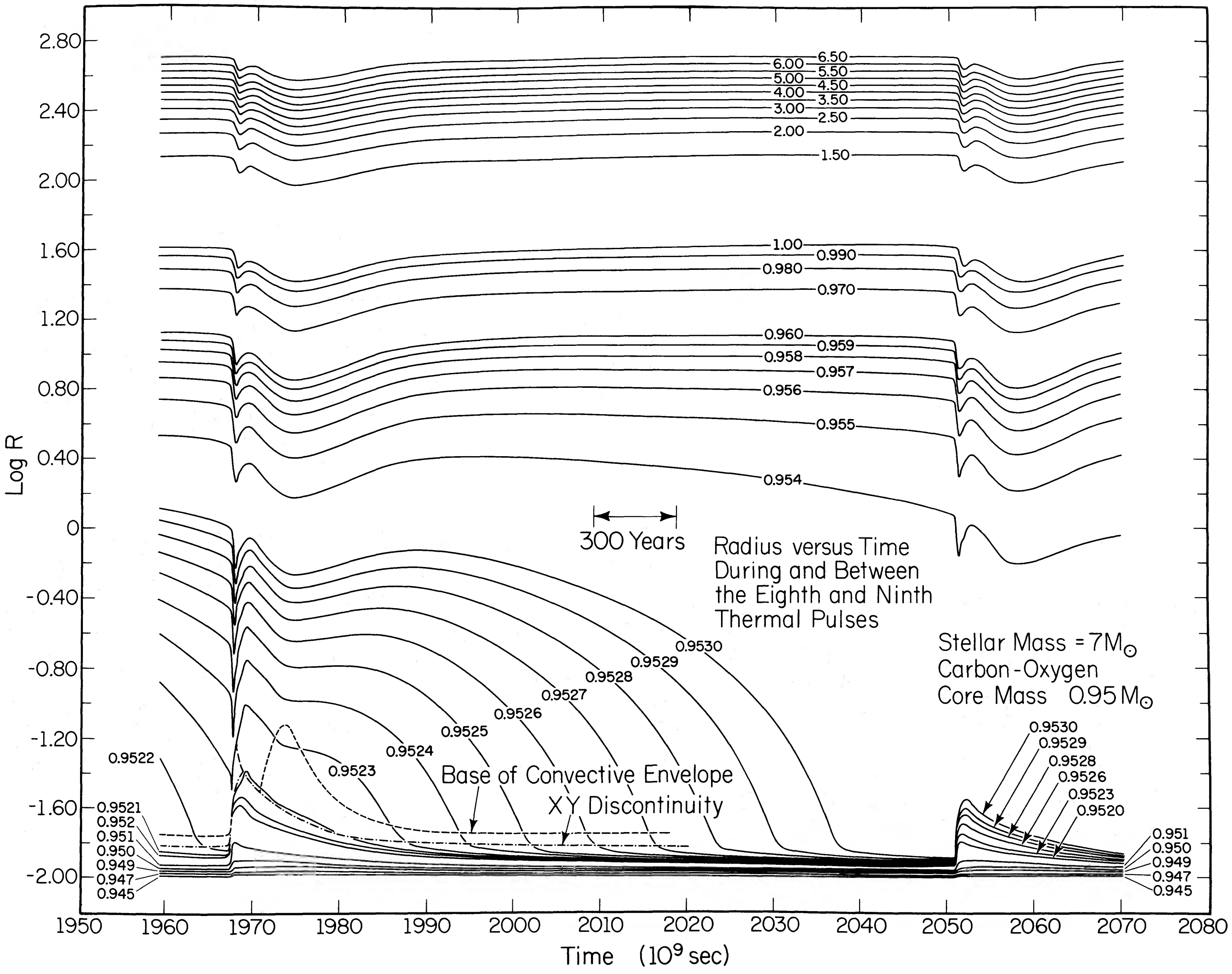

FIG. 3.—Radial location of various mass points during and between the eighth and ninth thermal pulses. Radius and mass are in solar units.

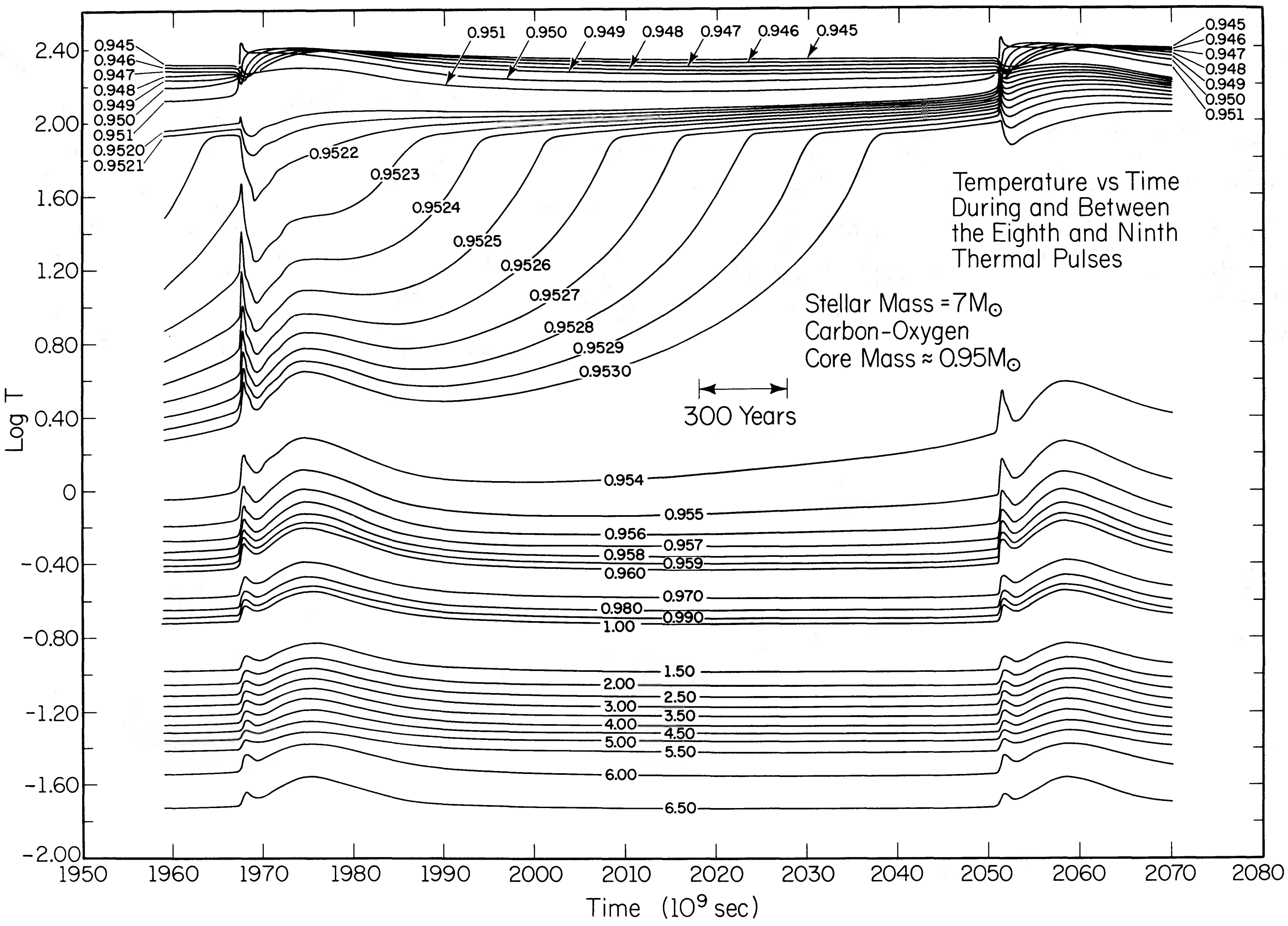

FIG. 4.—Temperature history of various mass points during and between the eighth and ninth pulses. Temperature is in 10^6 ° K.

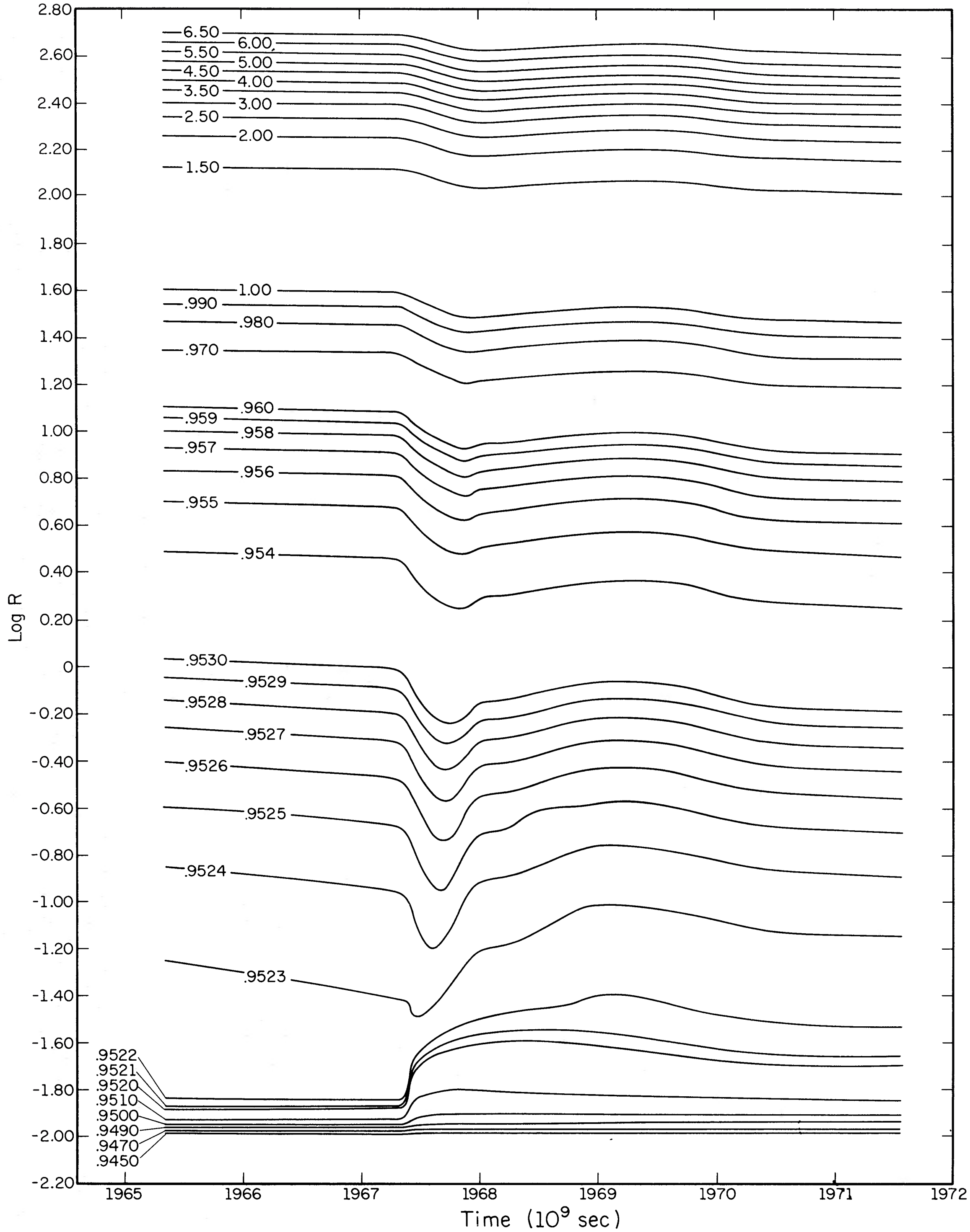

FIG. 5.—Radial location of various mass points as a function of time centered about the eighth thermal pulse. Radius and mass are in solar units.

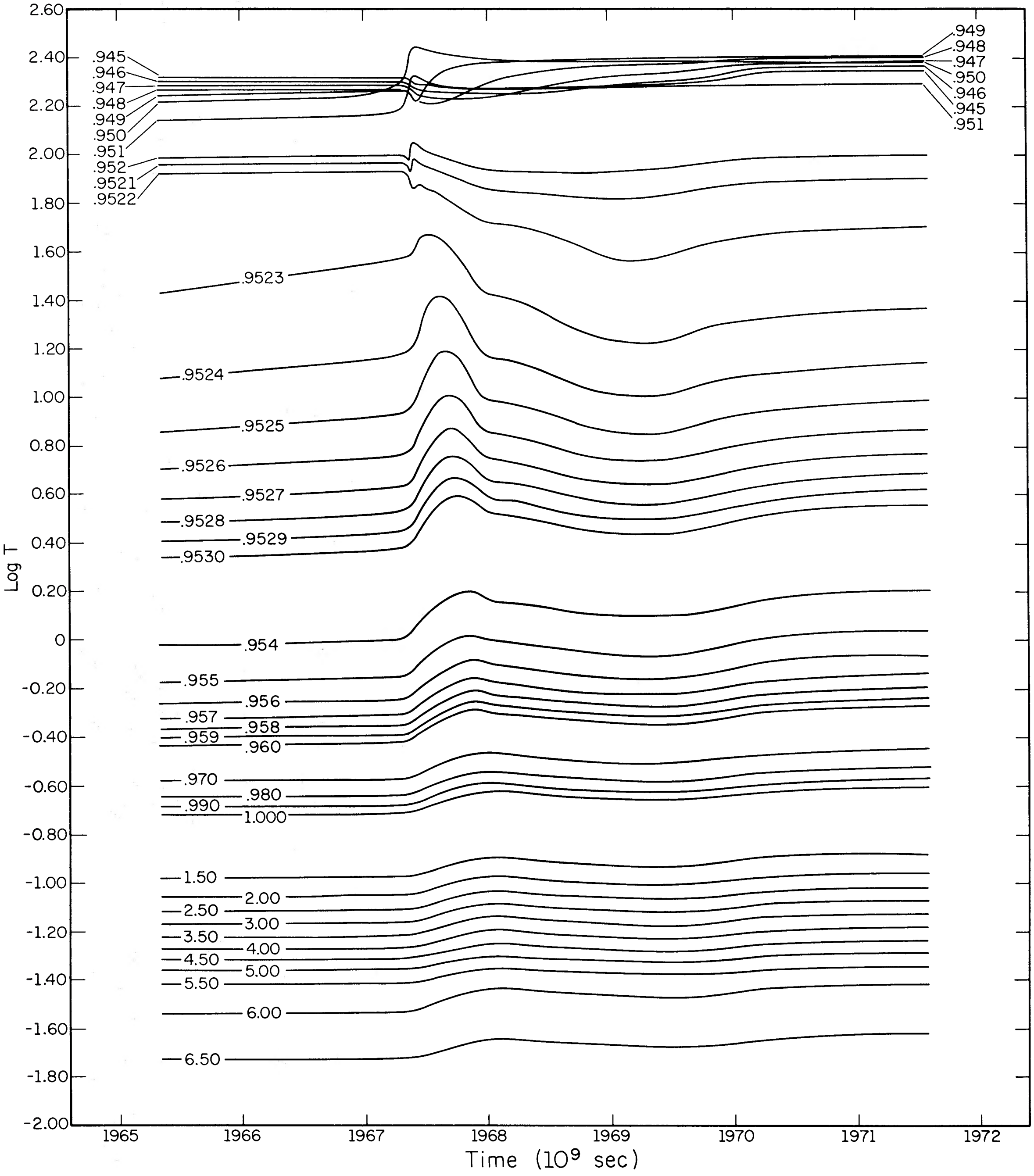

FIG. 6.—Temperature history of various mass points during the eighth thermal pulse. Temperature is in 10^6 ° K.

of the matter involved in furious helium-burning ($M/M_\odot \sim 0.949$–0.951) heats up rapidly and is propelled outward. Matter in the hydrogen-burning shell ($M/M_\odot \sim 0.95224$) is also propelled outward but, after a brief moment of heating, cools. In contrast, matter just outside the hydrogen-burning shell initially "collapses" inward and heats, at the same time liberating some gravitational potential energy to flow to the surface. The excess pressure buildup at the confluence of the outflowing and inflowing matter eventually forces all of the matter above the helium-burning region to flow outward.

It is interesting to note that the wave patterns evident in figures 3–6 are consequences of evolution in a quasi-static approximation that damps out all dynamic motions.

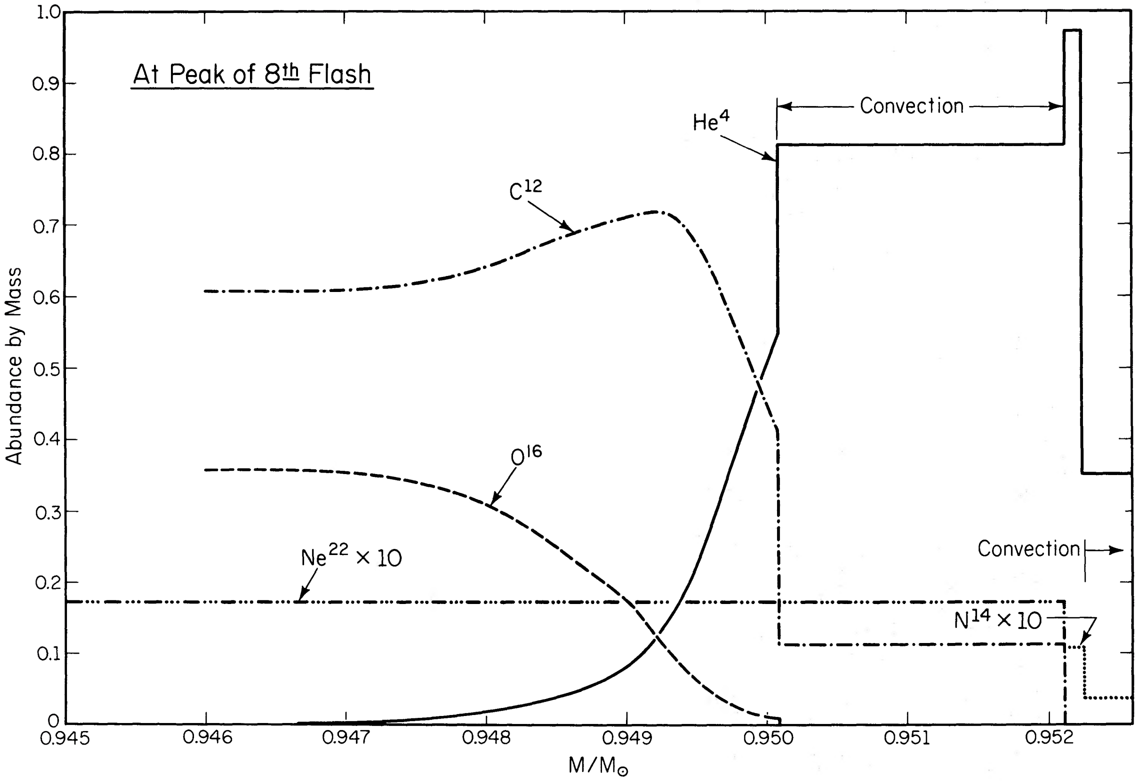

FIG. 7.—Composition (abundance by mass) versus mass (in solar units) at the peak of the eighth thermal pulse

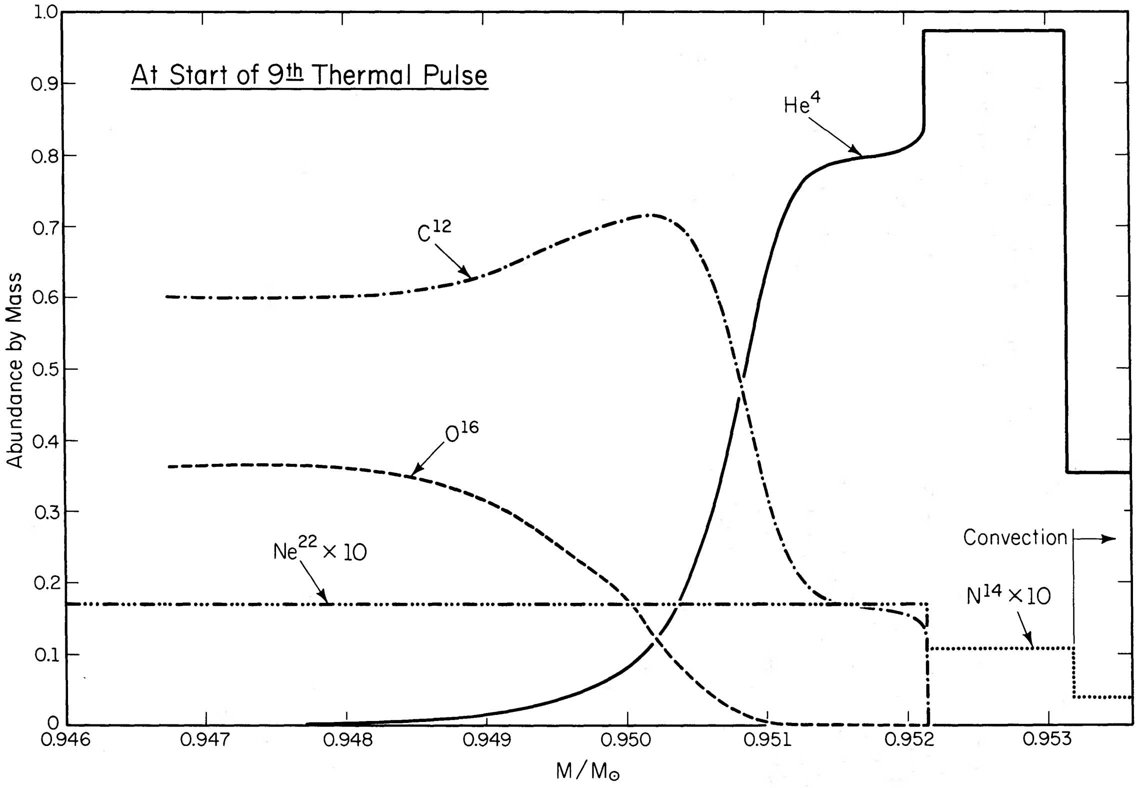

FIG. 8.—Composition versus mass just before the ninth thermal pulse

IV. NUCLEAR POWER OUTPUT, SHELL CONVECTION, AND NUCLEAR TRANSFORMATIONS DURING A THERMAL PULSE

The time dependence of the power output from various helium-burning reactions during a thermal pulse can be best understood following an examination of the composition characteristics within the star at several critical moments. In figure 7, composition characteristics are displayed near the peak of the eighth flash, when the mass in the convective shell is near maximum. Note that, in the entire region below the outer edge of the convective shell, all of the original ^{14}N left behind by the advancing hydrogen-burning shell has been converted into ^{22}Ne via the reactions $^{14}\mathrm{N}(\alpha, \gamma)^{18}\mathrm{F}(\beta^{+}\nu)^{18}\mathrm{O}(\alpha, \gamma)^{22}\mathrm{Ne}$. Within the convective shell, ^{12}C has reached a respectable abundance as a consequence of the triple-α process, but ^{16}O has not been appreciably enhanced by the reaction $^{12}\mathrm{C}(\alpha, \gamma)^{16}\mathrm{O}$. Finally, outside the hydrogen-burning shell, in the convective envelope, ^{12}C and ^{16}O must await passage into the hydrogen-burning region before being converted nearly completely into ^{14}N.

In figure 8 are shown composition characteristics shortly before a convective shell develops in the helium-burning region during the ninth pulse. Note that, in the interim following the eighth pulse, the advancing hydrogen-burning shell processes a mass of about 0.001 $M_{\odot}$. The processed matter consists primarily of ^{4}He and ^{14}N, contains very little ^{12}C and ^{16}O, and has no ^{22}Ne.

We are now in a position to understand figure 9, where the power output from several reactions and composition changes in the convective shell are shown as a function of time during the ninth thermal pulse. Until the outer edge of the convective shell reaches the discontinuity in abundances at mass 0.9522 $M_{\odot}$, the triple-α reaction makes the dominant contribution to the power output by helium-burning. When the outer edge of the convective shell crosses the discontinuity, ^{14}N is swept into the shell. There it burns rapidly and, in so doing, makes a contribution to power output equal to that of the triple-α process. Shortly thereafter, the ^{18}O progeny of ^{14}N burn α-particles to form ^{22}Ne and thereby make an additional contribution to the power output. The combined contributions of ^{14}N and ^{18}O α-burning to the flux of outgoing energy serve to accelerate the rate at which the convective shell grows outward. However, by the time that ^{14}N has been completely destroyed, the total power output from helium-burning reactions begins to decline and the convective shell slowly shrinks in size, eventually disappearing after a total duration of about 16 years.

The distribution of ^{4}He, ^{12}C, and ^{16}O just before the appearance and just after the disappearance of the convective shell is shown in figure 10. The major consequence of the thermal pulse has been to bring ^{12}C and ^{22}Ne in large abundance almost into contact with the hydrogen-helium discontinuity (within $\sim 10^{-4}$ $M_{\odot}$). The proximity in mass of the carbon discontinuity and the hydrogen-helium discontinuity is somewhat misleading. The spacial separation of the two discontinuities is, at minimum, about 6 percent of the distance of either discontinuity from the center. The pressures at the two discontinuities differ by an order of magnitude.

V. THE $^{22}\mathrm{Ne}\ (\alpha, n)^{25}\mathrm{Mg}$ REACTION AS A SOURCE OF NEUTRONS

The rate at which ^{22}Ne is converted into ^{25}Mg with the emission of neutrons may be written as

$$\frac{dX_{22}}{dt} = -RX_{22}X_4\,, \tag{1}$$

where X_{22} and X_4 are the abundances by mass of ^{22}Ne and ^{4}He, respectively. When time t is in seconds, density ρ in g cm^{-3}, and temperature T in 10^6 ° K,

$$R \sim 1.5 \times 10^{21}(\rho/T^{2/3}) \exp(-470/T^{1/3})\,. \tag{2}$$

This approximation for R is from Fowler, Caughlin, and Zimmerman (1975).

The "lifetime" of ^{22}Ne may be defined as $\tau_{22} = 1/RX_4$. In figure 11, this lifetime is shown as a function of time at the location of two mass points. Also shown is the mean lifetime in the convective shell, where $(\tau_{22})_{\text{mean}} = \Delta M_{\text{shell}}/X_4\int_{\text{shell}} R dM$. The time interval extends from shortly before the peak of the ninth flash to shortly after the disappearance of the convective shell (compare with fig. 9).

The mass point 0.951 $M_{\odot}$ lies slightly below the base of the convective envelope. At this mass point, τ_{22} drops to a minimum of about 10 yr and one may conclude that, over a brief interval of several years, some ^{22}Ne nuclei will disappear and an equal number of neutrons will be released.

The mass point 0.952 $M_{\odot}$ is located at roughly the midpoint of the convective shell. There, the lifetime of ^{22}Ne is, at minimum, over 4 times larger than the 2600-yr interval between two pulses. One might infer that no neutrons are released in the convective shell. Fortunately, however, the temperature sensitivity of the neutron-producing reaction is sufficiently high ($R \propto \rho T^{23}$) that the burning rate in matter near the base of the convective shell lowers the mean lifetime of ^{22}Ne in the convective shell to a value much nearer the lifetime at the base than at the center. The mean lifetime in the convective shell drops to a minimum of about 100 yr, compared with a minimum lifetime of about 11 yr at the base of the shell.

Since the base of the convective shell remains at a high temperature for only a few years, it is clear that only a minute fraction of the ^{22}Ne that is ultimately contained in the convective shell during the ninth pulse is converted into ^{25}Mg. One might despair were it not for the fact that the amplitude of every variation that characterizes the thermal pulse and the following relaxation phase increases with each oscillation.

It has already been shown (fig. 2) that the maximum power output by helium-burning reactions increases with each successive pulse. Figure 12 demonstrates that the peak temperature at the base of the convective shell increases with each pulse. Shown also in figure 12 is the minimum lifetime of ^{22}Ne against α-capture at

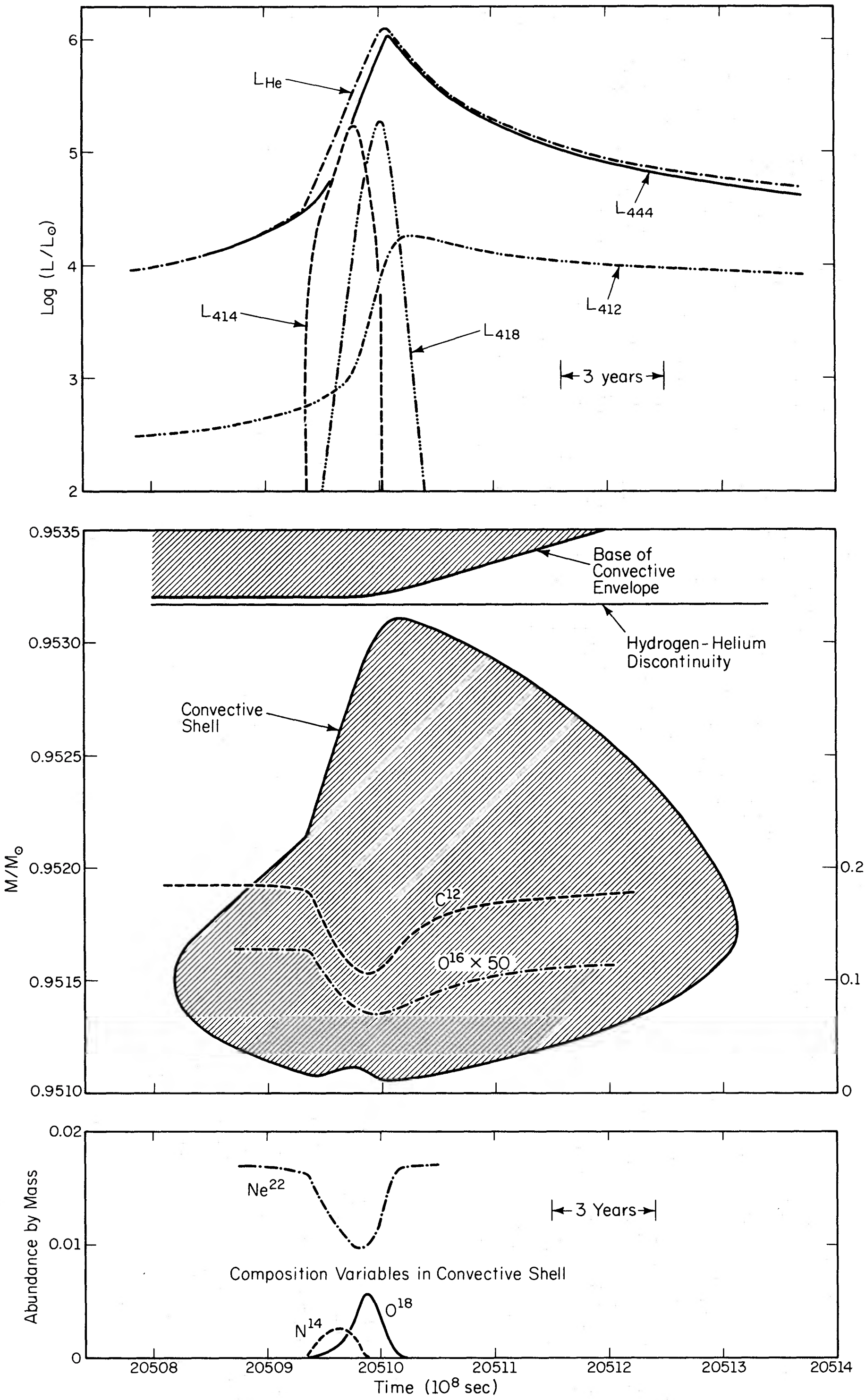

FIG. 9.—Characteristics of the helium-burning region during the ninth thermal pulse. *Upper panel*: power output from the triple-α reaction (L_{444}), the $^{12}C(\alpha, \gamma)^{16}O$ reaction (L_{412}), the $^{14}N(\alpha, \gamma)^{18}F(\beta^+\nu)^{18}O$ reactions (L_{414}), and from the $^{18}O(\alpha, \gamma)^{22}Ne$ reaction (L_{418}). All "luminosities" are in solar units. *Central panel*: shaded regions indicate the presence of convective motions. Also shown are the abundances by mass of ^{12}C and ^{16}O in the convective shell. *Lower panel*: abundances by mass of ^{14}N, ^{18}O, and ^{22}Ne in the convective shell.

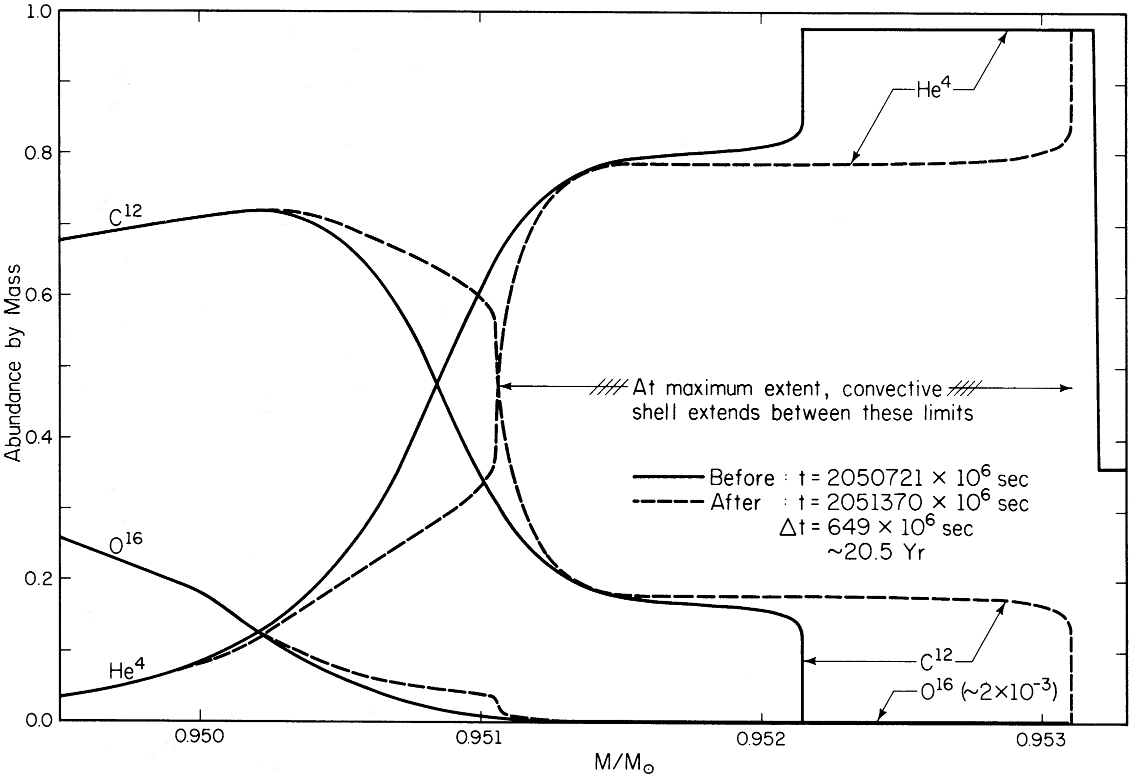

FIG. 10.—Abundances (by mass) of ^{4}He, ^{12}C, and ^{16}O as a function of mass in the model star just before the appearance of shell convection (*solid curve*) and just after the disappearance of shell convection during the ninth thermal pulse. ^{22}Ne is at an abundance by mass of about 0.0176 throughout the entire star below mass 0.9531 $M_\odot$.

the base of the shell (in obtaining this curve, a density $\rho = 2000$ g cm^{-3} has been adopted). Within another 10 pulses, the minimum lifetime at the base of the shell should drop below 1 yr and the mean lifetime in the shell should drop below 10 yr.

The duration of each pulse decreases with each pulse in such a way that the total nuclear energy released during a pulse remains nearly constant. The duration of a pulse is therefore roughly proportional to the lifetime of helium at some representative temperature in the helium-burning region, and the ^{22}Ne(α, n)^{25}Mg reaction will serve as a major source of neutrons only if the mean lifetime of ^{22}Ne drops below the mean lifetime of ^{4}He. At temperatures near $T_6 = 300$, the rate of ^{4}He-burning is proportional to about the 11th power of the temperature whereas the rate of ^{22}Ne burning goes as the 23d power. As temperature increases, then, the^{22} Ne lifetime decreases relative to the ^{4}He lifetime. A quantitative estimate gives $\tau_{22}/\tau_4 \sim 0.7$ at $T_6 = 314$ and $\rho = 2000$ g cm^{-3}. At $T_6 = 358$ and $\rho = 2000$ g cm^{-3}, $\tau_{22}/\tau_4 = 0.16$.

The maximum temperatures reached near the base of the convective shell, in the narrow region where most of the nuclear burning is occurring, are increasing at the rate of about 5 million degrees per pulse. Since the carbon-oxygen core of the star will not begin burning carbon until the core mass reaches about 1.4 $M_\odot$ and since the hydrogen-burning shell processes a mass of about 0.001 $M_\odot$ between pulses, one may estimate that at least 500 more pulses will occur. It seems quite reasonable to suppose that, long before the 500th pulse, the mean lifetime of ^{22}Ne in the convective shell will become comparable to or less than the duration-time of the convective shell.

However, it should be kept in mind that, although the maximum temperature at the base of the convective shell has been increasing almost linearly during the last three or four calculated pulses, the rate of increase per pulse is slowly decreasing. It is certainly possible that further calculation will show maximum base temperature approaching an asymptotic limit such that τ_{22}/τ_4 does not become small enough for ^{22}Ne to be a major source of neutrons for *s*-process nucleosynthesis. On the other hand, it is also possible that the cross section factor for the ^{22}Ne(α, n)^{25}Mg reaction is actually sufficiently larger than the currently estimated factor that neutrons are being copiously emitted already in the tenth pulse.

An additional uncertainty deserves airing. It has been assumed in the calculations that all elements in the convective shell are homogeneously distributed within this shell. This assumption is, of course, not valid for an element characterized by a lifetime small compared with a convective turnover time in the shell. An examination of lifetimes relative to estimates of

1975ApJ...196..351C

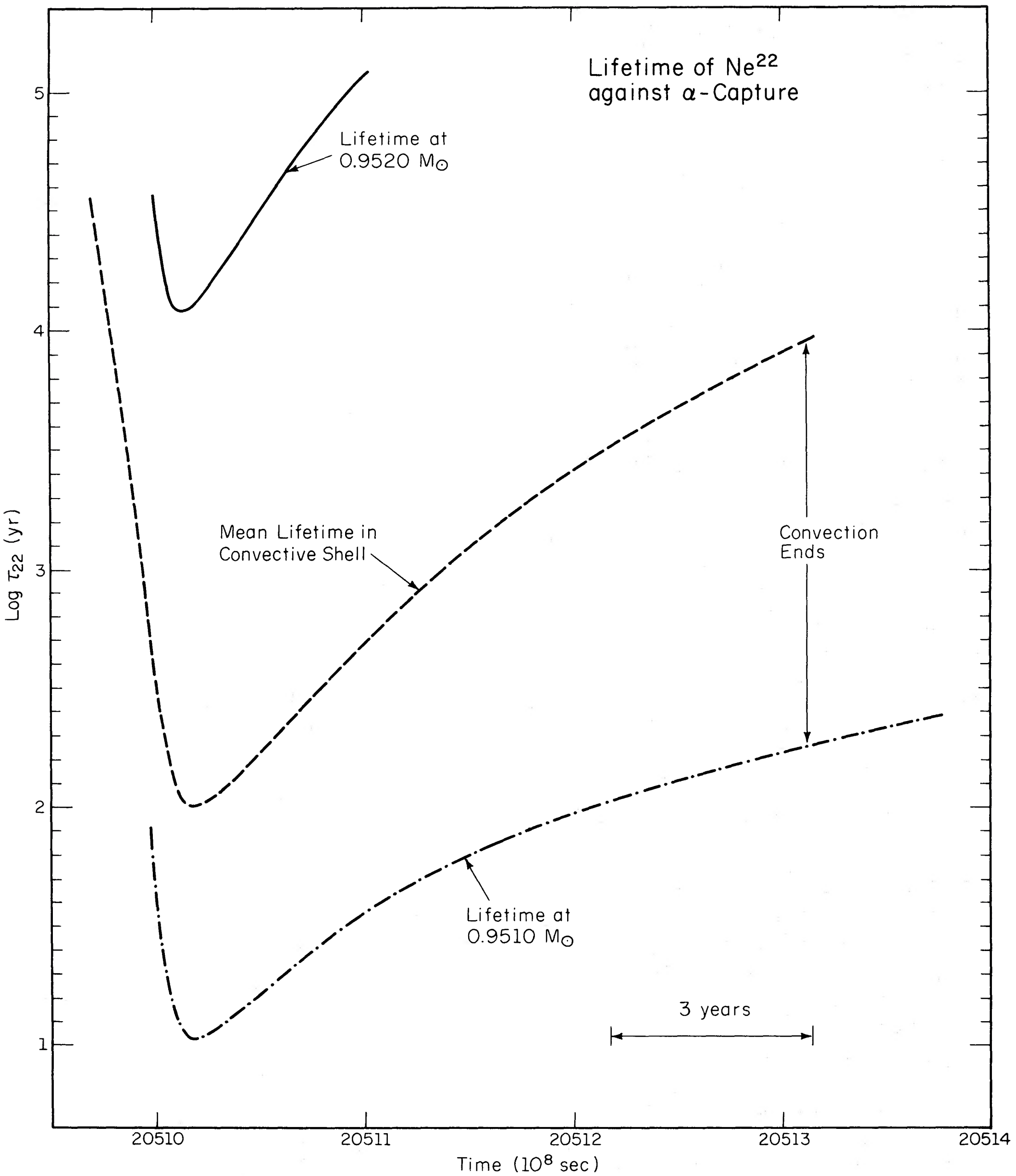

FIG. 11.—The "lifetime" of ^{22}Ne, X_{22}^{-1} $(dX_{22}/dt)^{-1}$, at two mass points, and the mean lifetime in the convective shell during the ninth thermal pulse.

mixing times indicates that departures from homogeneity will not appreciably alter the conclusions reached here. For example, at the peak of the eighth flash, the convective turnover time in the shell is on the order of 30 seconds compared with a ^{22}Ne lifetime on the order of tens of years at the base of the shell.

VI. THE MIXING OF FRESH PRODUCTS TO THE SURFACE

The possibility that products of helium-burning may be brought to the surface shortly after the convective shell disappears is demonstrated in figure 1 and is shown in greater detail in figure 13 where several properties of matter at the base of the convective envelope are given as a function of time before and after the eighth thermal pulse. At its maximum extent inward in mass, the base of the convective envelope reaches beyond the location in mass of the pre-pulse hydrogen-helium interface by about 5×10^{-5} $M_{\odot}$ and thus reaches to within about 5×10^{-5} $M_{\odot}$ of the carbon discontinuity left behind by the convective shell during the eighth pulse.

Figure 12 shows that the minimum mass separating the base of the convective envelope at its maximum

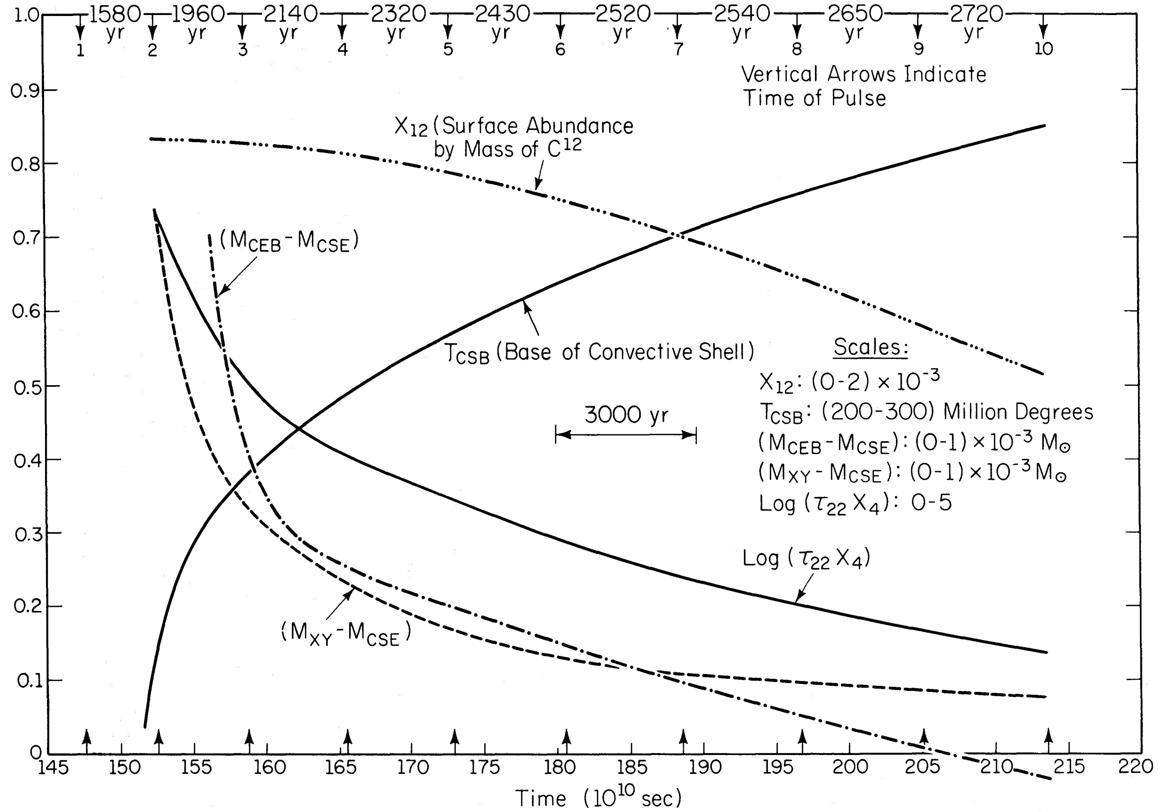

FIG. 12.—Relative extrema that occur during or shortly after a thermal pulse: minimum τ_{22}, minimum $M_{XY} - M_{\rm CSE}$, minimum $M_{\rm CEB} - M_{\rm CSE}$, and maximum $T_{\rm CSB}$, where τ_{22} = lifetime of ^{22}Ne at the base of the convective shell, M_{XY} = location in mass of the hydrogen-helium discontinuity, $M_{\rm CSE}$ = location in mass of the outer edge of convective shell, $M_{\rm CEB}$ = location in mass at the base of convective envelope, and $T_{\rm CSB}$ = temperature at the base of convective shell. Also shown is the surface abundance of ^{12}C.

inward extent following a thermal pulse ($M_{\rm CEB}$) and the maximum outward extent of the edge of the convective shell during the pulse ($M_{\rm CSE}$) decreases almost linearly with pulse number. Following the tenth pulse, $M_{\rm CEB} - M_{\rm CSE}$ goes negative by about 4×10^{-5} $M_\odot$. Convection then carries fresh ^{4}He, ^{12}C, and ^{22}Ne to the surface. Following more advanced pulses, when *s*-process elements may begin to be formed, rare earths should be carried to the surface by convection.

One may envision a slow change in surface abundances. During each interpulse relaxation phase, ^{16}O and ^{12}C are converted almost completely into ^{14}N within the radiative portion of the hydrogen-burning shell. During the following pulse, the fresh ^{14}N left behind by the hydrogen-burning shell is converted completely into ^{22}Ne within a convective shell which, at maximum, contains a mass of 0.002 $M_\odot$ and nearly touches the hydrogen-helium interface. The ^{22}Ne is, in turn, converted partially into ^{25}Mg within the convective shell, and the neutrons released in the conversion are captured by ^{56}Fe and its synthesized products to form heavy *s*-process elements. Neutrons are also captured by ^{22}Ne and ^{25}Mg and their progeny to form light *s*-process elements. Also found in the convective shell are fresh ^{4}He left behind by the hydrogen-burning shell and fresh ^{12}C made by the triple-α process. Immediately following the pulse, the convective envelope digs down into the region just vacated by the convective shell and brings out fresh ^{4}He, ^{12}C, ^{22}Ne, ^{25}Mg, and *s*-process elements. Concomitantly, the surface abundances of ^{1}H, ^{14}N, and ^{56}Fe drop slightly. The cycle completes when the base of the convective envelope recedes outward and hydrogen reignites. Then, during the interpulse phase, some of the new ^{12}C is processed by the hydrogen-burning shell into ^{14}N. Thus, the net abundance of neutron sources slowly increases with each cycle.

The curve $M_{\rm CEB} - M_{\rm CSE}$ in figure 12 shows that the extent to which the base of the convective envelope digs into the matter previously found in a convective shell increases almost linearly with pulse number. It is likely that, within another 20 pulses or so, the current rapid rate of increase will have abated and the magnitude of $M_{\rm CSE} - M_{\rm CEB}$ will have approached a limiting value. This inference is based on the supposition that the variations engendered by the thermal instability and the accompanying relaxation oscillations are limited in amplitude by the mass in the carbon-oxygen core. In particular, one might expect

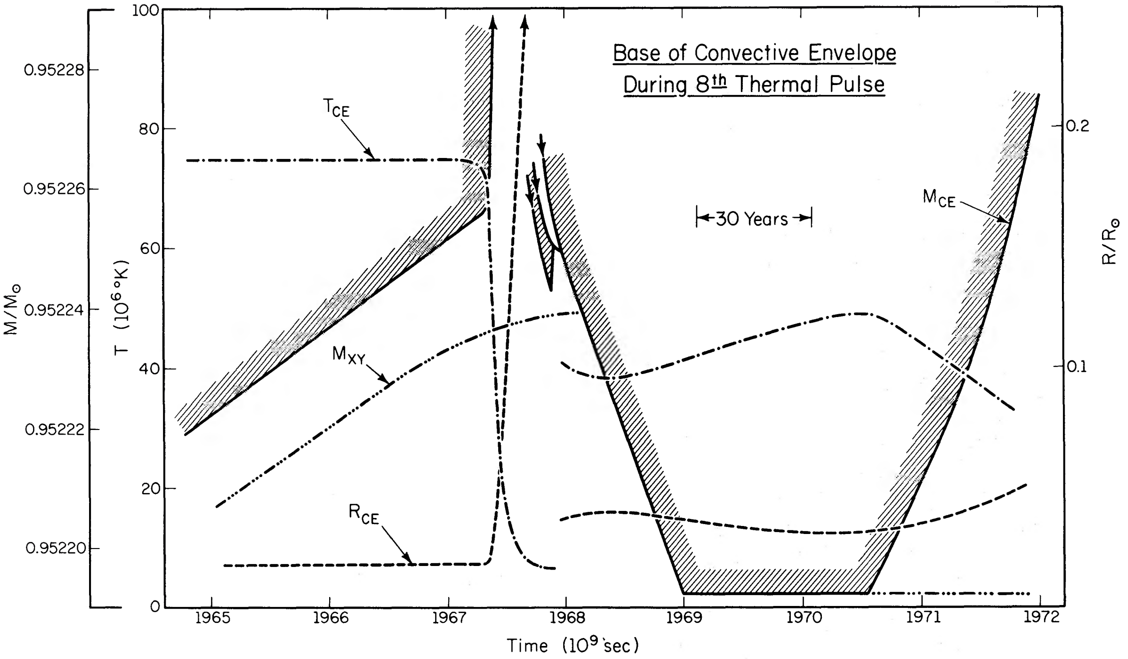

FIG. 13.—Properties at the base of the convective envelope before and after the eighth thermal pulse; M_{CE} = mass, R_{CE} = radial location, and T_{CE} = temperature. Also shown is the mass M_{XY} below which there is no hydrogen.

that the mass of fresh products deposited in the convective envelope following each pulse ($M_{CSE} - M_{CEB}$) will not exceed the mass carved out by the hydrogen-burning shell during the interpulse phase ($\sim 0.001\ M_\odot$).

The invasion of convection into the region left behind by the hydrogen-burning shell has the effect of increasing the duration of the double-shell-source phase. If a fraction f of the 0.001 $M_\odot$ processed by the hydrogen-burning shell during the interpulse phase is incorporated into the convective envelope immediately following each pulse, then the total number N of pulses to be expected in the present model (with an initial carbon-oxygen core mass of $\sim 0.95\ M_\odot$) is given by $0.001\ M_\odot (1 - f)N \approx 0.45\ M_\odot$. The total time expended in the double-shell-source phase is therefore proportional to $(1 - f)^{-1}$, and the total amount of matter that is processed at least once through helium-burning in a convective shell and is then mixed to the surface is proportional to $f/(1 - f)$.

VII. A CURABLE DEFICIENCY OF THE MODEL

Given the indication from the observations that there is some correlation between high surface abundances of *s*-process elements and higher-than-solar ratios of ^{12}C to ^{16}O in M, S, and N giants (see Wallerstein 1973; Scalo 1974; and references therein), a disturbing feature of the model star discussed here is the rapidity with which ^{12}C is depleted in the convective envelope during the interpulse phase. For example, during the eighth and ninth pulses, the surface abundance of ^{12}C decreases at the rate of $dX_{12}/dN \sim -0.1X_{12}$, where N is the cycle number. One may infer that, even though fresh carbon is added to the envelope just after each pulse, this carbon is rapidly converted during the interpulse phase into ^{14}N.

A quantitative estimate is possible. Let us suppose that, following each pulse, the mass ΔM_c of fresh carbon that is deposited in the envelope is

$$\Delta M_c \approx 0.001\ M_\odot \times f \times 0.15\,. \qquad (3)$$

Here, 0.15 is an approximation to the abundance by mass of ^{12}C left behind when the convective shell disappears and $0.001\ M_\odot \times f$ is the portion of the region vacated by the convective shell that is subsequently passed over by the base of the convective envelope. Since the hydrogen shell eats through a mass of 0.001 $M_\odot$ during each interpulse phase, one expects $f < 1$. If $6\ M_\odot\, g$ is the mean mass of the convective envelope, the abundance by mass of ^{12}C in this envelope undergoes an increment of

$$\Delta X_{12} = 2.5 \times 10^{-5} f/g \qquad (4)$$

immediately following each pulse. If ^{12}C were not destroyed during the interpulse phase, the surface abundance by number of ^{12}C would exceed the surface abundance by number of ^{16}O ($X_{16} = 7.3 \times 10^{-3}$ at the surface of the present model) after a number of cycles $\bar{N}$ determined by

$$\bar{N}\frac{dX_{12}}{dN} = (2.5 \times 10^{-5} f/g)\bar{N} \geq 6.25 \times 10^{-3}\,. \qquad (5)$$

Thus, after some $250g/f$ cycles, the present model would become a carbon star (C/O > 1).

However, the surface abundance of ^{12}C actually satisfies the equation

$$\frac{dX_{12}}{dN} = -\lambda X_{12} + \beta \tag{6}$$

so that

$$X_{12} = X_{12}(0)e^{-\lambda N} + \frac{\beta}{\lambda}(1 - e^{-\lambda N})\,. \tag{7}$$

Here $X_{12}(0)$ is the initial abundance by mass of ^{12}C, $\beta = 2.5 \times 10^{-5} f/g$, and λ is a function of the properties of the convective envelope. The burning of ^{14}N to form ^{12}C has been neglected. During the last few interpulse phases in the present model, $\lambda \sim 0.1$. Hence, after a very few cycles,

$$X_{12} \to \beta/\lambda \sim 2.5 \times 10^{-4} f/g\,, \tag{8}$$

and the present model will fail by a wide margin to become a carbon star.

There are several ways to remedy the apparent defect. One way is to reduce the mass of the diluting envelope (reduce g) either by invoking mass loss from the surface or by choosing an initially less massive star. Another way is to adjust the parameters in the treatment of envelope convection in such a way as to reduce the mean temperature at the base of the convective envelope during the interpulse phase. One may infer from figures 2 and 12 that, if this temperature can be reduced to less than 60 million degrees, λ in expressions (6)–(8) will be reduced to about 0.004 and, after several hundreds of cycles, the model will exhibit a surface ratio of C to O larger than 1. A slight reduction from 1.0 to 0.7 in the ratio of mixing length to pressure scale-height (l/H_p) reduces the temperature at the base of the convective envelope from 76 to 50 million degrees, quite sufficient to shut off the burning of ^{12}C.

It should be kept in mind, however, that a base temperature sufficiently low to prevent destruction of ^{12}C also hinders the production of ^{13}C. This suggests that small surface ratios of ^{12}C to ^{13}C should, in general, be correlated with low surface abundances of ^{12}C and that carbon stars should exhibit ^{12}C/^{13}C ratios considerably larger than the limiting value of 3.4.

A possible disadvantage of adjusting parameters to reduce the mean temperature at the base of the convective envelope is that, following each pulse, the extent to which the base of the convective envelope reaches down into the region of fresh ^{12}C and *s*-process elements may be reduced to such an extent that effectively no new elements are brought to the surface. On the other hand, using the current treatment of convection, the rate at which $M_{\rm CSE} - M_{\rm CEB}$ is increasing with each pulse would seem to be a bit excessive; in 20 cycles at the current rate, more newly processed matter will be engulfed by convection extending from the surface, just after each pulse, than has been processed by the hydrogen-burning shell during the interpulse phase. A different treatment that reduces $T_{\rm CEB}$ might also bring a welcome reduction in the rate of increase of $M_{\rm CSE} - M_{\rm CEB}$ (see note 2 added in proof).

VIII. THE LITHIUM PROBLEM

The fact that ^{7}Li appears in high abundance ($\sim 10^{-7}$ by number) at the surfaces of some luminous carbon stars coupled with the fact that the fraction of carbon stars that exhibit such anomalously high abundances is really very small (say 1 in 100) may offer a clue to the detailed nature of the mixing process in a convective envelope.

Following the suggestion of Cameron and Fowler, Iben (1973*b*), Smith *et al.* (1973), and Sackmann *et al.* (1974) have investigated the possibility of producing large abundances of ^{7}Li at the surfaces of convective envelopes having high base temperatures. Iben (1973*b*) shows that, if one assumes that *all* elements are distributed evenly throughout the envelope, then the abundance by mass of ^{7}Be in the envelope reaches a maximum of about 3×10^{-11} during the second interpulse phase. The equilibrium abundance by mass of ^{7}Li during this phase is about 4×10^{-13}. Iben argues that, during the ensuing pulse, when the temperature at the base of the envelope drops to a very low level (10 million degrees when $l/H_p = 1$), most of the ^{7}Be in the envelope will be converted by electron capture into ^{7}Li (over an interval of a few years) and the surface abundance of ^{7}Li will rise to 3×10^{-11}. A similar analysis of envelope matter during the sixth interpulse phase gives an equilibrium abundance of ^{7}Be of $\sim 10^{-10}$ and an equilibrium abundance of ^{7}Li of 5×10^{-13}. Thus, the assumption of homogeneity for all elements leads to the inference that the surface ^{7}Li abundance will rise to its highest values during the period of lowest base temperature (during the pulse) and will drop to its lowest values during the period of highest base temperature (during the long interpulse phase). Since the combined duration of the pulse phase and the phase immediately following each pulse (when base temperature hovers for a while at values intermediate between the minimum reached during the pulse and the mean obtaining during the interpulse phase) is very small relative to the duration of the interpulse phase, one has a very natural explanation for the paucity of lithium-rich carbon stars. However, the maximum surface ^{7}Li abundance predicted on this model is smaller than that found in several carbon stars by three or four orders of magnitude.

In addition to failing to provide a quantitative explanation of lithium-rich stars, the model suggested by Iben is based on incorrect physics. The assumption of homogeneity is even-roughly valid only for those elements such as ^{3}He and ^{12}C whose mean lifetimes against destruction are long compared with the mean turnover time in the convective envelope. For example, during the sixth interpulse phase, the mean lifetimes of ^{3}He and ^{12}C are both approximately 4×10^4 yr whereas a convective turnover time is on the order of several years. The assumption of homogeneity begins to break down even for these elements near the base of the envelope where lifetimes drop to roughly 10–20 days.

For ^{7}Be and ^{7}Li, the assumption of homogeneity is a very poor approximation. For example, during the sixth interpulse phase, the mean lifetimes of ^{7}Be and ^{7}Li would be (if these elements were distributed evenly) 2 months and 10 hours, respectively. Without further thought, one might suppose that a much better approximation would be achieved by assuming that ^{7}Be and ^{7}Li are *locally* in equilibrium. This is certainly the case near the base of the envelope where (during the sixth interpulse phase) the lifetimes of ^{7}Be and ^{7}Li are 3 hours and 0.05 seconds, respectively, and local equilibrium abundances are 1.6×10^{-7} and 1.08×10^{-17}, respectively. It is not the case, however, over most of the envelope where the lifetime of ^{7}Be against electron capture is locally roughly 2 months and the lifetime of ^{7}Li is essentially infinite.

Smith *et al.* (1973) and Sackmann *et al.* (1974) have attempted to approximate the actual distribution of elements in a convective envelope by supposing that the manner in which convection influences this distribution can be described by diffusion equations. The source terms in these equations are the ordinary nuclear interaction and β-decay rates. Although it may be permissible to describe some aspects of convective energy flow via a diffusion equation (interpreting this as an approximation to a "random walk" process and choosing a mean free path as a macroscopic "mixing length"), it is not clear that one can describe the transfer of individual element species by equations that are a mixture of two qualitatively different terms, one of which attempts to describe macroscopic behavior (convective motions) and the other of which describes microscopic behavior (nuclear reactions).

Nevertheless, the equations are easily solvable, and Smith *et al.* (1973) and Sackmann *et al.* (1974) show that they imply large abundances of ^{7}Li at the surface and that, for base temperatures near 50 million degrees, the magnitude of the maximum surface abundance achievable increases with increasing base temperature. The maximum amount of ^{7}Li that can be made in the envelope is, of course, also proportional to the amount of ^{3}He in the envelope. This is because the ^{7}Li that appears at the surface is the β-decay product of the ^{7}Be that is formed at the base of the convective envelope via the reaction $^3\mathrm{He}(^4\mathrm{He}, \gamma)^7\mathrm{Be}$ and that convectively diffuses out of the production region before beta decaying.

The fact that, on the diffusion model, both a high base temperature and a high ^{3}He abundance are necessary for a high surface ^{7}Li abundance provides a possible embarrassment for the diffusion model. First of all, since the surface ^{7}Li abundance would achieve and maintain its highest values during the interpulse phase, dropping to much lower values during the pulse and during the immediate post-pulse phase, one would expect the lithium-rich phenomenon to be the rule rather than the exception among carbon stars. Second, in order to achieve the highest abundances found in several carbon stars, one would require base temperatures large enough to destroy at roughly the same rates both ^{12}C (whose large abundance relative to ^{16}O is a characteristic signature of carbon stars) and ^{3}He (which is the ultimate source of ^{7}Li). Thus we would have the curious result that a super-^{7}Li-rich carbon star would cease being a carbon star in a matter of a few thermal pulses.

It is to be hoped that a more careful consideration of the physics of convective transfer will lead to models for the surface enhancement of Li that are in better accord with the observations.

IX. THE ENHANCEMENT OF *S*-PROCESS ELEMENTS AT THE SURFACE AND ANOTHER POSSIBLE EMBARRASSMENT

Having admitted to potentially embarrassing aspects of the model, it is permissible to remark on possible successes with regard to the predicted total surface abundance of *s*-process elements relative to the surface abundance of iron. The mass of ^{56}Fe that is first swallowed up by the convective shell, is next converted into heavier elements by neutron capture, and is then brought out as *s*-process elements may be written as

$$-\Delta M_{56} \approx X_{56}(0.001\, M_\odot f)\,, \tag{9}$$

where X_{56} is the envelope abundance by mass of ^{56}Fe before each pulse. Following each pulse, the surface abundance of ^{56}Fe is depleted by

$$\Delta X_{56} = -\Delta M_{56}/6M_\odot g = -1.7 \times 10^{-4} f/g X_{56}\,. \tag{10}$$

Hence, the surface abundance by number of ^{56}Fe follows the law

$$n_{56}(N) = n_{56}(0)\exp(-1.7 \times 10^{-4} Nf/g)\,. \tag{11}$$

Since (by definition) all ^{56}Fe nuclei that capture neutrons form *s*-process nuclei, the ratio of the total surface abundance of heavy *s*-process elements to the surface abundance of ^{56}Fe is just

$$n_s(N)/n_{56}(N) \approx \exp(1.7 \times 10^{-4} Nf/g) - 1$$
$$\approx 1.7 \times 10^{-4} Nf/g\,. \tag{12}$$

Ratios of this magnitude are found in some red supergiants (see Wallerstein 1973).

The number of neutrons released per ^{56}Fe seed nucleus may also be estimated. Defining the number abundance of any element as $n_i = X_i/A_i$, where X_i is the abundance by mass and A_i is the atomic number, the total initial abundance of CNO nuclei in the envelope of the present model is $n_{\mathrm{CNO}}(0) = 8.3 \times 10^{-4}$. Since the fresh ^{12}C injected into the envelope following each succeeding pulse increases the number abundance of ^{12}C in the envelope by $2 \times 10^{-6} f/g$, the hydrogen-burning shell will leave behind, during the interpulse phase, a number of ^{14}N nuclei equal to

$$n_{14} \approx 8.3 \times 10^{-4} + 2 \times 10^{-6} Nf/g\,. \tag{13}$$

The number abundance of ^{56}Fe left behind by the hydrogen-burning shell is very nearly the initial abundance, $n_{\mathrm{Fe}}(0) \sim 2 \times 10^{-5}$. If a fraction f^1 of the ^{22}Ne progeny of ^{14}N is converted into ^{25}Mg and neutrons, then the number of neutrons Δn_s released per ^{56}Fe seed nucleus in each cycle is approximately

$$\frac{\Delta n_s}{\Delta n_{56}} \sim 42 f^1(1 + 2.4 \times 10^{-3} Nf/g)\,. \qquad (14)$$

It is therefore plausible that, on the average, 20–60 neutrons are released for every fresh iron-seed nucleus. If all of the released neutrons are captured by ^{56}Fe and its progeny, heavy *s*-process elements will be produced in an abundance distribution that looks very different from the "cosmic" distribution (Ulrich 1973). This possible embarrassment is addressed in a companion paper (Iben 1975).

Equations (13) and (14) illustrate a feature of the present model that has ramifications for models of different initial composition. After a sufficiently large number of cycles, the fresh carbon brought into the envelope and then converted into ^{14}N by the hydrogen-burning shell can act as the ultimate source of neutrons for *s*-process nucleosynthesis even in the absence of a large initial abundance of CNO nuclei. Hence, the sensitivity of the total abundance of *s*-process elements produced in a given star to the initial abundance of light and of heavy elements (CNO nuclei and ^{56}Fe) is somewhat less than quadratic. Nevertheless, the sensitivity remains greater than the linear one suggested by other models which rely on the reaction $^{13}\mathrm{C}(\alpha, n)^{16}\mathrm{O}$ to provide neutrons.

Writing equation (14) again in the form

$$\frac{\Delta n_s}{\Delta n_{56}} = f^1(n_{\mathrm{CNO}}(0) + 2 \times 10^{-6} Nf/g)/n_{\mathrm{Fe}}(0)\,, \qquad (15)$$

it is evident that the number of neutrons liberated per fresh iron-seed nucleus may far exceed 20–60 in stars with initial iron and CNO abundances much smaller than solar. One infers that, in stars exhibiting anomalously high abundances of *s*-process elements relative to the abundance of iron, there should be an inverse correlation between the iron abundance and the mass weighted mean of the *s*-process elements.

A final point worth emphasizing is that the absolute abundance of ^{14}N at the surface of a double-shell-source star is likely to be at least as large as or larger than the surface abundance during previous stages. During all earlier entries onto the giant branch, the surface abundance of a model star increases as the base of the convective envelope extends into regions where ^{12}C has been converted nearly completely into ^{14}N. For example, on its first entry into the region of red giants, the 7 $M_\odot$ model discussed in this paper develops a surface abundance of ^{14}N that is 2.5 times larger than that with which it began on the main sequence (Iben 1972). When the model reaches the giant branch for the second time, the surface abundance of ^{14}N rises by another factor of 1.4. Then, during the course of the first 10 thermal pulses, the ^{14}N abundance increases at the expense of ^{12}C by another factor of 1.2, but this factor can be reduced by adjusting surface parameters.

When fresh ^{12}C begins to be injected into the envelope, ^{14}N will be concomitantly drained from the envelope, but at a very slow rate. If ^{12}C were not converted into ^{14}N within the envelope during the interpulse phase, the surface abundance of ^{14}N would drop at the same rate as the iron abundance, as given by equation (11). For stars with large envelopes, the change in ^{14}N would be imperceptible. If freshly injected ^{12}C is converted into ^{13}C at an appreciable rate within the envelope, then the abundance of ^{14}N will also rise, despite the depletions that immediately follow each pulse. One therefore expects that, in general, the mean surface abundance of ^{14}N will increase monotonically with time. There is some indication from the observations (Wallerstein 1973; Sneden 1974) that the absolute abundance of ^{14}N does indeed increase monotonically with each successive sojourn on the giant branch, as predicted.

It is a pleasure to thank those individuals who responded favorably to appeals for computer time: Dave Hummer of JILA who opened the door to the CDC 6600 and CDC 7600 computers at the National Center for Atmospheric Research; Jack Hildebrand who granted time on the NCAR machines despite opposition from the computer allocation advisory panel for this supposedly national facility; Dillon Mapother, Jack McManus, and David Stonehill at the University of Illinois who went out of their way to provide time on an IBM 360/75 and on an IBM 370/158 at the University of Illinois. Thanks to Jack Knott at the University of Illinois for easing the pain of attempting to use a saturated computer and to Gordon Chace at the same institution for acting as an efficient and effective interface between myself and the different computers used in obtaining the data for this paper. Thanks also to the Research Board of the University of Illinois for granting computer funds in abundance and to the National Science Foundation for contributing partial support for the massive computer usage required by modern studies of stellar structure and nucleosynthesis. Thanks to David Carlson for preparing graphs for figures 3–6, to Bob MacFarlane for his artistry in preparing the figures, and to Ann Carroll for her aid in preparing the manuscript. Further, thanks to Jim Truran for explaining the requirements for *s*-process nucleosynthesis and for critically commenting on the manuscript. Thanks to Mike Howard and Susan Lamb for serving as sounding boards and to Dave Arnett for helpful discussions on the lithium problem.

The first year of the three years involved in the investigation reported here was spent at the Joint Institute for Laboratory Astrophysics at the University of Colorado in Boulder and at the Santa Cruz campus of the University of California. I am most grateful for the hospitality extended to me during my visits to these stimulating institutions. Thanks to John Cox, Carl Hansen, John Faulkner, and Bob Kraft for making these visits possible.

A very warm thanks to the referee of the first version of this paper for insisting that: not only can

^{22}Ne not act as a significant source of neutrons but, even if it does, both it and its progeny will use up all of the emitted neutrons, leaving none for the production of heavier *s*-process elements.

Note 1 added in proof.—Following the initial submission and distribution of this paper, a number of investigators have communicated to me the results of thermal-pulse calculations for a variety of total masses and core masses (R. A. Gingold, P. Gross and A. Sweigert, D. Sugimoto and K. Nomoto, and H-C. Thomas). From these results it appears that (1) for a given core mass, a limiting pulse amplitude is reached after 15–25 pulses have been followed, and (2) the fraction of ^{22}Ne that is converted into ^{25}Mg plus neutrons in each pulse (at limiting amplitude) is a monotonically increasing function of core mass, the fraction exceeding 0.5 for core mass in the neighborhood of $(0.95–1.05)M_\odot$. Thus, all stars which develop a carbon-oxygen core of mass larger than $\sim M_\odot$ will exhibit at their surfaces an enhancement of *s*-process elements, the enhancement being greater the smaller the total mass of the star and the larger the core mass relative to the threshold mass of $\sim M_\odot$.

APPENDIX A

CONDUCTIVITY

Analytic fits to the electron conductivity calculated by Hubbard and Lampe (1969) have been constructed as functions of the parameters θ and $\langle\lambda\rangle/2R$ discussed by Iben (1968). The combination $\theta/\kappa_c T_6$, where θ is a momentum transfer factor, κ_c is the conductive opacity, and T_6 is the temperature (in units of 10^6 ° K), is a function of the degeneracy parameter,

$$\delta = \rho/\mu_e T_6^{3/2}\,, \tag{A1}$$

where ρ = density in g cm^{-3} and μ_e = nucleons per free electron. In good approximation,

$$\log(\theta/\kappa_c T_6) = -3.2862 + \log[\delta(1 + 0.024417\delta)] \tag{A2}$$

when $\log\delta < 0.645$;

$$\log(\theta/\kappa_c T_6) = -3.29243 + \log[\delta(1 + 0.02804\delta)] \tag{A3}$$

when $0.645 < \log\delta < 2.0$;

$$\log(\theta/\kappa_c T_6) = -4.80946 + \log[\delta^2(1 + 9.376/\eta_0^2)] \tag{A4}$$

when $\log\delta > 2.5$; and

$$\log(\theta/\kappa_c T_6) = 2a_1(2.5 - \log\delta) + 2b_1(\log\delta - 2) \tag{A5}$$

when $2 < \log\delta < 2.5$.

In expression (A5), a_1 and b_1 are the values of $\log(\theta/\kappa_c T_6)$ given by equations (A3) and (A4), respectively. In expression (A4),

$$\log\eta_0 = -0.52255 + (2\log\delta)/3\,. \tag{A6}$$

The quantity θ may be considered to be a function of

$$(\langle\lambda\!\!\!^{-}\rangle/2R)^2 = (9.24735 \times 10^{-3})\delta(n_e kT/P_e)T_6^{-1/2}(\mu_e \sum X_i Z_i^2/A_i + n_e^{-1}\partial n_e/\partial\eta)\,. \tag{A7}$$

Here $\langle\lambda\!\!\!^{-}\rangle$ = the wavelength of a free electron averaged over the Fermi distribution, R = Debye radius, n_e = electron density, $n_e kT$ = electron pressure when degeneracy is neglected, X_i = abundance by mass of element i, Z_i = number of protons in nucleus i, A_i = atomic mass of nucleus i, η = another degeneracy parameter (see, e.g., Iben 1968) that reduces to ϵ_F/kT (ϵ_F = Fermi energy) in the domain of degeneracy.

Adequate approximations are

$$(P_e/n_e kT) = 1 + 0.021876\delta \tag{A8}$$

when $\log\delta < 1.5$;

$$P_e/n_e kT = 0.4\eta_0(1 + 4.1124/\eta_0^2) \tag{A9}$$

when $\log\delta > 2.0$; and

$$\log(P_e/n_e kT) = 2a_2(2.0 - \log\delta) + 2b_2(\log\delta - 1.5) \tag{A10}$$

when $1.5 < \log\delta < 2.0$, where a_2 and b_2 are logarithms of $P_e/n_e kT$ given by expressions (A8) and (A9), respectively.

Further,

$$n_e^{-1}\partial n_e/\partial\eta = 1.0 - 0.01\delta(2.8966 - 0.034838\delta) \tag{A11}$$

when $\delta < 40$; and

$$n_e^{-1}\partial n_e/\partial\eta = (1.5/\eta_0)(1 - 0.8225/\eta_0^2) \tag{A12}$$

when $\delta > 40$.

Using expressions (A1)–(A12), Hubbard-Lampe tables of κ_c versus ρ and T_6 were converted into tables of log θ versus $\alpha = \log(\langle\lambda\rangle/2R)$ (see eq. [A7]) and ρ. Graphs of log θ versus α show that, to a very good approximation (within 20 percent for $0 < \log\rho < 6$), log θ is primarily a function of α, with ρ entering only in a secondary way. For pure hydrogen,

$$\log\theta_X = 1.048 - 0.124\alpha\,, \qquad \alpha \le -3\,; \tag{A13}$$

$$\log\theta_X = 0.13 - \alpha(0.745 + 0.105\alpha)\,, \qquad -3 < \alpha \le -1\,; \tag{A14}$$

and

$$\log\theta_X = 0.185 - 0.558\alpha\,, \qquad \alpha > -1\,. \tag{A15}$$

For pure helium,

$$\log\theta_Y = 0.937 - 0.111\alpha\,, \qquad \alpha \le -3\,; \tag{A16}$$

$$\log\theta_Y = 0.24 - \alpha(0.55 + 0.0689\alpha)\,, \qquad -3 < \alpha \le 0\,; \tag{A17}$$

and

$$\log\theta_Y = 0.24 - 0.6\alpha\,, \qquad \alpha > 0. \tag{A18}$$

For pure carbon,

$$\log\theta_C = 1.27 - 0.1\alpha\,, \qquad \alpha < -2.5\,; \tag{A19}$$

$$\log\theta_C = 0.727 - \alpha(0.511 + 0.0778\alpha)\,, \qquad -2.5 < \alpha \le 0.5\,; \tag{A20}$$

and

$$\log\theta_C = 0.843 - 0.785\alpha\,, \qquad \alpha > 0.5\,. \tag{A21}$$

For a mixture of elements, the net electron conductivity may be written as

$$\kappa_c = (X\theta_X + Y\theta_Y + Z_C\theta_C)/T_6 f \tag{A22}$$

where $f = (\theta/\kappa_c T_6)$ is given by expressions (A1)–(A6), X = abundance by mass of hydrogen, Y = abundance by mass of helium, and

$$Z_C = (3X_{12} + 3.5X_{14} + 4X_{16} + 3.56X_{18} + 4.54X_{22})/3\,. \tag{A23}$$

In expression (A23) the X_i are abundances by mass of ^{12}C ($i = 12$), ^{14}N ($i = 14$), ^{16}O ($i = 16$), ^{18}O ($i = 18$), and ^{22}Ne ($i = 22$).

The foregoing development for conductivity is not applicable when electrons are relativistically degenerate. Then, the results of Canuto (1970) are presumably applicable. An analytic approximation to Canuto's results may be constructed as a function of the parameters

$$\epsilon_F = [1 + (\rho_6/\mu_e)^{2/3}]^{1/2} - 1\,, \tag{A24}$$

and

$$\gamma = 22.76(\rho_6^{1/3}/T_6)Z_\alpha \tag{A25}$$

$$Z_\alpha = \Sigma_i Z_i^2 X_i/A_i^{1/3}\,, \tag{A26}$$

$$Z_\beta = \Sigma_i Z_i^2 X_i/A_i\,, \tag{A27}$$

where ρ_6 = density in 10^6 g cm^{-3}. This approximation is

$$\kappa_c = [(6.753 \times 10^{-8})(T_6^2/\epsilon_F^{2.5})Z_\beta/G]/(1 + \epsilon_F)\,, \qquad \text{(A28)}^1$$

where

$$\log G = [(0.873 - 0.298\log Z_\alpha) + (0.333 - 0.168\log Z_\alpha)M][1 - (1 + \gamma)^{-0.85}]\,, \tag{A29}$$

and

$$M = \min(1, 0.5 + \log\epsilon_F)\,. \tag{A30}$$

---

[1] As pointed out by Van Horn (1972), the expression for conductivity given by Canuto (1970) is too small by the factor $(1 + \epsilon_F)$.

1975ApJ...196..351C

In the calculations reported in the text, the approximation to the Hubbard-Lampe conductive opacity is used for all densities less than 10^6 g cm^{-3}. The approximation to the Canuto conductive opacity is used for densities in excess of 2×10^6 g cm^{-3}. For $6 < \log \rho < 6.3$, the following expression is used:

$$\log \kappa_c = (1 - f) \log \kappa_{\rm L} + f \log \kappa_{\rm H} , \tag{A31}$$

where

$$f = 0.5 \{1 - \cos [\pi(\log \rho - 6)/0.3]\} \tag{A32}$$

and $\kappa_{\rm H}$ = approximation to the Canuto conductive opacity, $\kappa_{\rm L}$ = approximation to the Hubbard-Lampe conductive opacity.

APPENDIX B

RADIATIVE OPACITY

Analytic fits to opacities given by Cox and Stewart (1970*a*, *b*), have been constructed. These take the form

$$\kappa = \kappa_e + \bar{\kappa} , \tag{B1}$$

where κ_e is an approximation to the opacity when all processes other than electron scattering are ignored.

For the mixtures characterized by ($X = 0$, $Y = 0.5$, $X_{12} = 0.5$), ($X = Y = 0$, $X_{12} = 1$), ($X = Y = 0$, $X_{12} = X_{16} = 0.5$), ($X = Y = X_{12} = 0$, $X_{16} = 1$), and ($X = 0$, $Y = 0.9999$, $Z = 0.0001$),

$$\log \kappa = \kappa_\rho \log (\rho/\bar{\rho}) + \log A_p , \tag{B2}$$

$$\log \bar{\rho} = -A + B \log T_6 , \tag{B3}$$

$$A = (1.25 + 0.488\mu^{1/2} + 0.092\mu)/0.67 , \tag{B4}$$

$$B = 3.86 + 0.252\mu^{1/2} + 0.018\mu , \tag{B5}$$

$$\mu = \sum_i Z_i^2 X_i/A_i - 1 , \tag{B6}$$

$$A_p = 1 + C(1 + C/24.55) , \tag{B7}$$

$$C = (2.019 \times 10^{-4} \rho/T_6^{1.7})^{2.425} , \tag{B8}$$

and

$$\kappa_\rho = 0.67 . \tag{B9}$$

An approximation to the electron-scattering component of κ is

$$\kappa_e = [0.2 - D - (D^2 + 0.004)^{1/2}](1 + X) , \tag{B10}$$

where

$$D = 0.05 (\log T_6 - 1.7) . \tag{B11}$$

For the mixtures characterized by ($X = 0.8$, $Y = 0.18$, $Z = 0.02$), ($X = 0.0$, $Y = 0.98$, $Z = 0.02$), ($X = 0.8$, $Y = 0.1999$, $Z = 0.0001$), and ($X = 0.0$, $Y = 0.9999$, $Z = 0.0001$),

$$\log \kappa = \kappa_\rho \log (\rho/\bar{\rho}) + A_z , \tag{B12}$$

where $\log \bar{\rho}$ is the smaller of

$$\log \bar{\rho}_1 = -2.3 + 4.833 \log T_6 , \tag{B13}$$

$$\log \bar{\rho}_2 = -(1.86 + 0.3125X) + 3.86 \log T_6 ; \tag{B14}$$

and

$$A_z = A_z^0(Z/0.02) , \tag{B15}$$

$$A_z^0 = A_1 \exp [-2.76 (\log \rho/\rho_0)^2/W^2] , \tag{B16}$$

$$\log \rho_0 = -(1.68 + 0.35X) + 1.8 \log T_6 \tag{B17}$$

when $\log T_6 > 0$; and

$$\log \rho_0 = -(1.68 + 0.35X) + (3.42 - 0.52X)\log T_6 \tag{B18}$$

when $\log T_6 < 0$.

The quantities A_1 and W in equation (B16) are given, respectively, by

$$A_1 = 1.22\exp[-(1.74 - 0.755X)(\log T_5 - 0.22 + 0.1375X)^2]\,, \tag{B19}$$

and

$$W = 4.05\exp[-(0.306 - 0.04125X)(\log T_6 - 0.18 + 0.1625X)^2]\,. \tag{B20}$$

In the calculations reported in the text, the opacity given by equations (B10)–(B20) was used for all $T_6 > 1.5$ and $X > 0$. For $X > 0$ and $T_6 < 1$, Christy's (1966) analytic expression was adopted. For $X > 0$ and $1 < T_6 < 1.5$, $\kappa = 2\kappa_1(1.5 - T_6) + 2\kappa_2(T_6 - 1)$, where κ_1 = Christy's approximation and κ_1 is given by equations (B10)–(B20). When $X = 0$ and $Z_B = X_{12} + X_{14} + X_{16} + X_{18} + X_{22} > Z$, expressions (B1)–(B11) were used. For $X = 0$ and $Z_{B0} < Z_B < Z$ ($Z_{B0} = Z_B$ at the surface of the star), $\kappa = [\kappa_1(Z_B - Z_{B0}) + \kappa_2(Z - Z_B)]/(Z - Z_{B0})$, where κ_1 is given by (B1)–(B11) and κ_2 is given by (B10)–(B20).

REFERENCES

Burbidge, E. M., Burbidge, G. R., Fowler, W. A., and Hoyle, F. 1957, *Rev. Mod. Phys.*, **29**, 547.
Cameron, A. G. W. 1954, *Phys. Rev.*, **93**, 932.
———. 1955, *Ap. J.*, **121**, 144.
Cameron, A. G. W., and Fowler, W. A. 1971, *Ap. J.*, **164**, 111.
Canuto, V. 1970, *Ap. J.*, **159**, 641.
Christy, R. F. 1966, *Ap. J.*, **144**, 108.
Clayton, D. D., Fowler, W. A., Hull, T. C., and Zimmerman, B. A. 1961, *Ann. Phys.*, **12**, 331.
Cox, A. N., and Stewart, J. 1970*a*, *Ap. J. Suppl.*, No. 174, **19**, 243.
———. 1970*b*, *ibid.*, p. 261.
Eggleton, P. P., Faulkner, J., and Flannery, B. P. 1973, *Astr. and Ap.*, **23**, 325.
Fowler, W. A., Caughlin, G. R., and Zimmerman, B. A. 1975, *Ann. Rev. Astr. and Ap.*, Vol. **13**, in press.
Hubbard, W. B., and Lampe, M. 1969, *Ap. J. Suppl.*, No. 163, **18**, 279.
Iben, I. Jr. 1968, *Ap. J.*, **154**, 557.
———. 1972, *ibid.*, **178**, 433.
———. 1973*a*, in *Explosive Nucleosynthesis*, ed. D. N. Schramm and W. D. Arnett (Austin: University of Texas Press), p. 115.
———. 1973*b*, *Ap. J.*, **185**, 209.
———. 1974*a*, *Ann. Rev. Astr. and Ap.*, **12**, 215.
———. 1974*b*, *Bull. AAS*, **6**, 316.
———. 1975, *Ap. J.*, **196**, 549.
Sackmann, I. J., Smith, R. L., and Despain, K. H. 1974, *Ap. J.*, **187**, 555.
Sanders, R. H. 1967, *Ap. J.*, **150**, 971.
Scalo, J. M. 1974, *Ap. J.*, **194**, 361.
Scalo, J. M., and Ulrich, R. K. 1973, *Ap. J.*, **183**, 151.
Schwarzschild, M., and Härm, R. 1967, *Ap. J.*, **150**, 961.
Seeger, P. A., Fowler, W. A., and Clayton, D. D. 1965, *Ap. J. Suppl.*, No. 97, **11**, 121.
Smith, R. L., Sackmann, I. J., and Despain, K. H. 1973, in *Explosive Nucleosynthesis*, ed. D. N. Schramm and W. D. Arnett (Austin: University of Texas Press), p. 168.
Sneden, C. 1974, *Ap. J.*, **189**, 493.
Sugimoto, D., and Nomoto, K. 1974, *Proc. IAU Symposium No. 66*, ed. R. J. Tayler (Warsaw), in press.
Sweigart, A. V. 1973, *Astr. and Ap.*, **24**, 459.
———. 1974, *Ap. J.*, **189**, 289.
Truran, J. W. 1973, *Proceedings of the Red Giant Conference*, ed. H. R. Johnson, J. P. Mutschlecner, and B. F. Peery (Bloomington: Indiana University Press), p. 394.
Ulrich, R. K. 1973, in *Explosive Nucleosynthesis*, ed. D. N. Schramm and W. D. Arnett (Austin: University of Texas Press), p. 139.
Ulrich, R. K., and Scalo, J. M. 1972, *Ap. J.* (*Letters*), **176**, L37.
Uus, U. 1970, *Nauch. Inform. Akad. Nauk. USSR*, **17**, 3, 25, 35, 48.
———. 1971, *ibid.*, **20**, 60, 64.
———. 1973, *ibid.*, **26**, 83, 96.
Van Horn, H. 1972, private communication.
Wallerstein, G. W. 1973, *Ann. Rev. Astr. and Ap.*, **11**, 115.
Weigert, A. 1966, *Zs. f. Ap.*, **64**, 395.

Note 2 added in proof.—Two additional pulses with $l/H = 0.7$ have been followed. The maximum inward extent of convection immediately following each pulse appears to be independent of l/H.

ICKO IBEN, JR.: Department of Astronomy, University of Illinois, Urbana, IL 61801

THE ASTROPHYSICAL JOURNAL, **196**: 549–558, 1975 March 1

NEON-22 AS A NEUTRON SOURCE, LIGHT ELEMENTS AS MODULATORS, AND *s*-PROCESS NUCLEOSYNTHESIS IN A THERMALLY PULSING STAR*

ICKO IBEN, JR.
University of Illinois, Champaign–Urbana

Received 1974 August 21

ABSTRACT

If the reaction ^{22}Ne(α, n)^{25}Mg is the major source of neutrons in the convective shell of a thermally pulsing star, the fraction of emitted neutrons that can be captured by ^{56}Fe and its neutron-capture progeny is controlled by ^{22}Ne, ^{25}Mg, and the neutron-capture progeny of ^{22}Ne and ^{25}Mg. Adopting currently quoted neutron-capture cross sections and choosing the initial ratio of ^{22}Ne to ^{56}Fe to be within a factor of 2 of the solar system value, it is shown that from three to six neutrons are captured by ^{56}Fe and its progeny for every fresh ^{56}Fe engulfed by the convective shell during a thermal pulse. The resultant distribution of heavy *s*-process elements resembles the solar system distribution.

Subject headings: abundances, stellar — convection — interiors, stellar — nucleosynthesis — stellar evolution

I. INTRODUCTION

In the preceding paper (Iben 1975) it is demonstrated that the reaction ^{22}Ne(α, n)^{25}Mg may serve as a major source of neutrons for transmitting ^{56}Fe into heavier neutron-rich elements on a slow time scale within the convective shell of a thermally pulsing star. If the abundance of the CNO progenitors of ^{22}Ne relative to the abundance of ^{56}Fe in the stellar envelope were the same as in the solar system, potentially 42 neutrons could be released in each pulse for every fresh ^{56}Fe seed nucleus. If all of these neutrons were captured by iron and its progeny, the resultant distribution of *s*-process elements would not at all resemble the solar system distribution, being *much* more heavily weighted toward Pb (see, e.g., Clayton 1968 and references therein). However, both ^{22}Ne and ^{25}Mg capture neutrons, as do their neutron-rich progeny. As a consequence, the light elements (^{22}Ne and ^{25}Mg and their progeny) filter out most of the neutrons, leaving a much smaller number for processing ^{56}Fe and its progeny. The resulting distribution of *s*-process elements heavier than iron may approach more closely the solar system distribution or deviate from it in the sense of an excessive underabundance of the heaviest neutron-rich elements.

A simple preliminary estimate of the extent of filtering is possible. If the mean neutron-capture cross section for the light elements is, say, 3–5 mb at 25–30 keV (290–350 million degrees) and if the mean neutron-capture cross section for elements heavier than ^{55}Mn is 15–20 mb at 25–30 keV, then, out of every 42 neutrons, the number that escape capture by the light elements is roughly $42 \times (15\text{–}20)/[42 \times (3\text{–}5) + 1 \times (15\text{–}20)] \sim 3.5\text{–}4.5$. In obtaining this estimate it has been assumed that ^{22}Ne is completely destroyed during a pulse, that the number ratio of fresh ^{22}Ne to fresh ^{56}Fe is 42, and that a mean cross section is obtained by weighting over the abundances actually prevailing during the neutron-active phase of the thermal pulse.

Ulrich (1973) argues that, in order to produce heavy *s*-process elements at abundances similar to those found in the solar system, the ratio of neutrons captured by ^{56}Fe and its progeny to the abundance of fresh ^{56}Fe brought in during each pulse must be about 3 or 4. It is amusing to note that such a ratio appears to follow naturally as a consequence of filtering by ^{22}Ne, ^{25}Mg, and the neutron capture progeny of these two elements if the ^{22}Ne(α, n)^{25}Mg reaction is the dominant source of neutrons. One is tempted to conclude that the solar system distribution of *s*-process elements demonstrates that the ^{22}Ne(α, n)^{25}Mg reaction is in fact the major source of neutrons for *s*-process nucleosynthesis in stars.

II. GROSS APPROXIMATIONS

A more quantitative estimate of the filtering action by light elements can be achieved. The treatment adopted here is patterned after that of Ulrich (1973) and therefore gives, in principle, a solution that will be approached asymptotically after many pulses.

Once all of the ^{14}N and ^{18}O has disappeared in the convective shell, the abundance of ^{22}Ne at any point obeys

$$\dot{n}_{22} = -n_{22}(\lambda + \langle\sigma_{22}v\rangle n)\,, \qquad (1)$$

where λn_{22} is the rate at which ^{22}Ne disappears via the (α, n) reaction, $\langle\sigma_{22}v\rangle n_{22}n$ is the rate at which ^{22}Ne disappears via neutron capture, n_{22} is the abundance of ^{22}Ne, n is the abundance of neutrons, and $\langle\sigma_{22}v\rangle$ is the product of velocity and the ^{22}Ne neutron-capture cross section averaged over a Maxwellian distribution of velocities.

The abundance of ^{25}Mg satisfies

$$\dot{n}_{25} = \lambda n_{22} + (\langle\sigma_{24}v\rangle n_{24} - \langle\sigma_{25}v\rangle n_{25})n\,, \qquad (2)$$

and the abundance of neutrons satisfies

$$\dot{n} = \lambda n_{22} - \left(\sum_i \langle\sigma_i v\rangle n_i\right)n\,. \qquad (3)$$

---

* Supported in part by the National Science Foundation (GP-35863).

In these equations n_{25} is the abundance of ^{25}Mg, n_{24} is the abundance of ^{24}Mg, n_i is the abundance of the ith type of nucleus that absorbs neutrons, and $\langle\sigma_i v\rangle$ is the thermal average of the product: velocity times neutron-capture cross section of the ith type of nucleus.

With the exception of a few elements that can be produced by (n, p) and (n, α) reactions on slightly heavier nuclei, most other nuclei between ^{23}Na and ^{55}Mn obey the equations

$$\dot{n}_i = (\langle\sigma_{i-1}v\rangle n_{i-1} - \langle\sigma_i v\rangle n_i)n\,. \tag{4}$$

The exceptions are discussed in Appendix A.

Since the lifetime of a neutron against capture is short compared with the time that elapses between successive neutron emissions, one may write, in good approximation,

$$n \approx \lambda n_{22} \Big/ \sum_i \langle\sigma_i v\rangle n_i\,. \tag{5}$$

For all constituents other than neutrons, the convective turnover time in the shell is short compared with the overall rate of change due to neutron capture. The abundances of these other constituents therefore change at nearly uniform rates throughout the shell.

An exact solution of equations (1)–(5) under conditions prevailing in a convective shell will not be attempted. Instead, approximations will be introduced that lead to a quicker and perhaps more revealing solution. One may define the sum

$$\bar{S} = \sum \bar{\sigma}_i \bar{n}_i\,, \tag{6}$$

where $\bar{n}_i$ is the mean abundance of the ith element in the convective shell during the neutron-active phase of the pulse and $\bar{\sigma}_i$ is the neutron-capture cross section appropriate to the mean temperature characterizing the narrow region near the base of the convective shell where neutron emission and capture are occurring at highest frequency. In first approximation,

$$\bar{\sigma}_i = \langle\sigma_i v\rangle / \langle v\rangle\,, \tag{7}$$

where averages are performed near the base of the convective shell. Assuming that the abundances of all elements obeying equations such as (4) do not vary by more than a factor of 2 during each pulse, one may approximate

$$\langle\sigma_i v\rangle \Big/ \sum_i \langle\sigma_i v\rangle n_i \sim \bar{\sigma}_i / \bar{S}\,. \tag{8}$$

On reinterpreting λ in all preceding equations as the mass and time weighted average of λ over the convective shell, equation (1) becomes directly integrable and the solution of the remaining equations is considerably simplified.

In equations such as (2) and (4) it is convenient to make the approximations

$$\int_B^A \langle\sigma_i v\rangle n_i n dt \approx \bar{n}_i \bar{\sigma}_i \phi\,, \tag{9}$$

where B and A refer, respectively, to before and after the neutron-active phase of a thermal pulse,

$$\phi = \frac{4}{3}\psi = \int_B^A \frac{\lambda n_{22}}{\bar{S}}\,dt$$
$$= -\int_B^A \frac{dn_{22}/\bar{S}}{1 + \bar{\sigma}_{22} n_{22}/\bar{S}} = \frac{1}{\bar{\sigma}_{22}} \ln \frac{1 + \bar{\sigma}_{22} {n_{22}}^B/\bar{S}}{1 + \bar{\sigma}_{22} {n_{22}}^A/\bar{S}}\,. \tag{10}$$

and

$$\bar{n}_i \approx ({n_i}^A + {n_i}^B)/2\,. \tag{11}$$

Approximate solutions of equation (4) are then

$${n_i}^A - {n_i}^B \approx (\bar{\sigma}_{i-1}\bar{n}_{i-1} - \bar{\sigma}_i \bar{n}_i)\phi\,. \tag{12}$$

The solution of equation (2) is approximately

$${n_{25}}^A - {n_{25}}^B \approx (\bar{\sigma}_{24}\bar{n}_{24} - \bar{\sigma}_{25}\bar{n}_{25} + \bar{S})\phi\,. \tag{13}$$

Because one portion of the equation for its abundance is integrable, ^{23}Na may be treated slightly differently. Writing

$$\dot{n}_{23} \approx \bar{\sigma}_{22} n_{22} \frac{\lambda n_{22}}{\bar{S}} - \bar{\sigma}_{23}\bar{n}_{23}\dot{\phi}\,, \tag{14}$$

one obtains

$${n_{23}}^A - {n_{23}}^B + \bar{\sigma}_{23}\bar{n}_{23}\phi \approx ({n_{22}}^B - {n_{22}}^A) - \bar{S}\phi\,. \tag{15}$$

For several of the light elements between ^{25}Mg and ^{55}Mn, neutron captures lead to proton and/or α-particle emission. Abundance details for the progeny of these elements are given in Appendix A.

Because its initial abundance may be large compared with the initial abundance of adjacent nuclei, ^{56}Fe deserves special treatment. Integrating

$$\dot{n}_{56} \approx (-\bar{\sigma}_{56} n_{56} + \bar{\sigma}_{55}\bar{n}_{55})\dot{\phi}\,, \tag{16}$$

one obtains

$$(\bar{\sigma}_{56}{n_{56}}^A - \bar{\sigma}_{55}\bar{n}_{55}) \approx (\bar{\sigma}_{56}{\bar{n}_{56}}^B - \bar{\sigma}_{55}\bar{n}_{55}) \exp(-\bar{\sigma}_{56}\phi)\,. \tag{17}$$

For ^{57}Fe an approximate solution is

$${n_{57}}^A - {n_{57}}^B \approx (\bar{\sigma}_{56}\bar{n}_{56} - \bar{\sigma}_{57}\bar{n}_{57})\phi\,, \tag{18}$$

where $\bar{n}_{56}$, the average of n_{56} suggested by equation (16), is given by

$$\bar{\sigma}_{56}\bar{n}_{56} \approx \bar{\sigma}_{55}\bar{n}_{55} + (\bar{\sigma}_{56}{n_{56}}^B - \bar{\sigma}_{55}\bar{n}_{55}) \frac{1 - \exp(-\bar{\sigma}_{56}\phi)}{\bar{\sigma}_{56}\phi}\,. \tag{19}$$

To make further progress, it is convenient to adopt a simplifying assumption introduced by Ulrich (1973) and to thereupon make use of the abundances of elements heavier than ^{56}Fe that Ulrich has estimated as a function of integrated neutron flux. Ulrich assumes that, prior to each thermal pulse, the matter between the hydrogen-helium discontinuity and the outer edge of the convective shell (at its maximum outward extent) during the previous pulse contains essentially only ^{56}Fe, ^{4}He, and other products of hydrogen burning. This assumption is a sensible one to make if the abundances of other elements produced in the convective shell are large compared with the abundances of these elements in the envelope. As will be demonstrated, the assumption is not a very good one for all elements in a Population I star. A proper treatment will be given in a subsequent communication. However, since the objective in this paper is to provide only rough estimates, it will be assumed hereinafter that, for all elements other than ^{22}Ne and ^{56}Fe,

$$n_i^B = r n_i^A\,, \tag{20}$$

where

$$r = 1 - h/d\,, \tag{21}$$

with d being the mass contained in the convective shell at maximum size and h being the mass processed through the hydrogen-burning shell during the interpulse phase. Clearly, the formalism is inappropriate when $h > d$.

For all elements heavier than ^{56}Fe one has from equation (12)

$$\bar{\sigma}_i \bar{n}_i = \bar{\sigma}_{i-1}\bar{n}_{i-1}(1 + \Lambda/\bar{\sigma}_i)^{-1}\,, \tag{22}$$

where

$$\Lambda = 2(1 - r)(1 + r)^{-1}\phi^{-1} \tag{23}$$

and

$$\bar{n}_i = n_i^A(1 + r)/2\,. \tag{24}$$

Equation (22) also connects most of the elements between ^{22}Ne and ^{55}Mn, with exceptions discussed in the Appendix.

Ulrich (1973) has calculated the sum

$$\sum_{i=56}^{209} \prod_{j=56}^{i} (1 + \Lambda/\bar{\sigma}_j)^{-1}$$

as a function of Λ, calling the result $N_n{}^0/N_{56}{}^0$. This means that

$$\sum_{i=56}^{209} \bar{\sigma}_i\bar{n}_i = \bar{\sigma}_{56}\bar{n}_{56}(1 + \Lambda/\bar{\sigma}_{56})N_n{}^0/N_{56}{}^0\,, \tag{25}$$

where $\bar{\sigma}_{56}\bar{n}_{56}$ follows from equation (19) when $\bar{n}_{55}$ is identified as $n_{55}{}^A(1 + r)/2$ and equation (17) is solved in conjunction with

$$n_{56}{}^B = r n_{56}{}^A + (1 - r)n_{56}(0) \tag{26}$$

to obtain $n_{56}{}^B$. The quantity $n_{56}(0)$ is the initial envelope abundance of ^{56}Fe.

Setting $\Delta n_{22} = n_{22}{}^B - n_{22}{}^A$, one may write

$$n_{22}{}^B = n_{22}(0) - r(1 - r)^{-1}\Delta n_{22} \tag{27}$$

and

$$n_{22}{}^A = n_{22}(0) - (1 - r)^{-1}\Delta n_{22}\,, \tag{28}$$

where $n_{22}(0)$ is the total abundance of CNO elements processed into ^{14}N by the hydrogen-burning shell and then processed into ^{22}Ne by helium burning in the convective shell.

With the further definitions

$$\sigma_s n_{56}(0) = \sum_{i=56}^{209} \bar{\sigma}_i\bar{n}_i\,, \tag{29}$$

$$\sigma_l 2\Delta n_{22} = (4/3)\sum_{i=23}^{55} \bar{\sigma}_i\bar{n}_i\,, \tag{30}$$

equation (10) may be rewritten as

$$\exp(\bar{\sigma}_{22}\phi) = 1 + \bar{\sigma}_{22}\Delta n_{22}/\bar{S}'\,, \tag{31}$$

where

$$\begin{aligned}\bar{S}' &= \bar{S} + n_{22}{}^A\bar{\sigma}_{22}\\ &= \bar{\sigma}_{22}(\bar{n}_{22} + n_{22}{}^A) + 1.5\sigma_l\Delta n_{22} + \sigma_s n_{56}(0)\,.\end{aligned} \tag{32}$$

III. SOLUTIONS

For any choice of r, Δn_{22}, $n_{22}(0)$, and $n_{56}(0)$, $\bar{S}'$ in equation (32) may be determined as a function of the parameter ϕ. The correct ϕ will be that one which satisfies equation (31). Inspection of the relevant neutron-capture cross sections (Allen, Gibbons, and Macklin 1971) suggests that $\sigma_s \sim 15$ mb, $\sigma_l \sim 3$–4 mb, and $\bar{\sigma}_{22} \ll \sigma_s$. Hence, for all values of Δn_{22} less than the maximum $[n_{22}(0)/2]$, $\sigma_{22}\Delta n_{22}\bar{S}' \ll 1$ and

$$\begin{aligned}\phi^{-1} \sim\ & \bar{\sigma}_{22}(\bar{n}_{22} + n_{22}{}^A)/\Delta n_{22}\\ & + 1.5\sigma_l + \sigma_s n_{56}(0)/\Delta n_{22}\,.\end{aligned} \tag{33}$$

If one supposes that $\Delta n_{22} \sim n_{22}(0)/2$ and chooses $n_{22}(0)/n_{56}(0) \sim 42$, as given by the Cameron (1973) abundance table, then

$$\phi^{-1} \rightarrow 0.5\bar{\sigma}_{22} + 1.5\bar{\sigma}_l + 0.7\ \text{mb} \tag{34}$$

or

$$\Lambda \rightarrow (1 - r)(1 + r)^{-1}(\bar{\sigma}_{22} + 3\bar{\sigma}_l + 1.4\ \text{mb})\,. \tag{35}$$

Thus, the "exposure" ϕ is determined primarily by the mean cross section for neutron capture on the light elements between ^{22}Ne and ^{55}Mn; and Λ, the parameter which characterizes the distribution of all of the *s*-process elements produced in the convective shell, is a function of only two quantities: (1) the mean neutron-capture cross section of the lighter elements and (2) the mass through which the hydrogen shell passes between pulses relative to the mass contained in the convective shell during a pulse.

In order to obtain the actual distribution, one needs a choice of r and an estimate of neutron-capture cross sections. The model of intermediate mass described in the preceding paper (Iben 1975) is characterized by $r \sim \frac{1}{2}$, and for the remainder of this paper it will be assumed that $r = \frac{1}{2}$.

Estimates of cross sections for the lighter elements at energies of 25–30 keV may be found in Allen *et al.*

1975ApJ...196..351C

TABLE 1

ABUNDANCES $n_{jA}/n_{22}(0)$ FOR VARIOUS CHOICES OF $2\Delta n_{22}/n_{22}(0)$

					$2\Delta n_{22}/n_{22}(0)$				
Element	Z	N	σ_j	Source	.2	.4	.6	.8	1.0
Ne^{22}	10	12	.05		0.80	0.60	0.40	0.20	0.0
Na^{23}	11	12	2.7	FCZ	6.51/-3	6.38/-3	5.31/-3	3.99/-3	2.53/-3
Mg^{24}	12	12	4	CSA	1.75/--3	1.98/-3	1.75/-3	1.35/-3	8.74/-4
Mg^{25}	12	13	3	MG	0.128	0.238	0.346	0.453	0.559
Mg^{26}	12	14	3	CSA	4.26/-2	9.34/-2	0.144	0.195	0.245
Al^{27}	13	14	4.6	AGM	1.21/-2	3.03/-2	4.91/-2	6.82/-2	8.73/-2
Si^{28}	14	14	3.8	AGM	5.65/-3	1.65/-2	2.82/-2	4.03/-2	5.26/-2
Si^{29}	14	15	10.4	AGM	1.31/-3	4.16/-3	7.34/-3	1.07/-2	1.40/-2
Si^{30}	14	16	1.9	AGM	1.79/-3	7.03/-3	1.35/-2	2.05/-2	2.77/-2
P^{31}	15	16	7	AGM	2.61/-4	1.15/-3	2.28/-3	3.54/-3	4.86/-3
S^{32}	16	16	3	AGM	2.03/-4	1.05/-3	2.22/-3	3.56/-3	4.98/-3
S^{33}	16	17	8	CSA	6.49/-6	3.40/-5	7.23/-5	1.16/-4	1.63/-4
			$\sigma_{n\alpha} = 80$						
S^{34}	16	18	3	CSA	5.77/-6	3.55/-5	8.02/-5	1.33/-4	1.90/-4
S^{36}	16	20	3	CSA	1.18/-6	9.23/-6	2.27/-5	3.95/-5	5.81/-5
Cl^{35}	17	18	13.5	AGM	8.88/-7	5.88/-6	1.36/-5	2.28/-5	3.29/-5
Cl^{36}	17	19	20	CSA	5.30/-8	3.53/-7	8.18/-7	1.38/-6	1.99/-6
			$\sigma_{np} = 200$						
Cl^{37}	17	20	3	AGM	5.10/-7	4.55/-6	1.17/-5	2.09/-5	3.13/-5
A^{38}	18	20	5	CSA	1.39/-7	1.41/-6	3.82/-6	7.00/-6	1.06/-5

(1971), in Couch, Schmeidekamp, and Arnett (1974), and in Fowler, Caughlin, and Zimmerman (1967). Those cross sections not found in these references have, for the initial attempt to estimate Λ, been chosen to be similar to cross sections of neighboring elements. All initial choices are given explicitly in column (4) of table 1 in units of millibarns. The capture cross section chosen for ^{22}Ne is slightly larger than is obtained by an extrapolation of the thermal (40^{-1} eV) cross section on the assumption that $\sigma \propto v^{-1}$.

The cross section for the $^{25}\text{Mg}(n, \gamma)^{26}\text{Mg}$ reaction is based on the work of Mughabghab and Garber (1974). These authors quote gamma and neutron widths in a cross section of Breit-Wigner form that fits the data for thermal neutron capture (at 40^{-1} eV) and the data for capture in the neighborhood of a resonance at 19.98 keV. They give $\Gamma_\gamma \sim 2.1$ eV and $\Gamma_n \approx 1.925(E/E_r)^{1/2}$ keV in a cross section of the form

$$\sigma_{25} = \pi \lambda\!\!\!^{-2} \frac{\Gamma_\gamma G \Gamma_n}{(E - E_r)^2 + \frac{1}{4}(\Gamma_n + \Gamma_\gamma)^2}, \qquad (36)$$

where the spin factor $G = (7/12)$ and $E_r = 19.98$ keV. E is the energy in the center of mass, and $\lambda\!\!\!^{-}$ is the de Broglie wavelength of the system.

The quantity $\langle \sigma_{25} v \rangle$ is integrable as it stands but is much more easily evaluated if one assumes $\Gamma_n \approx$ constant in the integrations. Then

$$\begin{aligned} \bar{\sigma}_{25} &\approx \langle \sigma_{25} v \rangle / \langle v \rangle \\ &\approx \pi^2(\hbar^2/\mu kT)(G\Gamma_\gamma/kT) \exp(-E_r/kT), \qquad (37) \end{aligned}$$

where $\hbar$ is Planck's constant, μ is the reduced mass of the system, and k is Boltzmann's constant. Inserting numbers, one obtains

$$\bar{\sigma}_{25} \sim (70 \text{ mb}/T_8^2) \exp(-2.32/T_8), \qquad (38)$$

where T_8 is the temperature in units of 10^8 ° K and $\bar{\sigma}_{25}$ is in millibarns.

For $T_8 = 1, 2, 3,$ and 4, expression (38) yields $\bar{\sigma}_{25} = 7.0, 5.5, 3.6, 2.5$ mb. Since the mean temperature in the convective shell must be slightly in excess of 300 million degrees for ^{22}Ne to burn rapidly enough to act as a major neutron source, a value $\bar{\sigma}_{25} \sim 3$–4 would seem appropriate.

Having settled on an initial set of cross sections (col. [4] of table 1) and making two additional choices—$n_{22}(0)/n_{56}(0) = 42$ and $(\bar{n}_{22} + n_{22}{}^A) \approx [2n_{22}(0) - 3.5\Delta n_{22}]$—equations (29)–(32) have been solved in conjunction

TABLE 1—*Continued*

Element	Z	N	σ_i	Source	$2\Delta n_{22}/n_{22}(0)$ .2	.4	.6	.8	1.0
A^{39}	18	21	5		4.54/-8	5.60/-7	1.63/-6	3.10/-6	4.83/-6
A^{40}	18	22	5		2.65/-8	3.60/-7	1.09/-6	2.11/-6	3.33/-6
K^{39}	19	20	16	AGM	4.19/-9	2.97/-8	6.70/-8	1.10/-7	1.55/-7
K^{40}	19	21	30	CSA	4.68/-9	5.35/-8	1.52/-7	2.86/-7	4.43/-7
			$\sigma_{np} = 30$						
K^{41}	19	22	22	AGM	9.75/-9	1.28/-7	3.81/-7	7.36/-7	1.16/-6
Ca^{42}	20	22	14	CSA	1.07/-8	1.51/-7	4.61/-7	9.01/-7	1.43/-6
Ca^{43}	20	23	30	CSA	4.17/-9	6.09/-8	1.89/-7	3.71/-7	5.91/-7
Ca^{44}	20	24	10	CSA	7.81/-9	1.25/-7	3.98/-7	7.97/-7	1.28/-6
Sc^{47}	22	24	44	AGM	1.56/-9	2.56/-8	8.26/-8	1.66/-7	2.68/-7
Ti^{46}	22	24	34	AGM	1.72/-9	2.92/-8	9.52/-8	1.93/-7	3.11/-7
Ti^{47}	22	25	92	AGM	5.96/-10	1.03/-8	3.36/-8	6.82/-8	1.11/-7
Ti^{48}	22	26	12	AGM	3.05/-9	5.67/-8	1.91/-7	3.93/-7	6.42/-7
Ti^{49}	22	27	20	AGM	1.41/-9	2.76/-8	9.47/-8	1.97/-7	3.23/-7
Ti^{50}	22	28	2	AGM	3.52/-9	8.31/-8	3.05/-7	6.58/-7	1.11/-6
V^{51}	23	28	25	AGM	2.27/-10	5.61/-9	2.09/-8	4.55/-8	7.68/-8
Cr^{52}	24	28	3.8	AGM	3.78/-10	1.66/-8	6.53/-8	1.46/-7	2.52/-7
Cr^{53}	24	29	40	AGM	4.78/-11	1.41/-9	5.61/-9	1.26/-8	2.18/-8
Cr^{54}	24	30	23	AGM	6.59/-11	2.04/-9	8.25/-9	1.87/-8	3.25/-8
Mn^{55}	25	30	50	AGM	2.71/-11	8.60/-10	3.50/-9	7.98/-9	1.39/-8
Fe^{56}	26	30	13.5	AGM	0.126	7.77/-2	6.24/-2	5.48/-2	5.03/-2

with all other equations that influence the terms that enter equations (29)–(32) for several values of Δn_{22}. In columns (6)–(10) of table 1 are shown the resultant abundances n_i^A. Abundances of all elements other than ^{56}Fe are normalized to $n_{22}(0)$. The abundance for ^{56}Fe is normalized to $n_{56}(0)$.

Comparison with solar system abundances (Cameron 1973) reveals that the convective shell of a thermally pulsing star is not a major site for the production of the lighter elements between ^{32}S and ^{55}Mn. These elements are produced at abundances far below those found in the solar system. On the other hand, elements between ^{22}Ne and ^{31}P are made in abundances comparable to those found in the solar system.

It is clear from these results that, if one is to obtain a distribution of the light elements between ^{32}S and ^{55}Mn in the convective shell that is correct to even first order, one must include in the analysis the initial envelope abundances of these elements, just as has been done here for ^{56}Fe and ^{22}Ne and has been done in another context for some of the light elements by Peters, Fowler, and Clayton (1972) and by Couch *et al.* (1974). On the other hand, if one is concerned only with the production of *s*-process elements heavier than ^{56}Fe, only the contribution of these elements to the value of σ_l is of importance and this contribution is completely dominated by the elements between ^{22}Ne and ^{31}P that are freshly produced in large abundance within the convective shell as progeny of ^{22}Ne.

The sensitivity of element distributions to several critical cross sections is illustrated in table 2. Cross sections for columns (2)–(5) are the same as in table 1 except for σ_{22} (0.25 mb for cols. [2] and [3], 0.5 mb for cols. [4] and [5]). The Woosley (1974) cross sections in column (6) are based on theoretical estimates of gamma widths, Γ_γ, and on the assumption of a high energy level density. Cross sections in column (9) are a hybrid of values based on laboratory measurements (where available) and values based on theory (Woosley).

The manner whereby model characteristics such as σ_l, σ_s, and Λ depend on several critical parameters is shown in table 3. The quantity $2\sigma_s\phi$ in this table is the number of neutrons captured by ^{56}Fe and by elements heavier than ^{56}Fe relative to the number of new ^{56}Fe nuclei added to the convective shell during each pulse. The quantity σ_{ls} is the mean neutron-capture cross

TABLE 2

ABUNDANCES $n_j^A/n_{22}(0)$ FOR DIFFERENT CHOICES OF CAPTURE CROSS SECTIONS

	σ_{22} = 0.25		σ_{22} = 0.50		Woosley Cross Sections			Hybrid Choice		
Element	Δ = .4	Δ = .8	Δ = .4	Δ = .8	$\bar{\sigma}_j$	Δ = .4	Δ = .8	$\bar{\sigma}_j$	Δ = .4	Δ = .8
Ne^{22}	.60	.20	.60	0.20	0.6	.60	.20	0.6	0.6	0.2
Na^{23}	2.84/-2	1.92/-2	5.03/-2	3.68/-2	2.7	5.62/-2	4.33/-2	2.7	6.05/-2	4.70/-2
Mg^{24}	8.10/-3	6.33/-3	1.28/-2	1.17/-2	1.8	7.52/-3	8.20/-3	1.8	1.95/-2	2.16/-2
Mg^{25}	0.235	0.452	0.231	0.451	4.7	0.199	0.366	3	0.219	0.421
Mg^{26}	8.31/-2	0.188	7.25/-2	0.180	1.4	0.108	0.286	1.4	8.28/-2	0.231
Al^{27}	2.47/-2	6.41/-2	1.95/-2	5.95/-2	4.3	1.31/-2	4.48/-2	4.6	1.04/-2	3.74/-2
Si^{28}	1.22/-2	3.69/-2	8.63/-3	3.30/-2	2.4	5.81/-3	2.74/-2	3.8	4.62/-3	2.19/-2
Si^{29}	2.93/-3	9.59/-3	1.93/-3	8.42/-3	5.1	1.13/-3	6.78/-3	10.4	1.04/-3	5.75/-3
Si^{30}	4.31/-3	1.76/-2	2.45/-3	1.46/-2	1.7	6.65/-4	5.91/-3	1.9	1.32/-3	1.09/-2
P^{31}	6.56/-4	2.98/-3	3.43/-4	2.41/-3	7.2	7.81/-5	8.50/-4	7	1.85/-4	1.88/-3
S^{32}	5.41/-4	2.90/-3	2.50/-4	2.25/-3	4.4	4.83/-5	6.78/-4	3	1.36/-4	1.86/-3
S^{33}	1.74/-5	9.42/-5	7.95/-6	7.31/-5	8.1	9.26/-7	1.32/-5	8.1	1.78/-6	2.47/-5
					$\sigma_{n\alpha}$ = 214			$\sigma_{n\alpha}$ = 214		
S^{34}	1.64/-5	1.05/-4	6.64/-6	7.81/-5	2.9	7.38/-7	1.42/-5	2.9	1.53/-6	2.87/-5
S^{36}	3.65/-6	2.96/-5	1.24/-6	2.09/-5	0.31	1.52/-7	5.34/-6	0.31	4.00/-7	1.37/-5
Cl^{35}	2.59/-6	1.77/-5	9.92/-7	1.30/-5	10.4	1.21/-7	2.74/-6	13.5	2.21/-7	4.75/-6
Cl^{36}	1.55/-7	1.07/-6	5.91/-8	7.83/-7	10.7	6.00/-9	1.37/-7	10.7	1.37/-8	2.98/-7
					σ_{np} = 192			σ_{np} = 192		
Cl^{37}	1.66/-6	1.53/-5	5.11/-7	1.04/-5	2.8	1.11/-8	4.21/-7	3	2.84/-8	1.05/-6
A^{38}	4.74/-7	4.99/-6	1.32/-7	3.30/-6	2.6	3.15/-9	1.63/-7	2.6	9.30/-9	4.74/-7

section for elements between ^{25}Mg and ^{55}Mn. Unless otherwise noted, $\bar{\sigma}_{25} = 3$ mb and $\bar{\sigma}_{22} = 0.05$ mb.

Ulrich (1973) states that a value of Λ between 4 and 5 leads to a distribution of *s*-process elements heavier than ^{56}Fe that closely resembles the solar system distribution of these elements. It is clear from table 3 that, for a wide latitude of input parameters, values of Λ between 4 and 6 characterize the neutron flux produced by ^{22}Ne and its absorbing progeny in a convective shell. It is quite natural to infer that most of the heavier *s*-process elements found in the solar system and in the remainder of the Universe were made in the convective shells of thermally pulsing stars wherein ^{22}Ne acts as the primary neutron source.

There are, of course, many uncertainties in the preceding arguments apart from those associated with the simplistic model chosen to approximate a very complex situation. As Couch *et al.* (1974) have pointed out, two crucial cross sections—one for the production of neutrons and the other for the destruction of ^{25}Mg at 30 keV—are highly uncertain. Fortunately, the uncertainty in the ^{22}Ne(α, n)^{25}Mg rate does not introduce as much uncertainty in the abundances produced in a convective shell as it does in the abundance produced in the center of a massive star, this latter situation being the one addressed by Couch *et al.* If the cross-section factor is increased, significant neutron production will begin in an earlier pulse; if it is decreased, significant neutron production will be delayed to a later pulse. In all events, significant neutron production will set in at some point, the ultimate result being essentially independent of the precise value of the cross-section factor.

Since the value of $\bar{\sigma}_{25}$ is an important factor in determining Λ, the uncertainty in $\bar{\sigma}_{25}$ could be more worrisome. In Appendix B it is shown that, for large $\bar{\sigma}_{25}$, one may approximate σ_l roughly by $(\sigma_{25}\sigma_{ls})^{1/2}$, demonstrating that the uncertainty in Λ due to an uncertainty in $\bar{\sigma}_{25}$ is considerably less than the uncertainty in $\bar{\sigma}_{25}$. This comforting result is also apparent from inspection of table 3. Perhaps the greatest uncertainty of all lies in the cross section for neutron capture on ^{22}Ne. The fact that Woosley's (1974) calculated cross sections agree in most cases to within a factor of 2 with available experimental cross sections at 25–30 keV suggests that a simple $\sigma \propto v^{-1}$ extra-

TABLE 2—*Continued*

	σ_{22} = 0.25		σ_{22} = 0.50		Woosley Cross Sections			Hybrid Choice		
Element	Δ = .4	Δ = .8	Δ = .4	Δ = .8	$\bar{\sigma}_j$	Δ = .4	Δ = .8	$\bar{\sigma}_j$	Δ = .4	Δ = .8
A^{39}	1.66/-7	2.13/-6	4.02/-8	1.34/-6	7.4	4.21/-10	2.99/-8	7.4	1.34/-9	9.44/-8
A^{40}	1.00/-7	1.42/-6	2.27/-8	8.71/-7	3.5	3.02/-10	2.69/-8	3.5	1.09/-9	9.75/-8
K^{39}	1.28/-8	8.75/-8	4.40/-9	6.55/-8	11	9.36/-11	3.41/-9	16	1.46/-10	3.54/-9
K^{40}	1.66/-8	1.98/-7	4.27/-9	1.27/-7	21.7	4.84/-11	2.91/-9	21.7	1.81/-10	1.12/-8
					σ_{np} = 24.2			σ_{np} = 24.2		
K^{41}	3.64/-8	4.97/-7	8.45/-9	3.08/-7	15.3	9.34/-11	7.89/-9	22	2.71/-10	2.24/-8
Ca^{42}	4.11/-8	6.01/-7	9.04/-9	3.67/-7	10.2	8.18/-11	8.15/-9	10.2	3.57/-10	3.46/-8
Ca^{43}	1.62/-8	2.46/-7	3.46/-9	1.49/-7	30	2.24/-11	2.40/-9	30	9.95/-11	1.04/-8
Ca^{44}	3.14/-8	5.20/-7	6.26/-9	3.08/-7	6.9	4.75/-11	6.25/-9	6.9	2.22/-10	2.84/-8
Sc^{47}	6.34/-9	1.08/-9	1.24/-9	6.35/-8	54.9	5.27/-12	7.24/-10	44	3.03/-11	4.07/-9
Ti^{46}	7.07/-9	1.24/-7	1.34/-9	7.26/-8	16.5	1.22/-11	1.88/-9	34	3.29/-11	4.71/-9
Ti^{47}	2.47/-9	4.39/-8	4.63/-10	2.56/-8	47.7	3.66/-12	5.94/-10	92	1.13/-11	1.67/-9
Ti^{48}	1.30/-8	2.49/-7	2.29/-9	1.43/-7	11.8	9.15/-12	1.72/-9	12	5.62/-11	9.55/-9
Ti^{49}	6.11/-9	1.24/-7	1.04/-9	6.99/-8	20.8	3.85/-12	8.00/-10	20	2.54/-11	4.76/-9
Ti^{50}	1.63/-8	3.98/-7	2.42/-9	2.15/-7	2.8	7.96/-12	2.24/-9	2	5.95/-11	1.57/-8
V^{51}	1.07/-9	2.73/-8	1.53/-10	1.46/-8	21.2	7.83/-13	2.43/-10	25	3.77/-12	1.08/-9
Cr^{52}	2.88/-9	8.52/-8	3.69/-10	4.40/-8	10.4	9.40/-13	3.43/-10	3.8	9.10/-12	3.44/-9
Cr^{53}	2.41/-10	7.32/-9	3.01/-11	3.76/-9	21.1	3.45/-13	1.39/-10	40	7.43/-13	2.97/-10
Cr^{54}	3.38/-10	1.08/-8	4.07/-11	5.46/-9	6.5	5.29/-13	2.63/-10	23	1.01/-12	4.39/-10
Mn^{55}	1.40/-10	4.57/-9	1.66/-11	2.31/-9	30.3	9.15/-14	4.90/-11	50	4.09/-13	1.87/-10
Fe^{56}	0.107	6.24/-2	0.146	7.24/-2		0.169	7.68/-2	13.5	0.145	5.76/-2

$\Delta = 2\Delta n_{22}/n_{22}(0)$

polation from 40^{-1} eV to 30 keV is inappropriate and that $\bar{\sigma}_{22}$ is larger than the 0.05 in mb obtained by such an extrapolation. An experimental estimate of $\bar{\sigma}_{22}$ in the 10–50 keV range would be most welcome.

IV. CONCLUDING REMARKS

A most attractive feature of the mechanism for producing *s*-process elements herein proposed is its near uniqueness as well as its universality. It will occur in all stars in the mass range (1.5–8) $M_\odot$. Such stars all develop nearly identical electron-degenerate carbon-oxygen cores capped by helium- and hydrogen-burning shells. If pulse amplitude is in one-to-one correspondence with the mass in the carbon-oxygen core, then neutron production via the ^{22}Ne(α, n)^{25}Mg reaction will be the same in all stars of a given core mass, regardless of the amount of mass in the envelope.

However, the amount of material that is brought out to the surface following each pulse may well depend upon envelope mass and upon surface composition to the extent that these attributes influence the depth to which the base of the convective envelope can reach following each pulse. Of course, even if the maximum depth of penetration were independent of envelope mass and composition, the degree of enrichment of surface abundances of *s*-process elements would increase strongly with decreasing envelope mass. This is because the total amount of contaminants added after each pulse would be the same in stars of varying envelope mass but the amount of diluting material would be less in stars with less massive envelopes. It may be anticipated that, at least among stars of intermediate mass at any given luminosity and for any given initial composition, the lightest stars should show the greatest enrichment of heavy *s*-process elements (as well as the greatest enrichment of ^{12}C).

It is a pleasure to thank Peter Axel, Charlie Barnes, Richard Couch, Richard Macklin, and Stan Woosley for informative discussions on neutron-capture cross

TABLE 3

AVERAGE CROSS SECTIONS AS A FUNCTION OF INPUT PARAMETERS

Cross Section	$\frac{n_{22}(0)}{n_{56}(0)}$	$\frac{2\Delta n_{22}}{n_{22}(0)}$	σ_ℓ	σ_s	$\sigma_{\ell s}$	Ψ	Λ	N_n^0/N_{56}^0	$2\sigma_s\phi$
$\sigma_{25} = 3$	42	.2	3.16	14.30	3.52	8.33/-2	6.00	2.52	3.18
	42	.4	3.23	14.91	3.60	1.08/-1	4.65	3.45	4.28
	42	.6	3.26	15.50	3.63	1.19/-1	4.20	4.00	4.92
	42	.8	3.28	15.84	3.65	1.26/-1	3.97	4.35	5.32
	42	1.0	3.29	16.13	3.66	1.30/-1	3.84	4.60	5.61
	21	.4	3.18	14.36	3.54	8.78/-2	5.69	2.67	3.36
	21	.8	3.24	15.09	3.61	1.11/-1	4.51	3.61	4.46
	84	.4	3.26	15.62	3.64	1.21/-1	4.12	4.12	5.06
	84	.8	3.29	16.12	3.66	1.30/-1	3.84	4.60	5.60
$\sigma_{25} = 2$	42	.4	2.56	15.73	3.65	1.24/-1	4.04	4.24	5.20
	42	.8	2.63	17.21	3.70	1.48/-1	3.38	5.63	6.78
$\sigma_{25} = 4$	42	.4	3.80	14.46	3.57	9.66/-2	5.18	2.98	3.72
	42	.8	3.81	15.13	3.61	1.12/-1	4.48	3.64	4.50
$\sigma_{25} = 6$	42	.4	4.74	14.26	3.51	8.19/-2	6.10	2.46	3.12
	42	.8	4.70	14.43	3.56	9.37/-2	5.34	2.88	3.60
$\sigma_{25} = 12$	42	.4	6.85	13.78	3.42	6.12/-2	8.17	1.75	2.25
	42	.8	6.67	13.87	3.46	6.86/-2	7.29	1.99	2.54
$\sigma_{22} = 0.25$	42	.4	3.17	14.40	3.55	9.12/-2	5.48	2.79	3.50
	42	.8	3.26	15.49	3.63	1.19/-1	4.20	4.00	4.91
$\sigma_{22} = 0.50$	42	.4	3.12	14.07	3.49	7.61/-2	6.57	2.25	2.85
	42	.8	3.23	15.11	3.61	1.11/-1	4.49	3.62	4.48
Woosley Cross Sections	42	.4	3.36	13.88	1.78	6.89/-2	7.26	2.00	2.55
	42	.8	3.23	14.94	1.92	1.08/-1	4.62	3.48	4.31
Hybrid Cross Sections	42	.4	2.63	14.08	1.96	7.63/-2	6.55	2.26	2.87
	42	.8	2.64	15.71	2.20	1.23/-1	4.06	4.21	5.16

sections and to thank Dave Carlson for checking the equations presented in the text. I am particularly grateful to Don Clayton for advising me to separate the crude treatment of possibly transitory significance presented here from the more secure results presented in the preceding paper. Finally, thanks to George Wallerstein and the referee of the previous paper for pointing out the necessity in the present context of considering neutron captures by elements lighter than ^{56}Fe.

APPENDIX A

ABUNDANCE RELATIONSHIPS AFFECTED BY (n, p) AND (n, α) REACTIONS

When (n, γ) and (n, α) reactions are taken into account, several relationships between element abundances are somewhat more complex than those given in the text. In this paper, only the reactions ^{33}S$(n, \alpha)^{30}$Si, ^{36}Cl$(n, p)^{36}$S, and ^{40}K(n, p) have been included in addition to the (n, γ) reactions already discussed in the text. A further complication is introduced by the fact that ^{39}Ar β-decays into ^{39}K with a half-life of 269 yr, long compared with the duration of a pulse, but short compared with the duration of the interpulse phase. The ^{39}Ar that is built up during each pulse disappears between pulses. For simplicity, only the relationships which result when $r = \frac{1}{2}$ will be given. They are

$$\bar{\sigma}_{30}n_{30}{}^{A} = \bar{\sigma}_{29}n_{29}{}^{A}(1 + \Lambda/\sigma_{30})^{-1}\left[1 - \frac{\bar{\sigma}_{33}{}^{n\alpha}}{\bar{\sigma}_{33}}\prod_{i=30}^{33}(1 + \Lambda/\bar{\sigma}_i)^{-1}\right]^{-1}, \tag{A1}$$

$$\bar{\sigma}_{39,\mathrm{Ar}}n_{39,\mathrm{Ar}}{}^{A} = \bar{\sigma}_{38}n_{38}{}^{A}\tfrac{3}{2}(1 + 3\Lambda/\bar{\sigma}_{39,\mathrm{Ar}})^{-1} \tag{A2}$$

$$n_{39,\mathrm{K}}{}^{A} = n_{39,\mathrm{Ar}}{}^{A}\epsilon/(2 - \epsilon)\,, \tag{A3}$$

where

$$\epsilon = \exp(-\bar{\sigma}_{39,\mathrm{Kr}}4\psi/3)\,, \tag{A4}$$

$$\bar{\sigma}_{36,\mathrm{S}}n_{36,\mathrm{S}}{}^{A} = \bar{\sigma}_{36,\mathrm{Cl}}n_{36,\mathrm{Cl}}{}^{A}(1 + \Lambda/\bar{\sigma}_{36,\mathrm{S}})^{-1}\,, \tag{A5}$$

$$\bar{\sigma}_{37}n_{37}{}^{A} = (\bar{\sigma}_{36,\mathrm{S}}n_{36,\mathrm{S}}{}^{A} + \bar{\sigma}_{36,\mathrm{Cl}}{}^{n\alpha}n_{36,\mathrm{Cl}}{}^{A})(1 + \Lambda/\bar{\sigma}_{37})^{-1}\,, \tag{A6}$$

$$\bar{\sigma}_{40,\mathrm{Ar}}n_{40,\mathrm{Ar}}{}^{A} = (\bar{\sigma}_{40,\mathrm{K}}{}^{np}n_{40,\mathrm{K}}{}^{A} + \tfrac{2}{3}\bar{\sigma}_{39,\mathrm{Ar}}n_{39,\mathrm{Ar}}{}^{A})(1 + \Lambda/\bar{\sigma}_{40,\mathrm{Ar}})^{-1}\,, \tag{A7}$$

$$\bar{\sigma}_{40,\mathrm{K}}n_{40,\mathrm{K}}{}^{A} = \bar{\sigma}_{39,\mathrm{K}}(n_{39,\mathrm{K}}{}^{A} + \tfrac{1}{3}n_{39,\mathrm{Ar}}{}^{A})(1 + \Lambda/\bar{\sigma}_{39,\mathrm{K}})^{-1}\,, \tag{A8}$$

and

$$\bar{\sigma}_{41}n_{41}{}^{A} = (\bar{\sigma}_{40,\mathrm{K}}{}^{n\gamma}n_{40,\mathrm{K}}{}^{A} + \bar{\sigma}_{40,\mathrm{Ar}}{}^{A}n_{40,\mathrm{Ar}}{}^{A})(1 + \Lambda/\bar{\sigma}_{41})^{-1}\,. \tag{A9}$$

In these relationships, a subscript letter Ar, Cl, K, or S refers, respectively, to the element argon, chlorine, potassium, or sulfur. A superscript $n\gamma$, np, or $n\alpha$ refers to capture of a neutron with emission of a photon, a proton, or an α-particle. Total cross sections are represented by lowercase sigmas without superscripts.

APPENDIX B

AN ALTERNATE SOLUTION WHEN σ_{22} IS SMALL

If the ^{22}Ne$(n, \gamma)^{23}$Ne reaction rate is assumed to be very small, a simpler approximate solution of the equations presented in the text may be constructed. On setting

$$n \approx -\dot{n}_{22}\Big/\sum\langle\sigma_i v\rangle n_i\,, \tag{B1}$$

equation (2) in the text for the abundance of ^{25}Mg becomes

$$\dot{n}_{25} \approx -\dot{n}_{22}\left(1 - \frac{\langle\sigma_{25}v\rangle n_{25}}{\sum\langle\sigma_i v\rangle n_i}\right). \tag{B2}$$

This may be approximated by

$$\dot{n}_{25} \cong -\dot{n}_{22}\left(1 - \frac{\bar{\sigma}_{25}n_{25}}{\sum\bar{\sigma}_i n_i}\right). \tag{B3}$$

Defining $\bar{\sigma}_{sl}$ and n_{sl} by

$$n_{sl}\sigma_{sl} = \sum_{i=26}^{55}\bar{\sigma}_i n_i \tag{B4}$$

and

$$n_{sl} = n_{22}(0) - n_{22} - n_{25}\,, \tag{B5}$$

and assuming $\sigma_{sl} \approx$ constant, equation (B2) has the solution

$$\tfrac{1}{2}\sigma_{ls}(n_{22} + n_{25})^2 - [\sigma_s n_{56}(0) + \sigma_{ls}n_{22}(0)](n_{22} + n_{25}) - \tfrac{1}{2}\sigma_{25}n_{25}{}^2 = \text{constant.} \tag{B6}$$

Choosing the parameter r defined in the text as $\frac{1}{2}$, so that $n_{25}{}^B = n_{25}{}^A/2$, $n_{ls}{}^B = n_{ls}{}^A/2$, and $2\Delta n_{22} = n_{25}{}^A + n_{ls}{}^A$, equation (B6) transforms into

$$(n_{25}{}^A)^2(\sigma_{ls} - \sigma_{25}) - \tfrac{4}{3}[\sigma_s n_{56}(0) + 3\sigma_{ls}\Delta n_{22}]n_{25}{}^A + \tfrac{8}{3}[\sigma_s n_{56}(0) + \tfrac{3}{2}\sigma_{ls}\Delta n_{22}]\Delta n_{22} = 0 \tag{B7}$$

or

$$n_{25}{}^{A} = \frac{2}{3}\,\frac{\sigma_s n_{56}(0) + 3\sigma_{ls}\Delta n_{22}}{\sigma_{ls} - \sigma_{25}} \left[\!\!\left[1 - \left\{ 1 - 6(\sigma_{ls} - \sigma_{25})\Delta n_{22}\, \frac{\sigma_s n_{56}(0) + 3\sigma_{ls}\Delta n_{22}/2}{[\sigma_s n_{56}(0) + 3\sigma_{ls}\Delta n_{22}]^2} \right\}^{1/2} \right]\!\!\right] . \tag{B8}$$

Expanding the square root in equation (B8) gives

$$n_{25}{}^{A} \sim 2\Delta n_{22}\, \frac{1.5\sigma_{ls}\Delta n_{22} + \sigma_s n_{56}(0)}{3\sigma_{ls}\Delta n_{22} + \sigma_s n_{56}(0)} , \tag{B9}$$

when $\sigma_{25} \sim \sigma_{ls}$ and/or $\sigma_{ls}\Delta n_{22} \ll \sigma_s n_{56}(0)$.

When $\sigma_{ls}\Delta n_{22} \gg \sigma_s n_{56}(0)$, another expansion gives

$$n_{25}{}^{A} \sim 2\Delta n_{22}\left(\frac{\sigma_{ls}}{\sigma_{25}}\right)^{1/2} \left[1 + \left(\frac{\sigma_{ls}}{\sigma_{25}}\right)^{1/2}\right]^{-1} \left[1 + \frac{\sigma_s n_{56}(0)}{3\sigma_{ls}\Delta n_{22}}\right] . \tag{B10}$$

The value of the parameter Λ is approximately

$$\Lambda \sim \frac{1.5\sigma_{ls}\Delta n_{22}(\sigma_{25} + \sigma_{ls}) + \sigma_s n_{56}(0)\sigma_{25}}{3\sigma_{ls}\Delta n_{22} + \sigma_s n_{56}(0)} + \frac{4}{3}\,\frac{\sigma_s n_{56}(0)}{2\Delta n_{22}} \tag{B11}$$

when $\sigma_{25} \sim \sigma_{ls}$ and/or $\sigma_{ls}\Delta n_{22} \ll \sigma_s n_{56}(0)$. When $\sigma_{ls}\Delta n_{22} \gg \sigma_s n_{56}(0)$, and $\sigma_{25} \not\simeq \sigma_{ls}$,

$$\Lambda \sim (\sigma_{ls}\sigma_{25})^{1/2} + \tfrac{4}{3}\sigma_s n_{56}(0)/2\Delta n_{22} . \tag{B12}$$

REFERENCES

Allen, B. J., Gibbons, J. H., and Macklin, R. L. 1971, *Advances in Nuclear Physics*, ed. M. Baranger and E. Vogt (New York: Plenum), **4**, 205.

Cameron, A. G. W. 1973, in *Explosive Nucleosynthesis*, ed. D. N. Schramm and W. D. Arnett (Austin: University of Texas Press), p. 3.

Clayton, D. D. 1968, *Principles of Stellar Evolution and Nucleosynthesis* (New York: McGraw-Hill).

Couch, R. G., Schmeidekamp, A. B., and Arnett, W. D. 1974, *Ap. J.*, **190**, 95.

Fowler, W. A., Caughlin, G. R., and Zimmerman, B. A. 1967, *Ann. Rev. Astr. and Ap.*, **5**, 525.

Iben, I. Jr. 1975, *Ap. J.*, **196**, 525.

Mughabghab, S. F. and Garber, D. I. 1974, Brookhaven National Laboratory Report 325, 3d ed., Vol. **1**.

Peters, J. G., Fowler, W. A., and Clayton, D. D. 1972, *Ap. J.*, **173**, 637.

Ulrich, R. K. 1973, in *Explosive Nucleosynthesis*, ed. D. N. Schramm and W. D. Arnett (Austin: University of Texas Press), p. 139.

Woosley, S. 1974, private communication.

Icko Iben, Jr.: Department of Astronomy, University of Illinois, Urbana, IL 61801

1975ApJ...196..351C

THE ASTROPHYSICAL JOURNAL, **196**: 559–563, 1975 March 1

ENVELOPE EJECTION TO FORM PLANETARY NEBULAE

PETER E. STRY
Joint Institute for Laboratory Astrophysics, University of Colorado
and National Bureau of Standards

Received 1974 July 26

ABSTRACT

Previous calculations at $L/L_{\rm crit} \approx 0.5$ are extended to higher luminosities to determine whether partial, small-scale ejections of mass continue to be the general result. The 0.2 $M_\odot$ envelope of a 1.2 $M_\odot$ star was perturbed by raising the interior boundary condition luminosity 10 percent to $L \approx L_{\rm crit}$. After a brief period of oscillation the entire envelope was ejected. The numerical methods include time dependent convection (not necessarily efficient) and a simplified version of a spherically extended atmosphere.

Subject headings: interiors, stellar — late-type stars — planetary nebulae

I. INTRODUCTION

At first glance it would appear that modeling the ejection of an envelope from a red supergiant star should present no problems. Generally the total energy of the envelope—thermal energy including energy of ionization minus gravitational binding energy—is positive. An adiabatic expansion would eject the envelope and yield just about the correct final velocity at infinity (Paczynski and Ziołkowski 1968). Furthermore, red supergiant stars on the asymptotic branch lie close to $L_{\rm crit}$, the critical luminosity given by the conventional formula

$$L_{\rm crit} = \frac{4\pi cGM_c}{\kappa_{\rm es}}, \qquad (1)$$

where $\kappa_{\rm es}$ is the electron scattering opacity, M_c is the mass interior to the envelope, and all other undefined symbols, here and below, have their usual meanings. $L_{\rm crit}$ is the luminosity at which the gradient of radiation pressure alone just balances the inward acceleration of gravity. As a star evolves to high luminosities approaching $L_{\rm crit}$, static models cease to exist (Rose and Smith 1972). These facts seem to imply a straightforward sequence of events. When the star reaches some fraction of $L_{\rm crit}$, stability breaks down, the positive total energy is converted into kinetic energy, and the envelope is ejected.

For realistic models, however, this process fails to occur. The problem lies in the presence of convection in the ionization zones which contribute most of the net positive energy to the envelope. When the envelope is expanding, the ionization zones cool and the gas begins to recombine. For an adiabatic process the ionization energy would be used to build up the pressure gradients and accelerate the envelope outward. The presence of convection changes all this. The energy of ionization released into the envelope is rapidly carried to the surface of the star, radiated away, and lost. Thus the additional outward acceleration is greatly reduced. Another way of describing this situation, considering the energy balance of the envelope as a whole, is that the surface luminosity rises so steeply with outward velocity that the total energy of the envelope is quickly depleted and ejection is rendered energetically impossible (Keeley 1970).

Thus most fully nonlinear dynamical calculations which have included convection have not demonstrated envelope ejection. If $L_{\rm crit}$ is defined as in equation (1), the most luminous of these calculations were carried out at $L/L_{\rm crit} \approx 0.5$: $L/L_{\rm crit} \approx 0.45$ (Sparks and Kutter 1973, 1974), $L/L_{\rm crit} \approx 0.48$ (Wood 1973), $L/L_{\rm crit} \approx 0.51$ (Keeley 1970), and $L/L_{\rm crit} \approx 0.57$ (Smith and Rose 1972). Of these only the first model, $L/L_{\rm crit} \approx 0.45$, ejected its entire envelope. The others at higher values of $L/L_{\rm crit}$ collapsed back inward and/or executed relaxation oscillations. A small amount of mass was lost from the atmosphere of the $L/L_{\rm crit} \approx 0.48$ and 0.57 models due to the presence of shock waves. This led Smith and Rose to postulate that the formation of planetary nebulae is a repetitive process of small scale mass loss rather than a one-step ejection.

The present work was undertaken to find out whether relaxation oscillations and the failure to achieve one-step ejection, which seems to be the general case at $L/L_{\rm crit} \approx 0.5$, continue to be the case for even higher values of $L/L_{\rm crit}$ or whether a point is finally reached at which the behavior of the luminosity can no longer prevent the ejection of the envelope.

II. METHODS

a) Spherically Extended Atmospheres

A combination of two circumstances makes the customary plane-parallel atmosphere a poor outer boundary condition for red supergiant stars. Of course, the atmospheres really are relatively thick, but this would not be of much significance for the interior structure except that the outer boundary for convection occurs at a very small optical depth, $\tau \approx 1$. The structure of a convective region is largely determined by the physical conditions at its outer edge (Cox and Giuli 1968*a*). These outer boundary conditions in turn

1975ApJ...196..351C

depend on those at the photosphere through terms of order

$$(T_e/T)^q\,,$$

where $q = 4 + \partial \ln x/\partial \ln \rho - \partial \ln T \geqslant 4$. The quantity T_e is the effective temperature, and κ is the opacity (Cox and Giuli 1968*b*). These terms become small compared with 1 for even modest inward increases in temperature T. However, if the outer boundary for convection occurs at small optical depth, $\tau \approx 1$ and $T \approx T_e$, obviously no neglect of the atmospheric boundary conditions is possible. The effects of the photosphere are not washed out, and the whole convective region, which in red supergiant stars contains most of the mass of the envelope, feels the effect of any errors at the surface.

A simple formula was devised semiempirically to take into account the spherical dilution of the radiative flux in the atmosphere:

$$T^4 = \frac{L}{8\pi\sigma R^2}\left(\frac{1}{\beta}\frac{R^2}{r^2} + 3\int_R^r \frac{R^2}{r^2}\,d\tau\right), \qquad (2)$$

where R is the outer radius of the model, taken at any sufficiently low value of τ, and β is a boundary parameter given below. The second term in the parentheses arises directly from the integration of the usual spherical diffusion formula

$$L = \frac{-64\pi\sigma r^2}{3\kappa\rho}\frac{\partial}{\partial r}(T^4)\,.$$

The first term is an ad hoc addition designed to take into account the nondiffusive outward streaming of the radiative flux in spherical geometry. It was motivated by anticipating the final solution and solving the transfer equation by discrete ordinates with one of the ordinates pointing directly outward. The boundary parameter β can be given to sufficient accuracy by simple interpolation between the diffusive and spherical streaming limits:

$$\beta = \frac{1/\sqrt{3} + \alpha}{1 + \alpha} \qquad \alpha = \frac{1}{\kappa\rho R}\,. \qquad (3)$$

Here α is a dimensionless parameter, the ratio of the photon mean free path to the radius of curvative, evaluated at $r = R$.

Of course, this sort of ad hoc formula can be justified only by comparison with exact numerical results. Equations (2) and (3) were compared with a series of extended gray atmospheres calculated by Hummer and Rybicki (1971). An example of this comparison is given in figure 1 for the case of a fairly extended atmosphere, $\alpha = 10$. In general, equations (2) and (3) did at least as well as the more conventional formulae for the less extended atmospheres and far better for the really extended ones in providing a good boundary condition at $\tau \approx 1$.

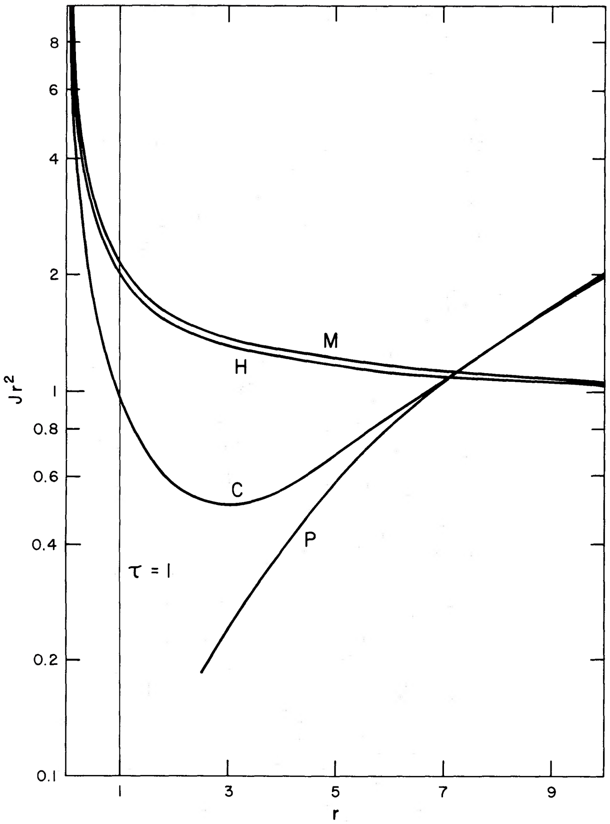

FIG. 1.—A comparison of three simple atmospheric formulae with the exact numerical solution from Hummer and Rybicki (1971) for the case $\kappa\rho = 1/r^2$ and $r_{\max} = 10$. The product Jr^2 in units of $L/(4\pi)^2$ is plotted versus radius for the cases: *P*, the plane-parallel formula; *C*, the diffusion approximation, $J = L(4\pi)^{-2}[1 + 3\int (R^2/r^2)d\tau]$; *M*, the method adopted in the text (eq. [2]); and *H*, the exact numerical solution.

b) *Time-dependent Convection*

Convection was handled by the usual local mixing-length equations which allowed for the possibility of inefficient convection. The ratio of mixing length to pressure scale height was always held at 1. Time dependence was handled by a method similar to that of Arnett (1969). The convective luminosity is written as

$$L_c = Gv\,, \qquad (4)$$

where v is convective velocity, and G is everything else in the convective luminosity formula (assumed to vary instantaneously). The time dependence of the convective velocity is written

$$\frac{dv}{dt} = \frac{1}{\tau}(v_i - v)\,, \qquad (5)$$

where τ is convective turnover time and v_i is instantaneous (equilibrium) convective velocity.

c) *Other Input*

The rest of the computational method was routine. The dynamical equations themselves were taken from Fraley (1968). Opacities were taken from the Los Alamos tables of A. N. Cox (Cox and Stewart 1969). The Massevitch II mix with $Z = 0.02$ was chosen

1975ApJ...196..351C

since it roughly corresponds to old Population I and the disk population, and opacities are given down to 1500° K. Water vapor opacity was included roughly by adding to these values the separate contribution of the water vapor taken from Auman (1967) for a turbulent velocity of 8 km s^{-1}. The thermodynamics included all ionized states of hydrogen and helium, radiation pressure, and the molecules H_2, OH, CO, and H_2O. The last three were unimportant and were calculated only to get the water vapor abundance for the opacity. All thermodynamic quantities were tabulated on a temperature-density grid, and interpolation was carried out with a two-dimensional local cubic spline.

III. RESULTS

a) *Initial Model*

The envelope to be perturbed was the most luminous of a series of "optimum" models, 0.2 $M_\odot$ envelopes of 1.2 $M_\odot$ red supergiant stars. Its luminosity was $\log (L/L_\odot) = 4.55$ ($L \approx 0.9\, L_{\rm crit}$) and effective temperature, $\log T_e = 3.49$. The run of some physical quantities through the envelope is shown in figure 2. Especially notable is the drop by five orders of magnitude in r^3P, proportional to the boundary term in the virial theorem. Despite the fact that convection carried most of the luminosity in the convective region, the local value of the ratio of the outward acceleration due to radiation pressure to the inward acceleration of gravity was greater than 1,

$$\frac{g(\text{rad})}{g(\text{grav})} = \frac{L(\text{rad})}{4\pi c G M(r)} \gtrsim 1 \, .$$

So the gas pressure (and thus the density) had to decrease drastically inward there to compensate for the net excess outward acceleration.

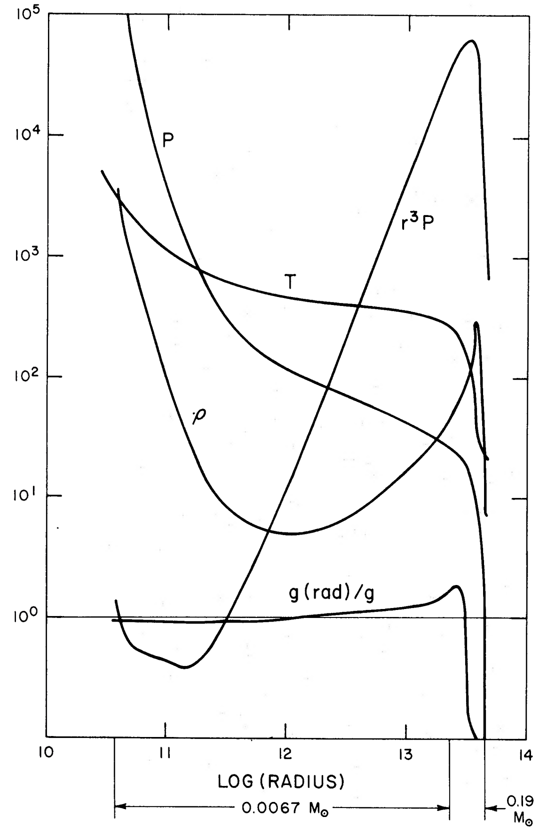

FIG. 2.—A static model envelope near the critical luminosity: $\text{Log}\, L/L_\odot = 4.55$, $\text{Log}\, T_e = 3.49$, $M_c = 1.0\, M_\odot$, and $M_{\rm env} = 0.2\, M_\odot$. The curves are labeled: *P*, the pressure in units of 10^2 dyn cm^{-2}; *T*, the temperature in units of 100° K; ρ, the density in units of 10^{-11} g cm^{-3}; the product r^3P in units of 10^{29} ergs; and $g(\text{rad})/g$, the nondimensional ratio of the outward acceleration due to radiation pressure to the inward acceleration of gravity.

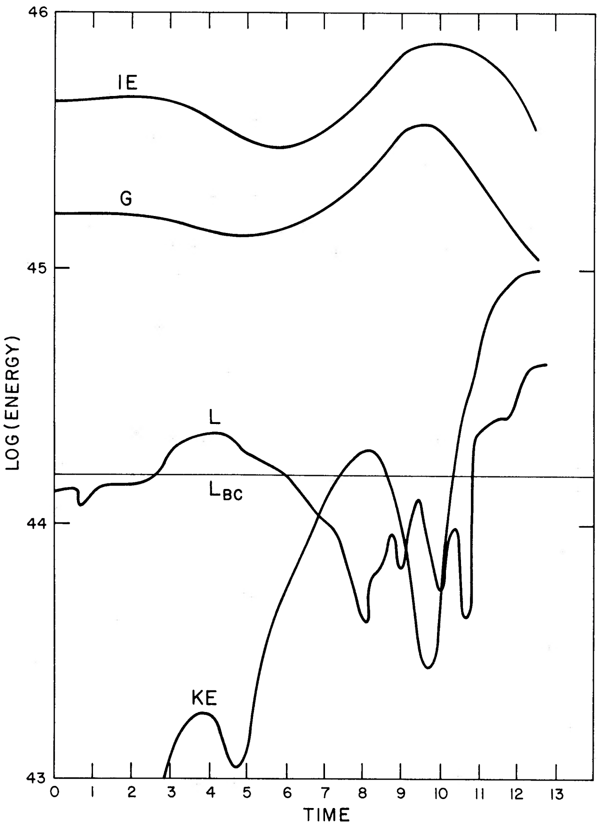

FIG. 3.—The time dependence of some energy parameters of the perturbed envelope. The logarithm of the quantities are plotted versus time in units of 10^7 seconds. IE is the internal energy (including ionization energy), G is the gravitational binding energy, and KE is the kinetic energy—all in units of ergs. *L* and L_{BC} are the logs of the surface luminosity and the luminosity inner boundary condition where the luminosities are expressed in units of 10^{-6} ergs s^{-1}.

This envelope was not calculated as part of an evolutionary series, but it lies quite close to true evolutionary models. For example, its luminosity is 20 percent above the formula given by Paczynski (1971):

$$L/L_\odot = 5.9 \times 10^4\, (M_c/M_\odot - 0.52)\, . \qquad (6)$$

b) *Dynamics*

This static model was perturbed by instantaneously increasing $L_{\rm BC}$, the boundary-condition luminosity at

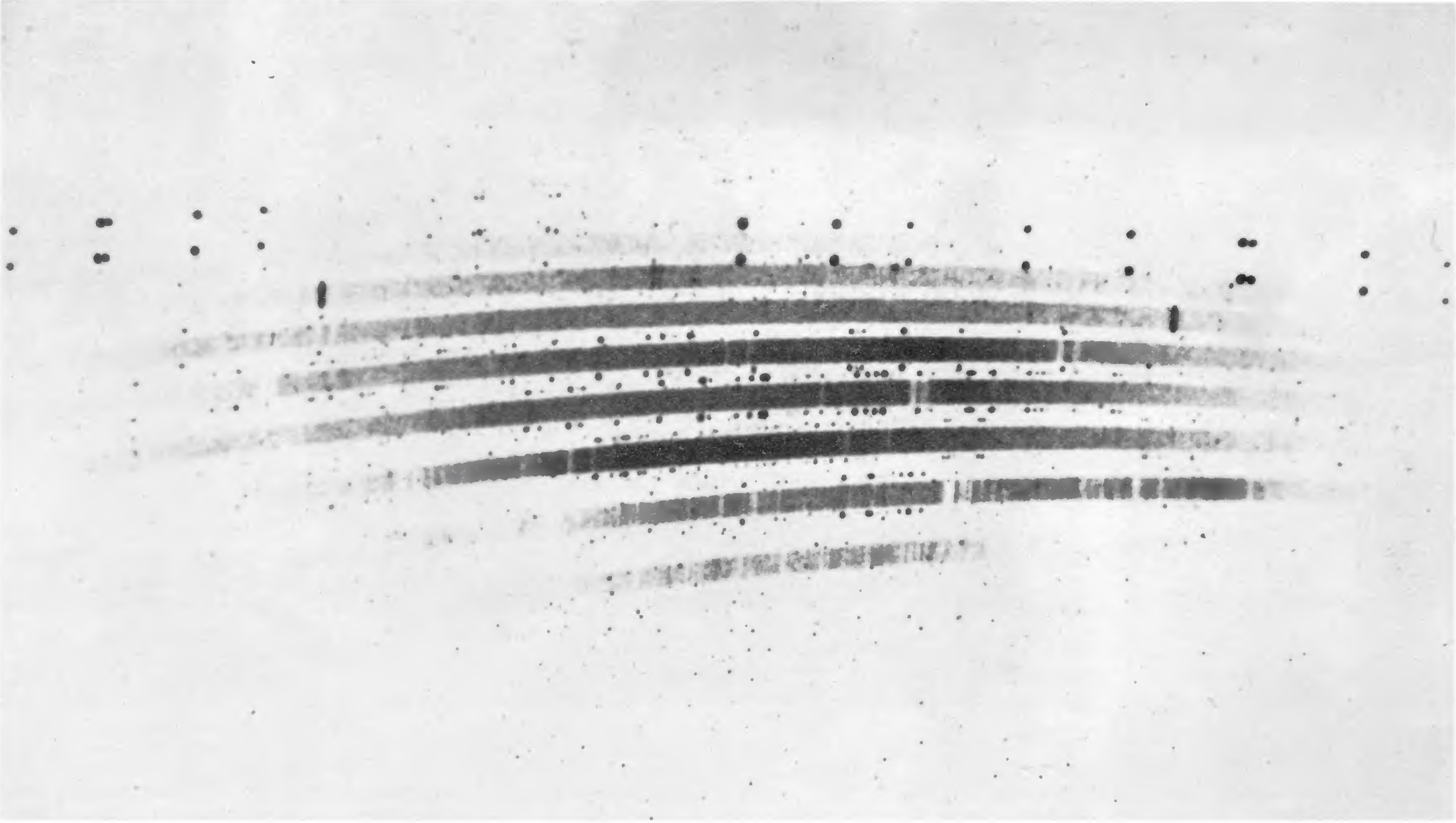

FIG. 2.—A reproduction of spectrogram SI 868 of 1331+170. The strong emission lines in the 9th and 11th orders are due to C IV λ1549 and Lα, respectively, at $z = 2.081$. The C IV absorption doublet at $z = 1.7754$ appears in the 10th order. The strong nightsky emission in the 7th and 8th orders is O I λ5577, and the nightsky Na I D lines are seen clearly resolved in the 7th order.

CARSWELL *et al.* (*see* page 353)